E.L. Ivchenko

OPTICAL SPECTROSCOPY OF SEMICONDUCTOR NANOSTRUCTURES

SPIN Springer's internal project number, if known

– Monograph –

August 8, 2004

Springer
Berlin Heidelberg New York
Hong Kong London
Milan Paris Tokyo

To Alla and Konstantin

Preface

What is the way to the abode of light?
And where does darkness reside?
Can you take them to their places?
Do you know the paths to their dwellings?
Job **38***: 19,20*

The present book is an attempt to create an impression of the contemporary optical spectroscopy of semiconductor nanostructures. It reviews new trends and notable progress attained in the field at the beginning of the third millennium. Nearly a decade ago G.E. Pikus and I published the book *Superlattices and Other Heterostructures: Symmetry and Optical Phenomena*. It had been written at the time of rapid transformation of research activities in semiconductor physics from bulk materials to systems of low dimensionality. At present nanophysics has become an established area which continues to accelerate and provides a fundamental base for tremendous technological developments. In order to keep pace, I decided to write a completely new book on optics of semiconductor nanostructures.

The new book reflects the success achieved during the recent decade in various optical studies of semiconductor nanostructures. Now the one- and zero-dimensional structures, quantum wires and quantum dots, are presented on an equal footing, alongside of superlattices and two-dimensional systems, heterojunctions and quantum wells. New concepts and phenomena included into consideration are exciton polaritons in resonant Bragg structures and photonic crystals, the strong Rabi splitting in quantum microcavities, trions, micro-photoluminescence of localized excitons in quantum wells, zero-dimensional excitons in quantum dots, giant magneto-optical effects in semimagnetic nanostructures, interface-induced lateral optical anisotropy, quantum-confined Pockels effect, chirality effects in carbon nanotubes, polariton-polariton scattering in the microcavities, etc. Moreover, in connection with the increasing interest in spintronics, special attention is paid to spin-related concepts and spin-dependent phenomena, including the spin splitting of electron and hole subbands, fine structure of excitonic levels, optical orientation of free-carrier spins and exciton angular momenta under inter- and intraband photoexcitation, sensitivity of the Zeeman spin splitting to the content, size and shape of a nanostructure, spin relaxation mechanisms, spin quantum beats, spin dynamics of exciton polaritons in the microcavities, circular photogalvanic and spin-galvanic effects in quantum wells. The organization of the book consisting of eight chapters is presented in Sect. 1.4.

Naturally, the present treatment was inspired by the book *Symmetry and Strained-Induced Effects in Semiconductors* by G.L. Bir and G.E. Pikus as

well as by my previous book with G.E. Pikus. For me, these three books are aligned in a kind of trilogy. Firstly, this is so because I feel greatly priviledged to belong to the physical school founded by my teacher G.E. Pikus who, together with A.G. Aronov and G.L. Bir, after introducing me to the world of theoretical physics taught, guided and supported me. Secondly, because, in each of the books, both the phenomenological and the microscopical description of physical phenomena is performed with emphasis on the symmetry analysis and the method of invariants, and the power of symmetry considerations is demonstrated.

I gratefully acknowledge that I learned and understood much of what follows due to my close research cooperation with M.M. Glazov, L.E. Golub, S.V. Goupalov, A.V. Kavokin, A.Yu. Kaminskii, A.A. Kiselev, A.I. Nesvizhskii, M.O. Nestoklon, S.A Tarasenko and M.M. Voronov, having grown up within the same school of theoretical physics; they represent the younger generations of physicists. Who knows, maybe some of them will write a book on sophisticated "nano-opto-bio-electronic" systems of the future. Then the trilogy would convert into a tetralogy.

Special thanks goes to my coauthors of the short textbook *Optical Properties of Semiconductor Nanostructures* by L.E. Vorobjev, E.L. Ivchenko, D.A. Firsov and V.A. Shalygin, published a few years ago in Russian. Perhaps, without that encouraging experience I would have never made the decision to write this monograph.

St. Petersburg *E.L. Ivchenko*
February 2004

Contents

1 Kingdom of Nanostructures

Let him lose himself in wonders as amazing in their littleness as the others in their vastness.
Of these two Infinites of science, that of greatness is the most palpable...
But the infinitely little is the least obvious. Philosophers have much oftener claimed to have reached it, and it is here they have all stumbled.

Blaise Pascal: Pensées

Due to continued progress in nanotechnology, novel semiconductor structures are fabricated with subnanometer accuracy and precisely controlled the electronic and optical properties. This progress in nanoscale engineering, as well as an improved understanding of the physical phenomena at the nanometer scale, have contributed to the rapid development of low-dimensional physics of semiconductors. At present a certain system of concepts and terms is accepted in this field of solid state physics. First of all the following vocabulary of semiconductor nanoscience has been developed: *Quantum Well* (QW), QW structure, *Single* and *Double* QWs, *Multiple* QWs (MQWs), *Superlattice* (SL), *Quantum Wire* (QWR) and *Quantum Well Wire* (QWW), *Quantum Dot* (QD) or *Quantum Box*, *Nanocrystal*, *Antidot*, *Quantum Microcavity*, *Photonic Crystals*, *Porous Semiconductor Material*, *Nanoclaster*, *Nanotube* and, particularly, *Carbon Nanotube*, *Type-I* and *Type-II* Heterostructures, *δ-Doped Structure*, *Strained Structure*, *Nanocontacts*, ... The nomenclature of novel quantum states in nanostructures includes *Quantum-Confined* states of free charge carriers and excitons, *Subbands* and *Minibands*, *Folded Acoustic Phonons*, *Confined Optical Phonons*, *Interface Phonon Modes*, *Low-Dimensional Magnetic Polarons*, *Composite Fermions*, *Edge States* in the Quantum Hall Effect.

In this chapter we briefly discuss the typical nanostructures progressing in the order from Two-Dimensional (2D) to One-Dimensional (1D) and Zero-Dimensional (0D) systems. Size-quantization and modification of energy spectra of quasi-particles in nanostructures are considered in Chap. 2.

1.1 Multilayered Heterostructures: Quantum Wells and Superlattices

The *Quantum Well* (QW) is a system in which the electron motion is restricted in one direction, thus producing the quantum confinement. In other words, the energy spectrum in one of the quantum numbers changes from continuous to discrete. For quantum confinement to be observable, the size

of a well must be less than the electron mean-free-pass length. This requirement imposes constraints on the well's geometric size, the sample quality and temperature.

The simplest 2D object on which the quantum confinement effects were revealed and studied are silicon-bases Metal-Oxide-Semiconductor (MOS) structures with a triangular confining potential formed at the semiconductor boundary and single GaAs/$Al_{1-x}Ga_xAs$ heterojunctions where a confining potential is created in the GaAs layer at the heterostructure boundary. It is on these structures that the quantum Hall effect, an unexpected and remarkable phenomenon occurring in a 2D electron gas, was discovered. However, in the following we will mainly concentrate on multilayered structures without built-in electric fields.

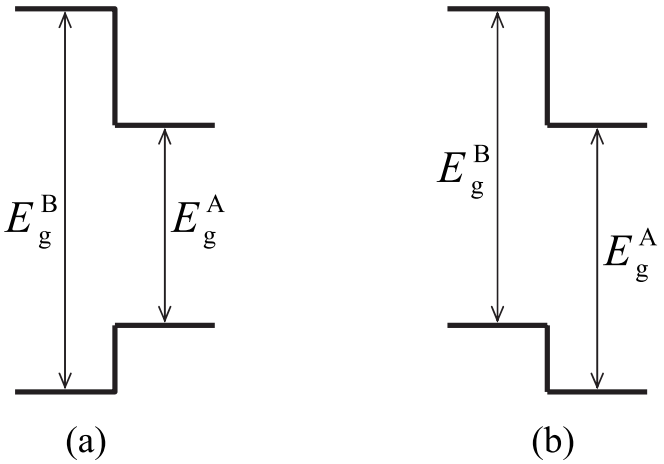

Fig. 1.1. Band diagrams of single type-I (**a**) and type-II (**b**) heterojunctions.

We start with a single heterojunction between two compositional semiconductors A and B, as illustrated in Fig. 1.1. In the figure, the higher and lower broken lines show the coordinate dependence of the conduction-band bottom and the valence-band top in the direction of the principal axis z, or the growth direction. One or both constituent materials can be alloy semiconductors, for instance, ternary solid solution $Al_{1-x}Ga_xAs$ or $Cd_{1-x}Mn_xTe$. Different examples of A/B heteropairs are GaAs/$Al_{1-x}Ga_xAs$, $In_{1-x}Al_xAs/Ga_{1-y}Al_yAs$, InAs/AlSb, $Ga_{1-x}In_xAs$/InP, CdTe/$Cd_{1-x}Mn_xTe$, $Zn_{1-x}Cd_xSe/ZnS_ySe_{1-x}$, ZnSe/BeTe, ZnSe/GaAs, $Si_{1-x}Ge_x$/Si and so forth, where the subscripts x, y or $1-x, 1-y$ show the fraction of atoms of particular kind at sites of the crystal lattice or one of its sublattice. By definition, in *type-I* heteropairs the band gap of one material, the material A in Fig. 1.1a, lies inside the band gap of another material. In this case the potential wells for the electrons and holes

are located in the same layer, e.g., GaAs layer in the GaAs/$Al_{1-x}Ga_xAs$ heterostructures with $x < 0.4$. The potential-barrier heights coincide with the conduction- and valence-band offsets, $\Delta E_c = E_c^{\rm B} - E_c^{\rm A}$ and $\Delta E_v = E_v^{\rm A} - E_v^{\rm B}$. The sum $\Delta E_c + \Delta E_v$ equals the difference ΔE_g between the band gaps $E_g^{\rm B}$ and $E_g^{\rm A}$. In the technologically important GaAs/$Al_{1-x}Ga_xAs$ heterosystem, the ratio $\Delta E_c/\Delta E_g$ is about 0.6.

In *type-II* structures the conduction-band bottom is lower in one layer, the layer A in Fig. 1.1b, whereas the valence-band top is higher in the neighboring layer B. It is clear that in type-II multilayered heterostructures, like GaAs/$Al_{1-x}Ga_xAs$ with $x > 0.4$, InAs/AlSb or ZnSe/BeTe, the electrons and holes are confined within different layers. A special case of type-II behavior is a heterostructure, e.g. InAs/GaSb, where the top $E_v^{\rm A}$ of the valence band in layer A lies above the bottom of the conduction band, $E_c^{\rm B}$. Heteropairs with one of the materials being a gapless semiconductor (e.g. HgTe/CdTe) are referred to as a *type-III* heterostructure.

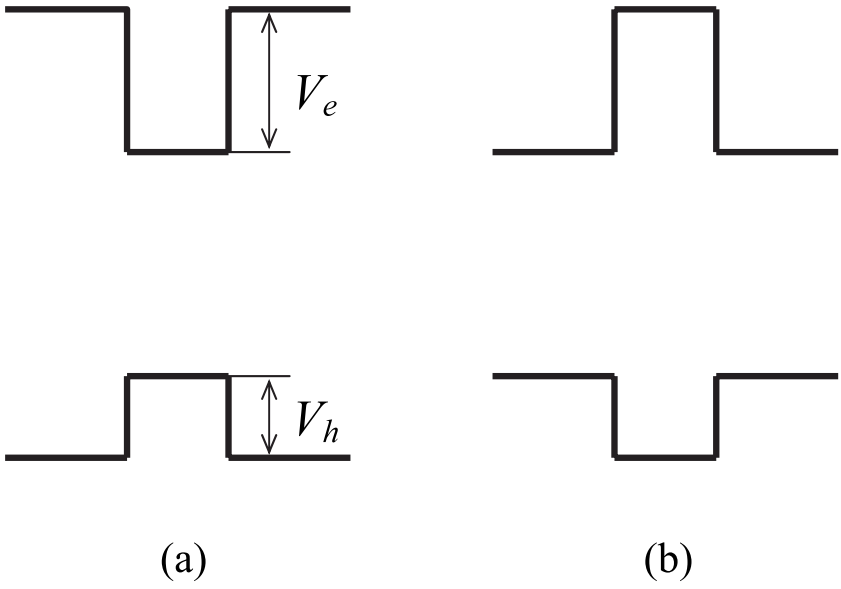

Fig. 1.2. Band diagrams of single QW (**a**) and single barrier (**b**) structures. $V_{e,h}$ are, respectively, the conduction- and valence-band offsets, or barrier heights.

A type-I double heterojunction B/A/B represents a *single QW structure* if $E_g^{\rm A} < E_g^{\rm B}$, see Fig. 1.2a, and a *single barrier structure* if $E_g^{\rm A} > E_g^{\rm B}$, Fig. 1.2b. In the former case the inner layer A forms a potential well size-quantizing the electron and hole states. In the latter, the layer A prevents free carriers from free exchange between the left- and right-hand-side layers B. It is clear

that a type-II double heterojunction is a single QW structure for one sort of carriers, say, for electrons, and, at the same time, a single barrier structure for charge carriers of the opposite sign. The structure with the confining potential shown in Fig. 1.2a is a *rectangular* QW. By varying properly the composition along the growth direction, one can produce wells of another shape, e.g., *parabolic*, *triangular*, etc.

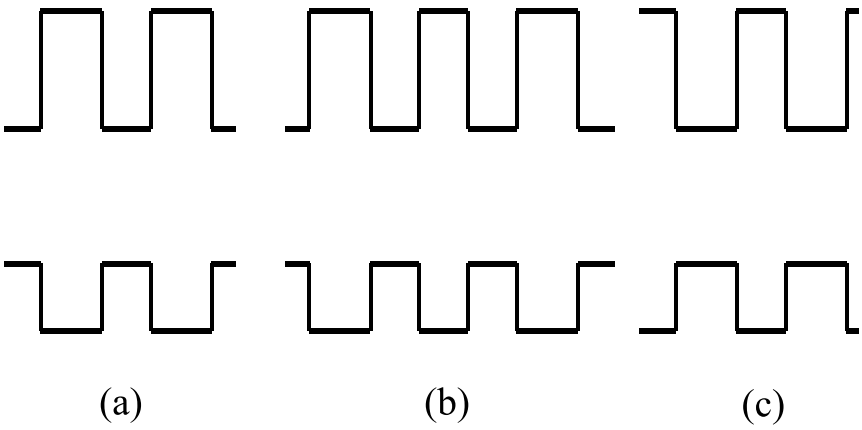

Fig. 1.3. Band diagrams of double-barrier (**a**), triple-barrier (**b**) and double-QW (**c**) structures.

A natural extension of a single barrier structure is *double-* and *triple-barrier* structures illustrated in Figs. 1.3a and b. Similarly, the concept of the single QW can be extended to *double QWs* (Fig. 1.3c), *triple QWs* and structures containing a set of QWs (Fig. 1.4). A periodic system of QWs separated by barriers thick enough to make them impenetrable for charge carriers is called *Multiple Quantum Wells* (MQWs). As regards electronic properties of MQWs, each of QWs is isolated from others. However, the electronic excitations within individual QWs can be coupled by electromagnetic fields and the presence of many wells affects noticeably optical characteristics of the structure. As the barriers get thinner, carrier tunnelling from one well to another becomes possible and, as a result, the quantum-confined states, or *subband* states, of an isolated well transform into *miniband* states. In that way the concept of MQWs transmutes into the concept of *SuperLattice* (SL). The miniband formation becomes actual when the SL period $d = a + b$ is smaller than the mean-free-path length, or phase-coherence length, in the growth direction. This length can be dependent on the sort of carriers, particularly, due to difference in the electron and hole effective masses. Therefore, the same periodic QW structure can be a SL for electrons which have, as a rule, a smaller effective mass and MQWs, or *thick-barrier SL*, for heavy holes. In this case the holes can also travel along the growth axis. However this motion

has no a coherent character and can be described as a series of incoherent tunnelling hoppings between neighboring wells. As the barrier thickness continues to decrease, the minibands corresponding to particular subbands of a single QW begin to overlap. Such *UltraThin SLs*, e.g. $(GaAs)_n(AlAs)_m$, with the layer thicknesses being usually not in excess of three-four monomolecular layers ($n, m = 2 \div 4$), behave as an anisotropic bulk crystal whose properties, however, differ substantially from those of the original materials. Strictly speaking, the definition of a SL presupposes that the layer thicknesses a and b must exceed the crystal-lattice constant in order to allow one to apply the effective mass approximation, or the envelope function method, for the description of electronic states. Nevertheless, it is instructive to include the ultrathin SLs, and even the compound $(GaAs)_1(AlAs)_1 = GaAlAs_2$, into the field of vision in the low-dimensional physics as the limiting case of a SL with $d \to 0$.

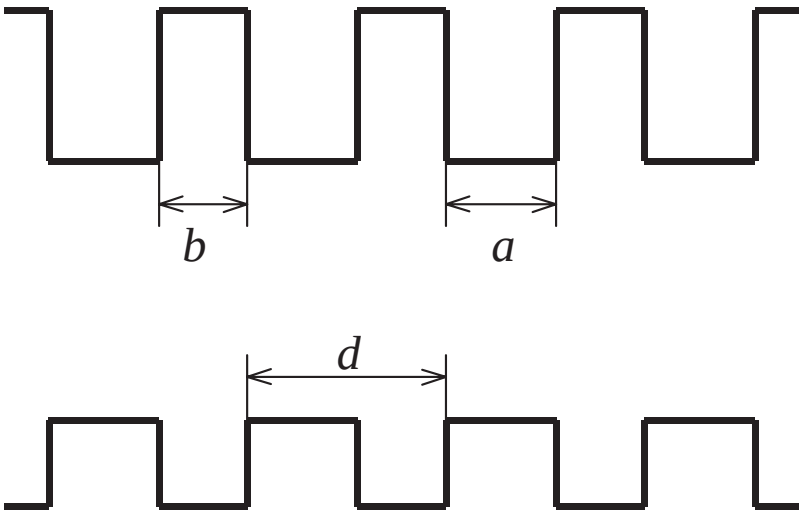

Fig. 1.4. Band diagram of a periodic structure consisting of the alternating well and barrier layers with the thicknesses a and b, respectively. It is called a multiple QW structure, if the barriers are thick, or a SL, if the barriers are thin.

Similarly to the above classification of heterostructures by the band alignment schemes, each SL belongs to one of three types, labelled *type-I*, *II* and *III*. The SLs consisting of alternating layers of different materials are called *compositional*. QWs and SLs were initially produced by choosing heteropairs with practically equal lattice constants a_0, for example, GaAs/AlGaAs pair. The structures with the lattice mismatch $\Delta a_0/a_0$ less or equal ≤ 0.01 are called *unstrained*, or *lattice matched*. Progress in growth technology has made it possible to obtain dislocation-free structures out of materials with notice-

ably different lattice constant. In this case at least one of the layers, A or B, must be thin enough, and the crystal lattices match because of internal stresses which result in a compression of one of the adjacent layers and a tension of the other. The QWs and SLs with $\Delta a_0/a_0 \geq 0.01$ are called *strained*. In *spin SLs* one or both layers A and B contain magnetic impurities or ions, e.g., CdTe/CdMnTe. Besides the compositional SLs produced by varying the composition, one can prepare SLs by modulation doping with a donor and an acceptor impurity (*modulation doped* SLs). The examples are a *n*-GaAs/*p*-GaAs SL and a *nipi* SL formed by *n*- and *p*-doped layers with intrinsic layers *i* between them. By varying smoothly the composition, one can produce SLs with wells and barriers of arbitrary shape, for instance, saw-tooth lattices with triangular wells. Keldysh [1.1] was the first to propose a superlattice by deforming a crystal with a strong standing acoustic wave. Esaki and Tsu [1.2] suggested instead composition modulation or selective doping, a method successfully implemented. In 1971, Kazarinov and Suris formulated a pioneer idea of a novel semiconductor laser, making use of stimulated light emission in a semiconductor SL by electrons making transitions between two levels of the different wells and emitting photons. This photon-assisted tunnelling mechanism, which does not involve the valence-band holes, had remained a purely theoretical prediction for over 20 years. The successful work on far infrared lasers based on this idea and called the *quantum cascade lasers* was reported in [1.6].

In addition to periodic structures, it is possible to produce and study aperiodic SLs. The Fibonacci SL may serve as an example of such a structure. It contains two basic elements (or blocks) $\mathbb{A}$ and $\mathbb{B}$. In the first realization [1.3] the basic elements were composed nominally of (17 Å AlAs)-(42 Å GaAs) and (17 Å AlAs)-(20 Å GaAs), respectively. The Fibonacci sequence, S_j, of order j is obtained from the blocks $\mathbb{A}$ and $\mathbb{B}$ following the rules: $S_0 = \mathbb{A}$, $S_1 = \mathbb{AB}$, $S_j = S_{j-1}S_{j-2}$ $(j \geq 2)$. In particular, $S_2 = \mathbb{ABA}$, $S_3 = \mathbb{ABAAB}$... The sequence S_j $(j \geq 2)$ comprises G_j elements $\mathbb{A}$ and G_{j-1} elements $\mathbb{B}$, G_j being the jth Fibonacci number given by the values $G_0 = G_1 = 1$ and the recurrent relation $G_j = G_{j-1}+G_{j-2}$. Particularly, $G_2 = 2, G_3 = 3, G_4 = 5, ...$ As j increases the ratio G_j/G_{j-1} converges toward $\tau = (1 + \sqrt{5})/2$. The Fibonacci SLs are, in some sense, an intermediate case between periodic and disordered 1D potentials. They reveal interesting and striking features in the band structure, wave-function localization and optical transitions [1.4].

1.2 Quantum Wires and Nanotubes

Technologically, the step from the 2D QW structures fabricated by thin-film growth down to one dimension is complicated. While several growth techniques are well suited to produce planar multilayer systems, the fabrication of *Quantum Wire* (QWR) structures in which charge carriers are quantum

confined in two dimensions is a very challenging task. The first methods suggested and attempted allowed to grow 1D structures called *Quantum Well Wires* (QWWs), i.e., 2D carrier-confinement structures in which carriers can move freely only in one direction. For example, a QWW can be prepared as a result of the lateral structuring of a QW by means of lithographic processing with etching and regrowth. The dimensionality of a 2D QW can be also reduced by using a special electrode configuration or strain lateral gradients to constrict the free carriers to a quasi-1D channel. Patterned interdiffusion and implantation locally alter the band gap of a QW also allowing fabrication of a QWW.

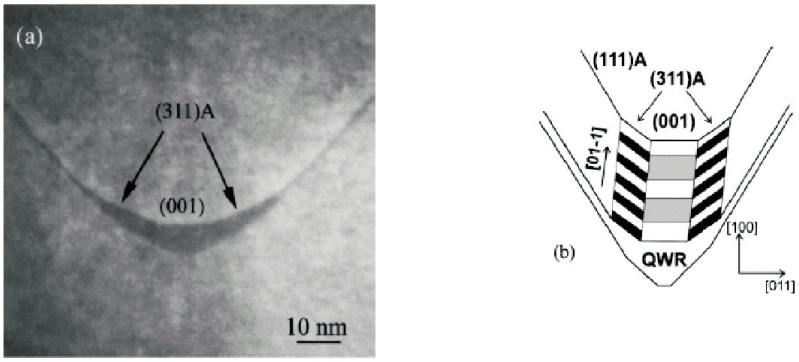

Fig. 1.5. (**a**) Typical cross-sectional TEM image of a V-shaped GaAs/AlGaAs QWR. (**b**) Schematic illustration of the QW crescent and the upper interface. Grey and dark stripes symbolize interface roughness. From [1.9].

Among methods suggested and attempted to fabricate QWRs different from QWWs, the growth on vicinal substrate has been suggested and attempted [1.7]. Another method that is utilized for growing uniform single and multiple semiconductor QWRs relies on deposition of thin layers on V-grooved substrates [1.8]. Figures 1.5a and 1.5b show a typical Transmission Electron Microscope (TEM) image of a V-shaped GaAs/AlGaAs QWR and a demonstrative illustration of the interface geometry [1.9]. The V-grooved substrates with a V-groove period of 2 or 4 μm were prepared by photolithography and wet chemical etching on (001)$\pm$0.1%-oriented GaAs substrate along the [1$\bar{1}$0] direction. Before epitaxial growth, the substrates were cleaned ultrasonically by organic solvent and additionally etched. This allowed to reduce greatly the interface roughness on the initial V-grooved substrates and improve uniformity of the grown QWRs. Epitaxial growth was performed with MetalOrganic Vapor Phase Epitaxy (MOVPE) system. The AlGaAs cladding layer grows to form a very sharp corner between two {111} crystal planes. The GaAs quantum well grows faster along the [001] direction, which results

in the formation of a crescent-shaped QW at the bottom of the groove. The GaAs to AlGaAs upper interface is composed of three clear crystalline facets, one (001) and two (311)A. The lateral tapering in the thickness of the QW crescent provides lateral variation in the effective band gap due to the increase in the carrier confinement energy with decreasing QW thickness. This lateral variation results in a 2D confining potential of the V-grooved QWR. By repeating the growth process it is possible to obtain vertically stacked multiple GaAs/AlGaAs QWR structures [1.10].

An effective Molecular Beam Epitaxy (MBE) technique called *Cleaved Edge Overgrowth* makes possible fabrication of a T-shaped intersection of two QWs, or a *T-shaped* QWR [1.11,1.12]. In this method, after conventional growth of a single QW, double QWs or MQWs on a [001] oriented substrate, the structure is further cleaved along the [110] direction and overgrown on the cleaved edge by a perpendicular QW and a barrier layer. Figure 1.6 shows a cross-sectional transmission electron micrograph of the multiple T-shaped GaAs/AlGaAs QWRs (a) and a schematic cross-sectional view of the QWR laser structure (b). One can see from Fig. 1.6a that T-shaped QW intersections are indeed located at the cleavage plane. The quantum mechanical bound states of an electron at two intersecting QWs are discussed in Sect. 2.2.2.

Carbon is a rare element that possesses the ability to form a wide variety of network-like sp^2 structures which can be looked upon as graphitic sheets curved in order to eliminate the dangling bonds. In particular, these network-like nanostructures include such nanoclusters as the fullerene molecule C_{60}, single carbon cages other than C_{60}, e.g., C_{70}, and multishell fullerenes, as well as carbon nanotubes, or carbon fibers. It is established that an arc discharge can produce either fullerenes or nanotubes by changing the conditions of the discharge. In fact, with the discovery by Iijima [1.14] of carbon nanotube structures, a new class of materials with the 1D dimensionality, or QWRs, has been introduced. The nanotubes are made of coaxial graphite cylinders, see Figs 1.7b and 1.7a. Each cylinder can be visualized as the conformal mapping of a 2D honeycomb graphene lattice (Fig. 1.7a) onto its surface. *Multiwalled*, or multiwall, carbon nanotubes consist of several concentric cylinders of the hexagonal network arranged around each other. In what follows we concentrate on *singlewalled*, or single-shell, nanotubes consisting of one cylinder.

A singlewalled nanotube is specified by a 2D hexagonal lattice vector $\boldsymbol{L}$ called the *chiral*, or circumferential, vector. Such a nanotube is obtained by rolling a graphite sheet along the vector $\boldsymbol{L}$ and joining one end of the vector to the other end as shown in Fig. 1.7. Thus, the length of circumference is $L = |\boldsymbol{L}|$ and the radius of the cylinder is $L/(2\pi)$. Each perfect carbon nanotube is translationally periodic along the tube principal axis with the period being dependent on the vector $\boldsymbol{L}$. Particular nanotubes with the chiral vector being parallel or perpendicular to one of elementary hexagon sides, see dashed and dotted lines in Fig. 1.7a, are called *armchair* and *zigzag* nan-

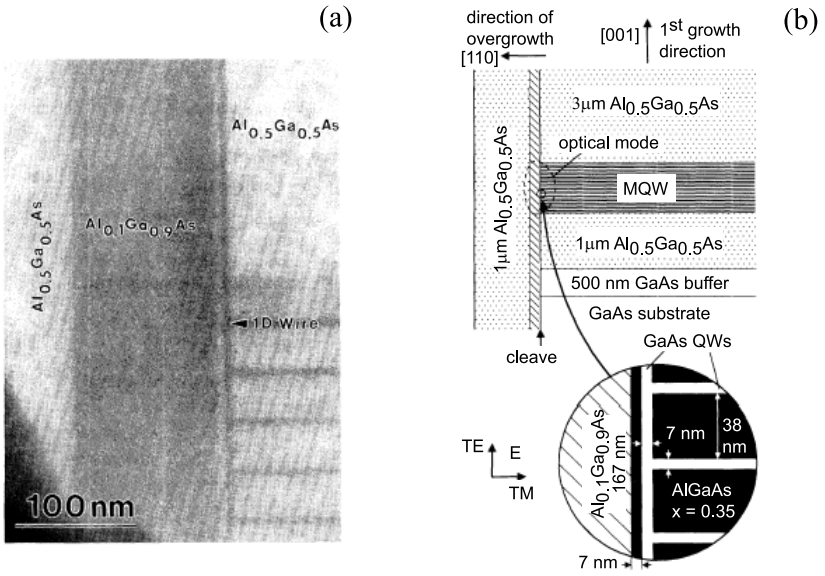

Fig. 1.6. (**a**) Cross-sectional bright-field transmission electron micrograph of a multiple T-shaped QWR structure taken in the [$\bar{1}$10] zone axis, i.e., with the electron beam aligned along the wire axis. Dark areas correspond to GaAs or GaAs-rich regions. (**b**) Schematic cross-section of the QWR laser structure. The MQW layer consists of 22 GaAs QWs separated by $Al_{0.35}Ga_{0.65}As$ barriers as illustrated in the magnified part of the QWR region. From [1.13].

otubes, respectively. Other nanotubes are characterized by a screw rotation symmetry and called the *chiral* nanotubes.

Introducing topological defects, pentagons, heptagons and octagons, in the carbon hexagonal network, one can connect different single-walled nanotubes to form three-terminal nanotube heterojunctions, in particular, T and Y junctions, which can be useful in nanoscale electronic devices, see [1.16, 1.17] and references therein.

1.3 Nanocrystals and Quantum Dot Structures

Quantum Dots (QDs) are nanoinclusions of one material inside another material. A semiconductor QD provides charge carrier confinement in all three directions and behaves as an artificial atom. Initially, QDs as well as QWRs were fabricated by the lateral structuring of QWs, including lithographic patterning and etching, selective intermixing by implantation and interdiffusion, strain-induced lateral confinement, growth on patterned substrates, see details in the book [1.18]. Here we discuss in more detail two other

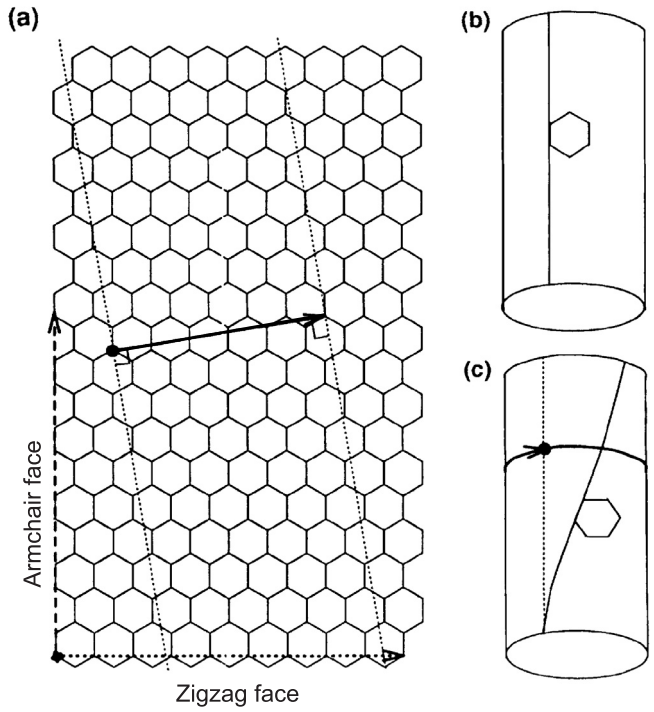

Fig. 1.7. (**a**) The hexagonal 2D lattice of a graphite monoatomic layer (graphene). A carbon nanotube is uniquely determined by the chiral vector, $\boldsymbol{L}$, shown by a solid arrow. Long-dashed and dotted vectors give rise to armchair and zigzag nanotubes. (**b**) A graphene sheet rolled up to form a zigzag nanotube. (**c**) A rolled graphene sheet representing chiral carbon nanotubes. From [1.15].

fabrication techniques for QDs, namely, Stranski-Krastanow growth of self-organized QDs [1.19–1.21] and formation of nanocrystals in semiconductor doped glasses [1.23].

There are three possible modes of heteroepitaxial growth, namely, Frank-van der Merve, Volmer-Weber and Stranski-Krastanow, representing respectively 'layer-by-layer', 'island' and 'layer-by-layer plus island' modes. The particular growth mode for a given heteropair depends on the interface energies and on the lattice mismatch. Experimental results and theoretical analysis [1.22] show that, in the lattice-mismatched InAs/GaAs system, the Stranski-Krastanow mode is realized. At the initial stage, the growth occurs layer by layer to form a *wetting layer* with the microscopic thickness of one or two monomolecular layers. With increasing InAs deposition three-dimensional (3D) coherent strained islands appear which can have the shape of a pyramid with a square base as illustrated in Fig. 1.8. For a *dilute* system

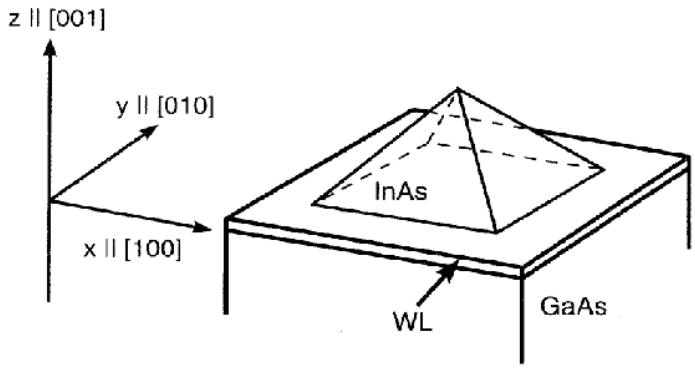

Fig. 1.8. Geometry of an InAs pyramid on an InAs wetting layer (WL) deposited on a GaAs(001) surface.

of islands, the elastic interaction between them via the strained substrate may be neglected. As the total InAs coverage increases and the system of islands transforms from dilute to *dense*, the elastic interaction between islands becomes essential, and a quasi-periodic array of self-organized islands with a narrow dot size distribution is formed. Therefore, the dense array of QDs is ordered both in shape, orientation, size and lateral arrangement.

An array of coherently strained InAs islands being covered and buried by the deposited GaAs creates a strain field in the surrounding GaAs matrix. When the next layer of InAs is grown, the modulated strain field pushes In ad-atoms on the surface towards buried islands resulting in vertical stacking of InAs islands in multisheet structures (*vertically coupled* QDs). With increasing separation-layer thickness the vertical correlation of InAs islands is lost because the surface strain field due to the underlying dots becomes too weak to influence the growth kinetics.

Figure 1.9 shows a TEM image of a CdSe nanocrystal in a glassy dielectric matrix. The sample was prepared by diffusion-controlled phase decomposition of an oversaturated solid solution. This three-stage technique makes it possible to vary the size of the grown nanocrystals in a controlled manner from some tens to thousands of Angstroms, but they are too small to form continuous bands of electronic state and represent a special class of QDs. Moreover, it is established that CdS and CdSe nanocrystals prepared by this method have nearly spherical form, small dispersion in size and retain the wurtzite crystalline structure.

As predicted in [1.25, 1.26], the cleaved edge overgrowth can be also employed to produce QDs at the juncture of three orthogonal QWs. The growth of the initial QW, the first cleave and overgrowth on the (110) plane used to obtain a T-shaped QWR are followed by the second cleave and overgrowth

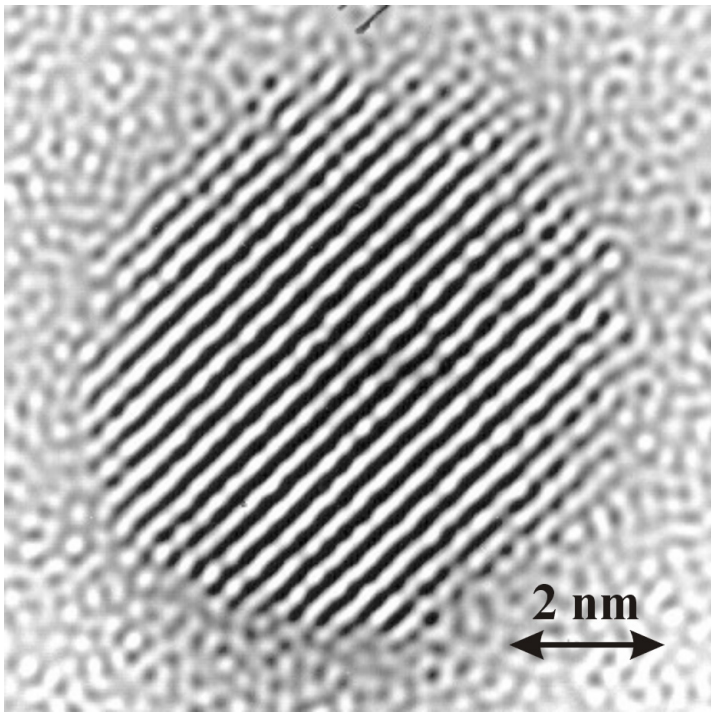

Fig. 1.9. High-resolution TEM image of a CdSe nanocrystal. The nanocrystal shape is close to spherical, the framework for Cd and Se atoms is a wurtzite lattice. From [1.24].

on top of the $(1\bar{1}0)$ plane. Such *twofold cleaved edge overgrowth* QDs have been realized in the GaAs/AlGaAs system using MBE [1.27].

1.4 Structure of the Book

The book is organized as follows: Chapter 1 which maps out the continuously expanding kingdom of semiconductor nanostructures is followed by Chapter 2 describing methods to calculate electron, exciton, phonon and photon states in various nanostructures. The consideration is based on the envelope-function approximation which provides a satisfactory accuracy and, on the other hand, allows a transparent physical interpretation. Other chapters are focused on particular fields of optical spectroscopy of nanostructures.

Chapter 3 deals with the reflection, propagation, absorption and transmission of light waves in nanostructures near the fundamental absorption edge. We focus the attention on coupling of excitons with electro-magnetic field and show that the concept of exciton polariton undergoes a substantial

modification in nanostructures. We calculate successively the reflection and transmission coefficients from a single quantum well, multiple quantum wells, periodic arrays of quantum dots and two-dimensional superlattices. Two final sections of Chapter 3 are devoted to electro- and magneto-optics.

Chapter 4 presents results on intraband optical spectroscopy including intra- and intersubband optical transitions in n- and p-doped periodic heterostructures and infrared dielectric response of undoped superlattices.

In Chapter 5 we review different aspects of photoluminescence spectroscopy emphasizing the role of excitons in the secondary emission of semiconductor nanostructures. We start with the description of macro- and microphotoluminescence spectra of localized excitons in undoped and modulation-doped quantum wells. Then we give a comprehensive introduction into optical spin orientation of free carriers and polarized photoluminescence of excitons under polarized photoexcitation. The description of polarized photoluminescence necessitates a detailed information about the electron and exciton spin-relaxation mechanisms, the g factor of free carriers and the fine structure of excitonic levels in low-dimensional systems. The chapter ends by describing the giant lateral optical anisotropy of type-II heterostructures.

Chapter 6 surveys various mechanisms of light scattering. We shall see that the semiconductor nanostructures offer new possibilities and enrich the Raman effect by scattering from intersubband excitations, confined and interface optical phonons as well as folded acoustic phonons.

Chapter 7 gives an account of nonlinear optical properties of nanostructures summarizing the studies of two-photon absorption, four-wave mixing and second-harmonic generation. Next, we describe optical properties of quantum microcavities. We discuss the energy dispersion and the Rabi splitting of low-dimensional exciton polaritons and then turn to nonlinear optical response of the microcavities. The chapter concludes with the description of angle-resolved polarization-dependent stimulated polariton-polariton scattering in quantum microcavities.

In Chapter 8 we give a consistent introduction to the physics of photogalvanic effects in noncentrosymmetric systems and summarize the results of recent theoretical and experimental studies on the circular and linear photogalvanic effects, the spin-galvanic effect and the photon drag effect in two- and one-dimensional structures.

In Conclusion (Chap. 9) we estimate perspective for low-dimensional physics of semiconductors, as a whole, and for the optical spectroscopy, in particular. The tables of characters of irreducible representations for some relevant point groups are presented in Appendix.

2 Quantum Confinement in Low-Dimensional Systems

So when Joseph came to his brothers,
they ... took him and threw him into the cistern.
Now the cistern was empty; there was
no water in it.

Genesis **37***: 23,24*

Nanostructures such as QWs, SLs, QWRs and QDs today constitute the main platforms for electronic structure engineering, or quantum-mechanical engineering. This calls for an efficient description and prediction of the electron energy spectra. At present different sophisticated microscopical approaches and atomistic theories have been proposed and developed to compute the free-carrier states in bulk semiconductors and semiconductor heteronanostructures. They are mostly based on empirical or first-principles pseudopotential and tight-binding methods. However, up to now the latter methods are not omnipotent and all-powerful. As in the past development of the physics of bulk semiconductors, the approximate continuum (not-atomistic) theories, by virtue of their simplicity and ease of interpretation, are by far the most popular methods for calculating the properties of electrons in semiconductor nanostructures. They are in the order (i) the *effective mass approximation* in case of a simple electronic band structure, (ii) the *effective Hamiltonian approach* for degenerate bands, and (iii) the envelope-function theory in the multi-band $\boldsymbol{k} \cdot \boldsymbol{p}$ models (e.g., the Kane model). In these methods of calculation, first, within each homogeneous layer of a multilayered structure or within a homogeneous region of lower dimensionality in QWR and QD structures, the solution is written as a linear combination of bulk wave functions. Then the sets of envelope functions in different regions are matched at the heterointerfaces by applying appropriate boundary conditions. In this chapter we will consider quantum confinement of electronic and excitonic states and modification of vibrational spectra in various nanostructures of different dimensionalities. The consideration is based on the approximate continuum methods but, from time to time, if it is pertinent we will refer to theoretical results obtained by using the refined atomistic theories.

2.1 Charge Carriers in Quantum Wells

2.1.1 Size-Quantization of Electrons with Simple Parabolic Energy Spectrum

Calculation of electron states in semiconductor nanostructures performed in the effective-mass approximation often looks like practical training in the quantum mechanics. Let us consider an A/B QW structure consisting of the well layer A sandwiched between two barrier half-subspaces B. For example, the materials A and B can be GaAs and $Al_xGa_{1-x}As$. For a simple isotropic and parabolic conduction band, the electron envelope function is separable and can be written as

$$\psi(\boldsymbol{r}) = \frac{1}{\sqrt{S}}\, \mathrm{e}^{\mathrm{i}\boldsymbol{k}_\parallel \cdot \boldsymbol{\rho}} \varphi(z)\,. \tag{2.1}$$

Here z is the structure growth axis, $\boldsymbol{k} = (k_x, k_y)$ is the 2D wave vector characterizing the electron's free motion in the interface plane (x, y) and S is the structure in-plane area. Notice that since translational invariance in the plane (x, y) is preserved, the space-group theorems concerning the $\boldsymbol{k}$ conservation apply to k_x and k_y but not to the z-component k_z. In the effective-mass method the z-dependent envelope satisfies the following Schrödinger equation inside the well

$$-\frac{\hbar^2}{2m_\mathrm{A}} \frac{d^2\varphi(z)}{dz^2} + \frac{\hbar^2 k_\parallel^2}{2m_\mathrm{A}}\, \varphi(z) = E\varphi(z)\,, \tag{2.2}$$

where m_A is the electron's effective mass in the material A. It is instructive to start from the electron states and energy spectrum in an idealized case of infinitely high (impenetrable) barriers. In this approximation, the envelope $\varphi(z)$ vanishes outside the QW and the boundary conditions are given by as

$$\varphi(\pm a/2) = 0\,, \tag{2.3}$$

where a is the well thickness and, since the origin of the coordinate system is chosen at the QW center, the points $\pm a/2$ are located at the interfaces. The system under consideration is invariant under the mirror reflection $z \to -z$. Therefore the totality of solutions of the Schrödinger equation splits into sets of even and odd functions of z, which can be written as $C\cos kz$ and $C\sin kz$, respectively, where C is the normalization factor. Taking into account the boundary conditions (2.3) we obtain that the electron wave-vector z-component, $k_z \equiv k$, is *size-quantized* and the allowed values of k and E are as follows

$$k = \frac{\nu\pi}{a}\,,\; E(k_\parallel) = \frac{\hbar^2}{2m_\mathrm{A}} \left[\left(\frac{\nu\pi}{a}\right)^2 + k_\parallel^2 \right]\,, \tag{2.4}$$

where $\nu = 1, 3, ...2n+1...$ for even solutions and $\nu = 2, 4...2n...$ for odd solutions. The corresponding electron quantum-confined states are labelled as $e\nu$.

The energy spectrum $E(k_\parallel)$ consists of the parabolic branches $E_{e\nu\boldsymbol{k}_\parallel}$, called *subbands*, which are shifted vertically with respect to each other. The electron total energy is the sum of the confinement energy $E_z = (\hbar^2/2m_\mathrm{A})(\nu\pi/a)^2$ and the kinetic energy $E_{xy} = (\hbar^2/2m_\mathrm{A})(k_x^2 + k_y^2)$ of the electron free motion in the (x, y) plane.

Now we turn to a finite barrier height $V = E_c^\mathrm{B} - E_c^\mathrm{A}$. Then the superstructure potential of a square QW B/A/B is

$$V(z) = \begin{cases} 0 & \text{for} \quad -a/2 < z < a/2\,, \\ V & \text{for} \quad z < -a/2 \quad \text{or} \quad z > a/2\,. \end{cases} \tag{2.5}$$

In QW structures with finite values of V, the envelope $\psi(\boldsymbol{r})$ is nonzero both in the A and B layers. Due to the translational symmetry, the components k_x, k_y are the same inside and outside the well. The equation for $\varphi(z)$ in the barrier layers is

$$-\frac{\hbar^2}{2m_\mathrm{B}}\frac{d^2\varphi(z)}{dz^2} + \left(\frac{\hbar^2 k_\parallel^2}{2m_\mathrm{B}} + V\right)\varphi(z) = E\varphi(z)\,. \tag{2.6}$$

Except for the fact that the masses m_A and m_B may be different, the equations (2.2, 2.6) are identical to those solved in quantum-mechanics textbooks for a particle confined in a 1D square-potential well. In general, there are two kinds of solutions to (2.2, 2.6). When $E - V - (\hbar^2 k_\parallel^2/2m_\mathrm{B})$ is positive, the solutions within each layer are linear combinations of two plane waves and their energy spectrum is continuous, even for a fixed in-plane wave vector $\boldsymbol{k}_\parallel$. In case of negative values of $E - V - (\hbar^2 k_\parallel^2/2m_\mathrm{B})$, which is considered below, the function $\varphi(z)$ is a linear combination of plane waves $\exp(\pm\mathrm{i}kz)$ inside the well, and exponentially decays as $\exp(\pm æz)$ in the left and right barriers, respectively, where

$$k = \left(\frac{2m_\mathrm{A}E}{\hbar^2} - k_\parallel^2\right)^{1/2}, \; æ = \left(\frac{2m_\mathrm{B}(V-E)}{\hbar^2} + k_\parallel^2\right)^{1/2}. \tag{2.7}$$

Since the potential (2.5) possesses reflection symmetry, the functions $\varphi(z)$ have a certain parity. For even solutions, one can write

$$\varphi(z) = \begin{cases} C\,\cos kz\,, & \text{if} \quad |z| \le a/2, \\ D\,\exp\left[-æ(|z| - a/2)\right], & \text{if} \quad |z| \ge a/2, \end{cases} \tag{2.8}$$

The coefficients C and D are found from the normalization condition

$$\int \varphi^2(z)\,dz = 1 \tag{2.9}$$

and boundary conditions that relate the envelopes $\varphi_\mathrm{A}, \varphi_\mathrm{B}$ and their derivatives $(d\varphi/dz)_\mathrm{A}, (d\varphi/dz)_\mathrm{B}$ on both sides of the interface between the materials A and B. The most popular are the so-called *Bastard boundary conditions* [2.1, 2.2]

$$\varphi_{\rm A} = \varphi_{\rm B}\,,\ \frac{1}{m_{\rm A}}\left(\frac{d\varphi}{dz}\right)_{\rm A} = \frac{1}{m_{\rm B}}\left(\frac{d\varphi}{dz}\right)_{\rm B}\,. \tag{2.10}$$

They ensure continuity of the envelope $\varphi(z)$ and the particle flux across the interface. For the solution (2.8) the boundary conditions lead to the following two linear homogeneous equations for C and D

$$C\,\cos k\frac{a}{2} = D\,,\ -\frac{k}{m_{\rm A}}C\,\sin k\frac{a}{2} = -\frac{æ}{m_{\rm B}}D\,. \tag{2.11}$$

After some algebra we obtain the transcendental equation for the energy of even solutions

$$\tan k\frac{a}{2} = \eta \equiv \frac{m_{\rm A}}{m_{\rm B}}\frac{æ}{k}\,. \tag{2.12}$$

For odd solutions, the envelope $\varphi(z)$ has the form

$$\varphi(z) = \begin{cases} C\,\sin kz\,, & \text{if} \quad |z| \le a/2\,, \\ D\,\text{sign}\{z\}\,\exp\left[-æ(|z| - a/2)\right], & \text{if} \quad |z| \ge a/2\,, \end{cases} \tag{2.13}$$

and the energy is found from

$$\cot k\frac{a}{2} = -\eta\,. \tag{2.14}$$

The coefficient C is derived from the normalization condition (2.9) and can be presented as

$$C = \sqrt{\frac{2}{a}}\left[1 \pm \frac{\sin ka}{ka} + \frac{1}{æa}(1 \pm \cos ka)\right]^{-1}\,, \tag{2.15}$$

where the sign $\pm$ corresponds to the even and odd solutions. By using (2.12) and (2.14) one can reduce the above expressions for C to

$$C = \sqrt{\frac{2}{a}}\left[1 + \frac{2}{(1+\eta^2)a}\left(\frac{\eta}{k} + \frac{1}{æ}\right)\right]^{-1}\,, \tag{2.16}$$

which is valid for solutions of both parities. It is known that in a symmetrical 1D well there is always at least one quantum-confined state. Therefore, for a finite value of V, the electron energy spectrum contains a finite number of subbands $e\nu$ ($\nu = 1...N$) and continuum of states with $E - (\hbar^2 k_\parallel^2/2m_{\rm B}) > V$. For the case of coinciding effective masses, $m_{\rm A} = m_{\rm B}$, the dispersion $E_{e\nu \boldsymbol{k}_\parallel}$ is parabolic with the same mass as in the bulk compositional materials. If the difference between $m_{\rm A}$ and $m_{\rm B}$ is relatively small, the subband dispersion is close to parabolic.

It is worthwhile to analyze the transition from a finite to an infinite barrier height. For this purpose we take $k_x = k_y = 0$ and assume V to be high enough and satisfy the condition

$$V \gg \frac{\hbar^2}{2m_{\rm A}} \left(\frac{\pi}{a}\right)^2 . \tag{2.17}$$

Then, for the ground state $e1$, we can replace æ by $æ_0 = \sqrt{2m_{\rm A}V/\hbar^2}$, rewrite (2.12) in the form $\cot(ka/2) = (m_{\rm B}k/m_{\rm A}æ) \approx (m_{\rm B}k/m_{\rm A}æ_0)$ and consider the ratio $k/æ_0$ as a small parameter. For the state $e1$, in the zero-order approximation we obtain $ka/2 = \pi/2$ or $k = \pi/a$ which coincides with (2.4) derived in the limit $V \to \infty$ for $\nu = 1$. In the first-order approximation we find

$$k \approx \frac{\pi}{a}\left(1 - \frac{m_{\rm B}}{m_{\rm A}}\frac{2}{æ_0 a}\right)$$

and

$$E_{e1} \approx \frac{\hbar^2}{2m_{\rm A}} \left(\frac{\pi}{a}\right)^2 \left(1 - \frac{m_{\rm B}}{m_{\rm A}}\frac{4}{æ_0 a}\right) . \tag{2.18}$$

If the masses $m_{\rm A}$ and $m_{\rm B}$ are comparable in the order of magnitude the criterion for validity of (2.18) is the inequality $æ_0 a \gg 4$. It follows then that the concepts "high barrier", "low barrier" are relative and, for a wide well, equation (2.18) is valid even in heterostructures with relatively small band offsets.

One should bear in mind that, for semiconductors with the simple band structure, the most general boundary conditions are (see, e.g., [2.3–2.7])

$$\varphi_{\rm A} = t_{11}\,\varphi_{\rm B} + t_{12}\,\dot\varphi_{\rm B}\,,\ \dot\varphi_{\rm A} = t_{21}\,\varphi_{\rm B} + t_{22}\,\dot\varphi_{\rm B}\,, \tag{2.19}$$

where

$$\dot\varphi_{\rm A} = l\left(\frac{\partial\varphi}{\partial z}\right)_{\rm A}\,,\ \dot\varphi_{\rm B} = l\,\frac{m_{\rm A}}{m_{\rm B}}\left(\frac{\partial\varphi}{\partial z}\right)_{\rm B}\,,$$

l is an arbitrarily chosen microscopic length introduced in order to get the matrix elements t_{ij} dimensionless. The matrix $\hat t$ is unimodular, i.e., it satisfies the condition $t_{11}t_{22} - t_{12}t_{21} = 1$ (to within an overall complex phase factor), to insure that the electron flux is continuous. For a sharp heterointerface A/B, the determination of the matrix $\hat t$ is beyond the competence of the envelope-function theory. Therefore the chosen set of components t_{ij} is either postulated or carried out by means of comparison with experiment or results of calculation performed in the frame of some microscopic model. Clearly, the Bastard boundary conditions (2.10) is a special case of the general conditions (2.19) with $t_{11} = t_{22} = 1, t_{12} = t_{21} = 0$. They are in a satisfactory agreement with the microscopical calculations in linear-chain tight-binding and empirical pseudopotential models [2.5]. Note that instead of solving the Schrödinger equation within each layer and sewing the solutions at the interfaces by using the boundary conditions in the form (2.10) one can equivalently use the Hamiltonian

$$\mathcal{H} = -\frac{\partial}{\partial z}\frac{\hbar^2}{2m(z)}\frac{\partial}{\partial z} - \frac{\hbar^2}{2m(z)}\left(\frac{\partial^2}{\partial x^2} + \frac{\partial^2}{\partial y^2}\right) + V(z)\,,$$

defined in the whole space. Here $m(z)$ is a discontinuous function jumping at the A/B interface from $m_{\rm A}$ to $m_{\rm B}$.

If the carrier spectrum is anisotropic but the normal, z, to the interface is directed along one of the principal axes $1, 2, 3$ of the effective-mass tensor, then the above equations for the electron energy are valid with minor modifications. Particularly, for $z \parallel 3$, the quantum-confinement energy E_z is governed by the effective masses $m_3^{\rm A}, m_3^{\rm B}$ while the kinetic energy E_{xy} is governed by the masses $m_i^{\rm A}, m_i^{\rm B}$ with $i = 1, 2$. If the carrier spectrum is anisotropic and the normal z is directed in an arbitrary way with respect to the principal axes $1, 2, 3$, then in the coordinate frame x, y, z the electron effective Hamiltonian within the well,

$$\mathcal{H} = \sum_{ij} \frac{\hbar^2}{2} \frac{\hat{k}_i \hat{k}_j}{m_{ij}^{\rm A}} \quad \text{with} \quad \hat{k}_j = -{\rm i}\frac{\partial}{\partial x_j} \, ,$$

contains nondiagonal components of the reciprocal effective-mass tensor ${m_{ij}^{\rm A}}^{-1}$. In this case, the solution of Schrödinger's equation can be also represented in the form (2.1). However, here,

$$\varphi(z) = \exp\left[-{\rm i}\left(\frac{m_{zz}}{m_{xz}}k_x + \frac{m_{zz}}{m_{yz}}k_y\right) z\right] \left(C_1 {\rm e}^{{\rm i}kz} + C_2 {\rm e}^{-{\rm i}kz}\right) \, . \tag{2.20}$$

For simplicity, we omit the superscript A indicating the effective mass in the layer A. The electron energy is given by

$$E = \frac{\hbar^2 k^2}{2m_{zz}} + E_{xy} \, , \tag{2.21}$$

where

$$E_{xy} = \frac{\hbar^2 k_x^2}{2m_{xx}}\left(1 - \frac{m_{xx}m_{zz}}{m_{xz}^2}\right) + \frac{\hbar^2 k_y^2}{2m_{yy}}\left(1 - \frac{m_{yy}m_{zz}}{m_{yz}^2}\right) + \frac{\hbar^2 k_x k_y}{2m_{xy}}\left(1 - \frac{m_{xy}m_{zz}}{m_{xz}m_{yz}}\right) \, .$$

In a QW structure, a value of k^2 is quantized. Just as in (2.4), for infinitely high barriers, $k = \nu\pi/a$.

The space confinement, or size-quantization, of hole states for the simple valence-band structure is treated in the same way, the hole subbands are labelled $h\nu$. Fig. 2.1 illustrates the size-quantized electron subbands $e1, e2$ in the conduction band and subbands $h1, h2$ in the valence band. For semiconductors with degenerate valence bands, the calculation of hole energy spectrum presents a more complicated procedure discussed in the next subsection.

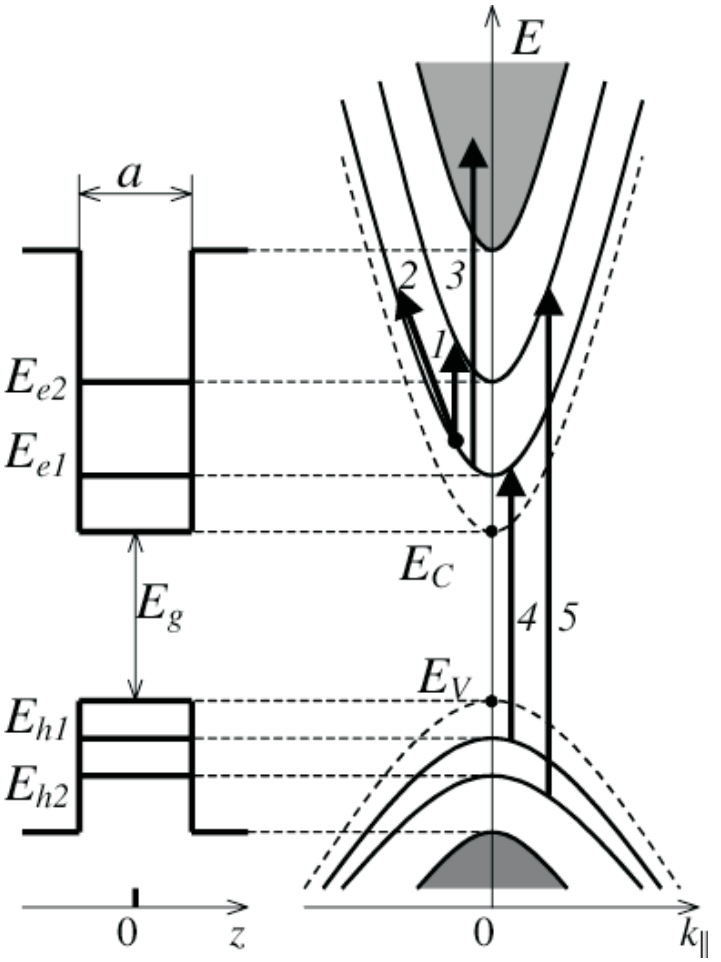

Fig. 2.1. Band diagram of a single QW and the electron energy dispersion in the 2D conduction and valence subbands. The arrows indicate possible optical transitions, namely, (*1*) direct intraband intersubband transitions, see Sect. 4.1, (*2*) indirect intrasubband transitions (Sect. 4.3), (*3*) transitions from quantum-confined to continuum states, and (*4*),(*5*) direct interband transitions (Sect. 2.6).

2.1.2 Luttinger Hamiltonian. Heavy- and Light-Hole Subbands

If we ignore the spin and spin-orbit interaction (the nonrelativistic approximation), the bottom conduction and top valence Γ-states in GaAs-like semiconductors are characterized by s- and p-type symmetries. The corresponding orbital Bloch functions are designated $S(\boldsymbol{r}) \equiv S$ and X, Y, Z. They form bases of the irreducible representations A_1 (Γ_1) and F_2 (Γ_{15}) of the point group T_d (see Appendix). However, one has to bear in mind that these functions are pe-

riodical with the periodicity of zinc-blende structure, say, $X(\boldsymbol{r}+\boldsymbol{a}_i)=X(\boldsymbol{r})$ with $\boldsymbol{a}_i$ being the primitive lattice vectors. The inclusion of the spin degeneracy doubles number of states at the Γ point: $\uparrow S, \downarrow S$ (the spinor irreducible representation Γ_6) for the conduction band and $\uparrow X, \uparrow Y, \uparrow Z, \downarrow X, \downarrow Y, \downarrow Z$ for the valence band. The spin-orbit interaction leads to splitting of the six degenerate valence states into the quartet

$$
\begin{aligned}
|\Gamma_8,+3/2\rangle &= -\uparrow \frac{X+\mathrm{i}Y}{\sqrt{2}}\,, \\
|\Gamma_8,+1/2\rangle &= \sqrt{\frac{2}{3}}\uparrow Z - \downarrow \frac{X+\mathrm{i}Y}{\sqrt{6}}\,, \\
|\Gamma_8,-1/2\rangle &= \sqrt{\frac{2}{3}}\downarrow Z + \uparrow \frac{X-\mathrm{i}Y}{\sqrt{6}}\,, \\
|\Gamma_8,-3/2\rangle &= \downarrow \frac{X-\mathrm{i}Y}{\sqrt{2}}\,,
\end{aligned}
\tag{2.22}
$$

that transforms according to the spinor representation Γ_8, and the doublet

$$
\begin{aligned}
|\Gamma_7,+1/2\rangle &= \frac{1}{\sqrt{3}}[\uparrow Z + \downarrow (X+\mathrm{i}Y)]\,, \\
|\Gamma_7,-1/2\rangle &= \frac{1}{\sqrt{3}}\,[-\downarrow Z + \uparrow (X-\mathrm{i}Y)]
\end{aligned}
\tag{2.23}
$$

that forms the spinor representation Γ_7. We use the canonical bases for the representations Γ_8, Γ_7, they transform under operations of the T_d group as the spherical functions $Y_{3/2,m}$ ($m=\pm 3/2, \pm 1/2$) and $Y_{1/2,m}$ ($m=\pm 1/2$). By analogy with spin-orbit splitting of the p-level of a hydrogen atom, the states Γ_8, Γ_7 are ascribed to those with the total angular momentum $J=3/2, 1/2$ and its z-components $m=\pm 3/2, \pm 1/2$ and $m=\pm 1/2$, respectively. This explains the notations of the corresponding basic functions in (2.22, 2.23).

The effective Hamiltonian for electrons in the valence band Γ_8 is a 4×4 matrix and, in the basis (2.22), has the form

$$
\mathcal{H}^{(\Gamma_8)} = \begin{bmatrix} F & H & I & 0 \\ H^* & G & 0 & I \\ I^* & 0 & G & -H \\ 0 & I^* & -H^* & F \end{bmatrix}\,,
\tag{2.24}
$$

where

$$
\begin{aligned}
F &= (A-B)\,k_z^2 + \left(A+\frac{B}{2}\right)(k_x^2+k_y^2)\,, \\
G &= (A+B)k_z^2 + \left(A-\frac{B}{2}\right)(k_x^2+k_y^2)\,, \\
I &= -\frac{\sqrt{3}}{2}\left[B(k_x^2-k_y^2) - 2\,\mathrm{i}\,\frac{D}{\sqrt{3}}k_x k_y\right]\,, \\
H &= -Dk_z(k_x-\mathrm{i}k_y)\,,
\end{aligned}
\tag{2.25}
$$

and x, y, z are the principal axes [100], [010] and [001]. This matrix, called the *Luttinger Hamiltonian* and depending on three band parameters, A, B and C, is derived in the second-order $\boldsymbol{k} \cdot \boldsymbol{p}$ perturbation theory or in the method of invariants. It describes the energy spectrum and electron (hole) states in the vicinity of the point $\boldsymbol{k} = 0$ in the band Γ_8 of zinc-blende-lattice semiconductors (e.g., GaAs, InP, CdTe, ZnSe) and in the band Γ_8^+ of centrosymmetric diamond-lattice semiconductors (Ge, Si). Notice that the symmetry forbids odd terms in the expansion of the Hamiltonian in powers of $\boldsymbol{k}$ in centrosymmetric crystals but allows such terms in T_d crystal classes. The linear- and cubic-in-$\boldsymbol{k}$ contributions to the effective Hamiltonian are discussed in Sect. 2.6.

The dispersion equation $\mathrm{Det}||\mathcal{H}^{(\Gamma_8)}_{m'm} - E\delta_{m'm}|| = 0$ is reduced to

$$\left[(E-F)(E-G) - \mid H \mid^2 - \mid I \mid^2\right]^2 = 0\,.$$

Its solutions are

$$\begin{aligned} E_{hh,lh} &= \frac{F+G}{2} \pm \sqrt{\left(\frac{F-G}{2}\right)^2 + |H|^2 + |I|^2} \\ &= Ak^2 \pm \sqrt{B^2k^4 + (D^2 - 3B^2)\left(k_x^2k_y^2 + k_y^2k_z^2 + k_z^2k_x^2\right)}\,. \end{aligned} \tag{2.26}$$

For most semiconductors with a zinc-blende lattice the band parameter A is negative. As a result, the effective masses $\hbar^2k^2/(2E_{hh,lh})$ are negative as well. Sometimes, instead of working in the electron representation with negative masses, it is more convenient to use the hole representation with positive masses and replace $\mathcal{H}^{(\Gamma_8)}$ by $-\mathcal{H}^{(\Gamma_8)}$. The energy in the latter representation will be labelled by the superscript 'h'. Thus for hole dispersion we have instead of (2.26)

$$\begin{aligned} E^h_{hh} &= \frac{\hbar^2k^2}{2m_{hh}}\,,\ m_{hh} = \frac{\hbar^2}{2(|A| - \sqrt{B^2 + C^2f})}\,, \\ E^h_{lh} &= \frac{\hbar^2k^2}{2m_{lh}}\,,\ m_{lh} = \frac{\hbar^2}{2(|A| + \sqrt{B^2 + C^2f})}\,, \end{aligned} \tag{2.27}$$

where

$$C^2 = D^2 - 3B^2\,,\ f = \frac{k_x^2k_y^2 + k_y^2k_z^2 + k_z^2k_x^2}{k^4}\,.$$

Usually values of A, B and $D/\sqrt{3}$ are close to each other because the $\boldsymbol{k} \cdot \boldsymbol{p}$ coupling of the Γ_8 valence band with the lowest conduction band Γ_6 is the strongest. As a result, the hole branch labelled 'hh' has a small dispersion and hence large mass, it is referred to as the *heavy-hole* subband. The other branch labelled 'lh' is known as the light-hole subband. Note that the heavy- and light-hole subbands are 3D bands and have nothing in common with the size-quantized subbands in QWs and QWRs.

The Luttinger Hamiltonian (2.24) can be conveniently presented in the following invariant form [2.8]

$$\mathcal{H}^{(\Gamma_8)}(\boldsymbol{k}) = \left(A + \frac{5}{4}B\right)k^2 - B\sum_i J_i^2 k_i^2 - \frac{D}{\sqrt{3}}\sum_{i'\neq i}\{J_{i'}J_i\}_s k_{i'}k_i \tag{2.28}$$

$$= \frac{\hbar^2}{2m_0}\left[-\left(\gamma_1 + \frac{5}{2}\gamma_2\right)k^2 + 2\gamma_2\sum_i J_i^2 k_i^2 + 2\gamma_3\sum_{i'\neq i}\{J_{i'}J_i\}_s k_{i'}k_i\right] .$$

Here $i, i' = x, y, z$, J_i are the matrices of the angular-momentum operators $\hat{J}_i$ in the basis $\mathrm{Y}_{3/2,m}$, the curly brackets with the subscript s mean the antisymmetrization: $\{MN\}_s = (MN + NM)/2$ for any operators or matrices M and N. The complete set of 4×4 matrices constructed from products of J_i is presented in Table 2.1. In the method of invariants, these matrices can be considered as objects transforming according to representations of the T_d group. Particularly, the matrices J_i and J_i^3 form equivalent bases of the representation F_1 (pseudovector) and the matrices V_i and $\{J_{i+1}J_{i+2}\}_s$ transform according to the representation F_2 (vector). The three matrices J_i^2 form a basis of the reducible representation which is reduced to $A_1 + E$. The invariant matrix is the sum $J_x^2 + J_y^2 + J_z^2$ which is equal $J(J+1)I$, where $J = 3/2$ and I is the 4×4 unit matrix with the components $I_{i'i} = \delta_{i'i}$. As a basis of the representation E one can use the pair $\sqrt{3}(J_x^2 - J_y^2), 2J_z^2 - J_x^2 - J_y^2$. Finally, the matrix $\{J_xJ_yJ_z\}_s$ is attributed to the representation A_2 (pseudoscalar). The matrices J_i, J_i^3, V_i and $\{J_xJ_yJ_z\}_s$ are odd and the matrices $J_i^2, \{J_{i+1}J_{i+2}\}_s$ are even under time inversion operation. The dimensionless constants γ_j called the *Luttinger* (or Kohn-Luttinger) band-structure parameters are connected with the constants A, B, D by

$$\frac{\hbar^2}{2m_0}\gamma_1 = -A\,,\ \frac{\hbar^2}{m_0}\gamma_2 = -B\,,\ \frac{\hbar^2}{m_0}\gamma_3 = -\frac{D}{\sqrt{3}}\,. \tag{2.29}$$

Table 2.1. Matrices J_i and their products for the representation Γ_8 in the basis $Y_{3/2,m}$ ($m = 3/2, 1/2, -1/2, -3/2$). The used notations are $V_i = \{J_i(J_{i+1}^2 - J_{i+2}^2)\}_s$, $\{J_xJ_yJ_z\}_s = \{J_x\{J_yJ_z\}_s\}_s$.

$$J_x = \begin{bmatrix} 0 & \sqrt{3}/2 & 0 & 0 \\ \sqrt{3}/2 & 0 & 1 & 0 \\ 0 & 1 & 0 & \sqrt{3}/2 \\ 0 & 0 & \sqrt{3}/2 & 0 \end{bmatrix},\quad J_y = \begin{bmatrix} 0 & -\mathrm{i}\sqrt{3}/2 & 0 & 0 \\ \mathrm{i}\sqrt{3}/2 & 0 & -\mathrm{i} & 0 \\ 0 & \mathrm{i} & 0 & -\mathrm{i}\sqrt{3}/2 \\ 0 & 0 & \mathrm{i}\sqrt{3}/2 & 0 \end{bmatrix},$$

$$J_z = \begin{bmatrix} 3/2 & 0 & 0 & 0 \\ 0 & 1/2 & 0 & 0 \\ 0 & 0 & -1/2 & 0 \\ 0 & 0 & 0 & -3/2 \end{bmatrix},$$

$$J_x^2 = \begin{bmatrix} 3/4 & 0 & \sqrt{3}/2 & 0 \\ 0 & 7/4 & 0 & \sqrt{3}/2 \\ \sqrt{3}/2 & 0 & 7/4 & 0 \\ 0 & \sqrt{3}/2 & 0 & 3/4 \end{bmatrix}, \quad J_y^2 = \begin{bmatrix} 3/4 & 0 & -\sqrt{3}/2 & 0 \\ 0 & 7/4 & 0 & -\sqrt{3}/2 \\ -\sqrt{3}/2 & 0 & 7/4 & 0 \\ 0 & -\sqrt{3}/2 & 0 & 3/4 \end{bmatrix},$$

$$J_z^2 = \begin{bmatrix} 9/4 & 0 & 0 & 0 \\ 0 & 1/4 & 0 & 0 \\ 0 & 0 & 1/4 & 0 \\ 0 & 0 & 0 & 9/4 \end{bmatrix},$$

$$2\{J_y J_z\}_s = \begin{bmatrix} 0 & -\mathrm{i}\sqrt{3} & 0 & 0 \\ \mathrm{i}\sqrt{3} & 0 & 0 & 0 \\ 0 & 0 & 0 & \mathrm{i}\sqrt{3} \\ 0 & 0 & -\mathrm{i}\sqrt{3} & 0 \end{bmatrix}, \quad 2\{J_z J_x\}_s = \begin{bmatrix} 0 & \sqrt{3} & 0 & 0 \\ \sqrt{3} & 0 & 0 & 0 \\ 0 & 0 & 0 & -\sqrt{3} \\ 0 & 0 & -\sqrt{3} & 0 \end{bmatrix},$$

$$2\{J_x J_y\}_s = \begin{bmatrix} 0 & 0 & -\mathrm{i}\sqrt{3} & 0 \\ 0 & 0 & 0 & -\mathrm{i}\sqrt{3} \\ \mathrm{i}\sqrt{3} & 0 & 0 & 0 \\ 0 & \mathrm{i}\sqrt{3} & 0 & 0 \end{bmatrix},$$

$$J_x^3 = \begin{bmatrix} 0 & 7\sqrt{3}/8 & 0 & 3/4 \\ 7\sqrt{3}/8 & 0 & 5/2 & 0 \\ 0 & 5/2 & 0 & 7\sqrt{3}/8 \\ 3/4 & 0 & 7\sqrt{3}/8 & 0 \end{bmatrix}, \quad J_y^3 = \begin{bmatrix} 0 & -\mathrm{i}7\sqrt{3}/8 & 0 & \mathrm{i}3/4 \\ \mathrm{i}7\sqrt{3}/8 & 0 & -\mathrm{i}5/2 & 0 \\ 0 & \mathrm{i}5/2 & 0 & -\mathrm{i}7\sqrt{3}/8 \\ -\mathrm{i}3/4 & 0 & \mathrm{i}7\sqrt{3}/8 & 0 \end{bmatrix},$$

$$J_z^3 = \begin{bmatrix} 27/8 & 0 & 0 & 0 \\ 0 & 1/8 & 0 & 0 \\ 0 & 0 & -1/8 & 0 \\ 0 & 0 & 0 & -27/8 \end{bmatrix},$$

$$V_x = \begin{bmatrix} 0 & -\sqrt{3}/4 & 0 & -3/4 \\ -\sqrt{3}/4 & 0 & 3/4 & 0 \\ 0 & 3/4 & 0 & -\sqrt{3}/4 \\ -3/4 & 0 & -\sqrt{3}/4 & 0 \end{bmatrix}, \quad V_y = \begin{bmatrix} 0 & -\mathrm{i}\sqrt{3}/4 & 0 & \mathrm{i}3/4 \\ \mathrm{i}\sqrt{3}/4 & 0 & \mathrm{i}3/4 & 0 \\ 0 & -\mathrm{i}3/4 & 0 & -\mathrm{i}\sqrt{3}/4 \\ -\mathrm{i}3/4 & 0 & \mathrm{i}\sqrt{3}/4 & 0 \end{bmatrix},$$

$$V_z = \begin{bmatrix} 0 & 0 & \sqrt{3}/2 & 0 \\ 0 & 0 & 0 & -\sqrt{3}/2 \\ \sqrt{3}/2 & 0 & 0 & 0 \\ 0 & -\sqrt{3}/2 & 0 & 0 \end{bmatrix},$$

$$2\{J_x J_y J_z\}_s = \begin{bmatrix} 0 & 0 & -\mathrm{i}\sqrt{3}/2 & 0 \\ 0 & 0 & 0 & \mathrm{i}\sqrt{3}/2 \\ \mathrm{i}\sqrt{3}/2 & 0 & 0 & 0 \\ 0 & -\mathrm{i}\sqrt{3}/2 & 0 & 0 \end{bmatrix}.$$

The method of invariants readily allows to write down a deformation-induced contribution to (2.28), the so-called *Bir-Pikus Hamiltonian*, as

$$\mathcal{H}_u^{(\Gamma_8)} = \left(a + \frac{5}{4}b\right) \mathrm{Tr}\{\hat{u}\} - b\sum_i J_i^2 u_{ii} - \frac{d}{\sqrt{3}} \sum_{i' \neq i} \{J_{i'} J_i\}_s u_{i'i}\,, \qquad (2.30)$$

where $\hat{u}$ is the strain tensor with the components $u_{i'i}$ and a, b, d are the deformation potential constants. The Zeeman Hamiltonian in the band Γ_8 reads

$$\mathcal{H}_{\boldsymbol{B}}^{(\Gamma_8)} = 2\mu_B \left[\mathcal{K}\boldsymbol{J}\cdot\boldsymbol{B} + q(J_x^3 B_x + J_y^3 B_y + J_z^3 B_z)\right] \tag{2.31}$$

and is characterized by two dimensionless coefficients $\mathcal{K}$ and q. Here $\boldsymbol{B}$ is the magnetic field and μ_B is the Bohr magneton. Note that the difference between γ_2 and γ_3 as well as nonzero value of q are due to the cubic symmetry of the zinc-blende lattice. The warping of the valence band, or the angular dependence of m_{hh}, m_{lh}, is directly related to the difference between γ_2 and γ_3. In the frequently used isotropic approximation, γ_3 is identified with γ_2 in which case the warping vanishes. In the effective Hamiltonian approach, the electron wave function is expanded in the Bloch states near the extremum point, here the Γ point, and written as a sum

$$\Psi(\boldsymbol{r}) = \sum_m \Phi_m(\boldsymbol{r})\,|3/2, m\rangle \tag{2.32}$$

of products of the smoothly-varying envelope functions Φ_m and the Γ-point Bloch functions $|3/2, m\rangle$, see (2.22).

In QW structures, the envelope functions Φ_m presented as a four-component column $\boldsymbol{\Phi}$ satisfy the matrix Schrödinger equation

$$\mathcal{H}\boldsymbol{\Phi}(\boldsymbol{r}) = E\boldsymbol{\Phi}(\boldsymbol{r})\,, \tag{2.33}$$

where the effective Hamiltonian $\mathcal{H}$ is the Luttinger Hamiltonian $\mathcal{H}^{(\Gamma_8)}(\hat{\boldsymbol{k}})$ with the superstructure potential $V(z)$ included into the diagonal, $\hat{\boldsymbol{k}} = -\mathrm{i}\nabla$. The simplest boundary conditions for the envelopes $\Phi_m(\boldsymbol{r})$ are

$$\boldsymbol{\Phi}_{\mathrm{A}} = \boldsymbol{\Phi}_{\mathrm{B}}\,,\ (\hat{v}_z\boldsymbol{\Phi})_{\mathrm{A}} = (\hat{v}_z\boldsymbol{\Phi})_{\mathrm{B}}\,, \tag{2.34}$$

where $\hat{v}_z$ is the normal component of the velocity operator

$$\hat{v}_z = \frac{1}{\hbar}\frac{\partial\mathcal{H}}{\partial k_z}\,. \tag{2.35}$$

In this subsection the consideration is restricted to zinc-blende-lattice QW structures grown along the direction [001]. QWs grown along low-symmetry directions are treated in Sect. 3.1.6. We start from quantum-confined valence states with zero in-plane wave vector, $k_x = k_y = 0$. Since in this case the non-diagonal elements of the Luttinger Hamiltonian vanish, heavy- and light-hole states are size-quantized independently and form two series of subbands, heavy-hole ($hh\nu$) and light-hole ($lh\nu$) subbands. At the same time the boundary conditions (2.34) reduce to (2.10). The hole quantum-confinement energies $E_{hh\nu}$ and $E_{lh\nu}$ are found from (2.12, 2.14) by substituting into these equations the hole masses and the valence band offset. For each state only one envelope $\Phi_i(z)$ is nonzero so that the heavy-hole states are characterized

by the angular momentum component $J_z = \pm 3/2$ whereas, for the lh states, $J_z = \pm 1/2$. Therefore, one has

$$\begin{aligned} \Psi_{hh\nu,\pm 3/2}(\boldsymbol{r}) &= \varphi_{hh\nu}(z)\,|3/2, \pm 3/2\rangle\,, \\ \Psi_{lh\nu,\pm 1/2}(\boldsymbol{r}) &= \varphi_{lh\nu}(z)\,|3/2, \pm 1/2\rangle\,, \end{aligned} \tag{2.36}$$

where the envelopes $\varphi_{hh\nu}(z), \varphi_{lh\nu}(z)$ are given by (2.8, 2.13).

For nonzero values of the in-plane wave vector $\boldsymbol{k}_\parallel$, the off-diagonal terms of the Luttinger Hamiltonian mix the heavy- and light-hole states and give rise to large nonparabolicities of the hole subbands [2.9–2.14]. In QWs with perfect interfaces, the in-plane motion may be factorized out of the envelope function

$$\boldsymbol{\Phi}(\boldsymbol{r}) = \mathrm{e}^{\mathrm{i}(k_x x + k_y y)}\boldsymbol{F}(z)\,, \tag{2.37}$$

where $\boldsymbol{F}$ is a four-component column, z and $\boldsymbol{k}_\parallel$-dependent. With no magnetic field, the solutions of (2.33) at each subband $hh\nu, lh\nu$ and in-plane wave vector $\boldsymbol{k}_\parallel$ are twofold degenerate. It is accepted to label the hole subbands as $E_{hh\nu,\boldsymbol{k}_\parallel}, E_{lh\nu,\boldsymbol{k}_\parallel}$ referring to the subband index $hh\nu$ or $lh\nu$ at $\boldsymbol{k} = 0$.

In symmetrical QWs, it is possible to classify the two degenerate states by a parity number $p = \pm$ under the mirror reflection $z \to -z$. It follows then that, for the hole state with parity p, the four-component envelope $\boldsymbol{F}(z)$ can be presented as [2.11, 2.13]

$$\boldsymbol{F}_p(z) = \begin{bmatrix} F_{3/2,p}(z) \\ F_{1/2,-p}(z) \\ F_{-1/2,p}(z) \\ F_{-3/2,-p}(z) \end{bmatrix}\,. \tag{2.38}$$

Particularly, this means that, if the component $F_{3/2,p}$ is even ($p = +$), then the component $F_{1/2,-p}$ is odd. In other words, the mth component of the column $\boldsymbol{F}_p(z)$ has parity p_m given by

$$p_m = (-1)^{3/2-m}\,p\,.$$

The fact that the Luttinger Hamiltonian is invariant under both time and space inversion allows to relate the even and odd solutions with the same $\boldsymbol{k}_\parallel$ by

$$\Psi_-(\boldsymbol{r}) = \hat{J}\hat{\mathcal{K}}\Psi_+(\boldsymbol{r})\,. \tag{2.39}$$

Here it is assumed that the time inversion operator $\hat{\mathcal{K}}$ acts both on the envelopes $\Phi_m(\boldsymbol{r})$ and the Bloch functions $|\Gamma_8, m\rangle$ whereas the space inversion operator $\hat{J}$ acts only on the envelopes, $\hat{J}\Phi_m(\boldsymbol{r}) = \Phi_m(-\boldsymbol{r})$. The operator $\hat{\mathcal{K}}$ is defined by

$$\hat{\mathcal{K}}u = -\mathrm{i}\sigma_y u^*\,, \tag{2.40}$$

where u is an arbitrary spinor function and σ_y is the Pauli matrix. In particular,

$$\hat{\mathcal{K}}\,|\Gamma_8,3/2\rangle = -\,|\Gamma_8,-3/2\rangle\ ,\ \hat{\mathcal{K}}\,|\Gamma_8,1/2\rangle = |\Gamma_8,-1/2\rangle\ , \qquad (2.41)$$
$$\hat{\mathcal{K}}\,|\Gamma_8,-1/2\rangle = -\,|\Gamma_8,1/2\rangle\ ,\ \hat{\mathcal{K}}\,|\Gamma_8,-3/2\rangle = |\Gamma_8,3/2\rangle\ .$$

A typical calculated hole energy spectrum is illustrated in Fig. 2.2 for a $GaAs/Al_{0.5}Ga_{0.5}As$ QW of the width $a = 200$ Å. Neglecting the off-diagonal terms in the Luttinger Hamiltonian, i.e., neglecting the heavy-light-hole hybridization, the $hh\nu$ and $lh\nu$ hole subbands are parabolas, see (2.25),

$$E_{hh\nu\boldsymbol{k}_\parallel} = E^0_{hh\nu} + \left(|A| + \frac{|B|}{2}\right) k_\parallel^2 \quad \text{and} \quad E_{lh\nu\boldsymbol{k}_\parallel} = E^0_{lh\nu} + \left(|A| - \frac{|B|}{2}\right) k_\parallel^2\,,$$

where $E^0_{j\nu} = E_{j\nu,k_\parallel=0}$ ($j = hh, lh$). The valence-subband coupling leads to anticrossing of these parabolic subbands and even to nonmonotonical dispersion for some of them. The nonparabolicity in the $hh2, lh1$ subbands is considerably larger than that in the $hh1$ subband because of the mutual repulsion of the $hh2, lh1$ subbands arising from the small energy separation between them.

The boundary conditions (2.34) ignore the anisotropy of chemical bonds at an interface. In fact, the point symmetry of a perfect GaAs/AlAs(001) interface, or of a CA/C′A′(001) interface between the zinc-blende-lattice semiconductors CA and C′A′, is C_{2v}. For this point group, the heavy-hole (hh) and light-hole (lh) states at $\boldsymbol{k}_\parallel = 0$ transform according to equivalent spinor representations and, hence, interface-induced lh-hh mixing is allowed even for zero in-plane wave vector. In [2.16, 2.17] this kind of mixing was postulated by including additional terms in the boundary conditions for the hole envelope functions. In a matrix form, the proposed boundary conditions for the envelopes $F_m(z)$ at $k_\parallel = 0$ are written as

$$\boldsymbol{F}_{\rm A} = \boldsymbol{F}_{\rm B}\ ,\ (\hat{v}_z\boldsymbol{F})_{\rm A} = (\hat{v}_z\boldsymbol{F})_{\rm B} - {\rm i}\frac{2}{\sqrt{3}}\frac{\hbar}{a_0 m_0} t_{l\text{-}h}\{J_x J_y\}_s \boldsymbol{F}_{\rm B}\ , \qquad (2.42)$$

where $x \parallel [100], y \parallel [010]$ The prefactor with Planck's constant $\hbar$, free electron mass m_0 and the lattice constant a_0 (assumed to be the same for CA and C′A′) is introduced to characterize the lh-hh mixing by the dimensionless real parameter $t_{l\text{-}h}$. The mixing under consideration has a nonrelativistic nature and is due to the interface-induced mixing of $|X\rangle$ and $|Y\rangle$ orbital Bloch functions under normal hole incidence. In [2.18] a tight-binding model has been used to relate the microscopic parameters with the coefficient $t_{l\text{-}h}$. The tight-binding estimation of $t_{l\text{-}h} = 0.44$ is in reasonable agreement with experiment on anisotropic exchange splitting of excitonic levels in type-II GaAs/AlAs SLs (Sect. 5.5.1). The additional term in the boundary conditions (2.42) plays a decisive role in the formation of interface optical anisotropy of heterostructures with no common atom (Sect. 3.1.7) and a large role in the quantum-confined Pockels effect (Sect. 3.4.3). Different theoretical aspects of the heavy-light-hole mixing at zinc-blende (001) interfaces under normal hole incidence were also analyzed in [2.19–2.26].

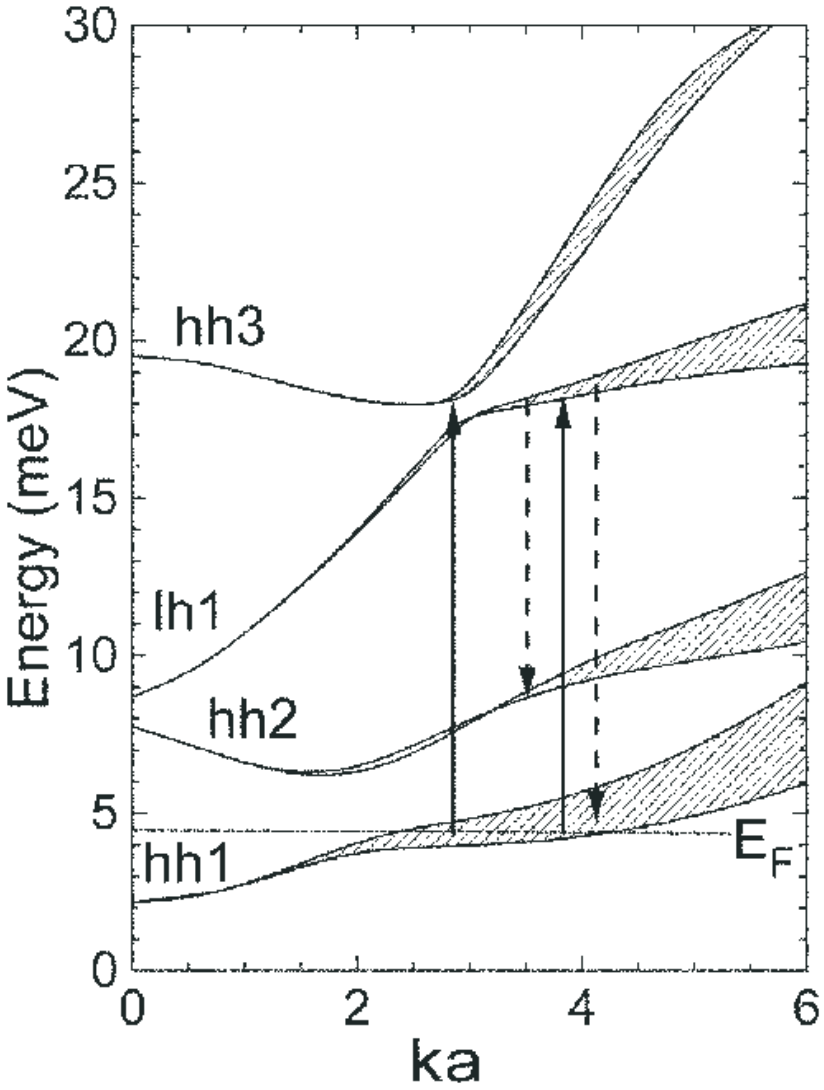

Fig. 2.2. Calculated in-plane energy dispersion of holes for the top-most valence subbands in a GaAs/$Al_{0.5}Ga_{0.5}As$ QW of the thickness $a = 200$ Å. The horizontal dashed-and-dotted line indicates the Fermi level position, E_F, corresponding to the 2D hole density $p_s = 2 \times 10^{11}$ cm^{-2}. The vertical arrows illustrate direct optical transitions accompanied by photon absorption (*solid*) or emission (*dashed*). The shaded areas demonstrate the anisotropy of the hole energy spectrum: the curves bounding these areas correspond to the dispersion along the [100] and [110] in-plane directions. From [2.15].

2.1.3 Effect of Nonparabolicity on the Confinement Energy

Effects of energy dispersion in bulk constituent semiconductors on quantum confinement of electrons and holes in nanostructures are naturally taken into account in multiband envelope-function theories. In a N-band model, the electron wave function is presented, similarly to (2.32), as a sum

$$\Psi(\boldsymbol{r}) = \sum_{n=1}^{N} \Phi_n(\boldsymbol{r})\, |n\rangle\,, \tag{2.43}$$

where $|n\rangle$ are the Bloch functions at the extremum point, here the Γ-point $\boldsymbol{k} = 0$, and N equals the number of involved basic states $|n\rangle$. The model effective Hamiltonian $\mathcal{H}(\boldsymbol{k})$ is a $N \times N$ matrix divided into three parts: the diagonal matrix $\mathcal{H}^{(0)}$ containing the energies E_n^0 at $\boldsymbol{k} = 0$, the matrix $\mathcal{H}^{(1)}$ describing the $\boldsymbol{k}\cdot\boldsymbol{p}$ and spin-orbit coupling between the chosen set $|n\rangle$ that is treated exactly, and the matrix $\mathcal{H}^{(2)}$ which takes into account by perturbation theory the coupling between the chosen set and remaining (remote) Bloch states. Among different $\boldsymbol{k}\cdot\boldsymbol{p}$ models used for description of electronic states, it is worth to mention (i) the 6×6 Luttinger model, $\Gamma_8^v + \Gamma_7^v$, of the coupled Γ_8 and Γ_7 valence bands [2.8, 2.27, 2.28], (ii) the Kane model [2.29–2.32] with a 8×8 Hamiltonian acting in the eightfold space $\Gamma_6^c + \Gamma_8^v + \Gamma_7^v$ of the conduction states Γ_6 and the valence states Γ_8, Γ_7, and (iii) the 14-band model [2.33–2.35] with a Hamiltonian $\mathcal{H}_{14\times14}$ acting in the space of states in the $\Gamma_6, \Gamma_8, \Gamma_7$ conduction bands and Γ_8, Γ_7 valence bands. Here we will apply the Kane model to demonstrate strengths of the multicomponent envelope-function theories and go beyond the parabolic-band approximation in calculations of conduction-band states.

The 8-band Kane model applied here explicitly takes into consideration the $\boldsymbol{k}\cdot\boldsymbol{p}$ mixing between the lowest conduction band Γ_{6c} and the highest valence-band Γ_{8v}, Γ_{7v} states and ignores coupling with other bands, $\mathcal{H}^{(2)} = 0$. Following Suris [2.36] we present the electron wave function in the form

$$\Psi = u\, S + v_x\, X + v_y\, Y + v_z\, Z\,, \tag{2.44}$$

where $u(\boldsymbol{r})$ and $\boldsymbol{v}(\boldsymbol{r})$ are scalar and vector spinor envelope functions. In terms of u and $\boldsymbol{v}$, the Schrödinger equation is conveniently written as follows

$$Eu = -\mathrm{i}P\,\hat{\boldsymbol{k}}\cdot\boldsymbol{v}\,, \tag{2.45}$$

$$\left(E + E_g + \frac{\Delta}{3}\right)\boldsymbol{v} = \ \mathrm{i}P\,\hat{\boldsymbol{k}}u + \mathrm{i}\frac{\Delta}{3}\,\boldsymbol{\sigma}\times\boldsymbol{v}\,.$$

Here E is the electron energy referred to the conduction band bottom Γ_6, $\hat{\boldsymbol{k}} = -\mathrm{i}\nabla$, E_g is the band gap, Δ is the spin-orbit splitting of the valence band and

$$P = \mathrm{i}\frac{\hbar p_{cv}}{m_0}\,,\ p_{cv} = \langle S|\hat{p}_z|Z\rangle\,. \tag{2.46}$$

By using the second equation of (2.45) one can express the vector spinor $\boldsymbol{v}$ via the gradient ∇u as

$$P\boldsymbol{v} = \frac{\hbar^2}{2m(E)}\nabla u - \mathrm{i}\frac{\hbar^2}{4m_0}[g(E) - g_0](\boldsymbol{\sigma} \times \nabla)u \,, \tag{2.47}$$

where

$$\frac{1}{m(E)} = \frac{2}{3}\frac{P^2}{\hbar^2}\left(\frac{2}{E_g + E} + \frac{1}{E_g + E + \Delta}\right) \,, \tag{2.48}$$

$$g(E) = g_0 - \frac{4}{3}\frac{m_0 P^2}{\hbar^2}\frac{\Delta}{(E_g + E)(E_g + E + \Delta)} \,.$$

Substituting (2.47) into the first equation of (2.45) we naturally come to a second-order differential equation for the conduction-band envelope

$$\frac{\hbar^2\hat{\boldsymbol{k}}^2}{2m(E)}\, u = E\, u \,. \tag{2.49}$$

Therefore, in a bulk material the electron dispersion equation is

$$2m(E)E = \hbar^2 k^2$$

or

$$E(E + E_g)(E + E_g + \Delta) = P^2 k^2 \left(E + E_g + \frac{2}{3}\,\Delta\right) \,. \tag{2.50}$$

Note that $m^{-1}(0)$ and the difference $g(0) - g_0$ describe the valence-band $\boldsymbol{k}\cdot\boldsymbol{p}$ contributions to the inverse effective mass and the g factor at the bottom of the conduction band (Sect. 5.3.3). Expanding the energy of the conduction band, $E_c(k)$, to k^4 we obtain from (2.50)

$$E_c(k) \approx \frac{\hbar^2 k^2}{2m^*}\left(1 - \frac{3 - 2\eta + \eta^2}{3 - \eta}\,\frac{\hbar^2 k^2}{2m^* E_g}\right) \,, \tag{2.51}$$

where $m^* = m(0)$ and $\eta = \Delta/(E_g + \Delta)$. It should be mentioned that in (2.45) the term $\hbar^2 k^2/(2m_0)$ is dropped because it is comparable with the contribution of neglected remote bands. The generalized Kane model contains this dropped term as well as the quadratic-in-$\boldsymbol{k}$ term $\mathcal{H}^{(2)}$. However, this modification deprives the model of its main asset, namely, the possibility of expressing all spectral parameters in terms of a limited number of the model constants.

The simplest boundary conditions for the envelope functions are the continuity of the spinor $u(\boldsymbol{r})$ and of the normal component of the vector $P\boldsymbol{v}(\boldsymbol{r})$ at the interfaces. For a QW structure with the growth axis along z, they reduce to

$$u_{\mathrm{A}} = u_{\mathrm{B}} \,,\; P_{\mathrm{A}}\,(v_z)_{\mathrm{A}} = P_{\mathrm{B}}\,(v_z)_{\mathrm{B}} \,, \tag{2.52}$$

where $P_{\rm A}, P_{\rm B}$ are values of P in materials A and B. One should bear in mind that if the energy E is referred to the conduction band bottom in the material A then, for the material B, the variable E in (2.45, 2.48, 2.49) must be replaced by $E - E_c^{\rm B}$. The more general form of boundary conditions in the Kane model is analyzed in [2.37] (see also [2.38]).

For the states at $k_{x,y} = 0$, spinor solutions of (2.48) can be presented in the form

$$u_s(z) = f(z)\, c_s, \tag{2.53}$$

where $f(z)$ is a scalar function and $c_{1/2} = \uparrow$, $c_{-1/2} = \downarrow$ are the spin-up and spin-down columns, respectively. In this case the boundary conditions take the form

$$f_{\rm A} = f_{\rm B}\ ,\ \frac{1}{m_{\rm A}(E)} \left(\frac{df}{dz}\right)_{\rm A} = \frac{1}{m_{\rm B}(E)} \left(\frac{df}{dz}\right)_{\rm B} \tag{2.54}$$

which differs from the Bastard conditions (2.10) by using the energy-dependent (nonparabolic) effective masses instead of those at the conduction band bottoms, $m_{\rm A}$ and $m_{\rm B}$. Hence, the electron quantum-confinement energy at $k_x = k_y = 0$ satisfies the transcendental equations (2.12) and (2.14) where the fixed parameters $m_{\rm A}, m_{\rm B}$ are replaced by the energy-dependent functions $m_{\rm A}(E), m_{\rm B}(E)$.

2.2 Electron States in Quantum Wires and Nanotubes

In a QW, a free carrier can freely move in two directions. From this a QW structure is said to be a 2D system, or a quasi-2D system taking into account that the size-quantized states have a finite extension in the third direction as well. Now we turn to a brief overview of electron states in QWRs, or systems of the dimensionality $d = 1$, where the free motion is possible only in one direction.

2.2.1 Cylindrical and Rectangular Quantum Wires

In this subsection we consider the kind of QWRs in which one material, A, is surrounded by another material, B. In the effective mass approximation, the 1D-electron envelope function is written in the factorized form

$$\psi(\boldsymbol{r}) = \frac{1}{\sqrt{L}}\, {\rm e}^{{\rm i}k_z z} \varphi(x, y)\ , \tag{2.55}$$

where z if the QWR principal axis and L is its length. Sometimes, they use the cylindrical coordinates, $\rho = \sqrt{x^2 + y^2}$ and ϕ (the azimuth angle), rather than x, y. For QWRs, the boundary conditions (2.10) are changed to

$$\varphi_{\rm A} = \varphi_{\rm B}\ ,\ \frac{1}{m_{\rm A}} \left(\boldsymbol{N} \cdot \nabla\varphi\right)_{\rm A} = \frac{1}{m_{\rm B}} \left(\boldsymbol{N} \cdot \nabla\varphi\right)_{\rm B}\ , \tag{2.56}$$

where $\boldsymbol{N}$ is the normal to the dividing surface between materials A and B.

In a *cylindrical QWR*, the electron states are characterized by a particular z-component, M, of the angular momentum. For the axially-symmetric states with $M = 0$, the function $\varphi(x, y) \equiv \varphi(\rho)$ is expressed via the Bessel functions $\mathrm{J}_0(x)$ and $\mathrm{K}_0(x)$ as follows

$$\varphi(x, y) = \begin{cases} C\,\mathrm{J}_0(k\rho)\,, & \text{if} \quad \rho \le R\,, \\ D\,\mathrm{K}_0(æ\rho)\,, & \text{if} \quad \rho \ge R\,, \end{cases} \tag{2.57}$$

where R is the wire radius, k and æ are related with the energy E by the equations

$$k = \left(\frac{2m_{\mathrm{A}}E}{\hbar^2} - k_z^2\right)^{1/2}\,,\ æ = \left(\frac{2m_{\mathrm{B}}(V-E)}{\hbar^2} + k_z^2\right)^{1/2} \tag{2.58}$$

similar to (2.7). Taking into account (2.56) we have $D = C\mathrm{J}_0(kR)/\mathrm{K}_0(æR)$ and come to the following equation for the electron energy

$$\frac{\mathrm{J}_1(kR)\mathrm{K}_0(æR)}{\mathrm{J}_0(kR)\mathrm{K}_1(æR)} = \frac{æ\,m_{\mathrm{A}}}{k\,m_{\mathrm{B}}}\,. \tag{2.59}$$

In a QWR with an infinite confining potential, when the wave function at the boundary can be set to zero, this equations reduces to $\mathrm{J}_0(kR) = 0$. The first three zeros of the function $\mathrm{J}_0(x)$ are 2.405, 5.520 and 8.654.

Let us now consider a less symmetrical QWR, namely, a QWR with the rectangular cross-section $a_x \times a_y$ along the axes x and y. In structures with infinitely high barriers, one has

$$\varphi(x, y) = \varphi_{\nu_x}(x; a_x)\varphi_{\nu_y}(y; a_y)\,, \tag{2.60}$$

where

$$\varphi_\nu(x; a) = \sqrt{\frac{2}{a}} \begin{cases} \cos(\nu\pi x/a) & \text{for odd } \nu\,, \\ \sin(\nu\pi x/a) & \text{for even } \nu\,. \end{cases} \tag{2.61}$$

Each electron subband is labelled by two quantum numbers ν_x, ν_y. The energy of an electron in the state (ν_x, ν_y, k_z) is given by

$$E_{e\nu_x\nu_y k_z} = \frac{\hbar^2}{2m_{\mathrm{A}}}\left[\left(\frac{\nu_x\pi}{a_x}\right)^2 + \left(\frac{\nu_y\pi}{a_y}\right)^2 + k_z^2\right]\,. \tag{2.62}$$

In the Kane model the electron states are described by the scalar and vector envelopes, u and $\boldsymbol{v}$, satisfying equations (2.47, 2.49) and boundary conditions

$$u_{\mathrm{A}} = u_{\mathrm{B}}\,,\ P_{\mathrm{A}}\,(\boldsymbol{N}\cdot\boldsymbol{v})_{\mathrm{A}} = P_{\mathrm{B}}\,(\boldsymbol{N}\cdot\boldsymbol{v})_{\mathrm{B}}\,. \tag{2.63}$$

One can present the spinor wave function $u(\boldsymbol{r})$ in the general form as

$$u_s(\boldsymbol{r}) = [f(\boldsymbol{r}) + \mathrm{i}\,\sigma_\alpha h_\alpha(\boldsymbol{r})]\,c_s\,, \tag{2.64}$$

where c_s ($s = \pm 1/2$) are the spin-up and spin-down states and, for $k_z = 0$, $f(\boldsymbol{r}), h_\alpha(\boldsymbol{r})$ are real functions. Symmetry of a nanoheterosystem imposes restrictions on coordinate dependence of these functions. In particular, in cylindrical wires, $f(\boldsymbol{r}) \equiv f(\sqrt{x^2+y^2})$ while the three functions $h_\alpha(\boldsymbol{r})$ are identically equal to zero because there exist no polynomials $\sum_{l,m} C_{l,m} x^l y^m$ which transform as pseudovector components with respect to operations from the point group $D_{\infty h}$. Taking into account the nonparabolicity in the Kane model, the equation for the electron energy in the state with $M = 0$ is obtained from (2.59) by substituting $m_{\rm A}(E), m_{\rm B}(E)$ instead of $m_{\rm A}, m_{\rm B}$.

For the conduction-electron state at the lowest-subband bottom $k_z = 0$ in a rectangular QWR, the envelopes $u, \boldsymbol{v}$ are independent of z and, hence,

$$f(\boldsymbol{r}) \equiv f(\boldsymbol{\rho}) = f(x^2, y^2)\ ,\ h_z(\boldsymbol{\rho}) = xyM(x^2, y^2)\ ,\ h_x(\boldsymbol{r}) \equiv h_y(\boldsymbol{r}) \equiv 0. \quad (2.65)$$

In the case of a quadratic cross section, one has

$$h_z(\boldsymbol{\rho}) = xy(x^2 - y^2)F(x^2, y^2)\ , \quad (2.66)$$

where $F(x^2, y^2) = F(y^2, x^2)$. The continuous envelopes $f(\boldsymbol{\rho})$ and $h(\boldsymbol{\rho}) \equiv h_z(\boldsymbol{\rho})$ satisfy equation (2.49), they are coupled at the interfaces by the continuity condition for the normal component of the spinor vector $P\boldsymbol{v}$ related to ∇u by (2.47). This condition imposes the continuity requirement on the two following linear combinations of the derivatives ∇f and ∇h:

$$\begin{aligned} &\mu\left(N_x\frac{\partial f}{\partial x} + N_y\frac{\partial f}{\partial y}\right) - \frac{G}{2}\left(N_x\frac{\partial h}{\partial y} - N_y\frac{\partial h}{\partial x}\right), \\ &\mu\left(N_x\frac{\partial h}{\partial x} + N_y\frac{\partial h}{\partial y}\right) + \frac{G}{2}\left(N_x\frac{\partial f}{\partial y} - N_y\frac{\partial f}{\partial x}\right)\ , \end{aligned} \quad (2.67)$$

where N_x, N_y are components of the 2D unit vector $\boldsymbol{N}$ normal to the A/B boundary, and $\mu = m_0/m(E)$, $G = g(E) - g_0$. In [2.39] the ground-state solutions $|e11, s\rangle$ of (2.49) in a wire of the cross section $2a \times 2b$ were calculated using the free relaxation technique described in [2.40]. The envelopes $f(\boldsymbol{\rho})$ and $h(\boldsymbol{\rho})$ calculated for the GaAs/$Al_{0.35}Ga_{0.65}$As QWR 80 Å × 120 Å are shown in Fig. 2.3 as contour maps. The origin of the coordinate system (x, y) is chosen in the wire center. Due to the rectangular symmetry, see (2.65), it is enough to present the variation of f and h only in the quadrant $x, y > 0$. The function $f(x, y)$ has the maximum value $f_{\max} \approx 7 \times 10^{-3}$ at the center and monotonously decreases with increasing the radial distance ρ. In accordance with (2.65) the function $h(x, y)$ is zero if $x = 0$ or $y = 0$. It follows from (2.66) that for coinciding a and b this function should vanish also at the diagonal $x = y$ and have opposite signs at the points (x, y) and (y, x). One can see in Fig. 2.3 areas of opposite signs in the map of $h(x, y)$ in spite of a remarkable difference between a and b. As a result, in every quadrant the function $h(x, y)$ exhibits a maximum and a minimum. As compared with $f_{\max}$, the extremum values of $h(x, y)$ are smaller by three orders of magnitude.

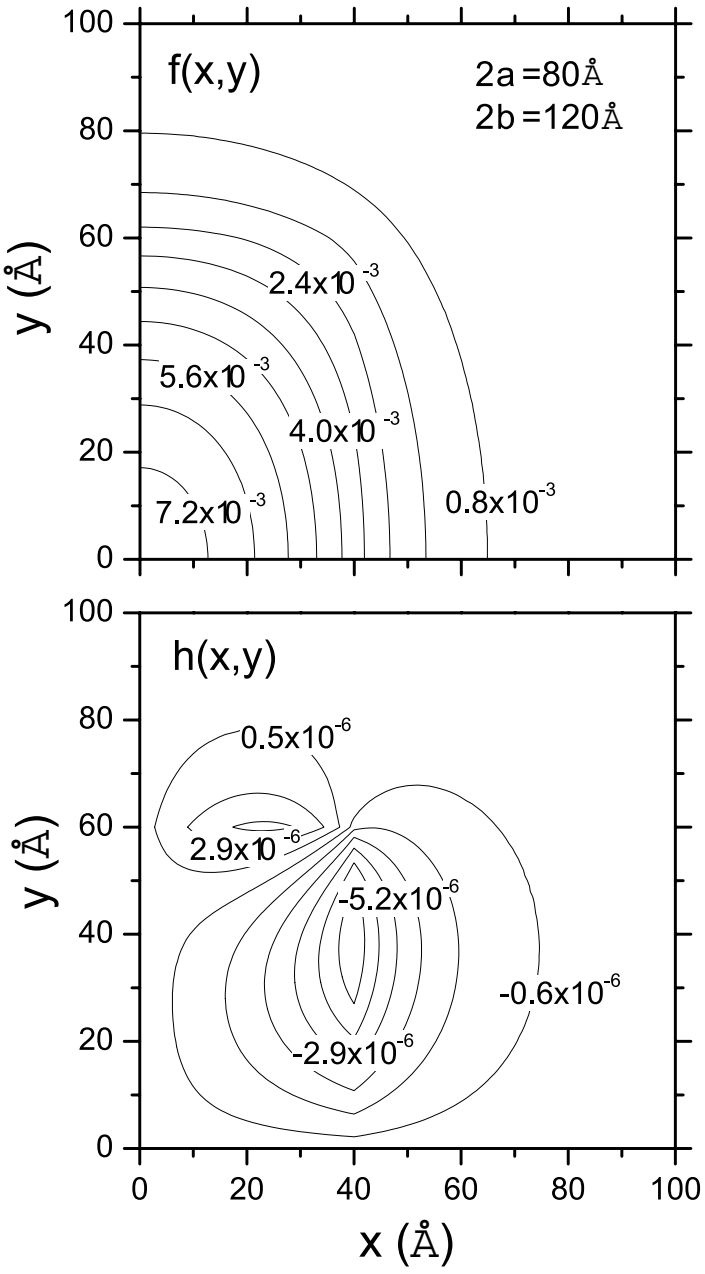

Fig. 2.3. Contour plots of the envelopes $f(x, y)$ and $h(x, y)$ for the electron lowest subband $e1$ (at the bottom, $k_z = 0$) in a $2a \times 2b$ rectangular GaAs/AlGaAs QWR with $a = 40$ Å and $b = 60$ Å. [2.39]

In QWRs with a confining potential of complicated shape, e.g., in V-shaped QWRs, the electron and hole states are calculated by direct solution of the full 2D Schrödinger equation, see [2.41].

2.2.2 T-shaped Quantum Wires

We consider a T-shaped QWR consisting of a cleaved QW of the thickness a and an overgrown QW of the thickness b, see inset in Fig. 2.4a. As compared to the QWR structures discussed in the previous subsection, the confining potential in T-shaped wires has openings so that free carriers are classically unbounded in such structures. However, the quantum mechanics allows formation of bound electron or hole states at the T intersection. The binding energy, ε_{1D}, of a 1D state is defined as an energy difference $E_{e1}(\max\{a,b\}) - E_{1D}$ between the lowest 2D-electronic state in the wider QW and the 1D-state under consideration. Here $E_{e1}(a)$ is the $e1$-subband quantum-confinement energy in a single QW of the thickness a. The solid line in Fig. 2.4a shows the calculated dependence of the energy of the lowest wire-like electron state on the width b at fixed $a = 50$ Å in the T-shaped $GaAs/Al_{0.35}Ga_{0.65}As$ structure. Physically, it is clear that, with changing the width b, the electron wave function is redistributed between the cleaved and overgrown QWs. For $b \to 0$, the energy E_{1D} asymptotically approaches that of a 2D electron in the overgrown well (indicated in Fig. 2.4a by the dotted horizontal line). In the opposite case, with b increasing and becoming much larger than a, the electron penetrates more and more into the cleaved well and $E_{1D} \to E_{e1}(b)$. The binding energy ε_{1D} is represented in the figure by the dashed line. Note that ε_{1D} is not an analytical function of b since at the point $b = a$ the meaning of the lowest 2D state changes. It is this point at which the binding energy, or the $2D$-$1D$ separation, reaches a maximum. According to Kiselev and Rössler [2.42], this simple criterion, i.e., the equality of the minimum energy values of 2D states in cleaved and overgrown QWs, can be applied to much more complex structures fabricated by the cleaved edge overgrowth technique. The probability density of the lowest electron states in the QRW with $a = b = 70$ Å is shown in Fig. 2.4b.

Some modifications of the conventional T-shaped structure can lead to an enhanced $2D$-$1D$ separation. One of the possibilities is the double T-shaped structure where two individual intersections are close enough to each other to permit 'bonding' and 'antibonding' 1D states. It is interesting to compare the tunnelling exponents that govern the coupling of 2D states in the cleaved QWs and of 1D states in the double T-shaped structure. According to (2.7), for the former coupling, it is $\exp(-æ_{2D}L_b)$ with L_b being the width of the barrier layer between two cleaved QWs and

$$æ_{2D} = \sqrt{2m_{\mathrm{B}}(V - E_{e1})/\hbar^2}\,.$$

The similar quantity $\exp(-æ_{2D}L_b)$ for the wire-like states is represented by

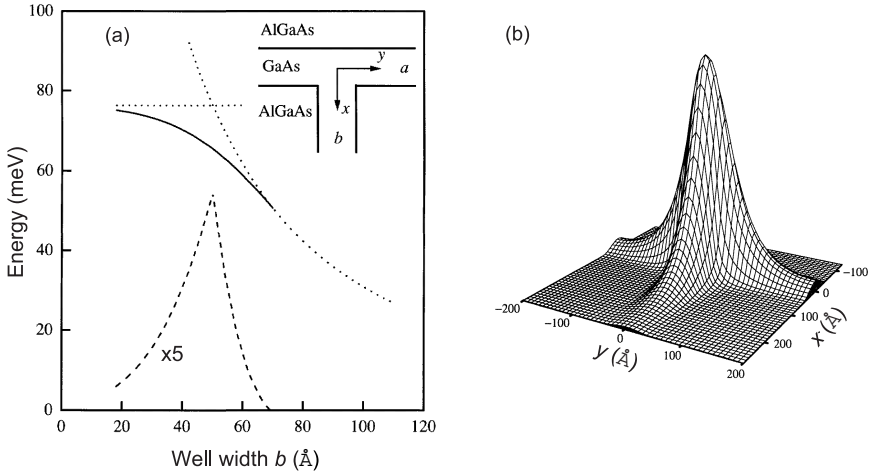

Fig. 2.4. (**a**) The dependence of the energy of the lowest electron state in a $GaAs/Al_{0.35}Ga_{0.65}As$ T-shaped structure (shown in inset) on the width b of the cleaved QW (*solid*) for a fixed width of the overgrown QW, $a = 50$ Å. The quantum-confinement energies of the lowest electron states $e1$ in the cleaved and overgrown QWs are represented by dotted lines. The 2D-1D difference is shown as a dashed line. (**b**) The electon probability density for the wire-like electron state in the structure with $a = b = 70$ Å. From [2.42].

$$æ_{1D} = \sqrt{2m_{\mathrm{A}}(E_{e1} - E_{1D})/\hbar^2}\,.$$

Thus, there is a range of barrier widths L_b where coupling of well states is negligible and, at the same time, the interaction of the wire-like states is strong.

Langbein et al. [2.43] calculated and optimized the confinement energies for electrons and holes in T-shaped QWRs using the effective-mass approximation for the simple conduction band and the six-band envelope-function theory (the Luttinger model) for the valence bands Γ_8, Γ_7. They showed that the conduction-band 1D state is confined more or less equally in different arms of the T-intersection, while the lowest valence-band state is more extended along the overgrown QW. This is a direct consequence of the isotropic conduction-band mass and the anisotropic valence-band mass. Moreover, due the large and anisotropic hole effective mass, the 1D valence-band states are only weakly bound at the T-shaped intersection.

Calculations of bound states in other opened QWR structures can be found in [2.44] (H-shaped structure, or double QW connected by a bridge grown from the well material), [2.45, 2.46] (barrier-modulated wires), [2.47] (L-shaped QWRs).

2.2.3 Carbon Nanotubes

We recall that a carbon nanotube is conceivable as a single hexagonal layer cut and rolled up into a cylinder. Thus, we start from the electron structure of a 2D graphite, or graphene. The carbon atoms in a graphene plane form a bipartite hexagonal lattice which can be divided into two sublattices A and B. The 2D basis vectors with the angle 120° between them can be defined by

$$\boldsymbol{a} = a(1,0)\ ,\ \boldsymbol{b} = a\left(-\frac{1}{2}, \frac{\sqrt{3}}{2}\right)\ , \tag{2.68}$$

where a is the lattice constant equal $\sqrt{3}$ times the interatomic distance $d = 1.44$ Å [2.48], and the coordinate system x, y in (2.68) is chosen in such a way that $x \parallel \boldsymbol{a}$, $y \perp \boldsymbol{a}$ and $b_y > 0$. The 2D reciprocal lattice is also hexagonal with the first Brillouin zone being a hexagon (Fig. 2.5).

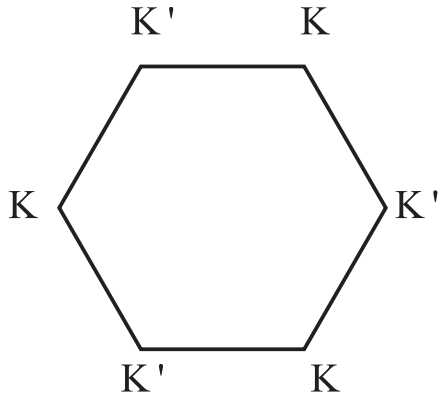

Fig. 2.5. 2D Brillouin zone of graphene.

We choose one of the B sites as the origin (0,0) of the coordinate system. Its three nearest A neighbors are located at the points

$$\boldsymbol{r}_1 = \frac{a}{\sqrt{3}}(0,-1)\ ,\ \boldsymbol{r}_2 = \frac{a}{\sqrt{3}}\left(\frac{\sqrt{3}}{2}\ ,\frac{1}{2}\right)\ ,\ \boldsymbol{r}_3 = \frac{a}{\sqrt{3}}\left(-\frac{\sqrt{3}}{2}\ ,\frac{1}{2}\right)\ . \tag{2.69}$$

In the tight-binding theory, the electron wave function in the state with the wave vector $\boldsymbol{k}$ is written as

$$\psi_{\boldsymbol{k}}(\boldsymbol{r}) = \sum_{\boldsymbol{R}\alpha} C_\alpha(\boldsymbol{k}) \exp\left[\mathrm{i}\boldsymbol{k}\cdot(\boldsymbol{R}+\boldsymbol{\tau}_\alpha)\right]\phi(\boldsymbol{r}-\boldsymbol{R}-\boldsymbol{\tau}_\alpha)\ . \tag{2.70}$$

Here $\boldsymbol{R}$ is the 2D translational vector which enumerates the unit cells, α enumerates two carbon atoms in the unit cell belonging to the sublattices

A and B, $\boldsymbol{\tau}_\alpha$ is the position of the atom α within the unit cell and $\phi(\boldsymbol{r})$ is an atomic π orbital. The coefficients $C_{\rm A}(\boldsymbol{k})$ and $C_{\rm B}(\boldsymbol{k})$ written as a two-component column $\hat{C}(\boldsymbol{k})$ satisfy the following matrix equation

$$\mathcal{H}\hat{C} = E\hat{C}\,,$$

where, in the nearest-neighbor approximation, the 2×2 effective Hamiltonian is given by

$$\mathcal{H} = \begin{bmatrix} E_0 & h^* \\ h & E_0 \end{bmatrix}\,, \qquad h(\boldsymbol{k}) = \gamma_0 \sum_{n=1}^{3} \exp\left(\mathrm{i}\boldsymbol{k}\cdot\boldsymbol{r}_n\right)\,, \tag{2.71}$$

γ_0 is the nearest-neighbor transfer integral, E_0 is the diagonal energy which in the following is set to zero. Substituting $\boldsymbol{r}_n$ from (2.69) into the exponents one obtains [2.49, 2.50]

$$h = \gamma_0 \left(\mathrm{e}^{-\mathrm{i}k_y a/\sqrt{3}} + 2\mathrm{e}^{\mathrm{i}k_y a/2\sqrt{3}} \cos\frac{k_x a}{2}\right)\,. \tag{2.72}$$

The energy dispersion is given by $E_\pm(\boldsymbol{k}) = \pm|h(\boldsymbol{k})|$. An important point is that the energy equals zero at each vortex of the 2D Brillouin zone (points K and K'), particularly at the left and right vortices

$$\boldsymbol{K} = \frac{4\pi}{3a}\,(-1,0)\,,\ \boldsymbol{K}' = \frac{4\pi}{3a}\,(1,0)\,. \tag{2.73}$$

Near these points the dispersion is linear, namely, $E_\pm(\boldsymbol{k}\approx\boldsymbol{K}) = \pm\gamma|\boldsymbol{k}-\boldsymbol{K}|$. At zero temperature the states with negative energies are occupied (valence band) whereas those with positive energies are empty (conduction band). Thus, a graphene is a zero-gap 2D crystal in the sense that the conduction and valence bands consisting of π states touch at the K and K' points.

Turning now to carbon nanotubes we write the circumferential vector as

$$\boldsymbol{L} = n_a\boldsymbol{a} + n_b\boldsymbol{b}\,, \tag{2.74}$$

where n_a, n_b are integers, and expand the electron effective Hamiltonian for a graphene sheet in the vicinity of the points $\boldsymbol{K}$ and $\boldsymbol{K}'$ [2.51, 2.52]. In the following we define $\boldsymbol{k}$ and $\boldsymbol{k}'$ as wave vectors referred respectively to the points $\boldsymbol{K}$ and $\boldsymbol{K}'$ and assume the products $ka, k'a \ll 1$ to be small. Then, in the second order in ka or $k'a$, the nondiagonal matrix element (2.72) of the Hamiltonian $\mathcal{H}$ is given by (see [2.53, 2.54])

$$h(\boldsymbol{k},\boldsymbol{K}) = \gamma\mathrm{e}^{-\mathrm{i}\theta}\left[k_\perp - \mathrm{i}k_z + \frac{a}{4\sqrt{3}}\mathrm{e}^{3\mathrm{i}\theta}\left(k_\perp + \mathrm{i}k_z\right)^2\right] \tag{2.75}$$

near the $\boldsymbol{K}$ point and

$$h(\boldsymbol{k}',\boldsymbol{K}') = \gamma\mathrm{e}^{\mathrm{i}\theta}\left[-k'_\perp - \mathrm{i}k'_z + \frac{a}{4\sqrt{3}}\mathrm{e}^{-3\mathrm{i}\theta}\left(k'_\perp - \mathrm{i}k'_z\right)^2\right] \tag{2.76}$$

near the $\boldsymbol{K}'$ point. Here $\gamma = (\sqrt{3}/2)\gamma_0 a$, θ is the angle between the vector $\boldsymbol{L}$ and the basis vector $\boldsymbol{a}$. The subscripts $z, \perp$ indicate components of a vector referred to the axes lying in the graphene plane and related to the vector $\boldsymbol{L}$ so as $z \perp \boldsymbol{L}$ and $k_z \perp \boldsymbol{L}$, $k_\perp \parallel \boldsymbol{L}$. In the same approximation the energy spectrum near the $\boldsymbol{K}$ point is given by

$$E_{c,v}(\boldsymbol{k}, \boldsymbol{K}) = \pm|h| \tag{2.77}$$
$$\approx \pm\gamma \left\{ |\boldsymbol{k}| + \frac{a}{4\sqrt{3}|\boldsymbol{k}|} \left[\left(k_\perp^3 - 3k_\perp k_z^2\right) \cos 3\theta + \left(k_z^3 - 3k_\perp^2 k_z\right) \sin 3\theta \right] \right\} ,$$

where $|\boldsymbol{k}| = \sqrt{k_\perp^2 + k_z^2}$, the upper and lower signs represent the conduction (subscript c) and valence (subscript v) bands, respectively. The similar spectrum near the $\boldsymbol{K}'$ point is obtained by changing $k_\perp \to -k'_\perp$, $k_z \to k'_z$, $\theta \to -\theta$ in agreement with the time inversion symmetry requirement $E_{c,v}(\boldsymbol{k}, \boldsymbol{K}') = E_{c,v}(-\boldsymbol{k}, \boldsymbol{K})$.

In a carbon nanotube specified by the vector $\boldsymbol{L}$ the electron wave function satisfies the cyclic boundary condition $\Psi(\boldsymbol{r}) = \Psi(\boldsymbol{r} + \boldsymbol{L})$. This enables one to find the allowed discrete values of $k_\perp$ as

$$k_\perp = \frac{2\pi}{L}\left(n - \frac{\nu}{3}\right) \; ; \; k'_\perp = \frac{2\pi}{L}\left(n + \frac{\nu}{3}\right), \tag{2.78}$$

where n is an integer $0, \pm1, \pm2...$ characterizing the angular momentum component of an electron, $L = |\boldsymbol{L}| = a\sqrt{n_a^2 + n_b^2 - n_a n_b}$, and ν equals one of three integers: $0, \pm1$ determined by the presentation of the sum $n_a + n_b$ as $3N + \nu$ with integer N. In the effective-mass approximation, the electron envelope functions can be written in the form

$$\psi_{c,v}(z; n, k_z) = \frac{\mathrm{e}^{\mathrm{i}n\varphi}}{\sqrt{2\pi}} \, \frac{\mathrm{e}^{\mathrm{i}k_z z}}{\sqrt{L_{CN}}} \, \hat{C}_{c,v}(n, k_z) \, , \tag{2.79}$$

where L_{CN} is the nanotube length and φ is the azimuth angle. The two-component columns $\hat{C}_{c,v}$ are eigenvectors of the 2×2 matrix Hamiltonian (2.71), given by

$$\hat{C}_c = \frac{1}{\sqrt{2}} \begin{bmatrix} h^*/|h| \\ 1 \end{bmatrix} \; , \; \hat{C}_v = \frac{1}{\sqrt{2}} \begin{bmatrix} 1 \\ -h/|h| \end{bmatrix} \tag{2.80}$$

with h defined by (2.75) for the 1D K-valley and by (2.76) for the 1D K'-valley where K, K' are the z-components of the vectors $\boldsymbol{K}, \boldsymbol{K}'$.

The dispersion in the conduction and valence subbands is obtained by substituting (2.78) into (2.75, 2.76 or 2.77). In the linear approximation, the conduction and valence band spectra are given by

$$E_{c,v}(n, k_z; K) = \pm\gamma \sqrt{\left(\frac{2\pi}{L}\right)^2 \left(n - \frac{\nu}{3}\right)^2 + k_z^2} \, , \tag{2.81}$$
$$E_{c,v}(n, k'_z; K') = \pm\gamma \sqrt{\left(\frac{2\pi}{L}\right)^2 \left(n + \frac{\nu}{3}\right)^2 + {k'_z}^2} \, .$$

It turns out that, for $\nu = 0$ when $n_a + n_b$ is a multiple of 3, a carbon nanotube is gapless (metallic, or semimetallic) since the valence and conduction subbands with $n = 0$ still touch each other: $E_{c,v}(0, k_z; K) = \pm\gamma|k_z|$. For $\nu = \pm 1$, a nanotube is semiconducting with the band gap $\Delta = (4\pi\gamma/3L)$. In the following we focus on the nanotubes characterized by a finite band gap and assume $\nu \neq 0$.

According to (2.77), for small values of k_z satisfying the condition $|k_z| \ll |k_\perp|$ in the K valley and similar condition in the K' valley, the electron spectrum has a parabolic form with terms linear in k_z

$$E_{c,v}(n, k_z; K) = \pm\left(\frac{\Delta_n}{2} + \frac{\hbar^2 k_z^2}{2m_n} + \beta_n k_z\right) , \tag{2.82}$$

$$E_{c,v}(n, k_z'; K') = \pm\left(\frac{\Delta_n'}{2} + \frac{\hbar^2 k_z'^2}{2m_n'} + \beta_n' k_z'\right) ,$$

where

$$\Delta_n = 2\gamma|k_\perp| \, , \; \Delta_n' = 2\gamma|k_\perp'| \, , \tag{2.83}$$

$$m_n = \frac{\hbar^2|k_\perp|}{\gamma} \, , \; m_n' = \frac{\hbar^2|k_\perp'|}{\gamma} \, , \tag{2.84}$$

$$\beta_n = -\frac{\sqrt{3}}{4}\gamma a|k_\perp| \sin 3\theta \, , \; \beta_n' = \frac{\sqrt{3}}{4}\gamma a|k_\perp'| \sin 3\theta \, , \tag{2.85}$$

and $k_\perp, k_\perp'$ are defined in (2.78). Note that the identity $E_{c,v}(n, k_z; K') = E_{c,v}(-n, -k_z; K)$ follows directly from the time inversion symmetry.

In the presence of an external magnetic field $\boldsymbol{B}$, the electron energy is modified just by changing $k_\perp, k_\perp'$ from (2.78) into

$$k_\perp = \frac{2\pi}{L}\left(n - \frac{\nu}{3} + \frac{\Phi}{\Phi_0}\right) \; ; \; k_\perp' = \frac{2\pi}{L}\left(n + \frac{\nu}{3} + \frac{\Phi}{\Phi_0}\right) , \tag{2.86}$$

where Φ is the magnetic flux passing through the cross section of a carbon nanotube, $\Phi = B_z L^2/(4\pi)$, and Φ_0 is the magnetic flux quantum, ch/e. Now the consequence of time inversion symmetry takes the form

$$E_{c,v}(n, k_z; \Phi; K') = E_{c,v}(-n, -k_z; -\Phi; K) \, .$$

Chirality (or spirality) of a nanotube manifests itself in a particular coupling between the angular momentum as described by n and the directed translational motion as described by k_z: due to the linear-in-k_z terms in (2.82) or, in general, due to odd-in-k_z terms in (2.77) the energy has a contribution which depends both on the *sign* of k_z and the *sign* of n (propeller effect).

It is interesting to analyze how this particular coupling disappears for zigzag and armchair tubes which are achiral from the symmetry point of view. In zigzag tubes, the angle θ between the circumferential vector $\boldsymbol{L}$ and

the vector $\boldsymbol{a}$ is an integer multiple of 60°, $\sin 3\theta$ is zero and odd-in-k_z terms in (2.77, 2.82) vanish. In armchair tubes, the angle θ equals $30° + N \cdot 60°$ with N integer leading to one of the following three relations between n_a and n_b: $n_a = 2n_b$ or $n_b = 2n_a$ or $n_b = -n_a$. This means that the sum $n_a + n_b$ is an integer multiple of 3 and the parameter ν is zero. As a result values of $|k_\perp|$ become independent of the sign of n, and the coupling between signs of n and k_z in the odd-in-k_z terms vanishes. This follows also from the symmetry considerations. In Sect. 8.6 we will show that the odd-in-k_z terms in the electron energy spectrum govern the chirality effects in carbon nanotubes.

It is worth to mention that, in actual nanotubes, σ and π bands of graphene are slightly mixed due to the presence of a finite cylinder curvature. This will lead to a small band-gap for the metallic nanotubes and a possible shift in the minimum position of the conduction band and the maximum position of the valence band in the 1D Brillouin zone. Moreover, local twists and bends may have an additional effect on electronic structure [2.55]. Reich et al. [2.56] compared the nearest-neighbor tight-binding approximation for the electron dispersion in graphene and carbon nanotubes with first-principles calculations and the tight-binding dispersion including up to third-nearest neighbors. They concluded that the nearest-neighbor tight-binding dispersion predicts the electronic energies correctly only for a very limited range of wave vectors. In order to establish the theoretical similarities between Si and C, Fagan et al. [2.57] performed first-principles calculations for a hypothetical material, silicon nanotubes. The band-structure calculations show that, similar to carbon structures, they may present metallic (armchair) or semiconductor (zigzag and mixed) behaviors.

2.3 Size Quantization in Quantum Dots

Different schemes are used for calculation of electronic states in QDs. They depend on the dot shape and size which, in their turn, are determined by the growth conditions, see the book [2.58] and references therein. Theoretically, the shape of a dot was modelled by spheres [2.59], cones [2.60], pyramids [2.61, 2.62], disks (or cylinders) [2.63, 2.64] and lenses [2.65]. The dots made from a QW heterostructure through a series of masking and etching steps are modelled by a continual lateral confining potential, as a rule a parabolic lateral potential (*parabolic QDs*) [2.66].

2.3.1 Rectangular and Spherical Quantum Dots

The simplest models are rectangular and spherical QDs with infinite barriers treated in the isotropic-effective-mass approximation. Similarly to (2.60), the envelope function of an electron confined in a $a_x \times a_y \times a_z$ rectangular QD, or a quantum box, is a product

$$\psi(\boldsymbol{r}) = \varphi_{\nu_x}(x, a_x)\, \varphi_{\nu_y}(y, a_y)\, \varphi_{\nu_z}(z, a_z) \tag{2.87}$$

of three envelopes (2.61) describing the size-quantization in one particular direction, respectively x, y or z. The electron energy levels are

$$E_{e\nu_x\nu_y\nu_z} = \frac{\pi^2\hbar^2}{2m_{\mathrm{A}}} \left[\left(\frac{\nu_x}{a_x}\right)^2 + \left(\frac{\nu_y}{a_y}\right)^2 + \left(\frac{\nu_z}{a_z}\right)^2 \right] . \tag{2.88}$$

The electronic states in a spherical QD dot are characterized by the electron *orbital* angular momentum l. The lowest-energy electron state corresponds to $l = 0$. For an infinitely high barrier, the ground-state electron wave function has the form

$$\psi_s(\boldsymbol{r}) = f(r)\, |s\rangle\ ,\ f(r) = \frac{1}{\sqrt{2\pi R}}\, \frac{\sin(\pi r/R)}{r}\ , \tag{2.89}$$

where the spin index s assumes the values $\pm 1/2$ and the Bloch function $|s\rangle = c_s S$. The confinement energy is

$$E = \frac{\pi^2\hbar^2}{2m_{\mathrm{A}}R^2}\ . \tag{2.90}$$

Refining the procedure by finite barriers we obtain for the ground state

$$f(r) = \frac{C}{r} \begin{cases} \sin kr & \text{for } r \le R\,, \\ \mathrm{e}^{-æ(r-R)} \sin kR & \text{for } r \ge R\,, \end{cases} \tag{2.91}$$

where C is a normalizing factor and $k, æ$ are defined by (2.58) taken at $k_z = 0$. The eigenenergies satisfy the equation

$$1 - kR\, \cot kR = \frac{m_{\mathrm{A}}}{m_{\mathrm{B}}}\, (1 + æR)\,. \tag{2.92}$$

In the Kane model, the influence of nonparabolicity is reduced to a replacement of $m_{\mathrm{A,B}}$ by $m_{\mathrm{A,B}}(E)$, the scalar envelope $u_s(\boldsymbol{r}) \equiv f(r)c_s$ is given by (2.91), and the vector envelope is determined from

$$P\boldsymbol{v}_s(\boldsymbol{r}) = \frac{\hbar^2}{2} \left[\frac{1}{m(E)}\, \frac{\boldsymbol{r}}{r} - \mathrm{i}\frac{g(E) - g_0}{2m_0} \left(\boldsymbol{\sigma} \times \frac{\boldsymbol{r}}{r} \right) \right] \frac{df}{dr}\, c_s\ .$$

The product VR^2 should exceed some critical value to allow at least one confined state. For $m_{\mathrm{A}} = m_{\mathrm{B}} \equiv m^*$, this critical value equals

$$(VR^2)_{\mathrm{cr}} = \frac{\pi^2\hbar^2}{8m^*}\ .$$

It is worth to mention that, for the ground electron state in a rectangular box (the point symmetry D_{2h}), all four functions in (2.64) are nonzero and allow the representation

$$f(\boldsymbol{r}) = f(x^2, y^2, z^2),\ \ h_x(\boldsymbol{r}) = yz\, M_x(x^2, y^2, z^2)\,,$$

$$h_y(\boldsymbol{r}) = zx\, M_y(x^2, y^2, z^2),\ h_z(\boldsymbol{r}) = xy\, M_z(x^2, y^2, z^2)\,,$$

where f and M_α are arbitrary functions of x^2, y^2 and z^2.

A confined-hole state formed from the four-fold spin-degenerate band of Γ_8 symmetry (the hole spin $J = 3/2$, its projection $m = \pm 3/2, \pm 1/2$) cannot be characterized by any definite value of the hole orbital angular momentum L. In the spherical approximation for the Luttinger Hamiltonian ($\gamma_2 = \gamma_3 \equiv \gamma$), this is the total hole angular momentum $\boldsymbol{F} = \boldsymbol{J} + \boldsymbol{L}$ which serves as a good quantum number. The hole state is, therefore, $(2F+1)$-fold degenerate due to the projection F_z of the angular momentum $\boldsymbol{F}$ along an arbitrary axis, z.

For the ground state we have $F = 3/2$, $F_z = \pm 3/2, \pm 1/2$. Orbital states with $L = 0, 2$ are involved in the formation of this four-degenerate state. Following (2.32) we present the hole wave functions at the ground level as

$$\psi^{(h)}_{F_z}(\boldsymbol{r}) = \sum_m \mathcal{R}_{m,F_z}(\boldsymbol{r})\, |3/2, m\rangle\,. \tag{2.93}$$

As a function of $\boldsymbol{r}$ and J_i, the matrix $\hat{\mathcal{R}}(\boldsymbol{r})$ with the components $\mathcal{R}_{m,F_z}$ must be a spherical invariant. There are only two linearly independent invariants, $\boldsymbol{r}^2 I$ and $(\boldsymbol{J}\cdot\boldsymbol{r})^2$, which can be constructed from products of the bilinear functions $r_i r_j$ and the 4×4 basic matrices presented in Table 2.1. Therefore, one has for the matrix $\hat{\mathcal{R}}(\boldsymbol{r})$ inside the dot [2.67–2.69]

$$\hat{\mathcal{R}}(\boldsymbol{r}) = \frac{1}{\sqrt{4\pi}R^{3/2}}\left\{f_0\left(\frac{r}{R}\right) - f_2\left(\frac{r}{R}\right)\,\left[\left(\boldsymbol{J}\cdot\frac{\boldsymbol{r}}{r}\right)^2 - \frac{5}{4}\right]\right\}\,. \tag{2.94}$$

The radial functions $f_l(x)$ are defined as

$$f_l(x) = C\left[\mathrm{j}_l\left(\phi x\right) - (-1)^{l/2}\frac{\mathrm{j}_0\left(\phi\right)}{\mathrm{j}_0\left(\sqrt{\beta}\phi\right)}\mathrm{j}_l\left(\sqrt{\beta}\phi x\right)\right]\,, \tag{2.95}$$

where $\mathrm{j}_l(x)$ are the spherical Bessel functions, C is determined by the normalization condition

$$\int_0^1 \left[f_0^2(x) + f_2^2(x)\right] x^2\, dx = 1\,,$$

β is the light-to-heavy hole mass ratio (in the spherical approximation), ϕ is the dimensionless parameter which determines, according to

$$E^h = \frac{\hbar^2\phi^2}{2m_{hh}R^2}\,, \tag{2.96}$$

the hole quantum-confinement energy at the ground state. For the infinite barrier potential the envelope function should vanish at $r = R$ which leads to a simple equation [2.59]

$$\mathrm{j}_0(\phi)\,\mathrm{j}_2\left(\sqrt{\beta}\phi\right) + \mathrm{j}_2(\phi)\,\mathrm{j}_0\left(\sqrt{\beta}\phi\right) = 0\,. \tag{2.97}$$

Note that the spherical Bessel functions allow the representation

$$\mathrm{j}_l(x) = \sqrt{\frac{\pi}{2x}}\,\mathrm{J}_{l+1/2}(x)$$

and the first three of them are

$$\mathrm{j}_0 = \frac{\sin x}{x}\,,\ \mathrm{j}_1 = \frac{\sin x}{x^2} - \frac{\cos x}{x}\,,$$

$$\mathrm{j}_2 = \left(\frac{3}{x^3} - \frac{1}{x}\right)\sin x - \frac{3\cos x}{x^2}\,.$$

For $\beta \to 1$, the light- and heavy-hole subbands in a bulk semiconductor merge to form one four-fold degenerate band. In this hypothetic limit the envelope function is spin-independent and, for the ground state, coincides with the electron envelope (2.89).

2.3.2 Parabolic Quantum Dots

Vertical QDs are artificial semiconductor 'atoms' produced by a combination of MBE and nanolithography. They are MBE-grown QW structures with a lateral confining potential due to electrostatic gates or some etching processing. The confinement along the growth direction z is much stronger than in the x-y plane. This allows to separate the vertical and in-plane motions and approximate the electron envelope by

$$\psi(\boldsymbol{r}) = \Phi(x,y)f(z)\,, \tag{2.98}$$

where $f(z)$ is one of the subband functions (2.8, 2.13) in a 2D QW, $\Phi(x,y)$ describes the in-plane confinement. In many vertical QDs the lateral potential, to a good approximation, has a cylindrical symmetry with a parabolic profile. For these dots, the function Φ satisfies the Schrödinger equation for a 2D harmonic oscillator

$$\left[-\frac{\hbar^2}{2m^*}\left(\frac{1}{\rho}\frac{\partial}{\partial\rho}\rho\frac{\partial}{\partial\rho} + \frac{1}{\rho^2}\frac{\partial^2}{\partial\varphi^2}\right) + \frac{1}{2}m^*\omega_0^2\rho^2\right]\Phi(\rho,\varphi) = E\Phi(\rho,\varphi)\,. \tag{2.99}$$

Here m^* is the in-plane electron effective mass, the last term in the square brackets is the 2D confining potential expressed via the oscillator characteristic frequency ω_0 and we use the cylindrical coordinates. The function $\Phi(\rho,\varphi)$ is separable into azimuthal and radial parts

$$\Phi(\rho,\varphi) = \frac{\mathrm{e}^{\mathrm{i}m\varphi}}{\sqrt{2\pi}}\, R(\rho)\,, \tag{2.100}$$

where m is the angular momentum component along z. The radial function R satisfies (2.99) where the operator $\partial^2/\partial\varphi^2$ is changed by $-m^2$. The solutions have the form [2.66]

$$R_{n_\rho,m}(\rho) = \sqrt{\frac{2n_\rho}{(n_\rho+|m|)!}}\,\left(\frac{\rho}{l_0}\right)^{|m|} \exp\left(-\frac{\rho^2}{2l_0^2}\right) \mathrm{L}^{|m|}_{n_\rho+|m|}\left(\frac{\rho^2}{l_0^2}\right)\,, \tag{2.101}$$

where l_0 is the natural harmonic oscillator length scale, $\sqrt{\hbar/(m^*\omega_0)}$, $n_\rho = 0,1,2...$ is the radial quantum number, $m = 0,\pm1,\pm2...$ is the quantum number for angular momentum component and $\mathrm{L}^m_{n+m}(\xi)$ is the associated Laguerre polynomial

$$\mathrm{L}^m_{n+m}(\xi) = \frac{(n+m)!}{n!}\mathrm{e}^{\xi}\xi^{-m}\frac{d^n}{d\xi^n}(\mathrm{e}^{-\xi}\xi^{n+m})\,. \tag{2.102}$$

The energy levels of the 2D oscillator are

$$E_{n_\rho m} = (2n_\rho + |m| + 1)\hbar\omega_0\,. \tag{2.103}$$

It follows then that the 2D parabolic potential forms shells, or degenerate orbitals including $\pm m$ and spin degeneracy. The shells $N = 1,2,3...$ are equally spaced in energy with the intershell spacing $\hbar\omega_0$ and the degeneracy $2N$.

Let the parabolic potential be anisotropic,

$$V(x,y) = \frac{1}{2}\, m^*(\omega_x^2x^2 + \omega_y^2y^2)\,,$$

where the resonant frequencies ω_x and ω_y are different. The solutions are, as before, separable

$$\Phi(x,y) = \Phi_{n_x}(x;\omega_x)\,\Phi_{n_y}(y;\omega_y)\,,$$

where n_x and n_y are non-negative integers enumerating the eigenstates of a 1D oscillator,

$$\Phi_n(x;\omega_0) = \frac{1}{\pi^{1/4}(2^n n! l_0)^{1/2}}\mathrm{H}_n\left(\frac{x}{l_0}\right)\exp\left(-\frac{x^2}{2l_0^2}\right)\,,$$

$l_0 = \sqrt{\hbar/(m^*\omega_0)}$ and $\mathrm{H}_n(\xi)$ is the Hermite polynomial

$$\mathrm{H}_n(\xi) = (-1)^n\mathrm{e}^{\xi^2}\frac{d^n}{d\xi^n}\mathrm{e}^{-\xi^2}\,.$$

The energy in the state (n_x,n_y) is given by [2.70]

$$E_{n_x,n_y} = \hbar\omega_x\left(n_x+\frac{1}{2}\right) + \hbar\omega_y\left(n_y+\frac{1}{2}\right)\,.$$

At $\omega_x = \omega_y \equiv \omega_0$, this set of levels reduces to the equidistant set $\hbar\omega_0(n_x + n_y + 1)$ equivalent to (2.103).

The above results are simply extended to the problem of an electron in a parabolic QD subject to a magnetic field $\boldsymbol{B} \parallel z$. In this case the eigenenergies are given by [2.71, 2.72]

$$E_{n_\rho m}(B) = (2n_\rho + |m| + 1)\,\hbar\sqrt{\omega_0^2 + \frac{1}{4}\omega_c^2} + \frac{m}{2}\,\hbar\omega_c\,, \tag{2.104}$$

where $\omega_c = |e|B/m^*c$ is the cyclotron frequency. This equation can be understood taking into account that, in the presence of magnetic field, two additional terms

$$\frac{1}{8}\,m^*\omega_c^2\rho^2 - \mathrm{i}\frac{\hbar\omega_c}{2}\frac{\partial}{\partial\varphi} = \frac{1}{8}\,m^*\omega_c^2\rho^2 + \frac{m}{2}\,\hbar\omega_c$$

appear in the electron effective Hamiltonian in (2.99). Therefore, as compared to (2.103) one should add the term $(m/2)\hbar\omega_c$ to the energy $E_{n_\rho m}$ and change the oscillator resonance frequency ω_0^2 by $[\omega_0^2 + (\omega_c^2/4)]^{1/2}$ which gives immediately (2.104).

For calculation of hole energy levels in a parabolic potential one needs to take into account the valence-band mixing. Pederson and Chang [2.66] proposed to expand the in-plane envelopes in terms of heavy-hole oscillator states. In this basis the light-hole block of the Luttinger Hamiltonian is not diagonal. However, the advantage of such a formulation is that all matrix elements can be calculated analytically. Then the energy spectrum is found by using a standard numerical diagonalization technique.

2.3.3 Cone-, Lens- and Pyramid-Shaped Quantum Dots

The first step of the calculation of InAs/GaAs or InGaAs/GaAs QDs formed on a wetting layer is to approximate pyramids with a square base by cones or lenses having the same height, h, and base surface. For a cone on the wetting layer of thickness d, the confining potential is modelled by the function

$$V_{\mathrm{cone}}(\rho, z) = V\,[1 - \theta(z)\,\theta(d - z) - \theta(z - d)\,\theta[h(1 - \rho/\rho_0) + d - z]]\,,$$

where ρ_0 is the base radius. The products of Heaviside functions in square brackets define the wetting-layer and cone regions. A lens is modelled as a part of a sphere with fixed height h and radius at the base ρ_0. The radius of the sphere R is related to h, ρ_0 by $R^2 = (R - h)^2 + \rho_0^2$, or $R = (h^2 + \rho_0^2)/2h$. The resulting confining potential is given by

$$V_{\mathrm{lens}}(\rho, z) = V\left\{1 - \theta(z)\,\theta(d - z) - \theta(z - d)\,\theta[R^2 - (z - d - h + R)^2 - \rho^2]\right\}.$$

It is clear that Hamiltonians with the above confining potentials are not separable in z and ρ and full 3D numerical diagonalization is needed to solve the

problem. However, complete numerical approaches justify the use of separable approximate treatments [2.60, 2.65], the latter being by far more physically intuitive. For illustration, we consider the adiabatic approximation applied by Wojs et al. [2.65] to calculate the electronic structure of a lens-shaped QD. They take advantage of the fact that the electron wave function is strongly confined to the lowest subband of the wetting layer and write the function in the separable form

$$\psi(\rho,\varphi,z) = \frac{\mathrm{e}^{\mathrm{i}m\varphi}}{\sqrt{2\pi}} R_m(\rho) f_\rho(z)\,, \tag{2.105}$$

where $f_\rho(z)$ is a slowly varying function of ρ and m is the angular momentum component along z. The functions $f_\rho(z)$ and $R_m(\rho)$ satisfy the separate equations

$$\left[-\frac{\hbar^2}{2m^*}\frac{\partial^2}{\partial z^2} \quad + \quad V(\rho,z)\right] f_\rho(z) = E_0(\rho) f_\rho(z)\,, \tag{2.106}$$

$$\left[\frac{\hbar^2}{2m^*}\left(-\frac{1}{\rho}\frac{\partial}{\partial\rho}\rho\frac{\partial}{\partial\rho} + \frac{M^2}{\rho^2}\right) + E_0(\rho)\right] R_m(\rho) = E R_m(\rho)\,.$$

For simplicity, the effective masses in the structure are assumed to be material independent, $m_\mathrm{A} = m_\mathrm{B} \equiv m^*$. The calculation starts with finding energy $E_0(\rho)$ corresponding to the electron motion in the z direction for a given thickness of the A layer,

$$a(\rho) = \sqrt{R^2 - \rho^2} + d + h - R\,.$$

Next, the radial motion in the potential $E_0(\rho)$ is solved for each angular momentum component m. The electron energy spectrum of a lens-shaped QD $\mathrm{In_{0.5}Ga_{0.5}As/GaAs}$ with $h = 44$ Å, $\rho_0 = 180$ Å, $d = 16$ Å consists of five shells, almost degenerate and almost equally spaced with intershell spacing of $\hbar\omega_0 = 30$ meV [2.66]. Thus, the energy spectrum is well approximated by the cutoff spectrum of the parabolic lateral potential.

Strain caused by the differences in the lattice constants a_0 of dot and matrix materials is decisive for Stranski-Krastanow self-organized growth. On the other hand, the strain distribution in and around dots modifies the electron band structure, due to deformation potential and piezoelectric fields. To illustrate, we remind the strain distribution in pseudomorphic slab and sphere. The term 'pseudomorphic' is used for heterostructures when they are lattice mismatched to their substrate, and the strain is accommodated entirely elastically without relaxation via dislocations and other defects. If the slab extends along the x and y directions the outer material B imposes the strain

$$u_{xx} = u_{yy} = \frac{a_0(B) - a_0(A)}{a_0(A)} \equiv u_\parallel \tag{2.107}$$

onto the inner material A, $a_0(\mathrm{A})$ and $a_0(\mathrm{B})$ being the lattice constants of bulk materials A and B. Since the slab can freely extend in the growth direction the stress along z is absent,

$$\sigma_{zz} = C_{11}u_{zz} + C_{12}(u_{xx} + u_{yy}) = 0\,,$$

and one finds

$$u_{zz} = -\frac{2C_{12}}{C_{11}}\,u_{\parallel}\,,$$

while the shear strain is zero and the outer material remains completely unstrained. Here $C_{11} = C_{xxxx}$, $C_{12} = C_{xxyy}$ are the *elastic stiffness constants*. In general, the stiffness tensor $\boldsymbol{C}$ relates the stress and strain components by

$$\sigma_{kl} = C_{klmn}u_{mn}\,, \tag{2.108}$$

For cubic crystal classes, it has three linearly independent components: C_{xxxx}, C_{xxyy} and $C_{xyxy} \equiv C_{44}$. Furthermore, in isotropic materials these three coefficients are related by $2C_{44} = C_{11} - C_{12}$ and then the stress-strain relation is written in terms of the Poisson ratio $\nu = C_{12}/(C_{11} + C_{12})$ and the Young modulus $E = (C_{11} - C_{12})(1 + \nu)$.

For a pseudomorphic sphere of the radius R, under the simplifying assumption of isotropic materials and material-independent elastic constants, the strains are [2.61]

$$u_{rr}^{\mathrm{in}} = u_{\theta\theta}^{\mathrm{in}} = u_{\varphi\varphi}^{\mathrm{in}} = \frac{2}{3}\,u_{\parallel}\frac{1-2\nu}{1-\nu}\,,$$

$$u_{rr}^{\mathrm{out}} = -2u_{\theta\theta}^{\mathrm{out}} = -2u_{\varphi\varphi}^{\mathrm{out}} = \frac{2}{3}\,u_{\parallel}\frac{1+\nu}{1-\nu}\left(\frac{R}{r}\right)^3\,,$$

where the superscripts $\mathrm{in}, \mathrm{out}$ refer to the inner (A) and outer (B) materials and we present the strain tensor components in the spherical coordinates,

$$u_{rr} = \frac{\partial u_r}{\partial r}\,,\; u_{\theta\theta} = \frac{1}{r}\frac{\partial u_\theta}{\partial \theta} + \frac{u_r}{r}\,,$$

$$u_{\varphi\varphi} = \frac{1}{r\sin\theta}\frac{\partial u_\varphi}{\partial \varphi} + \frac{u_\theta}{r}\cot\theta + \frac{u_r}{r}\,.$$

One can check that components of $\boldsymbol{u}^{\mathrm{in}}$ and $\boldsymbol{u}^{\mathrm{out}}$ at the dot surface, $r = R$, satisfy the conditions

$$(u_r^{\mathrm{in}} - u_r^{\mathrm{out}})|_{r=R} = u_{\parallel}R\,,$$

$$a_0(\mathrm{A})(1 + u_{\theta\theta}^{\mathrm{in}}) = a_0(\mathrm{A})(1 + u_{\varphi\varphi}^{\mathrm{in}}) = a_0(\mathrm{B})(1 + u_{\theta\theta}^{\mathrm{out}}) = a_0(\mathrm{B})(1 + u_{\varphi\varphi}^{\mathrm{out}})\,.$$

The strain distribution of a 3D dot of arbitrary shape and elastic properties cannot be presented in a closed analytical form but has to be solved numerically [2.61].

The strain gives rise to deformation-potential and piezoelectric contributions to the electron effective Hamiltonian. The former contribution is taken into account by including the Bir-Pikus Hamiltonian (2.30) for the Γ_8 valence band or the similar 6×6 matrix $\mathcal{H}_u$ for the valence bands $\Gamma_8+\Gamma_7$ considered together. For the conduction band Γ_6, this contribution is a scalar depending on the hydrostatic components of the strain,

$$\delta E_c = C_1 \left(u_{xx} + u_{yy} + u_{zz}\right) , \tag{2.109}$$

where C_1 is the conduction-band deformation-potential constant. In crystals with a zinc-blende lattice, the shear strain induces a piezoelectric polarization $\boldsymbol{P}$ with

$$P_i = e_{ijk} u_{jk} ,$$

e_{ijk} being the piezoelectric tensor and having only one linearly independent component $e_{xyz} \equiv e_{14}$. The strain-induced polarization creates fixed charges

$$\rho(\boldsymbol{r}) = -\mathrm{div}\boldsymbol{P}(\boldsymbol{r}) \tag{2.110}$$

and gives rise to the piezoelectric potential acting both on electrons and holes. Equation (2.110) reduces the symmetry of the electron Hamiltonian to C_{2v} even when the tensor u_{ij} possesses the C_{4v} point symmetry.

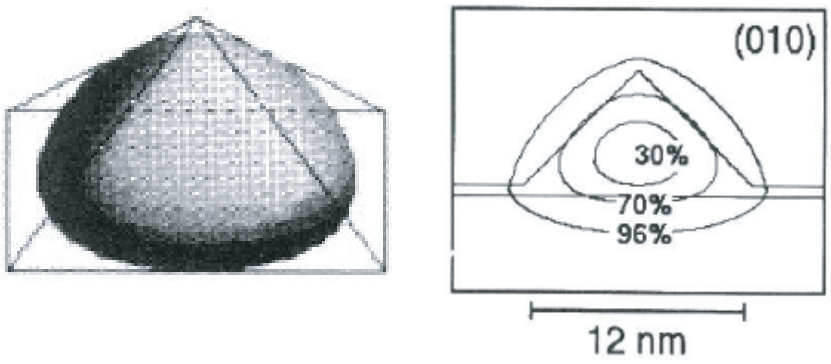

Fig. 2.6. 3D view of the isosurface (the probability of finding the electron inside is 70%), and cross section with isolines (30%, 70%, and 96% probabilities of finding the electron inside) of the squared electron ground-state wave function for an InAs QD. The cross section is a (010) plane through the dot center. From [2.61].

In Fig. 2.6 the calculated electron ground-state wave function in a pyramid QD is shown in a perspective view and in a (010) cross section [2.61]. The isosurface containing 70% of the wave-function probability lays almost completely within the dot. In [2.61] the calculation is performed in the simple

band model for both electrons and holes. A systematic theoretical investigation of electronic properties of InAs pyramid QDs in the frame of the eight-band $\boldsymbol{k} \cdot \boldsymbol{p}$ theory is presented in [2.62]. It is shown that the electron ground state is mainly represented by s-type Bloch functions with the envelope u in (2.44) while the hole ground state is almost completely described by p-type Bloch functions with the envelopes v_x, v_y, v_z. The first and second electron excited levels are two slightly split states with p-like envelopes, the energy separation between them is approximately proportional to the pyramid base length, b, in agreement with the proportionality between the piezoelectric potential and b. No remarkable intermixing of the confined-electron states with wetting-layer states is found. In contrast to the effective-mass calculation using the same strain distribution, the eight-band theory leads to the hole ground-state functions pronouncedly elongated along $[1\bar{1}0]$. Also the hole excited states in this theory are very different from previous effective mass results with respect to both the wave-function shapes and the level separations. The holes are generally confined to the bottom of the pyramid and do not reach the tip. However, experiments on Stark effect spectroscopy on InAs/GaAs self-assembled QDs [2.73] show that the hole is localized towards the top of the dot, above the electron, an alignment that is inverted relative to the predictions of previous calculations. This unexpected finding can be understood assuming that the nominally InAs dots contain significant concentration of Ga and have a graded $In_{1-x}Ga_xAs$ composition, with x decreasing from base to apex. Sheng and Leburton [2.74] address the issue of electron-hole alignment inversion in pyramidal QDs. They use the eight-band strain-dependent $\boldsymbol{k} \cdot \boldsymbol{p}$ effective Hamiltonian and consider three types of QDs, namely, pyramidal, truncated pyramidal and lens-shaped. Different models of Ga concentration profiles are analyzed, including dots containing five $In_{1-x}Ga_xAs$ monomolecular layers at the bottom with intervals 10% and dots with variable number of $In_{0.75}Ga_{0.25}As$ monomolecular layers. For structures with sizes studied experimentally, the theory allows to obtain inverted electron-hole alignments that are consistent with the experiment for several Ga diffusion profiles. However, the inverted alignment is not a universal property of self-organized QDs, but ultimately depends on diffusion profile and dot size that are imposed by fabrication processes, including the nominal composition of the dot layer, the growth temperature, composition changes during capping, post-growth annealing, etc. A microscopic pseudopotential description [2.75] also strongly suggests that to obtain accurate agreement between theory and experiment one needs to adopt a model that includes some Ga in-diffusion within the QD.

In [2.76] experimental and theoretical tools were used interactively to determine the geometric and compositional parameters and the resulting electronic properties of InGaAs/GaAs self-organized alloy QDs, grown by Metal-Organic Chemical Vapor Deposition (MOCVD) with nominal 50% In content and a deposition of four monolayers. Theoretically, an atomistic em-

pirical pseudopotential model was used as an alternative to the commonly used effective-mass and $\boldsymbol{k}\cdot\boldsymbol{p}$ envelope-function approximations. The QD structural model with best agreement between measured and predicted electronic properties of the studied samples is a truncated cone with height 35 Å, base diameter 200 Å, and top diameter 160 Å, having a nonuniform, peaked composition profile with average 60% In content.

In contrast to InAs and GaAs crystals, GaN and related nitride alloys generally have a hexagonal (wurtzite) structure, which leads to strong build-in piezoelectric fields in heterostructures, of the order of MV/cm. Electronic structure of nitride-based QDs, namely, GaN/AlN and $In_xGa_{1-x}N$/GaN QDs, was calculated for hexagonal prisms (prismatic QDs) and truncated hexagonal pyramids [2.77,2.78], respectively by using a multiband $\boldsymbol{k}\cdot\boldsymbol{p}$ model and a tight-binding method.

2.4 Spin Splitting of Electron Subbands: Bulk- and Structure-Inversion Asymmetry

It is well-known that, in centrosymmetric crystals, the electronic state at each band n and wave vector $\boldsymbol{k}$ is at least twofold degenerate (the so-called *Kramers degeneracy*, or *spin degeneracy*). In crystals lacking a center of inversion, the Kramers degeneracy of the Bloch states is lifted except for special points or lines in the Brillouin zone. Particularly, in zinc-blende-lattice semiconductors like GaAs, InAs, ZnSe, CdTe, etc. (the class T_d) the conduction band Γ_6 and the valence band Γ_8 are, respectively, twofold and fourfold degenerate at the Γ point. However, away from this point the conduction and valence bands are split into nondegenerate spin branches, even at zero magnetic field. The spin-dependent Hamiltonian can be constructed by expanding the effective Hamiltonian in powers of $\boldsymbol{k}$ and applying the method of invariants mentioned above in connection with the invariant form of the Luttinger Hamiltonian (2.28). For the T_d-symmetry crystals, one can show that the spin-dependent term in the conduction-band Hamiltonian appears starting with k^3 [2.79]

$$\mathcal{H}_{c3} = \gamma_c \left[\sigma_x k_x (k_y^2 - k_z^2) + \sigma_y k_y (k_z^2 - k_x^2) + \sigma_z k_z (k_x^2 - k_y^2)\right] , \qquad (2.111)$$

where σ_i are the Pauli matrices. For the band Γ_8 the main contribution is given by a similar expression

$$\mathcal{H}_{v3} = \gamma_v \sum_i J_i \kappa_i , \qquad (2.112)$$

where J_i are the 4×4 matrices defined in Table 2.1 and we use the notation

$$\kappa_x = k_x (k_y^2 - k_z^2) , \; \kappa_y = k_y (k_z^2 - k_x^2) , \; \kappa_z = k_z (k_x^2 - k_y^2) .$$

In contrast to the conduction band, the constant γ_v has a nonrelativistic nature. Indeed, this constant equals 2/3 of the similar constant in the 3×3 Hamiltonian for the nonrelativistic valence band Γ_{15}. Besides (2.112), the valence-band Hamiltonian expanded up to third order in $\boldsymbol{k}$ contains four relativistic terms, a linear-in-$\boldsymbol{k}$ term

$$\mathcal{H}_{v1} = \gamma_{v1} \sum_i V_i k_i$$

and three cubic terms

$$\delta\mathcal{H}_{v3} = \gamma'_{v3} \sum_i J_i^3 \kappa_i + \gamma''_{v3} k^2 \sum_i V_i k_i + \gamma'''_{v3} \sum_i V_i k_i \left(k_i^2 - \frac{k^2}{3} \right) .$$

In heterostructures, QWs or SLs, grown from zinc-blende-lattice semiconductors, the spin-dependent Hamiltonians contain both linear and cubic terms. Particularly, in (001)-grown QWs with symmetrical interfaces (D_{2d} point-group symmetry) the linear-$\boldsymbol{k}$ spin-dependent term in the conduction subband $e1$ has the form [2.80]

$$\mathcal{H}_{BIA} = \beta_1(\sigma_y k_y - \sigma_x k_x), \tag{2.113}$$

where $x\|[100]$, $y\|[010]$ and β_1 is a constant. This term can be obtained from the cubic-$\boldsymbol{k}$ term (2.111) describing the removal of spin degeneracy of the conduction-band states in a bulk semiconductor. Really, taking into account the quantum confinement effect we can replace in (2.111) k_z and k_z^2 by the average values $\langle k_z \rangle = 0$ and $\langle k_z^2 \rangle \neq 0$, respectively, and arrive at (2.113) with $\beta_1 = \gamma_c \langle k_z^2 \rangle$. Here the symbol $\langle k_z^l \rangle$ means the expectation value $\int \varphi_{e1}(z) \hat{k}_z^l \varphi_{e1}(z) dz$, $\varphi_{e1}(z)$ is the electron envelope function (2.8) at the lowest subband $e1$ and $\hat{k}_z = -\mathrm{i}\partial/\partial z$. Since the term $\mathcal{H}_{BIA}$ is due to the lack of inversion symmetry in the bulk material it is called the Bulk Inversion Asymmetry (BIA) term which explains the subscript BIA. Sometimes it is also called the Dresselhaus term [2.81].

In heterostructures with asymmetrical superstructural potential (the C_{2v} point group) there exists another spin-dependent contribution

$$\mathcal{H}_{SIA} = \beta_2(\sigma_x k_y - \sigma_y k_x) \tag{2.114}$$

which is called the Structure-Inversion Asymmetry (SIA) term, or the Rashba term. The structure asymmetry can be related with non-equivalent normal and inverted interfaces, external or built-in electric fields, compositionally stepped QWs etc. The spin-orbit interaction term in the form of (2.114) was first predicted in [2.82, 2.83] for bulk polar hexagonal crystals with the wurtzite structure (the C_{6v} point symmetry). Nature of the similar term in an asymmetrical 2D system has been analyzed by different authors ([2.84–2.90], see also [2.91] and references therein). Note that anisotropic orientation of

chemical bonds at the interfaces gives rise to an additional contribution to the linear-$\boldsymbol{k}$ Hamiltonian, even in symmetrical QWs [2.92, 2.93]. This is the so-called Interface Inversion Asymmetry (IIA) term. Since it has the same structure as the contribution (2.113), they can be described together by one inseparable Dresselhaus term with the common parameter β_1.

It is convenient to introduce the Cartesian coordinates $x' \| [1\bar{1}0]$, $y' \| [110]$, $z \| [001]$ which allow to write a sum of the BIA and SIA terms in the form

$$\mathcal{H}_{c1}(\boldsymbol{k}) = \frac{1}{2}\ (\beta_- \sigma_{x'} k_{y'} - \beta_+ \sigma_{y'} k_{x'})\ , \tag{2.115}$$

where $\beta_\pm = 2(\beta_2 \pm \beta_1)$ and from now on $\boldsymbol{k} \equiv \boldsymbol{k}_\parallel$. Introducing the effective Larmor frequency $\boldsymbol{\Omega_k}$ (at zero magnetic field) by

$$\mathcal{H}_{c1} = \frac{\hbar}{2}\, \boldsymbol{\sigma} \cdot \boldsymbol{\Omega_k} \tag{2.116}$$

and comparing with (2.115) we obtain

$$\Omega_{\boldsymbol{k},x'} = \beta_- k_{y'}/\hbar\,, \quad \Omega_{\boldsymbol{k},y'} = -\beta_+ k_{x'}/\hbar\,, \quad \Omega_{\boldsymbol{k},z} = 0. \tag{2.117}$$

Thus, in the parabolic approximation the resulting energy dispersion is

$$E_{e1\boldsymbol{k}} = E^0_{e1} + \frac{\hbar^2 k^2}{2m^*} \pm \frac{1}{2}\,\hbar\Omega_{\boldsymbol{k}}\,,$$

with the spin splitting given by

$$\Delta E = \hbar\Omega_{\boldsymbol{k}} = \sqrt{\beta_+^2 k_{x'}^2 + \beta_-^2 k_{y'}^2}. \tag{2.118}$$

If only one of the constants β_1, β_2 is nonzero then $\beta_-^2 = \beta_+^2 \equiv \beta^2$, and the splitting $\hbar\Omega_{\boldsymbol{k}} = \beta k$ is angular independent. Figure 2.7 illustrates the electron dispersion $E_{e1\boldsymbol{k}}$ (a,d) and contours of constant energy in the k_x-k_y plane for different relations between β_1 and β_2 (b,c,e). For $\beta_1 \neq 0, \beta_2 = 0$ and $\beta_1 = 0, \beta_2 \neq 0$ the dispersion has the same shape and consists of the well known *shifted parabolas in all directions*, displayed in Fig. 2.7a. However, the Rashba- and Dresselhaus spin-orbit coupling, or coupling between the spin and wave vector, results in different spin orientation of the eigenstates.

The spin orientation of split states at different $\boldsymbol{k}$ can be visualized by indicating the direction of the effective Larmor frequency $\boldsymbol{\Omega_k}$ which provides the relevant quantization axis for spin at given $\boldsymbol{k}$. The spin orientations for purely Rashba and purely Dresselhaus coupling are schematically shown in Fig. 2.7b and 2.7c by arrows. It is assumed that β_1 is negative and β_2 is positive. For the Rashba contribution the effective Larmor frequency and, hence, the spin is always perpendicular to the corresponding $\boldsymbol{k}$-vector (Fig. 2.7b). If the Dresselhaus term is dominant, the angle between $\boldsymbol{k}$-vector and spin depends on the crystallographic orientation of $\boldsymbol{k}$.

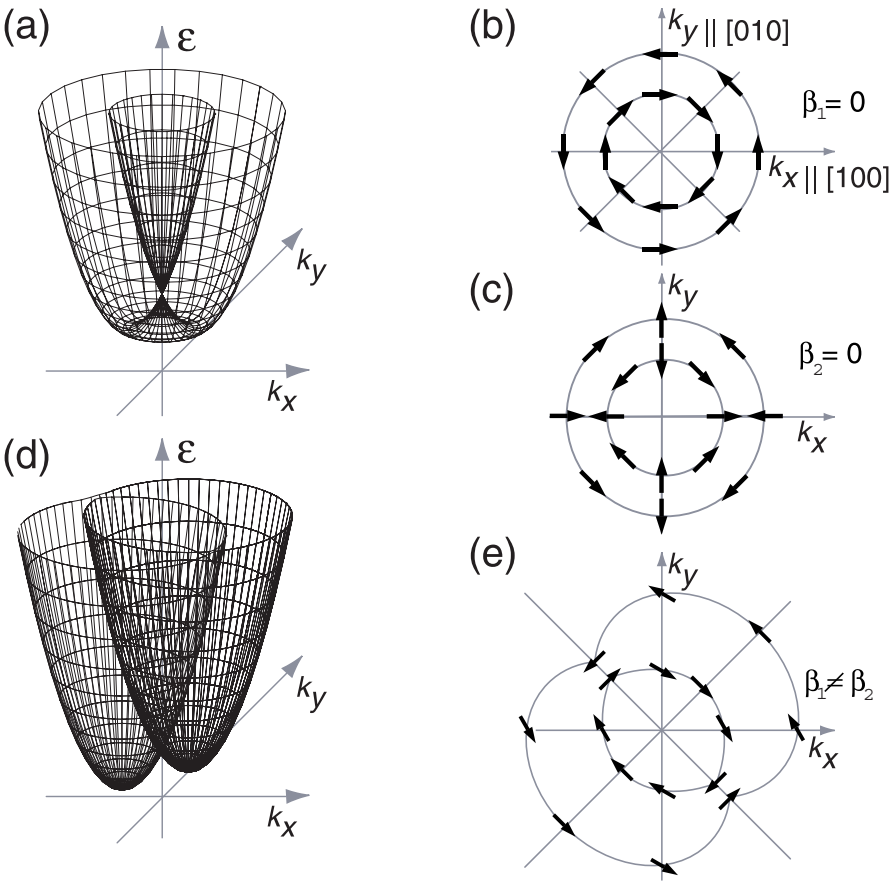

Fig. 2.7. Schematic 2D electron band structure with $\boldsymbol{k}$-linear terms for the C_{2v} symmetry for different strengths of the SIA and BIA contributions and the distribution of spin orientations at the 2D Fermi energy. (**a**) shows the case of only Rashba (**b**) or Dresselhaus (**c**) spin-orbit coupling, and (**d**, **e**) represent the case of simultaneous presence of both contributions. Arrows indicate the orientation of spins.

In the presence of both Rashba and Dresselhaus spin-orbit terms, relevant for the C_{2v} symmetry, the $[1\bar{1}0]$ and [110] axes become strongly nonequivalent. For $\boldsymbol{k} \parallel [110]$, the eigenvalues of the Hamiltonian are then given by $E_{e1} = \hbar^2 k^2/2m^* \pm (\beta_1 + \beta_2)k$ and, for $\boldsymbol{k} \parallel [1\bar{1}0]$, by $E_{e1} = \hbar^2 k^2/2m^* \pm (\beta_2 - \beta_1)k$. This anisotropic dispersion is sketched in Fig. 2.7d. The corresponding contours of constant energy together with the spin orientation for some $\boldsymbol{k}$-vectors are shown in Fig. 2.7e.

At low electron energies the spin splitting due to the linear-in-$\boldsymbol{k}$ term dominates. At higher energies relevant to high temperatures or large concen-

trations, the cubic-in-$\boldsymbol{k}$ term can be important as well. For the (001) QW structures the two Dresselhaus contributions to $\Omega_{\boldsymbol{k},i}$, linear and cubic, can be written as

$$\Omega_{\boldsymbol{k},x} = -\Omega_1 \cos\varphi - \Omega_3 \cos 3\varphi,\ \Omega_{\boldsymbol{k},y} = \Omega_1 \sin\varphi - \Omega_3 \sin 3\varphi,\ \Omega_{\boldsymbol{k},z} = 0, \quad (2.119)$$

where

$$\Omega_1 = \frac{2\gamma_c}{\hbar}\, k \left(\langle k_z^2 \rangle - \frac{1}{4}\, k^2 \right)\ ,\ \Omega_3 = \frac{\gamma_c}{2\hbar}\, k^3\ ,$$

$k^2 = k_x^2 + k_y^2$ and φ is the angle between $\boldsymbol{k}$ and the axis [100]. For the [111] structures, one has

$$\Omega_{\boldsymbol{k},x} = \Omega_1 \sin\varphi\ ,\ \Omega_{\boldsymbol{k},y} = -\Omega_1 \cos\varphi\ ,\ \Omega_{\boldsymbol{k},z} = -\Omega_3 \sin 3\varphi\ ,$$

where $x \parallel [11\bar{2}]$, $y \parallel [\bar{1}10]$, $z \parallel [111]$, φ is the angle between $\boldsymbol{k}$ and $[11\bar{2}]$, and

$$\Omega_1 = \frac{4\gamma_c}{\sqrt{3}\hbar}\, k \left(\langle k_z^2 \rangle - \frac{1}{4}\, k^2 \right)\ ,\ \Omega_3 = \sqrt{\frac{2}{3}} \frac{\gamma_c}{\hbar}\, k^3\ .$$

For the [110] structures, one has

$$\Omega_{\boldsymbol{k},x} = \Omega_{\boldsymbol{k},y} = 0\ ,\ \Omega_{\boldsymbol{k},z} = \Omega_1 \cos\varphi - \Omega_3 \cos 3\varphi\ ,$$

where $x \parallel [\bar{1}10]$, $y \parallel [001]$, $z \parallel [110]$, φ is the angle between $\boldsymbol{k}$ and $[1\bar{1}0]$, and

$$\Omega_1 = \frac{\gamma_c}{\hbar}\, k \left(\langle k_z^2 \rangle - \frac{1}{4}\, k^2 \right)\ ,\ \Omega_3 = \sqrt{\frac{3}{4}} \frac{\gamma_c}{\hbar}\, k^3\ .$$

The Rashba term can be presented in an invariant form as

$$\mathcal{H}_{SIA} = \beta_2 (\boldsymbol{\sigma} \times \boldsymbol{k}) \cdot \boldsymbol{N}\ , \quad (2.120)$$

where $\boldsymbol{N}$ is the unit vector directed along the normal to the interface. In a symmetrical QW subject to a homogeneous electric field $\boldsymbol{F} \parallel z$, the constant β_2 can be crudely estimated as [2.90]

$$\beta_2 = \frac{P^2}{3} \left\{ \frac{\Delta(2E_g + \Delta)}{E_g^2 (E_g + \Delta)^2}\, |e| F \right.$$
$$\left. + \left(\frac{\Delta}{E_g(E_g + \Delta)} - \frac{\Delta'}{E_g'(E_g' + \Delta')} \right) \left[\varphi_{e1}^2(a/2) - \varphi_{e1}^2(-a/2) \right] \right\}\ ,$$

where the band parameters E_g, Δ and E_g', Δ' refer to the well and barrier bulk materials, respectively, the parameter P is defined in (2.46), $\varphi_{e1}(z)$ is the envelope calculated in the presence of electric field, and $\pm a/2$ are the interface coordinates.

The BIA contribution to the valence band effective Hamiltonian responsible for removal of spin degeneracy of the hole subbands can be obtained by

averaging the linear and cubic terms, $\mathcal{H}_{1v}$ and $\mathcal{H}_{v3}+\delta\mathcal{H}_{3v}$, over the quantum-confined states $hh\nu$ or $lh\nu$ calculated neglecting the spin splitting. Note that this procedure applied to the nonrelativistic term (2.112) does not lead to linear-$\boldsymbol{k}$ splitting of heavy-hole states because the off-diagonal components $J_{i;\pm 3/2,\mp 3/2}$ equal zero. The Rashba spin splitting in 2D hole systems was analyzed by Winkler [2.95]. At small values of k, the heavy-hole spin splitting is of third order, in qualitative difference with the conduction-band and light-hole states in QWs.

Entin and Magarill [2.96] have derived the effective Hamiltonian for electrons confined near the curved surface and showed that the curved system has an additional spin-dependent term. For example, in a spherical QW where electrons are confined in a thin spherical layer of the radius R, the spin-orbit term is proportional to

$$\boldsymbol{\sigma}\cdot\left(\frac{\boldsymbol{R}}{R^2}\times\hat{\boldsymbol{p}}\right)\,,$$

where

$$\hat{\boldsymbol{p}}=\boldsymbol{o}_\theta\hat{p}_\theta+\boldsymbol{o}_\varphi\hat{p}_\varphi\,,\ \hat{p}_\theta=-\frac{\mathrm{i}}{R}\frac{\partial}{\partial\theta}\,,\ \hat{p}_\varphi=-\frac{\mathrm{i}}{R\sin\theta}\frac{\partial}{\partial\varphi}\,,$$

and the vectors $\boldsymbol{o}_\theta$, $\boldsymbol{o}_\varphi$, $\boldsymbol{o}_R=\boldsymbol{R}/R$ compose the orthogonal basis in the spherical coordinates.

Linear-in-$\boldsymbol{k}$ spin splitting of electron subbands in QWRs is described by a Hamiltonian

$$\mathcal{H}_1=(\boldsymbol{\sigma}\cdot\boldsymbol{\beta})\,k_z\,, \tag{2.121}$$

where z is the principal axis of the wire and $\boldsymbol{\beta}$ is a constant vector, its nonzero components are determined by symmetry of the structure. The effective Larmor frequency defined according to (2.116) is equal to $2\boldsymbol{\beta}k_z/\hbar$. Depending on the sign of k_z it is directed parallel or antiparallel to the fixed direction of $\boldsymbol{\beta}$. This is the main difference with QWs where the direction of $\boldsymbol{\Omega}_{\boldsymbol{k}}$ is independent of $\boldsymbol{k}$ only in asymmetrical QWs in the particular case $\beta_1=\pm\beta_2$ when either β_+ or β_- vanish. In [2.97] a simple 3D model of an asymmetric QWR is introduced in which the Rashba spin-orbit coupling (2.121) is derived from a realistic description of the bulk semiconductor electronic structure.

2.5 Electrons, Photons and Phonons in Superlattices

The effective-mass method, the formalism of macroscopic electrodynamics for photons, the dielectric model for optical phonons and the approximation of a homogeneous elastic medium for acoustic phonons allow a generalized description of the quasi-particle propagation in a semiconductor SL. We consider an infinite SL made up of alternating layers A and B with thicknesses a and b, respectively, and hence with the period $d=a+b$. The state of a generalized quasi-particle is described by the generalized envelope

$$\mathrm{e}^{-\mathrm{i}\omega t+\mathrm{i}\boldsymbol{q}\cdot\boldsymbol{\rho}}\varphi(z)\,,$$

where z is the SL principal axis, $\boldsymbol{\rho}$ is the in-plane component of the 3D radius-vector $\boldsymbol{r}$, $\boldsymbol{q}$ is the in-plane component of the quasi-particle wave vector. Within each homogeneous layer the z-dependent envelope $\varphi(z)$ is a linear combination of two exponential functions,

$$\varphi(z) = F_+\mathrm{e}^{\mathrm{i}k_\mathrm{A}z} + F_-\mathrm{e}^{-\mathrm{i}k_\mathrm{A}z} \quad \text{within the layers A}$$

and

$$\varphi(z) = G_+\mathrm{e}^{\mathrm{i}k_\mathrm{B}z} + G_-\mathrm{e}^{-\mathrm{i}k_\mathrm{B}z} \quad \text{within the layers B}\,.$$

The coefficients $F_\pm, G_\pm$ may depend on the layer number. At the interfaces the function $\varphi(z)$ satisfies the boundary conditions

$$\varphi_\mathrm{A} = \varphi_\mathrm{B}\,,\; C_\mathrm{A}\left(\frac{d\varphi}{dz}\right)_\mathrm{A} = C_\mathrm{B}\left(\frac{d\varphi}{dz}\right)_\mathrm{B}\,. \tag{2.122}$$

Physical meaning of the function $\varphi(z)$ and the coefficients $C_\mathrm{A,B}$ as well as the relation between the wave vectors $k_\mathrm{A}, k_\mathrm{B}$ and the frequency ω, or the energy $E = \hbar\omega$, will be discussed with reference to electrons, photons and phonons after deriving the dispersion equation for a generalized quasi-particle propagating in a SL. Let us present the function $\varphi(z)$ and its derivative as a two-component column

$$\hat{\varphi}(z) = \begin{pmatrix}\varphi\\ \dot{\varphi}\end{pmatrix}\,,\; \dot{\varphi}_j \equiv \frac{C_j}{C_\mathrm{A}}\frac{1}{k_\mathrm{A}}\frac{d\varphi}{dz} \quad (j = \mathrm{A},\mathrm{B})\,. \tag{2.123}$$

The transfer matrix through the layer (z_0, z) is a 2×2 matrix that relates the columns (2.123) at the points z and z_0, namely,

$$\hat{\varphi}(z) = \hat{t}(z, z_0)\hat{\varphi}(z_0)\,.$$

The transfer within a homogeneous layer A or B is realized by the matrix

$$\hat{t}(z, z_0) = \begin{bmatrix}\cos kl & \bar{N}^{-1}\sin kl\\ -\bar{N}\sin kl & \cos kl\end{bmatrix}, \tag{2.124}$$

where $l = z - z_0$, $\bar{N} = 1$ in the layer A and $\bar{N} = (C_\mathrm{B}k_\mathrm{B})/(C_\mathrm{A}k_\mathrm{A}) \equiv N$ in the layer B. Note that the transfer matrix is unimodular: $\mathrm{Det}\,\hat{t} = 1$.

According to the Bloch theorem one can seek eigensolutions satisfying the condition

$$\hat{\varphi}(d) = \hat{T}\hat{\varphi}(0) = \mathrm{e}^{iKd}\hat{\varphi}(0)\,,$$

where K is the wave vector characterizing the propagation of a quasi-particle along the principal axis z, $\hat{T}$ is the transfer matrix through a SL period, it is a product $\hat{t}_\mathrm{A}\hat{t}_\mathrm{B}$ of the transfer matrices through the layers A and B. As the first step in deriving the dispersion equation relating K and ω, we rewrite the above condition in terms of the components T_{ij} as follows

$$\mathrm{Det}\begin{bmatrix} T_{11}-\mathrm{e}^{iKd} & T_{12} \\ T_{21} & T_{22}-\mathrm{e}^{iKd} \end{bmatrix} = 0\,.$$

Taking into account the unimodularity of $\hat{T}$ we can present this equation in the form

$$\cos Kd = \frac{T_{11}+T_{22}}{2}\,. \tag{2.125}$$

By direct matrix multiplication we obtain

$$\hat{T} = \hat{t}_{\mathrm{A}}\hat{t}_{\mathrm{B}} = \begin{bmatrix} \cos k_{\mathrm{A}}a & \sin k_{\mathrm{A}}a \\ -\sin k_{\mathrm{A}}a & \cos k_{\mathrm{A}}a \end{bmatrix}\begin{bmatrix} \cos k_{\mathrm{B}}b & N^{-1}\sin k_{\mathrm{B}}b \\ -N\sin k_{\mathrm{B}}b & \cos k_{\mathrm{B}}b \end{bmatrix} =$$

$$\begin{bmatrix} \cos k_{\mathrm{A}}a\cos k_{\mathrm{B}}b - N\sin k_{\mathrm{A}}a\sin k_{\mathrm{B}}b & \text{.....} \\ \text{.....} & \cos k_{\mathrm{A}}a\cos k_{\mathrm{B}}b - N^{-1}\sin k_{\mathrm{A}}a\sin k_{\mathrm{B}}b \end{bmatrix}\,.$$

For the sake of brevity the off-diagonal components which do not enter into (2.125) are replaced by omission points. Substituting the expressions for T_{11} and T_{22} into (2.125) we finally arrive at

$$\cos Kd = \cos k_{\mathrm{A}}a\,\cos k_{\mathrm{B}}b - \frac{1}{2}\left(N+\frac{1}{N}\right)\sin k_{\mathrm{A}}a\,\sin k_{\mathrm{B}}b\,. \tag{2.126}$$

Now we pass on to particular cases and start with electrons in a short-period SL. In this case φ is the electron envelope function in the effective-mass approximation, $\omega = E/\hbar$, the coefficients in the boundary conditions are given by

$$C_{\mathrm{A}} = \frac{1}{m_{\mathrm{A}}}\,,\; C_{\mathrm{B}} = \frac{1}{m_{\mathrm{B}}}\,,\; N = \frac{m_{\mathrm{A}}}{m_{\mathrm{B}}}\frac{k_{\mathrm{B}}}{k_{\mathrm{A}}}\,.$$

For the states with the energy E lying below the barrier V, one has $k_{\mathrm{A}} = k$, $k_{\mathrm{B}} = \mathrm{i}æ$, see (2.7), and the dispersion equation can be conveniently rewritten in the form

$$\cos Kd = \cos ka\,\cosh æb\,+\,\frac{1}{2}\left(\eta-\frac{1}{\eta}\right)\sin ka\,\sinh æb\,, \tag{2.127}$$

where η is introduced in (2.12). In the reduced zone scheme values of K lie within the limits from $-\pi/d$ to π/d. At a fixed value of $\boldsymbol{q}$, for instance at $\boldsymbol{q} = 0$, the energy spectrum $E(\boldsymbol{q}, K)$ consists of alternating allowed and forbidden *minibands*. For SLs with thick potential barriers, the lower allowed minibands with $E < V$ are narrow and lie near the electron size-quantized levels in a QW of the same thickness a. As the barrier thickness b decreases the allowed minibands widen at the expense of the convergent forbidden minibands. In the limit $b \to 0$ the miniband character of the electron energy spectrum transforms into the parabolic dispersion of an electron in the host material A.

In order to analyze the dispersion at small values of K we can rewrite (2.127) in the following equivalent form

$$1 - \cos Kd = \frac{1}{2} \sin ka \, \sinh æb \, f_1 f_2 \equiv F \,, \tag{2.128}$$

$$f_1 = \tan k\frac{a}{2} - \eta \, \tanh æ\frac{b}{2} \,, \; f_2 = \frac{1}{\eta} \, \cot k\frac{a}{2} + \coth æ\frac{b}{2} \,.$$

For $|K| \ll \pi/d$ one has

$$E \approx E_{e\nu} + \frac{d^2}{2F'} K^2 \,, \tag{2.129}$$

where ν is the miniband index, $E_{e\nu}$ is the energy at $K = 0$ defined by the equations $f_1 = 0$ or $f_2 = 0$, F' is the derivative $dF(E)/dE$ at $E = E_{e\nu}$. Notice that, in the limit $b \to \infty$, the equations $f_1 = 0$, $f_2 = 0$ coincide with (2.12) and (2.14) for the confinement energy in a single QW. It follows from (2.129) that the electron effective mass for the motion along z is related to F' by

$$M_{zz} = F' \hbar^2 / d^2 \,. \tag{2.130}$$

For SLs with barriers thick enough so that $\exp(æb) \gg 1$, the allowed minibands can be described by

$$E(K) \approx E_{e\nu} + (1/F')(1 - \cos Kd) \,.$$

As regards the dependence of E on $\boldsymbol{q}$, it is parabolic if $m_\mathrm{A} = m_\mathrm{B}$, as in the bulk host materials. For $m_\mathrm{A} \neq m_\mathrm{B}$, the in-plane dispersion has a quasi-parabolic character with the effective mass slowly varying within the interval between m_A and m_B.

Next we consider the normal light waves in an optical SL with the layers A and B characterized by the local isotropic dielectric functions $æ_\mathrm{A}(\omega)$ and $æ_\mathrm{B}(\omega)$. For completeness we write down the Maxwell macroscopic equations

$$\mathrm{curl}\, \boldsymbol{B} = \frac{1}{c} \frac{\partial \boldsymbol{D}}{\partial t} \,, \; \mathrm{curl}\, \boldsymbol{E} = -\frac{1}{c} \frac{\partial \boldsymbol{B}}{\partial t} \,,$$

$$\mathrm{div} \boldsymbol{D} = 0 \,, \; \mathrm{div} \boldsymbol{B} = 0 \,.$$

Here $\boldsymbol{E}$ and $\boldsymbol{D}$ are the electric-field and electric-displacement vectors related by $\boldsymbol{D} = æ_j(\omega)\boldsymbol{E}$, and we use the form of material relation where the magnetic induction $\boldsymbol{B}$ coincides with the magnetic field $\boldsymbol{H}$. The space dispersion, or the dependence of $æ_{\mathrm{A,B}}(\omega)$ on the light wave vector $\boldsymbol{q}$, is neglected. As a rule, in what follows we omit the variable ω and use the notation $æ_{\mathrm{A,B}}$. For a monochromatic light wave the operator $\partial/\partial t$ may be replaced by the factor $-\mathrm{i}\omega$. Within each separate layer A or B the solution is a linear combination of plane waves $\exp\left[\mathrm{i}(\boldsymbol{q} \cdot \boldsymbol{\rho} \pm k_{\mathrm{A,B}} z)\right]$, where

$$k_\mathrm{A} = [(\omega/c)^2 æ_\mathrm{A} - q^2]^{1/2} \,, \; k_\mathrm{B} = [(\omega/c)^2 æ_\mathrm{B} - q^2]^{1/2} \,. \tag{2.131}$$

We fix the coordinate system x, y with $x \parallel \boldsymbol{q}$ in which case the 3D wave vectors $(q_x, q_y, \pm k_{\mathrm{A,B}})$ lie in the plane perpendicular to the y axis.

In a structure with isotropic layers, there are two types of Bloch solutions, or normal light waves, namely, TE waves (s-polarized waves) with $\boldsymbol{E} \parallel y$ and $\boldsymbol{B}$ lying in the (x, z) plane, and TM, or p-polarized waves with $\boldsymbol{B} \parallel y$. Obviously, for TE waves, the electric field $\mathcal{E}_y$ plays the role of the generalized envelope $\varphi(z)$. It follows from continuity of the tangential components $\mathcal{E}_y$ and B_x and from the relation $B_x \propto \partial\mathcal{E}_y/\partial z$, that $\mathcal{E}_y|_{\mathrm{A}} = \mathcal{E}_y|_{\mathrm{B}}$ and $(\partial\mathcal{E}_y/\partial z)|_{\mathrm{A}} = (\partial\mathcal{E}_y/\partial z)|_{\mathrm{B}}$. Therefore, for the TE-polarized light waves, we have $C_{\mathrm{A}} = C_{\mathrm{B}}$ and $N = k_{\mathrm{B}}/k_{\mathrm{A}}$.

Similarly, for TM waves, the role of $\varphi(z)$ is played by B_y, the first boundary condition is $B_y|_{\mathrm{A}} = B_y|_{\mathrm{B}}$, and from continuity of $\mathcal{E}_x \propto æ_j^{-1}(\partial B_y/\partial z)$ we obtain the second boundary condition

$$\frac{1}{æ_{\mathrm{A}}}\left(\frac{\partial B_y}{\partial z}\right)_{\mathrm{A}} = \frac{1}{æ_{\mathrm{B}}}\left(\frac{\partial B_y}{\partial z}\right)_{\mathrm{B}} ,$$

i.e., $C_{\mathrm{A}} = æ_{\mathrm{A}}^{-1}, C_{\mathrm{B}} = æ_{\mathrm{B}}^{-1}$, $N = (k_{\mathrm{B}}æ_{\mathrm{A}})/(k_{\mathrm{A}}æ_{\mathrm{B}})$. The dispersion equation for both TE- and TM-waves is given by the canonical equation (2.126).

In the long-wavelength approximation, when $|k_{\mathrm{A}}|a, |k_{\mathrm{B}}|b, |K|d \ll 1$, the optical SL may be considered a homogeneous uniaxial medium with the effective dielectric tensor

$$æ_{xx} = æ_{yy} = \frac{æ_{\mathrm{A}}a + æ_{\mathrm{B}}b}{a+b} , \; æ_{zz} = \left(\frac{a}{æ_{\mathrm{A}}} + \frac{b}{æ_{\mathrm{B}}}\right)^{-1} (a+b) . \qquad (2.132)$$

This result can be obtained by expanding the trigonometrical functions in (2.126) in powers of $k_{\mathrm{A}}a, k_{\mathrm{B}}b, Kd$. However, it can be also derived in a simple way if we take into account that, in the long-wavelength limit, the fields $\boldsymbol{E}$ and $\boldsymbol{B}$ change very little within each layer. The electric field $\mathcal{E}_y$ is continuous at the interface and the difference of its values in the neighboring layers may be ignored. The displacement D_y is approximately constant within each layer but its values jump at the interface from $D_{\mathrm{A},y} = æ_{\mathrm{A}}\mathcal{E}_y$ to $D_{\mathrm{B},y} = æ_{\mathrm{B}}\mathcal{E}_y$. The electric displacement averaged over the period is given by

$$\bar{D}_y = \frac{a\, D_{\mathrm{A},y} + b\, D_{\mathrm{B},y}}{a+b} = \frac{æ_{\mathrm{A}}\, a + æ_{\mathrm{B}}\, b}{a+b}\, \mathcal{E}_y ,$$

which agrees with the expression (2.132) for $æ_{yy}$. If we take into account the continuity of the normal component D_z of the displacement field and the relations $\mathcal{E}_{\mathrm{A},z} = D_z/æ_{\mathrm{A}}$, $\mathcal{E}_{\mathrm{B},z} = D_z/æ_{\mathrm{B}}$, we obtain for the average (macroscopic) field

$$\bar{\mathcal{E}}_z = \frac{a\, \mathcal{E}_{\mathrm{A},z} + b\, \mathcal{E}_{\mathrm{B},z}}{a+b} = \frac{a\, æ_{\mathrm{A}}^{-1} + b\, æ_{\mathrm{B}}^{-1}}{a+b}\, D_z ,$$

in agreement with the above expression for $æ_{zz}$.

Equation (2.126) for TM-modes suggests an important limiting case realized for

$$q^2 \gg \left(\frac{\omega}{c}\right)^2 |æ_{\mathrm{A,B}}| . \qquad (2.133)$$

In this case the retardation effects are negligible, one can use the approximations

$$k_{\mathrm{A}}, k_{\mathrm{B}} \to \mathrm{i}q_x \ , \ N \to \frac{æ_{\mathrm{A}}}{æ_{\mathrm{B}}} \ ,$$

and obtains, instead of (2.126), the secular equation for the so-called *interface modes* [2.98, 2.99]

$$\cos Kd = \cosh\left(q_x a\right)\cosh\left(q_x b\right) + \frac{1}{2}\left(\frac{æ_{\mathrm{B}}}{æ_{\mathrm{A}}} + \frac{æ_{\mathrm{A}}}{æ_{\mathrm{B}}}\right)\sinh\left(q_x a\right)\sinh\left(q_x b\right) . \tag{2.134}$$

Taking into account the condition (2.133) the above equation can be derived from a scalar potential $\phi(\boldsymbol{r})$ which determines the electric field $\boldsymbol{E} = -\nabla\phi$ if the retardation is neglected. In this approximation the magnetic field is zero. Within each A and B layer, the Laplace equation $\Delta\phi(\boldsymbol{r}) = 0$ is fulfilled by the exponential functions $\exp\left(\mathrm{i}q_x x \pm q_x z\right)$. Thus, the generalized envelope $\varphi(z)$ reduces to the potential ϕ and one indeed has $k_{\mathrm{A}} = k_{\mathrm{B}} = \mathrm{i}q_x$. The boundary conditions are $\phi_{\mathrm{A}} = \phi_b$ and $æ_{\mathrm{A}}(d\phi/dz)_{\mathrm{A}} = æ_{\mathrm{B}}(d\phi/dz)_{\mathrm{B}}$ which leads to $C_{\mathrm{A}} = æ_{\mathrm{A}}$, $C_{\mathrm{B}} = æ_{\mathrm{B}}$, $N = æ_{\mathrm{B}}/æ_{\mathrm{A}}$ and, finally, to (2.134).

For a SL with thick layers, $q_x a, q_x b \to \infty$, this equation reduces to

$$1 + \frac{1}{2}\left(\frac{æ_{\mathrm{B}}}{æ_{\mathrm{A}}} + \frac{æ_{\mathrm{A}}}{æ_{\mathrm{B}}}\right) = \frac{\left(æ_{\mathrm{A}} + æ_{\mathrm{B}}\right)^2}{2\, æ_{\mathrm{A}}\, æ_{\mathrm{B}}} = 0 \, .$$

This is nothing more than the well-known equation $æ_{\mathrm{A}}(\omega) + æ_{\mathrm{B}}(\omega) = 0$ for surface modes at a single interface between semiconductors A and B. It has solutions only if there are frequencies for which the dielectric functions $æ_{\mathrm{A}}(\omega)$ and $æ_{\mathrm{B}}(\omega)$ have opposite signs. To illustrate we consider the surface optical phonon. Let ω lie in the region of optical-phonon resonance frequency of the host material A. Then, one has

$$æ_{\mathrm{A}}(\omega) = æ_\infty \frac{\Omega_{LO}^2 - \omega^2}{\Omega_{TO}^2 - \omega^2} \ ,$$

where Ω_{TO}, Ω_{LO} are the resonance frequencies of transverse and longitudinal optical phonons. For simplicity, the dielectric function of the B material is assumed to be independent of ω and equal to the high-frequency dielectric constant of the A material, $æ_\infty$. Then, the frequency of the surface wave is $\Omega_s = \sqrt{(\Omega_{LO}^2 + \Omega_{TO}^2)/2}$. If $\Omega_{LO} - \Omega_{TO} \ll \Omega_{TO}$, the value Ω_s lies at the midpoint between Ω_{LO} and Ω_{TO}.

For a SL with the thick B layers, $q_x b \to \infty$, and the A layer of finite thickness, we obtain from (2.134)

$$\cosh\ q_x a + \frac{1}{2}\left(\frac{æ_{\mathrm{B}}}{æ_{\mathrm{A}}} + \frac{æ_{\mathrm{A}}}{æ_{\mathrm{B}}}\right)\ \sinh\ q_x a = 0 \, .$$

These are mixed left- and right-hand-side surface modes coupled because of the finite thickness a [2.100]. For the above simple model, the eigenfrequencies are given by

$$\omega^2 = \Omega_s^2 \pm \frac{1}{2}(\Omega_{LO}^2 - \Omega_{TO}^2)\mathrm{e}^{-q_x a} .$$

Particularly, if $\Omega_{LO} - \Omega_{TO} \ll \Omega_{TO}$, we have

$$\omega = \Omega_s \pm \frac{1}{2}\left(\Omega_{LO} - \Omega_{TO}\right)\mathrm{e}^{-q_x a} .$$

Now it is clear that the interface mode in a SL with finite a and b is a surface excitation transferred from one interface to another and propagating in that way along the SL principal axis.

The last problem involving wave propagation in SLs and related to the canonical equation (2.126) concerns *folded acoustic phonons*. Here we restrict ourselves to longitudinal acoustic phonons propagating along the principal axis z. The role of $\varphi(z)$ is played by the lattice displacement $u_z(z)$ along z. In the elastic limit the dispersion relations of the constituents are linear, namely, $\omega_{\mathrm{A}}(q) = s_{\mathrm{A}}q$ and $\omega_{\mathrm{B}}(q) = s_{\mathrm{B}}q$, where $s_{\mathrm{A,B}}$ is the longitudinal sound velocity. Therefore, k_{A} and k_{B} in the generalized description equal ω/s_{A} and ω/s_{B}, respectively. The first boundary condition is the continuity of u_z while the second condition follows from the continuity of the stress tensor component σ_{zz} related to the strain tensor component $u_{zz} = \partial u_z/\partial z$ by $\sigma_{zz} = \lambda u_{zz}$. Here λ is the elastic stiffness constant C_{zzzz} which can be expressed via the bulk density ρ and the longitudinal sound velocity s: $\lambda = \rho s^2$. Since the second boundary condition is rewritten as

$$\lambda_{\mathrm{A}} u_{zz}|_{\mathrm{A}} = \lambda_{\mathrm{B}} u_{zz}|_{\mathrm{B}} ,$$

we have

$$C_{\mathrm{A}} = \lambda_{\mathrm{A}} , \; C_{\mathrm{B}} = \lambda_{\mathrm{B}} , \; N = \frac{\lambda_{\mathrm{B}} k_{\mathrm{B}}}{\lambda_{\mathrm{A}} k_{\mathrm{A}}} = \frac{\rho_{\mathrm{B}} s_{\mathrm{B}}}{\rho_{\mathrm{A}} s_{\mathrm{A}}} ,$$

and equation (2.126) takes the form [2.99, 2.101]

$$\begin{aligned} \cos Kd = \cos\left(\frac{a\omega}{s_{\mathrm{A}}}\right)\cos\left(\frac{b\omega}{s_{\mathrm{B}}}\right) \\ - \frac{1}{2}\left(\frac{\rho_{\mathrm{B}} s_{\mathrm{B}}}{\rho_{\mathrm{A}} s_{\mathrm{A}}} + \frac{\rho_{\mathrm{A}} s_{\mathrm{A}}}{\rho_{\mathrm{B}} s_{\mathrm{B}}}\right)\sin\left(\frac{a\omega}{s_{\mathrm{A}}}\right)\sin\left(\frac{b\omega}{s_{\mathrm{B}}}\right) . \end{aligned} \tag{2.135}$$

Usually, in semiconductor SLs the parameter

$$\varepsilon = \frac{\rho_{\mathrm{B}} s_{\mathrm{B}} - \rho_{\mathrm{A}} s_{\mathrm{A}}}{\sqrt{\rho_{\mathrm{A}} \rho_{\mathrm{B}} s_{\mathrm{A}} s_{\mathrm{B}}}}$$

is small and (2.135) can be conveniently rewritten in the slightly modified form

$$\cos Kd = \cos\left[\omega\left(\frac{a}{s_{\rm A}} + \frac{b}{s_{\rm B}}\right)\right] - \frac{\varepsilon^2}{2}\sin\left(\frac{a\omega}{s_{\rm A}}\right)\sin\left(\frac{b\omega}{s_{\rm B}}\right). \qquad (2.136)$$

Neglecting the term proportional to ε^2 we obtain the dispersion relation

$$K = (k_{\rm A}a + k_{\rm B}b)/d = \omega/\bar{s}\,, \qquad (2.137)$$

which is that of a homogeneous medium with the average sound velocity

$$\bar{s} = (a+b)\left(\frac{a}{s_{\rm A}} + \frac{b}{s_{\rm B}}\right)^{-1}.$$

In the reduced zone scheme the straight line $\omega = \bar{s}K$ is folded within the first Brillouin zone of the SL, $-\pi/d < K \leq \pi/d$, as shown in Fig. 2.8 by the dashed curve. Allowance for nonzero value of ε results in the formation of *acoustic* allowed and forbidden *minibands*. For small values of the mismatch ε the width of the first forbidden miniband at $K = 0$ is found from the condition

$$0 = -\frac{1}{2}\left(\frac{\omega}{\bar{s}}\,d - 2\pi\right)^2 - \frac{\varepsilon^2}{2}\sin\left(\frac{\omega a}{s_{\rm A}}\right)\sin\left(\frac{\omega a}{s_{\rm B}}\right)$$

or $\Delta\omega = 2\,(\bar{s}/d)\,|\varepsilon\sin(\omega a/s_{\rm A})|$. Here we took into account that, at $\omega = \bar{s}(2\pi/d)$, one has $\sin k_{\rm B}b \approx \sin(2\pi - k_{\rm A}a) = -\sin k_{\rm A}a$.

Fig. 2.8 schematically represents the dispersion of folded acoustic phonons in a SL. The solid curve shows the spectrum at a nonzero value of the mismatch ε. The dispersion branches, or acoustic minibands, are labelled by the index l running through the integers $0, \pm1, \pm2...$ The branch outgoing from the point $\omega = 0, K = 0$ corresponds to $l = 0$, two next branches are labelled by $l = \pm1$ etc. Under such labelling the dashed curve in Fig. 2.8 is described analytically by

$$\Omega_{lK} = \bar{s}\left(|K|{\rm sign}\{l\} + \frac{2\pi}{d}|l|\right). \qquad (2.138)$$

Raman scattering of light by folded acoustic phonons is considered in Chap. 6.

2.6 Interband Optical Transitions

We shall now consider the optical transitions at the fundamental absorption edge in undoped semiconductors and semiconductor nanostructures. In a semi-classical approach the electromagnetic field is treated classically while the electronic subsystem is described quantum-mechanically. In the following we use the Coulomb gauge with a zero scalar potential. In this gauge the electric and magnetic fields, $\boldsymbol{E}$ and $\boldsymbol{B}$, are expressed via the vector potential $\boldsymbol{A}(\boldsymbol{r}, t)$ by

$$\boldsymbol{E} = -\frac{1}{c}\frac{\partial \boldsymbol{A}}{\partial t}\,,\ \boldsymbol{B} = {\rm curl}\,\boldsymbol{A}\,, \qquad (2.139)$$

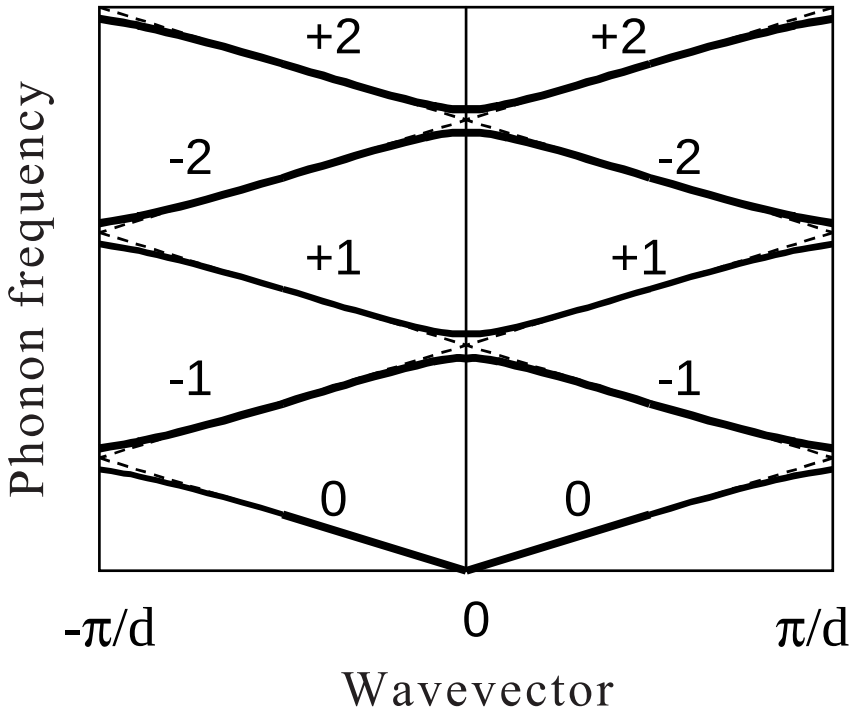

Fig. 2.8. Schematic representation of the dispersion of folded acoustic phonons in a SL. Dashed and solid lines show the dispersion, respectively, for zero and nonzero values of the parameter ε in (2.136).

where c is the light velocity in vacuum. For a plane monochromatic light wave propagating in a homogeneous medium, one has

$$\boldsymbol{A}(\boldsymbol{r},t) = \boldsymbol{A}_0 \mathrm{e}^{-\mathrm{i}\omega t + \mathrm{i}\boldsymbol{q}\cdot\boldsymbol{r}} + \boldsymbol{A}_0^* \mathrm{e}^{\mathrm{i}\omega t - \mathrm{i}\boldsymbol{q}\cdot\boldsymbol{r}} \,, \tag{2.140}$$

where $\boldsymbol{q}$ is the light wave vector and $\boldsymbol{A}_0$ is the amplitude related with the energy flux I by

$$A_0^2 = \frac{2\pi c}{n_\omega \omega^2}\, I \,, \tag{2.141}$$

n_ω being the refractive index of the medium at the frequency ω. It is convenient to present the vector $\boldsymbol{A}_0$ as a product $A_0\boldsymbol{e}$ of the real (positive) scalar amplitude A_0 and the polarization unit vector $\boldsymbol{e}$ satisfying the condition $|\boldsymbol{e}|^2 = 1$. We remind that for an elliptically polarized light wave the unit vector $\boldsymbol{e}$ is complex. In an interband optical absorption process, the radiation field transfers an electron from the occupied valence band to the unoccupied conduction band. In other words, the photon absorption is followed by the generation of an electron-hole pair. Here we treat the interband absorption in the single-particle approximation neglecting the interaction between the

photogenerated electron and hole. In the following section and other chapters of the book we will go beyond this approximation and include the effects of electron-hole Coulomb interaction, or excitonic effects, into consideration.

2.6.1 Transition Probability Rate

In linear optics, the perturbation operator of the electron-photon interaction has the form

$$-\frac{e}{c}\frac{1}{2m_0}[\hat{\boldsymbol{p}}\cdot\boldsymbol{A}(\boldsymbol{r},t)+\boldsymbol{A}(\boldsymbol{r},t)\cdot\hat{\boldsymbol{p}}]\,,$$

where $\hat{\boldsymbol{p}}$ is the momentum operator $-\mathrm{i}\hbar\nabla$. In the dipole approximation the coordinate dependence of $\boldsymbol{A}$ is neglected and the perturbation operator takes the form

$$-\frac{eA_0}{cm_0}\left(\boldsymbol{e}\,\mathrm{e}^{-\mathrm{i}\omega t}+\boldsymbol{e}^*\mathrm{e}^{\mathrm{i}\omega t}\right)\cdot\hat{\boldsymbol{p}}\,.$$

Using Fermi's golden rule to second order perturbation one can write for the optical transition rate

$$W^{(d)}_{e\nu,h\nu'}=\frac{1}{V_d}\,\frac{2\pi}{\hbar}\sum_{sm\boldsymbol{k}}|M(e\nu s,v\nu' m;\boldsymbol{k})|^2\,\delta(E_{e\nu s\boldsymbol{k}}-E_{v\nu' m\boldsymbol{k}}-\hbar\omega)\,, \quad (2.142)$$

where the matrix element of the one-photon direct transition $h\nu' m\boldsymbol{k}\to e\nu s\boldsymbol{k}$ is given by

$$M(e\nu s,v\nu' m;\boldsymbol{k})=-\frac{eA_0}{cm_0}\,\boldsymbol{e}\cdot\boldsymbol{p}_{e\nu s,v\nu' m}(\boldsymbol{k})\,, \quad (2.143)$$

$\boldsymbol{p}_{e\nu s,v\nu' m}(\boldsymbol{k})\equiv\langle e\nu s\boldsymbol{k}|\hat{\boldsymbol{p}}|v\nu' m\boldsymbol{k}\rangle$ is the matrix element of the momentum operator taken between the single-electron conduction- and valence-band states, and the indices ν,ν' enumerate the quantum-confined electron states in QWs ($d=2$), QWRs ($d=1$) and QDs ($d=0$). The valence-band energy $E_{v\nu' m\boldsymbol{k}}$ in the δ-function describing the energy conservation law is given in the electron representation. Note that it is related with the energy of the corresponding hole state by $E_{v\nu' m\boldsymbol{k}}=-E_{h\nu'\bar{m},-\boldsymbol{k}}$ where the bar over m means the spin opposite to m. The transition probability rate (2.142) is related to unit volume of the d-dimensional space, V_d being the macroscopic volume of the system, namely, the 3D volume of a bulk semiconductor, the lateral area of a QW, the wire length L for a QWR, and $V_d\to 1$ for a QD. The vector $\boldsymbol{k}$ in (2.142, 2.143) is a d-dimensional vector, if $d=1,2,3$, and this quantum number is absent for 0D systems.

In what follows we focus the attention on direct optical transitions in the vicinity of the Γ-point. Neglecting $\boldsymbol{k}$ dependence of the matrix element $\boldsymbol{p}_{e\nu s,v\nu' m}$ we can write it as

$$\boldsymbol{p}_{e\nu s,v\nu' m}=i_{\nu\nu'}\,\boldsymbol{p}_{cs,vm}\,. \quad (2.144)$$

The first multiplier called the *overlap integral* is defined for a QW as

$$i_{\nu\nu'} = \int \varphi_{e\nu}(z)\varphi_{h\nu'}(z)dz \tag{2.145}$$

and similarly for QWRs and QDs. The second multiplier is the matrix element of the momentum operator calculated between the Γ-point Bloch functions,

$$\boldsymbol{p}_{cs,vm} = \frac{1}{\Omega_0}\int_{\Omega_0} u^*_{cs}(\boldsymbol{r})\,\hat{\boldsymbol{p}}\,u_{vm}(\boldsymbol{r})\,d\boldsymbol{r}\,, \tag{2.146}$$

where Ω_0 is the unit-cell volume.

If the spin splitting of electronic states is neglected the probability rate is rewritten as

$$W^{\mathrm{QW}}_{e\nu,h\nu'} = \frac{e^2}{\hbar c n_\omega}\frac{I}{m_0^2\omega^2}\,g_{e\nu,h\nu'}(\hbar\omega)\,i^2_{\nu\nu'}\sum_{sm}|\boldsymbol{e}\cdot\boldsymbol{p}_{cs,vm}|^2\,, \tag{2.147}$$

where $g_{e\nu,h\nu'}(E)$ is the reduced density of states

$$g_{e\nu,h\nu'}(E) = \frac{1}{V_d}\sum_{\boldsymbol{k}}\delta(E_{e\nu\boldsymbol{k}} - E_{v\nu'\boldsymbol{k}} - E)\,. \tag{2.148}$$

To illustrate we consider the parabolic dispersion of the electron and hole bands, or subbands, assuming

$$E_{e\nu\boldsymbol{k}} = E^0_c + E_{e\nu} + \frac{\hbar^2k^2}{2m_e}\,,\; E_{v\nu\boldsymbol{k}} = E^0_v - E_{h\nu} - \frac{\hbar^2k^2}{2m_h}\,,$$

where E^0_c, E^0_v are the band edges in the well host material, $E_{e\nu}$ and $E_{h\nu}$ are the electron and hole quantum-confinement energies. For this simple band structure, we obtain the reduced densities of states

$$g_3(E) = \frac{1}{4\pi^2}\left(\frac{2\mu_{eh}}{\hbar^2}\right)^{3/2}\sqrt{E - E^0_{\nu\nu'}}\;\theta(E - E^0_{\nu\nu'})\,, \tag{2.149a}$$

$$g_2(E) = \frac{\mu_{eh}}{2\pi\hbar^2}\,\theta(E - E^0_{\nu\nu'})\,, \tag{2.149b}$$

$$g_1(E) = \frac{1}{2\pi}\left(\frac{2\mu_{eh}}{\hbar^2(E - E^0_{\nu\nu'})}\right)^{1/2}\theta(E - E^0_{\nu\nu'})\,, \tag{2.149c}$$

$$g_0(E) = \delta(E - E^0_{\nu\nu'})\,, \tag{2.149d}$$

where $\mu_{eh} = m_e m_h/(m_e + m_h)$ is the reduced effective mass, $E^0_{\nu\nu'}$ is the band gap attached to the pair of subbands $e\nu$ and $h\nu'$,

$$E^0_{\nu\nu'} = E_g + E_{e\nu} + E_{h\nu'}\,, \tag{2.150}$$

and $E_g = E^0_c - E^0_v$. The fundamental absorption edge

$$E^{\mathrm{QW}}_g \equiv E^0_{11} = E_g + E_{e1} + E_{h1} \tag{2.151}$$

corresponds to the absolute valence-band maximum and conduction-band minimum.

It follows from (2.149) that, in a QW, the density of states $g_2(E)$ looks like a horizontal step. In a QWR, the dependence $g(E)$ has a square-root peak and is similar to that for electron states in a bulk semiconductor subject to a quantizing magnetic field. In a QD, the energy level structure is discrete, the isolated levels are somewhat broadened only due to finite lifetimes of electrons and holes. The density of states for single electrons and holes is defined by expressions similar to (2.148). Note however that, as compared with (2.148), the single-particle density of states usually has an additional factor of 2 to take into account the spin degeneracy.

2.6.2 Selection Rules

In QW, QWR or QD structures with isotropic, both electron and hole, effective masses in the well host material and infinitely high barriers, the envelope functions $\varphi_{e\nu}$ and $\varphi_{h\nu}$ are identical and independent of the effective masses. Since, by definition, each of the sets is orthonormalized, we come to the selection rule

$$i_{\nu\nu'} = \delta_{\nu\nu'} \,. \tag{2.152}$$

Thus, the optical transitions take place only between conduction and valence subbands (or levels in QDs) with the coinciding quantum numbers.

For finite barriers, the shape of envelope wave function depends on the effective masses and the sets of envelopes for electrons and holes are different. Nevertheless, in many nanostructures, this difference is not dramatic and one can use the following soft selection rules

$$i_{\nu\nu} \approx 1 \quad \text{and} \quad |i_{\nu\nu'}| \ll 1 \quad \text{for} \quad \nu \neq \nu' \,. \tag{2.153}$$

If the confining potential has a center of symmetry, then the interband transitions between the states with envelopes $\varphi_{e\nu}, \varphi_{h\nu'}$ of opposite parity are of course forbidden.

Now we turn to the selection rules imposed by the second multiplier in (2.144). Table 2.2 presents the interband matrix elements $\boldsymbol{e} \cdot \boldsymbol{p}_{cs,vm}$ calculated between the conduction-band states $|\Gamma_6, s\rangle = \alpha_s S$ and the valence-band states $|\Gamma_8, m\rangle$ in the basis (2.22). The initial and final states, $|vm\rangle$ and $|cs\rangle$, are both taken in the electron representation. The values presented in the table should be multiplied by $p_{cv}/\sqrt{2}$, where the interband matrix element p_{cv} is defined in (2.46).

Table 2.2. The interband matrix elements of the momentum operator, $\boldsymbol{e} \cdot \boldsymbol{p}_{cs,vm}$, related to $p_{cv}/\sqrt{2}$. Here $\boldsymbol{e}$ is the light polarization unit vector.

	$v, +3/2$	$v, +1/2$	$v, -1/2$	$v, -3/2$
$c, +1/2$	$-(e_x + \mathrm{i}e_y)$	$2e_z/\sqrt{3}$	$(e_x - \mathrm{i}e_y)/\sqrt{3}$	0
$c, -1/2$	0	$-(e_x + \mathrm{i}e_y)/\sqrt{3}$	$2e_z/\sqrt{3}$	$e_x - \mathrm{i}e_y$

We remind that, in the electron and hole representations, the angular momenta of the valence states differ in sign and, therefore, the matrix elements in these two representation are related by $M(e\nu s, h\nu' m; \boldsymbol{k}) = M(e\nu s, v\nu', \bar{m}; -\boldsymbol{k})$. Now we take into account that, in QW structures, heavy- and light-holes at $k_x = k_y = 0$ are quantized independently. By using Table 2.2 and changing the sign of m we obtain the probability rates for the generation of electron-hole pairs $|e\nu s\,;\, hh\nu, m\rangle$ and $|e\nu s\,;\, lh\nu, m\rangle$ in QWs

$$
\begin{aligned}
&|M(e\nu, \pm 1/2\,;\, hh\nu, \mp 3/2)|^2 \propto |e_x \pm \mathrm{i}e_y|^2\,, \\
&|M(e\nu, \pm 1/2\,;\, hh\nu, \pm 3/2)|^2 = 0\,, \\
&|M(e\nu, \pm 1/2\,;\, lh\nu, \pm 1/2,)|^2 \propto \frac{1}{3}|e_x \mp \mathrm{i}e_y|^2\,, \\
&|M(e\nu, \pm 1/2\,;\, lh\nu, \mp 1/2)|^2 \propto \frac{4}{3}\,|e_z|^2\,.
\end{aligned}
\tag{2.154}
$$

Similar equations for the interband transitions from the spin-orbit (so) split valence band Γ_7, in the basis (2.23), are as follows

$$
\begin{aligned}
&|M(e\nu, \pm 1/2\,;\, h, so, \nu, \mp 1/2)|^2 \propto \frac{2}{3}|e_x \mp \mathrm{i}e_y|^2\,, \\
&|M(e\nu, \pm 1/2\,;\, h, so, \nu, \mp 1/2,)|^2 \propto \frac{2}{3}|e_z|^2\,,
\end{aligned}
\tag{2.155}
$$

where the symbol h reminds that here we use the hole representation for valence band states.

For the σ_+ circularly-polarized light propagating along z, the following equations hold

$$
\boldsymbol{e} = \frac{\boldsymbol{o}_x + \mathrm{i}\boldsymbol{o}_y}{\sqrt{2}}\,,\ e_z = 0 \quad \text{and} \quad |e_x + \mathrm{i}e_y|^2 = 0\,,\ |e_x - \mathrm{i}e_y|^2 = 2\,,
$$

whereas, for the σ_--polarized light, one has

$$
\boldsymbol{e} = \frac{\boldsymbol{o}_x - \mathrm{i}\boldsymbol{o}_y}{\sqrt{2}}\,,\ |e_x + \mathrm{i}e_y|^2 = 2\,,\ |e_x - \mathrm{i}e_y|^2 = 0\,,
$$

where $\boldsymbol{o}_x, \boldsymbol{o}_y$ are the unit vectors pointing in the directions x and y, respectively. The selection rules for the interband photoexcitation of an electron $(e\nu, s)$ and a hole $(hh\nu, m)$ in a QW for both linear and circular polarizations are presented in Table 2.3. One can see that, under interband transitions, the angular momentum component along z is conserved

$$
s + m = M\,, \tag{2.156}
$$

where $M = \pm 1$ for the $\sigma_\pm$ polarization and $M = 0$ for the linear polarization along z.

Table 2.3. Selection rules for interband optical transitions in QW structures. Numbers give values of squared matrix elements $|M(e\nu, s\,;\, j\nu, m)|^2$ $(j = hh, lh)$ in relative units. $|j\nu, m\rangle$ is the valence band state in the hole representation.

s, m	linear $\boldsymbol{e} \perp z$	linear $\boldsymbol{e} \parallel z$	circular σ_+ $e_y = \mathrm{i}e_x$	circular σ_- $e_y = -\mathrm{i}e_x$
$1/2, -3/2$	1	0	0	2
$-1/2, 3/2$	1	0	2	0
$1/2, 3/2$	0	0	0	0
$-1/2, -3/2$	0	0	0	0
$1/2, 1/2$	1/3	0	2/3	0
$-1/2, -1/2$	1/3	0	0	2/3
$1/2, -1/2$	0	4/3	0	0
$-1/2, 1/2$	0	4/3	0	0

2.7 Excitons in Semiconductors

2.7.1 Free Excitons in Bulk Crystals

Up to now we followed the single-particle Bloch scheme describing the independent motion of charge-carrying electrons and holes. The concept of excitons proposed by Frenkel in 1931 [2.102] goes beyond the scope of this scheme. The free exciton is an electron excitation which involves correlated motion of electrons and holes, does not carry current, but does carry energy. Frenkels's original model is appropriate for molecular crystals. Due to intermolecular interaction, an excited molecule can induce an upward transition in the neighboring molecule de-exciting itself. Thus, the molecular exciton can move and an exciton band is formed. In addition to *Frenkel excitons*, there are two other basic types of excitons [2.103]. In *charge-transfer excitons*, the excited state is formed by an electron and a hole lying on neighboring atoms. In the limit opposite to the Frenkel case and applicable for most semiconductors, the electron and hole are separated by many inter-atomic spacings and one can use the effective mass approximation to calculate the exciton energy levels and wave functions. This is the so-called *Wannier-Mott exciton* first considered in [2.104, 2.105].

The wave function of the Wannier-Mott exciton can be expanded in the states of noninteracting electron-hole pairs as follows

$$\Psi^{\mathrm{exc}} = \sum_{s\boldsymbol{k}_e, m\boldsymbol{k}_h} C_{s\boldsymbol{k}_e, m\boldsymbol{k}_h} |s\boldsymbol{k}_e, m\boldsymbol{k}_h\rangle \,. \tag{2.157}$$

Here s, m are the indices identifying the conduction- and valence-band spin branches, $\boldsymbol{k}_{e,h}$ is the electron or hole wave vector, $|s\boldsymbol{k}_e, m\boldsymbol{k}_h\rangle$ is the excited state of the crystal in which only one conduction-band state $|s\boldsymbol{k}_e\rangle$ is occupied and only one valence state $\hat{\mathcal{K}}|m\boldsymbol{k}_h\rangle$ is empty. In fact, $|s\boldsymbol{k}_e, m\boldsymbol{k}_h\rangle$ is a many-particle state. Sometimes it is presented in the effective form of a two-particle wave function

$$|s\boldsymbol{k}_e, m\boldsymbol{k}_h\rangle = \psi_{cs\boldsymbol{k}_e}(\boldsymbol{r}_e)\psi^h_{m\boldsymbol{k}_h}(\boldsymbol{r}_h)\,, \tag{2.158}$$

where $\psi_{cs\boldsymbol{k}_e}(\boldsymbol{r}_e)$ is the Bloch function for the electron in the conduction band, and $\psi^h_{m\boldsymbol{k}_h}(\boldsymbol{r}_h)$ is that in the hole representation obtained from the corresponding electron Bloch function for the valence band by the time inversion operator $\hat{\mathcal{K}}$ defined in (2.40). With the correspondence between the valence states in the electron and hole representations properly established, the use of (2.158) offers a number of advantages, rather than presents any difficulties.

By the envelope wave function of the exciton in the real-space representation, or the $\boldsymbol{r}$-representation, one understands the function obtained by inverse Fourier transform

$$\varphi_{sm}(\boldsymbol{r}_e, \boldsymbol{r}_h) = \sum_{\boldsymbol{k}_e\boldsymbol{k}_h} \mathrm{e}^{\mathrm{i}(\boldsymbol{k}_e\cdot\boldsymbol{r}_e + \boldsymbol{k}_h\cdot\boldsymbol{r}_h)} C_{s\boldsymbol{k}_e, m\boldsymbol{k}_h}\,. \tag{2.159}$$

In terms of the two-particle wave function (2.158) the exciton wave function takes the form

$$\Psi^{\mathrm{exc}} = \sum_{sm} \varphi_{sm}(\boldsymbol{r}_e, \boldsymbol{r}_h)\psi^0_{cs}(\boldsymbol{r}_e)\psi^{h0}_m(\boldsymbol{r}_h)\,, \tag{2.160}$$

where ψ^0_{cs}, ψ^{h0}_m are the Bloch functions at the extremum point, here the Γ point.

In the effective mass approximation, the envelopes $\varphi_{sm}(\boldsymbol{r}_e, \boldsymbol{r}_h)$ satisfy the two-particle (hydrogen-like) Schrödinger equation

$$\sum_{s'm'} \mathcal{H}_{sm,s'm'}\left(\hat{\boldsymbol{k}}_e, \hat{\boldsymbol{k}}_h\right)\varphi_{s'm'}(\boldsymbol{r}_e, \boldsymbol{r}_h) = E\varphi_{sm}(\boldsymbol{r}_e, \boldsymbol{r}_h)\,. \tag{2.161}$$

Here E is the exciton excitation energy, i.e., the energy of the excited state (2.157) referred to the energy of the crystal ground state $|0\rangle$ in which the conduction band is empty and the valence band is completely filled. Other notations are as follows: $\hat{\boldsymbol{k}}_e = -\mathrm{i}\partial/\partial\boldsymbol{r}_e$, $\hat{\boldsymbol{k}}_h = -\mathrm{i}\partial/\partial\boldsymbol{r}_h$, $\mathcal{H}_{sm,s'm'}(\boldsymbol{k}_e, \boldsymbol{k}_h)$ is the effective Hamiltonian of the electron-hole pair, which for a homogeneous semiconductor has the form

$$\begin{aligned}\mathcal{H}_{sm,s'm'}(\boldsymbol{k}_e, \boldsymbol{k}_h) = {} & \delta_{mm'}\mathcal{H}^e_{ss'}(\boldsymbol{k}_e) + \delta_{ss'}\mathcal{H}^h_{mm'}(\boldsymbol{k}_h) \\ & + \delta_{ss'}\delta_{mm'}\left(E_g - \frac{e^2}{æ|\boldsymbol{r}_e - \boldsymbol{r}_h|}\right)\,,\end{aligned} \tag{2.162}$$

and which can be also written in a more compact and symbolic form as

$$\mathcal{H}(\boldsymbol{k}_e, \boldsymbol{k}_h) = \mathcal{H}^e(\boldsymbol{k}_e) + \mathcal{H}^h(\boldsymbol{k}_h) + E_g - \frac{e^2}{æ|\boldsymbol{r}|}\,. \tag{2.163}$$

Here $\mathcal{H}^e$ and $\mathcal{H}^h$ are the effective single-particle Hamiltonians for the electron and hole, $\boldsymbol{r} = \boldsymbol{r}_e - \boldsymbol{r}_h$, æ is the low-frequency dielectric constant whose dispersion is neglected. Equation (2.161) with the Hamiltonian (2.162) describes

the state of the so-called *mechanical exciton*. The calculation of mechanical excitons does not include the *exchange interaction* between the electron and the hole in the exciton. This interaction as well as *exciton-photon coupling* will be discussed in Chaps. 3, 5 and 7.

For the simple conduction- and valence-band structure, the exciton envelope functions are hydrogen-like. For example, the ground-state exciton, or $1s$-exciton, is described by the envelope

$$\Psi_{1s}^{\mathrm{exc}}(\boldsymbol{r}_e, \boldsymbol{r}_h) = \frac{\mathrm{e}^{\mathrm{i}\boldsymbol{K}\cdot\boldsymbol{R}}}{\sqrt{V}}\, \varphi_{1s}(\boldsymbol{r})\,,\ \varphi_{1s}(\boldsymbol{r}) = \frac{\mathrm{e}^{-r/a_{\mathrm{B}}}}{\sqrt{\pi a_{\mathrm{B}}^3}}\,. \tag{2.164}$$

Here V is the crystal volume, $\boldsymbol{R}$ is the exciton center of mass,

$$\boldsymbol{R} = \frac{m_e\boldsymbol{r}_e + m_h\boldsymbol{r}_h}{m_e + m_h}\,, \tag{2.165}$$

$m_{e,h}$ is the electron or hole effective mass, a_{B} is the exciton Bohr radius

$$a_{\mathrm{B}} = \frac{æ\hbar^2}{\mu_{eh}e^2}\,, \tag{2.166}$$

and the reduced effective mass $\mu = m_e m_h/(m_e + m_h)$. The exciton excitation energy is

$$E = E_g - E_{\mathrm{B}} + \frac{\hbar^2 K^2}{2M}\,, \tag{2.167}$$

where the exciton translational mass $M = m_e + m_h$, and the binding energy for the $1s$-exciton, or *exciton Rydberg*, is given by

$$E_{\mathrm{B}} = \frac{\mu_{eh}e^4}{2æ^2\hbar^2}\,. \tag{2.168}$$

2.7.2 Free Exciton in a Quantum Well

The two-particle Hamiltonian describing the exciton in a QW includes superstructure potentials (2.5) for the electron and the hole

$$\mathcal{H}(\boldsymbol{k}_e, \boldsymbol{k}_h) = \mathcal{H}^e(\boldsymbol{k}_e) + \mathcal{H}^h(\boldsymbol{k}_h) + E_g - \frac{e^2}{æ|\boldsymbol{r}|} + V_e(z_e) + V_h(z_h)\,. \tag{2.169}$$

For the two-particle envelope $\varphi(\boldsymbol{r}_e, \boldsymbol{r}_h)$, the first Bastard boundary condition (2.10) takes the form

$$\varphi(\boldsymbol{r}_e, \boldsymbol{r}_h)|_{z_e=z_-} = \varphi(\boldsymbol{r}_e, \boldsymbol{r}_h)|_{z_e=z_+}\,,$$

$$\varphi(\boldsymbol{r}_e, \boldsymbol{r}_h)|_{z_h=z_-} = \varphi(\boldsymbol{r}_e, \boldsymbol{r}_h)|_{z_h=z_+}\,,$$

where z_- and z_+ are the left- and right-hand interface boundaries. The second boundary condition (2.10) taking into account the particle-flow continuity transforms to

$$\left[v_z^e\left(\hat{\boldsymbol{k}}_e\right)\varphi\right]_{z_e=z_-} = \left[v_z^e\left(\hat{\boldsymbol{k}}_e\right)\varphi\right]_{z_e=z_+} ,$$
$$\left[v_z^h\left(\hat{\boldsymbol{k}}_h\right)\varphi\right]_{z_h=z_-} = \left[v_z^h\left(\hat{\boldsymbol{k}}_h\right)\varphi\right]_{z_h=z_+} .$$

Here the components $\varphi_{sm}(\boldsymbol{r}_e, \boldsymbol{r}_h)$ are combined in one many-component vector $\varphi(\boldsymbol{r}_e, \boldsymbol{r}_h)$, $v_z^{e,h}$ is the projection of the electron or hole velocity operator

$$\boldsymbol{v}^e(\boldsymbol{k}) = \hbar^{-1}\nabla_{\boldsymbol{k}}\mathcal{H}^e(\boldsymbol{k}) , \; \boldsymbol{v}^h(\boldsymbol{k}) = \hbar^{-1}\nabla_{\boldsymbol{k}}\mathcal{H}^h(\boldsymbol{k}) . \tag{2.170}$$

For nondegenerate bands with effective masses m_e, m_h the exciton wave function can be presented in the factorized form

$$\varphi(\boldsymbol{r}_e, \boldsymbol{r}_h) = \chi_{sm}\phi(\boldsymbol{r}_e, \boldsymbol{r}_h) , \tag{2.171}$$

where χ depends only on the spin indices s, m. In the equation for the spin-independent function ϕ the variables can be partially separated

$$\phi(\boldsymbol{r}_e, \boldsymbol{r}_h) = \frac{\mathrm{e}^{\mathrm{i}\boldsymbol{K}_\parallel\cdot\boldsymbol{R}_\parallel}}{\sqrt{S}}\,\varphi(\boldsymbol{\rho}, z_e, z_h) , \tag{2.172}$$

where S is the sample area in the interface plane, $\boldsymbol{\rho} = \boldsymbol{\rho}_e - \boldsymbol{\rho}_h$, $\boldsymbol{\rho}_{e,h}$ is the in-plane component of the 3D vector $\boldsymbol{r}_{e,h}$, and the in-plane component of the exciton center of mass, $\boldsymbol{R}_\parallel$, is defined similarly to (2.165). The Schrödinger equation for $\varphi(\boldsymbol{\rho}, z_e, z_h)$ reduces to

$$\left(\mathcal{H}_0^e + \mathcal{H}_0^h + \mathcal{H}^{eh}\right)\phi(\boldsymbol{\rho}, z_e, z_h) = \left(E - E_g - \frac{\hbar^2 K_\parallel^2}{2M}\right)\varphi(\boldsymbol{\rho}, z_e, z_h) , \tag{2.173}$$

$$\mathcal{H}_0^e = -\frac{\hbar^2}{2m_e}\,\frac{\partial^2}{\partial z_e^2} + V_e(z_e) , \; \mathcal{H}_0^h = -\frac{\hbar^2}{2m_h}\,\frac{\partial^2}{\partial z_h^2} + V_h(z_h) ,$$
$$\mathcal{H}^{eh} = -\frac{\hbar^2}{2\mu_{eh}}\left(\frac{\partial^2}{\partial\rho_x^2} + \frac{\partial^2}{\partial\rho_y^2}\right) - \frac{e^2}{æ r} .$$

The binding energy of the exciton formed by an electron in the lowest conduction subband $e1$ and of a hole in the upper valence subband $h1$ is determined by

$$\varepsilon = E_{e1} + E_{h1} - \langle\varphi|\mathcal{H}_0^e + \mathcal{H}_0^h + \mathcal{H}^{eh}|\varphi\rangle , \tag{2.174}$$

where E_{e1}, E_{h1} are the electron and hole confinement energies at $\boldsymbol{k} = 0$.

We first consider the case of thick QWs such as $a \gg a_\mathrm{B}$. It corresponds to the weak confinement regime where the Coulomb interaction energy exceeds the intersubband separations $\Delta E_e, \Delta E_h$. In a thick well, one may neglect the distortion of internal motion of the electron-hole pair in the exciton and the exciton is quantized as a single whole,

$$\varphi(\rho, z_e, z_h) = F(Z)\,\varphi(\boldsymbol{r}) , \tag{2.175}$$

where $\varphi(\boldsymbol{r})$ is the wave function of the electron and hole relative motion in a homogeneous material and Z is the exciton center of mass on the z axis. For the exciton ground state, $\varphi(\boldsymbol{r})$ is given by (2.164) and $F(Z)$ by

$$F(Z) = \sqrt{\frac{2}{a}} \begin{cases} \cos(\nu\pi Z/a) & \text{for odd } \nu\,, \\ \sin(\nu\pi Z/a) & \text{for even } \nu\,, \end{cases} \tag{2.176}$$

where, for simplicity, we assumed the boundary conditions $F(\pm a/2) = 0$. For the excitation energy of the $1s$-exciton in the excitonic subband ν one has

$$E = E_g - E_{\mathrm{B}} + \frac{\hbar^2}{2M}\left[\left(\frac{\pi\nu}{a}\right)^2 + K_{\parallel}^2\right]\,. \tag{2.177}$$

As the well width a decreases, the quantum confinement of carriers begins to predominate over the Coulomb interaction and one can solve equation (2.173) by the variational technique using the trial function in the following factorized form

$$\varphi(\rho, z_e, z_h) = f(\rho, z)\varphi_{e1}(z_e)\varphi_{h1}(z_h)\,, \tag{2.178}$$

where $z = z_e - z_h$. The simplest trial function

$$f(\rho, z) = \sqrt{\frac{2}{\pi\tilde{a}^2}}\,\mathrm{e}^{-\rho/\tilde{a}} \tag{2.179}$$

has one variational parameter, the effective 2D Bohr radius $\tilde{a}$. A comparatively simple choice represents the trial function [2.106]

$$f(\rho, z) = C(1 + \alpha z^2)\mathrm{e}^{-\delta(\rho^2+z^2)^{1/2}}$$

with two variational parameters α and δ, C being a normalizing factor.

The left- and right-hand barriers of the QW press the electron and the hole to one another, with the result that the Coulomb interaction between them increases, as does also the binding energy, which in the case of infinitely-high barriers varies from E_{B} in a thick well to the 2D Rydberg $E_{\mathrm{B}}^{2D} = 4E_{\mathrm{B}}$ for $a \ll a_{\mathrm{B}}$. At the same time, the effective Bohr radius decreases from a_{B} to $a_{\mathrm{B}}^{2D} = a_{\mathrm{B}}/2$. As a result, in the 2D limit one has for the exciton ground state

$$\varphi(\rho, z_e, z_h) = \sqrt{\frac{2}{\pi}}\,\frac{4}{aa_{\mathrm{B}}}\cos\frac{\pi z_e}{a}\cos\frac{\pi z_h}{a}\mathrm{e}^{-2\rho/a_{\mathrm{B}}} \tag{2.180}$$

for $|z_{e,h}| < a/2$ and $\varphi(\rho, z_e, z_h) = 0$ otherwise.

Now we consider the exciton with the effective Hamiltonians $\mathcal{H}^e$ for the simple conduction band Γ_6, and $\mathcal{H}^h$ for the degenerate valence band Γ_8. Due to the quantum confinement the degeneracy of the valence band is removed as illustrated in Fig. 2.2. In the strong confinement regime the off-diagonal terms in the Luttinger Hamiltonian are neglected and both the conduction

subbands $e\nu$ and the valence subbands $hh\nu$ and $lh\nu$ are treated as isolated subbands from the point of view of exciton formation. This leads to the formation of two exciton systems, i.e., the heavy-hole and light-hole excitons associated with the hole angular momentum components $m = \pm 3/2$ and $m = \pm 1/2$, respectively. We rewrite the diagonal components of the 3D-hole Luttinger Hamiltonian (2.28) in the form

$$F(\boldsymbol{k}) = \frac{\hbar^2 k_z^2}{2m_\perp^{hh}} + \frac{\hbar^2 k_\parallel^2}{2m_\parallel^{hh}}\,,\; G(\boldsymbol{k}) = \frac{\hbar^2 k_z^2}{2m_\perp^{lh}} + \frac{\hbar^2 k_\parallel^2}{2m_\parallel^{lh}}\,, \tag{2.181}$$

where the masses $m_\perp^{hh}, m_\perp^{lh}$ coincide with the effective masses, m_{hh} and m_{lh}, of the heavy and light holes in the bulk material and determine the hole quantum-confinement energies $E_{hh\nu}, E_{lh\nu}$ in a single QW. Two other masses are defined by

$$\frac{\hbar^2}{2m_\parallel^{hh}} = |A| + \frac{|B|}{2}\,,\; \frac{\hbar^2}{2m_\parallel^{lh}} = |A| - \frac{|B|}{2}\,.$$

They govern the corresponding reduced effective masses in $\mathcal{H}^{eh}$, see (2.173), namely,

$$\mu_{e\text{-}hh} = m_e m_\parallel^{hh}/(m_e + m_\parallel^{hh}) \quad \text{and} \quad \mu_{e\text{-}lh} = m_e m_\parallel^{lh}/(m_e + m_\parallel^{lh})\,.$$

For the decoupled heavy and light holes, the wave functions of $e\nu$-$hh\nu'$ and $e\nu$-$lh\nu'$ excitons are written as

$$\Psi^{\rm exc} = \frac{\mathrm{e}^{\mathrm{i}\boldsymbol{K}_\parallel\cdot\boldsymbol{R}_\parallel}}{\sqrt{S}}\,\varphi(\boldsymbol{\rho}, z_e, z_h)\,\psi_{cs}^0(\boldsymbol{r}_e)\psi_m^{h0}(\boldsymbol{r}_h)\,. \tag{2.182}$$

Here, ψ_{cs}^0 are the spinor Bloch functions $\uparrow S$, $\downarrow S$ and ψ_m^{h0} are the Bloch functions $|\Gamma_8, m\rangle$ in the hole representation. For the $e\nu$-$hh\nu'$ and $e\nu$-$lh\nu'$ excitons, one can use the trial functions

$$\varphi_{e\text{-}hh}(\boldsymbol{\rho}, z_e, z_h) = f_{e\text{-}hh}(\boldsymbol{\rho}, z)\,\varphi_{e\nu}(z_e)\,\varphi_{hh\nu'}(z_h)\,, \tag{2.183}$$

$$\varphi_{e\text{-}lh}(\boldsymbol{\rho}, z_e, z_h) = f_{e\text{-}lh}(\boldsymbol{\rho}, z)\,\varphi_{e\nu}(z_e)\,\varphi_{lh\nu'}(z_h)\,.$$

Figs. 2.9a and 2.9b show the binding energies, ε_{hh} and ε_{lh}, of the heavy-hole exciton $e1$-$hh1(1s)$ and the light-hole exciton $e1$-$lh1(1s)$ as a function of the thickness a of the GaAs/$\mathrm{Al}_x\mathrm{Ga}_{1-x}$As QW, for two Al concentrations $x = 0.15, 0.30$ and for the model QW with infinitely high barriers [2.106]. The parameters used in the calculation are as follows: $m_e = 0.067m_0$, $m_{hh} = 0.45m_0$, $m_{lh} = 0.08m_0$, $\mu_{e\text{-}hh} = 0.04m_0$, $\mu_{e\text{-}lh} = 0.051m_0$, æ = 12.5. For the infinite potential well, the binding energy monotonously increases with decreasing a in accordance with the expected increase from $E_{\rm B}$ at $a \gg a_{\rm B}$ to $4E_{\rm B}$ at $a \ll a_{\rm B}$. For the finite barriers, the binding energies $\varepsilon_{hh}, \varepsilon_{lh}$ depend nonmonotonously on a, namely, as the well thickness decreases, they reach a

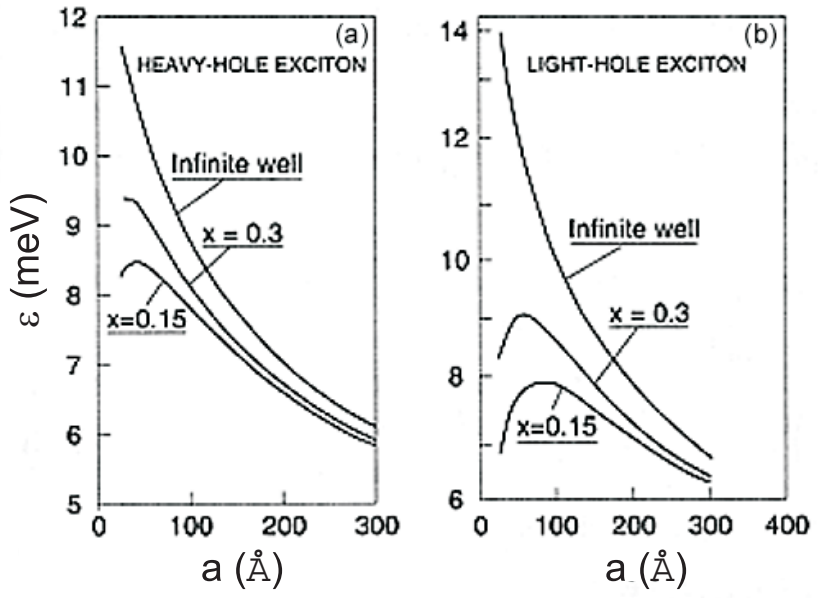

Fig. 2.9. Theoretical dependence of binding energy of $e1$-$hh1$ (**a**) and $e1$-$lh1$ (**b**) exciton on QW thickness in GaAs/$Al_xGa_{1-x}As$ heterostructure with $x = 0.15$ and 0.3, as well as in the infinitely high potential barrier model. From [2.106].

maximum and then fall off since at small a the electron and the hole bound in the exciton reside predominantly in the barrier regions. In the limit of very small thicknesses, this state of the $1s$-exciton may be considered a 3D exciton in the barrier material *attached* to a thin layer with a potential well for the electron and the hole. The binding energy of such an exciton is close to that of a free exciton in the bulk barrier material.

We discuss the hybridization of heavy- and light-hole states in the frame of combined description of strong-confinement regime for electrons and arbitrary regime for holes. In this case, for a stationary exciton with zero translational momentum, $\boldsymbol{K}_{\parallel} = 0$, the exciton wave function takes the form [2.107, 2.108]

$$\Psi^{\mathrm{exc}} = \frac{1}{\sqrt{S}}\,\varphi_{e\nu}(z_e)\sum_m F_m(\boldsymbol{\rho}, z_h)\psi^0_{cs}(\boldsymbol{r}_e)\psi^{h0}_m(\boldsymbol{r}_h)\,. \tag{2.184}$$

If the hole subband anisotropy is neglected and the QW is symmetrical, the envelopes $F_m(\boldsymbol{\rho}, z)$ are characterized by a particular parity with respect to the mirror reflection $z \to -z$ and a particular orbital angular-momentum component. As a result, they can be presented as

$$\boldsymbol{F}_p(\boldsymbol{\rho}, z) = \begin{bmatrix} F_{3/2,p}(\rho, z)\mathrm{e}^{\mathrm{i}l\varphi} \\ F_{1/2,-p}(\rho, z)\mathrm{e}^{\mathrm{i}(l+1)\varphi} \\ F_{-1/2,p}(\rho, z)\mathrm{e}^{\mathrm{i}(l+2)\varphi} \\ F_{-3/2,-p}(\rho, z)\mathrm{e}^{\mathrm{i}(l+3)\varphi} \end{bmatrix} , \tag{2.185}$$

where φ is the angle between the vector $\boldsymbol{\rho} = \boldsymbol{\rho}_e - \boldsymbol{\rho}_h$ and the x axis, the parity $p = \pm$ and l is an integer. The total angular momentum component of the exciton equals $s + 3/2 + l$. Comparing (2.185) with (2.182) we conclude that, for the $e1$-$hh1(1s)$ exciton with $m = 3/2$ or $m = -3/2$, one has $p = +$, $l = 0$ or $p = -$, $l = -3$. Similarly, for the $e1$-$lh1(1s)$ exciton with $m = 1/2$ or $m = -1/2$, one has $p = -$, $l = -1$ or $p = +$, $l = -2$. The four-component envelope (2.185) satisfies the equation

$$\left[\tilde{\mathcal{H}}(\hat{\boldsymbol{k}}) + E_g + E_{e\nu} + \tilde{V}_C(\rho, z)\right] \boldsymbol{F}(\boldsymbol{\rho}, z) = E\boldsymbol{F}(\boldsymbol{\rho}, z) \, .$$

Here $\tilde{\mathcal{H}}(\mathbf{k})$ differs from the Luttinger Hamiltonian (2.24) by the substitution

$$F \to \tilde{F} = F + \frac{\hbar^2 k_\parallel^2}{2m_e} \, , \; G \to \tilde{G} = G + \frac{\hbar^2 k_\parallel^2}{2m_e}$$

and $\tilde{V}_C(\rho, z)$ is the Coulomb potential averaged over the electron-density distribution,

$$\tilde{V}_C(\rho, z) = -\frac{e^2}{æ} \int dz_e \frac{\varphi_{e\nu}^2(z_e)}{\sqrt{\rho^2 + (z_e - z)^2}} \, .$$

The calculation shows that the model of uncoupled heavy- and light-hole states is a good approximation for the heavy-hole exciton $e1$-$hh1$ but can cause a significant error in calculating $e1$-$lh1$ excitons and, especially, excitons formed from holes in the higher hole subbands.

2.7.3 Excitons in Various Nanostructures

The physics of excitons has become a highly diversified field of science. The firm identification of exciton spectra were achieved for alkali halides in the 1930's, for molecular crystals in the 1940's and for semiconductors in the 1950's. Excitons have been found in most non-metallic crystals and rare earth metals as well as in photosynthetics and other biological systems. At present it is well known that the excitonic effects in bulk semiconductors dominate the optical properties near the fundamental band edge, at least at low temperatures and in undoped or moderately doped samples. In semiconductor nanostructures the electron-hole interaction is enhanced by confinement, which increases the overlap of the electron and hole wave functions. The development of new crystal-growth techniques and improvement in nanostructure fabrication allowed to study a significant enhancement of the excitonic binding energy, oscillator strength and exchange-induced splitting of exciton

levels with transition from 3D excitons in bulk semiconductors to 2D excitons in QWs and similar 2D-1D and 1D-0D transitions, respectively from QWs to QWRs and from QWRs to QD. Omnipresent and many-sided excitons play a central role in the band-edge optical spectroscopy of semiconductor nanostructures even at room temperature. Optical spectroscopic measurements of excitonic parameters, such as the energies of excitonic transitions, exciton oscillator strengths and lifetimes, the fine-structure splittings etc., present effective methods, contactless and nondestructive, for the characterization of nanostructures and give the information about the structure shape and size, the confining potential profile, interfacial quality, and so forth. In this subsection we briefly outline the theoretical description of excitons in nanostructures.

A simple extension of the *intrawell exciton* excited within a QW is the *interwell exciton* in a double QW structure. This indirect-exciton state is formed by an electron and a hole confined in different wells. In the presence of an electric field perpendicular to the interfaces the electron and hole ground states are localized in separate wells which allows the realization of a long-lived excitonic state and creates favorable conditions for Bose-Einstein condensation of excitons of high enough density [2.110–2.112]. Since the overlap of the electron and hole wave functions can be easily varied by changing the applied electric field, the lifetime of indirect excitons can be controlled externally. The interwell-exciton envelope function can be approximated by (2.178) where $\varphi_{e1}(z_e)$ and $\varphi_{h1}(z_h)$ are the single-particle envelopes of an electron and a hole spatially separated in the opposite wells.

In a single QW with a strong confining potential for conduction-band electrons and zero valence-band offset, the excitonic state can be considered as formed by a 2D electron and a 3D hole. The mixed 2D-3D exciton was realized in a $CdTe/Cd_{1-x}Mn_xTe$ QW by altering the barrier height in an external magnetic field [2.109]. In the variational approach one can take the envelope function (2.172) and choose a trial function in the form

$$\varphi(\rho, z_e, z_h) = \frac{1}{\sqrt{\pi a_\parallel a_\perp^2}} \exp\left[-\left(\frac{z_h^2}{a_\parallel^2} + \frac{\rho^2}{a_\perp^2}\right)\right] \varphi_{e1}(z_e)\,,$$

where $a_\parallel, a_\perp$ are variational parameters. Similar approach can be applied to a type-II QW structure where the conduction- and valence-band offsets are of opposite signs. If the B layers neighboring the layer A are thick, then, as well as for the mentioned above 2D-3D exciton, the hole is confined only due to the attractive Coulomb potential. In a periodic type-II structure with strong confinement of electrons and holes, respectively, in A and B layers, one can use the approximation (2.178) for the exciton envelope function.

A special case is realized in GaAs/AlAs periodic multi-layered structures. With decreasing the GaAs-layer thickness, they present a transition from type-I (Γ electron and Γ hole) to type-II (X-valley electron and Γ hole) [2.113,2.114]. The exciton $e1X$-$hh1\Gamma$ is doubly indirect, both in the real

space, because the envelope functions are spatially separated in the GaAs and AlAs layers, and in the $\boldsymbol{k}$ space, because the electron state is formed predominantly from the X-valley states. The oscillator strength for this exciton is much weaker than in type-I structures since no-phonon optical transitions between purely Γ-like valence and X-like conduction states are forbidden. This selection rule is removed due to the Γ-X mixing at interfaces [2.115–2.118].

In a MQW structure, excitons excited in individual QWs are coupled via electro-magnetic field to form exciton polaritons that are considered in Chap. 3. Exciton polaritons in quantum microcavities are discussed in Chap. 7. In a short-period SLs with 3D minibands, the exciton states are similar to those in a uniaxial 3D semiconductors (Sect. 3.1.3).

If the cross-sectional dimensions of a QWR or the sizes of a QD exceed the Bohr radius a_{B} of a 3D exciton (weak confinement regime) then the exciton wave function is written in the form similar to (2.175) with the function $F(X,Y)$ or $F(\boldsymbol{R})$ describing the translational motion of the exciton as a whole. The calculation of this function is performed analogously to size-quantization of single-particle motion in 1D and 0D nanostructures (Sects. 2.2 and 2.3).

In the strong confinement regime, the exciton wave function in a QWR is approximately presented as

$$\Psi^{\mathrm{exc}}_{\mathrm{QWR}} = \frac{\exp\left(\mathrm{i}K_z Z\right)}{\sqrt{L}} f(z)\, \varphi_{e1}(x_e, y_e)\, \varphi_{h1}(x_h, y_h)\, \psi^0_{cs}(\boldsymbol{r}_e)\, \psi^{h0}_m(\boldsymbol{r}_h)\,, \quad (2.186)$$

where $\varphi_{e1}(x_e, y_e), \varphi_{h1}(x_h, y_h)$ are the single-particle envelopes defined in (2.55). The envelope function describing the relative motion along the principal axis z satisfies a second-order differential equation

$$-\frac{\hbar^2}{2\mu_{eh}} \frac{d^2 f(z)}{dz^2} + \tilde{V}_C(z) f(z) = E f(z)$$

with the effective 1D Coulomb potential

$$\tilde{V}_C(z) = -\frac{e^2}{æ} \int dx_e dy_e dx_h dy_h \frac{\varphi^2_{e1}(x_e, y_e)\varphi^2_{h1}(x_h, y_h)}{\sqrt{(x_e - x_h)^2 + (y_e - y_h)^2 + z^2}}\,.$$

The simplest trial function is [2.119]

$$f(z) = \frac{1}{\sqrt{a_w}} \exp\left(-\frac{|z|}{a_w}\right)$$

with a single variational parameter, a_w. A slightly more complicated choice is to change $f(z)$ in (2.186) by $f(\rho, z)$, say, [2.120]

$$f(\rho, z) \propto \exp\left(-\frac{\sqrt{\rho^2 + z^2}}{a_w}\right),$$

where $\rho = |\boldsymbol{\rho}_e - \boldsymbol{\rho}_h|$.

Note that the 1D Coulomb potential $V_C(z) = -(e^2/æ|z|)$ leads to an infinite binding energy of the 1D exciton ground state. Loudon [2.121] considered analytically the ground-state problem for a regularized 1D Coulomb potential $V_C(z) \propto (|z| + R)^{-1}$ instead of $|z|^{-1}$ and obtained for the ground state the asymptotic solution with the binding energy ε satisfying the equation

$$\frac{R}{a_\mathrm{B}} = \frac{1}{2}\sqrt{\frac{E_\mathrm{B}}{\varepsilon}}\exp\left(-\frac{1}{2}\sqrt{\frac{E_\mathrm{B}}{\varepsilon}}\right).$$

One can see that as $R \to 0$ the ground-state binding energy diverges.

The exciton wave function in a QD satisfying the condition of strong-confinement regime is just a product

$$\Psi^{\mathrm{exc}} = \varphi_{e1}(\boldsymbol{r}_e)\ \varphi_{h1}(\boldsymbol{r}_h)\ \psi^0_{cs}(\boldsymbol{r}_e)\ \psi^{h0}_m(\boldsymbol{r}_h) \tag{2.187}$$

of the single-particle wave functions. The excitation energy of the ground-state exciton is given by

$$E = E_g + E_{e1} + E_{h1} + \tilde{V}_C\,,$$

where the last term is the Coulomb energy

$$\tilde{V}_C = -\frac{e^2}{æ}\int d\boldsymbol{r}_e d\boldsymbol{r}_h \frac{\varphi^2_{e1}(\boldsymbol{r}_e)\varphi^2_{h1}(\boldsymbol{r}_h)}{|\boldsymbol{r}_e - \boldsymbol{r}_h|}\,.$$

The exchange-interaction corrections to the 0D-exciton energy are analyzed in Chap. 5.

It is worth to mention that, in molecular crystals, the intermolecular interactions can be highly anisotropic. As a result, an effective dimensionality $d = 2$ or $d = 1$ for the energy transport may exist. Particularly, the organic crystals 1,2,4,5-tetrachlorobenzene and 1,4-dibromonaphthalene possess 1D-excitons [2.103].

Above we considered excitons in ideal nanostructures. Interface imperfections and composition fluctuations can give rise to localized exciton states which are quasi-0D states with a strong confinement along z and weak confinement in the interface plane (x, y). If the length of the exciton localization in a QW is much larger than the 2D Bohr radius, one can use the adiabatic approximation and represent the exciton envelope function in the form

$$\Psi_{\mathrm{exc}}(\boldsymbol{r}_e, \boldsymbol{r}_h) = F(X, Y)\ f(\rho)\ \varphi_{e1}(z_e)\ \varphi_{h1}(z_h)\,, \tag{2.188}$$

where the function $F(X, Y)$ describes the localization of the $e1$-$h1(1s)$ exciton as a whole in the interface plane, X and Y are the in-plane coordinates of the exciton center of mass. The fine structure of the heavy-hole exciton localized on a rectangular island in an imperfect QW structure is considered in Sect. 5.5.1.

2.7.4 Biexcitons and Trions

The existence of *biexcitons* and charged excitons, or *trions*, in semiconductors was predicted in 1958 by Lampert [2.122]. These complexes, called originally "excitonic molecule" and "excitonic ion", are analogous, respectively, to a hydrogen molecule H_2 and to an ion H^- or ionized molecule H_2^+. Semiconductor nanostructures allow to realize low-dimensional biexciton and trion states showing the strong increase of the binding energies as compared to the 3D case.

In the effective mass approximation the biexciton wave function is written as

$$\Psi^{\text{biexc}} = \varphi_{\text{biexc}}(\boldsymbol{r}_{e1}, \boldsymbol{r}_{e2}, \boldsymbol{r}_{h1}, \boldsymbol{r}_{h2},)\ \psi_{ee}(\boldsymbol{r}_{e1}, \boldsymbol{r}_{e2})\ \psi_{hh}(\boldsymbol{r}_{h1}, \boldsymbol{r}_{h2})\,, \qquad (2.189)$$

where the indices e, h indicate electrons and holes, the indices 1,2 enumerate the identical particles, φ_{biexc} is the four-particle envelope function and ψ_{ee}, ψ_{hh} are the Bloch parts. The total wave function has to be antisymmetrical with respect to the exchange of two electrons or two holes. In the biexciton ground state, the electrons and holes form separately spin singlets. This means that the functions ψ_{ee}, ψ_{hh} are antisymmetric, the electronic Bloch part is

$$\psi_{ee}(\boldsymbol{r}_1, \boldsymbol{r}_2) = \frac{1}{\sqrt{2}}\left[\psi^0_{c,1/2}(\boldsymbol{r}_1)\ \psi^0_{c,-1/2}(\boldsymbol{r}_2) - \psi^0_{c,-1/2}(\boldsymbol{r}_1)\ \psi^0_{c,1/2}(\boldsymbol{r}_2)\right]$$

and the hole part has a similar form. On the other hand, the ground-state envelope function must be symmetrical to the interchange $\boldsymbol{r}_{e1} \leftrightarrow \boldsymbol{r}_{e2}$ or $\boldsymbol{r}_{h1} \leftrightarrow \boldsymbol{r}_{h2}$. For a QW structure, in the strong-confinement regime, one can use the factored envelope

$$\varphi_{\text{biexc}} = \Phi(\boldsymbol{\rho}_{e1}, \boldsymbol{\rho}_{e2}, \boldsymbol{\rho}_{h2}, \boldsymbol{\rho}_{h2})\ \varphi_e(z_{e1})\ \varphi_e(z_{e2})\ \varphi_h(z_{h1})\ \varphi_h(z_{h2})\,, \qquad (2.190)$$

where the function Φ depends only on the in-plane coordinates, $\varphi_l(z_l)$ is the single-particle quantum-confined function with $l = e, h$. The envelope Φ satisfies the Schrödinger equation with the Hamiltonian

$$\begin{aligned}\mathcal{H} = &-\frac{1}{1+\sigma}\left(\nabla^2_{e1} + \nabla^2_{e2}\right) - \frac{\sigma}{1+\sigma}\left(\nabla^2_{h1} + \nabla^2_{h2}\right)\\ &+ 2\left(V_{e1,h1} + V_{e1,h2} + V_{e2,h1} + V_{e2,h2} + V_{e1,e2} + V_{h1,h2}\right)\,,\end{aligned}$$

where σ is the electron-hole mass ratio m_e/m_h, the units of energy and length are the 3D exciton Rydberg E_{B} and the 3D Bohr radius a_{B}, and the effective Coulomb interaction is defined by

$$V_{l1,l2}(\rho) = \int dz_1 dz_2 \frac{\varphi^2_l(z_1)\varphi^2_l(z_2)}{\sqrt{\rho^2 + (z_1 - z_2)^2}}\,,$$

$$V_{ei,hi'}(\rho) = -\int dz_e dz_h \frac{\varphi_e^2(z_e)\varphi_h^2(z_h)}{\sqrt{\rho^2 + (z_e - z_h)^2}} \qquad (i, i' = 1, 2) \,.$$

Since it is not possible to solve the four-body problem exactly they employ a variational technique. While calculating the biexciton in a single QW structure Kleinman [2.123] chose a trial function

$$\Phi = \xi(\beta; k\rho_{li,l'i'})\ \chi(\nu, \eta, \lambda, \tau; k\rho_{h1,h2}) \,,$$

$$\chi(\nu, \eta, \lambda, \tau; \rho_{h1,h2}) = u^\nu \mathrm{e}^{-\eta u} + \lambda \mathrm{e}^{-\tau u} \,,$$

$$\xi(\beta; \rho_{li,l'i'}) = \exp\left[-(s_1 + s_2)/2\right] \cosh\left[\beta(t_1 - t_2)/2\right] \,,$$

containing six variational parameters $k, \beta, \nu, \eta, \lambda, \tau$. Here

$$s_1 = \rho_{e1,h1} + \rho_{e1,h2} \,,\ s_2 = \rho_{e2,h1} + \rho_{e2,h2} \,,$$

$$t_1 = \rho_{e1,h1} - \rho_{e1,h2} \,,\ t_2 = \rho_{e2,h1} - \rho_{e2,h2} \,,$$

and $\rho_{li,l'i'}$ are the interparticle in-plane distances $|\boldsymbol{\rho}_{li} - \boldsymbol{\rho}_{l'i'}|$. The binding energy $\varepsilon_{\mathrm{bi}}$ of excitons in the biexciton is defined as the difference

$$\varepsilon_{\mathrm{bi}} = 2E_{\mathrm{exc}} - E_{\mathrm{bi}} \,, \tag{2.191}$$

where E_{exc} and E_{bi} are the exciton and biexciton excitation energies, accordingly. Calculations show that in the 2D limit $\varepsilon_{\mathrm{bi}}$ exceeds the biexciton binding energy in bulk GaAs by a factor of 3 to 4. An observation of the biexciton state in GaAs/$\mathrm{Ga}_{1-x}\mathrm{Al}_x$As QWs was reported in 1982 [2.124]. In II-VI compound semiconductors, it was observed convincingly by Bányai et al. [2.125]. The further enhancement of the biexiton binding energy is predicted for 1D QWR structures [2.125] and QDs or microcrystallites [2.126]. Multiexciton complexes in $\mathrm{In}_x\mathrm{Ga}_{1-x}$As/GaAs QDs of the lateral dot sizes varied around 500 Å were investigated in [2.127]. The formation of complexes consisting of three and four excitons becomes possible due to the 3D geometric confinement potential. Their binding energies are negative because the Pauli repulsion pushes additional electrons and holes into higher shells. Binding of two excitons into an excitonic molecule in type-II QW periodic systems is theoretically investigated by Shimura and Matsuura [2.128].

The first identification of charged excitons in a n-doped 2D structure was done by Kheng et al. [2.129]. Since then both the negatively and positively charged trions, X^- and X^+, composed of two electrons and one hole or two holes and one electron, have been observed and studied in III-V and II-VI 2D systems, see the review [2.130] and references therein. A three-body problem of 2D trions in semiconductor QWs was solved by applying a variational technique [2.131–2.133] or other simplified methods [2.134]. The ground-state wave functions for X^- and X^+ trions may be written respectively as

$$\Psi_{X^-,S} \tag{2.192}$$
$$= \varphi_{tr,S}(\boldsymbol{\rho}_{e1}, \boldsymbol{\rho}_{e2}, \boldsymbol{\rho}_h)\ \varphi_e(z_{e1})\ \varphi_e(z_{e2})\ \varphi_h(z_h)\ \psi_{ee}(\boldsymbol{r}_{e1}, \boldsymbol{r}_{e2})\ \psi_m^{h0}(\boldsymbol{r}_h) \,,$$

$$\Psi_{X^+,S} = \varphi_{tr,S}(\boldsymbol{\rho}_e, \boldsymbol{\rho}_{h1}, \boldsymbol{\rho}_{h2})\, \varphi_e(z_e)\, \varphi_h(z_{h1})\, \varphi_h(z_{h2})\, \psi^0_{cs}(\boldsymbol{r}_e)\, \psi_{hh}(\boldsymbol{r}_{h1}, \boldsymbol{r}_{h2})\,.$$

The negative 2D-trion effective Hamiltonian measured in units of 2D exciton binding energy, $E_{\rm B}^{2D} = 4E_{\rm B}$, and 3D exciton Bohr radius is [2.133]

$$\mathcal{H}(X^-) = -\frac{1}{4}\left(\nabla^2_{e1} + \nabla^2_{e2}\right) - \frac{\sigma}{1+\sigma}\nabla_{e1}\nabla_{e2} - \frac{1}{2}\left(\frac{1}{\rho_{e1,h}} + \frac{1}{\rho_{e2,h}} - \frac{1}{\rho_{e1,e2}}\right)\,,$$

where $\rho_{ei,h}$ is the distance between the electron i and the hole, $\rho_{e1,e2}$ is the interelectron distance. The similar Hamiltonian for X^+ trions is obtained by the change $e \leftrightarrow h$ and $\sigma \to \sigma^{-1}$. The trion binding energy is defined as

$$\varepsilon_{\rm tr} = E_{\rm exc} - E_{\rm tr}\,,$$

where $E_{\rm exc}, E_{\rm tr}$ are the exciton and trion excitation energies.

A reliable 6-parameter trial function for the singlet state,

$$\varphi_{tr,S} = \left[\exp\left(-a\rho_{13} - b\rho_{23}\right) + \exp\left(-b\rho_{13} - a\rho_{23}\right)\right] \times \frac{1 + c\rho_{12}}{1 + d(\rho_{12} - R_0)^2}\exp\left(-s\rho_{12}\right)\,, \tag{2.193}$$

is suggested by Sergeev and Suris [2.133]. Here the indices $1, 2$ refer to the identical particles, the index 3 refers to the unpaired particle and a, b, c, d, s, R_0 are variational parameters. The first multiplier is the symmetrized exciton-like function with different orbital radii, the second multiplier accounts for polarization effects. The parameter d takes into account vibrations of two identical particles around the average distance, R_0, between them. The parameter s optimizes the wave function at large distances ρ_{12}.

Figure 2.10 shows the calculated trion binding energy, $\varepsilon_{\rm tr}$, as a function of the mass ratio σ. Solid, dashed and dotted curves show results of calculation in three different approaches. One can see that the binding energy, $\varepsilon_{\rm tr}$, of the X^- trion is almost independent of σ whereas, for the X^+ trion, it remarkably increases with decreasing the mass ratio. At $\sigma \to 0$, it tends to 0.41.

A simple trial envelope function for the X^+ triplet state is [2.135]

$$\varphi_{tr,T} = \left[\exp\left(-a\rho_{13} - b\rho_{23}\right) + \exp\left(-b\rho_{13} - a\rho_{23}\right)\right] \times \frac{\exp\left(-s\rho_{12}\right)}{1 + d(\rho_{12} - R_0)^2}\left[x_1 - x_2 \pm {\rm i}(y_1 - y_2)\right]\,. \tag{2.194}$$

It is antisymmetrical with respect to the interchange $\boldsymbol{\rho}_1 \leftrightarrow \boldsymbol{\rho}_2$ of the hole coordinates. The bound triplet state vanishes as the mass ratio reaches a critical value $\sigma_{\rm cr}$ which, for isotropic effective masses, is close to 0.35. Near the critical point the triplet binding energy is found from

$$\varepsilon_{\rm tr} \ln\left(\frac{\varepsilon_0}{\varepsilon_{\rm tr}}\right) = A(\sigma_{\rm cr} - \sigma)\,,$$

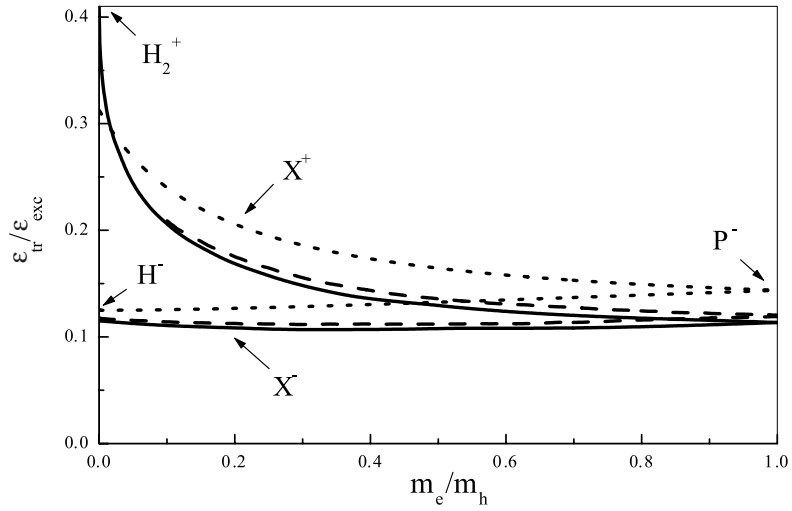

Fig. 2.10. Binding energies, $\varepsilon_{\rm tr}$, of the X^+ and X^- 2D-trion singlet states related to the exciton binding energy, $\varepsilon_{\rm exc}$, vs. the electron-to-hole mass ratio. Solid and dotted curves are calculated by using the variational method with six [2.133] and twenty two [2.131] fitting parameters. Dashed curve, calculation in a simple analytical model [2.134].

where $\varepsilon_0 \approx 2.70$ and $A \approx 1.17$ [2.135].

Excitonic trions in single and double QDs with Gaussian confinement potential were studied by the variational method in [2.136].

2.7.5 Dielectric Response of an Exciton

Here we will derive the relation between the exciton contribution to the dielectric polarization $\boldsymbol{P}_{\rm exc}$ and the macroscopic electric field $\boldsymbol{E}$ of the light wave. For that we consider the time-dependent wave function $|t\rangle$ of the electronic system in the presence of a monochromatic electromagnetic wave of a fixed polarization, α. We assume that the light frequency ω is close to an exciton resonance, ω_0, and selection rules allow the resonant photoexcitation only to one excitonic state, $|{\rm exc}, \alpha\rangle \equiv |{\rm exc}\rangle$, described by the two-particle envelope (2.172). Resonance frequencies of other excitons dipole-active in the same polarization are assumed to be far off enough and their dielectric response as well as that of continuum electron-hole-pair states modified by the Coulomb interaction are taken into account by the background dielectric constant $æ_b$. In the linear approximation one has

$$|t\rangle = |0\rangle + c(t)\,|{\rm exc}, \alpha\rangle\ ,\ c(t) = c_0 {\rm e}^{-{\rm i}\omega t} + c_0' {\rm e}^{{\rm i}\omega t}\ , \qquad (2.195)$$

where $|0\rangle$ is the ground state of the electronic system with the filled valence band and empty conduction band. In the following we neglect the nonresonant term $c_0' \exp(\mathrm{i}\omega t)$.

By definition, the excitonic contribution to the dielectric polarization is given by the quantum-mechanical average

$$P_{\mathrm{exc}}(\boldsymbol{r},t) = \langle t|\hat{d}_\alpha(\boldsymbol{r})|t\rangle = \langle 0|\hat{d}_\alpha(\boldsymbol{r})|\mathrm{exc}\rangle\, c(t) + \mathrm{c.c.}\,, \tag{2.196}$$

where $\hat{d}_\alpha(\boldsymbol{r})$ is the dipole-moment density operator. In the effective mass approximation the matrix element of $\hat{d}_\alpha(\boldsymbol{r})$ can be written as

$$\langle \mathrm{exc}|\hat{d}_\alpha(\boldsymbol{r})|0\rangle = \frac{\langle \mathrm{exc}|\hat{j}_\alpha(\boldsymbol{r})|0\rangle}{\mathrm{i}\omega_0} = -\frac{\mathrm{i}ep_{cv}}{\omega_0 m_0}\,\phi^*(\boldsymbol{r},\boldsymbol{r})\,. \tag{2.197}$$

For the heavy-hole exciton in a zinc-blende-lattice QW, the interband matrix element p_{cv} equals $\langle S|\hat{p}_x|X\rangle = \langle S|\hat{p}_y|Y\rangle = \langle S|\hat{p}_z|Z\rangle$. For the sake of simplicity, we consider in the following only the case of normal light incidence and the zero in-plane wave vector for an exciton in the QW. In this case the light electric field and excitonic polarization can be presented in the form

$$E_\alpha(\boldsymbol{r},t) = E_\alpha(z)\mathrm{e}^{-\mathrm{i}\omega t} + \mathrm{c.c.}\,,\; P_{\mathrm{exc}}(\boldsymbol{r},t) = P_{\mathrm{exc}}(z)\mathrm{e}^{-\mathrm{i}\omega t} + \mathrm{c.c.}$$

Moreover, the coordinate dependence of the exciton envelope function reduces to $\phi(\boldsymbol{r}_e,\boldsymbol{r}_h) \equiv S^{-1/2}\varphi(\boldsymbol{\rho}_e - \boldsymbol{\rho}_h, z_e, z_h)$, where $\boldsymbol{\rho}$ is the in-plane component of the 3D vector $\boldsymbol{r}$ and S is the sample in-plane area. Thus,

$$\langle \mathrm{exc}|\hat{d}_\alpha(\boldsymbol{r})|0\rangle = -\frac{\mathrm{i}ep_{cv}}{\sqrt{S}\omega_0 m_0}\,\Phi^*(z)\,, \tag{2.198}$$

where

$$\Phi(z) = \varphi(0,z,z)\,. \tag{2.199}$$

The state $|t\rangle$ satisfies the time-dependent Schrödinger equation

$$\mathrm{i}\hbar\frac{\partial}{\partial t}|t\rangle = (\mathcal{H}_0 + \hat{V})|t\rangle\,,\; \hat{V} = -\int d\boldsymbol{r}\;\hat{d}_\alpha(\boldsymbol{r})\,E_\alpha(\boldsymbol{r},t)\,, \tag{2.200}$$

where $\mathcal{H}_0$ is the Hamiltonian of the unperturbed electronic system. Multiplying the Schrödinger equation by $\langle \mathrm{exc}|$ we come to

$$\hbar\omega c_0 = \hbar\omega_0 c_0 - S\int dz'\langle \mathrm{exc}|\hat{d}_\alpha(\boldsymbol{r}')|0\rangle E_\alpha(z')\,. \tag{2.201}$$

Now we multiply (2.201) by $\langle 0|\hat{d}_\alpha(\boldsymbol{r})|\mathrm{exc}\rangle = \langle \mathrm{exc}|\hat{d}_\alpha(\boldsymbol{r})|0\rangle^*$ and obtain taking into account the relation (2.196) between $P_{\mathrm{exc}}(\boldsymbol{r},t)$ and $c(t)$

$$(\omega_0 - \omega)P_{\mathrm{exc}}(z) = \frac{1}{\hbar}\left(\frac{e|p_{cv}|}{\omega_0 m_0}\right)^2 \Phi(z)\int dz'\,\Phi^*(z')E_\alpha(z')\,. \tag{2.202}$$

Equation (2.202) is also valid for a bulk semiconductor. In this case one has

$$E_\alpha(z) = E_\alpha \, \mathrm{e}^{\mathrm{i}qz} \, , \; P_{\mathrm{exc}}(z) = P_{\mathrm{exc}} \, \mathrm{e}^{\mathrm{i}qz} \, , \; \Phi(z) = \frac{\varphi_{1s}(0)}{\sqrt{L}} \, \mathrm{e}^{\mathrm{i}qz} \, ,$$

where q is the wave vector for the light propagating along z, L is the sample length in this direction. After integration over z' and replacement of $\varphi_{1s}(0)$ by $(\pi a_{\mathrm{B}}^3)^{-1/2}$ we obtain

$$(\omega_0 - \omega) P_{\mathrm{exc}} = \left(\frac{e|p_{cv}|}{\omega_0 m_0} \right)^2 \frac{1}{\pi a_{\mathrm{B}}^3 \hbar} \, E_\alpha = \frac{æ_b \omega_{LT}}{4\pi} \, E_\alpha \, , \tag{2.203}$$

where ω_{LT} is the 3D-exciton longitudinal-transverse splitting,

$$\omega_{LT} = \frac{4}{\hbar} \left(\frac{e|p_{cv}|}{\omega_0 m_0} \right)^2 \frac{1}{æ_b a_{\mathrm{B}}^3} \, . \tag{2.204}$$

Equation (2.202) is used in the next chapter in the analysis of resonant light reflection and transmission in QW structures.

3 Resonant Light Reflection and Transmission

Do you send the lightning bolts on their way?
Do they report to you, 'Here we are'?

Job **38***: 35*

In bulk crystals, a photon and an exciton mix in the dispersion-crossover region, losing their identity in a combined quasi-particle called the *exciton polariton*. Physically, exciton polaritons can be conveniently considered in terms of an effective two-oscillator model. The uncoupled photonic and excitonic oscillators are characterized by the same wave vector $\boldsymbol{q}$ and the bare-particle eigenfrequencies

$$\omega_{\rm phot}(q) = \frac{c}{\sqrt{æ_b}}\, q \qquad \text{and} \qquad \omega_{\rm exc}(q) = \omega_0 + \frac{\hbar q^2}{2M}\,,$$

where $æ_b$ is the background dielectric constant, ω_0 is the exciton resonance frequency at $q = 0$, and M is the exciton effective mass. The coupling is governed by a value of the exciton longitudinal-transverse splitting, $\omega_{\rm LT}$, and the dispersion equation for coupled excitations can be written as

$$\left(\omega^2_{\rm phot}(q) - \omega^2\right)\left(\omega^2_{\rm exc}(q) - \omega^2\right) = 2\omega^2\omega_{\rm LT}\omega_0\,. \tag{3.1}$$

This is an equivalent form of the conventional dispersion equation

$$\left(\frac{cq}{\omega}\right)^2 = æ(\omega, \boldsymbol{q}) \tag{3.2}$$

with the one-pole dielectric function

$$æ(\omega, \boldsymbol{q}) = æ_b + \frac{2æ_b\omega_0\omega_{\rm LT}}{\omega^2_{\rm exc}(q) - \omega^2} \approx æ_b + \frac{æ_b\omega_{\rm LT}}{\omega_{\rm exc}(q) - \omega}\,. \tag{3.3}$$

Exciton polaritons were intensively studied in 1960's and 1970's, their manifestation in various optical phenomena, including light reflection and transmission, photoluminescence and resonant light scattering, is well-established and documented (see, e.g., the contributed volume [3.1] and references therein). Renewed interest and important developments in this field, see, e.g., [3.2–3.9], were stimulated by technological achievements in fabrication of high-quality nanostructures, multi-layered heterostructures, MQWs, SLs, regular arrays of quantum wires and dots, quantum microcavities. Moreover, the concept of exciton polariton has undergone a substantial modification,

in particular with respect to long-period MQW structures containing a finite number of wells [3.10–3.15]. In this chapter, while describing the light reflection and transmission, we will point out the exciton-polariton aspects of these optical processes in various nanostructures.

In short-period heterostructures the interference between "forward-scattered" and incident waves is described simply by a macroscopic dielectric function $æ_{\text{eff}}(\omega)$ or index of refraction $n_{\text{eff}} = \sqrt{æ_{\text{eff}}}$ (Sect. 3.1.3). However, such a description is no longer valid for long-period regular structures with the period comparable with the light wavelength λ as shown in Sects. 3.1.2 and 3.1.4. When the QWs are separated by a $\lambda/2$, interference between forward and backward waves can strongly attenuate the incident field and enlarge the reflected wave as it occurs in conventional multilayer thin-film dielectric mirrors or distributed Bragg reflectors (Chap. 7). A new and intriguing aspect of the Bragg reflectors is a MQW structure which satisfies the Bragg condition at the exciton resonance frequency, such structures are considered in Sects. 3.1.4 and 3.1.5.

In Sects. 3.1.6 and 3.1.7 we discuss optical properties of QWs grown along directions different from [001] and asymmetrical (001)-grown QWs. The electromagnetic response of 0D and 1D structures is described in Sect. 3.2. Electro- and magneto-optics in nanostructures are presented in Sects. 3.3 and 3.4, respectively.

3.1 Optical Reflection from Quantum Wells and Superlattices

We will first consider in detail the reflection of light from a single-QW structure and then turn to multiple-QW structures including short-period SLs and resonant Bragg structures.

3.1.1 Single Quantum Well Structure

The amplitude reflection coefficient from the four-layer system 'vacuum (0) - cap layer (1) - single QW (2) - semiinfinite barrier (3)' is connected with the coefficient r_{123} of reflection from the QW by

$$r = r_{01} + \frac{t_{01}t_{10}\mathrm{e}^{2\mathrm{i}\phi_1}}{1 - r_{10}r_{123}\mathrm{e}^{2\mathrm{i}\phi_1}}\, r_{123} = \frac{r_{01} + r_{123}\mathrm{e}^{2\mathrm{i}\phi_1}}{1 - r_{10}r_{123}\mathrm{e}^{2\mathrm{i}\phi_1}}\,. \tag{3.4}$$

Here r_{ij} $(= -r_{ji})$ and t_{ij} are the amplitude coefficients for reflection and transmission of the light falling from a half-infinite medium i ($i = 0$ in vacuum and $i = 1$ in layer 1) on the half-infinite medium j, $\phi_1 = q_{1z}d_1$ is the dephasing due to optical path from the external surface to the interface between the layers 1 and 2, q_{1z} is the z-component of the light wave vector in the layer 1, it is given by

$$q_{1z} = \frac{\omega}{c}\left(æ_b - \sin^2\theta_0\right)^{1/2} \ . \tag{3.5}$$

The incidence and refraction angles, θ_0 and θ, are related by $\sin\theta_0 = n_b \sin\theta$ with the refractive index $n_b = \sqrt{æ_b}$. It follows from (3.4) that the *reflectance* of the structure has the form

$$R = |r|^2 = \frac{r_{01}^2 + \mathrm{Re}\left\{r_{01}r_{123}\mathrm{e}^{2\mathrm{i}\phi_1}\right\} + |r_{123}|^2}{1 + 2\mathrm{Re}\left\{r_{01}r_{123}\mathrm{e}^{2\mathrm{i}\phi_1}\right\} + r_{01}^2|r_{123}|^2} \ . \tag{3.6}$$

Thus, the problem is reduced to the calculation of the amplitude reflection coefficient $r_{123}(\omega)$ for a monochromatic light wave of frequency ω.

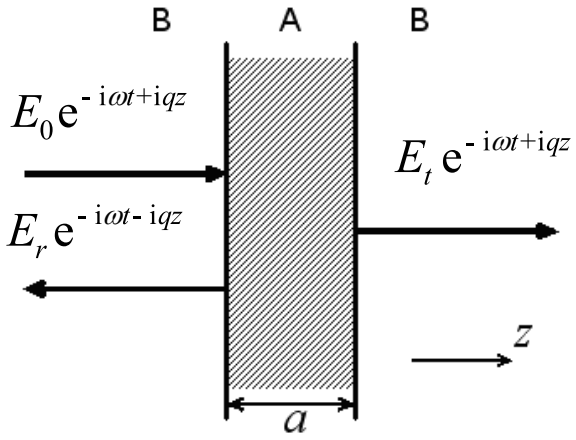

Fig. 3.1. Schematic representation of the normal-incidence light reflection from a single QW.

The problem of light reflection from a single QW neighboring two semi-infinite barrier layers (Fig. 3.1), was solved in 1991 [3.4, 3.5]. The solution has become an important milestone in the development of the quantum electrodynamics studying the coupling between 3D photons and low-dimensional excitons, 2D, 1D or 0D. For simplicity, we assume the normal incidence geometry, $\theta_0 = 0$. Then the final result will be reformulated for $\theta_0 \neq 0$. The amplitudes of the electric field for the initial, reflected and transmitted waves are denoted as $\boldsymbol{E}_0, \boldsymbol{E}_r$ and $\boldsymbol{E}_t$, respectively. For (001)-grown QWs, the three vectors are parallel and we can use the scalar amplitudes E_0, E_r, E_t shown in Fig. 3.1. The electric field outside the QW is given by

$$E(z,t) = \begin{cases} E_0 \exp\left(-\mathrm{i}\omega t + \mathrm{i}qz\right) + E_r \exp\left(-\mathrm{i}\omega t - \mathrm{i}qz\right) & \text{if} \quad z < -a/2 \ , \\ E_t \exp\left(-\mathrm{i}\omega t + \mathrm{i}qz\right) & \text{if} \quad z > a/2 \end{cases} \tag{3.7}$$

with $q = \sqrt{æ_b}\,\omega/c$. As far as we deal with the linear optics we can omit the factor $\exp\left(-\mathrm{i}\omega t\right)$. The amplitude reflection and transmission coefficients are

defined by

$$r_{\rm QW} = \frac{E_r}{E_0}\,,\; t_{\rm QW} = \frac{E_t}{E_0}\,. \tag{3.8}$$

In (3.7, 3.8) the coordinate z is referred to as the QW center while the coefficient r_{123} in (3.4) is defined with respect to the interface plane between the layers 1 and 2. This means that r_{123} and r_{QW} are related by

$$r_{123} = {\rm e}^{{\rm i}qa} r_{\rm QW}\,. \tag{3.9}$$

We derive $r_{\rm QW}$ and, hence, r_{123} in the frequency region close to a particular exciton resonance ω_0, say the heavy-hole exciton $e1$-$hh1(1s)$. Two different approaches will be used. The first is based on the solution of the wave equation

$$\frac{d^2E}{dz^2} = -\left(\frac{\omega}{c}\right)^2 D = -\left(\frac{\omega}{c}\right)^2 \left[æ_b E + 4\pi P_{\rm exc}(z)\right]\,, \tag{3.10}$$

where D is the electric displacement and $P_{\rm exc}(z)$ is the exciton contribution to the dielectric polarization depending on the electric field E. According to (2.202) the resonant dielectric response of a QW is nonlocal and given by

$$4\pi P_{\rm exc}(z) = G(\omega)\,\Phi(z) \int \Phi^*(z')E(z')\,dz'\,, \tag{3.11}$$

$$\Phi(z) = \varphi(0,z,z),\;\; \Phi^*(z) = \Phi(z)\,,\; G(\omega) = \frac{\pi a_B^3 æ_b \omega_{\rm LT}}{\omega_0 - \omega - {\rm i}\Gamma}\,.$$

Here $E(z)$ is the total electric field inside the QW, $a_{\rm B}$ and $\omega_{\rm LT}$ are the 3D-exciton Bohr radius and longitudinal-transverse splitting, Γ is the exciton nonradiative damping rate, the envelope function $\varphi(\rho, z_e, z_h)$ is introduced in (2.172). Note that, for the exciton ground state $e1$-$h1(1s)$, $\Phi(z)$ is an even function of z with the origin $z = 0$ chosen at the central plane of the QW.

We rearrange the wave equation (3.10) to a more convenient form

$$\frac{d^2E}{dz^2} + q^2 E = -q_0^2 4\pi P_{\rm exc}(z) \tag{3.12}$$

with q_0 being the light wave vector in vacuum

$$q_0 = \frac{\omega}{c}\,. \tag{3.13}$$

Now let us remind that the general solution of the linear second-order equation

$$\frac{d^2y}{dz^2} + q^2 y = F(z)$$

with an arbitrary inhomogeneous term $F(z)$ has the following general solution

$$y(z) = y_1 e^{iqz} + y_2 e^{-iqz} - \frac{i}{2q} \int dz' \, e^{iq|z-z'|} \, F(z') \, .$$

Therefore, (3.12) can be transferred into

$$E(z) = E_1 e^{iqz} + E_2 e^{-iqz} + 2\pi i \frac{q_0^2}{q} \int dz' \, e^{iq|z-z'|} \, P_{\rm exc}(z') \, . \tag{3.14}$$

The first two terms represent a pair of linearly independent solutions of the homogeneous equation, i.e., equation (3.12) with $P_{\rm exc} = 0$. They describe the plane waves incident on the QW from the left and right half-spaces. In other words, the amplitudes E_1 and E_2 are fixed by the external conditions. In the particular case of the initial light wave emerging from the left, one has $E_1 = E_0, E_2 = 0$. The third term in (3.14) is a particular solution of (3.12) with the inhomogeneous term $-q_0^2 4\pi P_{\rm exc}(z)$. It describes the electric field of the secondary wave induced coherently by the photoexcited 2D exciton.

In order to check that (3.14) is indeed a solution of (3.12) one can use the identity

$$\left(\frac{d^2}{dz^2} + q^2 \right) \frac{i}{2q} e^{iq|z-z'|} = -\delta(z - z') \, .$$

The δ-function appears on the left-hand side as a result of two successive differentiations, namely,

$$\frac{d}{dz} \, |z - z'| = \mathrm{sign}\{z - z'\} \equiv \begin{cases} 1 \text{ if } z > z' \, , \\ -1 \text{ if } z < z' \, , \end{cases}$$

$$\frac{d^2}{dz^2} \, |z - z'| = \frac{d}{dz} \, \mathrm{sign}\{z - z'\} = 2 \, \delta(z - z') \, .$$

It follows from (3.11, 3.14) that, for $E_1 = E_0, E_2 = 0$, the electric field satisfies the integral equation

$$E(z) = E_0 e^{iqz} + i \frac{q_0^2}{2q} G(\omega) \int dz' \, e^{iq|z-z'|} \Phi(z') \int \Phi(z'') E(z'') \, dz'' \, . \tag{3.15}$$

It allows an exact solution for arbitrary $\Phi(z)$ because after multiplying all the terms by $\Phi(z)$ and integrating over z one obtains a linear algebraic equation

$$\Lambda = \Lambda_0 + i \frac{q_0^2}{2q} \, G(\omega) \, \Lambda \int \int dz \, dz' e^{iq|z-z'|} \Phi(z) \Phi(z') \tag{3.16}$$

for the integral

$$\Lambda = \int \Phi(z) E(z) \, dz \, .$$

Here $\Lambda_0 = E_0 \int \Phi(z) \exp(iqz) \, dz$ or, taking into account the even symmetry of $\Phi(z)$,

$$\Lambda_0 = E_0 \int \Phi(z) \cos qz \, dz \, .$$

From (3.16) we readily find that

$$\mathit{\Lambda} = \frac{E_0 \int \mathit{\Phi}(z) \cos qz \, dz}{1 - \mathrm{i}(q_0^2/2q)\, G(\omega) \int\int dz \, dz' \mathrm{e}^{\mathrm{i}q|z-z'|} \mathit{\Phi}(z)\mathit{\Phi}(z')} \, . \tag{3.17}$$

The denominator can be rewritten in a more convenient form if we present the exponential function in the integrand as

$$\mathrm{e}^{\mathrm{i}q|z-z'|} = \cos q(z-z') + \mathrm{i} \sin q|z-z'| = \cos qz \cos qz' + \sin qz \sin qz' + \mathrm{i} \sin q|z-z'|$$

and introduce the parameters

$$\mathit{\Gamma}_0 = \frac{1}{2} \, q \, \omega_{\mathrm{LT}} \, \pi a_B^3 \left[\int \mathit{\Phi}(z) \cos qz \, dz \right]^2 \, , \tag{3.18}$$

$$\tilde{\omega}_0 = \omega_0 + \frac{1}{2} \, q \, \omega_{\mathrm{LT}} \, \pi a_B^3 \int\int dz \, dz' \mathit{\Phi}(z)\mathit{\Phi}(z') \sin q|z-z'| \, .$$

The final result for $\mathit{\Lambda}$ reads

$$\mathit{\Lambda} = E_0 \, \frac{(\omega_0 - \omega - \mathrm{i}\mathit{\Gamma}) \int \mathit{\Phi}(z) \cos qz \, dz}{\tilde{\omega}_0 - \omega - \mathrm{i}(\mathit{\Gamma} + \mathit{\Gamma}_0)} \, . \tag{3.19}$$

Taking z outside the QW layer where $\mathit{\Phi}(z)$ vanishes we can present the amplitude reflection and transmission coefficients as, see (3.15),

$$r_{\mathrm{QW}} = \frac{\mathit{\Lambda}}{E_0} \, \mathrm{i} \frac{q_0^2}{2q} \, G(\omega) \int \mathit{\Phi}(z') \cos qz' dz' \, , \; t_{\mathrm{QW}} = 1 + r_{\mathrm{QW}} \, . \tag{3.20}$$

Substitution of $\mathit{\Lambda}$ from (3.19) allows us to achieve our goal in finding the reflection and transmission coefficients [3.4, 3.5]

$$r_{\mathrm{QW}}(\omega) = \frac{\mathrm{i}\mathit{\Gamma}_0}{\tilde{\omega}_0 - \omega - \mathrm{i}(\mathit{\Gamma} + \mathit{\Gamma}_0)} \, , \; t_{\mathrm{QW}}(\omega) = \frac{\tilde{\omega}_0 - \omega - \mathrm{i}\mathit{\Gamma}}{\tilde{\omega}_0 - \omega - \mathrm{i}(\mathit{\Gamma} + \mathit{\Gamma}_0)} \, . \tag{3.21}$$

Now the physical meaning of the parameters (3.18) becomes transparent: $\tau_0 = (2\mathit{\Gamma}_0)^{-1}$ is the exciton radiative lifetime and $\tilde{\omega}_0$ is the renormalized exciton resonance frequency. The both parameters describe the modification of the 2D exciton complex eigenfrequency from $\omega_0 - \mathrm{i}\mathit{\Gamma}$ to $\tilde{\omega}_0 - \mathrm{i}(\mathit{\Gamma} + \mathit{\Gamma}_0)$ due to the exciton-photon coupling.

The second approach to derive r_{QW} and t_{QW} is based on the most general considerations and allows to perceive what in (3.21) is model-independent. As before we select an isolated excitonic level and consider a frequency region $\mathit{\Delta}\omega$ near the exciton resonance frequency ω_0 wide as compared to the inverse lifetime of the selected exciton and narrow as compared to the spacing $|\omega_0 - \omega_0'|$ between ω_0 and any other exciton resonance ω_0'. Under normal incidence the excitonic state with zero 2D wave vector, $K_x = K_y = 0$, is excited. The exciton can be scattered by an acoustic phonon or static defect into

$\boldsymbol{K} \neq 0$ states or trapped onto a localization site, it can also emit or absorb an optical phonon and leave the resonance frequency region at all. Let τ be the lifetime with respect to all such or similar processes. In addition, within some time τ_0 the exciton can coherently emit into the left or right barrier a photon of the initial frequency ω and the wave vectors $\pm q$. The meaning of the parameters ω_0, τ and τ_0 can be conveniently interpreted in terms of the time-resolved experiment: after a short-pulse photoexcitation of the exciton the time-variation of its wave function is described by the factor $\exp(-\mathrm{i}\Omega_0 t)$, where Ω_0 is the complex frequency $\omega_0 - \mathrm{i}(\Gamma + \Gamma_0)$ and $\Gamma_0 = (2\tau_0)^{-1}$, $\Gamma = (2\tau)^{-1}$ are called the exciton *radiative* and *nonradiative* damping rates.

The coefficients r_{QW} and t_{QW} represent a linear response of the QW to the action of a light wave. Let us analyze their dependence on the frequency ω extending this dependence on the whole complex plane $\omega = \omega' + \mathrm{i}\omega''$. According to the general theory of the linear response of the system to a periodic perturbation, the response function has poles in the plane ω at the complex eigenfrequencies of the system excited states. Therefore, within the interval $\Delta\omega$, the reflection and transmission coefficients are one-pole functions

$$r_{\mathrm{QW}}(\omega) = c_r + \frac{d_r}{\Omega_0 - \omega}\,,\; t_{\mathrm{QW}}(\omega) = c_t + \frac{d_t}{\Omega_0 - \omega}\,, \tag{3.22}$$

where $\Omega_0 = \omega_0 - \mathrm{i}(\Gamma + \Gamma_0)$ and c_r, d_r, c_t, d_t are constants.

In general, the background dielectric constant, $æ_a$, of the QW compositional material contributed by all electron-hole excitations, except for the fixed exciton ω_0, can be different from $æ_b$. However here, as well as in the first approach, we ignore the mismatch between $æ_a$ and $æ_b$. This means that, neglecting the exciton, the light wave would propagate through the QW as in a uniform medium as if $r_{\mathrm{QW}} = 0, t_{\mathrm{QW}} = 1$. The same holds if we take the exciton into consideration but move away into the off-resonant region $|\omega_0 - \omega| \gg \Gamma, \Gamma_0$. It follows then that

$$c_r = 0\,,\; c_t = 1\,. \tag{3.23}$$

The coefficients d_r, d_t characterize the exciton-photon coupling and are evidently independent of the nonradiative damping Γ. For a short time, in order to find them, we neglect the dissipation assuming $\Gamma = 0$. Then the energy conservation law imposes on r_{QW}, t_{QW} the condition

$$|r_{\mathrm{QW}}|^2 + |t_{\mathrm{QW}}|^2 = 1\,. \tag{3.24}$$

Hence, we can exclude Γ in the expressions (3.22), substitute the latter into (3.24) and obtain

$$\frac{|d_r|^2}{(\omega_0 - \omega)^2 + \Gamma_0^2} + \left|1 + \frac{d_t}{\omega_0 - \omega - \mathrm{i}\Gamma_0}\right|^2 = 1\,. \tag{3.25}$$

The next step is to write the light wave $E_t \exp(\mathrm{i}qz)$ in the right barrier as a sum of the initial wave $E_0 \exp(\mathrm{i}qz)$ and the secondary wave $E_{\mathrm{exc}} \exp(\mathrm{i}qz)$ emitted coherently by the exciton. Since the QW under consideration is assumed to be symmetrical the amplitude E_{exc} coincides with that of the reflected wave, E_r, and hence

$$t_{\mathrm{QW}}(\omega) = 1 + r_{\mathrm{QW}}(\omega) \tag{3.26}$$

which has been also obtained in the previous derivation, see (3.20). Comparing (3.26) with (3.22) we conclude that the constants d_r and d_t are equal. Replacing in (3.25) d_r by d_t we find

$$|d_t|^2 + \mathrm{Re}\{d_t(\omega_0 - \omega + \mathrm{i}\Gamma_0)\} = 0\,,$$

where $\mathrm{Re}\{Z\}$ means the real part of Z and ω is real. Representing d_t as a product of the modulus $|d_t|$ and the phase factor $\exp(\mathrm{i}\Phi_t)$ we reduce the above equation into

$$|d_t| + (\omega_0 - \omega)\cos\Phi_t - \Gamma_0 \sin\Phi_t = 0\,.$$

Thus, $\cos\Phi_t = 0$ and $|d_t| = \Gamma_0 \sin\Phi_t$. Since $|d_t|$ and Γ_0 are both positive we should choose the solution $\Phi_t = \pi/2$ of the equation $\cos\Phi_t = 0$. The final result, equations (3.22) with $c_r = 0, c_t = 1, d_r = d_t = \mathrm{i}\Gamma_0$, coincides with (3.21) if we change ω_0 in the complex frequency Ω_0 by the renormalized resonance frequency $\tilde{\omega}_0$. In fact, we had to define Ω_0 as $\tilde{\omega}_0 - \mathrm{i}(\Gamma + \Gamma_0)$ beginning from (3.22).

The reflectance $R_{\mathrm{QW}} = |r_{\mathrm{QW}}|^2$ and transmittance $T_{\mathrm{QW}} = |t_{\mathrm{QW}}|^2$ determine the fractions of the incident energy flux transferred to the reflected and transmitted waves. For $\Gamma \neq 0$, a part of the incident energy is absorbed inside the QW. This fraction is called the *absorbance* and given by

$$\eta_{\mathrm{QW}} \equiv 1 - R_{\mathrm{QW}} - T_{\mathrm{QW}} = \frac{2\Gamma\Gamma_0}{(\tilde{\omega}_0 - \omega)^2 + (\Gamma + \Gamma_0)^2}\,. \tag{3.27}$$

The reflection coefficient r_{QW} and radiative damping Γ_0 were derived in the frame of classical electrodynamics. Let us show that the same result is obtained by using the methods of quantum electrodynamics. In this connection we remind that the amplitude of the vector potential $\boldsymbol{A}(\boldsymbol{r})$ related to a single electromagnetic quantum $\hbar\omega$ propagating in a medium with the dielectric constant $æ_b = n_b^2$ is given by

$$\boldsymbol{A}_0 = \left(\frac{2\pi\hbar c^2}{æ_b V_0\,\omega}\right)^{1/2} \boldsymbol{e}\,, \tag{3.28}$$

where $\boldsymbol{e}$ is the polarization unit vector and V_0 is the macrovolume of Born - von Kármán. Next we write the Hamiltonian of radiation-matter interaction in the linear approximation

$$\hat{V} = -\frac{1}{c}\int d\boldsymbol{r}\;\; \boldsymbol{j}(\boldsymbol{r})\cdot\boldsymbol{A}(\boldsymbol{r},t)\,, \tag{3.29}$$

where $\boldsymbol{j}(\boldsymbol{r})$ is the current-density operator. According to (2.198) (Sect. 2.7.5) the matrix element of $\hat{V}$ for the photon-induced transition from the ground state of the system $|0\rangle$ into the excited state with an exciton, $|\,\mathrm{exc}, K_x = K_y = 0\rangle$, equals to

$$\langle \mathrm{exc}|\hat{V}|0\rangle = -\sqrt{S}\,\frac{ep_{cv}}{m_0 c}A_0\,\delta_{q_x,0}\,\delta_{q_y,0}\int dz\,\Phi(z)\cos q_z z\,,$$

where S is the sample area in the interface plane. Using Fermi's golden rule we can write for the exciton radiative lifetime

$$\frac{1}{\tau_0} = \frac{2\pi}{\hbar}\left(\frac{e|p_{cv}|}{m_0 c}\right)^2 V_0 A_0^2\int_{-\infty}^{\infty}\frac{dq_z}{2\pi}\left[\int \Phi(z)\cos q_z z\,dz\right]^2\delta\left(\hbar\frac{c}{n_b}|q_z| - \hbar\omega\right)\,. \tag{3.30}$$

Here the δ-function describes the energy conservation which selects two values of q_z, namely $q_z = \pm\omega\, n_b/c$. While deriving this equation, we performed the transformation from summation to integration in accordance to the rule

$$\sum_{q_z} \to \frac{V_0}{2\pi S}\int dq_z\,.$$

Substituting (3.28) into (3.30) and integrating over q_z we obtain

$$\Gamma_0 = \frac{1}{2\tau_0} = \frac{2\pi q(\omega_0)}{\hbar æ_b}\left(\frac{e|p_{cv}|}{m_0\omega_0}\right)^2\left[\int \Phi(z)\cos qz\,dz\right]^2$$

in agreement with (3.18) since, according to (2.204), one has

$$\frac{4}{æ_b}\left(\frac{e|p_{cv}|}{m_0\omega_0}\right)^2 = \hbar\omega_{\mathrm{LT}}\,a_B^3\,. \tag{3.31}$$

The reflected energy flux $J = (c/n_b)\hbar\omega|r_{\mathrm{QW}}(\omega)|^2$ per single photon can be also calculated by using Fermi's golden rule with the compound matrix element

$$\frac{\langle 0|\hat{V}|\,exc\rangle\,\langle exc|\hat{V}|0\rangle}{\hbar(\Omega_0 - \omega)} \tag{3.32}$$

for the two-step process "primary photon - exciton" and "exciton - secondary photon". The resonant denominator contains the complex energy of the excited state of the system, $\hbar\Omega_0 = \hbar[\tilde{\omega}_0 - \mathrm{i}(\Gamma + \Gamma_0)]$. It is worth to stress, however, that energies of the primary and secondary photons coincide because the same ground state $|0\rangle$ plays the role of the initial and final states of the electronic system. Thus, the process of light reflection from a QW can be interpreted in terms of the resonant fluorescence of a two-level quantum

system. In particular, the natural broadening of spectral lines is taken into account in the similar manner while calculating the reflection probability from a QW and scattering cross-section of an atom. However, there exists an important difference between these two quantum systems, namely, an atom is a 0D object and the light is elastically scattered in the broad solid angle whereas, in the case of a QW with perfect interfaces, the secondary photon propagates in the right and left barriers in the definite directions.

From (3.32) we obtain similarly to (3.30)

$$\frac{c}{n_b}\hbar\omega|r_{\rm QW}(\omega)|^2 = \hbar\omega\frac{2\pi}{\hbar}\left(\frac{e|p_{cv}|A_0}{m_0 c}\right)^4 (V_0 A_0^2)^2 \frac{1}{\hbar^2}\frac{1}{(\tilde{\omega}_0-\omega)^2+(\Gamma+\Gamma_0)^2}$$
$$\times \int_{-\infty}^{0}\frac{dq_z}{2\pi}\left[\int \Phi(z)\cos q_z z\, dz\right]^4 \delta(\hbar\frac{c}{n_b}|q_z|-\hbar\omega)$$

and, after additional simplification, come to

$$|r(\omega)|^2 = \frac{\Gamma_0^2}{(\tilde{\omega}_0-\omega)^2+(\Gamma+\Gamma_0)^2}$$

which agrees with (3.21).

The dielectric response (3.11) can be rewritten as

$$P_{\rm exc}(z) = \int dz\chi(z,z')\,E(z') \tag{3.33}$$

with the nonlocal susceptibility being equal to

$$\chi(z,z') = \frac{G(\omega)}{4\pi}\,\Phi(z)\,\Phi(z')\,. \tag{3.34}$$

Thus, the dielectric polarization at the point z lying inside the QW depends not only on a value of the electric field at this point but also on values of E at other points z'. It is instructive to consider a hypothetical four-layer structure containing the layer 2 of the thickness a characterized by a local single-pole dielectric function

$$æ_a(\omega) = æ_b + \frac{æ_b\,\omega_{\rm eff}}{\omega_0-\omega-{\rm i}\Gamma}\,. \tag{3.35}$$

Here $\omega_{\rm eff}$ is the effective longitudinal-transverse splitting being a measure of the interaction of light with the hypothetical exciton in the layer 2. The reflection coefficient from the layer 2 is calculated to be

$$r_{123}^{\rm eff} = \frac{1\ -\ {\rm e}^{2{\rm i}\phi}}{1-{\rm e}^{2{\rm i}\phi}\,r_{12}^2}\,r_{12}\,, \tag{3.36}$$

where $r_{12} = (n_b-n_a)/(n_b+n_a)$ is the Fresnel reflection coefficient on the interface between the layers 1 and 2, $n_a = \sqrt{æ_a(\omega)}$, $\phi = q_0 n_a a$. Assuming

$$\omega_{\rm eff} \ll \Gamma \tag{3.37}$$

we obtain

$$r_{123}^{\rm eff} = \frac{\rm i}{2}\, {\rm e}^{{\rm i}\phi} \frac{\omega_{\rm eff}\, \sin\phi}{\omega_0 - \omega - {\rm i}\Gamma}\,.$$

Comparing $r_{123}^{\rm eff}$ with the exact result for $r_{123} = {\rm e}^{{\rm i}\phi} r_{\rm QW}$, see (3.9, 3.21), we conclude that they coincide if we set

$$\omega_{\rm eff} = \frac{2\Gamma_0}{\sin q(\omega_0)a} \approx \frac{2\Gamma_0}{q(\omega_0)a}\,. \tag{3.38}$$

We can approximate $\sin\phi$ by ϕ because in typical nanostructures the QW thickness is small as compared with the light wavelength at the exciton resonance frequency ω_0. Together with (3.37) this means that Γ_0 and $\tilde{\omega}_0 - \omega_0$ are smaller than Γ and their contribution to the denominator $\Omega_0 - \omega$ can be neglected. Finally, the real QW structures with a nonlocal response may be replaced by a hypothetical structure with a local response only if

$$\frac{2\Gamma_0}{q(\omega_0)a} \ll \Gamma\,. \tag{3.39}$$

Otherwise one should use the exact result (3.21).

Additional simplifications follow if we take into consideration that the QW thickness a is usually small as compared to the light wavelength $2\pi/q$ and we can neglect corrections of the order $qa \ll 1$ replacing $\exp({\rm i}qz)$, $\cos qz$ by unity for values of z inside the QW. In this approximation the electric field (3.15) inside the QW equals to

$$E = E_0 + 2\pi{\rm i}\frac{q_0^2 a}{q} P = E_0 + \frac{\rm i}{\xi}\, P\,, \tag{3.40}$$

where P is the averaged polarization

$$P(t) = \frac{1}{a} \int dz\, P(z,t) \tag{3.41}$$

and the dimensionless parameter ξ is defined as

$$\xi = \frac{æ_b}{2\pi q a}\,. \tag{3.42}$$

In the same approximation we have for the radiative damping

$$\Gamma_0 = \frac{1}{2}\, q\, \omega_{\rm LT}\, \pi a_B^3 \left[\int \Phi(z)\, dz\right]^2\,, \tag{3.43}$$

and the material relation for $P_{\rm exc}(z)$ can be reduced to the following equation for the average

$$(\omega_0 - \omega - \mathrm{i}\Gamma)P = \xi\Gamma_0 E\,. \tag{3.44}$$

In the variational approach with one variable parameter $\tilde{a}$ (Chap. 2), we find

$$\int \Phi(z)\,dz = \sqrt{\frac{2}{\pi}}\,\frac{1}{\tilde{a}}\,i_{11}^0\,,$$

where $i_{11}^0 = \int \varphi_{e1}(z)\,\varphi_{h1}(z)\,dz$ is the overlap integral between the envelopes for an electron in the $e1$ subband and a hole in the $h1$ subband. In this case we come to

$$\Gamma_0 = \omega_{\mathrm{LT}}\,\frac{qa_B^3}{\tilde{a}^2}\left(i_{11}^0\right)^2\,. \tag{3.45}$$

For typical QWs values of $\hbar\Gamma_0$ lie in the range $0.01 \div 0.1$ meV, e.g., $\hbar\Gamma_0 \approx 0.12$ meV in 100-Å CdTe/$Cd_{0.13}Zn_{0.87}$Te QWs [3.12] and $\hbar\Gamma_0 \approx 30$ μeV in 85-Å $In_{0.04}Ga_{0.96}As$/GaAs QWs [3.16]. For crude estimations one can use the approximation of infinitely high barriers in which case $i_{11}^0 = 1$ and take for $\tilde{a}$ a value of the 2D Bohr radius, $a_{\mathrm{B}}^{(2D)} = a_{\mathrm{B}}/2$. Then one has

$$\Gamma_0 = 4qa_{\mathrm{B}}\omega_{\mathrm{LT}}\,. \tag{3.46}$$

Equation (3.21) for r_{QW} can be generalized to make allowance for two and more excitonic resonances. Each resonance adds an extra pole in the reflection coefficient $r_{QW}(\omega)$. Practically, if a wide frequency range is considered the two-pole response function

$$r_{\mathrm{QW}}(\omega) = \frac{\mathrm{i}\Gamma_0^h}{\omega_0^h - \omega - \mathrm{i}(\Gamma_h + \Gamma_0^h)} + \frac{\mathrm{i}\Gamma_0^l}{\omega_0^l - \omega - \mathrm{i}(\Gamma_l + \Gamma_0^l)} \tag{3.47}$$

is often used, where the indices h and l refer to the $e1$-$hh1(1s)$ and $e1$-$lh1(1s)$ excitons. The two-pole reflection coefficient was used as well to fit reflectivity spectra in doped QWs and deduce the parameters of the heavy-hole excitons and trions [3.17]. Astakhov et al. [3.18] found a linear dependence of the trion radiative damping and oscillator strength on the 2D electron concentration accompanied by some decrease in the exciton oscillator strength. As a result, an all-optical method has been proposed to obtain information about 2D electron gases of low density from 10^9 up to 10^{11} cm^{-2}.

A modification of equations (3.4, 3.9, 3.21) more suitable for comparison with experiment is obtained if we notice that the ratio

$$\frac{r_{123}\mathrm{e}^{2\mathrm{i}\varphi_1}}{1 - r_{10}r_{123}\mathrm{e}^{2\mathrm{i}\varphi_1}}$$

can be reduced to

$$\frac{\mathrm{i}\Gamma_0\mathrm{e}^{2\mathrm{i}\varphi_{0a}}}{\omega_0' - \omega - \mathrm{i}(\Gamma + \Gamma_0')}\,, \tag{3.48}$$

where

$$\varphi_{0a} = q\left(d_1 + \frac{a}{2}\right) = \phi_1 + \frac{1}{2}qa\,, \tag{3.49}$$
$$\omega_0' = \tilde{\omega}_0 + r_{10}\Gamma_0 \sin 2\varphi_{0a}\,,\ \Gamma_0' = \Gamma_0(1 + r_{10}\cos 2\varphi_{0a})\,.$$

Due to the self-consistent effect of reflection of the secondary light from the external surface, the cladding layer 1 modifies the exciton resonance frequency and radiative damping from ω_0, Γ_0 to ω_0', Γ_0'. Particularly, if the secondary wave that had been emitted by the exciton and the secondary wave which returned to the QW due to the reflection are in phase, i.e., $\cos 2\phi_{0a} = 1$, the exciton radiative damping increases by a factor of $2n_b/(n_b + 1)$.

By using (3.48) we can present the reflectance as

$$R(\omega) = |r(\omega)|^2 = R_0 + \frac{A + Bx}{1 + x^2}\,, \tag{3.50}$$

where

$$R_0 = r_{01}^2\,,\ x = \frac{\omega - \omega_0'}{\Gamma'}\,,\ \Gamma' = \Gamma + \Gamma_0'\,,$$
$$A = t_{01}t_{10}s(t_{01}t_{10}s - 2r_{01}\cos 2\varphi_{0a})\,,\ B = 2r_{01}t_{01}t_{10}s\sin 2\varphi_{0a}\,,\ s = \frac{\Gamma_0}{\Gamma}\,.$$

Under normal incidence, $r_{01} = (1 - n_b)/(1 + n_b)$, $t_{01}t_{10} = 4n_b/(n_b + 1)^2$. The phase ϕ_{0a} determines the shape of the reflection resonance profile [3.19]. Depending on the thickness of the top layer the reflectance spectrum can have a single dip or a peak when $2\phi_{0a}$ is an integral number of π, a system of equally pronounced maximum and minimum when $2\phi_{0a} = (m + 0.5)\pi$, and intermediate profiles for other values of ϕ_{0a}.

The homogeneous, nonradiative broadening of the reflectance spectrum is due to exciton scattering by heterostructure defects, phonons and free charges. However, when describing experimental optical spectra, the parameter Γ in (3.21) or (3.50) is frequently interpreted as a sum of two contributions, $\Gamma_\mathrm{h} + \Gamma_\mathrm{inh}$, the first of them being related to the real homogeneous broadening, and the second taking effectively into account the inhomogeneous broadening of the exciton resonance frequency.

The above equations (3.21) for the reflection and transmission coefficients can be extended for an oblique incidence geometry. Firstly, $q = q_0 n_b$ should be replaced by $q_z = (q^2 - q_\parallel^2)^{1/2}$, where $q_\parallel = q_0 \sin\theta_0 = q\sin\theta$ is the in-plane component of the wave vector, θ is the refractive angle connected with the incident angle in vacuum by $n_b \sin\theta = \sin\theta_0$. Secondly, the in-plane kinetic-energy term $\hbar q_\parallel^2/(2M)$ should be added to the resonant frequency ω_0. For the s-polarized light (TE polarization, the electric vector $\boldsymbol{E}$ being perpendicular to the incidence plane) the equations (3.21) exhibit a minor modification, i.e.,

$$r_\mathrm{QW}(\omega) = \frac{\mathrm{i}\Gamma_{0s}}{\tilde{\omega}_{0s} - \omega - \mathrm{i}(\Gamma + \Gamma_{0s})}\,,\ t_\mathrm{QW}(\omega) = 1 + r_\mathrm{QW}(\omega)\,, \tag{3.51}$$

where Γ_0 and $\tilde{\omega}_0$ have been changed by

$$\Gamma_{0s} = \frac{1}{2}\,\frac{q^2}{q_z}\,\omega_{\rm LT}\,\pi a_B^3\left[\int \Phi(z)\cos q_z z\,dz\right]^2\,, \tag{3.52}$$

$$\tilde{\omega}_{0s} = \omega_0(q_\parallel) + \frac{1}{2}\,q_z\,\omega_{\rm LT}\,\pi a_B^3\int\int dz\,dz'\Phi(z)\Phi(z')\sin q_z|z-z'|\,,$$

where $\omega_0(q_\parallel) = \omega_0 + (\hbar q_\parallel^2/2M)$. For the p-polarized light (TM polarization, $\boldsymbol{E}$ lies in the incidence plane) the reflection coefficient is given by the two-pole function

$$r^p_{\rm QW}(\omega) = \frac{{\rm i}\Gamma_{0p}}{\tilde{\omega}_{0p} - \omega - {\rm i}(\Gamma + \Gamma_{0p})} - \frac{{\rm i}\Gamma'_{0p}}{\tilde{\omega}'_{0p} - \omega - {\rm i}(\Gamma + \Gamma'_{0p})}\,, \tag{3.53}$$

where

$$\Gamma_{0p}(q_\parallel) = \frac{q_z^2}{q^2}\,\Gamma_{0s}\,,\ \Gamma'_{0p} = \frac{q_\parallel^2}{q^2}\,\frac{\omega'_{\rm LT}}{\omega_{\rm LT}}\,\Gamma_{0s}\,,\ \tilde{\omega}_{0p} = \tilde{\omega}_{0s}\,, \tag{3.54}$$

$$\tilde{\omega}'_{0p} = \omega_0(q_\parallel) + \omega'_{\rm LT}\pi a_{\rm B}^3\int \Phi^2(z)dz + (q_\parallel/q_z)^2[\tilde{\omega}_{0p} - \omega_0(q_\parallel)]\,.$$

The values of $\omega_{\rm LT}$ and $\omega'_{\rm LT}$ are proportional to the squared moduli of the interband optical matrix elements in the polarization $\boldsymbol{e} \perp z$ and $\boldsymbol{e} \parallel z$, respectively. The presence of two poles in (3.53) reflects the fact that there exist two excitonic states, the transverse and longitudinal excitons, which exhibit different renormalization due to the exciton-photon interaction. Heavy-hole excitons $e1$-$hh1$ in zinc-blende-based semiconductor heterostructures are optically inactive in the polarization $\boldsymbol{E} \parallel z$, $\omega'_{\rm LT} = 0$, and the second term in (3.53) vanishes.

Since the wave vector, K, of a photoexcited 2D exciton is equal to $q_\parallel = q(\omega_0)\sin\theta$, equations (3.52) and (3.54) also show a K-dependence of the exciton radiative lifetimes $\tau_{r,s} = (2\Gamma_{0s})^{-1}$ and $\tau_{r,p} = (2\Gamma_{0p})^{-1}$. The radiative exciton states lie within the circle $K \le (\omega_0/c)n_b$ because in this case $q_z = [q(\omega_0)^2 - K^2]^{1/2}$ is real and the exciton can annihilate with the emission of light into the barrier. An exciton with $K > (\omega_0/c)n_b$ (and hence with imaginary q_z) induces an electromagnetic field but it decays exponentially in the barriers as $\exp(-|z|\,{\rm Im}\{q_z\})$. The inverse influence of this field on the exciton leads to renormalization of its resonant frequency but does not create a new recombination channel.

If the background dielectric constant, $æ_a$, in the QW differs from $æ_b$, then $æ_b$ in the expression for $G(\omega)$, see (3.11), should be replaced by $æ_a$ and the factor q^2 in the left-side of (3.12) should be replaced by $q_0^2 æ_0(z)$, where $æ_0(z) = æ_a$ inside the QW and $æ_0(z) = æ_b$ outside the QW. The obtained integro-differential equation for $E(z)$ can be solved as well, and the following result is valid in the case of a dielectric constant mismatch [3.20]

$$r_{\rm QW} = r^{(0)} + r_{\rm exc}\,,\ t_{\rm QW} = t^{(0)} + r_{\rm exc}\,. \tag{3.55}$$

Here $r^{(0)}$ and $t^{(0)}$ are the reflection and transmission coefficients calculated, neglecting the exciton contribution. They are given by

$$r^{(0)} = \mathrm{e}^{-\mathrm{i}q_b a} r_{ba} \frac{1 - \mathrm{e}^{2\mathrm{i}q_a a}}{1 - r_{ba}^2 \mathrm{e}^{2\mathrm{i}\, q_a a}} \ , \ t^{(0)} = \mathrm{e}^{\mathrm{i}q_a a}(\mathrm{e}^{-\mathrm{i}q_b a} + r_{ab}\, r^{(0)}) \ , \tag{3.56}$$

$q_{a,b} = q_0 n_{a,b}$, $r_{ba} = -\, r_{ab} = (n_b - n_a)/(n_b + n_a)$, $n_{a,b} = \sqrt{æ_{a,b}}$ and $r_{ba} = -r_{ab} = (n_b - n_a)/(n_b + n_a)$. For a symmetric well with an even function $\Phi(z)$ the exciton contribution to $r_{\mathrm{QW}}, t_{\mathrm{QW}}$ can be written as

$$r_{\mathrm{exc}} = t^{(0)} \frac{\mathrm{i}\bar{\Gamma}_0}{\tilde{\omega}_0 - \omega - \mathrm{i}\left(\Gamma + \bar{\Gamma}_0\right)} \ , \ \bar{\Gamma}_0 = \frac{1 + r_{ab}\mathrm{e}^{\mathrm{i}q_a a}}{1 - r_{ab}\mathrm{e}^{\mathrm{i}q_a a}}\, \Gamma_0 \ , \tag{3.57}$$

where Γ_0 and $\tilde{\omega}_0$ differ from (3.18) by the replacement $q \to q_a$. As before, the reflected and transmitted waves are defined as $E_r \exp(-\mathrm{i}q_b z)$, $E_t \exp(\mathrm{i}q_b z)$ and the origin $z = 0$ is taken in the QW center. While deriving this equation we ignored the tunnel tails of $\Phi(z)$, and assumed $\Phi(z)$ to be nonzero only inside the QW. For coinciding n_a and n_b, or æ$_a$ and æ$_b$, the background reflection $r^{(0)}$ vanishes, $t^{(0)}$ reduces to unity, the parameter $\bar{\Gamma}_0$ reduces to the real damping Γ_0 and (3.55) coincide with (3.21). One can see that at $r_{ab} \neq 0$ the parameter $\bar{\Gamma}_0$ is complex and contributes both to the real and imaginary parts of the exciton complex eigenfrequency. For $q_a a \ll 1$, the correction $\tilde{\omega}_0 - \omega_0 + \mathrm{Im}\{\bar{\Gamma}_0\}$ to the resonance frequency ω_0 is negligibly small and can be disregarded.

3.1.2 Periodic Quantum Well Structure

Here we consider normal light waves propagating in the infinite equidistant system of QWs centered at the points $z_n = nd$, where n is an integer, d is a sum of the QW thickness a and the thickness b of a barrier between the nearest QWs. The latter is thick enough to prevent the quantum-mechanical tunnelling of an exciton from one QW to another. In this case the exciton contribution to the dielectric polarization is a sum of the single-QW contributions

$$P_{\mathrm{exc}}(z) = \sum_n P_{\mathrm{exc}}^{(n)}(z) \tag{3.58}$$

and the constitutive relation for $P_{\mathrm{exc}}^{(n)}(z)$ is given by (3.11) in which the envelope $\Phi(z)$ is replaced by the envelope $\Phi_n(z) = \Phi(z - z_n)$ with a shifted argument. Therefore,

$$P_{\mathrm{exc}}^{(n)}(z) = \frac{G(\omega)}{4\pi}\, \Phi_n(z) \int \Phi_n(z') E(z')\, dz' \ . \tag{3.59}$$

The initial electric field and the electric field induced by 2D excitons excited coherently in the QWs are given by

$$E(z) = E_1 \mathrm{e}^{\mathrm{i}qz} + E_2 \mathrm{e}^{-\mathrm{i}qz} + 2\pi \mathrm{i} \frac{q_0^2}{q} \sum_n \int dz' \, \mathrm{e}^{\mathrm{i}q|z-z'|} \, P^n_{\mathrm{exc}}(z') \, . \qquad (3.60)$$

Eigenexcitations in such a system in the frequency region close to ω_0 have a mixed exciton-photon nature. They comprise both the electro-magnetic and excitonic components. These are nothing more than exciton-polariton modes modified substantially, as compared with those in bulk crystals. In the absence of dissipation, $\Gamma = 0$, the exciton polariton propagates without limitation, experiencing continual coherent transformation from exciton into photon and from photon to exciton.

In order to derive the dispersion equation for exciton polaritons in periodic MQWs, let us consider the transfer matrix through a B/A/B layer of a thickness d with a single QW in its center. Here the length d has an arbitrary value but then it will be the period for a regular MQW structure. The transfer matrix connects the amplitudes of the electric field at the points $z = \pm d/2$

$$\begin{bmatrix} E'_+ \\ E'_- \end{bmatrix} = \begin{bmatrix} T_{11} \; T_{12} \\ T_{21} \; T_{22} \end{bmatrix} \begin{bmatrix} E_+ \\ E_- \end{bmatrix} \, .$$

The amplitudes are defined as follows: the incoming and outgoing waves on the left-hand side are, respectively,

$$E_+ \exp\left[\mathrm{i}q(z + d/2)\right] \quad \text{and} \quad E_- \exp\left[-\mathrm{i}q(z + d/2)\right]$$

and those on the right-hand side are

$$E'_- \exp\left[-\mathrm{i}q(z - d/2)\right] \quad \text{and} \quad E'_+ \exp\left[\mathrm{i}q(z - d/2)\right] .$$

The components T_{ij} are related to the reflection and transmission coefficients $\tilde{r} = \mathrm{e}^{\mathrm{i}qd} r_{\mathrm{QW}}$, $\tilde{t} = \mathrm{e}^{\mathrm{i}qd} t_{\mathrm{QW}}$ by

$$\hat{T} = \frac{1}{\tilde{t}} \begin{bmatrix} \tilde{t}^2 - \tilde{r}^2 & \tilde{r} \\ -\tilde{r} & 1 \end{bmatrix} \, . \qquad (3.61)$$

The above result can be demonstrated as follows. Consider first the light incoming from the left-hand side so that $E'_- = 0$. According to the definition of the transfer matrix, in this case

$$E'_+ = T_{11} E_+ + T_{12} E_- \, , \; 0 = T_{21} E_+ + T_{22} E_- \, .$$

It follows then that

$$\tilde{r} = \frac{E_-}{E_+} = -\frac{T_{21}}{T_{22}} \, , \; \tilde{t} = \frac{E'_+}{E_+} = \frac{T_{22} T_{11} - T_{12} T_{21}}{T_{22}} \, .$$

For the light incoming from the right-hand side we have $E_+ = 0$, $E'_+ = T_{12} E_-$, $E'_- = T_{22} E_-$, and hence

$$\tilde{r} = \frac{E'_+}{E'_-} = \frac{T_{12}}{T_{22}}\,,\ \tilde{t} = \frac{E_-}{E'_-} = \frac{1}{T_{22}}\,.$$

From a comparison we obtain $T_{12} = -T_{21}$ and

$$\mathrm{Det}\{\hat{T}\} = T_{22}T_{11} - T_{12}T_{21} = 1 \tag{3.62}$$

as well as the above equation for $\hat{T}$.

Now we turn from a single QW to a regular MQWs with the spacing $d = a + b$. For exciton polaritons propagating along the principal axis of the infinite regular MQWs, the frequency ω vs. wave vector K dependence can be derived by applying the Bloch theorem. According to this theorem the eigenwaves (or normal waves) can be sought in the form

$$\begin{bmatrix} E'_+ \\ E'_- \end{bmatrix} = \mathrm{e}^{\mathrm{i}Kd} \begin{bmatrix} E_+ \\ E_- \end{bmatrix} = \hat{T} \begin{bmatrix} E_+ \\ E_- \end{bmatrix} \tag{3.63}$$

which leads to the dispersion equation (2.125). Taking into account the relation (3.61) between T_{ij} and $\tilde{r}, \tilde{t}$ we obtain

$$\cos Kd = \frac{\tilde{t}^2 - \tilde{r}^2 + 1}{2\tilde{t}} = \cos qd + \mathrm{i}\sin qd \frac{r_{\mathrm{QW}}}{1 + r_{\mathrm{QW}}}\,. \tag{3.64}$$

From here and from (3.21), valid if $æ_a = æ_b$, we come to the dispersion equation [3.5]

$$\cos Kd = \cos qd - \frac{\Gamma_0}{\tilde{\omega}_0 - \omega - \mathrm{i}\Gamma}\,\sin qd\,. \tag{3.65}$$

The real part of K is defined within the superstructure Brillouin zone, $-\pi/d < \mathrm{Re}\{K\} \le \pi/d$. In the following we omit the *tilde* symbol reminding that $\tilde{\omega}_0$ is the renormalized exciton resonance frequency. An important point is that the denominator in the second term of (3.65) does not contain the exciton radiative damping in contrast with the denominators in (3.21). This agrees with the general property of exciton polaritons: in the absence of dissipative couplings they are stationary states and exciton-radiation interaction alone gives rise to no optical absorption.

It is instructive to rearrange (3.65) as

$$(\cos qd - \cos Kd)\,(\omega_0 - \omega - \mathrm{i}\Gamma) = \Gamma_0 \sin qd\,. \tag{3.66}$$

Similarly to (3.1), this form allows an interpretation in terms of the two-oscillatory model of exciton polaritons. Indeed, zeros of the functions inside the first and second parentheses of (3.66) determine eigenfrequencies of bare photons and excitons the latter coinciding with that for a quasi-2D exciton in a SQW. The right-hand side of (3.66) governs the strength of exciton-photon coupling, it is not completely determined by Γ_0 but also depends on the period and frequency.

Equation (3.65) can be extended to allow the mismatch $æ_a \neq æ_b$, then it has the form

$$\cos Kd = D_1 - \frac{\Gamma_0}{\omega_0 - \omega - \mathrm{i}\Gamma} D_2 \,, \tag{3.67}$$

where

$$D_1 = \cos q_a a \cos q_b b - \frac{1 + r_{ab}^2}{1 - r_{ab}^2} \sin q_a a \sin q_b b = \tag{3.68}$$

$$= \frac{\cos\left(q_a a + q_b b\right) - r_{ab}^2 \cos\left(q_a a - q_b b\right)}{1 - r_{ab}^2} \,,$$

$$D_2 = \frac{\sin(q_a a + q_b b) + r_{ab}^2 \sin(q_b b - q_a a) + 2 r_{ab} \sin(q_b b)}{1 - r_{ab}^2} \,,$$

other notations have been introduced in (3.56, 3.57). It is convenient to rewrite this equation in the equivalent form

$$\cos^2 \frac{Kd}{2} = \frac{D_3 D_4}{1 - r_{ab}^2}, \tag{3.69}$$

where

$$D_3 = \cos\phi_+ + r_{ab} \cos\phi_-, \tag{3.70}$$

$$D_4 = \cos\phi_+ - r_{ab} \cos\phi_- - \frac{\Gamma_0}{\omega_0 - \omega - \mathrm{i}\Gamma} \left(\sin\phi_+ + r_{ab} \sin\phi_-\right) \,,$$

and $\phi_\pm = (q_b b \pm q_a a)/2$.

3.1.3 Effective Dielectric Function of Short-Period Multiple Quantum Wells and Superlattices

In short-period structures, MQWs and SLs, with the period d smaller than the light wavelength $\lambda = 2\pi/q$, one can use the approximation of an effective uniform medium, introduce the effective dielectric function $æ_{\mathrm{eff}}(\omega)$ and apply the methods of resonant spectroscopy developed for bulk crystals.

For short-period MQWs, i.e., in the long-wavelength limit $|K|^2 d^2, qd \ll 1$, the equation for $æ_{\mathrm{eff}}$ is derived by expanding the trigonometric functions in (3.65) as follows

$$\cos Kd \approx 1 - \frac{1}{2}(Kd)^2 \,,\ \cos qd \approx 1 - \frac{1}{2}(qd)^2 \,,\ \sin qd \approx qd \,.$$

As a result, (3.65) can be reduced to

$$1 - \frac{1}{2}(Kd)^2 = 1 - \frac{1}{2}(qd)^2 - qd \, \frac{\Gamma_0}{\omega_0 - \omega - \mathrm{i}\Gamma} \,,$$

or [3.3, 3.22]

$$\left(\frac{c\,K}{\omega}\right)^2 = æ_{\rm eff}(\omega) \equiv æ_b + \frac{æ_b\,\omega_{\rm LT}^{\rm MQW}}{\omega_0 - \omega - {\rm i}\Gamma} \tag{3.71}$$

with

$$\omega_{\rm LT}^{\rm MQW} = \frac{2\Gamma_0}{q(\omega_0)d}\,. \tag{3.72}$$

In the 2D limit, from (3.46) we obtain the estimation

$$\omega_{\rm LT}^{\rm MQW} = \frac{8a_{\rm B}}{d}\omega_{\rm LT}\,. \tag{3.73}$$

For d comparable with $a_{\rm B}$, $\omega_{\rm LT}^{\rm MQW}$ exceeds the bulk value $\omega_{\rm LT}$. Physically, this enhancement of the exciton oscillator strength can be understood bearing in mind that the barriers press an electron and a hole excited inside the QW closer to each other, thus increasing the probability to find them at the same point, which, in turn, increases the exciton-photon coupling constant.

The criterion of validity $|K|^2d^2 \ll 1$ is equivalent to the inequality

$$(qd)^2\,\frac{\omega_{\rm LT}^{\rm MQW}}{|\omega_0 - \omega - {\rm i}\Gamma|} \ll 1\,.$$

This condition for MQWs is much weaker than the condition (3.39) for the approximation of a local response in a QW. Note that the effective oscillator strength $\omega_{\rm eff}$ in a QW, see (3.38), and the effective longitudinal-transverse splitting, $\omega_{\rm LT}^{\rm MQW}$, are related by

$$\omega_{\rm LT}^{\rm MQW} = \frac{a}{d}\,\omega_{\rm eff}\,.$$

If two or more exciton resonances are taken into account the effective dielectric function has the corresponding number of poles. Usually it is enough to consider a two-pole function

$$æ_{\rm eff}(\omega) = æ_b + \frac{\Omega^{(h)}}{\omega_0^h - \omega - {\rm i}\Gamma_h} + \frac{\Omega^{(l)}}{\omega_0^l - \omega - {\rm i}\Gamma_l}\,, \tag{3.74}$$

where h, l denote the heavy- and light-hole ground exciton states. The exciton oscillator strength $\Omega^{(j)}$ can be presented as a product $æ_b\omega_{{\rm LT},j}^{\rm MQW}$ where $\omega_{{\rm LT},j}^{\rm MQW}$ is the effective longitudinal-transverse splitting for the exciton $j = h, l$.

In MQWs with the dielectric constant mismatch the effective dielectric function takes the form

$$æ_{\rm eff}(\omega) \equiv \bar{æ} + \frac{æ_a\,\omega_{\rm LT}^{\rm MQW}}{\omega_0 - \omega - {\rm i}\Gamma}$$

with

$$\bar{æ} = \frac{æ_a a + æ_b b}{d}\,,\ \omega_{\rm LT}^{\rm MQW} = \frac{2\Gamma_0(q_a)}{q_a(\omega_0)d}\,.$$

The approximation of an effective uniform medium is also valid in SLs where the exciton envelope function is written as (Chap. 2)

$$\Psi_{\rm exc}(\boldsymbol{r}_e, \boldsymbol{r}_h) = \frac{{\rm e}^{{\rm i}\boldsymbol{K}\cdot\boldsymbol{R}}}{\sqrt{V}} f(\boldsymbol{r}) U_e(z_e) U_h(z_h)\,. \tag{3.75}$$

Here V is the volume, $U_e(z_e)$ and $U_h(z_h)$ are the single-particle envelope functions, respectively at the bottom of the conduction miniband $e1$ and at the top of the valence miniband $h1$, they are normalized by

$$\int\limits_0^d U^2(z)\,dz = d\,,$$

$f(\boldsymbol{r})$ is the envelope describing the relative electron-hole motion. This function satisfies Schrödinger's equation

$$\left[-\frac{\hbar^2}{2\mu_l}\frac{\partial^2}{\partial z^2} - \frac{\hbar^2}{2\mu_t}\left(\frac{\partial^2}{\partial x^2} + \frac{\partial^2}{\partial y^2}\right) - \frac{e^2}{æ r}\right] f(\boldsymbol{r}) = -\varepsilon f(\boldsymbol{r})\,,$$

where ε is the exciton binding energy, $\mu_{l,t}$ are the reduced effective masses μ_{zz} and $\mu_{xx} = \mu_{yy}$ of the electron-hole pair, æ is the low-frequency dielectric constant. Then the dielectric function is given by

$$æ_{\rm eff}(\omega) \equiv æ_b + \frac{æ_b\,\omega_{\rm LT}^{\rm SL}}{\omega_0 - \omega - {\rm i}\Gamma} \tag{3.76}$$

with the longitudinal-transverse splitting being [3.3]

$$\omega_{\rm LT}^{\rm SL} = \omega_{\rm LT}\frac{a_B^3}{a_l a_t^2}\left[\frac{1}{d}\int\limits_0^d U_e(z)U_h(z)\,dz\right]^2\,. \tag{3.77}$$

Here a_l and a_t are the longitudinal and transverse effective Bohr radii which are the variational parameters in the trial function

$$f(\boldsymbol{r}) = \frac{1}{\sqrt{\pi a_l a_t^2}}\exp\left[-\left(\frac{x^2+y^2}{a_t^2} + \frac{z^2}{a_l^2}\right)^{1/2}\right].$$

The dependence of the longitudinal-transverse splitting of the $e1$-$hh1(1s)$ exciton on the period d of the GaAs/AlGaAs heterostructure with GaAs and AlGaAs layers of equal thickness is shown in Fig. 3.2. The branches of the theoretical curve were calculated by (3.72, 3.77). The range of layer thicknesses in the regular heterostructures under investigations covers the limits of MQWs and SLs. At the sides of MQWs the longitudinal-transverse splitting of the heterostructure, $\omega_{\rm LT}^h$, equals to $\omega_{\rm LT}^{\rm MQW}$ given by (3.72). It increases approximately as d^{-1} with decreasing the period. As the period

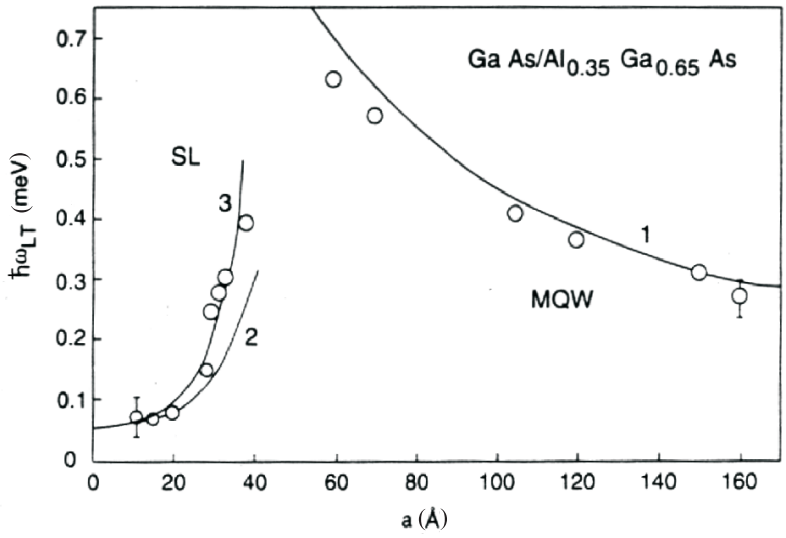

Fig. 3.2. The longitudinal-transverse splitting of heavy-hole excitons vs. a period of multilayered $GaAs/Al_{0.35}Ga_{0.65}As$ structure with equal thickness of wells and barriers. Curves 1 and 2 are calculated according to (3.73) and (3.77), respectively. Curve 3 is calculated taking into account nonparabolicity of the electron miniband spectrum [3.21]. From [3.22].

decreases still further, i.e., at the side of SLs where $\omega_{\rm LT}^{h} \approx \omega_{\rm LT}^{\rm SL}$, the overlap of electron states in neighboring wells increases, the subband $e1$ transfers into a miniband, the miniband electron effective mass decreases, and the character of the electron motion in the structure changes from 2D to 3D. As a result the effective longitudinal-transverse splitting reaches a maximum at a certain value of d and then starts to fall off. Thus, the nonmonotonic dependence of $\omega_{\rm LT}^{h}(d)$ is actually a manifestation of the 2D-3D transition in a periodic heterostructure.

3.1.4 Resonant Bragg Structures

Now we shall analyze the exciton-polariton spectrum in MQW heterostructures, see (3.65) and (3.69), focusing attention on resonant Bragg structures. Physically the analysis becomes more transparent if we disregard the nonradiative damping and inhomogeneous broadening.

As for any particle or quasi-particle moving in a periodic system, the exciton-polariton dispersion spectrum has allowed bands and forbidden energy (or frequency) regions, the latter are commonly called *band gaps*. The allowed bands are determined by the condition $|C(\omega)| \leq 1$, where $C(\omega)$ stands for the right-hand side of (3.65). If $|C(\omega)| > 1$ the corresponding solution

$K(\omega)$ of (3.65) has an imaginary part even for $\Gamma = 0$ and belongs to the band-gap damped modes. The band gap edges are found as solutions of the following equations

$$\omega_1 = \omega_0 + \Gamma_0 \cot \frac{n_b \omega_1 d}{2c} \,, \tag{3.78}$$

$$\omega_2 = \omega_0 - \Gamma_0 \tan \frac{n_b \omega_2 d}{2c} \,,$$

they touch the allowed bands at the points $K = 0$ and $K = \pm\pi/d$, respectively. If a value of $\phi_0 = (n_b \omega_0 d/c)$ lies far away from any integer number of π, then the band gap lies between

$$\omega_1 = \omega_0 + \Gamma_0 \cot \phi_0 \,,\ \omega_2 = \omega_0 - \Gamma_0 \tan \phi_0 \,. \tag{3.79}$$

For example, in structures with the periods $q(\omega_0)d = \pi/4, \pi/2$ (anti-Bragg structure) or $3\pi/4$, the gaps are defined by the pairs $\omega_0 + (1 \pm \sqrt{2})\Gamma_0$, $\omega_0 \pm \Gamma_0$ and $\omega_0 + (\pm\sqrt{2} - 1)\Gamma_0$, respectively.

The approximation (3.79) fails for resonant Bragg structures satisfying the condition

$$q(\omega_0)d = \pi \qquad \text{or} \qquad d = \frac{\lambda(\omega_0)}{2} \,, \tag{3.80}$$

where $\lambda(\omega_0)$ is the light wavelength at the frequency ω_0 in the medium with the dielectric constant $æ_b$. In the spectral region near the exciton resonance frequency, $|\omega - \omega_0| \ll \omega_0$, the values of K are close to $\pm\pi/d$ and one can approximate $\cos Kd, \cos qd, \sin qd$ in (3.65) or (3.66) by

$$-1 + \frac{1}{2}\,(Kd \mp \pi)^2 \,,\ -1 + \frac{1}{2}\left(\pi \frac{\omega - \omega_0}{\omega_0}\right)^2 \quad \text{and} \quad -\pi \frac{\omega - \omega_0}{\omega_0} \,,$$

respectively. As a result the dispersion equation reduces to

$$\left(\frac{Kd}{\pi} \mp 1\right)^2 = \left(\frac{\omega - \omega_0}{\omega_0}\right)^2 - \frac{2}{\pi}\frac{\Gamma_0}{\omega_0}\frac{\omega - \omega_0}{\omega - \omega_0 + \mathrm{i}\Gamma} \,. \tag{3.81}$$

At $\omega = \omega_0$, the wave vector K equals to $\pm\pi/d$ and the exciton-photon coupling vanishes which also follows immediately from (3.65) because $\sin q(\omega_0)d = \sin \pi = 0$. Physically this can be understood taking into account that, at $\omega = \omega_0$, the light wave and 2D-exciton are characterized by opposite parity properties, the exciton-photon mixing is forbidden and the light propagates as in a uniform medium with the dielectric constant $æ_b$. Really, we consider here the ground state of a 2D-exciton described by an envelope function symmetrical with respect to the mirror reflection $z \to -z$. On the other hand, for $q(\omega_0)d = \pi$, the normal light wave in the resonant Bragg structure is a standing wave with the electric field $E(z) = E_0 \sin(\pi z/d)$, where the origin is chosen in the center of one of the QWs, so that $E(z)$ is an odd function of z with respect to the center of any QW.

Detuning of the frequency ω from ω_0 removes the symmetry restrictions and, for $K \approx \pi/d$ and $\Gamma = 0$, the exciton-polariton dispersion transforms into [3.23]

$$\omega - \omega_0 = \pm\sqrt{\frac{2}{\pi}\Gamma_0\omega_0 + \omega_0^2\left(\frac{Kd}{\pi} - 1\right)^2} \tag{3.82}$$

or

$$K = \frac{\pi}{d}\left[1 \pm \sqrt{\left(\frac{\omega - \omega_0}{\omega_0}\right)^2 - \frac{2}{\pi}\frac{\Gamma_0}{\omega_0}}\right] .$$

The dispersion for K near the point $-\pi/d$ is obtained by changing the sign of K in the above equations. From (3.82) we conclude that the exciton-polariton spectrum has a broad band gap

$$\delta = 2\left(\frac{2\Gamma_0\omega_0}{\pi}\right)^{1/2} \tag{3.83}$$

with ω_0 being the central point of the gap.

In the near-Bragg structures the condition (3.80) is satisfied for the frequency

$$\omega_B = \frac{\pi c}{n_b d} \tag{3.84}$$

slightly differing from the exciton resonance frequency,

$$|\omega_B - \omega_0| n_b d/c = \pi|\omega_B - \omega_0|/\omega_B \ll 1 .$$

In this approximation one obtains two band gaps from (3.78). For $\omega_0 > \omega_B$ the gaps are given by [3.24]

$$\omega_- < \omega < \omega_B \ , \ \omega_0 - \frac{\pi}{2}\Gamma_0\frac{\omega_0 - \omega_B}{\omega_B} < \omega < \omega_+ \ , \tag{3.85}$$

where

$$\omega_\pm = \frac{\omega_0 + \omega_B}{2} \pm \sqrt{\left(\frac{\omega_0 - \omega_B}{2}\right)^2 + \frac{2}{\pi}\Gamma_0\omega_0} \ .$$

If the detuning has the opposite sign, $\omega_0 < \omega_B$, the band gaps are determined by

$$\omega_- < \omega < \omega_0 - \frac{\pi}{2}\Gamma_0\frac{\omega_B - \omega_0}{\omega_B} \ , \ \omega_B < \omega < \omega_+ \ . \tag{3.86}$$

The systems closely related to the resonant Bragg structures are periodic arrays of thin layers of resonant two-level systems separated by half-wavelength nonabsorbing dielectric layers (called *resonantly absorbing Bragg reflectors*) [3.25, 3.26] and 1D optical lattices of laser-cooled trapped atoms [3.27]. If the light wavelength exceeds the average distance between nearest two-level systems (or atoms) randomly arranged in a thin layer (or atomic plane) then the propagation of normal light waves and the formation of the photonic band gaps is similar to those described above for exciton polaritons in MQWs.

3.1.5 Finite Quantum Well Structure

The lifetime of exciton polaritons propagating through an infinite bulk crystal or infinite MQWs is limited by the exciton nonradiative damping rate. In contrast, a finite MQW structure is open and exciton polaritons in such a structure decay due to both nonradiative and radiative processes. Let us consider a system of N equidistant QWs sandwiched between semi-infinite barrier layers. The barrier layers separating the wells are thick enough to prevent the direct interwell transfer and, therefore, excitonic states in different QWs are coupled only via the electromagnetic field. The N-fold degeneracy of the bare-exciton subsystem is lifted. The coupled-mode frequencies $\omega_j = \omega_j' + \mathrm{i}\omega_j''$ are distributed in the lower complex semi-plane ω with negative $\mathrm{Im}\{\omega\}$. The effects of radiative coupling of excitons in different wells, i.e., multiple coherent reemission and reabsorption of photons, can strongly influence the resonant optical properties of high-quality MQWs, both linear and nonlinear, under cw excitation as well as in time-resolved experiments.

In this subsection we consider the reflection and transmission of light through a stack of N equidistant QWs. We start from the simple limiting case of weak exciton-photon coupling, assuming the reflection coefficient (3.21) to be small which is valid if

$$\Gamma_0 \ll |\omega_0 - \omega - \mathrm{i}\Gamma| \,.$$

In this case in order to find the reflectance of the whole system we can ignore multi-reflection processes and sum up the amplitudes of light waves reflected from distinct planes arriving at

$$r_N = (1 + \mathrm{e}^{2\mathrm{i}qd} + \mathrm{e}^{4\mathrm{i}qd} ...)\, r_{\mathrm{QW}} = \mathrm{e}^{\mathrm{i}(N-1)qd}\, \frac{\sin Nqd}{\sin qd}\, r_{\mathrm{QW}} \,. \tag{3.87}$$

At particular frequencies where the product qd is an integral number of π the reflectance $R_N = |r_N|^2$ shows maxima. The first maximum occurs at ω satisfying the condition (3.80). The anti-Bragg condition $d = \lambda/4$ determines another characteristic frequency. In this case the contributions to the reflected wave from neighboring QWs cancel each other, and the reflectance either vanishes if N is even or coincides with that for a single QW if N is odd.

If the coefficient r_{QW} is not small compared with unity then one has to take into account multi-reflection of the light waves and the reflectance of N planes is determined by a more complicated equation. In order to derive this equation we note that, according to (3.63), the eigenvalues of the transfer matrix (3.61) are $\exp(\pm\mathrm{i}Kd)$, where K means the wave vector of an exciton polariton propagating at the frequency ω in the infinite periodic MQW structure, it satisfies the dispersion equation (3.65) or (3.67).

We introduce the two-component eigencolumns of the transfer matrix [3.7]

$$\hat{T}\hat{C}_{1,2} = \mathrm{e}^{\pm\mathrm{i}Kd}\hat{C}_{1,2} \,.$$

They can be presented as

$$\hat{C}_{1,2} = \begin{bmatrix} 1 \\ a_{1,2} \end{bmatrix}, \; a_{1,2} = \frac{r_{\rm QW}}{{\rm e}^{-{\rm i}qd} - t_{\rm QW}\,{\rm e}^{\pm {\rm i}Kd}}\,. \tag{3.88}$$

Let $E_{\pm}^{\rm L}$ and $E_{\pm}^{\rm R}$ be the electric field amplitudes at the plane shifted, respectively, to the left by $d/2$ from the center of the leftmost QW and to the right by the same length $d/2$ from the rightmost QW and let the initial light wave of the amplitude E_0 be incident from the left semi-infinite barrier. Then we can use the equations

$$E_{+}^{\rm L} = E_0,\; E_{-}^{\rm L} = E_r,\; E_{+}^{\rm R} = E_t,\; E_{-}^{\rm R} = 0$$

as the effective boundary conditions. The reflection and transmission coefficients are defined as $r_N = E_r/E_0$, $t_N = E_t/E_0$. The pairs of amplitudes $E_{\pm}^{\rm L}, E_{\pm}^{\rm R}$ are conveniently presented as the two-component columns

$$\hat{E}^{\rm L} = E_0 \begin{bmatrix} 1 \\ r_N \end{bmatrix}, \; \hat{E}^{\rm R} = E_0 \begin{bmatrix} t_N \\ 0 \end{bmatrix}. \tag{3.89}$$

Rewriting $\hat{E}^{\rm L}$ as a superposition

$$\hat{E}^{\rm L} = f_1\hat{C}_1 + f_2\hat{C}_2$$

and acting on this column by the matrix $\hat{T}^N$ we obtain

$$\hat{E}^{\rm R} = f_1{\rm e}^{{\rm i}KNd}\hat{C}_1 + f_2{\rm e}^{-{\rm i}KNd}\hat{C}_2\,.$$

From the condition $E_{-}^{\rm R} = 0$ we find $a_1f_1{\rm e}^{{\rm i}KNd} + a_2f_2{\rm e}^{-{\rm i}KNd} = 0$ which allows to convert

$$r_N = \frac{a_1f_1 + a_2f_2}{f_1 + f_2}\,,\; t_N = \frac{{\rm e}^{{\rm i}KNd}f_1 + {\rm e}^{-{\rm i}KNd}f_2}{f_1 + f_2}$$

into

$$r_N = \frac{a_1a_2({\rm e}^{{\rm i}NKd} - {\rm e}^{-{\rm i}NKd})}{a_1{\rm e}^{{\rm i}NKd} - a_2{\rm e}^{-{\rm i}NKd}}\,,\; t_N = \frac{a_1 - a_2}{a_1{\rm e}^{{\rm i}NKd} - a_2{\rm e}^{-{\rm i}NKd}}\,.$$

Substitution of $a_{1,2}$ from (3.88) results in

$$r_N = \frac{\tilde{r}\sin NKd}{\sin NKd - \tilde{t}\sin(N-1)Kd}, t_N = \frac{\tilde{t}\sin Kd}{\sin NKd - \tilde{t}\sin(N-1)Kd}, \tag{3.90}$$

where $\tilde{r} = {\rm e}^{{\rm i}qd}r_{\rm QW}$, $\tilde{t} = {\rm e}^{{\rm i}qd}t_{\rm QW}$, and the coefficients $r_{\rm QW}, t_{\rm QW}$ are given by (3.21) if $æ_a = æ_b$, and (3.55) for structures with the dielectric constant mismatch.

For small values of $\tilde{r}$ we can replace K by q and $\tilde{t}$ by ${\rm e}^{{\rm i}qd}$. Then, taking into account that

$$\sin Nqd - {\rm e}^{{\rm i}qd}\sin(N-1)qd = {\rm e}^{-{\rm i}(N-1)qd}\sin qd$$

we can reduce (3.90) to (3.87).

Another limiting case that allows simplifications is a short-period MQW structure. Since in this case $|K|d, qd \ll 1$, we can replace $\mathrm{e}^{\mathrm{i}qd}, \mathrm{e}^{\pm \mathrm{i}Kd}$ by $1 + \mathrm{i}qd, 1 \pm \mathrm{i}Kd$ and, using (3.64), approximate $r_{\mathrm{QW}}, t_{\mathrm{QW}}$ by

$$\frac{(q^2 - K^2)d}{2\mathrm{i}q - (q^2 - K^2)d} \, , \; \frac{2\mathrm{i}q}{2\mathrm{i}q - (q^2 - K^2)d} \, .$$

Then the reflection and transmission coefficients are reduced to

$$r_N = \frac{1 - \mathrm{e}^{2\mathrm{i}\phi_N}}{1 - \mathrm{e}^{2\mathrm{i}\phi_N} r_{12}^2} r_{12} \, , \; t_N = \mathrm{e}^{2\mathrm{i}\phi_N} \frac{t_{12} t_{21}}{1 - \mathrm{e}^{2\mathrm{i}\phi_N} r_{12}^2} r_{12} \, ,$$

where $\phi_N = NKd$, the wave vector K satisfies (3.71),

$$r_{12} = \frac{q - K}{q + K} \, , \; t_{12} t_{21} = \frac{4qK}{(q + K)^2} \, .$$

The same result is obtained in the approximation of a uniform local medium where N QWs are replaced by an effective homogeneous layer of the thickness Nd and with the refractive index K/q_0.

Now, we turn to the resonant Bragg structures. According to (3.81) in the frequency region $|\omega - \omega_0| \ll \omega_0$ the exciton-polariton wave vector is given by

$$K = \pm \frac{\pi}{d}(1 \pm S) \, , \; S = \left[\left(\frac{\omega - \omega_0}{\omega_0} \right)^2 - \frac{2\Gamma_0}{\pi \omega_0} \, \frac{\omega - \omega_0}{\omega - \omega_0 + \mathrm{i}\Gamma} \right]^{1/2} \, .$$

In an N-well structure in the frequency region determined by the condition

$$\pi N |S| \ll 1 \tag{3.91}$$

we can replace $\tilde{r}, \tilde{t}$ by $-r_{\mathrm{QW}}, -t_{\mathrm{QW}}$ and the ratios

$$\frac{\sin (N-1)Kd}{\sin NKd} \, , \; \frac{\sin NKd}{\sin Kd}$$

by $-(N-1)/N$, $(-1)^{N-1}N$. As a result, the reflection and transmission coefficients (3.90) take on the surprisingly simple form

$$r_N = - \frac{\mathrm{i}N\Gamma_0}{\omega_0 - \omega - \mathrm{i}(\Gamma + N\Gamma_0)} \, , \; t_N = (-1)^N \frac{\omega_0 - \omega - \mathrm{i}\Gamma}{\omega_0 - \omega - \mathrm{i}(\Gamma + N\Gamma_0)} \, . \tag{3.92}$$

One can see that the reflection coefficient from the resonant Bragg structure is obtained from that for the single-QW case, see (3.21), just by substituting $N\Gamma_0$ for the radiative damping rate Γ_0.

In order to understand the above result and, more generally, to analyze the exact equations (3.90) we need to study the analytical properties of the

responses $r_N(\omega)$, $t_N(\omega)$, as it was done in Sect. 3.1.1 for a single-QW structure. The main idea is that poles of the coefficients r_N, t_N considered as a function of the complex variable $\omega = \omega' + \mathrm{i}\omega''$ coincide with the complex frequencies of the exciton-polariton modes. In the same way as for N coupled oscillators, the system of N QWs is characterized by N eigenfrequencies, ω_j. For a single QW the eigenfrequency equals to $\omega_0 - \mathrm{i}(\Gamma + \Gamma_0)$. For N identical QWs, in general, all ω_j are different, and the reflection coefficient has N different poles. The corresponding non-stationary eigenstates represent exciton polaritons in finite multiple QW structures which are, in this case, mixed excitations where 2D excitons are coupled with 3D photons. The system with a finite value of N is open and, hence, imaginary parts of the eigenfrequencies are nonzero even neglecting the nonradiative damping. The real parts ω_j' determine the position of peaks, dips and other features in the cw spectra. The spacing between the real parts can lead to quantum beats in the optical response to a short-pulse excitation. The imaginary parts of ω_j describe the decay and dynamics of modes and the broadening of the spectral features. The frequency distribution pattern is governed by the period d and the number of coupled wells, N.

The eigenfrequencies ω_j can be found from (3.59, 3.60) where the external fields E_1, E_2 are excluded. Substitution of (3.60) with $E_1, E_2 = 0$ into (3.59) leads to the following set of linear equations

$$(\omega_0 - \omega - \mathrm{i}\Gamma)P_n + \sum_{n'} \Lambda_{nn'} P_{n'} = 0\ ,\ \Lambda_{nn'} = -\mathrm{i}\Gamma_0 \mathrm{e}^{\mathrm{i}qd|n-n'|} \qquad (3.93)$$

for the average polarizations $P_n = a^{-1} \int dz\, P_{\mathrm{exc}}^{(n)}(z)$. Here as before we omit the *tilde* symbol over ω_0. It follows then that the problem of exciton polaritons in QW structures is indeed reduced to the problem of a linear chain of classical oscillators with only one resonance frequency ω_0, one damping rate $\Gamma + \Gamma_0$ and coupling coefficients $\Lambda_{nn'}$ between the oscillators n and n'. The coupling coefficients are proportional to the exciton radiative damping Γ_0 and the phase factor dependent on the inter-oscillator distances, $d|n - n'|$. Note that the matrix $\hat{\Lambda}$ is symmetrical but non-Hermitian. According to Gerschgorin's circle theorem, the eigenvalues of a complex square matrix a_{lm} of order N lie in a closed region of the complex plane $z = z' + \mathrm{i}z''$ formed by the circles

$$|z - a_{ll}| \le \sum_{m \ne l} |a_{lm}|\ .$$

Hence, it follows that the eigenfrequencies of a system of N QWs are localized in a circle with the center lying at the point $\omega_0 - \mathrm{i}\Gamma - \mathrm{i}\Gamma_0$ and the radius being equal to $(N-1)\Gamma_0$.

In the following we enumerate a sequence of N QWs from $n = -m$ to $n = m$, excluding zero for an even $N = 2m$ and including the value of $n = 0$ for an odd $N = 2m + 1$. The system has a mirror plane of symmetry in the center of the structure taken as $z = 0$ and, hence, for any normal mode

the dielectric polarization P_n and the electric field $E(z)$ are characterized by a definite parity: $P_{-n} = \pm P_n$, $E(-z) = \pm E(z)$. It can be shown that there are m odd and $N-m$ even solutions [3.10, 3.28]. Let us perform the unitary transformation $\hat{S}$ from the initial basis of single-well excitons $|n\rangle$ to the new basis $|n\rangle_\pm = (|n\rangle \pm |{-n}\rangle)/\sqrt{2}$ $(n = 1, ..., m)$ for even N and the basis $|n\rangle_\pm = (|n\rangle \pm |{-n}\rangle)/\sqrt{2}$ $(n = 1, ..., m)$, $|0\rangle_+ \equiv |0\rangle$ for odd N. Then the transformed matrix $\hat{S}^{-1}\hat{\Lambda}\hat{S}$ becomes quasi-diagonal

$$\begin{bmatrix} \hat{\Lambda}^+ & 0 \\ 0 & \hat{\Lambda}^- \end{bmatrix},$$

where the submatrices $\hat{\Lambda}^+$ and $\hat{\Lambda}^-$ specify the sets ω_j^+ and ω_j^- for the even and odd solutions, respectively. The diagonal elements of these matrices can be readily calculated: $\Lambda_{nn}^\pm = \mp \mathrm{i}\Gamma_0(1 \pm \eta^{2n-1})$ if N is even and $\Lambda_{nn}^\pm = \mp \mathrm{i}\Gamma_0(1 \pm \eta^{2n})$ $(n \neq 0)$, $\Lambda_{00}^+ = -\mathrm{i}\Gamma_0$ if N is odd, where $\eta = \exp(\mathrm{i}qd)$. It is convenient to use the eigenfrequency $\omega_0 - \mathrm{i}(\Gamma + \Gamma_0)$ for a single QW as a reference point and introduce the frequencies $\Omega_j^\pm = \omega_j^\pm - \omega_0 + \mathrm{i}(\Gamma + \Gamma_0)$. Since the trace of any square matrix is equal to the sum of its eigenvalues, we obtain for the sums [3.28]

$$\pm \sum_{j=1}^{m} \Omega_j^\pm = -\mathrm{i}\Gamma_0 \eta \frac{1-\eta^N}{1-\eta^2}\,, \tag{3.94}$$

$$\sum_{j=1}^{m+1} \Omega_j^+ = -\sum_{j=1}^{m} \Omega_j^- = -\mathrm{i}\Gamma_0 \eta^2 \frac{1-\eta^{N-1}}{1-\eta^2}$$

for even and odd N, respectively. In particular, it follows from (3.94) that the sum of all Ω_j equals to zero, i.e., the center-of-mass for the total set ω_j lies at the point $\omega_0 - \mathrm{i}(\Gamma + \Gamma_0)$. For $N = 1, ..., 4$, the frequencies $\Omega_j^\pm$ can be presented in an analytical form [3.10, 3.28]

$$\Omega_1^+ = 0 \qquad (N=1)\,; \qquad \Omega_1^\pm = \mp \mathrm{i}\Gamma_0 \eta \qquad (N=2)\,; \tag{3.95}$$

$$\Omega_{1,2}^+ = -\frac{\mathrm{i}}{2}\Gamma_0 \eta \left(\eta \pm \sqrt{\eta^2+8}\right)\,,\ \Omega_1^- = \mathrm{i}\Gamma_0 \eta^2 \qquad (N=3)\,;$$

$$\Omega_{1,2}^+(\eta) = \Omega_{1,2}^-(-\eta) = -\frac{\mathrm{i}}{2}\Gamma_0 \eta \left[1 + \eta^2 \pm \sqrt{(1+\eta^2)^2 + 4(1+2\eta)}\right] \quad (N=4)\,.$$

Taking into account the symmetry considerations and general analytical properties of a linear response the reflection coefficient can be written as [3.10]

$$\tilde{r}_N(\omega) = \frac{1}{2}\eta^N \left(\frac{P_{N,s}^{(*)}(y,\eta)}{P_{N,s}(y,\eta)} - \frac{P_{N,a}^{(*)}(y,\eta)}{P_{N,a}(y,\eta)} \right)\,. \tag{3.96}$$

Here $y = (\omega_0 - \omega + \mathrm{i}\Gamma)/\Gamma_0$, $P_{N,\gamma}(y,\eta)$ $(\gamma = s, a)$ is a polynomial with the unit coefficient in the term of the highest order in y and with other coefficients dependent on one parameter η. The corresponding coefficients in

the polynomials $P_{N,\gamma}(y,\eta)$ and $P^{(*)}_{N,\gamma}(y,\eta)$ are complex conjugate including the transformation from $\eta = \exp(\mathrm{i}qd)$ into η^*. The roots of the equations $P_{N,s}(y,\eta) = 0$ and $P_{N,a}(y,\eta) = 0$ determine the eigenfrequencies for the even and odd exciton-polariton modes, respectively. The polynomials of the N-th and $(N-2)$-th orders are related by the recurrent equations

$$P_{N,\gamma}(y) = (y+\mathrm{i})P_{N-2,\gamma}(y) \pm \mathrm{i}\eta^{N-1}P^{(*)}_{N-2,\gamma}(y)\,, \tag{3.97}$$

where the sign $\pm$ corresponds to $\gamma = s$ and $\gamma = a$, respectively, and one can start from $P_{0,\gamma} = 1$ and $P_{1,s}(y) = y + \mathrm{i}$, $P_{1,a} = 1$.

If the exciton resonance frequency ω_0 and the structure period d satisfy the inequality $|q(\omega)d - \pi| \ll 1$ or, strictly speaking, the condition (3.80), the reflection and transmission coefficients are given by (3.92). One can see that in this case the function $r_N(\omega)$ has only the one pole

$$\omega = \omega_0 - \mathrm{i}(\Gamma + N\Gamma_0). \tag{3.98}$$

This means that, for the resonant Bragg structures, among N eigenmodes $N-1$ modes are optically inactive, their frequencies $\omega_j = \omega_0 - \mathrm{i}\Gamma$ $(j = 1, ..., N-1)$ are not renormalized by the exciton-photon interaction, and only one mode (which can be called a *superradiant mode*) is optically active with the oscillator strength and the radiative damping being N times higher than those for the exciton in a SQW. Note that (3.92) are valid in the frequency region (3.91). Outside this region the constructive interference of light waves breaks down and one must use more complicated equations (3.90) for r_N and t_N. The N-dependence of the spectral width of the reflection coefficient from the resonant Bragg structure is linear up to a few dozens of QWs, until $N\Gamma_0 \ll \delta = 2\sqrt{2\hbar\omega_0\Gamma_0/\pi}$, and then saturates to the photonic band gap δ defined by (3.83).

According to (3.92) the amplitude and half-width of the reflection resonant contour must be strongly enhanced in the Bragg structures. Experimental studies of the resonant Bragg structures have been performed for heteropairs CdTe/CdMgTe [3.11], CdTe/CdZnTe [3.12,3.29], CdMnTe/CdZnMgTe [3.30], GaAs/GaAlAs [3.31], InGaAs/GaAs [3.16, 3.32, 3.33]. Figure 3.3a shows reflection spectra taken from CdTe/CdZnTe Bragg and anti-Bragg structures. In the latter case, the half-width and the amplitude of the reflection peak are remarkably smaller than those in the Bragg structure. The strong enhancement effects are observed on InGaAs/GaAs QWs, as seen in Fig. 3.3b. The detuning from the Bragg condition by 15% leads to a complete modification of the spectrum. A linear dependence of the reflection-peak linewidth on N, see (3.98), has been reported by Prineas et al. [3.16]

An independent verification of the theory is provided by time-resolved studies that show that the reflection signal decays much faster in a perfect Bragg structure than in a single QW [3.31]. Nonlinear four-wave mixing in resonant Bragg structures is touched in Sect. 7.3.

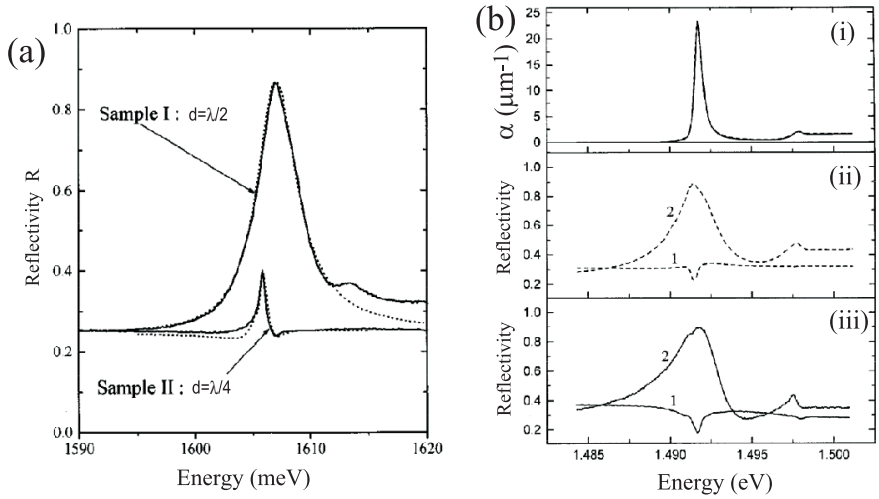

Fig. 3.3. (**a**) A comparison of the reflectivity spectra in the region of the $e1$-$hh1(1s)$ exciton for two stacks of ten QWs of $CdTe/Cd_xZn_{1-x}Te$ with the same thickness $\lambda/2$ of the cladding layer but with the periods d close either to $\lambda/2$ (sample I) or to $\lambda/4$ (sample II) in a magnetic field of 5 T. The dashed lines are theoretical, $\hbar\Gamma_0 = 0.12$ meV, and $\hbar\Gamma = 0.3$ meV. [3.12] (**b**) Absorption and reflection spectra of a structure containing thirty $In_{0.04}Ga_{0.96}As/GaAs$ QWs. (**i**) Experimental (*solid*) and calculated (*dashed*) absorption coefficient as a function of energy. The lines are hard to distinguish. (**ii**) Calculated and (**iii**) measured reflectivity at Bragg resonance (*curves* 2) and at $0.85\lambda/2$ spacing (*curves* 1) as a function of energy. [3.32]

3.1.6 Quantum Wells Grown along the Low-Symmetry Directions

Up to now we discussed the optical phenomena in zinc-blende-lattice heterostructures grown along the principal axis [001]. QW structures having growth axes different from [001] and [111] exhibit a remarkable *in-plane* anisotropy in the interband optical transitions [3.34–3.36]. This kind of anisotropy is attributed to the valence band warping of bulk semiconductors with zinc-blende and diamond lattices. We remind us that the warping is governed by a value of $D - \sqrt{3}B \propto \gamma_3 - \gamma_2$ where D, B, γ_i are the band parameters introduced in Chap. 2, see (2.28). While describing here the in-plane optical properties of QW structures we disregard the anisotropic orientation of chemical bonds at the interfaces, this will be done in the next subsection, and apply the conventional effective-Hamiltonian approach with the Luttinger Hamiltonian (2.28) and the simplest form of boundary conditions for flat interfaces, see (2.14). Then the point symmetry of a (hkl)-grown QW coincides with that of a bulk zinc-blende crystal subjected to a uniaxial deformation along the axis $[hkl]$. We concentrate on the particular case of $[hhl]$ heterostructures with the growth direction lying in the $(1\bar{1}0)$ plane. For arbi-

trary h the point group of the system has only two symmetry operations: the identity transformation e and the mirror reflection $\sigma_{(1\bar{1}0)}$. However, for the (001), (111) and (110) growth directions, the corresponding point groups are D_{2d}, C_{3v} and C_{2v}, they contain additional elements of symmetry, see Tables A.2, A.3 and A.4 in the Appendix.

Considering the short-period MQW structures we can introduce the effective dielectric tensor $\hat{\text{æ}}_{\text{eff}}(\omega)$. In the coordinate system $x \parallel [ll(\overline{2h})]$, $y \parallel [\bar{1}10]$, $z \parallel [hhl]$ related to the growth direction, the off-diagonal components $\hat{\text{æ}}_{\alpha\beta}$ with $\alpha = y$ or $\beta = y$ vanish and one has

$$\hat{\text{æ}}_{\text{eff}} = \begin{bmatrix} \text{æ}_{xx} & 0 & \text{æ}_{xz} \\ 0 & \text{æ}_{yy} & 0 \\ \text{æ}_{zx} & 0 & \text{æ}_{zz} \end{bmatrix} ,$$

where $\text{æ}_{xz} = \text{æ}_{zx}$. Under normal incidence the light propagates along z. One eigenwave (ordinary mode) is polarized along y and characterized by the refractive index $n_y = \sqrt{\text{æ}_{yy}}$. The electric field of another eigenwave (extraordinary mode) is perpendicular to y, its effective refractive index is given by

$$n_x = \sqrt{\text{æ}_{xx} - \frac{\text{æ}_{xz}^2}{\text{æ}_{zz}}} .$$

The in-plane anisotropy is described by the ratio

$$\rho = \frac{K_x - K_y}{\bar{K}} , \tag{3.99}$$

where K_α is the absorption coefficient in the polarization $\alpha = x, y$, and $\bar{K}$ is the average $(K_x + K_y)/2$. Since $K_\alpha = 2q_0 n''_\alpha$ with $n''_\alpha = \text{Im}\{n_\alpha\}$ we have $\rho = 2(n''_x - n''_y)/(n''_x + n''_y)$. We take into account two poles in the dielectric tensor,

$$\text{æ}_{\alpha\beta} = \text{æ}_b \delta_{\alpha\beta} + \frac{\Omega^{(h)}_{\alpha\beta}}{\omega_0^h - \omega - \mathrm{i}\Gamma_h} + \frac{\Omega^{(l)}_{\alpha\beta}}{\omega_0^l - \omega - \mathrm{i}\Gamma_l}$$

due to the heavy-hole (h) and light-hole (l) excitons, see (3.74). For large values of $\Gamma_{h,l}$ we can retain only linear terms in $\Omega^{(h,l)}_{\alpha\beta}$ and come to the equation

$$\rho_j = \frac{\Omega^{(j)}_{xx} - \Omega^{(j)}_{yy}}{\bar{\Omega}^{(j)}} \tag{3.100}$$

for the in-plane anisotropy of the absorption coefficient near the resonance ω_0^j, $j = hh, lh$.

The analytical result is possible in the first order in the difference $\gamma_3 - \gamma_2$. For this purpose we write the Luttinger Hamiltonian as a sum of the zero-order isotropic term

$$\mathcal{H}^0_{\Gamma_8} = \left(A + \frac{5}{4} B \right) k^2 - B(\boldsymbol{J} \cdot \boldsymbol{k})^2 \tag{3.101}$$

and the anisotropic perturbation

$$V_{\Gamma_8} = -2\left(\frac{D}{\sqrt{3}} - B\right)\left(\{J_1 J_2\}_s k_1 k_2 + \{J_2 J_3\}_s k_2 k_3 + \{J_3 J_1\}_s k_3 k_1\right). \quad (3.102)$$

Here $1, 2, 3$ are the principal axes [100], [010] and [001].

Four eigencolumns, $\hat{C}^{(0)}_{m\boldsymbol{k}}$, of the matrix $\mathcal{H}^0_{\Gamma_8}$ can be chosen to have a definite angular-momentum component, m, on the wave-vector direction

$$\left(\boldsymbol{J}\cdot\frac{\boldsymbol{k}}{k}\right)\hat{C}^{(0)}_{m\boldsymbol{k}} = m\hat{C}^{(0)}_{m\boldsymbol{k}}\,. \quad (3.103)$$

In the isotropic approximation the electron spectrum in the valence band Γ_8 is spherical and parabolic,

$$E^0_{\pm 3/2}(\boldsymbol{k}) = (A-B)k^2\,,\; E^0_{\pm 1/2}(\boldsymbol{k}) = (A+B)k^2\,. \quad (3.104)$$

The next step is to calculate the eigenvectors $\hat{C}_{m\boldsymbol{k}}$ of the matrix $\mathcal{H}_{\Gamma_8}$. In the first approximation they are written as

$$\hat{C}_{m\boldsymbol{k}} = \hat{C}^{(0)}_{m\boldsymbol{k}} + \sum_j{}' \frac{V_{jm}(\boldsymbol{k})}{E^0_m(k) - E^0_j(k)}\hat{C}^{(0)}_{j\boldsymbol{k}}\,. \quad (3.105)$$

The perturbation matrix elements

$$V_{jm}(\boldsymbol{k}) = \hat{C}^{(0)\dagger}_{j\boldsymbol{k}} V_{\Gamma_8}\hat{C}^{(0)}_{m\boldsymbol{k}}$$

can be calculated by expressing k_1, k_2, k_3 in terms of the components of $\boldsymbol{k}$ in the coordinate system x, y, z and the matrices J_1, J_2, J_3 in terms of their linear combinations related to the axes x, y, z

$$J_{1,2} = \frac{1}{\sqrt{2}}(\cos\theta J_x \mp J_y + \sin\theta J_z)\,,\; J_3 = -\sin\theta J_x + \cos\theta J_z\,,$$

where θ is the angle between the growth direction and the axis [001], $\cos\theta = l/\sqrt{l^2+2h^2}$, $\sin\theta = h\sqrt{2/(l^2+2h^2)}$. Note that, in the basis $\hat{C}^{(0)}_{m\boldsymbol{k}}$, the matrices J_x, J_y, J_z and their products have the same form as J_1, J_2, J_3 and related matrices in the basis (2.22). For the states at the Γ point, $k_x = k_y = 0$, the substitution

$$k_{1,2} \to \frac{\sin\theta}{\sqrt{2}}k_z\,,\; k_3 \to \cos\theta k_3$$

is applicable and we obtain

$$V_{\Gamma_8} = \left(B - \frac{D}{\sqrt{3}}\right)k_z^2\left\{\frac{1-\mu^2}{2}\left[(3\mu^2+1)(2J_z^2 - J_x^2 - J_y^2) - (3\mu^2-1)(J_x^2 - J_y^2)\right]\right.$$
$$\left. + \mu\sqrt{1-\mu^2}(3\mu^2-1)\{J_x J_z\}_s\right\}$$

or explicitly, see Table 2.1,

$$||V_{jm}(\boldsymbol{k})|| = \frac{1}{4}(\sqrt{3}B - D)k_z^2 \begin{bmatrix} u & v & w & 0 \\ v & -u & 0 & w \\ w & 0 & -u & -v \\ 0 & w & -v & u \end{bmatrix} \tag{3.106}$$

$$u = \sqrt{3}(1-\mu^2)(3\mu^2+1)\,,\ v = 2\mu\sqrt{1-\mu^2}(3\mu^2-1)\,, \tag{3.107}$$
$$w = (1-\mu^2)(1-3\mu^2)\,.$$

The valence-band wave function can readily be written in the limiting case of infinite barriers as

$$\psi_{j1,m}(\boldsymbol{r}) = \sqrt{\frac{2}{a}}\cos\frac{\pi z}{a}\sum_{m'} C_{m\boldsymbol{k},m'}u^0_{m'}(\boldsymbol{r})\,, \tag{3.108}$$

where $u^0_{m'}$ are the bulk Bloch functions at $\boldsymbol{k}=0$ and a is the QW thickness. It is a symmetrized combination of the Bloch states with the wave vectors $\pm\boldsymbol{k}$ where the vector $\boldsymbol{k}$ has the components

$$\frac{\pi}{a}\,\frac{1}{\sqrt{l^2+2h^2}}(h,h,l) \tag{3.109}$$

in the coordinate system $1,2,3$ and $(\pi/a)(0,0,1)$ in the coordinate system x,y,z. In this case a value of k_z^2 is equal to $(\pi/a)^2$. While calculating the interband optical matrix elements we use the basis of conduction electron states with the spin component $s=\pm1/2$ along the growth direction $[hhl]$. Then the matrix elements $\boldsymbol{p}_{cs,vjm}(\boldsymbol{k})$ of the momentum operator taken between the valence-band states $(vj,m,\boldsymbol{k})$ and conduction-band states $(c,s,\boldsymbol{k})$ are given by Table 2.2. The microscopic equation for the exciton oscillator strength $\Omega^{(j)}_{\alpha\beta}$ is given by

$$\Omega^{(j)}_{\alpha\beta} = \frac{8e^2\Lambda_{e1\text{-}h1}}{\hbar d(\omega_0^j m_0\tilde{a}_j)^2}\sum_{sm} p^{\alpha}_{vjm,cs}(\boldsymbol{k})p^{\beta}_{cs,vjm}(\boldsymbol{k})\,. \tag{3.110}$$

Here d is the period of the structure, the overlap integral $\Lambda_{e1\text{-}h1}$ for the infinite barriers equals to unity, $\tilde{a}_j$ is the effective Bohr radius different for the heavy- and light-hole excitons because the in-plane effective masses for heavy and light holes are different.

In the model under consideration the in-plane optical anisotropy comes from the transitions $(v,h,\pm3/2)\to(c,\pm1/2)$ and $(v,l,\pm1/2)\to(c,\mp1/2)$. Indeed, according to (3.105, 3.106) the state $(v,h,\pm3/2)$ has an admixture of the light-hole state $\hat{C}^{(0)}_{\mp1/2}$ described by the coefficient

$$f_{hl} = -\frac{V_{\mp1/2,\pm3/2}}{2Bk_z^2}\,.$$

Taking into account the selection rules presented in Table 2.2 we obtain

$$p^x_{c\pm1/2,vj\pm3/2}(\boldsymbol{k}) = -\frac{p_{cv}}{\sqrt{2}}\left(1-\frac{f_{hl}}{\sqrt{3}}\right)\,, \tag{3.111}$$
$$p^y_{c\pm1/2,vj\pm3/2}(\boldsymbol{k}) = -\mathrm{i}\frac{p_{cv}}{\sqrt{2}}\left(1+\frac{f_{hl}}{\sqrt{3}}\right)\,.$$

From here and (3.100, 3.106, 3.110) we find [3.37]

$$\rho_h = \mp\frac{2}{\sqrt{3}}f_{hl} = \frac{D-\sqrt{3}B}{2B}\,(1-\mu^2)(3\mu^2-1) \tag{3.112}$$
$$= \frac{\gamma_3-\gamma_2}{2\gamma_2}\,(1-\mu^2)(3\mu^2-1)\,.$$

For the light-hole exciton the anisotropy has the opposite sign and, in the considered approximation, we have

$$\rho_l = -3\rho_h\,.$$

One can see that the dependence of ρ_h, ρ_l on the growth direction is given by the product $g(\mu) = (1-\mu^2)(3\mu^2-1)$. In the interval $0 \le \mu \le 1$ this function has its absolute minimum $g = -1$ for the [110]-grown structure ($\mu = 0$) and a local maximum $g = 1/3$ for the [112] growth direction ($\mu = \sqrt{2/3}$). In agreement with the symmetry considerations, we have $\rho_{h,l} = 0$ for the structures grown along the high-symmetry axes [001] ($\mu = 0$) and [111] ($\mu = 1/\sqrt{3}$). In agreement with the experiment [3.35, 3.36, 3.38] the signs of ρ_h for the [110]- and [113]-grown QWs are opposite.

In the calculation based on the 4×4 Luttinger Hamiltonian and infinite barriers the anisotropy is insensitive to the QW thickness a. Allowance for the mixing between the band Γ_8 and spin-orbit-split band Γ_7 at nonzero k_z leads to a variation of the anisotropy with changing a. If we retain the terms linear in $|B|k_z^2/\Delta \ll 1$ then the result (3.112) for ρ_h is changed by the factor $1 + (8|B|/\Delta)(\pi/a)^2$ whereas ρ_l remains unchanged. The results of the numerical calculation for the 6×6 Hamiltonian describing simultaneously the bands Γ_8 and Γ_7 as well as comparison with experiment are presented in Fig. 3.4. For large well widths both ρ_h and ρ_l are independent of a and the values are very close to those based on the 4×4 Hamiltonian. With decreasing a, particularly for $a < 50 \div 60$ Å, the in-plane anisotropy becomes more pronounced. Armelles et al. [3.36] studied (113)-grown GaAs/AlAs QWs with and without corrugated interfaces. Since the observed optical anisotropy is of the same order in both kinds of samples one can conclude that the corrugation has a small effect on the anisotropy.

3.1.7 Interface Optical Anisotropy of Heterostructures without a Common Atom

In the conventional envelope-function approach with the boundary conditions (2.14) the (001)-grown QWs are uniaxially isotropic. The main goal of

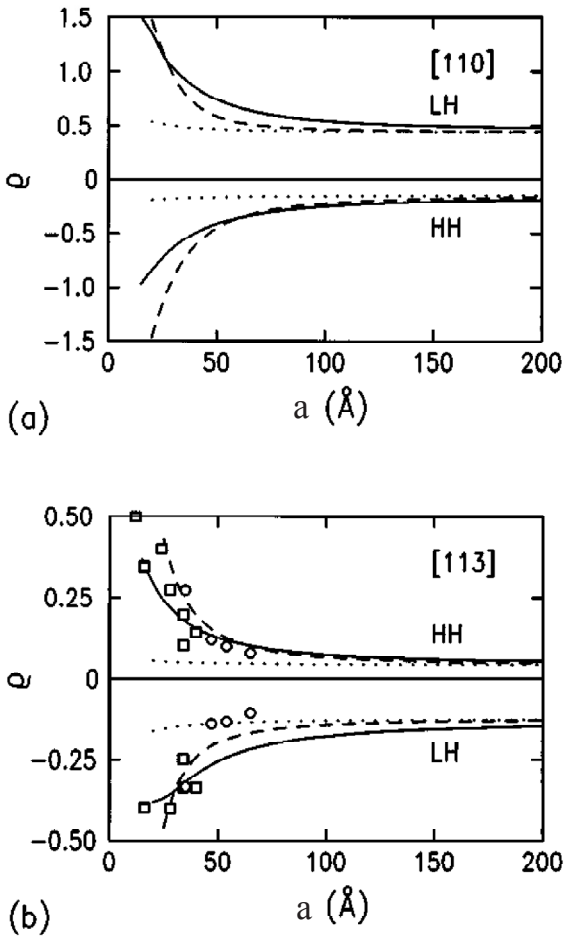

Fig. 3.4. Optical anisotropy ρ_h and ρ_l of a GaAs/AlAs QW, as a function of well width a for the growth direction (**a**) [110] and (**b**) [113]. *Dotted* lines correspond to a calculation based on the 4×4 Luttinger Hamiltonian (finite barriers). In the other two calculations, the 6×6 Hamiltonian was used, for infinitely high barriers (*dashed*) or finite barriers (*solid*). Experimental points in (**b**) were taken from [3.35] (circles) and [3.36, 3.39] (squares). From [3.40].

this subsection is to demonstrate that, in zinc-blende-lattice multi-layered heterostructures grown along the [001] principal direction, the interfaces induce a remarkable in-plane anisotropy, namely nonequivalence between the [110] and [1$\bar{1}$0] axes. The anisotropy can manifest itself both in optical and transport phenomena but we restrict the consideration to the optical manifestations only.

In a zinc-blende-lattice bulk semiconductor, say GaAs as a representative of III-V compounds or ZnSe as a representative of II-VI compounds, any lattice site is a center of the tetrahedral point symmetry. For any anion atom the right-hand-side bonds always lie in the same $\langle 110 \rangle$-like plane, say the (110) plane, whereas the bonds on the left lie in another plane which is perpendicular to the previous one.

Now we shift from a bulk semiconductor to a single heterojunction CA/C′A′. If the compositional materials CA and C′A contain the identical anion atoms, labelled A, the interface is formed by one atomic plane of anions neighboring the C atomic plane on one side and the C′ plane on the other side. As compared to bulk semiconductor crystals, the symmetry of a single heterojunction is reduced to the point group C_{2v} (Chap. 2). In this group the directions [110] and [1$\bar{1}$0] are nonequivalent. Thus, we conclude that, in general, a single heterojunction gives in-plane anisotropy. The particular mechanism and order of magnitude of the anisotropy can be obtained by using the microscopical model discussed below, and we shift the symmetry analysis from a single to double heterojunction, or to a QW. The symmetry of an ideal QW is higher than that of a single heterojunction because it contains the mirror rotation S_4 about the [001] axis by 90°. The second interface also induces the in-plane anisotropy. However, for the left and right interfaces, the role of the axes [110] and [1$\bar{1}$0] is interchanged, their contributions to the anisotropy cancel each other and, as a result, an ideal QW is isotropic in the interface plane, at least in the linear optics.

The next step is to consider an interface between two materials lacking common anions and cations, C ≠ C′, A ≠ A′. The heteroboundary CA-on-C′A′ consists of two nonstandard planes containing anions of one material and cations of another material. There are two possibilities of the transition from the layer C′A′ to the layer CA, either via the chemical bond C′-A in the sequence of atomic planes −C′−A′−C′ ∼A−C−A− (interface of kind *a*) or via the chemical bond A′-C in the sequence −A′−C′−A′ ∼C−A−C− (interface of kind *b*) where the standard and nonstandard bonds are indicated by the symbols − and ∼, respectively. The structure is assumed to grow from the left- to the right-hand side. Taking into account the similar alternative for the other interface, C′A′-on-CA, we conclude that, for a heteropair with no common atom, there exist four kinds of ideal QWs labelled as L*a*-R*a*, L*b*-R*b*, L*b*-R*a* and L*a*-R*b*. Here a, b indicate the interface chemical bond and R,L indicate the right- and left-hand-side interfaces. The first two have symmetrical interfaces related by the S_4 operation, such QWs are isotropic in the interface

plane. The remaining two kinds are characterized by the low symmetry C_{2v}, the left and right interfaces contribute differently to the in-plane anisotropy and these contributions do not compensate each other. It is accepted that under growth without a special control the interface is predominantly cation-terminated and the QWs are nominally La-Rb-like. Of course, one cannot exclude interfacial disorder and some admixture of a-like bonds at the right interface and b bonds at the left interface. At present technology allows the interfacial control in the process of layer-by-layer growth and fabrication of QW structures with both anion and cation-terminated interfaces [3.41].

Optical anisotropy in heterostructures without common cations and anions was predicted by Krebs and Voisin [3.42] and observed in GaInAs/InP QWs [3.43,3.44]. They used the experimental setup typical for measurements of birefringence and dichroism in bulk uniaxial crystals (Fig. 3.5a). In this setup the initial light linearly polarized by the polarizer P is focused onto the sample S, the transmitted light is filtered through an analyzer A and a spectrometer and finally detected by a photomultiplier. The sample can be rotated around the growth axis. In the particular experiment presented in Fig. 3.5 the sample contained 80 InGaAs QWs separated by InP barriers [3.44]. The curve (b) with the left-hand side scale shows the angular dependence of the transmitted intensity in the setup with parallel polarizer and analyzer with θ being the angle between the analyzer and the sample [100] axis. The curve (c) shows the ratio between the transmission signals in the crossed and parallel polarizer-analyzer configurations. From the curve (b) we conclude that the absorption exhibits a maximum and a minimum at the angle $\pm 45°$, respectively, or, in other words, when the light is polarized along the [110] and $[1\bar{1}0]$ axes. The curve (c) confirms this conclusion because the transmitted signal measured in the crossed configuration $P_{\perp}$-A reaches maxima at the angles equal to 0 and 90° when the polarization plane lies in the middle between the axes [110] and $[1\bar{1}0]$. From the maximum and minimum values of the transmission one can find the absorption coefficients K_{110} and $K_{1\bar{1}0}$. Remarkably, nearly no anisotropy effect is observed in InGaAs/AlInAs MQWs where the compositional materials share a common anion.

Let us calculate the lateral optical anisotropy of a quantum-well structure CA/C′A′ at the absorption edge, i.e., under the $hh1$-$e1$ interband transitions with zero 2D electron wave vector ($k_x = k_y = 0$, Γ point). In the envelope-function method, the electron and hole effective Hamiltonians within the well or in the barrier have the same form as in the corresponding bulk materials and, in particular, possess cubic symmetry T_d. The low symmetry of the interface is taken into account by including the additional term in the boundary conditions for the valence-band wave-function envelope, see (2.42).

Neglecting the relativistically small corrections, we shall use for the conduction-band electron commonly accepted boundary conditions (2.10), i.e., the continuity of the envelope and of its normal derivative divided by the effective mass. In this case the electron wave function at the bottom of the

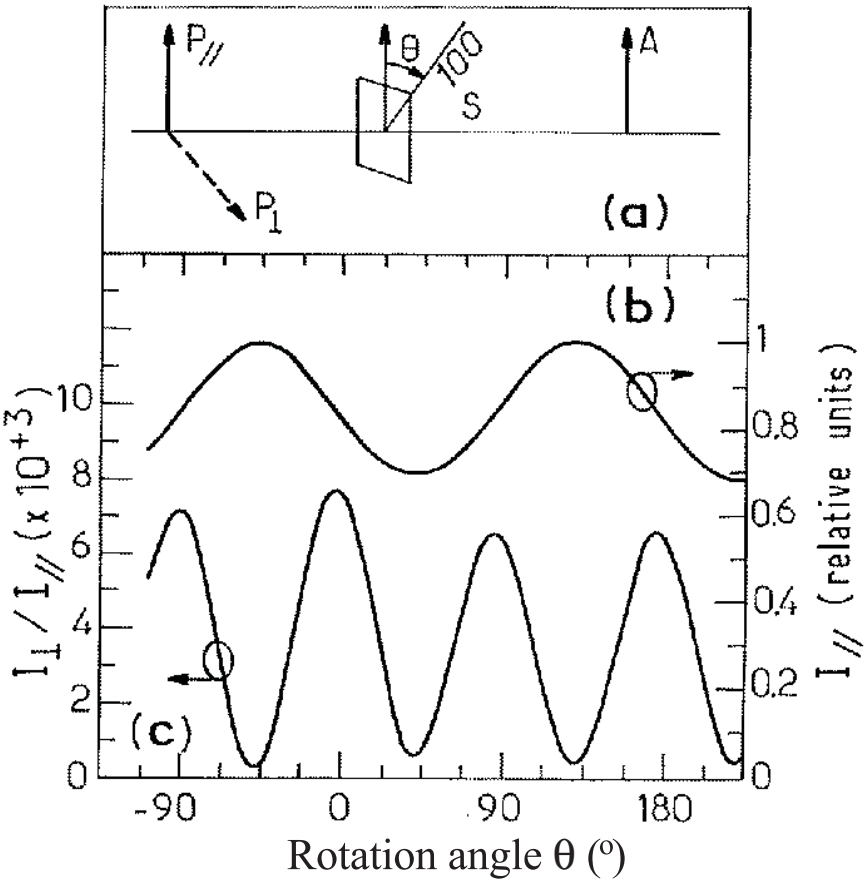

Fig. 3.5. Scheme of the experimental set-up for polarization-resolved transmission measurements (**a**), transmission signal at $\hbar\omega = 925$ meV, as a function of the angle θ between the sample [100] axis and the analyser, with parallel polarizer and analyzer (**b**) or with crossed polarizers (**c**). The small deviation from $\pi/2$ rotation invariance in (**c**) is due to a very small optical anisotropy generally observed in InP substrates. The studied sample S is 80-period InGaAs(45Å)/InP(68Å) MQWs. From [3.44].

$e1$ subband can be conveniently written as

$$\psi^{(e1)}_{\pm 1/2} = \varphi_{e1}(z)|\Gamma_6, \pm 1/2\rangle \,, \tag{3.113}$$

where $|\Gamma_6, \pm 1/2\rangle$ are the $\uparrow$ S and $\downarrow$ S Bloch functions, S is the coordinate function of the Γ_1 representation of group T_d, and $\varphi_{e1}(z)$ is given by (2.8).

For the four envelope functions φ_m ($m = \pm 3/2, \pm 1/2$) of the hole wave function

$$\psi = \frac{1}{\sqrt{S}} \sum_m \varphi_m(z) |\Gamma_8, m\rangle \tag{3.114}$$

we shall use the extended boundary conditions

$$\varphi_m = \varphi'_m \,,\ \nabla_m \varphi_m = \nabla'_m \varphi'_m + \frac{2}{\sqrt{3}}\, t_{l\text{-}h} \sum_n \{J_x J_y\}_{mn} \varphi'_n \,, \tag{3.115}$$

taking into account the mixing between the heavy- and light-hole states at the (001) interface, which is allowed by the interface symmetry even under normal incidence of the hole, i.e., for $k_x = k_y = 0$ (Sect. 2.1.2). The notation used in writing the boundary conditions is m, $n = \pm 3/2$, $\pm 1/2$,

$$\nabla_{\pm 3/2} = a_0 \frac{m_0}{m_{hh}} \frac{d}{dz} \,,\ \nabla_{\pm 1/2} = a_0 \frac{m_0}{m_{lh}} \frac{d}{dz} \,,$$

m_{hh}, m_{lh} are the heavy- and light-hole effective masses, which are different in the CA and C′A′ materials (here and subsequently the quantities pertaining to the C′A′ material are primed), J_α are the angular-momentum matrices for $J = 3/2$ in the Γ_8 basis (Table 2.1), and $t_{l\text{-}h}$ is a dimensionless parameter of heavy-light–hole mixing introduced in (2.42). For $t_{l\text{-}h} \neq 0$, the pair of the Kramers-conjugate states at the bottom of the $hh1$ hole subband contains an admixture of $m = \pm 1/2$ states:

$$\psi^{(hh1)}_{\pm 3/2} = F(z)\, |\Gamma_8, \pm 3/2\rangle \pm \mathrm{i} G(z)\, |\Gamma_8, \mp 1/2\rangle \,, \tag{3.116}$$

where $|\Gamma_8, m\rangle$ are the Bloch functions. Note that the second of the boundary conditions (3.115) for function $G(z)$ has the form

$$\frac{1}{m_{lh}} \frac{dG}{dz} = \frac{1}{m'_{lh}} \frac{dG'}{dz} + \frac{t_{l\text{-}h}}{a_0 m_0} F' \,. \tag{3.117}$$

Within the QW the real envelope functions $F(z)$ and $G(z)$ can be written as

$$\begin{aligned} F(z) &= A \cos k_h z + B \sin k_h z \,, \\ G(z) &= C \cos k_l z + D \sin k_l z \,, \end{aligned} \tag{3.118}$$

and in the barrier layers, $z > a/2$ and $z < -a/2$, they decay exponentially

$$\begin{aligned} F(z) &= F(\pm a/2)\, \exp\left[-æ_h(|z| - a/2)\right] \,, \\ G(z) &= G(\pm a/2)\, \exp\left[-æ_l(|z| - a/2)\right] \,. \end{aligned} \tag{3.119}$$

Here A, B, C, D are z-independent coefficients, the point $z = 0$ is chosen at the well center,

$$\begin{aligned} &k_h = (2m_{hh}\varepsilon/\hbar^2)^{1/2},\ k_l = (2m_{lh}\varepsilon/\hbar^2)^{1/2} = (m_{lh}/m_{hh})^{1/2} k_h \,, \\ &æ_h = [2m'_{hh}(V - \varepsilon)/\hbar^2]^{1/2},\ æ_l = (m'_{lh}/m'_{hh})^{1/2} æ_h \,, \end{aligned} \tag{3.120}$$

ε is the hole energy, and V is the barrier height, i.e., the valence-band offset at the interface. Note that the barrier height for conduction-band electrons is $\Delta E_g - V$, where ΔE_g is the difference between the band-gap widths in the compositional materials. In a common-anion structure the mixing coefficients $t^{\mathrm{L}}_{l\text{-}h}$ and $t^{\mathrm{R}}_{l\text{-}h}$ at the left- and right-hand interfaces, respectively, coincide, and therefore coefficients B and C in (3.118) vanish identically, and $F(a/2) = F(-a/2)$, $G(a/2) = -G(-a/2)$. For $t^{\mathrm{L}}_{l\text{-}h} \neq t^{\mathrm{R}}_{l\text{-}h}$, the $F(z)$, $G(z)$ functions do not possess definite parity under sign inversion of z.

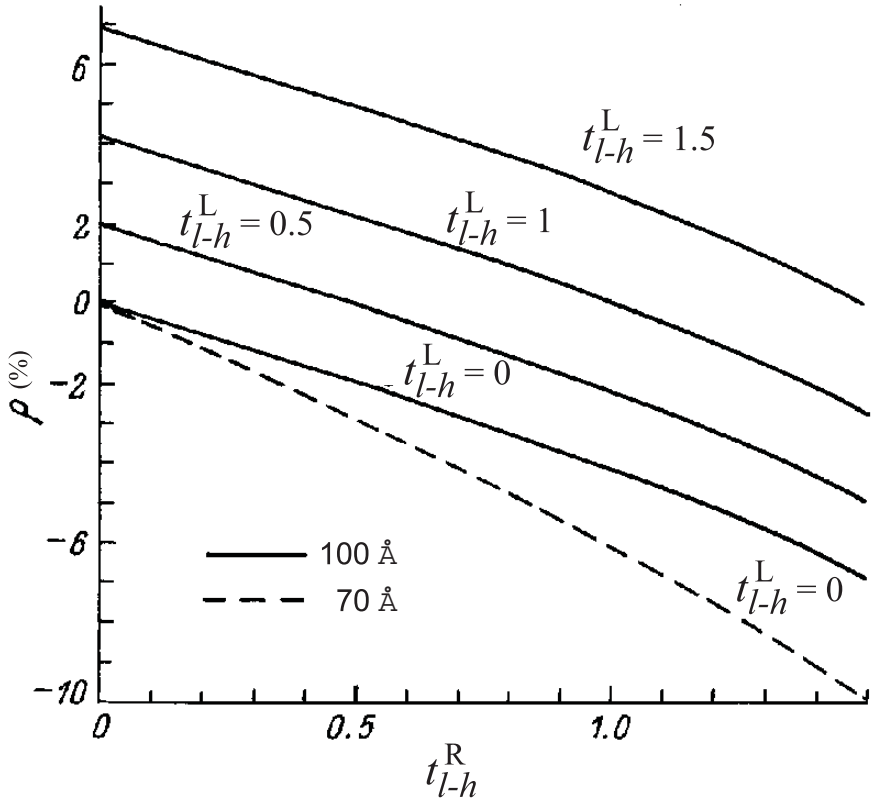

Fig. 3.6. Relative anisotropy of the absorption coefficient in a periodic QW structure $Ga_{0.47}In_{0.53}As/InP$ vs. dimensionless heavy-light-hole mixing coefficient $t^{\mathrm{R}}_{l\text{-}h}$ at the right-hand interface calculated for fixed values of $t^{\mathrm{L}}_{l\text{-}h}$. The solid lines are calculated for wells with thickness $a = 100$ Å, and the dashed line, for $a = 70$ Å. [3.45]

According to (3.113, 3.116, 3.118) and Tables 2.2, 2.3, the interband optical transitions allowed under normal incidence of the linearly polarized

light, $\boldsymbol{e} \perp z$, involve excitation of electron-hole pairs $(e1, -1/2; hh1, 3/2)$ and $(e1, 1/2; hh1, -3/2)$. The transition rates are proportional to [3.45]

$$|M_{-1/2,3/2}(\boldsymbol{e})|^2 = |M_{1/2,-3/2}(\boldsymbol{e})|^2 \tag{3.121}$$
$$= M_0^2 \left(I_1^2 + \frac{1}{3} I_2^2 + \frac{2}{\sqrt{3}} I_1 I_2 \cos 2\phi \right) ,$$

where M_0 is a constant, ϕ is the angle between the plane of polarization and the [110] axis, and

$$I_1 = \int \varphi_{e1}(z) F(z) dz , \qquad I_2 = \int \varphi_{e1}(z) G(z) dz .$$

In accordance with symmetry considerations, light absorption passes through extrema at $\phi = 0$ ($\boldsymbol{e} \| [110]$) and $\phi = \pi/2$ ($\boldsymbol{e} \| [1\bar{1}0]$). According to (3.121), the absorption anisotropy in a periodic quantum-well structure is described by the relation

$$\rho \equiv \frac{K_{[110]} - K_{[1\bar{1}0]}}{K_{[110]} + K_{[1\bar{1}0]}} = \frac{2}{\sqrt{3}} \frac{I_1 I_2}{I_1^2 + (I_2^2/3)} \approx \frac{2}{\sqrt{3}} \frac{I_2}{I_1} , \tag{3.122}$$

where the definition of ρ differs from (3.99) by a factor of 2. In a QW grown of materials with no-common cations and anions, and with no electric field present, the optical anisotropy is dominated by the difference between heavy-light–hole mixing coefficients $t_{l\text{-}h}$ for the CA/C′A′ and C′A′/CA heteroboundaries. It is assumed that the potential barriers at the left- and right-hand interfaces are the same. Figure 3.6 plots the absorption-coefficient anisotropy vs mixing parameters for the left-hand ($t_{l\text{-}h}^{\mathrm{L}}$) and right-hand ($t_{l\text{-}h}^{\mathrm{R}}$) interfaces. The calculation was done using (3.122) for $Ga_{0.47}In_{0.53}As$/InP QWs with thicknesses of 100 Å (solid lines) and 70 Å (dashed line). The main parameters of the materials are listed in Table 3.1. The band offsets used are $\Delta E_c = 0.262$ eV and $\Delta E_v = 0.348$ eV for the conduction and valence bands, respectively. For a fixed value of $t_{l\text{-}h}^{\mathrm{L}}$, the $t_{l\text{-}h}^{\mathrm{R}}$ dependencies presented in Fig. 3.6 reverse sign at $t_{l\text{-}h}^{\mathrm{L}} = t_{l\text{-}h}^{\mathrm{R}}$, which corresponds to a symmetric QW. A decrease in well thickness enhances the influence of interfaces and, hence, makes a steeper $\rho(t_{l\text{-}h}^{\mathrm{R}})$ dependence for a narrower QW.

Table 3.1. The band parameters of $Ga_{0.47}In_{0.53}As$ and InP used in the calculation of curves in Fig. 3.6.

	E_g(eV)	$m_e(m_0)$	$m_{hh}(m_0)$	$m_{lh}(m_0)$
GaInAs	0.81	0.041	0.377	0.052
InP	1.42	0.077	0.65	0.12

It was shown in the previous subsection that the in-plane anisotropy appeared due to the heavy-light hole mixing in (hhl)-grown QWs if the Luttinger band parameters γ_2, γ_3 (or $\sqrt{3}B, D$) are different. We see now that,

in no-common-atom (001)-grown QW structures with interfaces of different kinds, the in-plane anisotropy originates from heavy-light hole mixing taking place at the interfaces. The effect of an electric field on the anisotropy is considered in Sect. 3.4.3.

3.2 Reflection and Diffraction of Light from Arrays of Quantum Wires and Dots

In the previous sections we could trace the modification of the exciton-polariton concept in long-period MQW structures. Here we outline the framework for similar analysis of structures containing regular arrays of QWRs and QDs. The shift from MQWs to 3D lattices of QDs or QWRs allows to bridge the gap between multilayered structures and photonic crystals. The latter are defined as periodic dielectric structures with the period being comparable to the wavelength of the visible-range electromagnetic waves. In the simplest realization, a photonic crystal is thought of as a periodic lattice of spheres of dielectric constant $æ_a$ embedded in a uniform dielectric background $æ_b$ (see reviews [3.46, 3.47]). Other potential realizations are a 3D lattice of resonant two-level atoms [3.48] or semiconductor microcrystals embedded into the pores of periodic porous materials [3.49] (see also [3.50]). We pay more attention to the dots and present short information containing the wires because the both procedures are quite similar.

3.2.1 Rayleigh Scattering of Light by a Single Quantum Wire or Dot

We start with a single QD imbedded in an infinite barrier material of the dielectric constant $æ_b$. The excitonic states in the QD are 0D, or quasi-0D, due to the quantum-confinement effect. We consider a narrow frequency region near a particular exciton size-quantization level and solve the scattering problem of an incident electromagnetic wave on this QD. In the resonant frequency region the dielectric response to an electromagnetic wave is nonlocal and our goal is to show how the theory makes allowance for such kind of nonlocality and give the corrections to the line position and natural linewidth similar to the values $\tilde{\omega}_0$ and Γ_0 in (3.18).

We use the Maxwell equations

$$\begin{aligned} &\Delta \boldsymbol{E} - \text{grad div}\boldsymbol{E} = -\left(\frac{\omega}{c}\right)^2 \boldsymbol{D} \ , \\ &\text{div}\boldsymbol{D} = 0 \end{aligned} \tag{3.123}$$

for the electric field $\boldsymbol{E}$ and the displacement vector $\boldsymbol{D}$. In linear response the relation between $\boldsymbol{D}$ and $\boldsymbol{E}$ reads [3.51]

$$\boldsymbol{D}(\boldsymbol{r}) = æ_b \boldsymbol{E}(\boldsymbol{r}) + 4\pi \boldsymbol{P}_{\text{exc}}(\boldsymbol{r}) \ , \tag{3.124}$$

$$4\pi \boldsymbol{P}_{\rm exc}(\boldsymbol{r}) = \boldsymbol{p}\, G(\omega)\, \Phi(\boldsymbol{r})\ ,\ \boldsymbol{p} = \int \Phi(\boldsymbol{r}')\ \boldsymbol{E}(\boldsymbol{r}')\ d\boldsymbol{r}'\ . \tag{3.125}$$

Here $G(\omega)$ is the same one-pole function as that in (3.11) with ω_0 being the bare QD-exciton resonance frequency, $æ_b$ is the background dielectric constant, $\Phi(\boldsymbol{r})$ denotes the envelope function $\Psi_{\rm exc}(\boldsymbol{r}_e, \boldsymbol{r}_h)$ of an exciton excited in the QD at coinciding electron and hole coordinates: $\Phi(\boldsymbol{r}) = \Psi_{\rm exc}(\boldsymbol{r}, \boldsymbol{r})$. In addition, we neglect anisotropy of the bulk-exciton longitudinal-transverse splitting and consider, in fact, the case of the $\Gamma_6 \times \Gamma_7$ exciton. For simplicity, the QD background dielectric constant $æ_a$ is assumed to coincide with $æ_b$. Clearly, the length scale of non-locality is set by the exciton envelope function which is of the same order as the QD size.

It follows from (3.124) that div $\boldsymbol{E} = -(4\pi/æ_b)$ div $\boldsymbol{P}_{\rm exc}$ which allows to rewrite the first equation (3.123) as

$$\Delta \boldsymbol{E}(\boldsymbol{r}) + q^2 \boldsymbol{E}(\boldsymbol{r}) = -4\pi q_0^2 \left(1 + q^{-2}\ \text{grad div}\right) \boldsymbol{P}_{\rm exc}(\boldsymbol{r})\ . \tag{3.126}$$

We remind that $q_0 = \omega/c$, $q = q_0 n_b$ and $n_b = \sqrt{æ_b}$.

Instead of the 1D Green function used for QW structures we use now the 3D Green function

$$G_{3D}(\boldsymbol{r} - \boldsymbol{r}') = \frac{\exp\left(\mathrm{i}q|\boldsymbol{r} - \boldsymbol{r}'|\right)}{4\pi|\boldsymbol{r} - \boldsymbol{r}'|}\ , \tag{3.127}$$

satisfying the differential equation

$$(\Delta + q^2) G_{3D}(\boldsymbol{r} - \boldsymbol{r}') = -\delta(\boldsymbol{r} - \boldsymbol{r}')\,. \tag{3.128}$$

Green's function allows to express $\boldsymbol{E}(\boldsymbol{r})$ via the excitonic polarization as

$$\boldsymbol{E}(\boldsymbol{r}) = \boldsymbol{E}_0 \mathrm{e}^{\mathrm{i}\boldsymbol{q}\boldsymbol{r}} + 4\pi q_0^2 \int d\boldsymbol{r}' G_{3D}(\boldsymbol{r} - \boldsymbol{r}') \left(1 + q^{-2}\ \text{grad div}\right) \boldsymbol{P}_{\rm exc}(\boldsymbol{r}')\ , \tag{3.129}$$

where $\boldsymbol{q}$ and $\boldsymbol{E}_0$ are the wave vector and amplitude of the initial light wave. Integration by parts allows to rewrite (3.129) as

$$E_\alpha(\boldsymbol{r}) = E_{0,\alpha} \mathrm{e}^{\mathrm{i}\boldsymbol{q}\boldsymbol{r}} + 4\pi q_0^2 \int d\boldsymbol{r}' \sum_\beta G_{\alpha\beta}(\boldsymbol{r} - \boldsymbol{r}') P_{{\rm exc},\beta}(\boldsymbol{r}')\ , \tag{3.130}$$

where we introduced the matrix Green function [3.52]

$$G_{\alpha\beta}(\boldsymbol{r}) = \left(\delta_{\alpha\beta} + \frac{1}{q^2}\, \frac{\partial^2}{\partial r_\alpha \partial r_\beta}\right) \frac{\mathrm{e}^{\mathrm{i}qr}}{4\pi r} \tag{3.131}$$

$$= -\frac{1}{3q^2}\, \delta_{\alpha\beta}\, \delta(\boldsymbol{r}) + \frac{\mathrm{e}^{\mathrm{i}qr}}{4\pi r} \left[\frac{2}{3}\, \delta_{\alpha\beta} + \left(3\frac{r_\alpha r_\beta}{r^2} - \delta_{\alpha\beta}\right) \left(\frac{1}{(qr)^2} - \frac{\mathrm{i}}{qr} - \frac{1}{3}\right)\right]\ .$$

Using (3.125, 3.130) we obtain

$$p_\alpha = p_\alpha^0 + T_{\alpha\beta} p_\beta \, , \; \boldsymbol{p}^0 = \boldsymbol{E}_0 \int d\boldsymbol{r} \Phi(\boldsymbol{r}) \, , \tag{3.132}$$

$$T_{\alpha\beta} = q_0^2 G(\omega) \int d\boldsymbol{r} d\boldsymbol{r}' \; G_{\alpha\beta}(\boldsymbol{r} - \boldsymbol{r}') \Phi(\boldsymbol{r}) \Phi(\boldsymbol{r}') \; .$$

Equation (3.132), together with (3.130, 3.131), completes the solution of the electromagnetic scattering problem.

For spherical or cubic QDs, the matrix $\hat{T}$ is diagonal and isotropic, $T_{\alpha\beta} = T\delta_{\alpha\beta}$, with

$$T(\omega) = -\frac{\delta\omega_0 - \mathrm{i}\Gamma_{\mathrm{SQD}}}{\omega_0 - \omega - \mathrm{i}\Gamma} \, , \tag{3.133}$$

$$\delta\omega_0 = \frac{\pi}{3} a_{\mathrm{B}}^3 \omega_{\mathrm{LT}} \left(\int \Phi^2(\boldsymbol{r}) \, d\boldsymbol{r} - \frac{q^2}{2\pi} \int \int d\boldsymbol{r} d\boldsymbol{r}' \frac{\cos q|\boldsymbol{r} - \boldsymbol{r}'|}{|\boldsymbol{r} - \boldsymbol{r}'|} \Phi(\boldsymbol{r}) \Phi(\boldsymbol{r}') \right) \, , \tag{3.134}$$

$$\Gamma_{\mathrm{SQD}} = \frac{1}{6} q^2 a_{\mathrm{B}}^3 \omega_{\mathrm{LT}} \int \int d\boldsymbol{r} d\boldsymbol{r}' \frac{\sin q|\boldsymbol{r} - \boldsymbol{r}'|}{|\boldsymbol{r} - \boldsymbol{r}'|} \Phi(\boldsymbol{r}) \Phi(\boldsymbol{r}') \, . \tag{3.135}$$

Here $\delta\omega_0$ and Γ_{SQD} are the renormalization of the resonance frequency and radiative damping of the 0D exciton. We return to their interpretation in Chap. 5 while considering the fine structure of exciton levels in nanostructures.

The above procedure can be repeated for the elastic scattering of light by a QWR. In this case one can use the 2D Green function $G_{2D}(\boldsymbol{\rho}) = (\mathrm{i}/4)\mathrm{H}_0^{(1)}(q\rho)$ satisfying the equation

$$\left(\frac{\partial^2}{\partial x^2} + \frac{\partial^2}{\partial y^2} + q^2 \right) G_{2D}(x, y) = -\delta(x)\delta(y) \, , \tag{3.136}$$

where $\mathrm{H}_0^{(1)}(z)$ is a Hankel function. Under normal incidence of the monochromatic electromagnetic wave upon a single QWR the electric field is written similarly to (3.125, 3.130) as

$$E_\alpha(\boldsymbol{\rho}) = E_{0,\alpha} \mathrm{e}^{\mathrm{i}\boldsymbol{q}\boldsymbol{\rho}} + \tag{3.137}$$

$$+ q_0^2 G(\omega) \int d\boldsymbol{\rho}' \Phi(\boldsymbol{\rho}') \sum_\beta \left(\delta_{\alpha\beta} + \frac{1}{q^2} \frac{\partial^2}{\partial r_\alpha \partial r_\beta} \right) G_{2D}(\boldsymbol{\rho} - \boldsymbol{\rho}') \int d\boldsymbol{\rho}'' \Phi(\boldsymbol{\rho}'') E_\beta(\boldsymbol{\rho}'') \, ,$$

where $\Phi(\boldsymbol{\rho})$ is the 1D-exciton envelope function at coinciding coordinates of the electron and hole.

3.2.2 Periodic Arrays of Isolated Quantum Dots

Let us turn to an ensemble of QDs and consider first the photonic (or more precisely, exciton-polaritonic) band structure of a 3D periodic array of QDs (or, simply, QD lattices) and then, in the next subsection, the light reflection from and transmission through a planar quadratic QD lattice.

In the following the centers of QDs in the 3D array are indicated by the translation vectors $\boldsymbol{a}$. The nonlocal material equation relating $\boldsymbol{P}_{\rm exc}$ and $\boldsymbol{E}$ is obtained if we present the excitonic contribution to the dielectric polarization as a sum of individual contributions (3.125) over $\boldsymbol{a}$,

$$4\pi \boldsymbol{P}_{\rm exc}(\boldsymbol{r}) = G(\omega) \sum_{\boldsymbol{a}} \boldsymbol{p_a}\, \Phi_{\boldsymbol{a}}(\boldsymbol{r}) \;,\; \boldsymbol{p_a} = \int \Phi_{\boldsymbol{a}}(\boldsymbol{r}')\; \boldsymbol{E}(\boldsymbol{r}')\; d\boldsymbol{r}' \;, \tag{3.138}$$

where $\Phi_{\boldsymbol{a}}(\boldsymbol{r}) = \Phi(\boldsymbol{r}-\boldsymbol{a})$. In this subsection we neglect the overlap of exciton envelope functions $\Psi_{\boldsymbol{a}}$ and $\Psi_{\boldsymbol{a}'}$ with $\boldsymbol{a} \neq \boldsymbol{a}'$ so that excitons excited in different dots are assumed to be coupled only via the electromagnetic field. We seek for Bloch-like solutions of (3.126) satisfying the translational symmetry

$$\begin{aligned} \boldsymbol{E}_{\boldsymbol{K}}(\boldsymbol{r}+\boldsymbol{a}) &= \exp\left(\mathrm{i}\boldsymbol{K}\boldsymbol{a}\right) \boldsymbol{E}_{\boldsymbol{K}}(\boldsymbol{r}) \;, \\ \boldsymbol{P}_{\mathrm{exc},\boldsymbol{K}}(\boldsymbol{r}+\boldsymbol{a}) &= \exp\left(\mathrm{i}\boldsymbol{K}\boldsymbol{a}\right) \boldsymbol{P}_{\mathrm{exc},\mathbf{K}}(\boldsymbol{r}) \;, \end{aligned} \tag{3.139}$$

where the wave vector $\boldsymbol{K}$ is defined within the first Brillouin zone. The exciton-polariton dispersion $\omega(\boldsymbol{K})$ can be shown to satisfy the equation

$$\mathrm{Det}||\delta_{\alpha\beta} - R_{\alpha\beta}(\omega, \boldsymbol{K})|| = 0 \;, \tag{3.140}$$

where $\alpha, \beta = x, y, z$, $\delta_{\alpha\beta}$ is the Kronecker symbol and, for QD lattices,

$$R_{\alpha\beta}(\omega, \boldsymbol{K}) = G(\omega)\, \frac{q_0^2}{v_0} \sum_{\boldsymbol{g}} \frac{|I_{\boldsymbol{K}+\boldsymbol{g}}|^2\, S_{\alpha\beta}(\boldsymbol{K}+\boldsymbol{g})}{(\boldsymbol{K}+\boldsymbol{g})^2 - q^2} \;, \tag{3.141}$$

$$I_{\boldsymbol{Q}} = \int \Phi(\boldsymbol{r}) \mathrm{e}^{\mathrm{i}\boldsymbol{Q}\boldsymbol{r}} d\boldsymbol{r} \;,\; S_{\alpha\beta}(\boldsymbol{Q}) = \delta_{\alpha\beta} - \frac{Q_\alpha Q_\beta}{q^2} \;, \tag{3.142}$$

$\boldsymbol{g}$ are the reciprocal lattice vectors and v_0 is the volume of the lattice primitive cell.

Equations (3.140, 3.141) can be derived by using the two equivalent approaches: (i) to express the exciton dielectric polarization $\boldsymbol{P}_{\rm exc}(\boldsymbol{r})$ in terms of the electric field, $\boldsymbol{E}(\boldsymbol{r})$, and find solutions of the wave equation for $\boldsymbol{E}(\boldsymbol{r})$; (ii) by using Green's function of the wave equation, to express the electric field in terms of the exciton polarization and write a system of self-consistent equations describing electric-field-mediated coupling between the excitons excited in different QDs. In the first approach, we substitute (3.138) into (3.126) and expand the vector function $\boldsymbol{E}_{\boldsymbol{K}}(\boldsymbol{r})$ in the Fourier series as follows

$$\boldsymbol{E}_{\boldsymbol{K}}(\boldsymbol{r}) = \sum_{\boldsymbol{g}} \mathrm{e}^{\mathrm{i}(\boldsymbol{K}+\boldsymbol{g})\boldsymbol{r}}\; \boldsymbol{E}_{\boldsymbol{K}+\boldsymbol{g}} \,. \tag{3.143}$$

The integral (3.138) can be transformed into

$$\boldsymbol{p_a} = \mathrm{e}^{\mathrm{i}\boldsymbol{K}\boldsymbol{a}} \sum_{\boldsymbol{g}} I_{\boldsymbol{K}+\boldsymbol{g}}\; \boldsymbol{E}_{\boldsymbol{K}+\boldsymbol{g}} \equiv \mathrm{e}^{\mathrm{i}\boldsymbol{K}\boldsymbol{a}}\; \boldsymbol{\Lambda} \,. \tag{3.144}$$

The sum $\sum_{\boldsymbol{a}} \Phi_{\boldsymbol{a}}(\boldsymbol{r})\mathrm{e}^{\mathrm{i}\boldsymbol{K}\boldsymbol{a}}$ satisfies the translational symmetry similar to (3.139) and can be presented as

$$\sum_{\boldsymbol{a}} \Phi_{\boldsymbol{a}}(\boldsymbol{r})\ \mathrm{e}^{\mathrm{i}\boldsymbol{K}\boldsymbol{a}} = \sum_{\boldsymbol{g}} \mathrm{e}^{\mathrm{i}(\boldsymbol{K}+\boldsymbol{g})\boldsymbol{r}}\ \frac{I^*_{\boldsymbol{K}+\boldsymbol{g}}}{v_0}\,. \tag{3.145}$$

The system of linear equations for the space harmonics $\boldsymbol{E}_{\boldsymbol{K}+\boldsymbol{g}}$ can be written in the form

$$[(\boldsymbol{K}+\boldsymbol{g})^2 - q^2]\ \boldsymbol{E}_{\boldsymbol{K}+\boldsymbol{g}} = G(\omega)\ q_0^2\ \frac{I^*_{\boldsymbol{K}+\boldsymbol{g}}}{v_0}\ \hat{S}(\boldsymbol{K}+\boldsymbol{g})\ \boldsymbol{\Lambda}\,, \tag{3.146}$$

where the vector $\boldsymbol{\Lambda}$ is introduced in (3.144) and $\hat{S}(\boldsymbol{Q})\boldsymbol{\Lambda}$ is a vector with the components $S_{\alpha\beta}(\boldsymbol{Q})\Lambda_\beta$. Dividing both parts of (3.146) by $(\boldsymbol{K}+\boldsymbol{g})^2 - q^2$, multiplying them by $I_{\boldsymbol{K}+\boldsymbol{g}}$ and summing over $\boldsymbol{g}$ we arrive at the vector equation $\boldsymbol{\Lambda} = \hat{R}(\omega,\boldsymbol{K})\boldsymbol{\Lambda}$, where the matrix $\hat{R}$ is defined by (3.141), and hence at the dispersion equation (3.140).

In the second approach, we use the 3D Green function (3.127) rewriting it as

$$G_{3D}(\boldsymbol{r}-\boldsymbol{r}') = \frac{1}{V}\sum_{\boldsymbol{Q}} \frac{\exp\left[\mathrm{i}\boldsymbol{Q}(\boldsymbol{r}-\boldsymbol{r}')\right]}{\boldsymbol{Q}^2 - q^2}\,, \tag{3.147}$$

where V is the 3D QD-lattice volume. Green's function allows to express the electric field $\boldsymbol{E}(\boldsymbol{r})$ of the normal light wave via the polarization in the form of (3.130) with the initial field amplitude set to zero. For the Bloch solutions (3.139) one has $\boldsymbol{p}_{\boldsymbol{a}} = \mathrm{e}^{\mathrm{i}\boldsymbol{K}\boldsymbol{a}}\boldsymbol{p}_0$. Taking $\boldsymbol{a} = 0$ in (3.144) and using (3.130,3.143) we obtain

$$\begin{aligned}\boldsymbol{p}_0 = G(\omega)\int d\boldsymbol{r}\ \Phi_0(\boldsymbol{r})\int d\boldsymbol{r}'\ G_{3D}(\boldsymbol{r}-\boldsymbol{r}') \\ \times\left(1 + q^{-2}\ \mathrm{grad}\ \mathrm{div}\right)\boldsymbol{p}_0\ \sum_{\boldsymbol{a}} \Phi_{\boldsymbol{a}}(\boldsymbol{r}')\ \mathrm{e}^{\mathrm{i}\boldsymbol{K}\boldsymbol{a}}\,.\end{aligned} \tag{3.148}$$

If we now use equations (3.142, 3.145) and the presentation (3.147) of Green's function we finally come to the equation $\boldsymbol{p}_0 = \hat{R}(\omega,\boldsymbol{q})\boldsymbol{p}_0$ and rederive (3.140).

In the particular case of spherical QDs with the radius R exceeding the Bohr radius a_B one has

$$I_{\boldsymbol{Q}} = \pi\left(\frac{2R}{a_\mathrm{B}}\right)^{3/2}\frac{\sin QR}{QR[\pi^2 - (QR)^2]}\,. \tag{3.149}$$

Then (3.141) can be transformed into

$$R_{\alpha\beta}(\Omega,\boldsymbol{K}) = \xi\frac{\Omega^2}{\Omega^2 - 1}\sigma_{\alpha\beta}(\Omega,\boldsymbol{K})\,, \tag{3.150}$$

$$\sigma_{\alpha\beta}(\Omega, \boldsymbol{K}) = \sum_{\boldsymbol{b}} \frac{f(|\boldsymbol{K}+\boldsymbol{b}|R)\, S_{\alpha\beta}(\boldsymbol{K}+\boldsymbol{b})}{\Omega^2 - \Omega^2(\boldsymbol{K}+\boldsymbol{b})} \ , \tag{3.151}$$

$$\Omega = \frac{\omega}{\omega_0} \ , \ \xi = \frac{64}{\pi}\frac{\omega_{\rm LT}}{\omega_0}\left(\frac{R}{a}\right)^3 \ , \ f(x) = \left(\frac{\pi^2 \sin x}{x(\pi^2 - x^2)}\right)^2 \ , \tag{3.152}$$

$\Omega(\boldsymbol{Q}) = cQ/(n_b\omega_0)$. Equation (3.140) is equivalent to the three separate equations $R_j(\Omega, \boldsymbol{K}) = 1$, where R_j $(j = 1, 2, 3)$ are eigenvalues of the matrix $R_{\alpha\beta}$. The further simplification follows taking into account a small value of the parameter ξ since, in semiconductors, the ratio $\omega_{\rm LT}/\omega_0$ typically lies between 10^{-4} and 10^{-3}. Then one can change the factor $\Omega/(\Omega+1)$ in (3.150) by 1/2.

For high-symmetry points of the Brillouin zone, the symmetry imposes certain relations between the $R_{\alpha\beta}$ components, and the eigenvalues R_j can be readily expressed via them. Table 3.2 illustrates these relations for the points Γ, X, L, W, K and U of a face-centered-cubic QD lattice. The coordinates of the points in the reciprocal space are given in the first column (in terms of π/a). Note that in this case the lattice constant a and the unit-cell volume v_0 are related by $v_0 = a^3/4$.

Table 3.2. Nonzero components of the matrix $R_{\alpha\beta}$ and dispersion equations written in terms of $R_{\alpha\beta}$ for different $\mathbf{K}$ points in the Brillouin zone of a face-centered-cubic QD lattice.

$\boldsymbol{K}$ (π/a)	Nonzero components of $R_{\alpha\beta}$	Dispersion equations
Γ $(0,0,0)$	$R_{xx} = R_{yy} = R_{zz}$	$R_{xx} = 1$
X $(0,0,2)$	$R_{xx} = R_{yy}$, R_{zz}	$R_{xx} = 1$, $R_{zz} = 1$
L $(1,1,1)$	$R_{\alpha\alpha} = R_{xx}$, $R_{\alpha\beta} = R_{xy} (\alpha \neq \beta)$	$R_{xx} - R_{xy} = 1$, $R_{xx} + 2R_{xy} = 1$
W $(1,0,2)$	R_{xx}, $R_{yy} = R_{zz}$	$R_{xx} = 1$, $R_{yy} = 1$
K $(3/2,0,3/2)$	$R_{xx} = R_{zz}$, R_{yy} , $R_{xz} = R_{zx}$	$R_{xx} \pm R_{xz} = 1$, $R_{yy} = 1$
U $(1/2,1/2,2)$	$R_{xx} = R_{yy}$, R_{zz}, $R_{xy} = R_{yx}$	$R_{xx} \pm R_{xy} = 1$, $R_{zz} = 1$

According to (3.141, 3.150) the dispersion near the point $\boldsymbol{K}$ satisfying the condition $cK/n_b \approx \omega_0$ should be characterized by a giant anticrossing between the branches of bare transverse photon and exciton modes. Note that the anticrossing can be described with a high accuracy by retaining in the sum over $\boldsymbol{b}$ in (3.151) the two terms due to $\boldsymbol{b} = 0, -(4\pi/a)(0,0,1)$ if the resonant Bragg condition is satisfied for the (001) planes, i.e., if $(2\pi/a)(c/n_b) \approx \omega_0$, or two terms due to $\boldsymbol{b} = 0, -(2\pi/a)(1,1,1)$ if $(\pi\sqrt{3}/a)(c/n_b) \approx \omega_0$.

3.2.3 Diffraction by a Planar Array of Quantum Dots

We assume the array of QDs to be regularly packed in one plane normal to z. For simplicity, we consider here the normal incidence of the light and a quadratic lattice of spherical or cubic QDs with the translational vectors $\boldsymbol{a}$

being integer combinations of the basic vectors $\boldsymbol{a}_1 = a(1,0,0)$, $\boldsymbol{a}_2 = a(0,1,0)$. In this case the electric field can be expanded in the 2D Fourier series as

$$\boldsymbol{E}(\boldsymbol{r}) = \sum_{\boldsymbol{b}} \boldsymbol{E}_{\boldsymbol{b}}(z) \exp\left(\mathrm{i}\boldsymbol{b}\boldsymbol{\rho}\right) , \tag{3.153}$$

where $\boldsymbol{b} = l\boldsymbol{b}_1 + m\boldsymbol{b}_2$ are the 2D reciprocal-lattice vectors, $\boldsymbol{b}_1 = (2\pi/a)(1,0,0)$, $\boldsymbol{b}_2 = (2\pi/a)(0,1,0)$, l and m are integers, a is the constant of the 2D QD quadratic lattice.

The integral in (3.125) can be transformed into

$$\begin{aligned} \int \Phi_{\boldsymbol{a}}(\boldsymbol{r})\ \boldsymbol{E}(\boldsymbol{r})\ d\boldsymbol{r} &= \sum_{\boldsymbol{b}} \mathrm{e}^{\mathrm{i}\boldsymbol{b}\boldsymbol{a}} \int \boldsymbol{E}_{\boldsymbol{b}}(z)\Phi(\boldsymbol{\rho}, z) \exp\left(\mathrm{i}\boldsymbol{b}\boldsymbol{\rho}\right) d\boldsymbol{\rho} dz \\ &= \sum_{\boldsymbol{b}} \int \varphi_{\boldsymbol{b}}(z)\boldsymbol{E}_{\boldsymbol{b}}(z)\ dz \equiv \boldsymbol{\Lambda}_1 , \end{aligned} \tag{3.154}$$

where $\boldsymbol{\rho} = (x, y)$,

$$\varphi_{\boldsymbol{b}}(z) = \int \Phi(\boldsymbol{\rho}, z) \exp\left(\mathrm{i}\boldsymbol{b}\boldsymbol{\rho}\right) d\boldsymbol{\rho} \tag{3.155}$$

and we used the identity $\exp\left(\mathrm{i}\boldsymbol{b}\boldsymbol{a}\right) = 1$. We will also use the expansion

$$\sum_{\boldsymbol{a}} \Phi_{\boldsymbol{a}}(\boldsymbol{r}) = \frac{1}{a^2} \sum_{\boldsymbol{b}} \varphi_{\boldsymbol{b}}(z) \exp\left(\mathrm{i}\boldsymbol{b}\boldsymbol{\rho}\right) , \tag{3.156}$$

where a^2 is the 2D unit cell area.

The function $\boldsymbol{E}_{\boldsymbol{b}}(z)$ satisfies the equation

$$\left(\frac{d^2}{dz^2} + q_{\boldsymbol{b}}^2\right) \boldsymbol{E}_{\boldsymbol{b}}(z) = -G(\omega)\frac{q_0^2}{a^2} \left(1 + \frac{1}{q^2}\ \mathrm{grad}\ \mathrm{div}\right)_{\boldsymbol{b}} \varphi_{\boldsymbol{b}}(z)\boldsymbol{\Lambda}_1 , \tag{3.157}$$

where $q_{\boldsymbol{b}} = \sqrt{q^2 - \boldsymbol{b}^2}$,

$$\left(\frac{\partial^2}{\partial r_\alpha \partial r_\beta}\right)_{\boldsymbol{b}} = -K_\alpha K_\beta\ ,\ K_x = b_x, K_y = b_y, K_z = -\mathrm{i}\frac{\partial}{\partial z} . \tag{3.158}$$

The solution can be presented as

$$\begin{aligned} \boldsymbol{E}_{\boldsymbol{b}}(z) &= \boldsymbol{E}^{(0)}\mathrm{e}^{\mathrm{i}qz}\delta_{\boldsymbol{b},0} \\ &\quad + \frac{\mathrm{i}q_0^2}{2q_{\boldsymbol{b}}a^2} G(\omega) \int dz'\ \mathrm{e}^{\mathrm{i}q_{\boldsymbol{b}}|z-z'|} \left(1 + q^{-2}\mathrm{grad}\ \mathrm{div}\right)_{\boldsymbol{b}} \varphi_{\boldsymbol{b}}(z')\boldsymbol{\Lambda}_1 , \end{aligned} \tag{3.159}$$

where $\boldsymbol{E}^{(0)}$ is the amplitude of the initial wave. Multiplying the both parts of (3.159) by $\varphi_{\boldsymbol{b}}(z)$, integrating over z and summing over $\boldsymbol{b}$ we obtain

$$\begin{aligned} \boldsymbol{\Lambda}_1 &= \boldsymbol{\Lambda}_1^0 \\ &\quad + \sum_{\boldsymbol{b}} \frac{\mathrm{i}q_0^2}{2q_{\boldsymbol{b}}a^2} G(\omega) \int dz dz'\ \mathrm{e}^{\mathrm{i}q_{\boldsymbol{b}}|z-z'|} \varphi_{\boldsymbol{b}}(z) \left(1 + q^{-2}\mathrm{grad}\ \mathrm{div}\right)_{\boldsymbol{b}} \varphi_{\boldsymbol{b}}(z')\boldsymbol{\Lambda}_1 , \end{aligned} \tag{3.160}$$

where

$$\boldsymbol{\Lambda}_1^0 = \boldsymbol{E}^{(0)} \int \varphi_0(z) \mathrm{e}^{\mathrm{i}qz}\, dz = \boldsymbol{E}^{(0)} \int \varphi_0(z) \cos qz\, dz\,. \tag{3.161}$$

Let us denote by β the star of the vector $\mathbf{b}$. If $\boldsymbol{b} = l\boldsymbol{b}_1 + m\boldsymbol{b}_2$, the star β contains the vectors $\pm l\boldsymbol{b}_1 \pm m\boldsymbol{b}_2, \pm m\boldsymbol{b}_1 \pm l\boldsymbol{b}_2$ of equal absolute values. For $l \neq m \neq 0$ the star consists of eight vectors, otherwise it has four vectors ($l = m \neq 0$ or $l = 0, m \neq 0$ or $l \neq 0, m = 0$) and one vector in the particular case $l = m = 0$. Then the second term in the right-hand side of (3.160) can be rewritten

$$G(\omega) \sum_\beta \frac{\mathrm{i}q_0^2 n_\beta}{2q_\beta a^2} \int\int dz dz'\, \mathrm{e}^{\mathrm{i}q_\beta |z-z'|} \varphi_\beta(z)$$

$$\times \left[\left(1 - \frac{\beta^2}{2q^2}\right) \boldsymbol{\Lambda}_{1,\parallel} + \left(1 - \frac{1}{q^2}\frac{\partial^2}{\partial z'^2}\right) \boldsymbol{\Lambda}_{1,\perp} \right] \varphi_\beta(z')\,,$$

where $\boldsymbol{\Lambda}_{1,\parallel}, \boldsymbol{\Lambda}_{1,\perp}$ are vectors with the components $(\Lambda_{1,x}, \Lambda_{1,y}, 0)$ and $(0, 0, \Lambda_{1,z})$, respectively, n_β is the number of vectors in the star β and $\beta^2 = |\boldsymbol{b}|^2$, $q_\beta \equiv q_{\boldsymbol{b}}$. Taking into account that $\boldsymbol{\Lambda}_1^0 = (\Lambda_{1,x}^0, \Lambda_{1,y}^0, 0)$ we obtain

$$\begin{aligned} \boldsymbol{\Lambda}_1 &= \boldsymbol{\Lambda}_1^0 \left[1 - G(\omega) \sum_\beta \frac{\mathrm{i}q_0^2 n_\beta}{2q_\beta a^2} \left(1 - \frac{\beta^2}{2q^2}\right) \int dz dz'\, \mathrm{e}^{\mathrm{i}q_\beta |z-z'|} \varphi_\beta(z) \varphi_\beta(z') \right]^{-1} \\ &= \boldsymbol{\Lambda}_1^0 \frac{\omega_0 - \omega - \mathrm{i}\Gamma}{\tilde{\omega}_0 - \omega - \mathrm{i}(\Gamma + \Gamma_0)}\,. \end{aligned} \tag{3.162}$$

Here $\tilde{\omega}_0$ is the normalized exciton resonant frequency, the difference between $\tilde{\omega}_0$ and ω_0 consists of two terms

$$\begin{aligned} \delta\omega_1 &= \omega_{\mathrm{LT}} \frac{q^2 \pi a_{\mathrm{B}}^3}{2a^2} \sum_{\beta \in B_1} \frac{n_\beta}{q_\beta} \left(1 - \frac{\beta^2}{2q^2}\right) \\ &\quad \times \int dz dz'\, \sin(q_\beta |z - z'|)\, \varphi_\beta(z) \varphi_\beta(z')\,, \\ \delta\omega_2 &= -\omega_{\mathrm{LT}} \frac{q^2 \pi a_{\mathrm{B}}^3}{2a^2} \sum_{\beta \in B_2} \frac{n_\beta}{æ_\beta} \left(1 - \frac{\beta^2}{2q^2}\right) \\ &\quad \times \int dz dz'\, \mathrm{e}^{-æ_\beta |z-z'|} \varphi_\beta(z) \varphi_\beta(z')\,, \end{aligned} \tag{3.163}$$

B_1 and B_2 represent the sets of stars β with real and imaginary q_β, respectively, $æ_\beta = \mathrm{Im}\{q_\beta\}$. The exciton radiative damping rate is given by

$$\Gamma_0 = \omega_{\mathrm{LT}} \frac{q^2 \pi a_{\mathrm{B}}^3}{2a^2} \sum_{\beta \in B_1} \frac{n_\beta}{q_\beta} \left(1 - \frac{\beta^2}{2q^2}\right) \lambda_\beta^2\,, \tag{3.164}$$

$$\lambda_\beta = \int \varphi_\beta(z) \cos q_\beta z \, dz = \int \Phi(\boldsymbol{r}) \cos\left(\boldsymbol{b\rho} + q_\beta z\right) d\boldsymbol{r} \,. \tag{3.165}$$

The light waves diffracted in the backward and forward directions are written as

$$\sum_{\boldsymbol{b}} \boldsymbol{E}_{\boldsymbol{b}}^{(r)} \exp\left[\mathrm{i}(\boldsymbol{b\rho} - q_{\boldsymbol{b}} z)\right] \text{ and } \sum_{\boldsymbol{b}} \boldsymbol{E}_{\boldsymbol{b}}^{(t)} \exp\left[\mathrm{i}(\boldsymbol{b\rho} + q_{\boldsymbol{b}} z)\right] . \tag{3.166}$$

The amplitudes $\boldsymbol{E}_{\boldsymbol{b}}^{(r)}, \boldsymbol{E}_{\boldsymbol{b}}^{(t)}$ are given by [3.53]

$$\boldsymbol{E}_{\boldsymbol{b}}^{(r)} = \mathrm{i}\frac{q^2 \pi a_{\mathrm{B}}^3}{2 q_{\boldsymbol{b}} a^2} \frac{\omega_{\mathrm{LT}} \lambda_{\boldsymbol{b}} \lambda_0}{\tilde{\omega}_0 - \omega - \mathrm{i}(\Gamma + \Gamma_0)} \left(1 - \frac{\widehat{\boldsymbol{K}_r \boldsymbol{K}_r}}{q^2}\right) \boldsymbol{E}^{(0)} \,, \tag{3.167}$$

$$\boldsymbol{E}_{\boldsymbol{b}}^{(t)} = \left[\delta_{\boldsymbol{b},0} + \mathrm{i}\frac{q^2 \pi a_{\mathrm{B}}^3}{2 q_{\boldsymbol{b}} a^2} \frac{\omega_{\mathrm{LT}} \lambda_{\boldsymbol{b}} \lambda_0}{\tilde{\omega}_0 - \omega - \mathrm{i}(\Gamma + \Gamma_0)} \left(1 - \frac{\widehat{\boldsymbol{K}_t \boldsymbol{K}_t}}{q^2}\right)\right] \boldsymbol{E}^{(0)} \,,$$

where $(\widehat{\boldsymbol{K}\boldsymbol{K}}\boldsymbol{E})_i = K_i \sum_j K_j E_j$, $\boldsymbol{K}_r = (b_x, b_y, -q_{\boldsymbol{b}})$, $\boldsymbol{K}_t = (b_x, b_y, q_{\boldsymbol{b}})$. While deriving (3.167) we took into account that $\Lambda_{1,z}^{(0)} = 0$ and

$$\int \mathrm{e}^{\mathrm{i}q_{\boldsymbol{b}} z}(-\mathrm{i}d/dz)\varphi_{\boldsymbol{b}}(z) \, dz = -q_{\boldsymbol{b}} \int \mathrm{e}^{\mathrm{i}q_{\boldsymbol{b}} z} \varphi_{\boldsymbol{b}}(z) \, dz = -q_{\boldsymbol{b}} \lambda_{\boldsymbol{b}} \,.$$

One can check that (3.167) satisfies the energy-flux conservation law. Really, for zero dissipation, i.e. for $\Gamma = 0$, we have

$$\sum_{\boldsymbol{b} \in B_1} q_{\boldsymbol{b}} \left(|\boldsymbol{E}_{\boldsymbol{b}}^{(r)}|^2 + |\boldsymbol{E}_{\boldsymbol{b}}^{(t)}|^2\right) = q |\boldsymbol{E}^{(0)}|^2 \,. \tag{3.168}$$

For short-period 2D QD lattices, where $qa \ll 1$ and B_1 contains only one element $\beta = 0$, we obtain for the reflection and transmission coefficients

$$r = \frac{E_0^{(r)}}{E^{(0)}} = \frac{\mathrm{i}\Gamma_{\mathrm{QD}}}{\tilde{\omega}_0 - \omega - \mathrm{i}(\Gamma + \Gamma_{\mathrm{QD}})} \,, \; t = \frac{E_0^{(t)}}{E^{(0)}} = 1 + r \,, \tag{3.169}$$

where the exciton radiative damping, $\Gamma_0 \equiv \Gamma_{QD}$, is given by [3.51, 3.54]

$$\Gamma_{\mathrm{QD}} = \frac{3\pi}{(aq)^2} \Gamma_{\mathrm{SQD}} \tag{3.170}$$

and Γ_{SQD} is the exciton damping in a single QD, see (3.135). For $qa \ll 1$, the latter reduces to

$$\Gamma_{\mathrm{SQD}} = \frac{1}{6} \omega_{\mathrm{LT}} \left(q a_{\mathrm{B}}\right)^3 \left(\int d\boldsymbol{r} \Phi(\boldsymbol{r})\right)^2 \,.$$

The superradiance factor $3\pi/(aq)^2$ substantially enhances the radiative damping rate in dense QD arrays. This factor evidences that identical QDs located at distance a from each other emit coherently the secondary light.

The dependence of the reflection spectra on the number of equidistant QD planes, N, was studied theoretically in [3.53]. If the period d satisfies the Bragg condition at the exciton resonance frequency ω_0, then the halfwidth of the reflection spectrum is almost linearly increasing as a function of N. This is similar to the enhancement by a factor of N of the radiative damping of the superradiant mode in resonant Bragg MQW structures, see (3.92).

The theory presented in the above two subsections can also be used to generalize the theory of resonant diffraction of γ-radiation by nuclei from bulk crystals [3.55] to synthesized multilayers like the nuclear multilayer [^{57}Fe(22 Å)/Sc(11 Å)/Fe(22 Å)/Sc(11 Å)]×25 studied by Chumakov et al. [3.56]. The developed approach takes into account a contribution of only one confined-exciton resonance. This is valid if the separation between the exciton size-quantization levels is much larger than the bulk value of the exciton longitudinal-transverse splitting, ω_{LT}. In the opposite limit of extremely large bulk-exciton translational effective mass one can use the local material relation $\boldsymbol{D}(\boldsymbol{r}) = æ(\boldsymbol{r},\omega)\boldsymbol{E}(\boldsymbol{r})$. This was done by Sigalas et al. [3.57] for phonon-polaritons in a 2D lattice consisting of semiconductor cylinders.

Similar formula can be derived for the amplitude reflection coefficient from a grating of QWRs. In particular, for a short-period grating of thin QWRs and the polarization parallel to the wire principal axis, y, the radiative damping Γ_{QWR} is given by [3.51]

$$\Gamma_{\mathrm{QWR}} = \Gamma_{\mathrm{QW}} \frac{1}{d_x} \left(\frac{\int \Phi_{\mathrm{QWR}}(\rho)\, d^2\rho}{\int \Phi_{\mathrm{QW}}(z)\, dz} \right)^2 , \tag{3.171}$$

where d_x is the spacing between QWRs, Γ_{QW} is given by (3.18), $\Phi_{\mathrm{QW}}(z) = \sqrt{S}\Psi_{\mathrm{exc}}^{\mathrm{QW}}(\boldsymbol{r},\boldsymbol{r})$, $\Phi_{\mathrm{QWR}}(\rho) = \sqrt{L_y}\Psi_{\mathrm{exc}}^{\mathrm{QWR}}(\boldsymbol{r},\boldsymbol{r})$, $\Psi_{\mathrm{exc}}^{\mathrm{QW}}$ and $\Psi_{\mathrm{exc}}^{\mathrm{QWR}}$ are the single-QW and single-QWR exciton envelope functions, L_y is the wire (macroscopic) length. Note that the exciton radiative dampings in a single QWR and in an array of QWRs are related by: $\Gamma_{\mathrm{QWR}} = (2/qd_x)\Gamma_{SQWR}$.

3.2.4 Two-Dimensional Quantum-Dot Superlattices

In the previous subsection the resonant optical reflection from a lateral array of QDs was calculated neglecting the overlap of the exciton envelope functions excited at different dots. Now we extend the theory allowing an exciton to tunnel coherently from one potential minimum to another [3.58].

We consider a QW with a periodic 2D potential $V(x,y) = V(x+a,y) = V(x,y+a)$ acting at an exciton like at a single particle. It has no effect on the exciton internal state, i.e., x, y are the in-plane coordinates of the exciton center-of-mass. Note that here a is the lateral period, not the QW thickness as in other parts of this book. For simplicity, we assume the potential $V(x,y)$ to have the point symmetry of a quadrate: $V(x,y) = V(\pm x,\pm y) = V(y,x)$. Due to the potential $V(x,y)$ the exciton energy spectrum is transformed from the parabolic dispersion $E_{\mathrm{exc}}(k_x,k_y) = \hbar^2(k_x^2+k_y^2)/(2M)$ in an ideal

QW with $V \equiv 0$ into a series of 2D minibranches (M is the exciton in-plane translational effective mass). The two-particle envelope function is written as

$$\Psi_{\rm exc}(\boldsymbol{r}_e, \boldsymbol{r}_h) = \psi(\boldsymbol{\rho}) F(\boldsymbol{\rho}_e - \boldsymbol{\rho}_h) \varphi_e(z_e) \varphi_h(z_h) \,. \tag{3.172}$$

Here the functions φ_e, φ_h describe one-particle quantization of an electron (e) and a hole (h) along the growth axis z, $\boldsymbol{\rho}_{e,h}$ is the position of the electron or hole in the interface plane, F describes the relative motion of the electron-hole pair within the exciton in an ideal QW in the absence of an additional lateral potential (in the following the $1s$-exciton level is considered), the envelope ψ is a function of the exciton center-of-mass position $\boldsymbol{\rho} = (x, y)$. It should be noted that one can neglect the effect of the lateral potential $V(\boldsymbol{\rho})$ on the exciton internal state if the effective 2D Bohr radius is small in the scale of the potential variation. We consider the lowest electron and hole subbands in a symmetric QW in which case $\varphi_e(z_e)$ and $\varphi_h(z_h)$ are even functions of z if the origin $z = 0$ is taken at the QW central plane.

Under normal incidence of the light the excitonic states are excited at the Γ point of the 2D Brillouin zone, $k_x = k_y = 0$. The envelopes, $\psi(\boldsymbol{\rho})$, of these states are enumerated by the discrete index ν. They are periodic with the SL period and can be expanded in the Fourier series

$$\psi^\nu(\boldsymbol{\rho}) = \frac{1}{a} \sum_{\boldsymbol{b}} c_{\boldsymbol{b}}^{(\nu)} \exp\left(\mathrm{i}\boldsymbol{b}\boldsymbol{\rho}\right) , \; c_{\boldsymbol{b}}^{(\nu)} = \frac{1}{a} \int_{\Omega_0} \psi^\nu(\boldsymbol{\rho}) \exp\left(-\mathrm{i}\boldsymbol{b}\boldsymbol{\rho}\right) d\boldsymbol{\rho} \tag{3.173}$$

over the space harmonics with the wave vectors equal to the 2D reciprocal vectors $\boldsymbol{b} = (2\pi/a)(l, m)$ introduced in (3.153). We choose the normalization condition

$$\int_{\Omega_0} |\psi|^2 \, dxdy = 1 \,,$$

where Ω_0 is the unit cell, say the area $-a/2 < x, y < a/2$. Thus, the expansion coefficients $c_{\boldsymbol{b}}$ satisfy the condition

$$\sum_{\boldsymbol{b}} |c_{\boldsymbol{b}}^{(\nu)}|^2 = 1 \,.$$

Moreover, taking into account that the states with $\nu \neq \nu'$ are orthogonal we obtain

$$\sum_{\boldsymbol{b}} c_{\boldsymbol{b}}^{(\nu)*} c_{\boldsymbol{b}}^{(\nu')} = \delta_{\nu\nu'} \,,$$

from which it also follows that

$$\sum_{\nu} c_{\boldsymbol{b}}^{(\nu)*} c_{\boldsymbol{b}'}^{(\nu)} = \delta_{\boldsymbol{b}\boldsymbol{b}'} \,. \tag{3.174}$$

Note that by an appropriate choice of the phase factors the Bloch functions at the Γ-point can be assumed real. Because of the high symmetry of the

potential $V(\boldsymbol{\rho})$, the coefficients $c_{\boldsymbol{b}}^{(\nu)}$ are also real and the asterisk in (3.174) can be omitted.

In bulk semiconductors with the allowed interband optical transitions, only s-excitons, $1s$, $2s$ etc., are allowed in the dipole approximation. Due to a similar reason, under normal incidence of the light upon the 2D lateral SL, the dipole-allowed excitonic states are invariant with respect to any operation from the point group of a quadrate (the representation Γ_1). In the following the index ν enumerates only such states. For them the coefficients $c_{\boldsymbol{b}}$ in (3.173) with the reciprocal vectors belonging to the same star β, see the definition of a star in the previous subsection, coincide and the index $\boldsymbol{b}$ in $c_{\boldsymbol{b}}$ can be replaced by β: $c_{\boldsymbol{b}} \equiv c_\beta$.

To complete the Maxwell equations we use the material relation (3.124) where the exciton contribution, $\boldsymbol{P}_{\rm exc}$, to the dielectric polarization is connected with the total electric field by

$$4\pi \boldsymbol{P}_{\rm exc}(\boldsymbol{r}) = æ_b \omega_{\rm LT} \pi a_{\rm B}^3 \sum_\nu \frac{\Psi^\nu_{\rm exc}(\boldsymbol{r},\boldsymbol{r})}{\omega_{0\nu} - \omega - {\rm i}\Gamma_\nu} \boldsymbol{\Lambda}_\nu \,, \tag{3.175}$$

$$\boldsymbol{\Lambda}_\nu = \int dz' \int_{\Omega_0} d\boldsymbol{\rho}'\, \Psi^\nu_{\rm exc}(\boldsymbol{r}',\boldsymbol{r}')\, \boldsymbol{E}(\boldsymbol{r}') \,.$$

Here $\omega_{0\nu}$ is the exciton resonance frequency in the state ν, the integration in the plane (x,y) is carried out over the unit cell Ω_0. In (3.175) we take into account a set of excitonic states, as distinct from (2.202) where the linear response contains only one pole.

By using the Green function approach we can express the amplitude, $\boldsymbol{E}_r$, of the normally reflected (backscattered) wave via the vectors $\boldsymbol{\Lambda}_\nu$

$$\boldsymbol{E}_r = {\rm i}\Gamma_0^{\rm QW} \sum_\nu \frac{c_0^{(\nu)} \eta_0}{\omega_{0\nu} - \omega - {\rm i}\Gamma_\nu}\, \boldsymbol{\Lambda_\nu} \,, \tag{3.176}$$

where $c_0^{(\nu)}$ is the expansion coefficient in (3.173) for $\boldsymbol{b} = 0$, the set of values $\boldsymbol{\Lambda}_\nu$ satisfies the system of linear equations

$$\boldsymbol{\Lambda}_\nu = \boldsymbol{\Lambda}^0_\nu + {\rm i} \sum_{\nu'} \boldsymbol{\Lambda}_{\nu'} \frac{\Gamma_{\rm QW}}{\omega_{0\nu} - \omega - {\rm i}\Gamma_\nu} [A_{\nu\nu'} + {\rm i}(B_{\nu\nu'} + C_{\nu\nu'})] \,. \tag{3.177}$$

Here

$$\boldsymbol{\Lambda}^0_\nu = \boldsymbol{E}_0 c_0^{(\nu)} \eta_0 \,,\ \eta_0 = \int \varphi_e(z)\varphi_h(z) \cos qz\, dz \,, \tag{3.178}$$

$\Gamma_{\rm QW}$ is the exciton radiative damping in an ideal QW given by (3.18),

$$A_{\nu\nu'} + {\rm i}B_{\nu\nu'} = \sum_{\beta\in B_1} n_\beta \frac{q}{q_\beta} \left(1 - \frac{\beta^2}{2q^2}\right) c_\beta^{(\nu)} c_\beta^{(\nu')} \left[\left(\frac{\eta_\beta}{\eta_0}\right)^2 + {\rm i} I_{\nu\beta}\right] \,, \tag{3.179}$$

$$C_{\nu\nu'} = -\sum_{\beta\in B_2} n_\beta \frac{q}{æ_\beta}\left(1-\frac{\beta^2}{2q^2}\right) c_\beta^{(\nu)} c_\beta^{(\nu')} J_{\nu\beta}\,, \tag{3.180}$$

$$\eta_\beta = \int \varphi_e(z)\varphi_h(z)\cos q_\beta z\, dz\,,$$

B_1, B_2 are subsets of the set of stars β introduced in (3.163) and satisfying the condition $|\boldsymbol{b}| < q$ or $|\boldsymbol{b}| > q$, respectively, n_β is the number of vectors in the star β, $q_\beta = \sqrt{q^2-\beta^2}$, $æ_\beta = \sqrt{\beta^2-q^2}$,

$$I_{\nu\beta} = \eta_0^{-2}\int\int dz dz' S_{eh}(z,z')\sin q_\beta|z-z'|\,,$$

$$J_{\nu\beta} = \eta_0^{-2}\int\int dz dz' S_{eh}(z,z')\mathrm{e}^{-æ_\beta|z-z'|}\,,$$

$$S_{eh}(z,z') = \varphi_e(z)\varphi_h(z)\varphi_e(z')\varphi_h(z')\,.$$

While deriving (3.179), (3.180) we took into account that the values of $b_x^2, b_y^2, b_x b_y$ averaged over the vectors $\boldsymbol{b} = (b_x, b_y)$ belonging to the star β are equal to $\beta^2/2, \beta^2/2$, 0, respectively.

For a function $\psi(\boldsymbol{\rho})$ belonging to a basis of any representation different from Γ_1 the coefficient $c_0^{(\nu)}$ is zero. Therefore, the reflection of the light wave is indeed mediated only by the invariant excitonic states Γ_1. Then the vectors $\boldsymbol{\Lambda}_\nu$, $\boldsymbol{\Lambda}_\nu^0$, $\boldsymbol{E}_r$ are parallel to $\boldsymbol{E}_0$ and we can replace the vectors in (3.176)–(3.178) by scalar amplitudes. Then, if we divide both parts of (3.176) by E_0, we find the reflection coefficient $r = E_r/E_0$.

If the spacing between resonant frequencies of optically active excitons exceeds the exciton damping then the reflection coefficient is a sum of individual terms

$$r_\nu(\omega) = \frac{\mathrm{i}\Gamma_{\mathrm{QW}} c_0^{(\nu)2}}{\tilde{\omega}_{0\nu} - \omega - \mathrm{i}(\Gamma_\nu + \Gamma_{0\nu})}\,, \tag{3.181}$$

where

$$\Gamma_{0\nu} = \Gamma_{\mathrm{QW}} \sum_{\beta\in B_1} c_\beta^{(\nu)2} n_\beta \frac{q}{q_\beta}\left(\frac{\eta_\beta}{\eta_0}\right)^2\left(1-\frac{\beta^2}{2q^2}\right)\,, \tag{3.182}$$

$$\tilde{\omega}_{0\nu} - \omega_{0\nu} = \Gamma_0^{\mathrm{QW}}(B_{\nu\nu} + C_{\nu\nu})\,. \tag{3.183}$$

In this case $\Gamma_{0\nu}$ is the total radiative damping rate of the exciton ν and $\tilde{\omega}_{0\nu}$ is its renormalized resonant frequency. It is worth to mention that for $2\pi/a > q$ the subset B_1 consists of one element $\boldsymbol{b} = 0$ while other reciprocal vectors belong to the subset B_2. In this particular case $\Gamma_{0\nu}$ equals to $\Gamma_{\mathrm{QW}} c_0^{(\nu)2}$. For the sake of convenience, we define the ν-exciton oscillator strength as

$$f_\nu = c_0^{(\nu)2} \tag{3.184}$$

because the squared coefficient $c_0^{(\nu)}$ enters into the numerator in (3.181). The sum of oscillator strengths is conserved because according to (3.174) one has

$$\sum_{\nu} c_0^{(\nu)2} = 1\,. \tag{3.185}$$

In the method of plane waves defined by (3.173) the Schrödinger equation reads

$$\left(\frac{\hbar^2\beta^2}{2M} - E\right) c_\beta + \sum_{\beta'} c_{\beta'} \sum_{\boldsymbol{b}'\in\beta'} V_{\boldsymbol{b}\boldsymbol{b}'} = 0\,, \tag{3.186}$$

$$V_{\boldsymbol{b}\boldsymbol{b}'} = \frac{1}{a^2}\int\int_{\Omega_0} V(x,y)\,\cos\left\{\frac{2\pi}{a}[(l'-l)x + (m'-m)y]\right\} dxdy\,.$$

Here E is the exciton energy referred to the bottom of the exciton band in an ideal QW, $\boldsymbol{b}' = (2\pi/a)(l', m')$ and we remind that $\beta^2 = (2\pi/a)^2(l^2+m^2)$.

As an example, we define the lateral potential as a periodic array of disks, namely,

$$V(x,y) = \sum_{n_1 n_2} v(x - n_1 a, y - n_2 a)\,, \tag{3.187}$$

$$v(x,y) \equiv v(\rho) = \begin{cases} -v_0\,, & \text{if} \quad \rho \le R \\ 0\quad, & \text{if} \quad \rho > R\,, \end{cases}$$

where n_1, n_2 are integers and $\rho = \sqrt{x^2+y^2}$. Then one has

$$V_{lm,l'm'} = -v_0 \frac{R}{a}\,\frac{\mathrm{J}_1\left(2\pi\sqrt{(l'-l)^2+(m'-m)^2}\,R/a\right)}{\sqrt{(l'-l)^2+(m'-m)^2}}\,, \tag{3.188}$$

where $\mathrm{J}_1(t)$ is the Bessel function. The result of calculation is convenient to present in the dimensionless variables

$$\varepsilon = \frac{E}{E_0}\,,\; u_0 = \frac{v_0}{E_0}\,,\; \mu = \frac{R}{a}\,, \quad \text{where} \quad E_0 = \frac{\hbar^2}{2M}\left(\frac{2\pi}{R}\right)^2\,. \tag{3.189}$$

Figures 3.7 and 3.8 represent calculations of E_ν and f_ν as functions of u_0 and R/a for the four lowest excitonic states. The sum of f_ν over ν = 1-4 is shown by curves 5 in Figs. 3.7b and 3.8b. Since this sum is close to unity in the whole range of u_0 up to 1.2 and of R/a from 0 up to 0.5, we conclude that the oscillator strengths for excitons with $\nu > 4$ is negligible. The dotted curves in Fig. 3.7 and 3.8 are calculated in the tight-binding approximation while the dashed curves illustrate calculation in the approximation of almost free excitons.

In an ideal QW, i.e. for $u_0 = 0$, the dimensionless energy of the exciton ν equals $\mu^2\tilde{\beta}^2$ and possesses the values 0, μ^2, $2\mu^2$, $4\mu^2$... , the optically active is only the exciton $\nu = 1$. This agrees with the behavior of curves in Fig. 3.7 as u_0 tends to zero. For $u_0 \neq 0$, the lateral potential mixes the space harmonics belonging to different stars. As a consequence the states ν = 2-4 become optically active. Because of the sum rule (3.185) the oscillator strength is redistributed from the exciton $\nu = 1$ to other excitons. One can see from

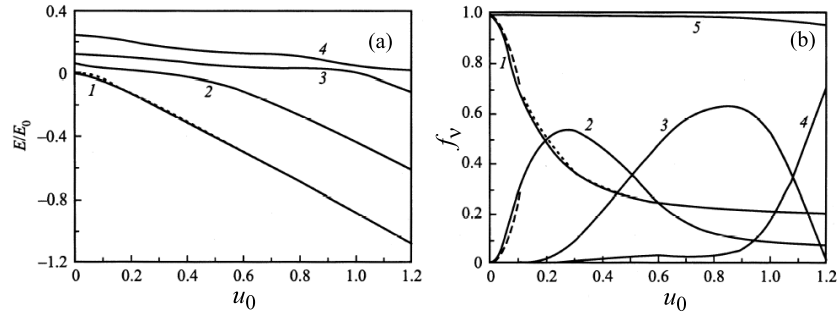

Fig. 3.7. The energy (**a**) and the oscillator strength (**b**) vs. the relative depth, u_0, of the potential disc for four lower exciton states in a 2D SL. The index $\nu = 1 - 4$ enumerates the optically-active exciton Bloch states with $k_x = k_y = 0$. The calculation is performed for the lateral array of quantum discs of the radius $R = a/4$. *Solid* curves, the exact calculation in the method of plane waves; *dotted* curves, calculation of E_1 (**a**) and f_1 (**b**) in the tight-binding approximation. *Dashed* curves 1 and 2 in (**b**) are obtained in the approximation of almost free excitons. Curve 5 in (**b**) represents the sum of f_ν over the four lowest energy states. [3.58]

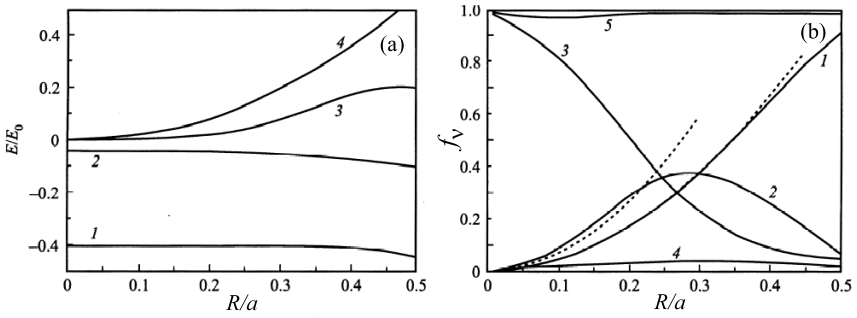

Fig. 3.8. Dependence of energy E_ν (**a**) and the oscillator strength f_ν (**b**) on the ratio R/a for the exciton states $\nu = 1 - 4$ in a 2D SL with an array of quantum discs. The calculation is performed for the relative depth $u_0 = 0.5$. The index ν enumerates the exciton Bloch states with $k_x = k_y = 0$; curve 5 in (**b**) represents the sum of f_ν over the four lowest energy states. Dotted curves 1 and 2 in (**b**) are obtained by using the tight-binding approximation. [3.58]

Fig. 3.7b that up to $u_0 = 0.25$ this redistribution occurs only in favor of the state $\nu = 2$. This phenomenon can be interpreted as anticrossing of the states 1 and 2 with increasing u_0. For large enough periods, the exciton states $\nu = 1, 2$ with negative values of E are bound-like, they can be approximated by the tight-binding functions

$$\psi^\nu(x, y) = \sum_{n_1 n_2} \varphi_\nu(x - la, y - ma) \,,$$

where $\varphi_\nu(x,y)$ are the normalized excitonic functions localized at a single potential $V(\boldsymbol{\rho})$ and characterized by the uniaxial symmetry. Another important point to be mentioned is that for large a, i.e. for small ratios R/a, the oscillator strength for the exciton $\nu = 3$ is prevailing or, in other words, the state $\nu = 3$ is free-like, it is close to the free exciton state in an ideal QW which is described by (3.173) with $c_0 = 1$, $c_{lm} = 0$ if $l \neq 0$ or/and $m \neq 0$ and, therefore, $f = 1$. With increasing R/a the oscillator strength is redistributed in favor of the bound-like states $\nu = 1$ and $\nu = 2$. This redistribution can be used for a qualitative analysis of "stealing oscillator strength" from neutral excitons X to charged excitons X^- mentioned by Kheng et al. [2.129] (as far as we ignore that the electrons filling the conduction band are not distributed periodically in the interface plane). Anyway the lateral SL allows to analyze a co-existence of bound- and free-like exciton states for different values of the disk potential depth and ratio R/a.

3.3 Electro-Optics of Nanostructures

Here we briefly discuss effects of an applied electric field $\boldsymbol{F}$ on optical properties of nanostructures. The effect of an in-plane electric field, $\boldsymbol{F}_\parallel \parallel (x,y) \perp z$, on free carriers and excitons in QW structures is similar to that in a bulk semiconductor, namely, free carriers contribute to the dc electric current and the bound excitonic state becomes nonstationary in moderate electric fields. In order to estimate the corresponding value of $F_\parallel$ we take into account that, in an electric field, the potential energy of an electron-hole pair changes by

$$-e\,\boldsymbol{F}_\parallel \cdot (\boldsymbol{\rho}_e - \boldsymbol{\rho}_h)\,, \tag{3.190}$$

where $\boldsymbol{\rho}_{e,h}$ is the electron or hole in-plane position. Now either of the particles (primarily that with the lower mass) can tunnel through the Coulomb barrier. For $1s$-exciton the height of the barrier is the exciton Rydberg E_B and its width is estimated as $\varDelta x \sim (E_\mathrm{B}/|e|F_\parallel)$. One can therefore write for the halfwidth $\varGamma$ of the exciton bound state

$$-\ln \varGamma \propto \frac{\varDelta x}{a_\mathrm{B}} \propto \frac{E_\mathrm{B}}{|e|F_\parallel a_\mathrm{B}}\,.$$

The broadening of the exciton absorption peak determined by $\varGamma$ occurs in fields of $F \sim (E_\mathrm{B}/|e|a_\mathrm{B}) \sim (10^3 - 10^4)$ V/cm where no noticeable shift of the absorption peak is observed to occur.

In a field applied perpendicularly to interfaces, $\boldsymbol{F}_\perp \perp (x,y) \parallel z$, the electron transport in a SQW structure is suppressed at all. In a periodic MQW structure with thick enough barriers transport along the normal to the layers can occurs due to incoherent hopping from one well to another and, thus, is rather hindered. In this case the height of the barrier for the tunnelling dissociation of excitons equals the potential barrier V. This keeps

the excitonic states well defined up to $F_\perp \sim (V/|e|a) \sim 10^5$ V/cm although the exciton level is meanwhile red-shifted by values comparable and even exceeding the 2D-exciton Rydberg. This is the so-called *quantum-confined Stark effect*, see the next subsection. As for SLs with the 3D character of charge-carrier motion, the increasing electric field leads to the free-carrier localization along the growth direction of the SL (Sect. 3.4.2). Sect. 3.4.3 is devoted to modification of the Pockels effect due to the quantum-confinement and interface-induced in-plane anisotropy of heterostructures.

3.3.1 Quantum-Confined Stark Effect

The electric-field induced change of the 2D-exciton excitation energy consists of three contributions

$$\Delta E_{\rm exc} = \delta E_{e1} + \delta E_{h1} - \delta\varepsilon \,, \tag{3.191}$$

where $\delta E_{e1,h1}$ is the change of single-particle confinement energy and $\delta\varepsilon$ is the change of the exciton binding energy. The Stark shift (3.191) mainly comes from the first two contributions.

At low fields, $|eF|a \ll (\hbar^2/2m^*)(\pi/a)^2$, the electron (or hole) level shift δE_ν is quadratic in the field $F \equiv F_z$. It can be found from the second-order perturbation theory. For the lowest level $\nu = 1$ one obtains

$$\delta E_1 = -\sum_{\nu\neq 1} \frac{(eFz_{\nu 1})^2}{E_\nu - E_1} \,, \tag{3.192}$$

where $z_{\nu 1}$ is the matrix element of the coordinate z and E_ν are the energies of unperturbed states. In symmetric QWs they have a definite parity and therefore only even ν contribute to the sum (3.192). Moreover, estimations show that the term with $\nu = 2$ is determinative and

$$\delta E_1 \approx -\frac{(eFz_{21})^2}{E_2 - E_1} \,.$$

For infinitely high barriers $z_{21} = (4/3\pi)^2 a$, $E_2 - E_1 = 3E_1$ and $E_1 = (\hbar^2/2m^*)(\pi/a)^2$ and we obtain the estimation

$$\delta E_1 \approx -C\frac{(eFa)^2}{E_1} \,, \qquad C = \frac{1}{3}\left(\frac{4}{3\pi}\right)^4 \,.$$

The factor $C = 0.0108295...$ slightly differs from the exact result

$$C = \left(\frac{15}{\pi^2} - 1\right)\frac{1}{48} = 0.0108152...$$

obtained in the limit of infinitely high barriers, $V_{e,h} \to \infty$.

For arbitrary values of the electric field one must solve the following Schrödinger equation

$$\left(-\frac{\hbar^2}{2m^*_{e,h}}\frac{d^2}{dz^2}+V(z)\pm|e|Fz-E_{e,h}\right)\varphi(z)=0\,, \tag{3.193}$$

where the sign $\pm$ and indices e,h correspond to an electron and a hole, respectively, and the Stark shifts $\delta E_{e1},\delta E_{h1}$ are given by the differences between $E_{e,h}$ and E_{e1}, E_{h1}. Airy's functions $\mathrm{Ai}(X)$ and $\mathrm{Bi}(X)$ are two linearly independent solutions of this equations. Thus, inside the QW its general solution has the form

$$\varphi(z)=c_1\mathrm{Ai}(X)+c_2\mathrm{Bi}(X)\,,\ X=\left(\frac{2m^*_{e,h}|e|F}{\hbar^2}\right)^{1/3}\left(\pm z-\frac{E_{e,h}}{|e|F}\right)\,. \tag{3.194}$$

Note that Airy's function $\mathrm{Ai}(X)$ is defined as

$$Ai(X)=\frac{1}{\pi}\int_0^\infty\cos\left(uX+\frac{u^3}{3}\right)du\,.$$

The asymptotic representations of the two functions are as follows

$$\mathrm{Ai}(X\to+\infty)\to\frac{1}{2\sqrt{\pi}X^{1/4}}\exp\left(-\frac{2}{3}X^{3/2}\right),$$

$$\mathrm{Bi}(X\to+\infty)\to\frac{1}{2\sqrt{\pi}X^{1/4}}\exp\left(\frac{2}{3}X^{3/2}\right)$$

and

$$\mathrm{Ai}(X\to-\infty)\to\frac{1}{\sqrt{\pi}|X|^{1/4}}\sin\left(\frac{2}{3}|X|^{3/2}+\frac{\pi}{4}\right),$$

$$\mathrm{Bi}(X\to-\infty)\to\frac{1}{\sqrt{\pi}|X|^{1/4}}\cos\left(\frac{2}{3}|X|^{3/2}+\frac{\pi}{4}\right).$$

For a high electric field the lower levels in a QW with infinitely high barriers are determined by the transcendental equation

$$\mathrm{Ai}\left[-\left(\frac{2m^*|eF|}{\hbar^2}\right)^{1/3}\left(\frac{a}{2}+\frac{E}{|eF|}\right)\right]=0 \tag{3.195}$$

or

$$E_{e,h}=-\frac{1}{2}|eF|a+\mu\left(\frac{(eF\hbar)^2}{2m^*_{e,h}}\right)^{1/3}\,,$$

where $\mu\approx 2.338;\ 4.088;\ 5.520...$ are the roots of equation $\mathrm{Ai}(-\mu)=0$. The variational function, $\varphi=2\alpha^{3/2}z\mathrm{e}^{-\alpha z}$, used frequently in the case of a triangle

potential yields for the lowest-level energy the coefficient $\mu = 2.47$, which differs from the exact value by less than 6%.

The equations presented for the limit $V_{e,h} \to \infty$ overestimate the Stark effect shifts. In a real system, e.g., in a $GaAs/Al_{0.35}Ga_{0.65}As$ QW, the quantum-confined Stark effect shifts the lowest electron and hole states in the field $F = 10^5$ V/cm by 6 and 15 meV, for a 100 Å-thick QW, and by 55 and 81 meV for $a = 250$ Å [3.59].

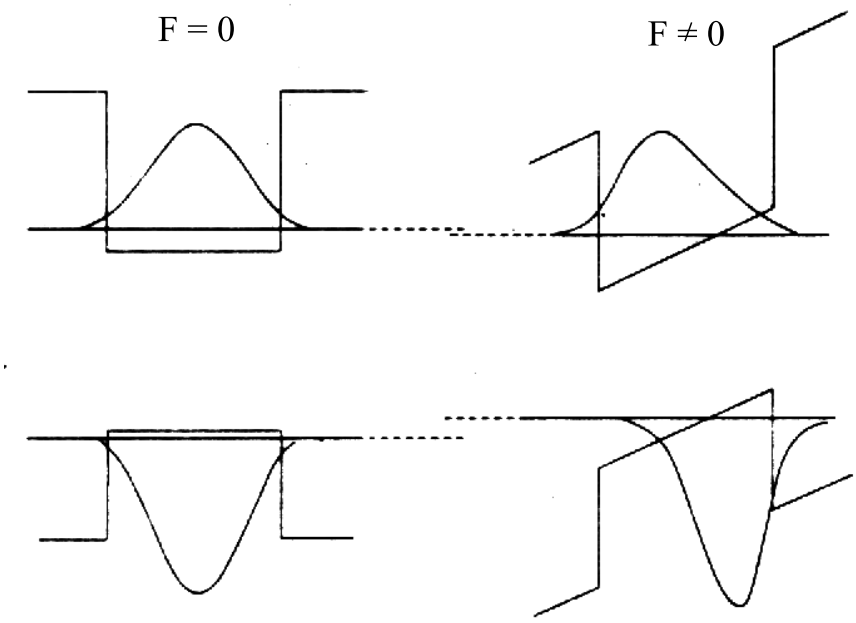

Fig. 3.9. Schematic representation of electron (*above*) and hole (*below*) wave functions for the lowest confined states in the absence of ($\boldsymbol{F} = 0$) and with ($\boldsymbol{F} \neq 0$) electric field parallel to z.

At the same time, the envelope wave functions $\varphi_{e,h}(z)$ undergo deformation, as is shown schematically in Fig. 3.9. In low fields, $|eF|a \ll E_1$, the level shift is quadratic in F while the shift of the center of mass $\bar{z}_{e,h} \propto F$. The existence of barriers prevents the breakup of the exciton. As the field increases, the electron and the hole are pressed towards to the opposite interfaces and both δE_1 and $\bar{z}$ saturate. While the electron and hole binding energy in the exciton is decreased, its change $\delta\varepsilon$ is small compared to the sum of single-particle shifts, $\delta E_{e1} + \delta E_{h1}$. In contrast to the binding energy of the exciton, its oscillator strength does not saturate with increasing the electric field because the overlap integral $\int \varphi_e(z)\varphi_h(z)dz$ vanishes in the limit of very

strong electric fields. The oscillator strength of the $e1$-$h1$ exciton decreases monotonously. On the other hand, the $v\nu \to c\nu'$ interband transitions, forbidden in the absence of an electric field by parity conservation, become allowed. In weak fields, the oscillator strength is proportional to F^2 for the transitions $v2 \to e1$ and $v1 \to e2$.

3.3.2 Stark Ladder in a Superlattice

In 1960, Wannier [3.60] predicted that when subjected to a uniform electric field the continuous energy bands in perfect crystals would pass into discrete, evenly spaced subbands forming a ladder. Since then this phenomenon is known as the *Wannier-Stark localization*, and the ladder-like spectrum is called the *Stark* (or *Wannier-Stark*) *ladder*. However, the field-induced localization could be reliably observed and investigated only in semiconductor SLs with a period exceeding by far the microscopic lattice constant.

The formation of a Stark ladder in a SL is easier perceived in the framework of tight-binding description valid when the overlap of the single-QW wave functions in the neighboring wells is small and the electron wave function in the SL can be written in the form

$$\varphi(z) = \frac{1}{\sqrt{NS}} \exp\left(\mathrm{i}\boldsymbol{K}_{\parallel} \cdot \boldsymbol{\rho}\right) \sum_n C_n \varphi_n(z) \,. \tag{3.196}$$

Here $\boldsymbol{K}_{\parallel}$ is the in-plane electron wave vector, d is the period of the SL, n labels the wells, $\varphi_n(z) = \varphi(z - nd)$, $\varphi(z)$ is the envelope function of the quantum-confined state $e\nu$ in a single QW centered at $z = 0$ (in the following $\nu = 1$), S is the in-plane area and N is the total number of periods in the regular structure. The tight-binding coefficients satisfy the following set of linear equations

$$IC_{n-1} + E_0 C_n + IC_{n+1} = EC_n \,, \tag{3.197}$$

where E is the electron energy, $E_0 \equiv E_{e1}$ is the quantum-confinement energy in a single QW, and I is the transfer integral between nearest neighbors. If we disregard the difference of electron effective masses in the well and barrier materials it has the form

$$I = -V \int_{-a/2}^{a/2} \varphi(z)\varphi(z \pm d)dz \tag{3.198}$$

and is negative for the $\nu = 1$ state. For the Bloch solutions in an unperturbed SL the coefficients C_n are given by $C_n = \exp\left(\mathrm{i}K_z dn\right)$ and the electron miniband has a cos-like dispersion

$$E(K_z) = E_0 + 2I \cos K_z d \,. \tag{3.199}$$

Thus, in the tight-binding approximation the miniband width Δ is equal to $4|I|$. This approximation is applicable if the width is small compared to the energy difference between the subbands $\nu = 2$ and $\nu = 1$. For small $K_z d$ we can expand the cosine function and approximate $E(K_z)$ by $E^0 + (\hbar^2 K_z^2/2M)$ where $E^0 = E_0 - 2|I|$ and the normal effective mass $M \equiv M_{zz}$ is connected with I by

$$M = \frac{\hbar^2}{2|I|d^2} \,. \tag{3.200}$$

The application of the electric field $\boldsymbol{F} \parallel z$ contributes a linear term $|e|Fz$ to the electron Hamiltonian. In terms of the tight-binding description this means that the diagonal single-particle energy E_0 is replaced by $E_0 + |e|Fdn$ and (3.197) transform to

$$I(C_{n-1} + C_{n+1}) + (E_0 + |e|Fdn - E)C_n = 0 \,, \tag{3.201}$$

or

$$\frac{-2I}{|e|Fd}(C_{n-1} + C_{n+1}) = 2\left(n + \frac{E_0 - E}{|e|Fd}\right) C_n \,,$$

or, in the dimensionless variables,

$$x(C_{n-1} + C_{n+1}) = 2(n - \lambda)C_n \,,$$

where $x = 2|I|/(|e|Fd)$, $\lambda = (E - E_0)/|e|Fd$. Let us recall that the Bessel functions satisfy the recurrent relations

$$x[y_{\mu-1}(x) + y_{\mu+1}(x)] = 2\,\mu\, y_\mu(x) \,. \tag{3.202}$$

Hence, the solution for C_n can be presented as [3.61]

$$C_n = D_1 \mathrm{J}_{n-\lambda}(x) + D_2 \mathrm{N}_{n-\lambda}(x) \,. \tag{3.203}$$

Since the Neumann function $\mathrm{N}_\mu(x)$ tends to ∞ for $\mu \to \infty$, we have to set $D_2 = 0$. The Bessel function $\mathrm{J}_{n-\lambda}(x)$ is limited for $n \to -\infty$ if λ is an integer. Denoting this integer by n_0 and the corresponding electron energy by E_{n_0} we obtain

$$C_n \propto \mathrm{J}_{n-n_0}\left(\frac{2|I|}{|e|Fd}\right) \text{ and } E_{n_0} = E_0 - eFdn_0 \,. \tag{3.204}$$

Thus, each electron miniband in the SL splits into a series of subbands separated by $|eF|d$. The spread of the electron wave function along the growth direction is governed by the parameter

$$\mathcal{N}_F = \frac{\Delta}{|eF|d} \,. \tag{3.205}$$

The quantum number n_0 indicates the QW where the probability to find an electron in the state (3.204) is the highest. As one moves away from this

well the probability decreases but remains non-negligible within $\mathcal{N}_F$ QWs, if $\mathcal{N}_F \gg 1$, or within a single n_0-th well, if $\mathcal{N}_F < 1$ (strong-localization limit). Another important parameter, $\mathcal{N}'_F$, is the ratio between the spacing $|eF|d$ and the energy uncertainty $\hbar/\tau_p$, where τ_p is the electron relaxation time for available scattering mechanisms. In a SL, by definition, the free-path or coherence length $l = v\tau_p$ exceeds the period d. At small fields, $\mathcal{N}'_F \ll 1$, the Stark ladder can be ignored and the electric field causes the conventional dissipative transport of miniband electrons. In the opposite limit, $\mathcal{N}'_F \gg 1$, the Stark-ladder levels are well defined and can be observed in the optical spectra.

In a GaAs/Al_xGa_{1-x}As SL, for $a = 40$ Å, $b = 20$ Å, $x = 0.35$ the width of the lowest electron miniband $\Delta \sim 0.07$ eV, and the parameter $\mathcal{N}_F$ is of the order of unity at $F \sim 10^5$ V/cm. Figure 3.10 presents experimental spectra of the photocurrent induced in a GaAs/AlGaAs SL at various electric fields. Being proportional to the absorption spectra, the photocurrent spectra show strong oscillations periodic in the reciprocal of the electric field. Therefore the absorption spectra reveal not only one intra-well transition but rather a series of transitions

$$E_{n_0 n'_0} = E_{00} + (n_0 - n'_0)|e|Fd \tag{3.206}$$

between conduction- and valence-band Wannier-Stark states of indices n_0 and n'_0, respectively. The interband optical transitions are illustrated in Fig. 3.11. At zero or small fields, $\mathcal{N}'_F \ll 1$, the absorption edges correspond to the difference between the bottom of the conduction miniband and the top of the valence minibands, see the transitions T_1 and T_2 involving heavy- and light-hole delocalized states. At moderate electric fields where $\mathcal{N}'_F \gg 1$ but yet $\mathcal{N}_F \gg 1$, see sketch in Fig. 3.11b, the electronic wave functions are localized but extend over $\mathcal{N}_F$ periods. Usually, in this regime the heavy holes are practically localized in one well. It follows then from (3.204) that the oscillator strength for the optical transition $hh1, n'_0 \to e1, n_0$ is proportional to $\mathrm{J}^2_{n_0 - n'_0}(\mathcal{N}_F/2)$ and is remarkable up to $|n_0 - n'_0|d = \mathcal{L}$ where $\mathcal{L}$ is the Wannier-Stark localization length

$$\mathcal{L} = \mathcal{N}_F d = \frac{\Delta}{|eF|} \,. \tag{3.207}$$

In a high electric field the electron states in neighboring wells are so widely separated in energy ($\mathcal{N}_F \ll 1$) that the electron is localized within one QW, the coefficients C_n for $n \neq n_0$ are negligible, overlap integrals for the $n'_0 \neq n_0$ interband transitions become very small, and only the intrawell transitions can be observed in the photocurrent spectrum, see the lower curve in Fig. 3.10 and Fig. 3.11c. Note that for very high fields the interminiband Zener tunneling becomes appreciable and gives rise to an additional broadening of the Wannier-Stark levels.

The Wannier-Stark localization is a phenomenon interpreted in terms of the energy levels and the electron packet spreading in real space. The

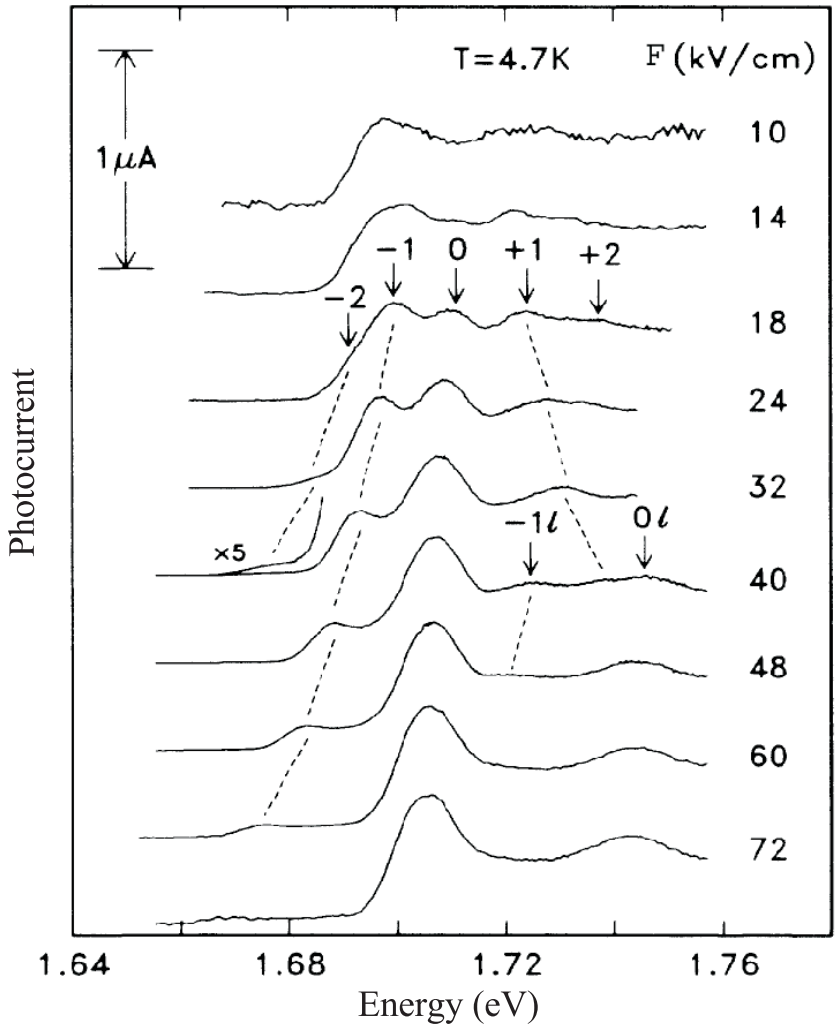

Fig. 3.10. Low-temperature spectra in the GaAs/$Al_{0.35}Ga_{0.65}As$ SL for different electric fields $\boldsymbol{F} \parallel z$. For convenience, the spectra are displaced vertically with respect to one another. The numbers refer to the peaks corresponding to $hhn' \rightarrow e1n$ transitions ($n - n' = 0, \pm 1, \pm 2...$) in the moderate fields. Analogous transitions from light holes are denoted by $0l$ and $-1l$. From [3.62].

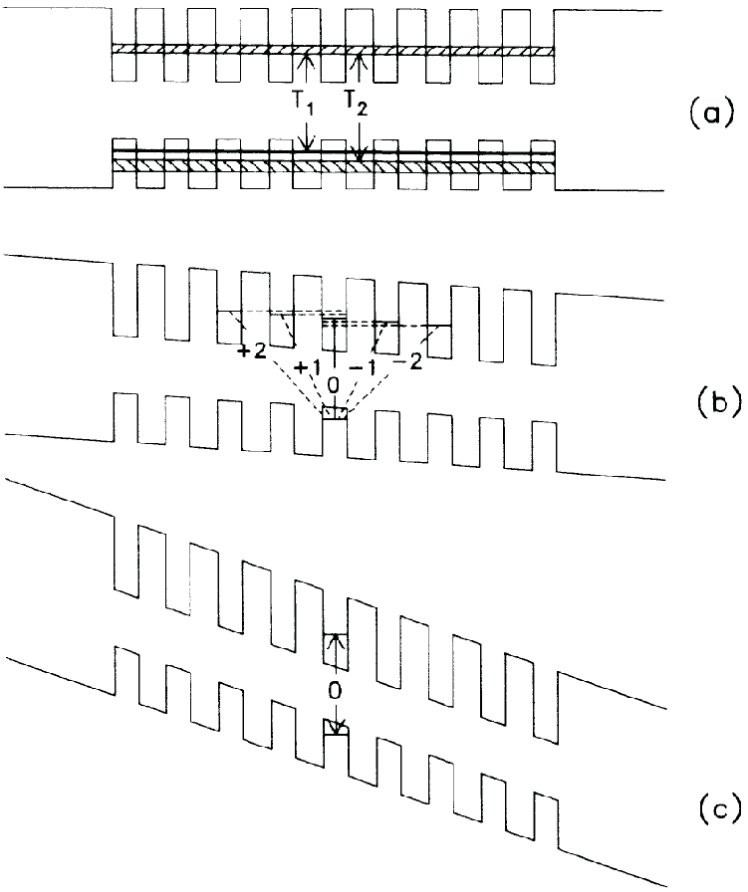

Fig. 3.11. Sketches of the conduction- and valence-band potential profiles for the GaAs/$Al_xGa_{1-x}As$ SL under a small (**a**), moderate (**b**), and high (**c**) electric field. From [3.62].

Bloch oscillations is another manifestation of the electric-field effect on free charges where observable values are measured as a function of time, see [3.63] and references therein. This manifestation can be better visualized if one uses the gauge $\boldsymbol{A} = (0, 0, -Fct)$, where c is the light velocity, and considers nonstationary solutions of the Schrödinger equation

$$i\hbar\frac{\partial\psi}{\partial t} = E\left(K_z + \frac{|e|A_z}{\hbar c}\right)\psi = E\left(K_z - \frac{|e|Ft}{\hbar}\right)\psi\,,$$

where the miniband dispersion $E(K_z)$ is a periodic function of the electron wave vector in a SL, see (3.199). The solution can be written as

$$\psi(t) = c \exp\left[-\frac{\mathrm{i}}{\hbar}\int\limits_0^t E\left(K_z - \frac{|e|Ft'}{\hbar}\right)dt'\right].$$

The electron motion is periodic with the period

$$\mathcal{T} = \frac{2\pi}{d}\frac{\hbar}{|eF|}\,.$$

Since the electron velocity is $v = \hbar^{-1}\,\partial E/\partial K_z = -(|e|F)^{-1}\,\partial E/\partial t$, the total distance passed from the minimum to maximum (or from left to right) at $K_z = 0, F > 0$ is

$$\mathcal{L} = \frac{1}{|e|F}\int\limits_0^{T/2}\frac{\partial E}{\partial t}dt = \frac{\Delta}{|eF|}$$

which coincides with the Wannier-Stark localization length defined by (3.207). Obviously, the Bloch oscillations can be also understood as quantum beats in a system of split levels (Chap. 5).

In addition to the clear physical interpretation, the tight-binding approximation can be used as an effective tool in the quantum-mechanical engineering. The first example can be the Stark ladder states in a semi-infinite SL. In this case $n = 0, 1, 2...$ and the boundary condition is $C_{-1} = 0$ because QWs with $n = -1, -2...$ are taken away. The solution for C_n can be presented as $C_n = D_1 \mathrm{J}_{n-\lambda}(x)$. In order to have nontrivial solutions the following equation for λ needs to be satisfied

$$\mathrm{J}_{-1-\lambda}(x) = 0\,.$$

We showed above that, for an infinite regular SL, the numbers $\lambda \equiv n_0$ are integers and the Stark ladder is equidistant. For the semi-infinite SL, the values of λ differ from integers and the set of the first few levels is not equidistant.

Two other examples are a semi-infinite SL with a wider terminating QW [3.64, 3.65] and a non-periodic finite SL with a miniband formed at a certain electric field F_{cr} [3.66, 3.67]. In the latter structure the series a_n, b_n of the successive layer thicknesses ($n = 1, 2 \cdots N$) satisfy the relations

$$E^0_{n+1} = E^0_n - |e|F_{\mathrm{cr}}\left(\frac{a_n + a_{n+1}}{2} + b_n\right),\ I_{n,n+1} = I\,, \tag{3.208}$$

where E^0_n is the diagonal energy in the n-th QW, $I_{n,n+1}$ is the transfer integral between n-th and $n+1$-th QWs. The values of a_1 (or E^0_1), F_{cr} and transfer integral I are chosen arbitrarily while other thicknesses $(b_1, a_2, b_2, \cdots)$ are found recursively from the above equations. At $F = F_{\mathrm{cr}}$, all single-QW levels $E_n = E^0_n + |e|F\overline{z}_n$, are equalized ($\overline{z}_n$ is the center of the n-th QW). Since all transfer integrals are chosen to be identical, the miniband of discrete levels,

$$E(k) = E^0_1 + 2I\cos\frac{\pi m}{N+1},\ m = 1, 2 \cdots N, \tag{3.209}$$

is formed just as in the case of a finite ideal SL in zero electric field.

3.3.3 Quantum-Confined Pockels Effect

The electric field $\boldsymbol{E}\|[001]$ applied to a bulk zinc-blende semiconductor results in a linear-in-field birefringence with the principal axes of the dielectric permittivity tensor oriented along the three directions $[1\bar{1}0]$, [110], and [001]. This is the well-known *Pockels effect*. Two mechanisms of the Pockels effect in QW structures were discussed in [3.68]. One of them involves uniaxial strain $u_{xy} \propto E$ ($x\|[100]$, $y\|[010]$) induced by the electric field (*piezoelectric effect*), and the mixing of heavy- and light-hole states induced by this strain, i.e., a contribution to function $G(z)$ in (3.116) and to the overlap integral I_2 proportional to u_{xy}. The second mechanism is purely electronic in nature, namely, one has to take into account that the interband matrix element of the momentum operator $\langle c, s, \boldsymbol{k}|\boldsymbol{e}\cdot\boldsymbol{p}|v, m, \boldsymbol{k}\rangle$ in a semiconductor of the T_d class contains terms linear in the electron wave vector $\mathbf{k}$. For $\boldsymbol{k}\|z$ we have

$$\begin{aligned}\langle c, 1/2, k_z|\boldsymbol{e}\cdot\boldsymbol{p}|v, 3/2, k_z\rangle &= -Pe_+ - Qk_ze_- \,, \\ \langle c, -1/2, k_z|\boldsymbol{e}\cdot\boldsymbol{p}|v, -3/2, k_z\rangle &= Pe_- - Qk_ze_+ \,,\end{aligned} \tag{3.210}$$

where $\mathbf{e}$ is the light-polarization unit vector, $e_\pm = e_x \pm \mathrm{i}e_y$, and P and Q are constants. When calculating the optical anisotropy by the envelope-function method, k_z has to be replaced by the operator $-\mathrm{i}d/dz$. In the lowest order in the small parameters I_2/I_1 and $Q/(aP)$ we obtain instead of (3.122)

$$\rho = \frac{2}{\sqrt{3}}\frac{I_2}{I_1} - \frac{2Q}{aP}\frac{I_3}{I_1} \,, \tag{3.211}$$

where $I_3 = a\int dz\,\varphi_{e1}(z)\,dF/dz$, and the factor a is introduced for the sake of convenience so that the quantities I_1, I_2, I_3 have the same dimension. In an electric field, the envelope $F(z)$ becomes asymmetrical even for $t_{l\text{-}h}^{L,R} = 0$, and the integral I_3 is nonzero.

Besides the above two bulk mechanisms, in QWs with $t_{l\text{-}h}^{\mathrm{L}}$, $t_{l\text{-}h}^{\mathrm{R}} \neq 0$, there is an additional mechanism of the Pockels effect, which involves the interfaces [3.69]. Indeed, an electric field changes the values of the envelope function $G(z)$ at the interfaces, and, as follows from (3.117), this results in a change in (3.116) of the extent of admixture of the $|\Gamma_8, \mp 1/2\rangle$ to $|\Gamma_8, \pm 3/2\rangle$ states, and, hence, to a change in the overlap integral I_2.

We have been assuming until now that the potential barriers at the C′A′/CA and CA/C′A′ interfaces are the same. But in a general case for C≠C′ and A≠A′ the effective dipole moments corresponding to the C-A′ and C′-A bonds are different, so that the difference between the band offsets V_L and V_R at the left- and right-hand interfaces may be as high as 50–100 meV [3.43]. At equilibrium, this difference generates a built-in electric field which equalizes the electrochemical potential and leads to an electric-field-induced contribution to the anisotropy. Application of a positive or negative external field F increases or compensates the built-in field and the dependence of ρ on F becomes asymmetric [3.45].

It is known that in zinc-blende lattice heterostructures, at $\boldsymbol{k} = 0$, the second heavy-hole $hh2$ and the lowest light-hole $lh1$ subbands at $\boldsymbol{k} = 0$ lie close to each other and far from other quantum-confined states crossing at a particular thickness $a_{\rm cr}$. Therefore even a small mixing perturbation can result in a remarkable modification of the interband optical matrix elements from these two valence subbands. We first consider this particular mixing in the absence of an external electric field. If the mixing is neglected, only one of the envelope functions φ_m in (3.114) is nonzero for the states $(hh2, \pm 3/2)$ and $(lh1, \pm 1/2)$ at $\boldsymbol{k} = 0$. It is given by

$$\varphi_{hh2}(z) = C_h \begin{cases} \sin k_h z\,, & \text{if } |z| \le \frac{a}{2}\,, \\ \pm \sin\phi_h \exp\left[-æ_h\left(|z| - \frac{a}{2}\right)\right], & \text{if } |z| \ge \frac{a}{2} \end{cases}$$

for the states $(hh2, \pm 3/2)$, and

$$\varphi_{lh1}(z) = C_l \begin{cases} \cos k_l z\,, & \text{if } |z| \le \frac{a}{2}\,, \\ \cos\phi_l \exp\left[-æ_l\left(|z| - \frac{a}{2}\right)\right], & \text{if } |z| \ge \frac{a}{2} \end{cases}$$

for the states $(lh1, \pm 1/2)$. According to (2.15), the normalization coefficients are

$$C_h = \left[\frac{a}{2}\left(1 - \frac{\sin k_h a}{k_h a} + \frac{1 - \cos k_h a}{2æ_h a}\right)\right]^{-1/2},$$
$$C_l = \left[\frac{a}{2}\left(1 + \frac{\sin k_l a}{k_l a} + \frac{1 + \cos k_l a}{2æ_l a}\right)\right]^{-1/2},$$

$\phi_h = k_h a/2$, $\phi_l = k_l a/2$ and $k_h, k_l, æ_h, æ_l$ are expressed via the hole quantum-confinement energies E^0_{hh2}, E^0_{lh1} and satisfy the standard equations

$$\cot\phi_h = -\frac{m^{\rm A}_{hh}}{m^{\rm B}_{hh}}\frac{æ_h}{k_h}\,,\ \tan\phi_l = \frac{m^{\rm A}_{lh}}{m^{\rm B}_{lh}}\frac{æ_l}{k_l}\,,$$

see (2.14) and (2.12), respectively. The Γ_8-hole Hamiltonian contains a specific contribution

$$H_{l\text{-}h} = \frac{\hbar^2}{\sqrt{3}m_0 a_0}\{J_x J_y\}_s\Big[\, t^{\rm R}_{l\text{-}h}\,\delta(z - z_{\rm R}) \,- t^{\rm L}_{l\text{-}h}\,\delta(z - z_{\rm L})\Big], \tag{3.212}$$

describing the heavy-light hole mixing. Then the coupling matrix element is derived as

$$\langle hh2, \pm 3/2|H_{l\text{-}h}|lh1, \mp 1/2\rangle = \tag{3.213}$$
$$\frac{\hbar^2}{2m_0 a_0}\left[t^{\rm L}_{l\text{-}h}\varphi_{hh2}(z_{\rm L})\varphi_{lh1}(z_{\rm L}) - t^{\rm R}_{l\text{-}h}\varphi_{hh2}(z_{\rm R})\varphi_{lh1}(z_{\rm R})\right],$$

where $z_{\rm L,R}$ is the coordinate of the left or right interface. In the two-level approximation, the energies of the mixed states labelled as h_+ and h_- are given by

$$E_{h_\pm} = \frac{1}{2}\left(E^0_{hh2} + E^0_{lh1}\right) \pm W \,, \tag{3.214}$$

where

$$W = \sqrt{\bar{\Delta}^2 + \bar{V}^2}\,,\ \bar{\Delta} = \frac{1}{2}\left(E^0_{hh2} - E^0_{lh1}\right)$$

and $\bar{V}$ is the modulus of the coupling matrix element (3.213).

Since at zero electric field the optical transitions $hh2 \to e1$ are forbidden the matrix element $M_{e1,h_\pm}$ is proportional to the admixture of the $lh1$ state in the $h_\pm$ hybrid. It follows then that the relative squared matrix element $Q(e1\text{–}\,h_\pm) = |M_{e1,h_\pm}/M_{e1,lh1}|^2$ can be written as

$$Q(e1\text{–}\,h_-) = \frac{W + \bar{\Delta}}{2W}\,,\ Q(e1\text{–}\,h_+) = \frac{W - \bar{\Delta}}{2W}\,. \tag{3.215}$$

Thus, in the vicinity of the crossing point the both transitions are allowed and the sum of $Q(e1\text{–}\,h_-)$ and $Q(e1\text{–}\,h_+)$ should be constant and equal to unity. However, in the considered two-band approximation and at zero electric field the both transition rates are uniaxially symmetrical.

Winkler [3.70] applied a multiband $\boldsymbol{k}\cdot\boldsymbol{p}$ Hamiltonian and reproduced the essential details of experimental absorption spectra. However a weak electric field in the growth direction was assumed in order to make $e1$-$hh2(1s)$ excitons dipole-allowed and describe the $e1$-$hh2$ spectral peak observed by Reynolds et al. [3.71]. The above considerations remove the restrictions [3.72, 3.73] imposed on the selection rules for the exciton angular momentum. In particular, due to the $hh2$-$lh1$ mixing not only $2p$ but also $1s$ excitons $e1$-$hh2$ or $e2$-$lh1$ become dipole active and can contribute to the optical spectra [3.71, 3.74] even in the absence of electric fields. It should be mentioned that Schulman and Chang [3.75, 3.76] solved the tight-binding model and reported for the first time the mixing of heavy- and light-hole states with $\boldsymbol{k} = 0$ in the (001)-grown zinc-blende-lattice heterostructures.

In the presence of an electric field the envelopes $\varphi_m(z)$ lose particular parity and both the $hh2 \to e1$ and $lh1 \to e1$ transitions from the unmixed valence states are allowed. In this case the mixing due to the Hamiltonian (3.212) leads to an in-plane anisotropy of the optical transitions from the split states $h_\pm$. This is another manifestation of the quantum-confined Pockels effect for resonating transitions $e1$-$hh2$ and $e1$-$lh1$. The above band-to-band description gives a reasonable understanding of the experimental observations, but misses the role of excitons which obviously affect the shape of absorption spectra in high-quality samples. In particular, a significant discrepancy between band-to-band calculations and experiment was systematically observed in the vicinity of the nearly degenerated $e1$-$lh1$ and $e1$-$hh2$ transitions to the $e1$ conduction-electron subband [3.77]. It is shown in [3.69] that, for the resonating $hh2$ and $lh1$ subbands, the related excitonic states are also strongly coupled by the interface Hamiltonian $H_{l\text{-}h}$, which explains the discrepancy. A theoretical model developed in [3.69] in the perturbative scheme, see (3.212, 3.213), shows quantitative agreement with experimental results.

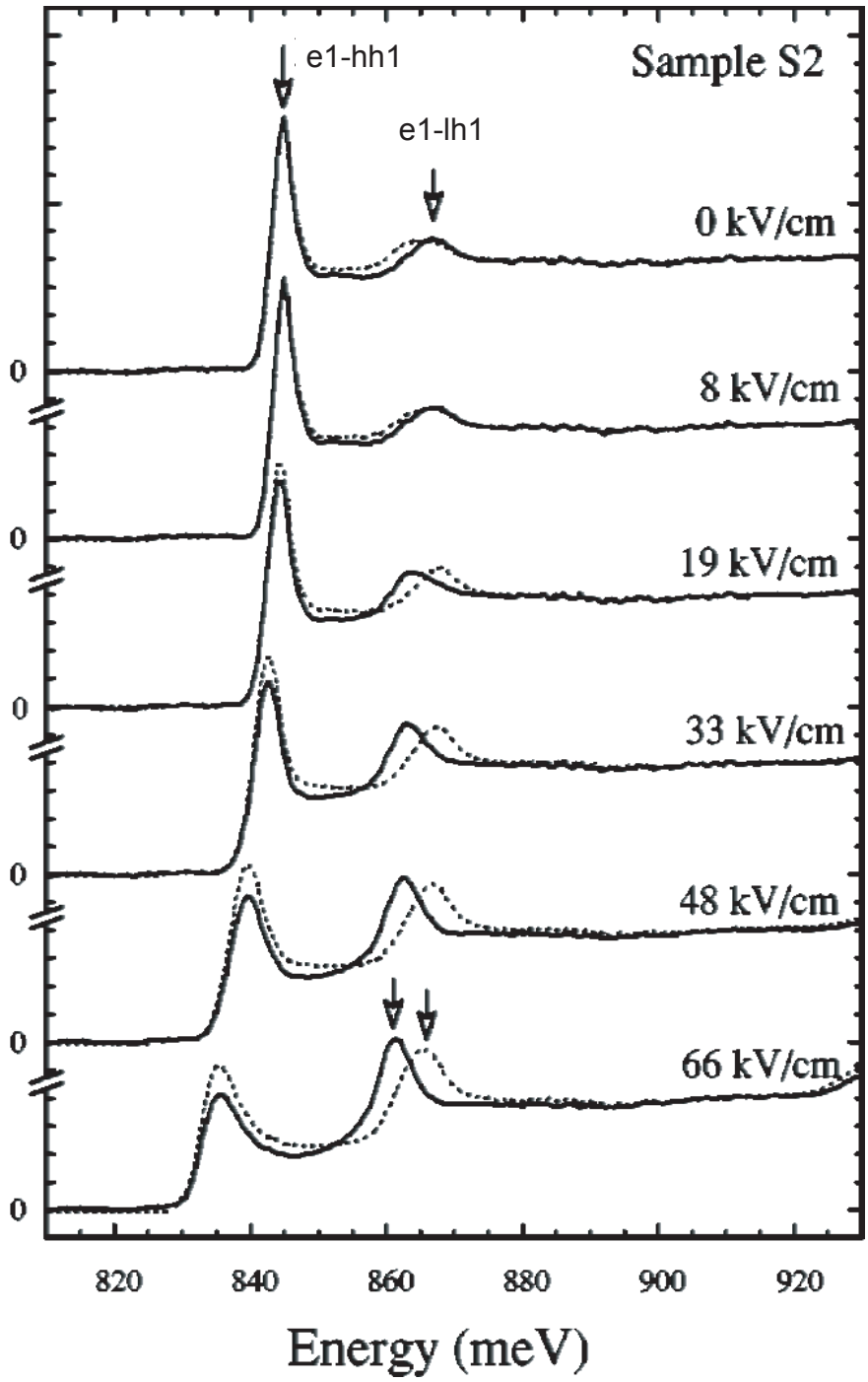

Fig. 3.12. Polarization-resolved absorption spectra of $In_xGa_{1-x}As/InP$ MQWs (a = 100 Å) measured for different electric fields at 77 K. The incident light is polarized along the [110] (solid line) and [$\bar{1}$10] (dashed line) eigenaxes of the sample. Besides the usual features of the quantum confined Stark effect (red-shift of the $e1$-$hh1$ transition, redistribution of the total oscillator strength), a large optical anisotropy develops in the $e1$-$lh1$ region. At high fields, one can distinguish a doublet of excitonic transitions, split by 6 meV and almost 100 % polarized. From [3.69].

Absorption spectra of $In_xGa_{1-x}As$(100 Å)/InP(80 Å) MQWs with $x = 0.83$ measured for linear polarizations parallel to [110] and [1$\bar{1}$0] directions and various applied voltages are displayed in Fig. 3.12. The most obvious part of the experimental results displayed in Fig. 3.12 is the classical scenario of the quantum-confined Stark effect: redshift of the absorption edge, associated with decrease of its absorption strength, and appearance of the $e1$-$hh2$ transition which was parity forbidden at zero field. The red-shifts and weak broadening of the transitions when increasing the bias show that the field is quite homogeneous through the MQWs. The second effect which can be observed in Fig. 3.12 is the variation of polarization properties related to the quantum-confined Pockels effect . One can see that the $e1$-$hh1$ exciton is also weakly polarized at zero field and gains some polarization (up to 10 %) at large field. A strong polarization feature develops in the region of the $e1$-$hh2$ and $e1$-$lh1$ transitions, revealing two optical resonant transitions with orthogonal linear polarizations.

Figures 3.13(a-d) are confined to on the region of $e1$-$hh2$ and $e1$-$lh1$ excitons at fields larger than 19 kV/cm, where the quantum-confined Pockels effect dominates over the zero-field contributions to the in-plane anisotropy. There are two observations allowing one to adjust the theoretical simulation to the experimental spectra. Firstly, the excitonic peak intensities are clearly redistributed as the electric field increases, so that the intensities of the two peaks equalize at $\sim$ 30 kV/cm. Secondly, the energy distance between the peaks decreases with increasing the field. According to (3.215) the oscillator strengths of the split excitonic transitions are equal at the field matching the crossing of the unmixed $e1$-$hh2$ and $e1$-$lh1$ excitonic levels. The respective transition energies are plotted in Fig. 3.13e by dotted curves. The theoretical absorption spectra were calculated as a sum of both excitonic and continuum contributions related to three transitions to the conduction subband $e1$ from the lowest valence subband $hh1$ and two higher valence subbands originating from the mixing of $lh1$ and $hh2$ states. The inhomogeneous spectral broadening was introduced by means of a Gaussian distribution function with the broadening factor taken the same for both of the split polarized excitonic transitions and their respective continuum contributions. As seen in Fig. 3.13, a satisfactory fit of the spectral shape is achieved, especially at large fields where the quantum-confined Pockels effect is the dominant contribution to the in-plane anisotropy. The simulation results allowed to estimate the matrix element of the heavy-light-hole mixing operator (3.212) as a function of the electric field. In particular, this matrix element decreases from 2.9 meV at 19 kV/cm to 1.9 meV at 66 kV/cm. As a result, we can determine simultaneously both of the $t^{\mathrm{L}}_{l\text{-}h}$ and $t^{\mathrm{R}}_{l\text{-}h}$ parameters which enter into (3.212). By using a standard least-square optimization algorithm, the values of $t^{\mathrm{L}}_{l\text{-}h} = 1.7 \pm 0.1$ and $t^{\mathrm{R}}_{l\text{-}h} = 0.1 \pm 0.1$ were obtained. The left and right interfaces appear to be not symmetrical (D_{2d} symmetry requires $t^{\mathrm{L}}_{l\text{-}h}$ and $t^{\mathrm{R}}_{l\text{-}h}$ to be equal) which is consistent with the small (but nonzero) anisotropy of the $e1$-$hh1$ transition

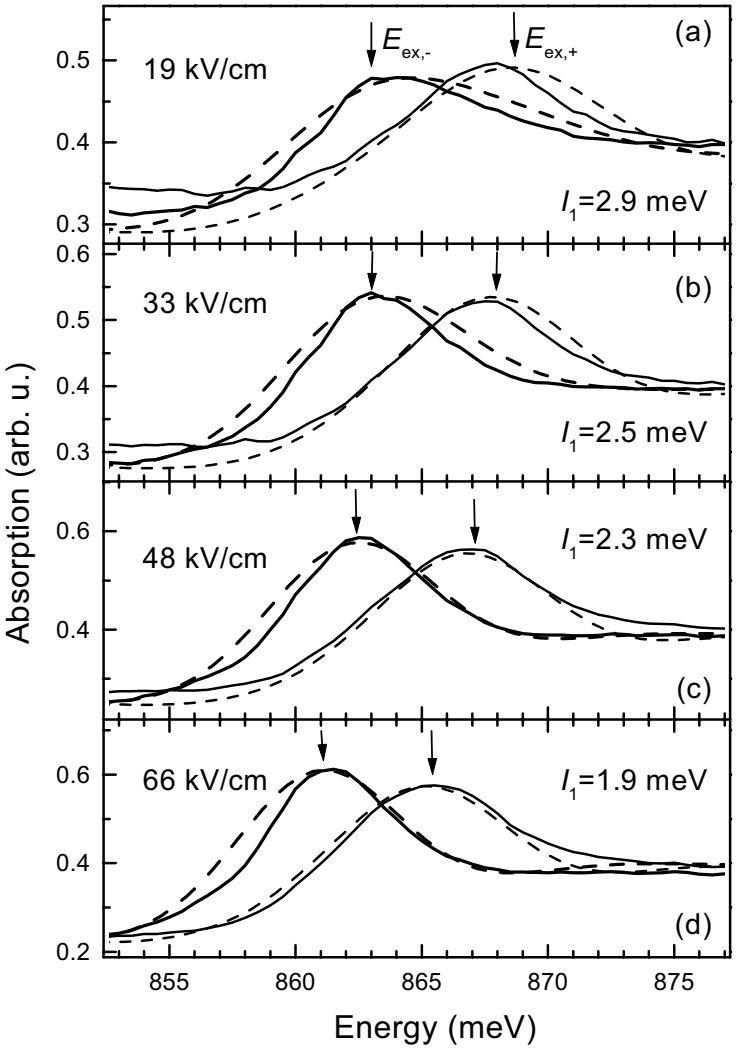

Fig. 3.13. Polarization-resolved absorption spectra of the $In_xGa_{1-x}As/InP$ sample in the region of $e1$-$hh2$ and $e1$-$lh1$ transitions. Figures (**a**)-(**d**) correspond to different fields. The incident light is polarized along the [110] (gray curves) and [$\bar{1}$10] (black curves) eigenaxes of the sample. Continuous lines display experimental data, whereas simulation results are represented by dashed lines. [3.69]

at zero-field. Yet, note that the estimated anisotropy of the $e1$-$hh1$ transition is small enough ($< 4 \div 5\%$) to justify the disregard of this effect as compared to the quantum-confined Pockels effect observed in the vicinity of $e1$-$hh2$ and $e1$-$lh1$ excitons. Going back to the structural properties of the studied QWs, it has been found that the stronger interface potential is associated to the left interface which corresponds to the interface "InGaAs grown on InP".

3.4 Magneto-Optics of Nanostructures

3.4.1 Magneto-Excitons in Quantum Well Structures

In the effective mass approximation, the exciton Hamiltonian in an external magnetic field $\boldsymbol{B}$ can be presented as a sum, $\mathcal{H}_{\rm exc}^{(0)} + \mathcal{H}_{\rm exc}^{(1)} + \mathcal{H}_{\rm exc}^{(2)}$, of the unperturbed Hamiltonian and terms linear and quadratic in $\boldsymbol{B}$, respectively. Weak magnetic-field effects are calculated by perturbation theory assuming the parameter

$$\beta = \frac{\hbar\omega_c}{2E_{\rm B}} = \frac{a_{\rm B}}{\lambda_B} \tag{3.216}$$

to be small, where $\omega_c = (|e|B/\mu_\parallel c)$ is the cyclotron frequency for the electron-hole in-plane reduced effective mass $\mu_\parallel$, $E_{\rm B}$ and $a_{\rm B}$ are the exciton binding energy and Bohr radius, $\lambda_B = (\hbar c/|e|B)^{1/2}$ is the magnetic length. For $\beta \ll 1$, the first-order term $\mathcal{H}_{\rm exc}^{(1)}$ leads to the splitting of excitonic spin sublevels (the Zeeman effect) while the second-order term gives a diamagnetic shift $\Delta E_{\rm dia} \propto B^2$. In the opposite limiting case of very strong magnetic fields, $\beta \gg 1$, the cyclotron motion of free carriers is quantized forming the Landau levels, the carrier motion is effectively reduced from 3D to 1D and the Coulomb interaction is considered as a perturbation. Then the interband optical transitions are those with coinciding Landau quantum numbers, $N_c = N_v$, and the band gaps

$$E_{cv,N} = E_g + \left(N + \frac{1}{2}\right)\hbar\omega_c\,, \tag{3.217}$$

where $N = 0, 1, 2...$ Moreover, the magnetic field increases the exciton binding energy and oscillator strength and, as a result, the absorption spectrum contains a series of excitonic peaks linked to the energies $E_{cv,N}$. Such quasi-1D electron-hole excitations differ substantially from conventional 3D excitons and are called *diamagnetic excitons* [3.78]. The contribution of continuum electron-hole excitations to the absorption results in an asymmetrical shape of each absorption peak.

In QW structures the motion of carriers along the growth direction z is quantized and, therefore, in a strong magnetic field $\boldsymbol{B} \parallel z$ their states become localized in all three directions. The density of states in this case is a sum of δ-functions, each of them corresponding to a separate 0D excitation. For the same reason, the absorption spectrum consists of separate peaks whose width

is determined by the homogeneous and inhomogeneous broadening. Since the broadening occurs equally towards higher and lower energies, the interband magneto-optical absorption peaks in QWs have symmetric shape [3.79].

The Zeeman effect will be considered in the next subsection and in Chap. 5. Here we ignore the exciton fine structure and concentrate on the diamagnetic effect in a QW structure subjected to a magnetic field $\boldsymbol{B} \parallel z$. In the approximate numerical calculation of the $e\nu$-$h\nu$ exciton envelope function, the separation ansatz

$$\Psi^{\mathrm{exc}} = F(\boldsymbol{\rho}_e, \boldsymbol{\rho}_h)\varphi_{e1}(z_e)\varphi_{h1}(z_h) \tag{3.218}$$

is used where the envelope $F(\boldsymbol{\rho}_e, \boldsymbol{\rho}_h)$ satisfies the Schrödinger equation with the Hamiltonian

$$\begin{aligned}\mathcal{H}_{\mathrm{exc}} &= E_g + E_{e\nu} + E_{h\nu} + V_C(\boldsymbol{\rho}_e - \boldsymbol{\rho}_h) \\ &+ \frac{1}{2m_e}\left[-\mathrm{i}\hbar\frac{\partial}{\partial\boldsymbol{\rho}_e} - \frac{e}{c}\boldsymbol{A}(\boldsymbol{\rho}_e)\right]^2 + \frac{1}{2m_h}\left[-\mathrm{i}\hbar\frac{\partial}{\partial\boldsymbol{\rho}_h} + \frac{e}{c}\boldsymbol{A}(\boldsymbol{\rho}_h)\right]^2 .\end{aligned} \tag{3.219}$$

Here $E_{e\nu}$, $E_{h\nu}$ are the quantum-confinement energies, V_C is the effective 2D Coulomb potential

$$V_C(\rho) = -\frac{e^2}{æ}\int\int dz_e dz_h \frac{\varphi_{e1}^2(z_e)\varphi_{h1}^2(z_h)}{\sqrt{\rho^2 + (z_e - z_h)^2}} ,$$

and we use the gauge

$$\boldsymbol{A} = \frac{1}{2}\,\boldsymbol{B} \times \boldsymbol{\rho} \tag{3.220}$$

for the vector potential. The two-particle eigenfunctions can be sought in the form [3.80]

$$F(\boldsymbol{\rho}_e, \boldsymbol{\rho}_h) = \exp\left[\frac{\mathrm{i}}{\hbar}\,\boldsymbol{R}_\parallel \cdot \left(\boldsymbol{P} - \frac{e}{c}\,\boldsymbol{B} \times \boldsymbol{\rho}\right)\right] \exp\left(\mathrm{i}\frac{\gamma}{2\hbar}\,\boldsymbol{\rho} \cdot \boldsymbol{P}\right) f(\boldsymbol{\rho} - \boldsymbol{\rho}_0) , \tag{3.221}$$

where $\boldsymbol{\rho} = \boldsymbol{\rho}_e - \boldsymbol{\rho}_h$, $\boldsymbol{R}_\parallel$ is the in-plane center of mass, $\boldsymbol{P}$ is the generalized 2D momentum of the exciton and

$$\boldsymbol{\rho}_0 = \frac{\lambda_B^2}{\hbar}\left(\frac{\boldsymbol{B}}{B} \times \boldsymbol{P}\right) , \; \gamma = \frac{m_h - m_e}{m_h + m_e} .$$

For the $e\nu$-$h\nu$ excitons, the envelope function of the relative motion satisfies the equation

$$\begin{aligned}E f(\boldsymbol{\rho}) = \Bigg[&E_g^{(\nu)} + \frac{\boldsymbol{P}^2}{2M_\parallel} - \frac{\hbar^2}{2\mu_\parallel}\Delta_{\boldsymbol{\rho}} + \frac{e^2B^2}{8\mu_\parallel c^2}\rho^2 \\ &- \frac{\mathrm{i}e\gamma}{2\mu_\parallel c}\boldsymbol{B} \cdot \left(\boldsymbol{\rho} \times \frac{\partial}{\partial\boldsymbol{\rho}}\right) + V_C(\boldsymbol{\rho} + \boldsymbol{\rho}_0)\Bigg] f(\boldsymbol{\rho}) ,\end{aligned} \tag{3.222}$$

where $M_{\parallel} = m_e + m_h$, $E_g^{(\nu)} = E_g + E_{e\nu} + E_{h\nu}$, and

$$\Delta_{\boldsymbol{\rho}} = \frac{\partial^2}{\partial x^2} + \frac{\partial^2}{\partial y^2} \,.$$

In the following we consider only axially-symmetric excitonic states excited under normal incidence, set their in-plane momentum $\boldsymbol{P}$ and the $\boldsymbol{P}$-dependent shift $\boldsymbol{\rho}_0$ to zero and seek solutions independent of the azimuth angle of the 2D vector $\boldsymbol{\rho}$, $f(\boldsymbol{\rho}) \equiv f(\rho)$. This also allows to throw away the term in (3.222) proportional to γ and reduce $\Delta_{\boldsymbol{\rho}}$ to

$$\frac{1}{\rho}\frac{\partial}{\partial\rho}\left(\rho\frac{\partial}{\partial\rho}\right) \,.$$

In the weak-field limit, the diamagnetic shift for the s-excitonic states with angle-independent $f(\boldsymbol{\rho})$ is given by

$$\Delta E_{\rm dia} = \frac{\pi}{4}\frac{e^2B^2}{\mu_{\parallel}c^2}\int f^2(\rho)\rho^3\,d\rho \tag{3.223}$$

with $f(\rho)$ calculated at zero field.

In the very strong magnetic field, the function of the relative motion for axially-symmetric excitons can be approximated by

$$f_N(\rho) = \frac{1}{\sqrt{2\pi}\,N!\,\lambda_B}\;\; \mathrm{L}_N\left(\frac{\rho^2}{2\lambda_B^2}\right)\;\; \exp\left(-\frac{\rho^2}{4\lambda_B^2}\right), \tag{3.224}$$

where $\mathrm{L}_N(x) \equiv \mathrm{L}_N^0(x)$ is Laguerre polynomial

$$\mathrm{L}_N(x) = \mathrm{e}^x\frac{d^N}{dx^N}\left(\mathrm{e}^{-x}x^N\right) \,.$$

The exciton excitation energy is written as

$$E = E_g^{(\nu)} + \left(N + \frac{1}{2}\right)\hbar\omega_c - \varepsilon \,, \tag{3.225}$$

where ε is the exciton binding energy which in this approximation is just the energy of the Coulomb interaction in the state (3.224) given by the triple integral

$$\varepsilon_{N,\nu} = \frac{e^2}{æ}\int\limits_0^{\infty} 2\pi\rho d\rho \int\limits_{-\infty}^{\infty}\int\limits_{-\infty}^{\infty} dz_e dz_h \frac{f^2(\rho)\varphi_{e\nu}^2(z_e)\varphi_{h\nu}^2(z_h)}{\sqrt{\rho^2 + (z_e - z_h)^2}} \,.$$

Analytical results are allowed in the limit of infinitely high barriers, narrow QWs and ultra-high magnetic field such as

$$a < \lambda_B < a_{\mathrm{B}} \, .$$

Then one can obtain [3.80, 3.81]

$$\varepsilon_{N,\nu} = D_N \frac{e^2}{æ\lambda_B} \, , \tag{3.226}$$

where the dimensionless parameters D_N tend to constant values with decreasing the ratio a/λ_B, particularly $D_0 \to (\pi/2)^{1/2}$ [3.80]. Thus, the energy (3.225) increases linearly with B due to the Landau quantization and has a negative contribution proportional to $\sqrt{B}$ due to the Coulomb interaction.

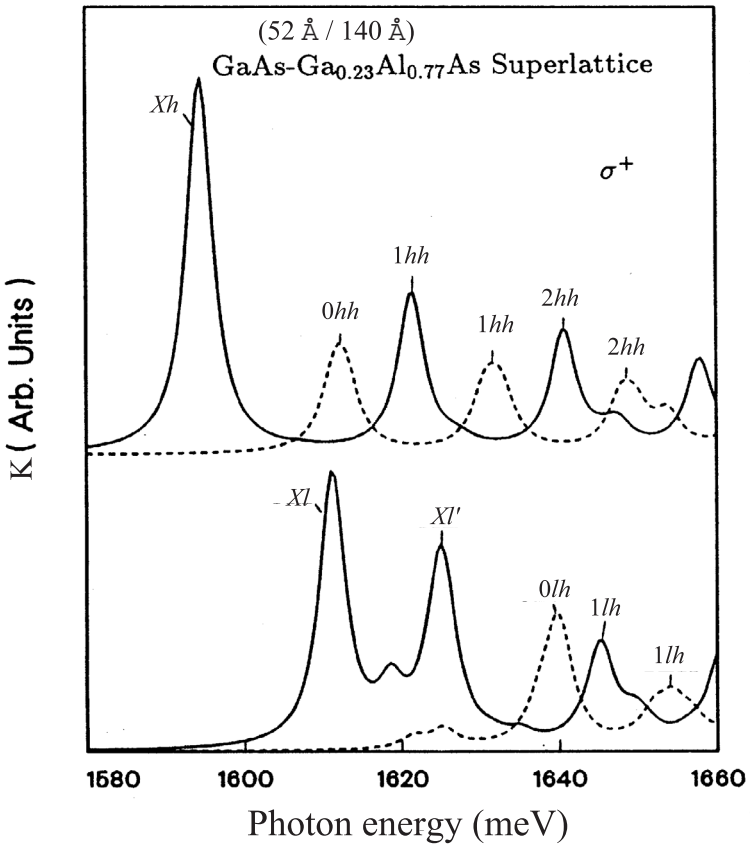

Fig. 3.14. Absorption spectra of periodic $\mathrm{GaAs/Al}_x\mathrm{Ga}_{1-x}\mathrm{As}$ heterostructure with $a = 52$ Å, $b = 140$ Å calculated for the magnetic field $B = 10$ T for σ_+ polarization with (*solid*) and without inclusion (*dotted*) of the exciton effects. The upper and lower curves describe the contributions to absorption coming from the $hh1 \to e1$ and $lh1 \to e1$ transitions, respectively. From [3.86].

Three comments concerning the above consideration are relevant. For intermediate magnetic fields where the parameter β in (3.216) is comparable with unity the exciton states can be found only numerically, see, e.g., [3.82–3.85]. Secondly, the separation (3.218) neglects any electron-hole correlation along the z axis. This correlation can be approximately taken into account keeping the separation (3.218) where the single-particle envelopes are found self-consistently from the Schrödinger equations where the confinement potential has a contribution dependent on $f(\rho)$ [3.81]. Thirdly, the exciton states can be substantially modified because of the heavy-light-hole mixing described by the Luttinger Hamiltonian. Figure 3.14 illustrates a sophisticated calculation of magnetoabsorption spectra in MQWs performed neglecting and taking into account the Coulomb interaction [3.86]. The inclusion of this interaction shifts the absorption peaks to lower energies and results in a redistribution of oscillator strength between the peaks. The lower peaks are labelled by Xh and Xl rather than by $0hh$ and $0lh$, since the corresponding states contain a remarkable admixture of other Landau levels. The anomalous peak Xl' arises due to a strong admixture of the $0lh$ Landau level to heavy-hole states with a nonzero component of the orbital moment.

3.4.2 Polarized Reflection Spectra in an External Magnetic Field

Before we go into details of polarized optical reflection let us remind some characteristics of the polarized electromagnetic wave. This information will be useful in other chapters as well. We consider a transverse quasi-monochromatic electromagnetic wave with the electric field

$$\boldsymbol{E}(t) = \boldsymbol{E}_0(t)\mathrm{e}^{-\mathrm{i}\omega t} + \boldsymbol{E}_0^*(t)\mathrm{e}^{\mathrm{i}\omega t}\,,$$

where $\boldsymbol{E}_0(t)$ is the amplitude slowly varying in time, the vector $\boldsymbol{E}$ is assumed to be perpendicular to the propagation axis 3. We define the polarization density matrix as the time-averaged products

$$d_{\alpha\beta} = \langle E_{0,\alpha}E_{0,\beta}^*\rangle \;\; (\alpha,\beta = 1,2)\,.$$

If the light intensity is defined as $I = \langle |E_1|^2 + |E_2|^2\rangle$ then the density matrix can be presented in the form

$$\hat{d} = \frac{I}{2}\begin{bmatrix} 1+P_l & P_{l'} - \mathrm{i}P_c \\ P_{l'} + \mathrm{i}P_c & 1-P_l \end{bmatrix}\,. \tag{3.227}$$

Here the Stokes parameters

$$P_c = \frac{I_+ - I_-}{I_+ + I_-}\,,\; P_l = \frac{I_1 - I_2}{I_1 + I_2}\,,\; P_{l'} = \frac{I_{1'} - I_{2'}}{I_{1'} + I_{2'}} \tag{3.228}$$

are, respectively, the degrees of circular polarization, of linear polarization in the axes $1,2$ and of linear polarization in the axes $1',2'$ rotated around the axis 3 by 45^o with respect to the axes $1,2$.

The above density matrix is written in the basis of the linearly polarized components $\boldsymbol{E} = E_1\boldsymbol{e}_1 + E_2\boldsymbol{e}_2$, where $\boldsymbol{e}_1, \boldsymbol{e}_2$ are the unit vectors along 1 and 2. Note that, in the basis of circular polarized components

$$\boldsymbol{E} = E_+\boldsymbol{e}_+ + E_-\boldsymbol{e}_- \,,\; \boldsymbol{e}_\pm = \frac{\boldsymbol{e}_1 \pm \mathrm{i}\boldsymbol{e}_2}{\sqrt{2}} \tag{3.229}$$

the density matrix has the form

$$\hat{d}^{(c)} = \frac{I}{2}\begin{bmatrix} 1+P_c & P_l - \mathrm{i}P_{l'} \\ P_l + \mathrm{i}P_{l'} & 1-P_c \end{bmatrix} . \tag{3.230}$$

This is demonstrated by applying the relations

$$\boldsymbol{e}_1 = \frac{1}{\sqrt{2}}(\boldsymbol{e}_+ + \boldsymbol{e}_-) \,,\; \boldsymbol{e}_2 = -\frac{\mathrm{i}}{\sqrt{2}}(\boldsymbol{e}_+ - \boldsymbol{e}_-) \,, \tag{3.231}$$

$$\boldsymbol{e}_{1'} = \frac{1}{\sqrt{2}}(\boldsymbol{e}_1 + \boldsymbol{e}_2) = \frac{1-\mathrm{i}}{2}\boldsymbol{e}_+ + \frac{1+\mathrm{i}}{2}\boldsymbol{e}_- \,.$$

Thus, say, for $\boldsymbol{E} \parallel \boldsymbol{e}_1$ or $\boldsymbol{E} \parallel \boldsymbol{e}_{1'}$ we have respectively

$$\hat{d}^{(c)} = \frac{I}{2}\begin{bmatrix} 1 & 1 \\ 1 & 1 \end{bmatrix} \text{ and } \hat{d}^{(c)} = \frac{I}{2}\begin{bmatrix} 1 & -\mathrm{i} \\ \mathrm{i} & 1 \end{bmatrix} .$$

A magnetic field applied in the Faraday configuration, $\boldsymbol{B} \parallel z$, induces a difference between the amplitude reflection coefficients, r_+ and r_-, for the σ_+ and σ_- circularly-polarized light normally incident on a (001)-grown QW structure. As a result, under reflection the normally-incident and linearly-polarized light exhibits a rotation of the polarization plane and gains an ellipticity. The first effect, the Faraday rotation in reflection geometry, is also known as the *polar Kerr effect*. As will be shown below, in the exciton resonance frequency region this difference appears mainly due to the Zeeman splitting of the exciton radiative level into two circularly-polarized sublevels. If the initial light $\boldsymbol{E}_0$ is polarized along the axis 1 then, according to (3.231), the amplitude of the reflected light is equal to

$$\boldsymbol{E}_r = \frac{\boldsymbol{E}_0}{\sqrt{2}}(r_+\boldsymbol{e}_+ + r_-\boldsymbol{e}_-) = \frac{\boldsymbol{E}_0}{\sqrt{2}}\, r_+ \left(\boldsymbol{e}_+ + \frac{r_-}{r_+}\boldsymbol{e}_-\right)$$

The Faraday angle under reflection is readily calculated as

$$\theta = \frac{1}{2}\arg\left\{\frac{r_-}{r_+}\right\} \tag{3.232}$$

and the acquired circular polarization is given by

$$P_c = \frac{R(\sigma_+) - R(\sigma_-)}{R(\sigma_+) + R(\sigma_-)} \,, \tag{3.233}$$

where $R(\sigma_\pm) = |r_\pm|^2$.

In the linear-in-field approximation, one can neglect the diamagnetic shift of the exciton excitation energy and take into account the Zeeman splitting of the exciton levels. In symmetric zinc-blende-lattice (001)-grown QWs, the degenerate radiative doublet of the $e1$-$hh1$ (or $e1$-$lh1$) exciton splits into the sublevels $\omega_{0,\pm} = \omega_0 \pm (\Omega_B/2)$ with angular momentum component $M = \pm 1$, which are optically active in the σ_+ and σ_- polarizations, respectively. The splitting $\hbar\Omega_B$ equals to $g_{zz}\mu_B B_z$, where g_{zz} is the exciton g-factor, see for details Chap. 5. The amplitude reflection coefficients, $r_\pm(\omega)$, from a single QW structure or MQWs are expressed via the corresponding zero-field reflection coefficient $r(\omega)$ where the variable ω is shifted by $\mp\Omega_B/2$, namely,

$$r_\pm(\omega) = r\left(\omega \mp \frac{\Omega_B}{2}\right) , \tag{3.234}$$

where r is found from (3.4) and (3.21, 3.55) or (3.90).

In the case where the Zeeman splitting Ω_B exceeds the exciton damping Γ, it can be readily measured spectroscopically. In the other limiting case, $|\Omega_B| \ll \Gamma$, the splitting can be found by studying normal-incidence reflection of unpolarized or linearly polarized light and measuring the spectral behavior of the degree of circular polarization of reflected light

$$P_c = -\frac{\Omega_B}{2}\,\frac{1}{R(\omega)}\frac{\partial R(\omega)}{\partial \omega} , \tag{3.235}$$

where R is given by (3.50).

In the same way, for small magnetic fields the rotation angle θ is given by

$$\theta = \frac{\Omega_B}{2r_{01}}\,\mathrm{Im}\left\{\frac{\partial r(\omega)}{\partial \omega}\right\} . \tag{3.236}$$

In particular, for a single-QW structure with $\Gamma_0 \ll \Gamma$ one has

$$\theta = \frac{4n_b}{n_b^2 - 1}\Omega_B\Gamma_0\frac{[\Gamma^2 - (\omega_0 - \omega)^2]\cos 2\varphi_{0a} + 2(\omega_0 - \omega)\Gamma \sin 2\varphi_{0a}}{[(\omega_0 - \omega)^2 + \Gamma^2]^2} , \tag{3.237}$$

where the phase φ_{0a} is defined according to (3.48).

3.4.3 Giant Magneto-Optical Effects in Semimagnetic Nanostructures

Semimagnetic or diluted magnetic semiconductors are semiconducting compounds in which a fraction x of the cations is randomly replaced by transition metal ions, e.g., $3d^n$ ions. Most often, they are solid solutions $A_{1-x}M_xB$ with A = Cd, Zn, Hg, B = Te, Se, S, and M = Mn^{2+}, Fe^{2+}, Co^{2+}. The magnetic subsystem interacts effectively with charge carriers, electrons and holes,

due to the strong *sp-d* exchange interaction between the carrier spins and magnetic moments of the ions. The semimagnetic bulk semiconductors and nanostructures are known for giant magneto-optical properties and magnetic polarons. Particularly, in this systems the Zeeman splitting of the carrier or exciton spin states are described by the effective g-factors being in excess of a hundred.

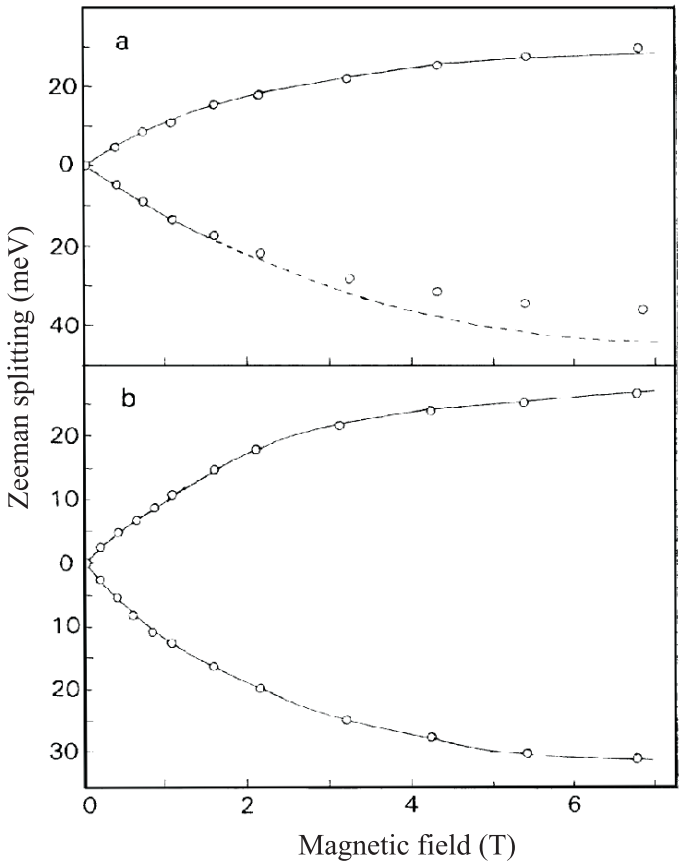

Fig. 3.15. Zeeman splitting of the heavy-hole exciton in an 18-Å-thick single QW (**a**) and a 40-Å-period SL (**b**) with $x = 0.1$. Curves are calculated with use of (3.238) and parameters $T_{\rm AF} = 2.4$ K, $\tilde{x} = 0.05$, or 0.07 for the single QW, or SL, respectively. [3.87]

Usually, the *sp-d* interaction of magnetic ions with free carriers is described by two constants, α and β, of the exchange interaction. For example, the normal magnetic field, $\boldsymbol{B} \parallel z$, changes the carrier energy by

$$\Delta E_{e,s} = \frac{\alpha}{v_0} x s \langle S_z \rangle \, , \; \Delta E_{h,j} = \frac{\beta}{3v_0} x j \langle S_z \rangle \, , \tag{3.238}$$

where $s = \pm 1/2$, $j = \pm 3/2, \pm 1/2$ are the electron and hole spin indices, x is the content of magnetic ions, v_0 is the unit cell volume (for the zinc-blende lattice, $v_0 = a_0^3/4$), and $\langle S_z \rangle$ is the average spin component of a magnetic ion along z. In the thermal equilibrium one has

$$\langle S_z \rangle = -S \, B_S(Sg\mu_B B_z / 2k_B T) \, , \tag{3.239}$$

where S is the atomic spin of a magnetic ion (5/2 for Mn^{2+}, 3/2 for Co^{2+}), $g = 2$ is the ion g-factor, and $\mathrm{B}_S(X)$ is the Brillouin function

$$\mathrm{B}_S(X) = \frac{2S+1}{2S} \coth \frac{2S+1}{2S} X - \frac{1}{2S} \coth \frac{X}{2S} \, . \tag{3.240}$$

Note that at small X this function is approximated by

$$\mathrm{B}_S(X) \approx \frac{S+1}{3} X \, .$$

In order to take into account the antiferromagnetic Mn-Mn spin coupling two additional fitting parameters are introduced, namely, the content x in (3.238) is replaced by the effective content $\tilde{x}$ and T in (3.239) is shifted by some value T_{AF}. In the paramagnetic phase $\tilde{x} = x$ and $T_{\mathrm{AF}} = 0$ whereas in the spin-glass phase $\tilde{x} < x$ and $T_{\mathrm{AF}} > 0$. In the $Cd_{1-x}Mn_xTe$ system, $\alpha/v_0 = 220$ meV and $\beta/v_0 = 880$ meV. Opportunities of resonance reflection spectroscopy to study the magneto-optical properties in CdTe/CdMnTe QWs and SLs are demonstrated in [3.87]. Figure 3.15 shows the Zeeman splitting of the heavy-hole exciton states $|\pm 1\rangle$ measured at magnetic fields parallel to the growth axis in a 18-Å-thick single QW and 40-Å-period SL. Since in the studied structures only barriers are semimagnetic, there exists a certain magnetic field B_{cr} at which the valence band offset for one of the heavy-hole states vanishes resulting in the magnetic-field induced type-I–type-II transition. According to (3.238) the value of B_{cr} satisfies the condition

$$\frac{\beta}{2v_0} \tilde{x} \langle S_z \rangle + V_{hh} = 0 \, ,$$

where V_{hh} is the heavy-hole subband offset at zero field. In $CdTe/Cd_{0.9}Mn_{0.1}Te$ QWs, B_{cr} equals 1.3 T. At this particular field one of the heavy-hole exciton can be considered approximately as formed by a 2D electron and a 3D hole. Reduction of the effective oscillator strength of the low-energy σ_+-polarized exciton observed in [3.87] is a convincing demonstration of the type-I–type-II transition.

The large Faraday rotation in bulk diluted magnetic semiconductors is further enhanced in semimagnetic QWs with larger excitonic oscillator strength. Particularly, this has opened the way for using CdMnTe heterostructures as

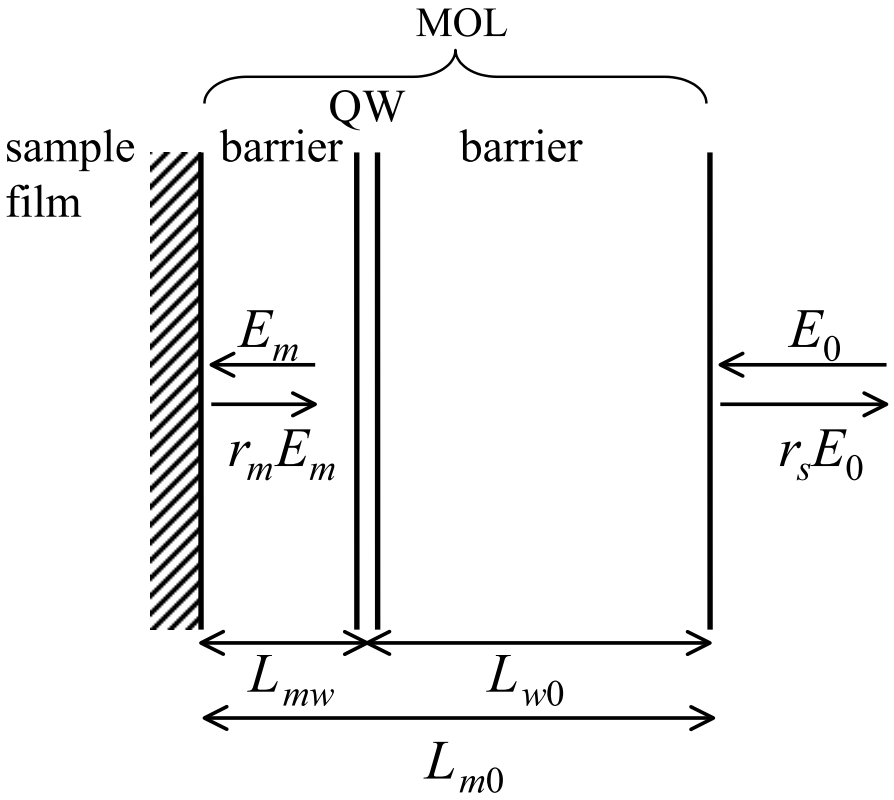

Fig. 3.16. Schematic representation of the optical cavity with an embedded QW.

magneto-optic layers for high resolution Faraday microscopy at low temperature in order to make a cartography of the magnetic field at the surface of a superconductor [3.88, 3.89]. The structure is schematically depicted in Fig. 3.16. It consists of a metal, an inner barrier layer, a QW and a top barrier layer with CdMnTe and CdMgTe used, respectively, as the QW and barrier compositional materials. In fact it is an optical cavity with an embedded QW. The metal is illuminated through the magneto-optical layers by linearly polarized light. The plane of light polarization is rotated in the areas that carry magnetic flux. After passing through a crossed (or slightly uncrossed) analyser the reflected light is focused on a detector. Since the magnetic field lines diverge out of the surface plane of the superconducting film, the semimagnetic QW must be as close as possible to the superconducting film to achieve a good spatial resolution.

The reflection coefficients $r_{\pm}$ from the structure shown in Fig. 3.16 can be presented in the form

$$r = r^{(0)} + \frac{\mathrm{i}\Gamma_0 C}{\omega_0 - \omega - \mathrm{i}(\Gamma + \Gamma_0 B)} \,. \tag{3.241}$$

Here the first term describes the reflection when the exciton contribution is ignored

$$r^{(0)} = \frac{r_{0b} + r_m \mathrm{e}^{2\mathrm{i}\varphi_{m0}}}{1 - r_{b0} r_m \mathrm{e}^{2\mathrm{i}\varphi_{m0}}} \,,$$

$$C = t_{b0} t_{0b} \mathrm{e}^{2\mathrm{i}\varphi_{w0}} A \,, \qquad A = \left(\frac{1 + r_m \mathrm{e}^{2\mathrm{i}\varphi_{mw}}}{1 - r_{b0} r_m \mathrm{e}^{2\mathrm{i}\varphi_{m0}}} \right)^2 \,, \tag{3.242}$$

$$B = 1 + \frac{r_{b0}(2 r_m \mathrm{e}^{2\mathrm{i}\varphi_{m0}} + \mathrm{e}^{2\mathrm{i}\varphi_{w0}}) + r_m \mathrm{e}^{2\mathrm{i}\varphi_{mw}}}{1 - r_{b0} r_m \mathrm{e}^{2\mathrm{i}\varphi_{m0}}} \,.$$

Other notations are as follows: Γ_0 and Γ are the exciton radiative and non-radiative damping rates in a single QW,

$$r_{b0} = -r_{0b} = \frac{n_b - 1}{n_b + 1} \,,\; t_{0b} t_{b0} = 1 - r_{b0}^2 \,,$$

n_b is the refractive index of the barrier assumed to coincide with that of the QW, the phases are given by

$$\varphi_{w0} = (\omega/c) n_b L_{w0} \,,\; \varphi_{mw} = (\omega/c) n_b L_{mw} \,,$$

the thicknesses L_{w0}, L_{mw} and the reflection coefficient, r_m, from the metal to the barrier are defined in Fig. 3.16. In the following we use ρ_m and φ_m for the modulus and phase of r_m.

The amplification of rotation in the optical cavity occurs mostly due to the factor A defined in (3.242). This factor exhibits a maximum when two conditions are fulfilled. Firstly, the total dephasing $2\varphi_{m0} + \varphi_m$ must be an integer number of 2π. The reflection coefficient $r^{(0)}$ then exhibits a minimum value of $(\rho_m - r_{b0})/(1 - \rho_m r_{b0})$. For a perfect metal ($\varphi_m = \pi$) the optical thickness of the cavity is equal to $(2p+1)\lambda/4$ with p an integer and λ the wavelength of light. Secondly, the QW must be located at an anti-node of the electric field which means that $2\varphi_{mw} + \varphi_m = 2l\pi$ with l being an integer. In this particular case the amplification factor equals to

$$A = \left(\frac{1 + \rho_m}{1 - r_{b0} \rho_m} \right)^2 \,.$$

If the contribution of the QW to the reflected signal is small even at the minimum of reflectivity, i.e.,

$$\left| r^{(0)} \right| \gg |t_{b0} t_{0b} \Gamma_0 A / \Gamma| \,, \tag{3.243}$$

then the rotation angle is given by

$$\theta = \frac{t_{b0}t_{0b}A}{2r^{(0)}}\frac{\Gamma_0\Omega_B}{\Gamma^2}F(\Omega,\Omega_B)\,,$$

where $\Omega = \omega - \omega_0$ and

$$F(\Omega,\Delta) = \frac{\Gamma^2[\Gamma^2 + (\Delta/2)^2 - \Omega^2]}{[\Gamma^2 - (\Delta/2)^2 + \Omega^2]^2 + \Gamma^2\Delta^2}\,.$$

For small magnetic fields one can set $\Delta = 0$ in the expression for F. Note that the function $F(\Omega, 0)$ has a maximum value of 1 at $\Omega = 0$, changes sign at the points $\Omega = \pm\Gamma$ and reaches minima $-1/8$ at $\Omega = \pm\sqrt{3}\Gamma$. An additional enhancement of the rotation angle can be achieved by using few QWs with the Bragg spacing instead of one [3.89].

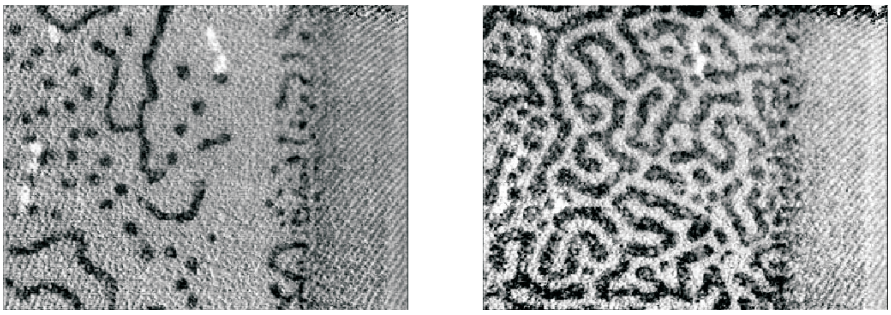

Fig. 3.17. Images of the magnetic flux pattern at the surface of the 10 μm Indium layer obtained at 1.8 K and $H = 28$ Oe (left), $H = 77$ Oe (right). Normal and superconducting domains appear in black and gray, respectively. The size of each image is 264×191 μm^2. The analyser was uncrossed by 15° with respect to the polarizer. [3.89]

The above magneto-optical layers allowed an observation of the intermediate state pattern in a superconductor layer with spatial and magnetic resolutions of 1 μm and 10 mT (Fig. 3.17). As it can be seen from the figure, the intermediate state is formed by normal flux tubes (dark spots) and long corrugated lamellae with typical width and spacing of ~ 10 μm. These normal state regions are separated by superconducting state domains (in gray). Figure 3.17 demonstrates wide possibilities to use the low-dimensional physics for studies of hybrid systems containing semiconductor and superconductor layers.

4 Intraband Optical Spectroscopy of Nanostructures

The light shines in the darkness,
but the darkness has not overcome it.

John **1***: 5*

The physics of intersubband transitions in QWs and SLs has attracted increased attention in recent decades, mainly due to the promise of applications in the mid- and far-infrared regions (2–20 μm) such as detection, modulation, harmonic generation, emission, quantum cascade lasers and photogalvanics.

4.1 Intersubband Optical Transitions. Simple Band Structure

In bulk semiconductor with a simple band structure direct intraband optical transitions are forbidden by the momentum and energy conservation laws

$$\boldsymbol{k}' = \boldsymbol{k} + \boldsymbol{q}\,, \; \frac{\hbar^2 k'^2}{2m} = \frac{\hbar^2 k^2}{2m} + \hbar\omega$$

because they cannot be satisfied simultaneously. Here $\boldsymbol{k}, \boldsymbol{k}'$ are the electron wave vectors in the initial and final states, and $\boldsymbol{q}, \omega$ are the light wave vector and frequency. The intraband absorption can only occur by absorption of a photon and simultaneous scattering by "third particle", e.g., a phonon, another free carrier or a static defect. This process called an *indirect optical transition* is described by second-order matrix elements involving virtual intermediate states.

Quantum-confinement effects transform the free-carrier energy spectrum into a series of subbands in QWs or minibands in SLs. As a result we find here an additional mechanism of intraband absorption associated with *direct* optical transitions of free carriers between the subbands or minibands. Choosing the well and barrier compositional materials one can vary the well dimensions, its height and width, and tune the resonance frequency of intersubband optical transitions to a given value. This opens a clear way for using MQWs and other nanostructures as novel devices and systems in infrared technologies.

4.1.1 Intersubband Light Absorption in a Quantum Well

The transition rate from the electron states i to f is given by Fermi's golden rule. We consider here the direct optical transitions $e1 \to e2$ between the

lowest and first excited subbands in a QW, the transitions $e\nu \to e\nu'$ with arbitrary ν and ν' are treated in a similar way. By using equations analogous to (2.142, 2.147) one can present the total transition rate $W_{e2,e1}$ per unit area in the form

$$W_{e2,e1} = \frac{4\pi^2 e^2 I}{\hbar\omega^2 c n_\omega S} \sum_{ss'\boldsymbol{k}} |\boldsymbol{e}\cdot\boldsymbol{v}_{e2s',e1s}(\boldsymbol{k})|^2 (f_{e1s\boldsymbol{k}} - f_{e2s'\boldsymbol{k}}) \delta(E_{e2s'\boldsymbol{k}} - E_{e1s\boldsymbol{k}} - \hbar\omega) \,. \tag{4.1}$$

Here I is the light intensity, see (2.141), s, s' are the spin indices, $f_{e\nu s\boldsymbol{k}}$ is the electron distribution function, $\boldsymbol{v}_{e\nu' s',e\nu s}(\boldsymbol{k})$ is the matrix element of the velocity operator and S is the sample area.

In a heterostructure consisting of semiconductor layers with a simple conduction band, isotropic and parabolic, one has

$$\boldsymbol{v}_{e\nu' s',e\nu s}(\boldsymbol{k}) = \delta_{s's} \left[\hbar\left(\boldsymbol{k}\cdot\boldsymbol{e}_\parallel\right) \langle\nu'|m^{-1}(z)|\nu\rangle + e_z \langle\nu'|\hat{v}_z|\nu\rangle\right] \,, \tag{4.2}$$

where

$$\hat{v}_z = -\mathrm{i}\frac{\hbar}{2}\left(\frac{1}{m(z)}\frac{\partial}{\partial z} + \frac{\partial}{\partial z}\frac{1}{m(z)}\right) \,.$$

For a rectangular QW, in the limit of infinitely high barriers, equation (4.2) simplifies to

$$\boldsymbol{e}\cdot\boldsymbol{v}_{e\nu' s',e\nu s}(\boldsymbol{k}) = \delta_{s's}\frac{\hbar}{m_\mathrm{A}}\left[\left(\boldsymbol{k}\cdot\boldsymbol{e}_\parallel\right)\delta_{\nu'\nu} + k_z^{(\nu'\nu)} e_z\right] \,, \tag{4.3}$$

where

$$k_z^{(\nu'\nu)} = \mathrm{i}\frac{2}{a}\left[1 - (-1)^{\nu'+\nu}\right]\frac{\nu'\nu}{\nu'^2 - \nu^2} \,. \tag{4.4}$$

The direct intersubband transitions are allowed in the $\boldsymbol{e} \parallel z$ polarization between the subbands of opposite parity. The selection rules, expressed by (4.3), hold for finite barriers as well, provided the effective masses m_A and m_B in the well and barrier materials coincide. However, the expression for $k_z^{(\nu'\nu)}$ becomes more complicated. If the masses $m_\mathrm{A}, m_\mathrm{B}$ are different, the matrix elements $\langle\nu'|m^{-1}(z)|\nu\rangle$ are nonzero not only for $\nu' = \nu$ but also for ν' and ν of the same parity. However the probability of the latter transitions is very small and other corrections to $k_z^{(\nu'\nu)}$ including those connected with the band nonparabolicity can play a role.

For a single QW structure the conventional concept of the absorption coefficient, K, is meaningless in the strict sense. Instead one can introduce the *absorbance* η_{21}, or the fraction of the energy flux absorbed in the QW due to the transitions between the subbands $e1$ and $e2$. It can also be defined as, see (3.27),

$$\eta_{21} = 1 - |r_{21}|^2 - |t_{21}|^2 \,,$$

where r_{21}, t_{21} are the related reflection and transmission coefficients. The absorbance is connected with $W_{e2,e1}$ by

$$W_{e2,e1} = \frac{\eta_{21} I}{\hbar\omega} \tag{4.5}$$

and, therefore, the electromagnetic energy absorbed in a unit area of the QW equals to

$$\hbar\omega W_{e2,e1} = \eta_{21} I \,.$$

For the intersubband transitions the reflectivity $|r_{21}|^2$ is negligibly small as compared with η_{21} and, conditionally, one can define an effective absorption coefficient K_{SQW} for a single QW by

$$\eta_{21} = 1 - \exp\left(-K_{SQW} a\right) \approx K_{SQW} a \,.$$

However one should be careful not to overestimate the meaning of K_{SQW}. On the other hand, in short-period MQW structures one can use the approximation of an effective uniform medium (Sect. 3.1.3) and the effective absorption coefficient is well defined by

$$K_{\mathrm{MQW}} = \frac{\eta_{21}}{d} \,, \tag{4.6}$$

where d is the period.

Substituting (4.3, 4.4) into (4.1) and integrating over $\boldsymbol{k}$ we obtain

$$\eta_{21} = \frac{512}{27} \frac{e^2\hbar}{c m_{\mathrm{A}} n_\omega} (N_1 - N_2) \left|e_z\right|^2 \delta(E_2^0 - E_1^0 - \hbar\omega) \,, \tag{4.7}$$

where N_ν is the 2D density of electrons in the ν-th subband; in the following we assume that the 2D equilibrium electrons occupy only the lowest subband $\nu = 1$. The δ-function in (4.7) is $\boldsymbol{k}$-independent because we assume the same dispersion parabolas in the subbands $e1$ and $e2$. The relaxation of electrons results in a homogeneous spectral width, Γ_{21}, of the $e2$-$e1$ resonant transition, namely

$$\eta_{21} = \frac{512}{27} \frac{e^2\hbar}{c m_{\mathrm{A}} n_\omega} (N_1 - N_2) \left|e_z\right|^2 \frac{1}{\pi} \frac{\hbar\Gamma_{21}}{(E_2^0 - E_1^0 - \hbar\omega)^2 + (\hbar\Gamma_{21})^2} \,. \tag{4.8}$$

Allowance for nonparabolicity of the electron dispersion in the bulk compositional materials, linear-$\boldsymbol{k}$ spin-dependent terms and other effects removing the equidistance between $E_{e2s'\boldsymbol{k}}$ and $E_{e1s\boldsymbol{k}}$ lead to an additional broadening of the peak in the intersubband absorption spectrum.

To interpret (4.8) let us replace the system of 2D electron gas by a system of 3D classical electrons confined within a narrow slab of the effective thickness a_{eff} and characterized by the sheet density N_1 and conductivity in a unit area given by

$$\sigma_{zz}(\omega) = \frac{N_1 e^2 f_{21}}{m_{\rm A} a_{\rm eff}} \frac{-{\rm i}\omega}{\omega_{21}^2 - \omega^2 - 2{\rm i}\omega\Gamma_{21}} \,, \tag{4.9}$$

where $\hbar\omega_{21} = E_{21}$ and f_{21} is the so-called *oscillator strength*. This equation can be derived by solving the equation of motion

$$\frac{d^2 z}{dt^2} + 2\Gamma_{21}\frac{dz}{dt} + \omega_{21}^2 z = \frac{e}{m_{\rm A}} f_{21} E(t)$$

for a classical oscillator excited by a monochromatic electric field

$$E(t) = E_0 \exp(-{\rm i}\omega t) + {\rm c.c.}$$

The solution is $z(t) = z_0 \exp(-{\rm i}\omega t) + {\rm c.c.}$ with the amplitude

$$z_0 = \frac{e}{m_{\rm A}} \frac{f_{21} E_0}{\omega_{21}^2 - \omega^2 - 2{\rm i}\omega\Gamma_{21}} \,.$$

One can check that the amplitude of the induced current $j_z = eN_{3D}dz/dt$ with $N_{3D} = N_1/a_{\rm eff}$ can be written as $\sigma_{zz}E_0$ with the conductivity given exactly by (4.9). For weakly-damped oscillators, $\Gamma_{21} \ll \omega_{21}$, the denominator can be approximated near the resonance by $2\omega_{21}(\omega_{21} - \omega - {\rm i}\Gamma_{21})$.

Equalizing the energy losses $\eta_{21} I$ to $2a_{\rm eff}\,{\rm Re}\{\sigma_{zz}\}|E_0|^2$ we obtain

$${\rm Re}\{\sigma_{zz}\} = \frac{c n_\omega}{4\pi a}\,\eta_{21} \,.$$

By comparing this equation with the expressions (4.9) for the conductivity and (4.8) for the absorbance we find that the effective slab model describes the behavior of a 2D electron gas confined in a QW if one takes the dimensionless oscillator strength equal to

$$f_{21} = \frac{256}{27\pi^2} \approx 0.96 \,.$$

Clearly, the best way to study the subband structure is to observe intersubband optical transitions in the absorption or scattering spectra (the latter will be discussed in Chap. 6). One has however to bear in mind that there are additional effects which shift the resonance energy from the corresponding subband separation calculated in the single-particle approximation. One of them is called the *depolarization effect*. It can be readily understood in the slab model. Actually, the external electric field $E_{{\rm ext},z}$ differs from the field E_z inside the slab. If we introduce the local dielectric function

$$æ_{zz}(\omega) = æ_b + \frac{4\pi{\rm i}}{\omega}\sigma_{zz}(\omega)$$

with σ_{zz} given by (4.9) we can write the relation

$$æ_b E_{{\rm ext},z} = æ_{zz}(\omega) E_z$$

which is nothing more than the boundary condition for the normal component of the electric displacement vector. Therefore the equation $j_z = \sigma_{zz} E_z$ can be rewritten in terms of the external field as $j_z = \tilde{\sigma}_{zz} E_{\mathrm{ext},z}$ with the renormalized conductivity [4.1]

$$\tilde{\sigma}_{zz} = \frac{æ_b}{æ_{zz}}\,\sigma_{zz} = \frac{N_1 e^2 f_{21}}{m_{\mathrm{A}} a_{\mathrm{eff}}} \frac{-\mathrm{i}\omega}{\tilde{\omega}_{21}^2 - \omega^2 - 2\mathrm{i}\omega\Gamma_{21}}\,, \tag{4.10}$$

where the renormalized resonance frequency is given by

$$\tilde{\omega}_{21}^2 = \omega_{21}^2 + \omega_{21,\mathrm{pl}}^2$$

and the intersubband plasmon frequency by

$$\omega_{21,\mathrm{pl}}^2 = \frac{4\pi N_1 e^2 f_{21}}{æ_b m_{\mathrm{A}} a_{\mathrm{eff}}}\,. \tag{4.11}$$

Taking into account the depolarization effect the rate of energy losses is given by $2a_{\mathrm{eff}}\,\mathrm{Re}\{\tilde{\sigma}_{zz}\}|E_{\mathrm{ext},z}|^2$ instead of $2a_{\mathrm{eff}}\,\mathrm{Re}\{\sigma_{zz}\}|E_z|^2$ and exhibits its maximum at the frequency $\tilde{\omega}_{21}$.

Physically, the depolarization effect arises because each electron feels a field which is different from the external field by the mean Hartree field of other electrons perturbed by the external field. In fact, the Hartree approximation is valid when the average kinetic energy of electrons is much larger than the average interaction energy. Otherwise this approximation overestimates the Coulomb repulsive force of other electrons, many-body effects such as exchange and correlation can play an important role and reduce the renormalization of the resonance energy $\hbar\omega_{21}$ [4.1]. A more rigorous treatment of the linear response of an n-doped QW to an external electric field, $E_{\mathrm{ext},z}$, leads the conductivity $\tilde{\sigma}_{zz}(\omega)$ given in the form of (4.10) with $f_{21} = (2m_{\mathrm{A}}\omega_{21}/\hbar)\langle 2|z|1\rangle^2$ and

$$\tilde{\omega}_{21}^2 = \omega_{21}^2(1 + \alpha_{21} - \beta_{21})\,. \tag{4.12}$$

The coefficients α_{21}, β_{21} describe the depolarization and exchange-correlation effects, respectively. The former is defined by

$$\alpha_{21} = \frac{8\pi N_1 e^2 L_{21}}{\hbar\omega_{21} æ_b}\,, \tag{4.13}$$

where

$$L_{21} = \int\limits_{-\infty}^{\infty} dz\; \varphi_2(z)\; \varphi_1(z) \int\limits_{-\infty}^{z} dz' \int\limits_{-\infty}^{z'} dz''\; \varphi_2(z'')\; \varphi_1(z'')$$

and $\varphi_\nu(z)$ is the electron envelope in the subband ν. Therefore, the intersubband plasmon frequency can be written as

$$\omega_{21,\mathrm{pl}}^2 \equiv \omega_{21}^2 \alpha_{21} = \frac{8\pi N_1 e^2 L_{21}\omega_{21}}{\hbar æ_b} \,, \tag{4.14}$$

which coincides with (4.11) if we set

$$\frac{f_{21}}{a_{\mathrm{eff}}} = \frac{2L_{21}\omega_{21}m_{\mathrm{A}}}{\hbar} \,.$$

An explicit equation for the coefficient β_{21} can be found in [4.1]. Note that the corresponding term includes the exciton-like correction which appears due to the interaction between the excited electrons in the $e2$ subband and the empty state, or holes, in the $e1$ subband.

In an ideal QW, the energy spacing $E_{21} = E_2^0 - E_1^0$ exhibits no random variations in the interface plane and the spectral width of the absorption can be estimated by

$$\delta_{21} \sim \max\left(\frac{\hbar^2\bar{k}^2}{2m}\,\frac{\delta m}{m}\,, \Gamma_{21}\,, |\beta_\nu|\bar{k}\right) \,, \tag{4.15}$$

where δm is the difference of the electron effective masses in the subbands $e1$ and $e2$ due to the nonparabolicity, β_ν is the coefficient describing linear-$\boldsymbol{k}$ terms in the electron effective Hamiltonian, and $\bar{k}$ is an average value of the wave vector in the equilibrium 2D electron gas occupying states in the lower subband $e1$. The latter has an order of magnitude of the Fermi wave vector in case of the degenerate statistics and the thermal wave vector $\sqrt{2m_1^* k_B T/\hbar^2}$ for the Maxwell distribution. As a rule, in available QW structures the width, Δ_{21}, of inhomogeneous broadening of the gap E_{21} exceeds the width δ_{21} of absorption spectrum in an ideal QW. The inhomogeneous broadening can be taken into consideration by introducing the distribution function, $F(E_{21})$, of the gap E_{21} and replacing (4.6, 4.7) by

$$K_{\mathrm{MQW}} = \frac{256\pi^2 e^2\hbar^2(N_1 - N_2)}{9n_\omega c a^2 m_{\mathrm{A}}^2 \omega d} F(\hbar\omega)|e_z|^2 \,. \tag{4.16}$$

The shape of the function $F(E_{21})$ can be found from a comparison with experiment [4.2] or calculated by using a particular model of the interface roughness [4.3].

In the above description of an intersubband resonance in a QW the confinement dictates that the electric vector of the light wave must have a nonzero component e_z along the growth direction in order to excite the $e2$-$e1$ intersubband transition. This one-band picture is modified in a multiband description of the band structure. The main result is that through $\boldsymbol{k}\cdot\boldsymbol{p}$ band coupling, notably mixing of the conduction states with the heavy, light and spin-orbit-split hole states, all four transitions $e1, \pm 1/2 \rightarrow e2, \pm 1/2$ are allowed, some of them in the polarization $\boldsymbol{e} \parallel z$ plane and others in the polarization $\boldsymbol{e} \perp z$ plane. For a QW of the D_{2d} point symmetry, the $e1$ and $e2$

subband states at $\boldsymbol{k} = 0$ transform according to the spinor representations Γ_6 and Γ_7. In the D_{2d} point group, the direct product

$$\Gamma_6 \times \Gamma_7 = \Gamma_1 + \Gamma_2 + \Gamma_5 \tag{4.17}$$

with excitations of the symmetry Γ_2 and Γ_5 (or B and E in other notations) being optically active, respectively, in the polarization $\boldsymbol{e} \parallel z$ and $\boldsymbol{e} \perp z$. Therefore, the intersubband matrix elements of the velocity operator at $\boldsymbol{k} = 0$ are, in general, characterized by two linearly-independent coefficients. One may show that they can be presented in the form

$$||\boldsymbol{e} \cdot \boldsymbol{v}_{e2s',e1s}|| = \begin{bmatrix} Ve_z & V'(e_x - \mathrm{i}e_y) \\ -V'(e_x + \mathrm{i}e_y) & Ve_z \end{bmatrix} . \tag{4.18}$$

The coefficients V and V' describe the spin-conserving ($s' = s$) and spin-flip ($s' - s = \pm 1$) transitions, respectively. By using the Kane model we can present the electron wave function in the subband ν at $\boldsymbol{k} = 0$ as

$$\psi_{e\nu,1/2} = \left[u_{\Gamma_6,1/2} + \frac{\hbar p^*_{cv}}{\sqrt{3} m_0} \left(\frac{\sqrt{2} u_{\Gamma_8,1/2}}{E_g + E^0_\nu} - \frac{u_{\Gamma_7,1/2}}{E_g + \Delta + E^0_\nu} \right) \hat{k}_z \right] \varphi_\nu(z) ,$$

$$\psi_{e\nu,-1/2} = \left[u_{\Gamma_6,-1/2} + \frac{\hbar p^*_{cv}}{\sqrt{3} m_0} \left(\frac{\sqrt{2} u_{\Gamma_8,-1/2}}{E_g + E^0_\nu} + \frac{u_{\Gamma_7,-1/2}}{E_g + \Delta + E^0_\nu} \right) \hat{k}_z \right] \varphi_\nu(z) ,$$

where the admixture of the valence-band states is included. An important point is that the energy denominators are dependent on the quantum-confinement energy which leads to a nonzero value of V'. Taking into account that $m^* \ll m_0$ one has in the non-vanishing approximation [4.4]

$$V \equiv v_{21} = \frac{\hbar}{m^*} k_z^{(21)} , \tag{4.19}$$

$$V' \equiv v_{21} \Lambda , \; \Lambda = \frac{E_{21} \Delta (2E_g + \Delta)}{2E_g (E_g + \Delta)(3E_g + 2\Delta)} .$$

Therefore, taking into account off-diagonal components in (4.18) we can rewrite (4.16) in a more general form

$$K_{\mathrm{MQW}}(\boldsymbol{e}) = K_z \, |e_z|^2 + K_\parallel \left(|e_x|^2 + |e_y|^2 \right) , \tag{4.20}$$

where

$$K_z = \frac{256 \pi^2 e^2 \hbar^2 (N_1 - N_2)}{9 n_\omega c a^2 m_{\mathrm{A}}^2 \omega d} F(\hbar\omega) , \; K_\parallel = \Lambda^2 K_z \tag{4.21}$$

and, for simplicity, the depolarization and exchange-correlation effects are ignored.

Figure 4.1 illustrates the geometry of experiment on light transmission through a MQW structure. Since $\Lambda^2 \ll 1$ and, in the $\boldsymbol{e} \perp z$ polarization, the

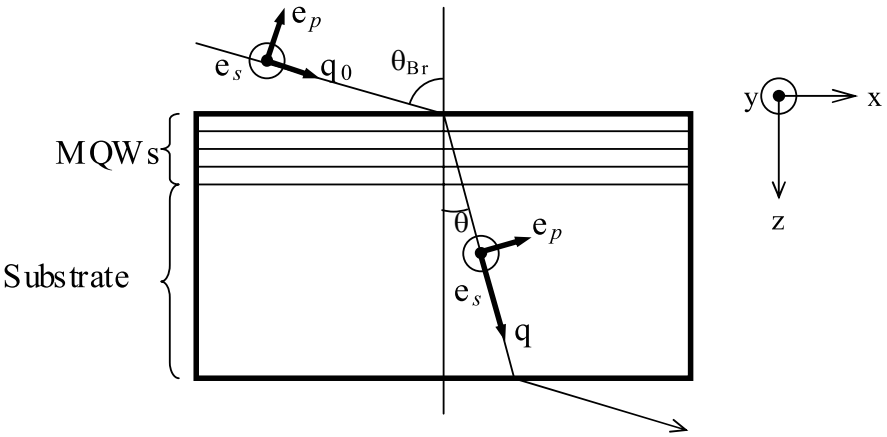

Fig. 4.1. Schematic representation of light reflection from a MQW structure under oblique incidence at Brewster's angle $\theta_{\rm Br}$.

intersubband transitions are very weak, the oblique incidence of p-polarized light is used [4.5]. To exclude the losses associated with reflection from the top and bottom faces of the sample, one may conveniently shine the infrared light under the Brewster angle, $\theta_{\rm Br}$, satisfying the condition $\tan\theta_{\rm Br} = \sqrt{æ_b}$, where $æ_b$ is the dielectric constant of the barrier. Neglecting the light absorption in the barrier, we obtain for the transmission coefficient

$$-\ln T = \frac{K_z N d}{\cos\theta}\left(\sin^2\theta + \Lambda^2\cos^2\theta\right), \tag{4.22}$$

where N is the number of wells in the structure, and θ is the refraction angle related with the Brewster angle by $\sqrt{æ_b}\sin\theta = \sin\theta_{\rm Br}$. Taking into account that in the Brewster geometry

$$\cos\theta = \sqrt{\frac{æ_b}{æ_b+1}}\,,\quad \frac{\sin^2\theta}{\cos\theta} = \frac{1}{\sqrt{æ_b(æ_b+1)}}\,,$$

one has

$$-\ln T = K_z N d\,\frac{1+\Lambda^2 æ_b}{\sqrt{æ_b(æ_b+1)}}\,. \tag{4.23}$$

Figure 4.2 shows an experimental intersubband absorption spectrum of the sample containing a MQW structure with 40-Å $In_{0.45}Ga_{0.55}As$ wells and 80-Å $Al_{0.45}Ga_{0.55}As$ barriers. The absorption was measured by a Fourier-transform infrared spectrometer with p-polarized light at Brewster's angle. The dashed and broken lines in Fig. 4.2 are the best fits with the Lorentzian and the Voigt line shapes, respectively. Note that the Voigt profile is a convolution of a Gaussian representing an inhomogeneous broadening with a Lorentzian representing a homogeneous broadening.

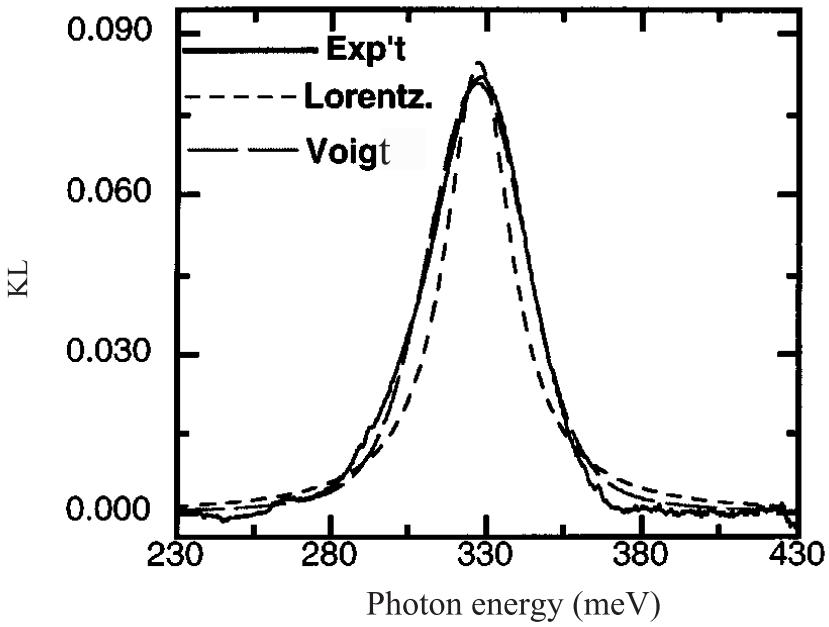

Fig. 4.2. Experimental (Exp't) absorption spectrum of InGaAs/AlGaAs MQW structure using p-polarized light at Brewster's angle, along with the best Lorentzian (Lorentz.) and Voigt line shapes. From [4.2].

Using QW infrared detectors with either GaAs or InGaAs QWs, Liu et al. [4.6] experimentally investigated the accuracy of the polarization selection rule for the conduction band intersubband transitions. Figure 4.3 plots the normalized photosignal taken at the Brewster angle incidence at the wavelength 8.1 μm and 4.6 μm from GaAs/$Al_{0.26}Ga_{0.74}As$ and $In_{0.1}Ga_{0.9}As/Al_{0.44}Ga_{0.56}As$ QW detectors, respectively. In the figure, squares represent the photoresponse signal as a function of the angle between the plane of incidence and the plane of polarization. For quantitative comparisons, the reflection (69%) of the s-polarized light at the sample/vacuum interface must be taken into account. The experiments imply that the s-to-p ratio does not exceed 0.22% in the GaAs QWs and 3% in the InGaAs QWs in agreement with a small value of the parameter Λ.

To increase the radiation energy absorbed in the sample containing MQWs, the side faces of the sample can be prepared in the so-called *waveguide geometry* by cleaving or polishing two parallel side faces at some angle. In this case the light is directed through the faces, as illustrated in Fig. 4.4, thus exciting the waveguide modes. Figure 4.5 shows the resonance behavior of absorption measured in n-GaAs/AlGaAs MQWs by making use of trans-

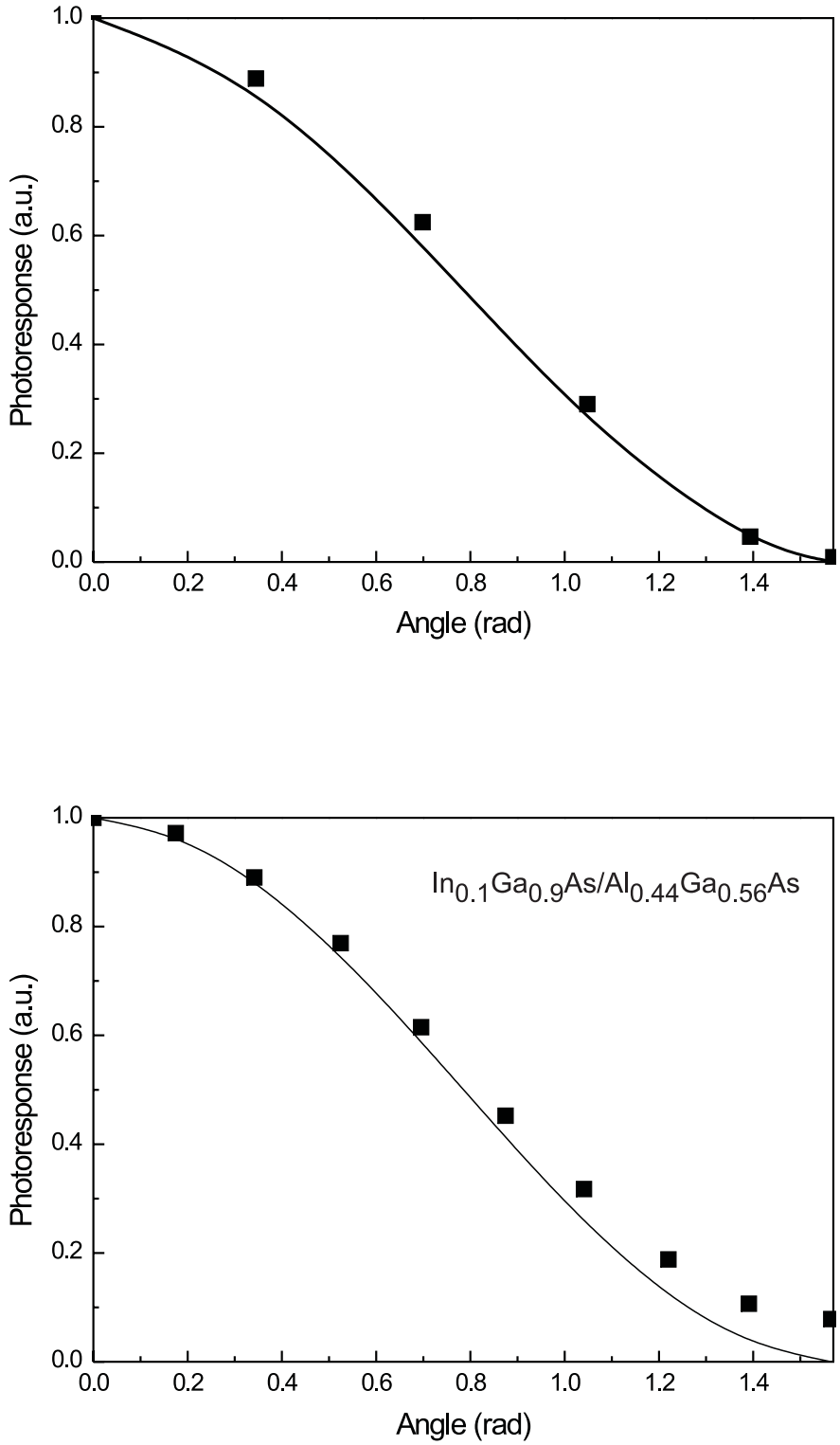

Fig. 4.3. Measured photoresponse signal vs. polarization azimuthal angle φ for (**top** panel) a GaAs/AlGaAs and (**bottom** panel) an InGaAs/AlGaAs QW (T = 80 K). The ideal $\cos^2\varphi$ relation is shown by the solid line. The size of the symbol represents the measurement error bar. From [4.6].

mission Fourier spectroscopy in the multiple-reflection waveguide geometry (see the inset). The points indicate values of the spin-galvanic current (see Sect. 8.2) observed under photoexcitation of the structure by a CO_2 laser, which causes direct transitions within each QW. One can see from Fig. 4.5 that both spectra repeat each other in agreement with the theory because the photocurrent is proportional to $K_\parallel(\hbar\omega)$ and, according to (4.21), the coefficient $K_\parallel(\hbar\omega)$ is proportional to $K_z(\hbar\omega)$.

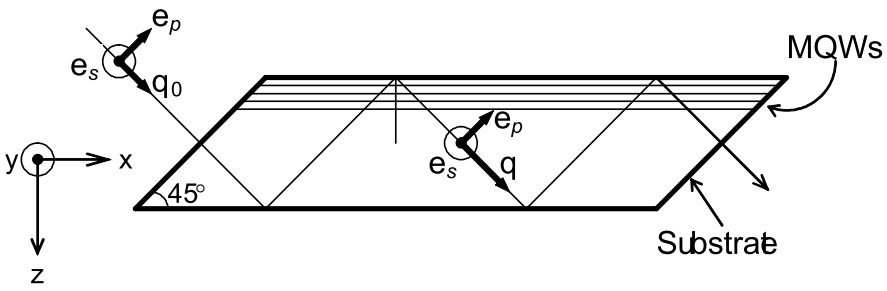

Fig. 4.4. Illustration of light transmission in the multiple-reflection wave-guide geometry.

Intersubband optical transitions in n-doped QW structures can be appreciable in the in-plane polarization ($\boldsymbol{e} \perp z$) if the effective mass in the conduction band of a compositional bulk semiconductor is anisotropic, and none of the principal axes of the reciprocal effective-mass tensor $m^{-1}_{\alpha\beta}$ coincides with the growth axis. Such a situation arises when the nanostructure is grown from many-valley semiconductors along the direction different from the principal axis of a particular valley. This can be achieved, for example, in Ge/Si_xGe_{1-x} QW structures grown in the direction [001]. In bulk Ge the electron dispersion in one of the L valleys, say the $[1\bar{1}1]$ valley, is

$$E_{\boldsymbol{k}} = \frac{\hbar^2}{2}\left(\frac{k_1^2 + k_2^2}{m_t} + \frac{k_3^2}{m_l}\right), \tag{4.24}$$

where m_t, m_l are the transverse and longitudinal effective masses, $\boldsymbol{k}$ is the electron wave vector referred to the extremum point $\boldsymbol{k}_0 = (\pi/a_0)(1,-1,1)$ and k_1, k_2, k_3 are the components of $\boldsymbol{k}$ along the axes $[1\bar{1}\bar{2}]$, [110] and $[1\bar{1}1]$, respectively. In the coordinate system $x \parallel [1\bar{1}0]$, $y \parallel [110]$, $z \parallel [001]$ relevant for (001)-grown structure, the dispersion (4.24) will be

$$E_{\boldsymbol{k}} = \frac{\hbar^2}{2}\left(\frac{k_x^2}{m_{xx}} + \frac{k_y^2}{m_{yy}} + \frac{k_z^2}{m_{zz}} + 2\,\frac{k_x k_z}{m_{xz}}\right), \tag{4.25}$$

where

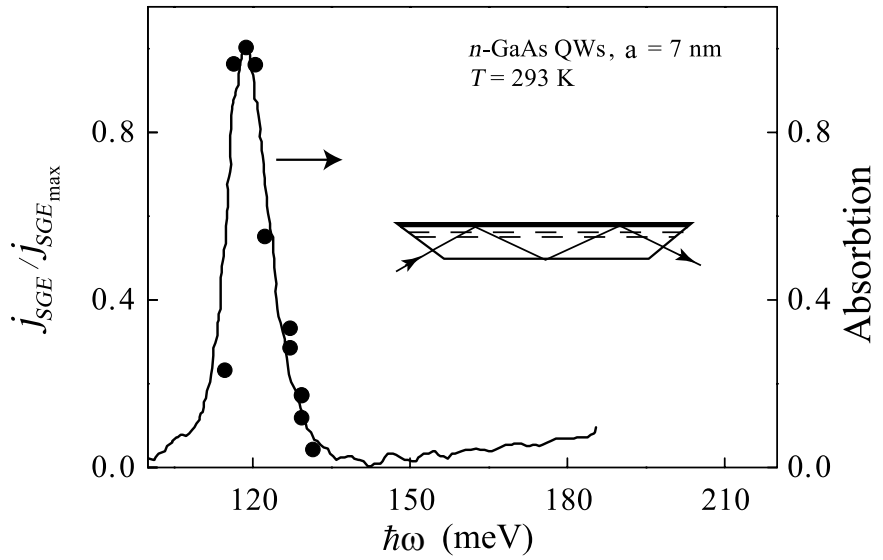

Fig. 4.5. Absorption spectrum (full line) of an n-doped (001)-grown GaAs/AlGaAs MQW structure (a = 70 Å) obtained from transmission in a multiple-reflection wave-guide geometry, see the inset. Points show the spectral dependence of the spin-galvanic current caused by the spin orientation due to direct optical transitions between $e1$ and $e2$ conduction subbands. [4.7]

$$\frac{1}{m_{xx}} = \frac{\cos^2\theta}{m_t} + \frac{\sin^2\theta}{m_l}\,,\ \frac{1}{m_{zz}} = \frac{\sin^2\theta}{m_t} + \frac{\cos^2\theta}{m_l}\,,$$
$$m_{yy} = m_t\,,\ \frac{1}{m_{xz}} = \cos\theta\sin\theta\left(\frac{1}{m_l} - \frac{1}{m_t}\right)\,,$$

and $\theta = \arccos(1/\sqrt{3})$ is the angle between the axes $[1\bar{1}1]$ and z. Notice that equation (4.25) is a particular case of the more general equation (2.21).

The x-component of the velocity, $v_x = \hbar^{-1}\partial E_{\boldsymbol{k}}/\partial k_x$, has a linear-in-$k_z$ contribution

$$v_x = \frac{\hbar k_x}{m_{xx}} + \frac{\hbar k_z}{m_{xz}}\,,$$

which allows nonzero $e2$-$e1$ intersubband matrix elements

$$v_{21,x} = -\mathrm{i}\frac{\hbar}{m_{xz}}\left\langle e2\left|\frac{\partial}{\partial z}\right|e1\right\rangle\,. \tag{4.26}$$

For the intersubband transitions at the point $k_x = k_y = 0$ in a high-barrier QW, we have

$$v_{21,x} = \frac{\hbar k_z^{(2,1)}}{m_{xz}} = \mathrm{i}\frac{8\hbar}{3a}\cos\theta\sin\theta\left(\frac{1}{m_l} - \frac{1}{m_t}\right)\,.$$

For the two lowest subbands in a Metal-Oxide-Semiconductor (MOS) structure, one sometimes chooses trial functions in the form

$$\varphi_1(z) = C_1 z \mathrm{e}^{-\alpha_1 z}\,,\ \varphi_2(z) = C_2 z \left(1 - \frac{\alpha_1+\alpha_2}{3}\, z\right) \mathrm{e}^{-\alpha_2 z}$$

with the normalizing factors

$$C_1 = 2\alpha_1^{3/2}\,,\ C_2 = 2\left(\frac{3\alpha_2^5}{\alpha_1^2 - \alpha_1\alpha_2 + \alpha_2^2}\right)^{1/2}\,.$$

In this case, one has

$$v_{21,x} = -2\mathrm{i}\frac{\hbar\alpha_2}{m_{xz}}\left(\frac{4t^3}{3(1+t^3)(1+t)^3}\right)^{1/2}\,,$$

where $t = \alpha_2/\alpha_1$.

4.1.2 Interminiband Light Absorption in a Superlattice

Now we turn to interminiband optical properties of SLs in order to show how infrared spectroscopy can reveal their miniband structure. In contrast to a MQW structure, in a SL the electron energy depends on an additional quantum index, namely, the z-component of the wave vector k_z. The transition rate in a unit 3D volume is given by (4.1) where the area S is replaced by the SL volume V and the 2D vector $\boldsymbol{k}$ by the 3D wave vector $\boldsymbol{K}$. For the absorption coefficient due to the $e1 \to e2$ transitions, one can write

$$\begin{aligned} &K_{\mathrm{SL}}(\boldsymbol{e} \parallel z) \qquad (4.27)\\ &= \frac{4\pi^2 e^2}{\omega c n_\omega}\frac{2}{V}\sum_{\boldsymbol{K}} |v_{21,z}(\boldsymbol{K})|^2 \left(f_{e1\boldsymbol{K}} - f_{e2\boldsymbol{K}}\right)\delta(E_{e2\boldsymbol{K}} - E_{e1\boldsymbol{K}} - \hbar\omega)\,. \end{aligned}$$

In the particular case of equal masses, $m_{\mathrm{A}} = m_{\mathrm{B}}$, the electron dispersion in a SL can be expressed in the form

$$E_{e\nu\boldsymbol{K}} = \frac{\hbar^2 K_\parallel^2}{2m_{\mathrm{A}}} + E_\nu(K_z)$$

so that

$$E_{e2\boldsymbol{K}} - E_{e1\boldsymbol{K}} = E_2(K_z) - E_1(K_z)\,,$$

the parabolic in-plane dispersions cancel in the argument of the δ-function in (4.27). One is left with a purely 1D reduced density of miniband states

$$\begin{aligned} \rho_{21}(\hbar\omega) &= \int \frac{dK_z}{2\pi}\,\delta\left[E_2(K_z) - E_1(K_z) - \hbar\omega\right] \qquad (4.28)\\ &= \frac{1}{\pi\hbar}\frac{1}{|v_{e2z}(K_\omega) - v_{e1z}(K_\omega)|}\,, \qquad (4.29) \end{aligned}$$

where the z component of the electron velocity is

$$v_{e\nu z}(K_z) = \frac{1}{\hbar}\frac{\partial E_\nu}{\partial K_z}$$

and K_ω satisfies the equation $E_2(K_\omega) - E_1(K_\omega) = \hbar\omega$.

The function $\rho_{21}(\hbar\omega)$ has a shape of a two-pronged fork and exhibits two square-root singularities at the high- and low-energy edges, respectively,

$$\hbar\omega_{21} = E_{21}^0 \equiv E_2^0 - E_1^0 \quad \text{and} \quad \hbar\omega'_{21} = E_2(\pi/d) - E_1(\pi/d)\,.$$

By using this function Eq. (4.27) can be rewritten as

$$K_{\rm SL}(\boldsymbol{e} \parallel z) \tag{4.30}$$
$$= \frac{4\pi^2 e^2}{\omega c n_\omega}\rho_{21}(\hbar\omega)\left[\frac{2}{S}\sum_{\boldsymbol{K}_\parallel}|v_{21,z}(\boldsymbol{K})|^2\,(f_{e1\boldsymbol{K}} - f_{e2\boldsymbol{K}})\right]_{K_z=K_\omega}.$$

Equation (4.30) can be analyzed by using different approximations. As the first limiting case let us assume $\hbar\omega$ to be close to the minigap E_{21}^0 at the Γ point. Then the parabolic approximation

$$E_\nu(K_z) = E_\nu^0 + \frac{\hbar^2 K_z^2}{2M_\nu}$$

is valid and, for the 3D Boltzmann electron gas, we come to

$$K_{\rm SL}(\boldsymbol{e} \parallel z) \tag{4.31}$$
$$= \frac{4\pi e^2}{\hbar c n_\omega}\frac{N_{3D}\,|v_{21,z}|^2}{\omega}\left(\frac{\pi\hbar^2\mu_{21}}{k_B T(E_{21}^0 - \hbar\omega)M_1}\right)^{1/2}\exp\left(-\frac{E_{21}^0 - \hbar\omega}{k_B T}\frac{\mu_{21}}{M_1}\right).$$

Here N_{3D} is the volume electron concentration, $v_{21,z}$ is the interminiband matrix element of the velocity operator at $\boldsymbol{K} = 0$, the reduced effective mass $\mu_{21} = M_1|M_2|/(M_1 + |M_2|)$. Note that M_1 is positive and M_2 is negative. The thermal energy is assumed to be small compared to the width of the lower miniband.

In a wide-barrier SL, the electron dispersion can be approximated by

$$E_1(K_z) = E_1^0 + \frac{1}{2}\Delta_1(1 - \cos K_z d)\,,\; E_2(K_z) = E_2^0 - \frac{1}{2}\Delta_2(1 - \cos K_z d)$$

and one has

$$\sin\frac{K_\omega d}{2} = \left(\frac{E_{21}^0 - \hbar\omega}{\Delta_1 + \Delta_2}\right)^{1/2},$$

$$|v_{e2z}(K_\omega) - v_{e1z}(K_\omega)| = (2\hbar)^{-1}(\Delta_1 + \Delta_2)d\sin K_\omega d\,.$$

The reduced density of miniband states is symmetric around the energy $E_{21}^0 - (\Delta_1 + \Delta_2)/2$ [4.8]

$$\rho_{21}(\hbar\omega) = \left\{\pi d\sqrt{(E_{21}^0 - \hbar\omega)[\hbar\omega - (E_{21}^0 - \Delta_1 - \Delta_2)]}\right\}^{-1} . \tag{4.32}$$

These equations can also be derived in the tight-binding approximation, where one starts with the energy levels calculated for a single QW and takes into account the coupling between the states in the nearest neighboring wells. In the same approximation the matrix element $v_{21,z}(\boldsymbol{K})$ is independent of $\boldsymbol{K}$ and equal to that for intra-well intersubband transitions. The absorption spectrum has in this case the shape of an asymmetric two-pronged fork

$$K_{\mathrm{SL}}(\boldsymbol{e} \parallel z) \propto \frac{\rho_{21}(\hbar\omega)}{\omega} \exp\left(-\frac{\Delta_1}{\Delta_1 + \Delta_2}\frac{E_{21}^0 - \hbar\omega}{k_B T}\right) .$$

The relative intensity of the low-energy peak at

$$\hbar\omega = E_{21}^0 - \Delta_1 - \Delta_2 \equiv \hbar\omega_{21}'$$

decreases with decreasing temperature.

It is instructive to trace the transition of the absorption spectrum from 3D to 2D. With increasing the barrier thickness the miniband width $\Delta_{1,2}$ decreases and the function $\rho_{21}(\hbar\omega)$ tends to $d^{-1}\delta(E_{21}^0 - \hbar\omega)$ while the expression in the square brackets in (4.30) reduces to $|v_{21,z}|^2 N_1$, where N_1 is the 2D electron density in a single QW. As a result (4.27) reduces to the absorption coefficient of a MQW structure given by (4.6).

4.2 Intersubband Optical Transitions. Complicated Band Structure

In a bulk semiconductor with the degenerate band Γ_8 (zinc-blende lattice) or Γ_8^+ (diamond lattice), direct optical transitions between the heavy- and light-hole subbands are possible under arbitrary light polarization. In the isotropic approximation, $D = \sqrt{3}B$, the coefficient of such an absorption is expressed by

$$K = \frac{e^2 k}{\hbar c n_\omega}\left[f(E_{hh}^*) - f(E_{lh}^*)\right] , \tag{4.33}$$

where the initial, heavy, and final, light, hole energies are related with the photon energy by

$$E_{hh}^* = \frac{m_{lh}}{m_{hh} - m_{lh}}\hbar\omega\ ,\ E_{lh}^* = \frac{m_{hh}}{m_{hh} - m_{lh}}\hbar\omega = E_{hh}^* + \hbar\omega\ ,$$

and the wave vector of the holes involved in the transition is given by

$$\hbar k = \left(\frac{2m_{lh}m_{hh}}{m_{hh} - m_{lh}}\hbar\omega\right)^{1/2} .$$

In QW structures, each 3D subband, hh or lh, gives birth to its series of subbands of quantum-confined states, $hh\nu$ or $lh\nu$. At the point $k_x = k_y = 0$ they are purely $\pm 3/2$ or $\pm 1/2$ states, provided the heavy-light hole mixing at the interfaces discussed in Sect. 3.3.3, see (3.212), is ignored. For nonzero $\boldsymbol{k}$, the QW subband states are intermixed and the energy dispersion has a complicated nonparabolic character, see Chap. 2 for details . For illustration Fig. 4.6 depicts the hole energy spectrum of an $In_{0.49}Ga_{0.51}P/GaAs$ QW. Because of the aforementioned admixture and nonparabolicity the subband dispersion cannot be described by a certain value of the angular momentum component and a certain effective mass. Usually the valence subbands are labelled as $j\nu$ with j standing for hh or lh in accordance with the corresponding value of m at $\boldsymbol{k} = 0$, see (2.16). There are two important consequences of this kind of band structure.

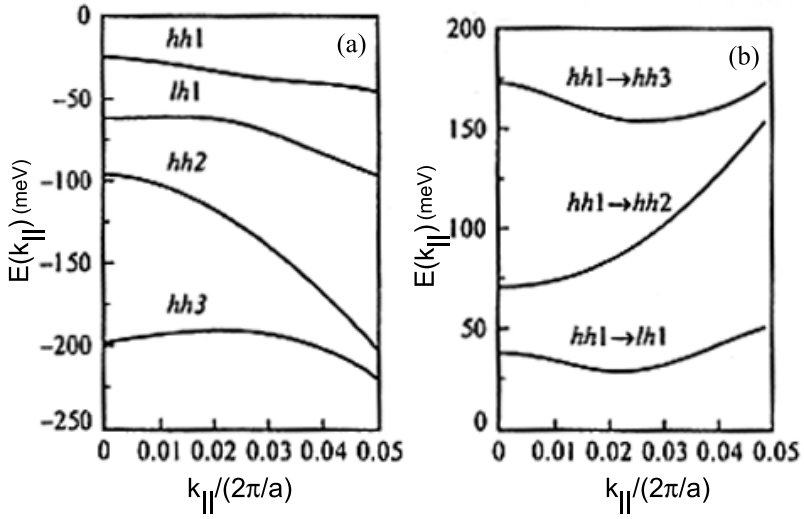

Fig. 4.6. (**a**) Valence subbands in an InGaP/GaAs QW. (**b**) The energy spacing between the lowest valence subband $hh1$ and the first three higher subbands. From [4.9].

Firstly, in contrast to the conduction-band subbands, the hole intersubband energy spacing is k-dependent and this dependence for the particular pairs ν', ν can be nonmonotonous as one can see in Fig. 4.6b. In the spherical approximation the reduced density of states

$$\rho_{j'\nu',j\nu}(\hbar\omega) = \frac{2}{S}\sum_{\boldsymbol{k}} \delta\left(E_{j'\nu'k} - E_{j\nu k}\right)$$

can be transformed to

$$\rho_{j'\nu',j\nu}(\hbar\omega) = \sum_i \frac{k_i}{\pi} \left| \frac{d(E_{j'\nu'k} - E_{j\nu k})}{dk} \right|^{-1}_{k=k_i} , \tag{4.34}$$

where k_i are roots of the equation $E_{j'\nu'k} - E_{j\nu k} = \hbar\omega$. The absorbance $\eta_{j'\nu',j\nu}$ is connected with $\rho_{j'\nu',j\nu}$ by

$$\eta_{j'\nu',j\nu}(\hbar\omega) = \frac{2\pi^2 e^2}{\omega n_\omega c} \sum_i \rho^{(i)}_{j'\nu',j\nu}(\hbar\omega) \times [f^h(E_{j\nu k_i}) - f^h(E_{j'\nu' k_i})] \sum_{p'p} \left\langle |\boldsymbol{e} \cdot \boldsymbol{v}_{j'\nu'p',j\nu p}(\boldsymbol{k})|^2 \right\rangle_{k=k_i} , \tag{4.35}$$

where $\rho^{(i)}_{j'\nu',j\nu}$ is the i-th term in the sum (4.34) and the angular brackets mean averaging over the azimuthal angle, φ, of the vector $\boldsymbol{k}$. The reduced density of states as well as the absorbance have square-root singularities near the point k_0 where the spacing $\Delta_{j'\nu',j\nu}(k) = E_{j'\nu'k} - E_{j\nu k}$ exhibits an extremum, e.g., a minimum. Expanding this energy spacing in up to the second order in $k - k_0$,

$$\Delta_{j'\nu',j\nu}(k) = \Delta_{j'\nu',j\nu}(k_0) + \frac{\hbar^2}{2\mu}(k - k_0)^2 ,$$

we obtain two roots

$$k_{1,2} = k_0 \pm \sqrt{\frac{2\mu}{\hbar^2}[\hbar\omega - \Delta_{j'\nu',j\nu}(k_0)]} .$$

The corresponding density of states becomes

$$\rho_{j'\nu',j\nu}(\hbar\omega) = \frac{k_0}{\pi\hbar} \sqrt{\frac{2\mu}{\hbar\omega - \Delta_{j'\nu',j\nu}(k_0)}} . \tag{4.36}$$

Note that, for the structure with the spectrum shown in Fig. 4.6, square-root singularities must manifest themselves at $\hbar\omega \approx 25$ meV (transitions $hh1 \to lh1$) and $\hbar\omega \approx 150$ meV (transitions $hh1 \to hh3$). Allowance for warping of the valence band, $D \neq \sqrt{3}B$, results in angular dependence of the roots $k_i(\varphi)$, broadening of the singularities and final values of $\rho_{j'\nu',j\nu}(\hbar\omega)$ and $\eta_{j'\nu',j\nu}(\hbar\omega)$. In order to get the final value of $\rho_{lh1,hh1}(\hbar\omega)$ at the point k_0, we may notice that the function $\Delta_{lh1,hh1}(\boldsymbol{k})$ has a minimum at the points $(\pm k_0, 0)$, $(0, \pm k_0)$ of the 2D $\boldsymbol{k}$-space. It can be expanded near one of these four 2D valleys, say, the valley $(k_0, 0)$, as

$$\Delta_{lh1,hh1}(\boldsymbol{k}) = \Delta_{lh1,hh1}(k_0, 0) + \frac{\hbar^2}{2\mu_x}(k_x - k_0)^2 + \frac{\hbar^2 k_y^2}{2\mu_y} , \tag{4.37}$$

where μ_x coincides with μ and μ_y tends to ∞ as the warping is vanishing. The reduced density of states for four equivalent valleys is

$$\rho_{lh1,hh1}(\max) = \frac{4\sqrt{\mu_x \mu_y}}{\pi\hbar^2} \,.$$

Secondly, intersubband transitions in p-type QWs are more complicated than those in n-type QWs because, due to the $\boldsymbol{k}$-dependent band-mixing effect, there are no simple selection rules at $\boldsymbol{k} \neq 0$ so that both the normal ($\boldsymbol{e} \parallel z$) and in-plane ($\boldsymbol{e} \perp z$) polarizations are allowed with the transition rates being comparable. In the effective-mass approximation the intersubband matrix elements $\boldsymbol{v}_{j'\nu'p',j\nu p}(\boldsymbol{k})$ are calculated starting from the velocity operator expressed as the gradient in $\boldsymbol{k}$ space of the Luttinger Hamiltonian

$$\boldsymbol{e} \cdot \boldsymbol{v}(\boldsymbol{k}) = \hbar^{-1} \boldsymbol{e} \cdot \nabla_{\boldsymbol{k}} \mathcal{H}_{\Gamma_8}(\boldsymbol{k}) = \sum_{\alpha\beta} e_\alpha Q_{\alpha\beta} k_\beta \,, \tag{4.38}$$

where

$$Q_{\alpha\beta} = \frac{2}{\hbar}\left[\left(A - \frac{5}{4}B + BJ_\alpha^2\right)\delta_{\alpha\beta} + (1-\delta_{\alpha\beta})\frac{D}{\sqrt{3}}\{J_\alpha J_\beta\}_s\right] \,.$$

In terms of the four-component envelope functions expressed as columns $\hat{F}_{j\nu p\boldsymbol{k}}(z)$, see (2.37), the matrix elements are written in the form

$$\boldsymbol{e} \cdot \boldsymbol{v}_{j'\nu'p',j\nu p}(\boldsymbol{k}) = \sum_{\alpha\beta} e_\alpha \int dz\, \hat{F}^\dagger_{j'\nu'p'\boldsymbol{k}}(z)\, Q_{\alpha\beta}\, \hat{k}_\beta\, \hat{F}_{j\nu p\boldsymbol{k}}(z) \,, \tag{4.39}$$

where $\hat{\boldsymbol{k}} = (k_x, k_y, -\mathrm{i}\partial/\partial z)$ and the index p takes into account the double degeneracy of the hole states.

For a symmetric QW, the two degenerate states are classified by a parity p under the mirror reflection, $z \to -z$, which transforms the electron spinor wave function $\psi(x,y,z)$ into $\hat{\sigma}_z\psi(x,y,-z)$. We remind us (Chap. 2) that, for symmetric states labelled with the index $p = +$, the m-th component $F_{j\nu+\boldsymbol{k},m}(z)$ of the column $\hat{F}_{j\nu+\boldsymbol{k}}(z)$ has the parity $p_m = (-1)^{3/2-m}$. The envelope $F_{j\nu-\boldsymbol{k},m}(z)$ of an antisymmetrical state is obtained from the corresponding symmetrical state by changing z into $-z$ and m into $-m$, complex conjugation and multiplication by a factor $(-1)^{3/2-m}$ relating the Bloch function $|\Gamma_8, m\rangle$ with the function $\hat{\mathcal{K}}\,|\Gamma_8, -m\rangle$, see (2.41). In the polarization $\boldsymbol{e} \parallel (x,y)$, the parity is conserved under intersubband transitions, $p' = p$, whereas, in the polarization $\boldsymbol{e} \perp (x,y)$, the parity is reversed. Moreover, the symmetry imposes additional conditions upon nonzero matrix elements

$$|\boldsymbol{e}_\parallel \cdot \boldsymbol{v}_{j'\nu'+,j\nu+}(\boldsymbol{k})|^2 = |\boldsymbol{e}^*_\parallel \cdot \boldsymbol{v}_{j'\nu'+,j\nu+}(\boldsymbol{k})|^2 \,,$$

$$|v^z_{j'\nu'-,j\nu+}(\boldsymbol{k})|^2 = |v^z_{j'\nu'+,j\nu-}(\boldsymbol{k})|^2 \,.$$

The phenomenon inverse to the absorption is the spontaneous emission of hot carriers heated up, e.g., by an external electric field [4.10]. The heating results in occupation of higher-energy states. Direct optical transitions from

these states to the lower subbands is accompanied by emission of light. We define the spectral intensity of the secondary radiation by

$$I(\hbar\omega) = \frac{\hbar\omega\ \Delta W}{\Delta(\hbar\omega)\ \Delta\Omega}\ , \tag{4.40}$$

where ΔW is the rate of emission of photons in the frequency region $\Delta\omega$ within a solid angle $\Delta\Omega$ from a unit area of the illuminating QW. For the intersubband transitions, the spectral intensity of spontaneous emission can be presented in the form

$$I(\hbar\omega) = \frac{e^2\omega^2 n_\omega}{\pi c^3}\frac{1}{S}\sum_{j'j\nu'\nu\boldsymbol{k}} f_{j'\nu'\boldsymbol{k}}(1-f_{j\nu\boldsymbol{k}})\,\delta(E_{j'\nu'\boldsymbol{k}}-E_{j\nu\boldsymbol{k}}-\hbar\omega) \tag{4.41}$$

$$\times\ \sum_{p'p}|\boldsymbol{e}^*\cdot\boldsymbol{v}_{j\nu p,j'\nu'p'}(\boldsymbol{k})|^2\ .$$

The emission matrix element $\boldsymbol{e}^*\cdot\boldsymbol{v}_{j\nu p,j'\nu'p'}(\boldsymbol{k})$ equals the complex conjugate matrix element $[\boldsymbol{e}\cdot\boldsymbol{v}_{j'\nu'p',j\nu p}(\boldsymbol{k})]^*$ for the intersubband absorption. Equation (4.41) can be derived by using the straightforward expression for the differential of the emission rate due to the $j',\nu'\to j,\nu$ transitions

$$\Delta W_{j\nu,j'\nu'} = \frac{2\pi}{\hbar}\frac{V_0 q^2\Delta q\Delta\Omega}{(2\pi)^3}\left(\frac{e}{c}A_0\right)^2\sum_{\boldsymbol{k}} f_{j'\nu'\boldsymbol{k}}(1-f_{j\nu\boldsymbol{k}}) \tag{4.42}$$

$$\times\ \delta(E_{j'\nu'\boldsymbol{k}}-E_{j\nu\boldsymbol{k}}-\hbar\omega)\,\frac{2}{S}\sum_{p'p}|\boldsymbol{e}^*\cdot\boldsymbol{v}_{j\nu p,j'\nu'p'}(\boldsymbol{k})|^2\ .$$

Here $q = n_\omega(\omega/c)$ is the light wave vector, the differential Δq equals to $n_\omega\Delta\omega/c$, $A_0 = (2\pi\hbar c^2/n_\omega^2 V_0\,\omega)^{1/2}$ is the amplitude of the vector potential related to a single electromagnetic quantum, see (3.28). We consider the radiation emitted in a small solid angle $\Delta\Omega$ around the normal to the interfaces. In this case the transition probability rate is independent of the secondary photon polarization and $\boldsymbol{e}$ is any in-plane unit vector. An additional factor of 2 in (4.42) takes into account two polarization states of a transverse electromagnetic wave. After various simplifications the equations (4.40, 4.42) reduce to (4.41).

A spectrum of the spontaneous emission from a p-doped GaAs/AlGaAs QW structure in the electric field 450 V/cm is plotted in Fig. 4.7 with the solid curve. The dashed curve is calculated as a half-sum of two spectra obtained for $\boldsymbol{e}\parallel z$ and $\boldsymbol{e}\perp z$. To take into account the homogeneous and inhomogeneous broadening as well as the resolution of the detector, the theoretical spectrum is convoluted with a Gaussian of the width 2 meV. The hole energy distribution was described by the Fermi-Dirac function with the hot-hole effective temperature of 80 K. One can see a satisfactory agreement between the theory and experiment.

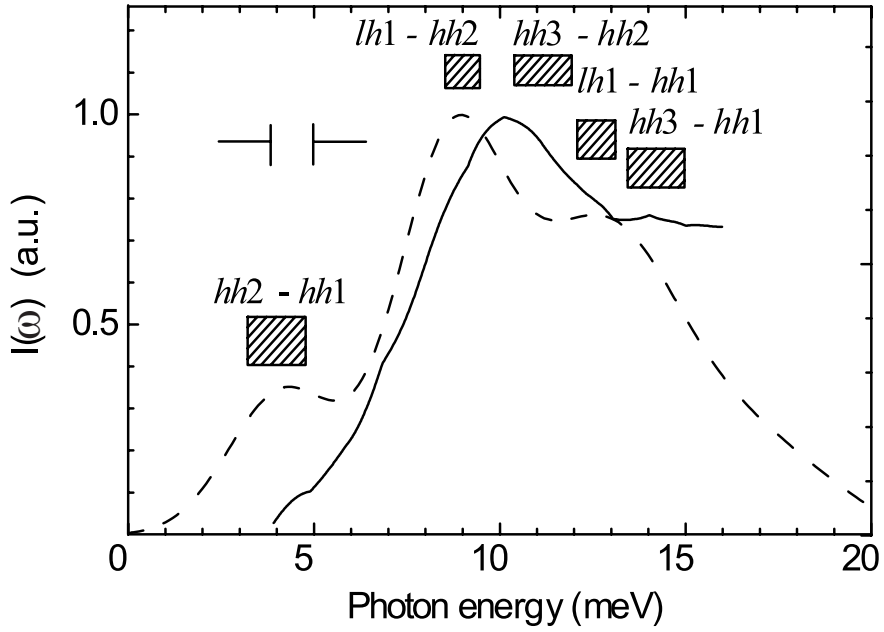

Fig. 4.7. Measured (*solid*) and calculated (*dashed*) emission spectra for the applied electric field $F = 450$ V/cm. Rectangles show estimated spectral widths expected from the analysis of the reduced density of states in an ideal homogeneous structure. [4.10]

4.3 Intrasubband Optical Transitions

4.3.1 Intrasubband Light Absorption in a Quantum Well

Considering free-carrier intrasubband absorption in a QW in the Drude model, we start from the classical equation for in-plane motion of an electron

$$\dot{\boldsymbol{v}}(t) + \gamma \boldsymbol{v}(t) = \frac{e}{m^*}\, \boldsymbol{E}(t)\,, \tag{4.43}$$

where γ is the phenomenological damping constant. In a QW where an electron moves freely in the interface plane and is effected only by the in-plane component of an external electric field, equation (4.43) reduces to

$$\dot{\boldsymbol{v}}_{\parallel}(t) + \gamma \boldsymbol{v}_{\parallel}(t) = \frac{e}{m^*}\, \boldsymbol{E}_{\parallel}(t)\,.$$

The amplitudes of the in-plane current and the electric field are related by

$$\boldsymbol{j}_{\parallel}(\omega) = eN_{2D}\boldsymbol{v}_{\parallel}(\omega) = \frac{e^2 N_{2D}}{m(-\mathrm{i}\omega + \gamma)}\, \boldsymbol{E}_{\parallel}(\omega)\,.$$

The absorbance

$$\eta = \frac{\hbar\omega}{I}\, W \tag{4.44}$$

can be expressed in terms of current and field, and be written as

$$\eta = \frac{2}{I}\,\mathrm{Re}\left\{\boldsymbol{j}_{\parallel}(\omega)\cdot\boldsymbol{E}^{*}_{\parallel}(\omega)\right\} = \frac{4\pi e^2 N_{2D}\gamma}{m^* c n_\omega(\omega^2+\gamma^2)}\,. \tag{4.45}$$

Here W is the photon absorption rate and $I = (cn_\omega/2\pi)|\boldsymbol{E}_{\parallel}(\omega)|^2$ is the light intensity.

For $\hbar\omega \ll \bar{E}$, the expression for η can be derived by solving the kinetic equation

$$-\mathrm{i}\omega\,\delta f_{\boldsymbol{k}}(\omega) + \frac{e}{\hbar}\boldsymbol{E}_{\parallel}\cdot\nabla_{\boldsymbol{k}} f^0(E_k) + \frac{\delta f_{\boldsymbol{k}}(\omega)}{\tau_p} = 0$$

for the deviation of the electron distribution function, $\delta f_{\boldsymbol{k}}$, induced by the in-plane electric field. The result coincides with (4.45) if γ^{-1} is set equal to the momentum scattering time.

In the limit $\omega \gg \tau_p^{-1}$ the absorption rate W (or absorbance η) can be calculated by using Fermi's golden rule for indirect transitions. For *scattering by static defects* this rule reads

$$W = \frac{2\pi}{\hbar}\frac{2\pi e^2 I}{\omega^2 c n_\omega}\frac{2}{S}\sum_{\boldsymbol{k}'\boldsymbol{k}}\sum_i |R^{(i)}_{\boldsymbol{k}'\boldsymbol{k}}|^2 (f^0_k - f^0_{k'})\delta(E_{k'} - E_k - \hbar\omega) \tag{4.46}$$

with the second-order matrix element for defect-assisted electron-photon interaction being

$$\begin{aligned} R^{(i)}_{\boldsymbol{k}'\boldsymbol{k}} &= \frac{(\boldsymbol{e}\cdot\boldsymbol{v}_{\boldsymbol{k}'})V^{(i)}_{\boldsymbol{k}'\boldsymbol{k}}}{E_{k'} - E_k} + \frac{V^{(i)}_{\boldsymbol{k}'\boldsymbol{k}}(\boldsymbol{e}\cdot\boldsymbol{v}_{\boldsymbol{k}})}{-\hbar\omega} \\ &= \frac{\hbar}{m^*}\,\frac{V^{(i)}_{\boldsymbol{k}'\boldsymbol{k}}}{\hbar\omega}\,\boldsymbol{e}\cdot(\boldsymbol{k}' - \boldsymbol{k})\,. \end{aligned} \tag{4.47}$$

Here $\boldsymbol{v}_{\boldsymbol{k}} = \hbar\boldsymbol{k}/m^*$ is the electron velocity, $V^{(i)}_{\boldsymbol{k}'\boldsymbol{k}}$ is the matrix element of spin-conserving elastic scattering $\boldsymbol{k} \to \boldsymbol{k}'$ and the index i enumerates the elementary scatterers. The corresponding momentum relaxation time that determines the mobility is given by

$$\frac{1}{\tau_p(E)} = \frac{2\pi}{\hbar}\frac{2}{S}\sum_{\boldsymbol{k}'}\sum_i |V^{(i)}_{\boldsymbol{k}'\boldsymbol{k}}|^2(1-\cos\theta)\delta(E_{k'} - E)\,,$$

where θ is the scattering angle. Further analysis is readily performed assuming $V^{(i)}_{\boldsymbol{k}'\boldsymbol{k}}$ is $\boldsymbol{k}$ and $\boldsymbol{k}'$ independent which is valid for defects with a short-range in-plane scattering potential. Then the absorbance in the high-frequency limit can be presented as

$$\eta = \frac{4\pi e^2 N_{2D}\gamma(\omega)}{m^* c n_\omega \omega^2}\,, \tag{4.48}$$

where γ is a function of the light frequency. In accordance with the kinetic-theory result, at low frequencies, i.e. for $\hbar\omega \ll \bar{E}$, the damping γ coincides with τ_p^{-1}, while in the high-frequency region, $\hbar\omega \gg \bar{E}$ but $\hbar\omega < E_{21}$, the damping constant becomes $(2\tau_p)^{-1}$.

For intrasubband optical transitions *assisted by phonons*, the transition probability rate is similar to (4.46)

$$W = \frac{2\pi}{\hbar}\frac{2\pi e^2 I}{\omega^2 c n_\omega}\frac{2}{S}\sum_{\boldsymbol{k'k}}\sum_{\boldsymbol{q},\pm}|R_{\boldsymbol{k'k}}(\boldsymbol{q})|^2\delta(E_{k'}-E_k-\hbar\omega\pm\hbar\Omega_{\boldsymbol{q}}) \tag{4.49}$$
$$\times\left[f_k(1-f_{k'})\left(m_{\boldsymbol{q}}+\frac{1}{2}\pm\frac{1}{2}\right)-f_{k'}(1-f_k)\left(m_{\boldsymbol{q}}+\frac{1}{2}\mp\frac{1}{2}\right)\right].$$

Here f_k is the electron distribution function, the sign + or − indicates the process of phonon emission or absorption, $\boldsymbol{q}$, $\Omega_{\boldsymbol{q}}$ and $m_{\boldsymbol{q}}$ are the phonon wave vector, frequency and occupation number, respectively. For equilibrium phonons the latter is described by the Planck function $[\exp(\hbar\Omega_{\boldsymbol{q}}/k_BT)-1]^{-1}$. The matrix element of the indirect electron-photon interaction is presented in the form

$$R_{\boldsymbol{k'k}}(\boldsymbol{q}) = \left[\frac{(\boldsymbol{e}\cdot\boldsymbol{v}_{\boldsymbol{k'}})V^{\pm}_{\boldsymbol{k'k}}(\boldsymbol{q})}{E_{k'}-E_k\pm\hbar\Omega_{\boldsymbol{q}}}+\frac{V^{\pm}_{\boldsymbol{k'k}}(\boldsymbol{q})(\boldsymbol{e}\cdot\boldsymbol{v}_{\boldsymbol{k}})}{-\hbar\omega}\right]\delta_{\boldsymbol{k'}\pm\boldsymbol{q}_\parallel,\boldsymbol{k}}$$
$$= \frac{\hbar}{m^*}\,\frac{V^{\pm}_{\boldsymbol{k'k}}}{\hbar\omega}\,\boldsymbol{e}\cdot(\boldsymbol{k'}-\boldsymbol{k})\,\delta_{\boldsymbol{k'}\pm\boldsymbol{q}_\parallel,\boldsymbol{k}}\,, \tag{4.50}$$

where $V^{\pm}_{\boldsymbol{k'k}}(\boldsymbol{q})$ is the matrix element of electron-phonon interaction, and the δ-symbol describes the in-plane momentum conservation in the scattering act. The first term in the right-hand side of (4.50) corresponds to the process of electron scattering by a phonon to the virtual state $\boldsymbol{k'}$ followed by absorption of a photon while the second term describes the transition where the photon absorption precedes the scattering by a phonon.

The main features of the phonon-assisted intrasubband absorption can be understood neglecting interface effects on the phonon energy spectrum and treating the electron-phonon interaction as that between 2D electrons and conventional 3D phonons. Then for the matrix element of electron interaction with polar-optical phonons in a zinc-blende QW structure one has

$$V^{\pm}_{\boldsymbol{k'k}}(\boldsymbol{q}) = \pm\mathrm{i}|e|\left[\frac{2\pi\hbar\Omega_{LO}}{V_0(q_\parallel^2+q_z^2)}\left(\frac{1}{æ_\infty}-\frac{1}{æ_0}\right)\right]^{1/2}J^{(\pm)}(q_z)\,, \tag{4.51}$$

where

$$J^{(+)}(q_z) = J^{(-)*}(q_z) = \int \mathrm{e}^{-\mathrm{i}q_z z}\varphi_{e1}^2(z)\,dz \tag{4.52}$$

and $\varphi_{e1}(z)$ is the envelope function of a quantum-confined electron. In symmetrical QWs, $J^{(+)}(q_z)$ and $J^{(-)}(q_z)$ coincide and are real. A similar form has the matrix element for deformation-potential or piezoelectric interaction of

electrons with acoustic phonons. Particularly, for the deformation-potential interaction one has

$$V^{\pm}_{\boldsymbol{k}'\boldsymbol{k}}(\boldsymbol{q}) = \mp \mathrm{i}\, \Xi_c \left(\frac{\hbar \sqrt{q_\parallel^2 + q_z^2}}{2\rho V_0 s_{LA}} \right)^{1/2} J^{(\pm)}(q_z)\,, \tag{4.53}$$

where Ξ_c is the deformation-potential constant, ρ is the density of the semiconductor and s_{LA} is the longitudinal sound velocity.

In a symmetric QW with infinitely high barriers, the integral (4.52) equals to

$$J^{(\pm)}(q_z) = \frac{\sin x}{x} \left(1 + \frac{\pi x}{\pi^2 - x^2} \right)\,,$$

where $x = q_z a/2$. Values of $[J^{(\pm)}(q_z)]^2$ are close to unity for $x < \pi/2$ and become negligible for $x > 3\pi/2$. Therefore, a typical value of q_z in (4.53) is π/a while

$$q_\parallel^2 \sim \frac{2m^*}{\hbar^2} \max\left(\bar{E}, \hbar\omega\right)\,.$$

This differs from intraband optical transitions in a bulk semiconductor where the square modulus $q_x^2 + q_y^2 + q_z^2$ is determined by $\max\left(\bar{E}, \hbar\omega\right)$.

Figure 4.8 presents the calculated temperature dependence of the absorption coefficient of GaAs/AlGaAs MQWs, $K = \eta/d$, at the wavelength $\lambda = 92$ μm ($\hbar\omega = 13$ meV) [4.11]. One can see the separate contributions to indirect absorption due to scattering by optical phonons, impurities and interface imperfections as well as a sum of these contributions.

Since the LO-phonon energy $\hbar\Omega_{LO}$ in GaAs is 36 meV and $\omega < \Omega_{LO}$, at low temperatures the light absorption of electrons interacting with LO-phonons can be ignored and the scattering by static defects is dominating. With increasing temperature the role of transitions accompanied by LO-phonon absorption increases. At the same time the step-like energy distribution of the degenerate 2D electron gas is smeared, and photon absorption followed by emission of a LO phonon also becomes possible. As a result, the optical-phonon assisted absorption is dominating starting with $T = 200$ K.

Agethe and Vass [4.12] have calculated the LO-phonon limited intrasubband photon absorption in n-doped QWs taking into account that the actual phonon spectrum is more complicated and consists of confined, interface (symmetric and antisymmetric), half-space and bulk modes. They analyzed the contribution to the absorption from each phonon mode as a function of four controllable parameters, namely, the light frequency ω, QW thickness a, electron temperature T_e and density N_{2D}.

4.3.2 Electron Cyclotron Resonance in a Superlattice

Cyclotron resonance is the most powerful technique for measuring the effective masses in solids. In the classical description of the cyclotron resonance

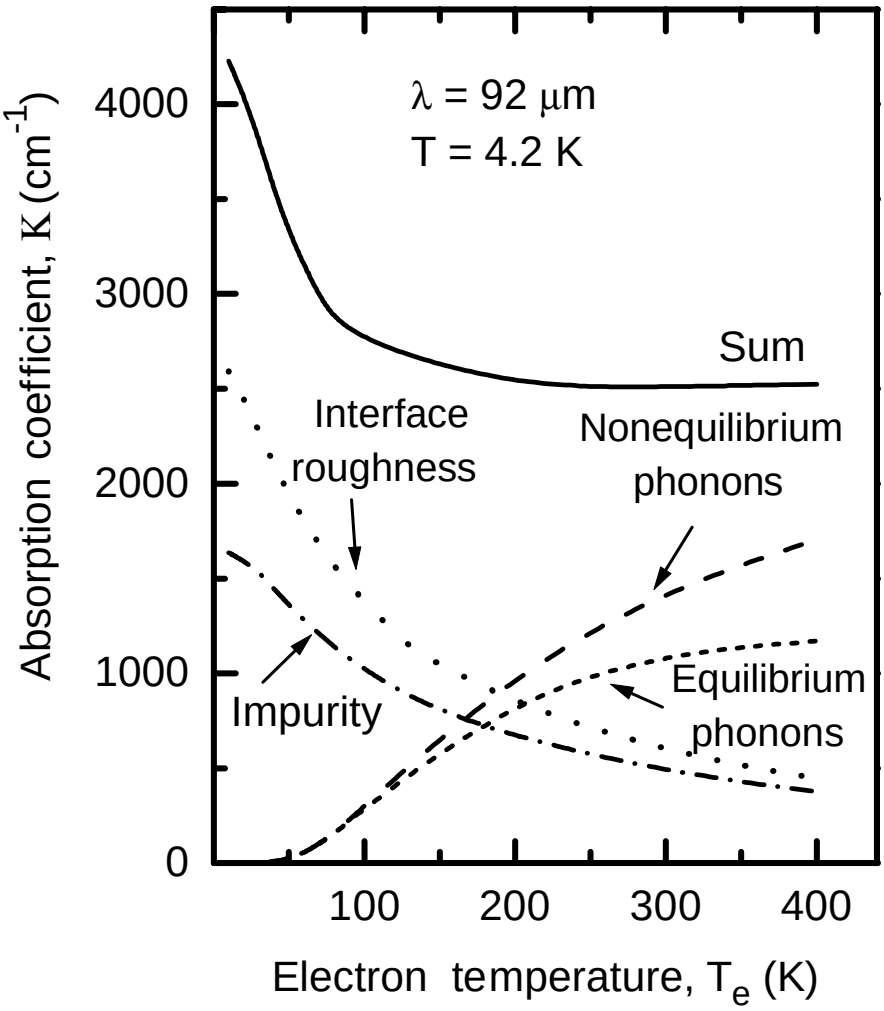

Fig. 4.8. Calculated contributions of various scattering mechanisms to the far-infrared absorption coefficient of a biased n-doped GaAs/AlGaAs MQW structure for s-polarized light. In the calculation, interface scattering, impurity scattering, scattering by equilibrium and nonequilibrium phonons are taken into account. The sum of all contributions is shown by the solid line. From [4.11].

in the 3D space, the equation of motion (4.43) is replaced by the *Lorentz equation*

$$\dot{\boldsymbol{v}}(t) + \gamma \boldsymbol{v}(t) = \frac{e}{m^*} \left[\boldsymbol{E}(t) + \frac{\boldsymbol{v}(t)}{c} \times \boldsymbol{B} \right] , \tag{4.54}$$

where $\boldsymbol{B}$ is an external static magnetic field and $\boldsymbol{E}(t)$ is an oscillating electric field. We assume $\boldsymbol{E}(t) \perp \boldsymbol{B}$ and use the system of coordinates with $z \parallel \boldsymbol{B}$. Equation (4.54) is readily solved and the current-density combinations $j_\pm = j_x \pm \mathrm{i} j_y$ are given by

$$j_\pm(\omega) = eN_{3D} v_\pm = \frac{e^2 N_{3D}}{m^*} \frac{E_\pm(\omega)}{-\mathrm{i}(\omega \pm \omega_c) + \gamma} , \tag{4.55}$$

where ω_c the classical cyclotron frequency $|e|B_z/(m^*c)$. When the frequency ω passes through the cyclotron frequency, either j_+ (if $B_z < 0$) or j_- (if $B_z > 0$) exhibits a resonant behavior and one observes the resonant absorption of electromagnetic radiation (microwave or far-infrared).

In quantum-mechanical terms, the cyclotron resonance originates from optical transitions of charged particles between the Landau levels. Measurement of the dependence of the cyclotron-resonance frequency on the magnitude and direction of the magnetic field provides a direct and reliable way for determining the electron or hole effective mass, as well as for studying the nonparabolicity and nonsphericity of an electronic band in a semiconductor.

In a bulk semiconductor with a parabolic conduction band

$$E_{\boldsymbol{k}} = \frac{\hbar^2}{2} \left(\frac{k_1^2}{m_1} + \frac{k_2^2}{m_2} + \frac{k_3^2}{m_3} \right) , \tag{4.56}$$

the Schrödinger equation for the envelope wave function in a homogeneous magnetic field can be simplified by change of the coordinates

$$x_i \to \tilde{x}_i = \sqrt{\frac{m_i}{\bar{m}}}\, x_i \qquad (i = 1, 2, 3)$$

to an equivalent equation for an electron with the isotropic mass $\bar{m} = (m_1 m_2 m_3)^{1/3}$ in an effective field $\tilde{\boldsymbol{B}}$ with the components

$$\tilde{B}_i = \sqrt{\frac{m_i}{\bar{m}}}\, B_i \, . \tag{4.57}$$

Therefore, the energy spacing between the nearest Landau levels assumes the form

$$\hbar\omega_c = \hbar \frac{|e|\tilde{B}}{\bar{m}c} = \hbar \frac{|e|B}{m_c c} , \tag{4.58}$$

where the cyclotron mass

$$m_c = \bar{m} \left(\sum_i \frac{m_i}{\bar{m}} \cos^2 \theta_i \right)^{-1/2} , \tag{4.59}$$

θ_i is the angle between $\boldsymbol{B}$ and the axis i.

If two of the three masses m_i coincide, for instance, if $m_1 = m_2 \equiv m_t$, the expression for the cyclotron mass simplifies to

$$m_c(\theta_3) = \left(\frac{\sin^2 \theta_3}{m_t m_l} + \frac{\cos^2 \theta_3}{m_t^2} \right)^{-1/2} , \tag{4.60}$$

where $m_l \equiv m_3$. By measuring the cyclotron resonance in the $\boldsymbol{B} \parallel 3$ and $\boldsymbol{B} \perp 3$ geometries, one can determine the cyclotron masses $m_c(\theta_3 = 0) = m_t$ and $m_c(\theta_3 = \pi/2) = \sqrt{m_t m_l}$ and, hence, the longitudinal mass

$$m_l = \frac{m_c^2(\pi/2)}{m_c(0)} . \tag{4.61}$$

If $\boldsymbol{B} \parallel x_3$, the cyclotron orbit is a circle and has the scale of the magnetic length

$$\lambda_B = \left(\frac{\hbar c}{|e|B} \right)^{1/2} .$$

If $\boldsymbol{B} \perp x_3$, say, $\boldsymbol{B} \parallel x_2$, the cyclotron orbit is elliptical with different magnetic lengths along x_1 and x_3,

$$\lambda_{B,x_1} = \left(\frac{m_l}{m_t} \right)^{1/4} \left(\frac{\hbar c}{|e|B} \right)^{1/2} , \; \lambda_{B,x_3} = \left(\frac{m_t}{m_l} \right)^{1/4} \left(\frac{\hbar c}{|e|B} \right)^{1/2} . \tag{4.62}$$

If the electron dispersion $E_{\boldsymbol{k}}$ has a more complex form than (4.56), one can use for determination of the cyclotron mass m_c the semi-classical approach

$$m_c(E, k_z) = \frac{\hbar^2}{2\pi} \int \int dk_x dk_y \delta(E_{\boldsymbol{k}} - E) , \tag{4.63}$$

where the z axis of the Cartesian coordinate system x, y, z is directed along the magnetic field. Of the states with a fixed electron energy E, the main contribution to the cyclotron resonance comes from those characterized by extremal orbits corresponding to a maximum or minimum of the k_z-dependence of m_c.

In QWs, the electron motion along the growth direction is quantized and the cyclotron orbits are confined to the interface plane. In terms of a 3D semiconductor it is equivalent to setting $m_l \to \infty$ in (4.60), which results in a cosine dependence of the cyclotron mass

$$m_c(\theta) = m^* \cos \theta \tag{4.64}$$

on the angle θ between the normal to the interfaces and the magnetic field direction. This angular dependence, as a signature of the confinement of cyclotron orbits in MQWs with thick barriers, was first confirmed in the

optically detected cyclotron resonance in a structure consisting of 180-Å-thick GaAs wells separated by 230-Å $Al_{0.33}Ga_{0.67}As$ barriers [4.13]. These indirect methods for observing cyclotron and magnetic resonances, Optically Detected Cyclotron Resonance (ODCR) and Optically Detected Magnetic Resonance (ODMR), involve the monitoring of microwave-induced changes in the luminescence intensity.

In the case of SLs, coupling between wells through thin penetrable barriers transforms subbands of electron quantum-confined states into minibands of extended states. The energy dispersion of the latter has a 3D character. Therefore, the cyclotron resonance in SLs should reveal properties similar to those in a uniaxial semiconductor crystal with the longitudinal effective mass drastically dependent on the barrier thickness. Particularly, the Landau levels are formed not only in the $\boldsymbol{B} \parallel z$ geometry as in the case of QWs but also in a magnetic field lying in the interface plane. According to (4.60), in the latter configuration the cyclotron mass is the geometric mean of the in-plane mass m_t and the "superstructural" mass m_l, and the spacing between Landau levels is smaller than in the former configuration. Landau levels in a SL were first observed in both configurations of the magnetic field by Belle et al. [4.14] who studied the photoluminescence excitation spectra of the structure containing 40 periods of 39.2-Å GaAs wells and 11.2-Å $Al_{0.4}Ga_{0.6}As$ barriers. The first direct cyclotron-resonance measurements on extended states in a semiconductor SL were performed by Duffield et al. [4.15]. Figure 4.9 illustrates their measurements of the normal (m_l) and in-plane (m_t) effective masses in a $GaAs/Al_xGa_{1-x}As$ as a function of the aluminum fraction x in the barriers. The curves bounding the shaded areas represent the $m_l(x)$ dependence calculated for a SL with rectangular wells and barriers, and for the conduction-band offset $V = 0.65\Delta E_g$ or $V = 0.61\Delta E_g$ using the Kronig-Penney boundary conditions

$$\varphi_{\mathrm{A}} = \varphi_{\mathrm{B}} \,, \left(\frac{d\varphi}{dz}\right)_{\mathrm{A}} = \left(\frac{d\varphi}{dz}\right)_{\mathrm{B}} \tag{4.65}$$

or the Bastard boundary conditions (2.10).

The above picture of the cyclotron orbits in the geometry $\boldsymbol{B} \parallel x_2$ is valid at low magnetic fields when the magnetic length $\lambda_{B,z}$ is larger than the SL period d, and an electron can complete its elliptical cyclotron orbit through several barriers. If the lattice periodicity and cyclotron orbit radius are comparable the electron energy gets dependent on the position of the cyclotron orbit along the growth axis z and one needs to solve explicitly the Schrödinger equation for the electron envelope function $\psi(\boldsymbol{r})$ in a SL [4.16]. With $\boldsymbol{B} \parallel y$ and using the Landau gauge, $A_x = Bz, A_y = A_z = 0$, this function can be sought in the form

$$\psi(\boldsymbol{r}) = \mathrm{e}^{\mathrm{i}(k_x x + k_y y)} \varphi(z) \,, \tag{4.66}$$

where $\varphi(z)$ satisfies the equation

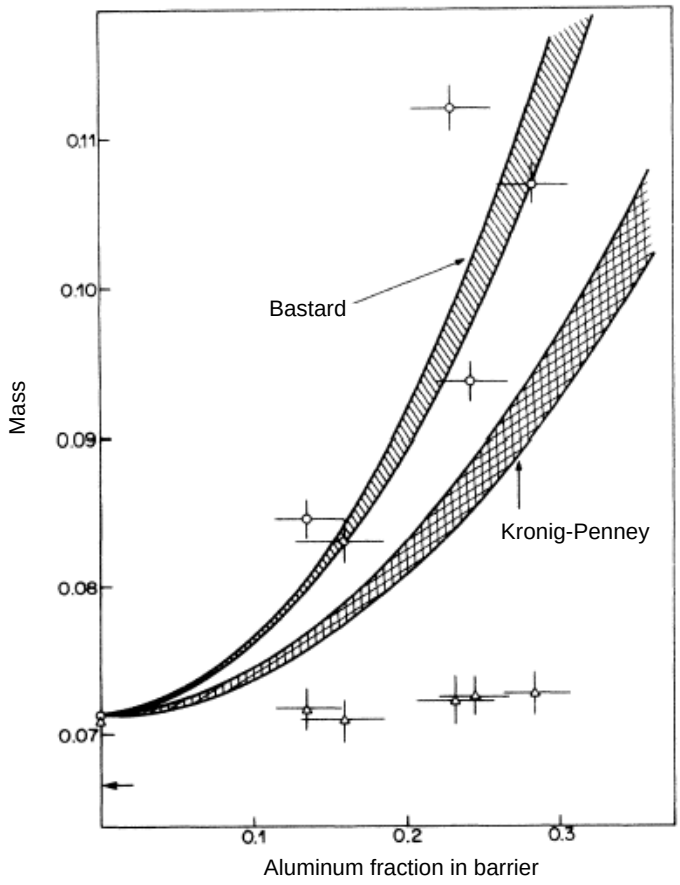

Fig. 4.9. Effective electron mass related to the free electron mass in the lowest miniband $e1$ in GaAs/Al_xGa_{1-x}As SL with $a = 80$ Å, $b \approx 20$ Å vs. composition x. The experimental data were obtained from a cyclotron resonance study. Circles, the normal mass $m_l \equiv m_{zz}$; triangles, the in-plane mass $m_t \equiv m_{xx} = m_{yy}$. The calculations performed for the boundary conditions (4.65) and (2.10) are displayed by shaded areas. The curves bounding these areas correspond to the conduction-band offset $V = 0.65\Delta E_g$ (*top* curve) and $V = 0.61\Delta E_g$ (*bottom* curve). From [4.15].

$$\frac{\hbar^2}{2m^*}\left[\left(k_x - \frac{eB}{c\hbar}\,z\right)^2 + k_y^2\right]\varphi(z) - \left(\frac{d}{dz}\frac{\hbar^2}{2m^*}\frac{d}{dz}\right)\varphi(z) + V(z)\varphi(z) = E\varphi(z)\,.$$

Here the notations x, y, z are used instead of x_1, x_2, x_3, $V(z)$ is the superstructure potential, and the effective mass m^* is allowed to be different in the well and barrier materials. The position of the cyclotron orbit $z_0 = k_x\lambda_B^2$ is a good quantum number. In the limit $\lambda_{B,z} = (m_t/m_l)^{1/4}\lambda_B \gg d$, the Landau levels are flat, i.e., they have the same energy for all values of z_0. At

higher fields, as the cyclotron energy approaches the miniband width, $\lambda_{B,z}$ and d become comparable and the interlevel energy spacing as a function of B tends to saturate. Simultaneously, the Landau levels develop dispersion, and the resonant absorption spectrum broadens [4.17].

4.4 Infrared Reflection from Quantum Wells and Superlattices

Optical phonon modes dominate the infrared absorption and spectroscopic ellipsometry in undoped bulk semiconductors and multi-layered heterostructures. Infrared reflectance can be used as a simple, contactless and nondestructive, characterization technique to provide the information on the thicknesses of the various layers, alloy composition, phonon frequencies and broadening parameters. We consider here the infrared reflection spectroscopy from an undoped SL and its description in the effective-medium dielectric function model.

For a crystal of cubic symmetry with two different atoms in the unit cell, the dielectric function in the infrared region can be represented in the form

$$æ(\omega) = æ_\infty \frac{\Omega_L^2 - \omega^2 - 2\mathrm{i}\Gamma_L\omega}{\Omega_T^2 - \omega^2 - 2\mathrm{i}\Gamma_T\omega} , \tag{4.67}$$

where Ω_L and Ω_T are the resonance frequencies of the LO and TO phonon, respectively, $æ_\infty$ is the high-frequency dielectric constant, and Γ_L, Γ_T are the phonon damping rates. In general, $\Gamma_L \neq \Gamma_T$ but usually these constants are assumed to coincide.

Let a SL consist of alternating layers of semiconductors A and B with the isotropic dielectric functions $æ_\mathrm{A}(\omega)$ and $æ_\mathrm{B}(\omega)$, described by (4.67) with a given set of parameters $æ_\mathrm{A}^\infty, \Omega_{T1}, \Omega_{L1}$ for the layer A, and $æ_\mathrm{B}^\infty, \Omega_{T2}, \Omega_{L2}$ for the layer B. For simplicity, in the main part of this section, we neglect the phonon damping. For an arbitrary relation between the light wavelength and the SL period $d = a+b$, one needs to use the straightforward treatment of the normal light waves in a periodic medium presented in Chap. 2. If the light wavelength is large compared to the SL period $d = a + b$, then, according to (2.132), the SL may be treated as a homogeneous uniaxial medium with two linearly independent components of the dielectric tensor,

$$\begin{aligned} æ_\perp(\omega) \equiv æ_{xx} = æ_{yy} &= \frac{æ_\mathrm{A}(\omega)a + æ_\mathrm{B}(\omega)b}{a+b} , \\ æ_\parallel(\omega) \equiv æ_{zz} &= \frac{(a+b)æ_\mathrm{A}(\omega)æ_\mathrm{B}(\omega)}{æ_\mathrm{A}(\omega)b + æ_\mathrm{B}(\omega)a} . \end{aligned} \tag{4.68}$$

The function $æ_\perp(\omega)$ has poles at the points $\omega = \omega_{T1}, \omega_{T2}$ and the function $æ_\perp(\omega)$ has zeros at the points $\omega = \omega_{L1}, \omega_{L2}$. Denoting the zeroes of the function

$$æ_{\rm A}(\omega)a + æ_{\rm B}(\omega)b$$

by $\omega_{\perp,1}, \omega_{\perp,2}$ and those of the function

$$æ_{\rm A}(\omega)b + æ_{\rm B}(\omega)a$$

by $\omega_{\parallel,1}, \omega_{\parallel,2}$ we can represent the frequency dependence of the components (4.68) in a factorized form

$$æ_\perp(\omega) = æ_\perp^\infty \frac{(\omega_{\perp,1}^2 - \omega^2)(\omega_{\perp,2}^2 - \omega^2)}{(\Omega_{T1}^2 - \omega^2)(\Omega_{T2}^2 - \omega^2)} , \tag{4.69}$$

$$æ_\parallel(\omega) = æ_\parallel^\infty \frac{(\Omega_{L1}^2 - \omega^2)(\Omega_{L2}^2 - \omega^2)}{(\omega_{\parallel,1}^2 - \omega^2)(\omega_{\parallel,2}^2 - \omega^2)} ,$$

where

$$æ_\perp^\infty = \frac{æ_{\rm A}^\infty a + æ_{\rm B}^\infty b}{a+b} , \; æ_\parallel^\infty = \frac{(a+b)æ_{\rm A}^\infty æ_{\rm B}^\infty}{æ_{\rm A}^\infty b + æ_{\rm B}^\infty a} . \tag{4.70}$$

Note that in a SL with layers of equal thicknesses, $a = b$, the frequencies $\omega_{\perp,j}$ and $\omega_{\parallel,j}$ coincide.

In a uniaxial medium, solutions of the Maxwell equations split into ordinary and extraordinary waves. For the ordinary waves (s- or TE-polarization), the electric vector $\boldsymbol{E}$ is perpendicular to the plane containing the light wave vector $\boldsymbol{q}$ and the principal axis. The dispersion equation has the form

$$q^2 = \left(\frac{\omega}{c}\right)^2 æ_\perp(\omega) .$$

For the extraordinary waves (p- or TM-polarization), the vector $\boldsymbol{E}$ lies in the plane $(\boldsymbol{q}, z)$, and the dispersion equation is

$$q^2 = \left(\frac{\omega}{c}\right)^2 \frac{æ_\perp(\omega) æ_\parallel(\omega)}{æ_\perp(\omega)\cos^2\theta + æ_\parallel(\omega)\sin^2\theta} ,$$

where θ is the angle between $\boldsymbol{q}$ and z. For the reflection coefficient from the boundary between the vacuum and semi-infinite SL, one obtains

$$R_\mu = |r_\mu|^2 , \; r_\mu = \frac{1 - \bar{n}_\mu}{1 + \bar{n}_\mu} ,$$

where the index $\mu = {\rm s}, {\rm p}$ indicates the polarization of the incident wave,

$$\bar{n}_{\rm s} = \frac{\left(æ_\perp - \sin^2\theta_0\right)^{1/2}}{\cos\theta_0} , \; \bar{n}_{\rm p} = \frac{1}{\cos\theta_0}\left(\frac{æ_\parallel - \sin^2\theta_0}{æ_\parallel æ_\perp}\right)^{1/2} , \tag{4.71}$$

and θ_0 is the external angle of incidence.

If a SL is finite and grown on a substrate with an isotropic dielectric constant $æ_b$, one has to take into account the light reflection at the boundary

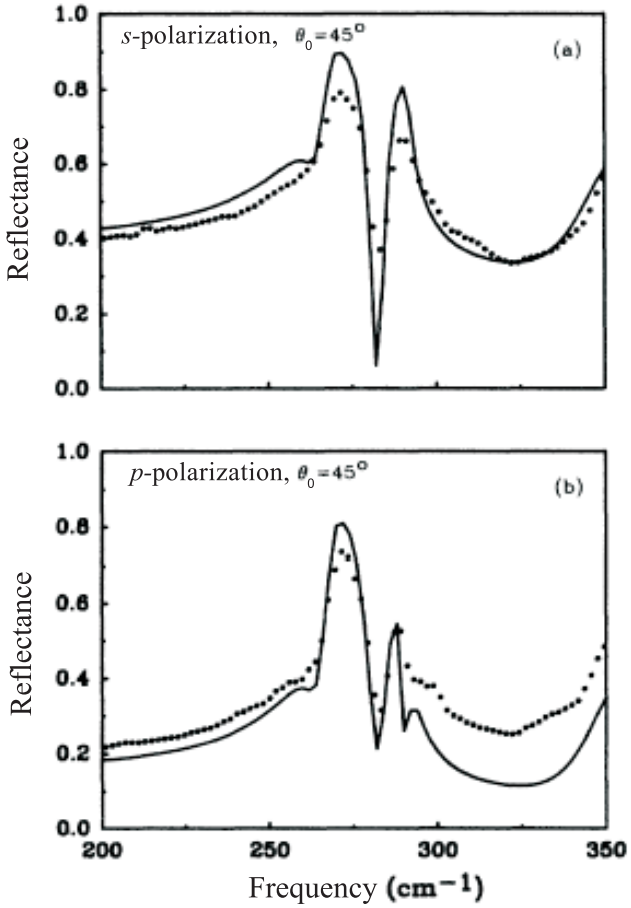

Fig. 4.10. Theoretical (*solid*) and experimental (*dotted*) infrared reflectance spectra under oblique incidence with the $\theta_0 = 45^\circ$ for the *s*-polarized (**a**) and *p*-polarized (**b**) light. The strong peak at 270 cm^{-1} is the GaAs TO mode. From [4.18].

'SL – substrate' and interference of waves reflected from the external and internal SL boundaries. If the substrate is thick enough in order to neglect the reflection from its back face, we obtain for the reflection coefficients r_s and r_p [4.18]

$$r_\mu = \frac{(1-\bar{n}_{b,\mu})\cos\Phi_\mu - \mathrm{i}\left(\frac{\bar{n}_{b,\mu}}{\bar{n}_\mu} - \bar{n}_\mu\right)\sin\Phi_\mu}{(1+\bar{n}_{b,\mu})\cos\Phi_\mu - \mathrm{i}\left(\frac{\bar{n}_{b,\mu}}{\bar{n}_\mu} + \bar{n}_\mu\right)\sin\Phi_\mu}\,. \tag{4.72}$$

Here

$$\bar{n}_{b,s} = \frac{\left(æ_b - \sin^2\theta_0\right)^{1/2}}{\cos\theta_0}\ ,\ \bar{n}_{b,p} = \frac{\left(æ_b - \sin^2\theta_0\right)^{1/2}}{æ_b\cos\theta_0}\ ,$$

$$\Phi_s = \frac{\omega}{c}L\left(æ_\perp - \sin^2\theta_0\right)^{1/2}\ ,\ \Phi_p = \frac{\omega}{c}L\left[\left(æ_\parallel - \sin^2\theta_0\right)\frac{æ_\perp}{æ_\parallel}\right]^{1/2}\ ,$$

and L is the SL thickness. Figure 4.10 shows reflectance spectra of a GaAs/AlAs SL grown on a GaAs substrate measured and analyzed by Lou et al. [4.18] It should be noted that the solid-solution layer in a GaAs/$Al_xGa_{1-x}As$ SL with $x \neq 0, 1$ (or in any other similar zinc-blende-lattice SL) contains two optical modes associated with the vibrations of the Ga–As and Al–As atomic pair, and

$$æ_B(\omega) = æ_B^\infty\,\frac{(\Omega_{L,1}^2 - \omega^2 - 2i\Gamma_{L,1}\omega)(\Omega_{L,2}^2 - \omega^2 - 2i\Gamma_{L,2}\omega)}{(\Omega_{T,1}^2 - \omega^2 - 2i\Gamma_{T,1}\omega)(\Omega_{T,2}^2 - \omega^2 - 2i\Gamma_{T,2}\omega)}\ . \tag{4.73}$$

Here $æ_B^\infty$ is close to the average

$$(1-x)æ_\infty(\mathrm{GaAs}) + xæ_\infty(\mathrm{AlAs})$$

and $\Omega_{T,1}, \Omega_{T,2}$ are close to the transverse optical vibrational frequencies 268 cm^{-1} and 362 cm^{-1} in homogeneous GaAs and AlAs, respectively. For illustration, the parameters for the solid solution $Al_{0.3}Ga_{0.7}As$ derived from comparison of experimental and theoretical normal-reflection spectra are as follows [4.19]: $\Omega_{T,1} = 265.2$ cm^{-1}, $\Omega_{L,1} = 278.3$ cm^{-1}, $\Omega_{T,2} = 360.2$ cm^{-1}, $\Omega_{L,2} = 379.1$ cm^{-1}, $\Gamma_{T,1} = 4.32$ cm^{-1}, $\Gamma_{L,1} = 3.07$ cm^{-1}, $\Gamma_{T,2} = 6.05$ cm^{-1}, $\Gamma_{L,2} = 4.71$ cm^{-1}, $æ_B^\infty = 10.16$.

The above approach can be readily extended to consider the vibrational spectra of wurtzite-lattice SLs grown along the hexagonal axis, for example, CdSe/CdS [4.20] or GaN/AlN [4.21] SLs. We recall that the wurtzite crystals belong to the symmetry group C_{6v}. For this lattice, the group theory predicts one A_1 and one E_1 type optical phonon modes that are Raman and infrared active, two E_2 modes which are Raman active and two B_1 inactive modes. Within each layer, A or B, the dielectric tensor is characterized by two linearly independent components

$$æ_\perp(\omega) = æ_\perp^\infty\,\frac{\Omega_{L,\perp}^2 - \omega^2 - 2i\Gamma_{L,\perp}\omega}{\Omega_{T,\perp}^2 - \omega^2 - 2i\Gamma_{T,\perp}\omega}\ ,$$

$$æ_\parallel(\omega) = æ_\parallel^\infty\,\frac{\Omega_{L,\parallel}^2 - \omega^2 - 2i\Gamma_{L,\parallel}\omega}{\Omega_{T,\parallel}^2 - \omega^2 - 2i\Gamma_{T,\parallel}\omega}$$

with the parameters dependent on A or B. The effective dielectric tensor in a short-period SL is given by (4.68) where the components $æ_{xx} = æ_{yy}$ are expressed in terms of $æ_{A,\perp}, æ_{B,\perp}$ whereas $æ_{zz}$ is related to $æ_{A,\parallel}$ and $æ_{B,\parallel}$.

5 Photoluminescence Spectroscopy

Light is sweet,
and it pleases the eyes to see the sun.

Ecclesiastes **11***: 7*

The light of the righteous shines brightly,
but the lamp of the wicked is snuffed out.

Proverbs **13***: 9*

Luminescence, or fluorescence, is an efficient tool to study the excited electronic states in solids. Since the luminescence intensity is determined both by the population of the excited states and the optical-transition probabilities, luminescence, in many cases, offers an advantage in analyzing the fine structure of excited states, which does not show up in absorption or reflection spectra. Moreover, it provides the possibility to investigate the kinetics of population and relaxation of the excited states. By studying the luminescence for different populations of the electronic states, one can examine effects of electron-electron interaction on electronic spectra.

In the present chapter we pay attention to *PhotoLuminescence* (PL), i.e., to emission of radiation induced by the optical excitation of a sample by using an external source of light. The conventional PL spectroscopy is based on measurements of secondary-emission spectrum at fixed parameters of the primary radiation. In this set-up the measured spectrum is mainly determined by the oscillator strength and lifetime of the radiative states with the energies lying close to the fundamental absorption edge and, indirectly, by processes of energy relaxation of "hot" excited states. In another technique known as PhotoLuminescence Excitation (PLE) spectroscopy the spectrometer is set to detect emission of a particular photon energy from the sample. The intensity of this emission is recorded as a function of the excitation photon energy. PLE spectra give information about the oscillator strength and the density of states above the fundamental absorption edge but not about their lifetime. Photoluminescence of semiconductor nanostructures has its own specific features which will be successively considered in the following sections.

5.1 Mechanisms of Photoluminescence

In semiconductors, depending on the character of the radiative transition, one distinguishes between intrinsic, extrinsic and exciton luminescence. Intrinsic, or band-to-band, luminescence is connected with the recombination of free electrons and holes. Extrinsic or impurity luminescence originates from the

radiative recombination of free electrons with holes bound to acceptors, or of free holes with bound-to-donor electrons, the so-called *bound-to-free emission*, as well as from radiative donor-acceptor recombination and optical transitions between the levels of the same impurity center. Exciton luminescence appears due to the recombination of free, impurity-bound or localized excitons. Other exciton-related mechanisms of light emission are exciton-polariton, biexciton (or multi-exciton) and trion luminescence. If the kinetic energy of the free carriers or excitons involved in recombination exceeds substantially the thermal energy, such light emission is called *hot luminescence*.

Low-temperature luminescence of undoped QW structures is attributed to radiative recombination of excitons localized by interface microroughness, substitutional alloy disorder, or both. The fluctuations in the well width and alloy composition modulate the local 2D potential giving rise to localized states forming the exciton-band tail. If the exciton hopping is ineffective the PL lineshape is governed by the density of localized states. In the multiple hopping regime to be considered in the next section, the population of the exciton-band tail and, hence, the PL spectrum are being formed as a result of competition between exciton recombination and acoustic-phonon-assisted transfer from higher- to lower-energy localized sites. The same holds true for QWR structures even more so because in this case the width of a nanoobject fluctuates in two dimensions.

At higher temperatures excitons are delocalized and characterized by the quasi-equilibrium distribution function $f(K) = C \exp\left(-\hbar^2 K^2 / 2Mk_BT\right)$, where $\boldsymbol{K}$ is the d-dimensional wave vector, $d = 2$ for QWs and $d = 1$ for QWRs, the normalization coefficient C is proportional to $T^{d/2}N$, N is the exciton density. The PL decay time is given by

$$\tau_{PL}^{-1} = \frac{\int d^d K \, \tau_r^{-1}(K) \, f(K)}{\int d^d K \, f(K)} \,, \tag{5.1}$$

where $\tau_r(K) = [2\Gamma_0(K)]^{-1}$ is the exciton radiative lifetime. Bearing in mind that only excitons with $K < (\omega_0/c)n_b$ can emit photons while those with $K > (\omega_0/c)n_b$ are "dark" (Sect. 3.1.1) one can derive the following equation for the inverse decay time

$$\tau_{PL}^{-1} \approx \frac{f(0) \int d^d K \, \tau_r^{-1}(K)}{\int d^d K \, f(K)} \propto T^{d/2} \,. \tag{5.2}$$

Here we assumed that the exciton thermal wave vector $K_T = (2Mk_BT/\hbar^2)^{1/2}$ considerably exceeds a value of the light wave vector $(\omega_0/c)n_b$.

Gershoni et al. used the temperature dependence of the PL decay time as an unambiguous signature of a 1D- or 2D-system [5.1]. They performed measurements of PL transients in GaAs/$Al_{1-x}Ga_xAs$ QWs and nanometer-scale QWRs. The latter were prepared by cleaved-edge epitaxial overgrowth. In the temperature range 10–90 K the PL decay times followed roughly a

temperature power-law dependence, $\tau_{PL}(T) = AT^{\beta}$. The best-fitted slope β obtained for the 80-Å QW was 1.05±0.1 whereas, for the 34-Å and 80-Å strain-induced QWRs, the slopes were 0.4±0.1 and 0.33±0.1 in reasonable agreement with theoretical prediction $\beta = 1$ for a QW and $\beta = 0.5$ for a QWR, see (5.2).

5.2 Emission Spectra of Localized Excitons

5.2.1 Stokes Shift of the Low-Temperature Photoluminescence Peak

The PL spectral peak from undoped QW or QWR structures at low temperatures is usually red-shifted with respect to the peak in absorption or PLE spectra. This so-called *Stokes shift* is explained taking into account that the excitation spectrum is dominated by optical transitions to extended free-exciton states, while the low-temperature PL arises from radiative recombination of localized excitons. In this subsection we outline the main features of the theory describing the low-temperature multi-hopping relaxation of localized excitons and discuss experiments on cw and time-resolved PL spectroscopy. Theoretically, the key problem for the multi-hopping regime is a description of excitonic kinetics making allowance for a wide scatter in the intersite times because of the random spatial distribution of the sites.

Let us consider the temporal evolution of the PL peak under the pulsed optical excitation of a QW or QWR. Hereafter, to denote the localized states, we use the localization energy ε instead of the exciton excitation energy

$$E = E_0 - \varepsilon \,, \tag{5.3}$$

where E_0 is the mobility edge separating the extended and localized states. To minimize the number of parameters entering into the theory we assume a simplified model with the following properties:

(1) The density of localized-exciton states, $g(\varepsilon)$, decays exponentially with increasing the localization energy

$$g(\varepsilon) = g_0 \exp\left(-\varepsilon/\varepsilon_0\right) , \tag{5.4}$$

where g_0 and ε_0 are constants.

(2) Let $w(\varepsilon, \varepsilon', r)$ be the exciton hopping transfer rate for the transition $\varepsilon \to \varepsilon'$ between the localization sites separated by a distance r. The temperature is set to zero and the probability of such a hopping is nonzero only if $\varepsilon' > \varepsilon$ (or $E > E'$). Therefore, one can write

$$w(\varepsilon, \varepsilon', r) = \theta(\varepsilon' - \varepsilon)\, w_h(r) \,, \tag{5.5}$$

where $\theta(x)$ is the Heaviside step function.

(3) The rate $w(r)$ is independent of ε and ε', and decays exponentially with increasing the separation

$$w_h(r) = \omega_0 \, \mathrm{e}^{-2r/L} \, , \tag{5.6}$$

because, for a localized exciton, the envelope wave function exhibits an exponential asymptotic behavior, $\Psi(R) \to R^{(1-d)/2} \exp(-R/L)$, where L is the localization length and d is the space dimensionality.

(4) The localized-exciton recombination time τ_0 is independent of ε.

The pulsed interband optical excitation of the structure is followed by fast energy relaxation of photocreated electrons and holes to the bottom of conduction band and top of the valence band, binding of the photoelectrons and photoholes into free excitons and the free-exciton initial localization. In the multiple-trapping process, the excitons with small values of ε hop to the deeper states with larger localization energies and the PL peak red-shifts in time. We shall analyze the temporal evolution of the PL peak by using quite general physical considerations.

According to (5.4), the concentration of sites with the localization energy exceeding ε is given by

$$\rho(\varepsilon) = \int_{\varepsilon}^{\infty} d\varepsilon' \, g(\varepsilon') = g_0 \varepsilon_0 \mathrm{e}^{-\varepsilon/\varepsilon_0} \, . \tag{5.7}$$

It follows then that the average distance, $\bar{r}_\varepsilon$, between the localization sites with $\varepsilon' > \varepsilon$ can be estimated from the condition to find in the circle of the radius $\bar{r}_\varepsilon$, on the average, one of such centers of localization. This is equivalent to the equation

$$V_d(\bar{r}_\varepsilon)\rho(\varepsilon) = 1 \, , \tag{5.8}$$

where $V_d(r)$ is the volume of the sphere of radius r in the d-dimensional space

$$V_3(r) = \frac{4\pi}{3} r^3 \, , \; V_2(r) = \pi r^2 \, , \; V_1(r) = 2r \, . \tag{5.9}$$

An exciton trapped onto the site ε hops within the distance $\bar{r}_\varepsilon$. The lifetime with respect to the hopping is given by

$$\tau_\varepsilon = w_h^{-1}(\bar{r}_\varepsilon) = \omega_0^{-1} \mathrm{e}^{2\bar{r}_\varepsilon/L} \, . \tag{5.10}$$

The PL peak position $E_{\max} = E - \varepsilon_{\max}$ at the delay time t following the pulsed photoexcitation is found from the evident relation $\tau_{\varepsilon_{\max}} = \omega_0^{-1} \exp(2\bar{r}_\varepsilon/L) = t$, or

$$\varepsilon_{\max}(t) = \varepsilon_0 \ln \left[g_0 \varepsilon_0 V_d(L/2) \ln^d(\omega_0 t) \right] = d\varepsilon_0 \ln\ln(\omega_0 t) + A \, , \tag{5.11}$$

where the constant $A = \varepsilon_0 \ln[g_0 \varepsilon_0 V_d(L/2)]$. Therefore, for localized excitons, the time-dependent Stokes shift is described by the double logarithmic law.

Using the same line of reasoning one can come to the conclusion that, under the cw photoexcitation above the mobility edge, the position of the PL peak is determined by (5.11) where the time t is replaced by the exciton recombination lifetime

$$\varepsilon_{\max}^{cw} = d\,\varepsilon_0 \ln\ln\left(\omega_0\tau_0\right) + A\,. \tag{5.12}$$

Now we obtain the same result in the frame of a more rigorous kinetic theory. We proceed from the approximation of optimal hopping transfers. This means that an exciton localized at any site O is allowed to hop to a lower-energy site O′ characterized by the maximum value of $w(\varepsilon,\varepsilon',r)$, see (5.5), for a given microscopic configuration near the site O. Then we can label every excitonic state by two parameters: the localization energy ε and distance r to the nearest site with the localization energy $\varepsilon' > \varepsilon$. The acoustic-phonon-assisted hopping of localized excitons is described by the kinetic equation

$$\left(\frac{\partial}{\partial t} + \frac{1}{\tau_0}\right) f(\varepsilon,r,t) + I_{\varepsilon,r}\{f\} = \Gamma^{(0)}(\varepsilon,t)\,. \tag{5.13}$$

Here $f(\varepsilon,r)$ is the population, or occupancy, of the state (ε,r), $\Gamma^{(0)}(\varepsilon)$ is the generation rate at level ε due to phonon-assisted transitions from extended excitonic states (or under resonant optical excitation), and the intersite transfer term $I_{\varepsilon,r}\{f\}$ is an analogue of the collision integral in the conventional Boltzmann equation. In the approximation of optimal hopping it has the form

$$\begin{aligned} I_{\varepsilon,r}\{f\} &= w_h(r)\, f(\varepsilon,r,t) \\ &\quad - \int\limits_0^{\varepsilon} d\varepsilon_1 \int\limits_0^{\infty} dr_1\, \frac{g(\varepsilon_1)}{\rho(\varepsilon_1)}\, P_{\varepsilon_1}(r_1)\, w_h(r_1)\, f(\varepsilon_1,r_1,t)\,. \end{aligned} \tag{5.14}$$

The first term on the right-hand side describes the hopping down from the state (ε,r) while the second term accounts the rate for hopping to this particular state from the higher localized states with $\varepsilon_1 < \varepsilon$. The function $P_\varepsilon(r)$ is the distribution of the optimal neighbors in energy and space. For an uncorrelated system of localized sites it can be presented as

$$P_\varepsilon(r) = \rho(\varepsilon) S_d(r) \exp\left[-V_d(r)\rho(\varepsilon)\right]. \tag{5.15}$$

Here $S_d(r) = dV_d(r)/dr$ is the area of the generalized sphere

$$S_3 = 4\pi r^2\,,\; S_2 = 2\pi r\,,\; S_1 = 2\,. \tag{5.16}$$

Note that, for the exponential density of states defined in (5.4), the ratio $g(\varepsilon_1)/\rho(\varepsilon_1)$ equals to ε_0^{-1}.

An exciton localized in the state ε emits a photon of the energy

$$\hbar\omega = E_0 - \varepsilon \,. \tag{5.17}$$

Therefore, the PL spectral intensity, $I(\omega)$, is proportional to the exciton energy distribution function, $N(\varepsilon) = N(E_0 - \hbar\omega)$, related with $f(\varepsilon, r)$ and $P_\varepsilon(r)$ by

$$N(\varepsilon) = g(\varepsilon) \int\limits_0^\infty dr P_\varepsilon(r) f(\varepsilon, r) \,.$$

Note that, as soon as τ_0 is independent of ε, the integral intensity of PL radiation decays exponentially according to

$$J(t) = \int I(\omega, t)\, d\omega = J(0)\, \mathrm{e}^{-t/\tau_0} \,, \tag{5.18}$$

where $I(\omega, t)$ is the spectral intensity at the time t.

Let us introduce the total generation rate $\mathit{\Gamma}(\varepsilon)$ at the level ε including the income from both delocalized (extended) and localized states

$$\mathit{\Gamma}(\varepsilon) = \mathit{\Gamma}^{(0)} + \int\limits_0^\varepsilon \frac{d\varepsilon_1}{\varepsilon_0} \int\limits_0^\infty dr_1\, P_{\varepsilon_1}(r_1)\, w_h(r_1)\, f(\varepsilon_1, r_1) \,. \tag{5.19}$$

Using the same assumptions as in deriving (5.11, 5.12), we neglect the dependence of $\tau_0, \mathit{\Gamma}^{(0)}$ and $w_h(r)$ on ε. In the steady-state regime the time derivative in (5.13) vanishes and the occupancy $f(\varepsilon, r)$ is time-independent. Then (5.13) can be rewritten as

$$\left[\frac{1}{\tau_0} + w_h(r)\right] f(\varepsilon, r) = \mathit{\Gamma}(\varepsilon) \,, \tag{5.20}$$

or

$$f(\varepsilon, r) = \frac{\mathit{\Gamma}(\varepsilon)}{\tau_0^{-1} + w_h(r)} \,. \tag{5.21}$$

Substituting the latter expression into (5.19) an integral equation containing only $\mathit{\Gamma}(\varepsilon)$ is obtained

$$\mathit{\Gamma}(\varepsilon) = \mathit{\Gamma}^{(0)} + \int\limits_0^\varepsilon \frac{d\varepsilon_1}{\varepsilon_0} \mathit{\Gamma}(\varepsilon_1) W_h(\varepsilon_1) \,, \tag{5.22}$$

where $W_h(\varepsilon)$ is the probability that the exciton in the state ε prefers to hop down rather than to recombine. It is defined by

$$W_h(\varepsilon) = \int\limits_0^\infty dr P_\varepsilon(r) \frac{w_h(r)}{\tau_0^{-1} + w_h(r)} \,.$$

Differentiating (5.22) over ε we come to the equation

$$\frac{d}{d\varepsilon}\Gamma(\varepsilon) = \frac{W_h(\varepsilon)}{\varepsilon_0}\,\Gamma(\varepsilon)\,.$$

Its solution with the boundary condition $\Gamma(0) = \Gamma^{(0)}$, see (5.19), is given by

$$\Gamma(\varepsilon) = \Gamma^{(0)} \exp\left[\int\limits_0^{\varepsilon} \frac{d\varepsilon_1}{\varepsilon_0} W_h(\varepsilon_1)\right]. \tag{5.23}$$

From this equation and (5.21) we finally arrive at

$$f(\varepsilon, r) = \frac{\Gamma^{(0)}}{\tau_0^{-1} + w_h(r)} \exp\left[\int\limits_0^{\varepsilon} \frac{d\varepsilon_1}{\varepsilon_0} W_h(\varepsilon_1)\right]. \tag{5.24}$$

Further simplifications are possible following the approximate replacement of the ratio

$$\frac{w_h(r)}{\tau_0^{-1} + w_h(r)}$$

by the step function $\theta(\tilde{r} - r)$, where the critical radius $\tilde{r}$ satisfies the condition

$$w_h(\tilde{r}) = \frac{1}{\tau_0} \quad \text{or} \quad \tilde{r} = \frac{L}{2}\ln(\omega_0\tau_0)\,, \tag{5.25}$$

and the ratio

$$\frac{\tau_0^{-1}}{\tau_0^{-1} + w_h(r)} = 1 - \frac{w_h(r)}{\tau_0^{-1} + w_h(r)}$$

by $1 - \theta(\tilde{r} - r) = \theta(r - \tilde{r})$. Then we successively obtain for the probability to hop

$$W_h(\varepsilon) \approx \int\limits_0^{\tilde{r}} dr P_\varepsilon(r) = 1 - \mathrm{e}^{X(\varepsilon)}\,,$$

the total generation rate

$$\Gamma(\varepsilon) \approx \Gamma^{(0)} \exp\left[\int\limits_0^{\varepsilon} \frac{d\varepsilon_1}{\varepsilon_0}\left(1 - \mathrm{e}^{X(\varepsilon_1)}\right)\right]$$

and the occupancy

$$f(\varepsilon, r) \approx \theta(r - \tilde{r})\tau_0\Gamma(\varepsilon)\,,$$

where

$$X(\varepsilon) = \rho(\varepsilon)V_d(\tilde{r})\,. \tag{5.26}$$

As a result, the energy distribution function can be simplified to

$$N(\varepsilon) = I^{(0)}\tau_0 g(\varepsilon) \int\limits_{\tilde{r}}^{\infty} dr P_\varepsilon(r) \exp\left[\int\limits_0^{\varepsilon} \frac{d\varepsilon_1}{\varepsilon_0} W_h(\varepsilon_1)\right]$$
$$= I^{(0)}\tau_0 g_0 \exp\left[-\frac{\varepsilon}{\varepsilon_0} - X(\varepsilon) + \int\limits_0^{\varepsilon} \frac{d\varepsilon_1}{\varepsilon_0}\left(1 - \mathrm{e}^{X(\varepsilon_1)}\right)\right] .$$

The PL peak position, $\omega_{\max}$, is found from $\hbar\omega_{\max} = E_0 - \varepsilon_{\max}$ with $\varepsilon_{\max}$ being a root of the equation $d \ln N(\varepsilon)/d\varepsilon = 0$ or, in the explicit form,

$$-\frac{1}{\varepsilon_0} - \frac{dX(\varepsilon)}{d\varepsilon} + \frac{1}{\varepsilon_0}\left(1 - \mathrm{e}^{X(\varepsilon)}\right) = 0$$

which reduces to the transcendental equation

$$X = \mathrm{e}^{-X} \tag{5.27}$$

that has a single solution $\bar{X} \approx 0.567$. According to (5.26), the position of the PL peak is given by $\rho(\varepsilon^{cw}_{\max})V_d(\tilde{r}) = \bar{X}$ or, explicitly,

$$\varepsilon^{cw}_{\max} = \varepsilon_0 \ln\left[g_0\varepsilon_0 V_d(\tilde{r})\right] + \bar{X}\varepsilon_0 = d \ln\ln\left(\omega_0\tau_0\right) + A + \bar{X}\varepsilon_0 , \tag{5.28}$$

where the constant A was introduced in (5.11). This result can formally be obtained from the approximate equation (5.12) just by adding the constant $\bar{X}\varepsilon_0$. It is worth to stress that the kinetic theory allows not only to find the peak position but also to calculate the PL spectral shape.

Adding the time derivative to the kinetic equation one can solve various time-dependent problems. Golub et al. [5.2] numerically calculated the time-resolved PL spectra assuming that a nanostructure is excited by a short pulse and, at the initial moment $t = 0$, all the localized states (ε, r) are equally populated, $f(\varepsilon, r, t = 0) = \text{const}$. At very short times the spectral intensity $I(\omega)$ repeats the density of states, $I(\omega) \propto g(E_0 - \hbar\omega)$, and is monotonic. For times

$$t > \omega_0^{-1} \exp\left[\rho(0)V_d(L/2)^{-1/d}\right]$$

the PL maximum shifts from the mobility edge and moves continuously into the band gap with increasing t. The numerical results obtained for a QW structure ($d = 2$) are well described by the dependence

$$\varepsilon_{\max}(t) = \varepsilon_0\{\ln\left[N_0 \ln^2(\omega_0 t)\right] + \bar{X}'\} , \tag{5.29}$$

where $N_0 = g_0\varepsilon_0\pi(L/2)^2$, $\bar{X}'$ is a constant slightly differing from $\bar{X}$ and weakly dependent on N_0 and $\omega_0\tau_0$. One can see that (5.29) differs by a constant term $\varepsilon_0\bar{X}'$ from (5.11) taken for $d = 2$.

Equations (5.28, 5.29) can be presented in the equivalent form

$$\varepsilon^{cw}_{\max} = \varepsilon_0\left\{\ln\left[N_0 \ln^2(\omega_0\tau_0)\right] + \bar{X}\right\} , \tag{5.30}$$

$$\varepsilon_{\max}(t) = \varepsilon_{\max}^{cw} + \varepsilon_0 \left(2 \ln \frac{\ln \omega_0 t}{\ln \omega_0 \tau_0} + \bar{X}' - \bar{X} \right)$$

more convenient for comparison between theory and experiment on 2D systems.

According to (5.17, 5.30) the simplest theory of localized-exciton energy relaxation contains five parameters: $E_0, \varepsilon_0, N_0, \omega_0, \tau_0$ and, additionally, the sixth parameter $\bar{X}' - \bar{X}$. The recombination lifetime τ_0 can be found by measuring the PL integral intensity J as a function of time delay and comparing the observed dependence with (5.18). A single-exponential character of the decay $J(t)$ is of a crucial importance: linear variation of $\ln J(t)$ with time serves as the main reason for assuming τ_0 to be energy-independent. The mobility edge E_0 can be found from the peak position of the absorption or PLE spectrum. This allows to relate the emitted photon energy $\hbar\omega$ to the localization energy $\varepsilon = E_0 - \hbar\omega$, see (5.17). A value of $\varepsilon_{\max}^{cw}$ is found from the Stokes shift of the cw PL spectral peak with respect to E_0. This imposes one condition on three parameters, ε_0, ω_0 and N_0. The final choice of these parameters is made from fitting both the experimental curve $\varepsilon_{\max}(t)$ and PL spectral shape $I(\omega, t)$.

For the purposes of illustration, Figs. 5.1 and 5.2 show the time evolution $\varepsilon_{\max}(t)$ and cw spectrum of low-temperature PL measured at T = 2 K from a 20Å-thick $Zn_{0.8}Cd_{0.2}Se/ZnSe$ QW. Other experimental data including the time-resolved PL integral intensity $J(t)$, time-resolved spectral intensity $I(\omega, t)$ for several frequencies ω and spectra $I(\omega, t)$ at different delay times t are presented in [5.3]. The best fit parameters are $\tau_0 = 170$ ps, $\varepsilon_{\max}^{cw} = 13$ meV, $\varepsilon_0 = 8$ meV, $\omega_0 = 10^{13}$ s^{-1}, $N_0 = 0.053$. Note that for this set of parameters the correction $\bar{X}' - \bar{X}$ in (5.30) equals to ≈ 0.18.

It should be noted that in the transfer term (5.14) we neglect the spatial correlation between two successive hops related to a non-Markovian nature of the hopping processes. An existence of the correlation can be explained by considering the nth and the $(n+1)$th hops, respectively, from site $\boldsymbol{r}_{n-1}$ to $\boldsymbol{r}_n$ and from site $\boldsymbol{r}_n$ to $\boldsymbol{r}_{n+1}$ $(n > 1)$. Since we take into account only hops to the optimal neighbors then, for the given configuration of sites, the site $\boldsymbol{r}_{n+1}$ certainly lies outside the sphere V_d of radius $|\boldsymbol{r}_n - \boldsymbol{r}_{n-1}|$ centered at $\boldsymbol{r}_{n-1}$. Otherwise the exciton would have jumped directly from $\boldsymbol{r}_{n-1}$ to $\boldsymbol{r}_{n+1}$ avoiding the site $\boldsymbol{r}_n$. Thus, the straightforward theory must exclude the possibility of hopping into this sphere from the site $\boldsymbol{r}_n$, see details in [5.2]. The dotted curve in Fig. 5.2 is calculated by making allowance for the correlation between successive hops. One can see no remarkable deviation from the theory disregarding the non-Markovian correlation (dashed curve).

5.2.2 Nonmonotoneous Behavior of the Stokes Shift with Temperature

Baranovskii et al. [5.4] used the Monte-Carlo simulation procedure to model the same scenario of multi-hopping relaxations of localized excitons and, for

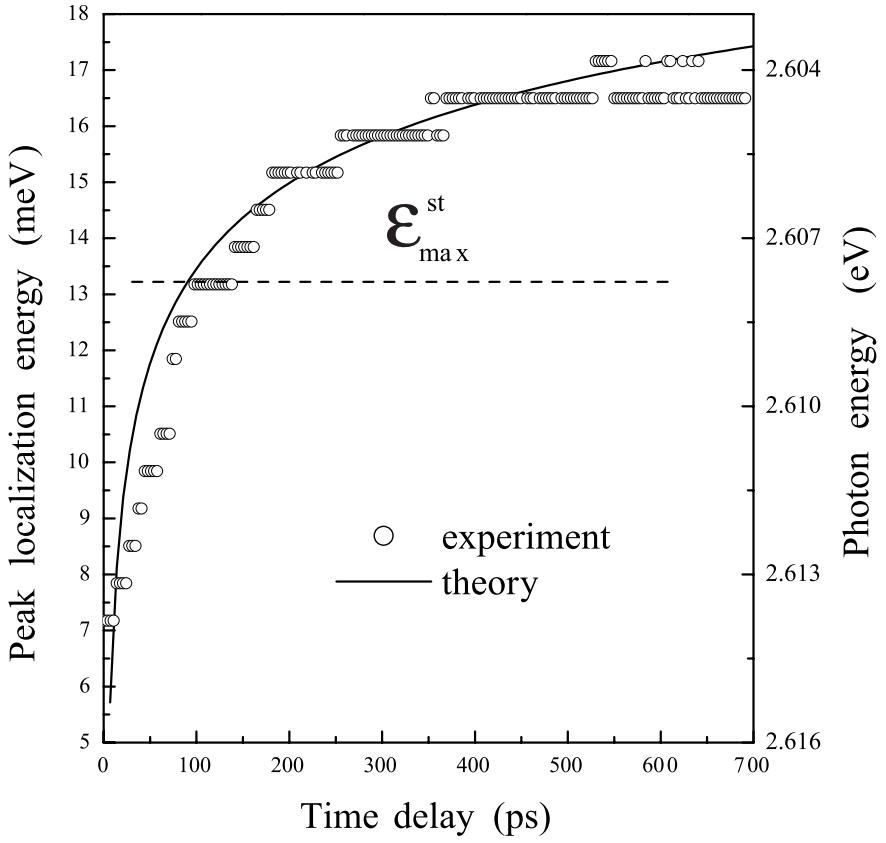

Fig. 5.1. The temporal shift of the PL peak measured at T = 2 K in the 20 Å $Zn_{0.8}Cd_{0.2}Se/ZnSe$ QW and calculated from (5.30) with the values of parameters indicated in the text. The dashed horizontal line indicates the position of the PL peak under steady-state excitation. [5.3]

the identical set of parameters, obtained an excellent agreement between the simulation and the kinetic analytical theory represented by (5.14, 5.22). They employed a similar simulation technique for finite temperatures and confirmed the non-monotonous temperature dependence of the cw PL maximum demonstrated previously by Zimmermann et al. [5.5]. Physically, this curious phenomenon can be interpreted taking into account that, at T = 0, the PL is dominated by excitons finding themselves on accidentally isolated localization sites acting as pores. For such sites, or traps, the lifetime with respect to hopping down to the nearest lower-energy neighbor exceeds the recombination time. At low, but finite temperatures, an exciton trapped by an effective pore has an opportunity for further energy relaxation by hopping

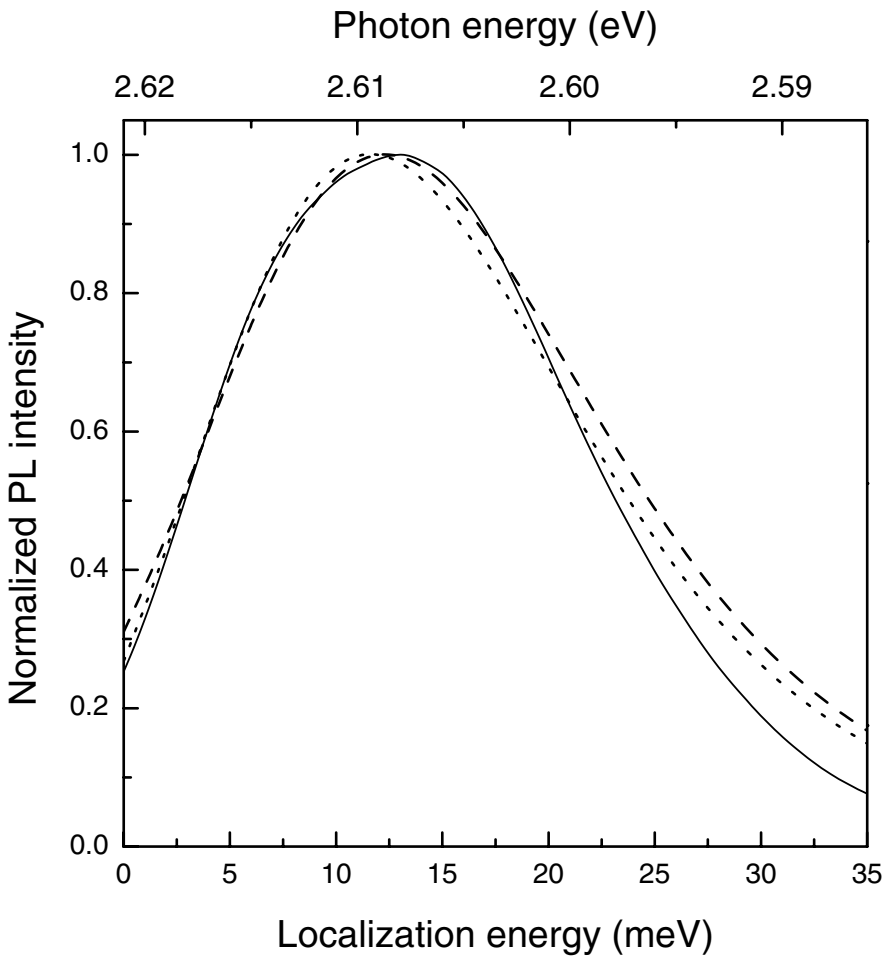

Fig. 5.2. Comparison of the experimental time-integrated PL spectrum (*solid*) with the steady-state PL spectrum calculated neglecting (*dashed*) and taking into account (*dotted*) the correlation between successive hops. [5.3]

first up to the nearest higher-energy neighbor and then down to a deeper-energy site.

To illustrate and make the physics of the PL-peak temperature shift more transparent, let us consider three sites O, O′ and O_1 with the localization energies $\varepsilon, \varepsilon', \varepsilon_1$ ($\varepsilon' < \varepsilon < \varepsilon_1$) assuming the initial exciton generation to occur only to the site O. Then the steady-state occupancies f, f', f_1 of these three sites satisfy the following set of rate equations

$$(\tau_0^{-1} + w_{O'O} + w_{O_1O})f - w_{OO'}f' = \Gamma_O \,,$$
$$(\tau_0^{-1} + w_{O_1O'} + w_{OO'})f' - w_{O'O}f = 0 \,,$$
$$\tau_0^{-1} f_1 - w_{O_1O}f - w_{O_1O'}f' = 0 \,.$$

Here Γ_O is the generation rate to the site O, $w_{\alpha\beta}$ is the hopping rate for the acoustic-phonon assisted transition from site β to the site α, and the upward transitions $O_1 \to O$ and $O_1 \to O'$ are ignored. If the site O is a pore at zero temperature then $w_{O_1O} < \tau_0^{-1}$. Let site O′ be the optimal at $T \neq 0$ with respect to O, which means that $w_{O'O} > w_{O_1O}$. Site O_1 is assumed to satisfy the condition $w_{O_1O'} > w_{OO'}$. It can be shown that, under the above assumptions and for $w_{O'O} > \tau_0^{-1}$, the ratio $f_1/(f+f')$ is given approximately by the product $\tau_0 w_{O'O}$. At T = 0, i.e., for vanishing $w_{O'O}$, this ratio is equal to $\tau_0 w_{O_1O}$ which is small as compared with $\tau_0 w_{O'O}$. Thus, the average exciton energy indeed shifts downwards (the localization energy shifts upwards) with allowance made for the effective relaxation channel $O \to O' \to O_1$.

Here we generalize the kinetic theory presented in the previous subsection from zero to finite temperatures [5.6]. We use the Miller-Abrahams expression

$$w(\varepsilon, \varepsilon', r) = \omega_0 \exp\left[-\frac{2r}{L} - \theta(\varepsilon - \varepsilon')\frac{\varepsilon - \varepsilon'}{k_B T}\right] \tag{5.31}$$

for the hopping transition rate between the sites ε and ε' separated by the distance r. In the limit $T \to 0$ this expression reduces to (5.6). In the light of (5.31) we characterize each localized-exciton state by three parameters $\varepsilon, \varepsilon'$ and r, where ε is the localization energy for a given site, while ε' and r are the localization energy and the distance to an optimal site with the maximum value of $w(\varepsilon, \varepsilon', r)$ in the given local configuration. The probability to occupy such a state is denoted by $f(\varepsilon, \varepsilon', r)$. The energy distribution $N(\varepsilon)$ which determines the photoluminescence spectral intensity, $I(\omega) \propto N(E_0 - \hbar\omega)$, is related to $f(\varepsilon, \varepsilon', r)$ by

$$N(\varepsilon) = g(\varepsilon) \int_0^\infty d\varepsilon' \int_0^\infty dr P_\varepsilon(\varepsilon', r) f(\varepsilon, \varepsilon', r) \,, \tag{5.32}$$

where $P_\varepsilon(\varepsilon', r)$ is the distribution of optimal neighbors. In the following we restrict the consideration to 2D systems. Then, for uncorrelated localized sites distributed in the 2D space, one can write instead of (5.15)

$$P_\varepsilon(\varepsilon', r) = 2\pi r g(\varepsilon') \exp\left[-U(\varepsilon, \varepsilon', r)\right] \,, \tag{5.33}$$

$$U(\varepsilon, \varepsilon', r) = \int_\Omega \int d\varepsilon_2 dr_2 \; 2\pi r_2 \; g(\varepsilon_2) \,, \tag{5.34}$$

the integration is performed over the area Ω in the (ε_2, r_2) space, where

$$w(\varepsilon, \varepsilon_2, r_2) > w(\varepsilon, \varepsilon', r) \,.$$

If the correlation between the successive hopping processes is ignored the kinetic equation for $f(\varepsilon, \varepsilon', r)$ under the cw photoexcitation has the form

$$\frac{1}{\tau_0}\, f(\varepsilon, \varepsilon', r, t) + I_{\varepsilon,\varepsilon',r}\{f\} = \Gamma^{(0)}(t) \tag{5.35}$$

similar to (5.13) but with the modified transfer term

$$\begin{aligned} I_{\varepsilon,\varepsilon',r}\{f\} &= w(\varepsilon, \varepsilon', r)\; f(\varepsilon, \varepsilon', r) \\ &\quad - \int_0^\infty \int_0^\infty d\varepsilon_1 dr_1\; \frac{g(\varepsilon_1)}{g(\varepsilon)}\; P_{\varepsilon_1}(\varepsilon, r_1)\; w(\varepsilon_1, \varepsilon, r_1)\; f(\varepsilon_1, \varepsilon, r_1)\,. \end{aligned} \tag{5.36}$$

In the limit of zero temperature one has, respectively,

$$w(\varepsilon, \varepsilon', r) = w(r)\theta(\varepsilon' - \varepsilon) = \omega_0 \exp(-2r/L)\; \theta(\varepsilon' - \varepsilon)\,,$$

$$P_\varepsilon(\varepsilon', r) = \frac{g(\varepsilon')}{\rho(\varepsilon)} P_\varepsilon(r)\theta(\varepsilon' - \varepsilon)\,,$$

$$f(\varepsilon, \varepsilon', r) = \frac{f(\varepsilon, r)}{\rho(\varepsilon)}\theta(\varepsilon' - \varepsilon)\,,$$

and (5.35) reduces to (5.20).

Figure 5.3 compares the results of calculation with the PL experimental data obtained in a cubic CdS/ZnSe 19Å/19Å SL in the temperature range 5–35 K. The circles (experiment) and curves (theory) show the purely kinetic contribution to the PL-peak shift

$$\Delta E_{\max}(T) = \hbar\omega_{\max}(T) - \hbar\omega_{\max}(0) - \delta E_g(T)\,, \tag{5.37}$$

where $\omega_{\max}(T)$ is the spectral position of the PL maximum at the temperature T, $\delta E_g(T)$ is the non-kinetic shift which appears due to temperature variation of the SL band gap and is found from the micro-PL spectra, see the next subsection. The solid curve in Fig. 5.3 is the result of computer simulation, the dashed curve was obtained by numerically solving (5.35, 5.36). In order to qualitatively take into account the inhomogeneous broadening, the theoretical spectra $I(\omega, E_0)$ calculated for a fixed value of the exciton mobility edge E_0 were convoluted with a Gaussian

$$J(\hbar\omega) \propto \int dE_0\; F(E_0 - \bar{E}_0) J_0(E_0 - \hbar\omega)\,,$$

$$F(E_0 - \bar{E}_0) = \frac{1}{\sqrt{\pi}\Delta} \exp\left[- \left(\frac{E_0 - \bar{E}_0}{\Delta} \right)^2 \right]\,.$$

The dimensionless parameters chosen to calculate the PL spectra are as follows: $\omega_0\tau_0 = 10^3$ and $N_0 = g_0\varepsilon_0\pi(L/2)^2 = 0.4$. The inhomogeneous broadening was described by a Gaussian with $\Delta = 2\;\varepsilon_0$. At zero temperature the PL

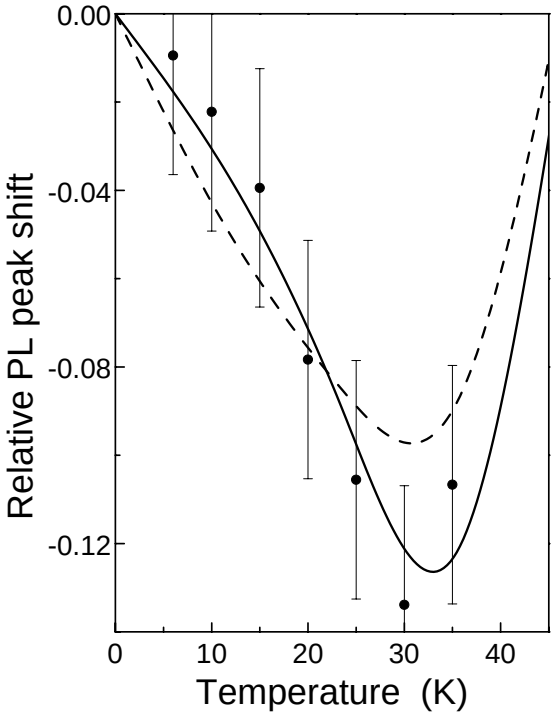

Fig. 5.3. Temperature dependence of the PL-peak shift in a 19 Å/19 Å CdS/ZnSe SL. The shift is defined in accordance with (5.37) and normalized to the low-temperature PL Stokes shift of 18 meV. Full circles, experiment; full curve, computer simulation; broken curve, kinetic theory. [5.6]

peak occurred at $\varepsilon_{\max} \equiv E_0 - \hbar\omega_{\max} = 3.53\ \varepsilon_0$. The Stokes shift $\varepsilon_{\max}^{cw}$ was estimated from the energy difference between the PL and PLE maxima to be 18 meV. From the PL Stokes shift a value of (18/3.53) meV or ≈ 5 meV was obtained for ε_0. One can see that the simulated PL shift $\Delta E_{\max}(T)$ and that calculated by using the kinetic theory are in good agreement.

5.2.3 Micro-Photoluminescence Spectroscopy

Usually optical studies of nanostructures, including those presented in Figs. 5.1–5.3, are carried out by illuminating macroscopic sample areas. This *macro-PL* probes large ensembles of localized sites in QWs or QWRs and

QDs in quantum-dot arrays. In this case narrow spectral features of individual quasi-0D excitons are hidden in PL spectral peaks inhomogeneously broadened and smoothed. At present, in PL or catodoluminescence spectroscopy, it has become possible to probe only a few localized sites or dots using a micrometer and even submicrometer spatial-resolution technique and combining it with high spectral and temporal resolution [5.7–5.10]. This can be achieved either by reducing the size of the laser spot on the sample or by reducing the area of the sample, e.g., by opening a series of apertures in an opaque metal film deposited on the surface of semiconductor nanostructure [5.11, 5.12]. Novel techniques have been developed that have led to the measurements of the Raman scattering, optically-detected nuclear-magnetic-resonance and nonlinear-optical microscopical spectra of individual 0D excitons, in addition to the *micro-PL* spectra.

Figure 5.4 shows three selected micro-PL spectra taken with a spatial resolution of $\sim 1\ \mu$m and recorded at different temperatures from the CdS/ZnSe 19Å/19Å SL used to measure the temperature shift of macro-PL peak (Fig. 5.3). The spectra are normalized with respect to the PL-intensity maximum and shifted vertically against each other for clarity. In addition to a broad PL background, a structure of narrow superimposed lines is observed with the full-width half-magnitude of 300 μeV. These lines show up due to the radiative recombination of strongly localized excitons forming quasi-0D states. Above 35 K, the narrow line emission is hardly observable, indicating enhanced delocalization of excitons. Within the experimental accuracy, the shift of the line positions with increasing temperature is identical for all the lines and corresponds to the temperature-induced shift of the SL band gap δE_g deducted in (5.37) in order to define a purely kinetic change, $\Delta E_{\max}$, in the PL-peak shift. The shifts $\delta E_g(T)$ for T=5 K and T=35 K differ by -1.4 meV. As one can see from Fig. 5.3, with the temperature increasing from 5 to 35 K, macro-PL spectra show a more pronounced red shift of the emission peak (-3.5 meV). This effect, also seen for the envelope of the micro-PL spectra, is clear evidence in favor of phonon-assisted exciton multi-hopping to deeper localized states, described in the previous subsection.

In Fig. 5.5, the results of a computer simulation of micro-PL spectra are displayed. For the simulation 50 subsystems were taken each containing 1000 localized-exciton sites randomly distributed with equal probabilities in the 2D space within a square area and with weight $g(\varepsilon)$. The exciton mobility edge in each subsystem was chosen randomly in accordance with the Gaussian distribution. The spectra were calculated for the same configuration of localized sites but for different temperatures, $k_BT = 0$, $0.4\varepsilon_0$ and $0.8\varepsilon_0$. The parameters of the theory are the same as those used to calculate the macro-PL spectra and the temperature dependence of $\Delta E_{\max}$ presented in Fig. 5.3 by solid line. The simulated PL spectrum is calculated as the sum

$$I(\omega) = \sum_{m=1}^{M} \sum_{i=1}^{n} f_i^{(m)}\, \Delta(\omega - \omega_i^{(m)})\,,$$

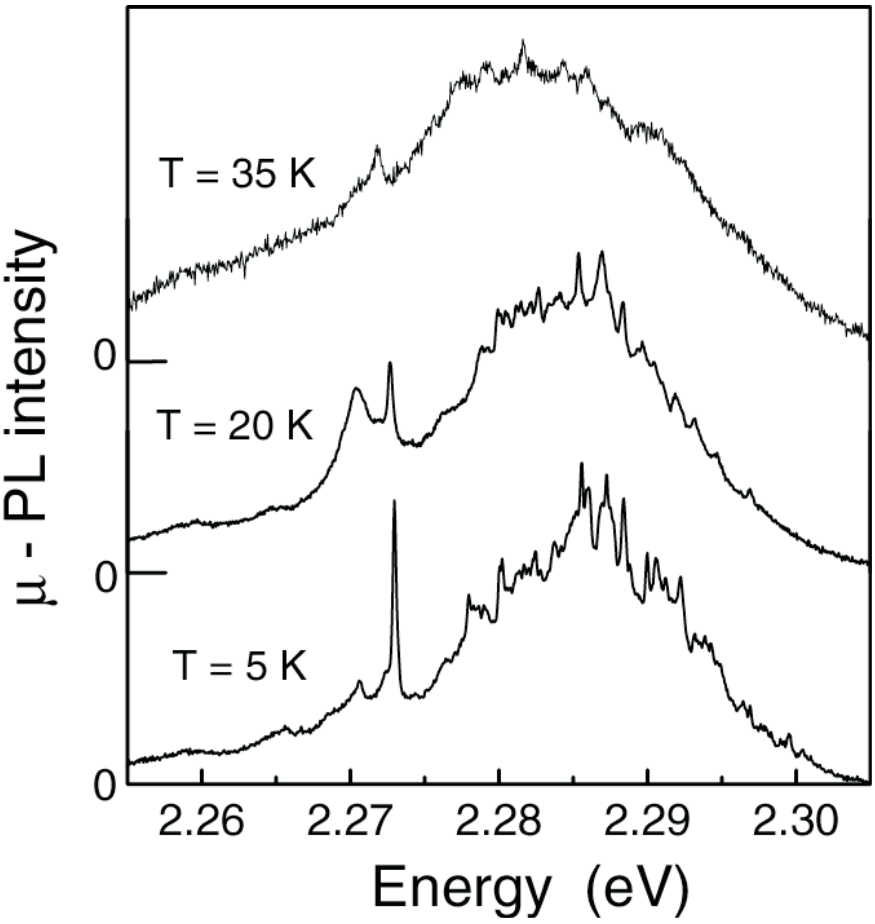

Fig. 5.4. Temperature dependent μ-PL spectra (spatial resolution $\approx 1\,\mu m$) taken from a 19 Å/19 Å CdS/ZnSe SL. [5.6]

where the index m enumerates the subsystems from 1 to $M = 50$, $\omega_i^{(m)}$ is the resonance frequency of the i-th localized-exciton state ($1 \leq i \leq 1000$) in the m-th subsystem, $f_i^{(m)}$ is the occupation number of the states (m, i), and the function $\Delta(\Omega)$ describes the homogeneous broadening of a single line. It is taken in the Lorentzian form

$$\Delta(\Omega) = \frac{1}{\pi} \frac{\gamma}{\gamma^2 + \Omega^2}$$

with γ being equal to $0.02\varepsilon_0/\hbar$.

In agreement with the experiment, a smooth spectral background can be seen in Fig. 5.4, reflecting the macro-PL spectrum, with a set of narrow lines corresponding to individual contributions of localized sites. Varying the

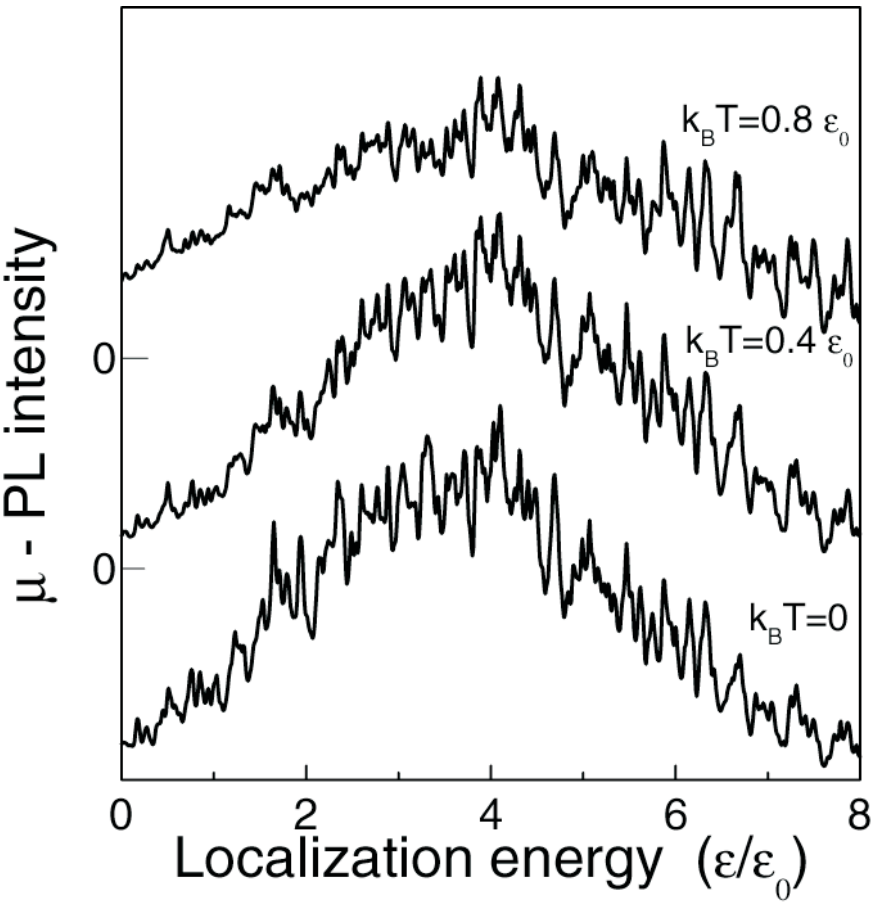

Fig. 5.5. μ-PL spectra computer-simulated for three different temperatures. [5.6]

temperature leads to exciton redistribution over the localization sites and, therefore, to changes in the intensities of the narrow lines and to evolution of the PL background. Since the band gaps are kept constant in the simulation procedure, the energy positions of the individual narrow lines remain unchanged.

5.2.4 Excitons in Quantum Wells Containing Free Carriers

Doping of QW structures can be unintentional, homogeneous, or selective. Selectively- or *modulation-doped quantum well* is a heterostructure in which a layer of donors (or acceptors) is introduced within the barrier region. The spatial separation between these donors and the 2D gas of electrons (or holes) formed in the well, strongly inhibits carrier scattering. The flexibility in the

choice of the structure parameters, such as the *spacer* width, doping concentration, etc., allows one to obtain a 2D electron gas (2DEG) with widely varying properties. Applying a gate voltage enables one to alter the system from a high-density quasi-metallic 2DEG to a low-density noninteracting one. In another method to study the system of coexisting excitons and 2D-carrier gas, the latter is generated by photoexciting the structure above the band gap and its density is controlled by the excitation intensity. At a large electron density the excitons are suppressed due to the screening and band-filling effects. When the electrons are removed from the well, an exciton line is gradually restored in the optical spectra. We discuss here two problems related to excitons localized in modulation-doped QWs, namely localized trions (see, e.g., [5.13,5.14]) and scattering of free carriers by localized excitons [5.15, 5.16].

Although extensive work has been carried out on the 2D trions X^-, in many of these studies a recurrent and controversial question keeps arising from time to time: how localized are the trion states and how does confinement affect the Coulomb interaction. An existence of localized trion states in modulation-doped GaAs/AlGaAs QWs was demonstrated by Finkelstein et al. [5.13] who observed a correlation between the decrease of the conductivity and the appearance of excitons and trions as the electron density is lowered. Another evidence of localized trions comes from comparison of the theoretical and experimental binding energies of negatively charged exciton X^- as a function of the well width a. Although the qualitative behavior of the binding energy $\varepsilon_{\rm tr}$ as a function of well width a agrees with theoretical predictions, values of $\varepsilon_{\rm tr}$ for the narrow QWs is at least twice the predicted value [5.17]. This discrepancy between theory and experiment is likely a consequence of the localization of the trion due to QW width fluctuations. Tischler et al. [5.14] have demonstrated single-trion spectroscopy using high spatial resolution. They presented a comparative study of the fine structure of single localized excitons and trions discussed in Sect. 5.4.1.

In addition to the formation of a three-particle bound state, negatively or positively charged exciton, a free carrier and exciton can collide scattering each other. In the quantum theory of scattering, the problem of 'electron - hydrogen atom' scattering is next in simplicity to that concerning collisions between two elementary particles. In the physics of semiconductors, similar process is represented by scattering of a free electron or hole by Wannier-Mott exciton. New aspects of this three-body problem were revealed in recent studies of the 'free carrier - exciton' interaction in 2D systems, namely in QW structures [5.18, 5.19]. Of special interest is a problem of interaction between localized excitons and free carriers photoexcited by an additional above-gap radiation at low temperatures [5.15, 5.20]. The theoretical aspects of this particular problem were studied by Golub et al. [5.16]. Following this study, we discuss the delocalization of localized excitons by free carriers in a QW structure. We use the Born approximation, take into account that the

incident and excitonic electrons are nondistinguishable and make allowance for both direct and exchange processes.

We consider a collision process with a free quasi-2D electron and a localized exciton in the initial state, and a free (delocalized) exciton and an electron of lower kinetic energy in the final state. Schematically the process can be presented in the form

$$(\boldsymbol{k}_0,\ s_0) + (\text{loc. exc.},\ s_0',\ m) \longrightarrow (\boldsymbol{k}_f,\ s_f) + (\text{free exc.},\ \boldsymbol{K},\ s_f',\ m).$$

Here $\boldsymbol{k}_0, \boldsymbol{k}_f$ are the wave vectors of the initial and scattered electron waves, $\boldsymbol{K}$ is the free-exciton wave vector, and s_0, s_0', s_f, s_f' is the spin component $\pm 1/2$ of the corresponding electron referred, say, to the structure principal axis z; m is the hole spin index. Hereafter we neglect the electron-hole exchange interaction which means that m is conserved in the collision process. The vectors $\boldsymbol{k}_0, \boldsymbol{k}_f, \boldsymbol{K}$ satisfy the energy conservation law

$$\frac{\hbar^2 k_0^2}{2m_e} - E_{\text{loc}} = \frac{\hbar^2 k_f^2}{2m_e} + \frac{\hbar^2 K^2}{2M}\,, \tag{5.38}$$

where m_e, M are the in-plane electron and exciton effective masses, and E_{loc} is the exciton localization energy.

Bearing in mind the electron nondistinguishability we write the wave function of the three-body system 'electron + exciton' as the Slater determinant

$$\Psi(\boldsymbol{r}_1, \boldsymbol{r}_2, \boldsymbol{r}_h) = \frac{1}{\sqrt{2}} \begin{vmatrix} \psi_{\boldsymbol{k}\,s}(\boldsymbol{r}_1) & \psi_{\boldsymbol{k}\,s}(\boldsymbol{r}_2) \\ \psi^{(\text{exc})}_{j;s'm}(\boldsymbol{r}_1, \boldsymbol{r}_h) & \psi^{(\text{exc})}_{j;s'm}(\boldsymbol{r}_2, \boldsymbol{r}_h) \end{vmatrix}\,, \tag{5.39}$$

where 3D vectors $\boldsymbol{r}_1, \boldsymbol{r}_2, \boldsymbol{r}_h$ describe positions of the two electrons and the hole, $\psi_{\boldsymbol{k}\,s}(\boldsymbol{r})$ and $\psi^{(\text{exc})}_{j;s'm}(\boldsymbol{r}_e, \boldsymbol{r}_h)$ are, respectively, the wave functions of a free electron in the state $(\boldsymbol{k}, s)$ and of an exciton in the localized state $j = \text{loc}$ or the free state $j = \boldsymbol{K}$. In the actual calculation the following approximate wave functions are used

$$\psi_{\boldsymbol{k}\,s}(\boldsymbol{r}_e) = \frac{1}{\sqrt{\Omega}} \mathrm{e}^{\mathrm{i}\boldsymbol{k}\boldsymbol{\rho}_e}\, \varphi_e(z_e)\, |s\rangle\,, \tag{5.40}$$

$$\psi^{(\text{exc})}_{j;s'm}(\boldsymbol{r}_e, \boldsymbol{r}_h) = F_j(\boldsymbol{R}) f(\rho)\, \varphi_e(z_e)\, \varphi_h(z_h)\, |s'; m\rangle\,.$$

Here $|s\rangle$ and $|s'; m\rangle$ are the Bloch functions at the center of the Brillouin zone, $\varphi_e(z_e)$ and $\varphi_h(z_h)$ are the envelopes for the lowest electron $(e1)$ and hole $(h1)$ quantum-confined states, the variational function $f(\rho) = (2/\pi)^{1/2} \tilde{a}^{-1} \exp(-\rho/\tilde{a})$ describes the relative electron-hole motion in the exciton, $\tilde{a}$ is the effective Bohr radius of the quasi-2D exciton in the $1s$ ground state, $\rho = |\boldsymbol{\rho}_e - \boldsymbol{\rho}_h|$, $\boldsymbol{\rho}_e$ and $\boldsymbol{\rho}_h$ are the 2D vectors (x_e, y_e) and (x_h, y_h), $\boldsymbol{R} = (m_e\boldsymbol{\rho}_e + m_h\boldsymbol{\rho}_h)/M$ is the exciton in-plane center-of-mass and Ω is the sample normalization area. The function $F_j(\boldsymbol{R})$ describes the translational

motion of the exciton as a whole. In the initial state it is approximated by the exponential function

$$F_{\rm loc}(\boldsymbol{R}) = \sqrt{\frac{2}{\pi L^2}}\,{\rm e}^{-R/L} \tag{5.41}$$

with L being the effective localization radius. The final state is represented by the plane wave $F_{\boldsymbol{K}}(\boldsymbol{R}) = \Omega^{-1/2}\ \exp({\rm i}\boldsymbol{K}\boldsymbol{R})$.

In order to calculate the matrix element of the electron-exciton interaction

$$M = \langle \boldsymbol{k}_f, s_f; \boldsymbol{K}, s'_f, m|\hat{H}|\boldsymbol{k}_0, s_0; {\rm loc}, s'_0, m\rangle$$

we start with the total three-body Hamiltonian $H = T_1 + T_2 + T_h + V_{1\text{-}2} + V_{1\text{-}h} + V_{2\text{-}h} + U_1 + U_2 + U_h$, where T stands for the kinetic energy operator, V is the Coulomb potential

$$V_{1\text{-}2} = \frac{e^2}{æ|\boldsymbol{r}_1 - \boldsymbol{r}_2|}\,, \qquad V_{i\text{-}h} = -\frac{e^2}{æ|\boldsymbol{r}_i - \boldsymbol{r}_h|} \quad (i = 1, 2)\,,$$

æ is the dielectric constant of the medium, U is the superstructural potential. It is worth to note that U contains as well the perturbation arising because of the QW-width fluctuation and leading to the exciton localization.

In the band-structure model under consideration the electron orbital motion is spin-independent and, therefore, it is possible to bring the matrix element M into the form

$$V = \mathcal{A}\,\delta_{s_f\,s_0}\delta_{s'_f\,s'_0} + \mathcal{B}\,(\boldsymbol{\sigma}_{s_f\,s_0}\cdot\boldsymbol{\sigma}_{s'_f\,s'_0})\,, \tag{5.42}$$

where $\boldsymbol{\sigma}$ is the vector matrix with components being equal to the Pauli matrices $\sigma_x, \sigma_y, \sigma_z$. The coefficients $\mathcal{A}$, $\mathcal{B}$ depend upon the wave vectors $\boldsymbol{k}_0, \boldsymbol{k}_f$, $\boldsymbol{K}$ but are independent on the spin indices. These coefficients can be expressed as

$$\mathcal{A} = V_{\uparrow\downarrow,\uparrow\downarrow} + \frac{1}{2}\,V_{\uparrow\downarrow,\downarrow\uparrow}\,, \qquad \mathcal{B} = \frac{1}{2}\,V_{\uparrow\downarrow,\downarrow\uparrow} \tag{5.43}$$

via matrix elements for the direct and exchange collision processes in the case where spins of the initial and excitonic electrons are antiparallel

$$V_{\uparrow\downarrow,\uparrow\downarrow} = \int d\boldsymbol{r}_1 d\boldsymbol{r}_2 d\boldsymbol{r}_h \psi^*_{\boldsymbol{k}_f}(\boldsymbol{r}_1)\psi^{({\rm exc})*}_{\boldsymbol{K}}(\boldsymbol{r}_2, \boldsymbol{r}_h)V_{12h}\psi_{\boldsymbol{k}_0}(\boldsymbol{r}_1)\psi^{({\rm exc})}_{\rm loc}(\boldsymbol{r}_2, \boldsymbol{r}_h)\,,$$
$$V_{\downarrow\uparrow,\uparrow\downarrow} = -\int d\boldsymbol{r}_1 d\boldsymbol{r}_2 d\boldsymbol{r}_h \psi^*_{\boldsymbol{k}_f}(\boldsymbol{r}_2)\psi^{({\rm exc})*}_{\boldsymbol{K}}(\boldsymbol{r}_1, \boldsymbol{r}_h)V_{12h}\psi_{\boldsymbol{k}_0}(\boldsymbol{r}_1)\psi^{({\rm exc})}_{\rm loc}(\boldsymbol{r}_2, \boldsymbol{r}_h)\,. \tag{5.44}$$

Here we use the notation $V_{12h} = V_{1\text{-}2} + V_{1\text{-}h}$. It follows from (5.42,5.43) that the similar matrix element, $V_{\uparrow\uparrow,\uparrow\uparrow}$, for the parallel spin configuration is given by the sum $V_{\uparrow\downarrow,\uparrow\downarrow} + V_{\downarrow\uparrow,\uparrow\downarrow}$.

In the Born approximation the probability rate for delocalization of the exciton (s'_0, m) by the s_0-electron is expressed by

$$w_{s_0,s_0'}(E_0) = \frac{2\pi}{\hbar} \sum_{s_f,s_f'} \sum_{\boldsymbol{k}_f,\boldsymbol{K}} |V|^2 \, \delta(E_f + E_{\rm exc} - E_0 + E_{\rm loc}) \; . \tag{5.45}$$

To simplify the writing we denote the kinetic energies $\hbar^2 k_0^2/2m_e$, $\hbar^2 k_f^2/2m_e$, $\hbar^2 K^2/2m_{\rm exc}$ by E_0, E_f and $E_{\rm exc}$, respectively. The total delocalization time, τ, can be written as $1/\tau = W_{1/2,s_0'} + W_{-1/2,s_0'}$, where

$$W_{s_0,s_0'} = \Omega \int w_{s_0,s_0'}(E_0) \, f_{s_0}(E_0) \, g_{2D} \, dE_0 \; , \tag{5.46}$$

$g_{2D}^s = m_e/(2\pi\hbar^2)$ is the density of 2D-electron states with a fixed spin and $f_s(E)$ is their energy distribution function. We assume the Boltzmann character of the distribution: $f_s(E) = \exp[(\mu_s - E)/k_B T]$, where T is the effective temperature which can be changed by microwave irradiation of the sample [5.20]. The chemical potential μ_s is related to the 2D concentration, N_s, of electrons with the spin s by the equation

$$\mu_s = k_B T \ln\left(\frac{N_s}{g_{2D}^s k_B T}\right) \; . \tag{5.47}$$

In experiments the electron gas may be unpolarized ($N_{1/2} = N_{-1/2}$) as well as completely spin-polarized ($N_{1/2} \gg N_{-1/2}$ or $N_{1/2} \ll N_{-1/2}$).

Figure 5.6 illustrates results of the numerical calculation of the probability rate $w_{s_0,s_0'}(E_0)$ and the delocalization time $\tau_{s_0,s_0'}$ performed assuming the electron gas to be polarized and by applying (5.42, 5.45) for the configurations $s_0 = -s_0'$ (curves 1) and $s_0 = s_0'$ (curves 2). The used parameters correspond to the GaAs/AlGaAs QW structures: $m_e = 0.067 m_0$, $m_h = 0.15 m_0$, the Bohr radius of the quasi-2D exciton $\tilde{a} = 100$ Å, the well width $a = 75$ Å. A value of $L = 180$ Å is chosen as the best fit to the envelope wave function calculated in the method of free relaxation [5.21] for a circular island of monolayer-high fluctuation of the QW width (the localization energy $E_{\rm loc} = 2$ meV is obtained for the island radius 80 Å). The envelopes $\varphi_e(z), \varphi_h(z)$ in (5.40) are approximated by the function $(2/a)^{1/2} \cos(\pi z/a)$.

The delocalization probability has a threshold in energy of the ingoing electron: $w_{s_0,s_0'}(E_0) = 0$ if $E_0 < E_{\rm loc}$. Near the threshold we can neglect the dependence of the coefficients $\mathcal{A}$, $\mathcal{B}$ on E_0 and obtain

$$w_{s_0,s_0'}(E_0) \propto \int\int dE_f \, dE_{\rm exc} \, \delta(E_f + E_{\rm exc} - E_0 + E_{\rm loc}) = E_0 - E_{\rm loc} \; . \tag{5.48}$$

One can see from Fig. 5.6a that the linear dependence is a good approximation up to $E_0 - E_{\rm loc} = 0.5$ meV. The curves $w_{s_0,s_0'}(E_0)$ reach maximum values at $E_0 - E_{\rm loc} \approx 1.5$ meV ($k_0 L \approx 1.4$) and smoothly decrease with the further increase in E_0. Note that the main contribution to $w_{\uparrow\uparrow}$ and $w_{\uparrow\downarrow}$ comes from the exchange processes. This can be understood taking into account that, in the Born approximation, for equal masses $m_e = m_h$ and for coinciding

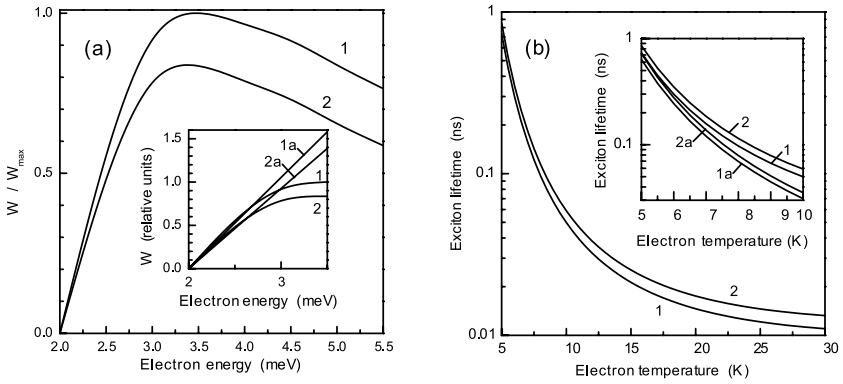

Fig. 5.6. (**a**) Relative probability of the exciton delocalization vs. the initial energy for antiparallel (*curve* 1) and parallel (*curve* 2) electron spin configurations. $w_{\max}$ is the maximum value of the function $w_{\uparrow\downarrow}(E_0)$. Inset shows the same dependence in the region of small $E_0 - E_{\rm loc}$. Curves 1a and 2b are calculated assuming the matrix element of the electron-exciton interaction to be constant. (**b**) Temperature dependence of the exciton delocalization time due to the 2D electron gas polarized antiparallel (*curve* 1) and parallel (*curve* 2) with respect to the electron spin orientation in the localized exciton. Inset shows the same dependence near the threshold; curves 1a and 2a are calculated for E_0-independent matrix elements of the electron-exciton interaction. [5.16]

envelopes $\varphi_e(z) = \varphi_h(z)$, the direct Coulomb interaction between an electron and an exciton vanishes, the matrix element $V_{\uparrow\downarrow,\uparrow\downarrow}$ is equal to zero and, hence, the matrix elements $V_{\uparrow\uparrow,\uparrow\uparrow}$, $V_{\downarrow\uparrow,\uparrow\downarrow}$ coincide and are entirely determined by the exchange contribution to electron-exciton interaction. For $m_e \neq m_h$, a value of $V_{\uparrow\downarrow,\uparrow\downarrow}$ differs from zero. However the estimation shows that, even for $m_h = 2m_e$, it is small as compared to $V_{\uparrow\uparrow,\uparrow\uparrow}$, $V_{\downarrow\uparrow,\uparrow\downarrow}$. This explains why the probabilities $w_{\uparrow\uparrow}(E_0)$, $w_{\uparrow\downarrow}(E_0)$ differ only by $10 \div 20\%$.

For the electron gas of the density $n = 10^9$ cm^{-2} at the temperature $T = 5$ K the exciton delocalization time is ~ 1 ns. With heating the electrons their average energy increases, the electron-exciton interaction is enhanced (Fig. 5.6a) and the time τ decreases. Figure 5.6b shows that, at low temperatures, this time is very sensitive to variation of T. In fact, it becomes shorter by an order of magnitude, as T increases from 5 K to 8 K. If the E_0-dependence of the matrix elements V is ignored, i.e., if $w_{s_0,s_0'} \propto E_0 - E_{\rm loc}$, then the delocalization rate is proportional to $T\exp(-E_{\rm loc}/k_BT)$ (curves 1a and 2a in the inset in Fig. 5.6b). It should be mentioned that the time τ corresponding to the electron density $n \neq 10^9$ cm^{-2} is obtained by multiplying the values in Fig. 5.6b by $10^9/n$. To illustrate, the inverse time τ^{-1} for an unpolarized electron gas is given by $(\tau_{\uparrow\uparrow}^{-1} + \tau_{\uparrow\downarrow}^{-1})/2$.

It is to be noted in conclusion that above we considered only one of possible mechanisms of the interaction between an electron and a localized exciton.

The photoluminescence intensity and polarization can be effected by other processes: the spin-flip elastic scattering of an electron or a hole by a localized exciton, the delocalization of an exciton with the free carrier captured in the final state by the localization site, free-carrier-induced hopping of an exciton between two different localized levels, etc.

5.3 Optical Spin Orientation of Free Carriers

Spin properties attract the great attention in recent years due to attempts to realize electronic devices based on the spin of electrons. Conduction electrons are obvious candidates for such devices, particularly in nanostructures where electron energy spectrum and shape of the envelope functions can effectively be engineered by the growth design, application of electric or magnetic fields as well as by illumination with light. Thus, spin electronics, or *spintronics*, is aimed at the study of the role played by electron spin in solid-state physics and creation of possible devices that exploit spin properties in addition to or even instead of the charge degree of freedom. In this connection the behavior of hole and exciton spins in semiconductors and the role of nuclear spins are of great importance in spintronics as well. The key topics of this field to be considered are the methods used to polarize electronic spins, particularly optical orientation of spins (Sect. 5.3.1), relevant spin-relaxation mechanisms (Sect. 5.3.2), the Zeeman effect and modification of the effective g factors in nanostructures due to the quantum confinement (Sect. 5.3.3) and manifestations of non-equilibrium spin polarization in time-resolved PL spectroscopy (Sect. 5.3.4). In this section we focus upon the spin optical orientation of free carriers, mainly on the orientation of conduction-electron spins. PL of polarized excitons will be considered in Sect. 5.4.

5.3.1 Principles of Optical Orientation

Since the pioneer work by Lampel [5.22] the *optical orientation* of free-carrier spins has become an effective method, contactless and nondestructive, for investigations of semiconductor band and kinetic parameters, see [5.23]. The essence of the method is to analyze the PL polarization as a function of the polarization of the initial light. We first formulate the basic principles of optical orientation of free-carrier spins.

Principle 1. Under optical interband excitation by circularly polarized light, the angular momentum component of σ_+ (or σ_-) photons is transferred to the spin (or angular momenta) of free carriers.

The electron-spin orientation under interband excitation follows immediately from the selection rules (2.154), see also Table 2.3. One can see that, for the σ_+-induced transition from $\pm 3/2$ states the photoelectrons with $s = -1/2$ are generated. Similarly, the transitions from the states $\pm 1/2$ lead to the generation of electrons with $s = 1/2$. Note that, for simplicity, we assume that

the light propagates along z and the PL is registered in the backscattering geometry.

The steady-state rate equations for the densities, n_+ and n_-, of electrons with the spin up (or 1/2) and down (or $-1/2$) have a simple form

$$\frac{n_+}{\tau_0} + \frac{1}{2\tau_s}(n_+ - n_-) = g_+ \,, \tag{5.49}$$

$$\frac{n_-}{\tau_0} + \frac{1}{2\tau_s}(n_- - n_+) = g_- \,.$$

Here $g_\pm$ are the photogeneration rates, τ_0 is the lifetime of photoelectrons in the conduction band, τ_s is the spin relaxation time. It is convenient to introduce the following notations: $n = n_+ + n_-$ as the total density, $g = g_+ + g_-$ as the total generation rate, $s_z = (n_+ - n_-)/2$ as the total average electron spin, and

$$p = \frac{n_+ - n_-}{n_+ + n_-} \tag{5.50}$$

as the degree of electron spin polarization. Then the solution of the above two rate equations can be presented as $n = g\tau_0$ and $p = p_0(T/\tau_0)$, where

$$p_0 = \frac{g_+ - g_-}{g_+ + g_-} \,, \; \frac{1}{T} = \frac{1}{\tau_0} + \frac{1}{\tau_s} \,, \tag{5.51}$$

T being the lifetime of photoelectron oriented spins.

Hence, *Principle 2* reads: If the photoelectron lifetime τ_0 is not too long as compared to the spin relaxation time τ_s, then the photoelectrons retain spin polarization (at least partially).

Under steady-state excitation, one has

$$s_z = \frac{p_0}{2}\, Tg = \frac{p_0}{2}\, \frac{\tau_s \tau_0}{\tau_0 + \tau_s}\, g \,. \tag{5.52}$$

The initial degree of spin polarization, p_0, is proportional to the degree of circular polarization of the initial light: $p_0 = æ P_c^0$. The coefficient æ depends on the selection rules: for the interband transitions $\Gamma_8 \to \Gamma_6$ in the bulk GaAs-type semiconductors, $æ = -1/2$, while for the optical transitions $hh1 \to e1$ in a GaAs-based QW one has $æ = -1$.

Principle 3. Due to the same selection rules for interband optical transitions, the radiative recombination of spin-polarized photocarriers gives rise to a (partial) circular polarization of the PL, or in an analytical form

$$P_c = æp = P_c^0 æ^2 \frac{T}{\tau_0} \,. \tag{5.53}$$

This equation is valid for recombination with unpolarized carriers of another sort, e.g., for recombination of spin-polarized electrons with unpolarized holes. If both degrees of spin polarization, p_e and p_h, are nonzero the circular

polarization is given by a more complicated equation. For the recombination of $e1$ electrons and $hh1$ holes ($æ = -1$) it has the form

$$P_c = \frac{p_h - p_e}{1 - p_e p_h} \,, \tag{5.54}$$

where $p_h = (n_+^h - n_-^h)/(n_+^h + n_-^h)$, and $n_\pm^h$ is the density of heavy holes with the angular momentum $\pm 3/2$.

Principle 4. The transverse magnetic field, $\boldsymbol{B} \perp z$, leads to depolarization of the photoluminescence. The rate equations for n and $\boldsymbol{s}$ in the transverse magnetic field can be written in the form

$$\frac{n}{\tau_0} = g \,, \; \frac{\boldsymbol{s}}{T} + \boldsymbol{s} \times \boldsymbol{\Omega}_L = \dot{\boldsymbol{s}} \,, \tag{5.55}$$

where $\boldsymbol{\Omega}_L = g_e \mu_B \boldsymbol{B}/\hbar$ is the *Larmor* frequency, g_e is the electron's effective g factor, and $\dot{\boldsymbol{s}}$ is the spin generation rate. These equations are derived from the equation for the so-called electron spin-density matrix

$$\frac{\hat{\rho}}{\tau_0} - \left(\frac{\partial \hat{\rho}}{\partial t}\right)_{s.r.} + \frac{\mathrm{i}}{\hbar}[\mathcal{H}_{\boldsymbol{B}}, \hat{\rho}] = \hat{g} \,. \tag{5.56}$$

The components of the spin-density matrix, $\rho_{11} \equiv \rho_{1/2,1/2}$, $\rho_{12} = \rho_{1/2,-1/2}$ etc., are expressed via the electron density n and components of the average electron spin $\boldsymbol{s}$ as

$$\hat{\rho} = \frac{1}{2} \begin{bmatrix} n + s_z & s_x - \mathrm{i}s_y \\ s_x + \mathrm{i}s_y & n - s_z \end{bmatrix} . \tag{5.57}$$

The spin relaxation term is conveniently approximated by [5.24]

$$-\left(\frac{\partial \hat{\rho}}{\partial t}\right)_{s.r.} = \frac{1}{2\tau_s} \begin{bmatrix} \rho_{11} - \rho_{22} & 2\rho_{12} \\ 2\rho_{21} & \rho_{22} - \rho_{11} \end{bmatrix} .$$

Let $\boldsymbol{B} \parallel x$, then $\mathcal{H}_{\boldsymbol{B}} = \hbar \Omega_L \sigma_x/2$ and

$$\frac{\mathrm{i}}{\hbar}[\mathcal{H}_{\boldsymbol{B}}, \hat{\rho}] = \frac{\mathrm{i}}{2} \Omega_L \begin{bmatrix} \rho_{21} - \rho_{12} & \rho_{22} - \rho_{11} \\ \rho_{11} - \rho_{22} & \rho_{12} - \rho_{21} \end{bmatrix} . \tag{5.58}$$

The vector equation (5.55) for $\boldsymbol{s}$ is equivalent to three scalar equations

$$\frac{s_x}{T} = \dot{s}_x \,, \; \frac{s_y}{T} + \Omega_L s_z = \dot{s}_y \,, \; \frac{s_z}{T} - \Omega_L s_y = \dot{s}_z \,.$$

Under normal incidence $\dot{s}_x = \dot{s}_y = 0$ and

$$s_z(B) = \frac{s_z(0)}{1 + (\Omega_L T)^2} \,, \; s_y(B) = -\frac{\Omega_L T}{1 + (\Omega_L T)^2} \, s_z(0) \,, \; s_x = 0 \,, \tag{5.59}$$

where $s_z(0)$ is given by (5.52). One can see that in the transverse magnetic field the average electron spin is rotated around $\boldsymbol{B}$ and depolarized. This is the so-called *Hanle effect*.

Note that, in general, one has to introduce the tensor g_{ij} of g factors and write $\mathcal{H}_{\boldsymbol{B}}$ in the form of the sum (5.86) (Sect. 5.3.3). Only in the particular case of an isotropic g factor the Larmor frequency $\boldsymbol{\Omega}_L$ is directed parallel to the in-plane magnetic field $\boldsymbol{B}$ and (5.55, 5.59) are valid.

5.3.2 Spin-Relaxation Mechanisms

For conduction-band electrons in bulk zinc-blende-lattice semiconductors, the following four mechanisms of spin relaxation, or spin decoherence, are relevant, see [5.25, 5.26] and references therein. The *Elliott-Yafet* mechanism is related to electron spin-flip scattering owing to a wave-vector dependent admixture of valence-band states to the conduction-band wave function. In the *D'yakonov-Perel'* mechanism the spin coherence is lost not in an act of scattering as in the previous case but during the time between successive acts of scattering due to the wave-vector dependent spin splitting of electron subbands [5.27]. In p-doped samples the conduction electrons loose their spin polarization via scattering by holes (the *Bir-Aronov-Pikus* mechanism) [5.28]. In samples containing paramagnetic centers the spin relaxation is contributed by spin-flip scattering processes as a result of the exchange interaction between free electrons and electrons bound on paramagnetic centers. In bulk semiconductor crystals the Elliott-Yafet mechanism can be essential only in narrow-gap materials with a large spin-orbit valence-band splitting, e.g., in InSb. The Bir-Aronov-Pikus mechanism predominates at low temperatures and sufficiently high hole densities [5.28]. The main spin relaxation at high temperatures is due to the D'yakonov-Perel' mechanism.

With reducing the dimensionality from 3D to 2D, the importance of the D'yakonov-Perel' mechanism is greatly enhanced and, in QWs with a moderate hole concentration, it is dominant. To consider this mechanism in more detail for (001)-grown QWs we take into account the linear-$\boldsymbol{k}$ Hamiltonian in the form (2.115) rewriting it as

$$\mathcal{H}_{c1} = \frac{1}{2}\left(\beta_- \sigma_{x'} k_{y'} - \beta_+ \sigma_{y'} k_{x'}\right) , \tag{5.60}$$

where $\beta_\pm = 2(\beta_2 \pm \beta_1)$ and the coordinate system $x' \parallel [1\bar{1}0], y' \parallel [110], z \parallel [001]$ is used.

A simple physical picture of what happens is as follows. Let us first consider an electron gas of the density N occupying the lowest conduction subband $e1$ and assume that, at the initial moment $t = 0$, the electrons are spin-polarized in the same direction, say along the growth direction z, and somehow distributed in the $\boldsymbol{k}$ space. It is useful to present $\mathcal{H}_{c1}(\boldsymbol{k})$ as the scalar product $(\hbar/2)\boldsymbol{\sigma} \cdot \boldsymbol{\Omega}_{\boldsymbol{k}}$, see (2.116). Then the linear-$\boldsymbol{k}$ spin-splitting of the electron subband plays the role of an effective magnetic field and results in spin precession with the angular velocity $\boldsymbol{\Omega}_{\boldsymbol{k}}$ during the time between collisions. The in-plane components of $\boldsymbol{\Omega}_{\boldsymbol{k}}$ are nonzero and given by (2.117).

We start from analysis of the large splitting limit

$$|\boldsymbol{\Omega}_{\boldsymbol{k}}| \gg \frac{1}{\tau} ,$$

where τ is a microscopic time of electron scattering. According to (2.117) the Larmor frequency $\boldsymbol{\Omega}_{\boldsymbol{k}}$ lies in the interface plane and is perpendicular to the

growth direction z. If $\boldsymbol{s}(t=0) \parallel z$ then the spin component of an electron in the state $\boldsymbol{k}$ oscillates as

$$s_z(t) = s_z(0)\cos\Omega_{\boldsymbol{k}}t.$$

If $\Omega_{\boldsymbol{k}} = |\boldsymbol{\Omega}_{\boldsymbol{k}}|$ is angular independent, the spin polarized electrons occupying the circle of the fixed radius in the $\boldsymbol{k}$ space show the similar oscillatory behavior for s_z component. However, if $\beta_-^2 \neq \beta_+^2$ or/and the electrons are occupying states with different values of $|\boldsymbol{k}|$, the scatter in $\boldsymbol{\Omega}_{\boldsymbol{k}}$ results in a decoherence of s_z.

In particular case where $\beta_-^2 = \beta_+^2$ and the electrons occupying the lowest conduction subband $e1$ have the same spin $\boldsymbol{s} \| z$ at the initial moment $t = 0$ and are distributed equally within the energy interval $0 < E < E_0$ the average $\bar{s}_z$ over the ensemble varies in the time domain $0 < t \ll \tau$ as

$$\bar{s}_z(t) = 2\, s_z(0)\, \left(\frac{\sin\Omega_0 t}{\Omega_0 t} + \frac{\cos\Omega_0 t - 1}{(\Omega_0 t)^2}\right)$$

where Ω_0 equals to $|\boldsymbol{\Omega}_{\boldsymbol{k}}|$ at $k = \sqrt{2mE_0/\hbar^2}$. One can see that $\bar{s}_z(t)$ decays non-exponentially, and the decay time scale is given by Ω_0^{-1}.

D'yakonov and Perel' [5.27] were the first to show that the electron-momentum scattering processes slow down the spin relaxation. In the collision-dominated limit

$$|\boldsymbol{\Omega}_{\boldsymbol{k}}| \ll \frac{1}{\tau}$$

the Larmor frequency direction changes randomly too fast, the spin rotation angle $\Delta\varphi \approx \Omega_k\tau$ between two successive acts of scattering is small and the time variation of s_z is described by the exponential function

$$s_z(t) = s_z(0)\exp\left(-\frac{t}{\tau_s}\right),$$

where τ_s is given by

$$\tau_s^{-1} \propto \langle \boldsymbol{\Omega}_{\boldsymbol{k}}^2 \tau \rangle \tag{5.61}$$

and the angle brackets mean averaging over the electron energy distribution. The dimensionless coefficient in (5.61) can be derived by solving the Boltzmann kinetic equation for the electron spin density matrix [5.27, 5.29].

In the frame of kinetic theory, the electron distribution in the wave vector and spin spaces is described by a 2×2 spin-density matrix

$$\hat{\rho}_{\boldsymbol{k}} = f_{\boldsymbol{k}} + \boldsymbol{s}_{\boldsymbol{k}} \cdot \boldsymbol{\sigma}. \tag{5.62}$$

Here $f_{\boldsymbol{k}} = \mathrm{Tr}\{\hat{\rho}_{\boldsymbol{k}}/2\}$ is the average occupation of the two spin states with the wave vector $\boldsymbol{k}$, or distribution function of electrons in the $\boldsymbol{k}$-space, and the average spin in the $\boldsymbol{k}$ state is $\boldsymbol{s}_{\boldsymbol{k}} = \mathrm{Tr}\{\hat{\rho}_{\boldsymbol{k}}(\boldsymbol{\sigma}/2)\}$. The macro- and microscopic spin-density matrices (5.57) and (5.62) are related by

$$\hat{\rho} = \sum_{\boldsymbol{k}} \hat{\rho}_{\boldsymbol{k}} \,. \tag{5.63}$$

If we neglect the spin splitting then, for arbitrary degeneracy of an electron gas with non-equilibrium spin-state occupation but equilibrium energy distribution within each spin branch, the electron spin-density matrix can be presented as

$$\hat{\rho}^0_{\boldsymbol{k}} = \left[\exp\left(\frac{E_{\boldsymbol{k}} - \bar{\mu} - \tilde{\mu}\,(\boldsymbol{\sigma}\cdot\boldsymbol{o_s})}{k_BT}\right) + 1\right]^{-1} , \tag{5.64}$$

where $E_{\boldsymbol{k}} = \hbar^2k^2/2m$, k_B is the Boltzmann constant, T is the temperature, $\boldsymbol{o_s}$ is the unit vector in the spin polarization direction, $\mu_\pm = \bar{\mu} \pm \tilde{\mu}$ are the effective Fermi energies for electrons with the spin component $1/2$ or $-1/2$ along $\boldsymbol{o_s}$ so that the energy distribution functions of electrons with the spin $\pm1/2$ are given, respectively, by

$$f^0_{k,\pm} = \left[\exp\left(\frac{E_{\boldsymbol{k}} - \mu_\pm}{k_BT}\right) + 1\right]^{-1} . \tag{5.65}$$

Note that (5.64) can be rewritten in the equivalent form [5.27]

$$\hat{\rho}^0_{\boldsymbol{k}} \equiv f^0_k + \boldsymbol{s}^0_k\cdot\boldsymbol{\sigma} = \frac{1}{2}\left[f^0_{k,+} + f^0_{k,-} + (f^0_{k,+} - f^0_{k,-})\,(\boldsymbol{\sigma}\cdot\boldsymbol{o_s})\right] .$$

The densities $n_\pm$ of 2D electrons with a particular spin can be related with the effective Fermi energies by

$$n_\pm = \frac{m}{2\pi\hbar^2}\,k_BT\,\ln(1 + \mathrm{e}^{\mu_\pm/k_BT}) \,. \tag{5.66}$$

If the spin splitting is non-zero but small compared to $\hbar/\tau$, the distribution function $\mathrm{Tr}\{\rho_{\boldsymbol{k}}/2\} = f^0_{\boldsymbol{k}}$ does not change, whereas the spin vector obtains a correction $\delta\boldsymbol{s}_{\boldsymbol{k}} = \boldsymbol{s}_{\boldsymbol{k}} - \boldsymbol{s}^0_k$ proportional to the spin splitting. Therefore, the spin-density matrix may be presented as

$$\hat{\rho}_{\boldsymbol{k}} = \hat{\rho}^0_{\boldsymbol{k}} + \delta\boldsymbol{s}_{\boldsymbol{k}}\cdot\boldsymbol{\sigma} \,. \tag{5.67}$$

The quantum kinetic equation for the spin-density matrix has the form

$$\frac{\partial\hat{\rho}_{\boldsymbol{k}}}{\partial t} + \frac{\mathrm{i}}{\hbar}[\mathcal{H}_{c1}(\boldsymbol{k}), \hat{\rho}_{\boldsymbol{k}}] + \hat{Q}_{\boldsymbol{k}}\{\hat{\rho}\} = 0 \,, \tag{5.68}$$

where $[P, R] = PR - RP$ and the third term in the left-hand side is the collision integral or the scattering rate, in this equation it is a 2×2 matrix. It follows from (5.68) that the kinetic equation for the pseudovector $\boldsymbol{s}_{\boldsymbol{k}}$ can be written as

$$\frac{d\boldsymbol{s}_{\boldsymbol{k}}}{dt} + \boldsymbol{s}_{\boldsymbol{k}}\times\boldsymbol{\Omega}_{\boldsymbol{k}} + \boldsymbol{Q}_{\boldsymbol{k}}\{\boldsymbol{s}\} = 0 \,, \tag{5.69}$$

where $\boldsymbol{Q}_{\boldsymbol{k}}\{\boldsymbol{s}, f\} = (1/2)\mathrm{Tr}\Big\{\boldsymbol{\sigma}\hat{Q}_{\boldsymbol{k}}\{\hat{\rho}\}\Big\}$. While considering the D'yakonov-Perel' mechanism, we ignore spin flips under scattering. Then, say, for the elastic scattering one has

$$\boldsymbol{Q}_{\boldsymbol{k}}\{\boldsymbol{F}\} = \sum_{\boldsymbol{k}'} W_{\boldsymbol{k}'\boldsymbol{k}}(\boldsymbol{F}_{\boldsymbol{k}} - \boldsymbol{F}_{\boldsymbol{k}'})\,,$$

where $W_{\boldsymbol{k}'\boldsymbol{k}}$ is the probability rate for the electron transition from the state $\boldsymbol{k}$ to $\boldsymbol{k}'$. For the equilibrium distribution $\hat{\rho}^0_{\boldsymbol{k}}$, the collision integral vanishes identically. This integral also vanishes after the summation over $\boldsymbol{k}$ which allows, in particular, to derive from (5.69) the following equation of balance for the total average spin

$$\frac{d\boldsymbol{s}}{dt} + \sum_{\boldsymbol{k}} \delta\boldsymbol{s}_{\boldsymbol{k}} \times \boldsymbol{\Omega}_{\boldsymbol{k}} = 0\,. \tag{5.70}$$

The angular dependence of the non-equilibrium correction $\delta\boldsymbol{s}_{\boldsymbol{k}}$ is the linear combination of $\cos\Phi_{\boldsymbol{k}} = k_{x'}/k$ and $\sin\Phi_{\boldsymbol{k}} = k_{y'}/k$, where $\Phi_{\boldsymbol{k}}$ is the angle between $\boldsymbol{k}$ and the axis x'. Retaining in the kinetic equation (5.69) terms proportional to the first angular harmonics we obtain an equation for $\delta\boldsymbol{s}_{\boldsymbol{k}}$ with the inhomogeneous term linear in $\boldsymbol{s}$. Then one can substitute the solution in the second term of (5.70). The final result is that the tensor of inverse spin relaxation times, $1/\tau^s_{\alpha\beta}$, is diagonal in the coordinate system x', y', z and given by [5.29, 5.30]

$$\frac{1}{\tau^s_{x'x'}} = \frac{1}{2}\left(\frac{\beta_+}{\hbar}\right)^2 \langle k^2\tau_p\rangle\,, \qquad \frac{1}{\tau^s_{y'y'}} = \frac{1}{2}\left(\frac{\beta_-}{\hbar}\right)^2 \langle k^2\tau_p\rangle\,, \tag{5.71}$$

$$\frac{1}{\tau^s_{zz}} = \frac{1}{\tau^s_{x'x'}} + \frac{1}{\tau^s_{y'y'}}\,,$$

where τ_p is the momentum relaxation time. In the time relaxation approximation valid for elastic or quasi-elastic scattering it can be introduced by

$$Q_{\boldsymbol{k}}\{\delta\boldsymbol{s}\} = \frac{\delta\boldsymbol{s}_{\boldsymbol{k}}}{\tau_p}\,,$$

where τ_p is in general a function of the energy $E_{\boldsymbol{k}}$.

If among the two contributions, BIA and SIA, to the spin splitting one is dominant and $|\beta_+| = |\beta_-|$, the spin relaxation times are interconnected by [5.29]

$$\tau^s_{x'x'} = \tau^s_{y'y'} = 2\tau^s_{zz}\,.$$

Interplay between the BIA and SIA contributions can lead to a giant spin relaxation anisotropy [5.30]. In particular, if these contributions coincide, $\beta_1 = \beta_2$, so that $\beta_- = 0$ one has $\tau^s_{x'x'} = \tau^s_{zz}$ and $\tau^s_{y'y'} = \infty$. In the case $\beta_1 = -\beta_2$ the coefficient $\beta_+ = 0$, the time $\tau^s_{x'x'}$ is infinite and $\tau^s_{y'y'}$ coincides with τ^s_{zz}.

The spin relaxation due to the spin splitting is slowed down by any process which changes the direction of $\boldsymbol{k}$, not only by momentum relaxation processes governing the electron mobility. The cyclotron movement of free carriers in a magnetic field suppresses the spin relaxation as well and can be considered one of such processes [5.31]. In a magnetic field $\boldsymbol{B} \parallel z$ applied to a (001)-grown QW, the decrease in spin relaxation rate is described by [5.32]

$$\frac{1}{\tau^s_{\alpha\alpha}(B)} = \frac{1}{\tau^s_{\alpha\alpha}(0)} \, \frac{1}{1+(\omega_c\tau_p)^2} \, , \tag{5.72}$$

where $\omega_c = |e|B/(mc)$ is the cyclotron frequency and the zero-field time $\tau^s_{\alpha\alpha}(0)$ ($\alpha = x', y', z$) is defined according to (5.71). Equation (5.72) can be understood taking into account that, due to the Lorentz force $(e/c)\boldsymbol{v} \times \boldsymbol{B}$, the free-electron wave vector varies in time as

$$k_{x'}(t) = \mathrm{Re}\left\{(k_{x'} + \mathrm{i}k_{y'})\mathrm{e}^{\mathrm{i}\omega_c t}\right\} \, , \; k_{y'}(t) = \mathrm{Im}\left\{(k_{x'} + \mathrm{i}k_{y'})\mathrm{e}^{\mathrm{i}\omega_c t}\right\} \, ,$$

the time-averaged values of k_α ($\alpha = x', y'$) are

$$\bar{k}_\alpha = \tau_p \int\limits_0^\infty k_\alpha(t) \exp\left(-t/\tau_p\right) dt \, ,$$

so that $\bar{k}_{x'} + \mathrm{i}\bar{k}_{y'} = (k_{x'} + \mathrm{i}k_{y'})(1 - \mathrm{i}\omega_c\tau_p)^{-1}$, and values of k^2_α averaged over the angle $\Phi_{\boldsymbol{k}}$ reduce to

$$\int\limits_0^{2\pi} \bar{k}^2_\alpha \, \frac{d\Phi_{\boldsymbol{k}}}{2\pi} = \frac{k^2}{2} \, \frac{1}{1+(\omega_c\tau_p)^2} \, .$$

Another possibility to change the direction of $\boldsymbol{k}$ is electron-electron collisions which make no effect on the electron mobility. Really, as shown in [5.33], electron-electron collisions change the direction of $\boldsymbol{k}$ and $\boldsymbol{\Omega}_{\boldsymbol{k}}$ and, therefore, they control the D'yakonov-Perel' spin relaxation, i.e., the time τ in (5.61), exactly in the same way as any other scattering processes do. In order to estimate a value of the time τ governed by the electron-electron collisions we use the kinetic equation in the same form

$$\frac{d\boldsymbol{s}_{\boldsymbol{k}}}{dt} + \boldsymbol{s}_{\boldsymbol{k}} \times \boldsymbol{\Omega}_{\boldsymbol{k}} + \boldsymbol{Q}_{\boldsymbol{k}}\{\boldsymbol{s}, f^0\} = 0 \tag{5.73}$$

as (5.69) but now retain in the collision integral for the spin distribution function $\boldsymbol{s}_{\boldsymbol{k}}$ only the contribution $Q_{\boldsymbol{k}}\{\boldsymbol{s}, f^0\}$ arising from the electron-electron scattering. Neglecting the exchange interaction as well as spin-flip scattering processes one has in the particular case of nondegenerate electron distribution

$$-\left(\frac{\partial \boldsymbol{s}_{\boldsymbol{k}}}{\partial t}\right)_{ee} \equiv \boldsymbol{Q}_{\boldsymbol{k}}\{\boldsymbol{s}, f^0\} = \sum_{\boldsymbol{k}'\boldsymbol{p}\boldsymbol{p}'} W_{\boldsymbol{p}\boldsymbol{p}',\boldsymbol{k}\boldsymbol{k}'}(\boldsymbol{s}_{\boldsymbol{k}} f^0_{k'} - \boldsymbol{s}_{\boldsymbol{p}} f^0_{p'}) \, , \tag{5.74}$$

where $W_{\boldsymbol{pp'},\boldsymbol{kk'}}$ is the probability rate for the scattering $\boldsymbol{k},\boldsymbol{k'} \to \boldsymbol{p},\boldsymbol{p'}$, and we assume the electron distribution function $f_{\boldsymbol{k}} = \mathrm{Tr}\{\hat{\rho}_{\boldsymbol{k}}/2\}$ to coincide with the Boltzmann function

$$f^0_{\boldsymbol{k}} = \exp\left[(\mu - E_{\boldsymbol{k}})/k_B T\right] \tag{5.75}$$

where $E_{\boldsymbol{k}} = \hbar^2 k^2/2m$, μ is the chemical potential derived from the equation for the 2D electron density $N = 2\sum_{\boldsymbol{k}} f^0_{\boldsymbol{k}}$. A sum of the direct Coulomb and exchange contributions can be presented as

$$\boldsymbol{Q}_{\boldsymbol{k}}\{\boldsymbol{s}, f^0\} = \frac{2\pi}{\hbar} \sum_{\boldsymbol{k'pp'}} \delta_{\boldsymbol{k}+\boldsymbol{k'},\boldsymbol{p}+\boldsymbol{p'}}\, \delta(E_k + E_{k'} - E_p - E_{p'}) \tag{5.76}$$

$$\times \left[2V^2_{\boldsymbol{k}-\boldsymbol{p}}(\boldsymbol{s}_{\boldsymbol{k}} f^0_{k'} - \boldsymbol{s}_{\boldsymbol{p}} f^0_{p'}) - V_{\boldsymbol{k}-\boldsymbol{p}} V_{\boldsymbol{k}-\boldsymbol{p'}}(\boldsymbol{s}_{\boldsymbol{k}} f^0_{k'} + \boldsymbol{s}_{\boldsymbol{k'}} f^0_k - 2\boldsymbol{s}_{\boldsymbol{p}} f^0_{p'})\right] .$$

Here $V_{\boldsymbol{q}}$ is the Fourier transform of the 2D Coulomb potential

$$V_{\boldsymbol{q}} = \frac{2\pi e^2}{æ q \Sigma} , \tag{5.77}$$

e is the elementary charge, æ is the dielectric constant, and Σ is the sample area in the interface plane. The exchange part is given by the term proportional to $V_{\boldsymbol{k}-\boldsymbol{p}} V_{\boldsymbol{k}-\boldsymbol{p'}}$.

In order to analyze the role of the quasi-2D character of the electron wave function confined in a QW of the finite thickness a one can replace $U^{2D}(\rho)$ by the effective potential obtained by averaging the 3D Coulomb potential as follows

$$U(\rho) = \frac{e^2}{æ} \int\int \frac{\varphi^2_{e1}(z)\, \varphi^2_{e1}(z')}{\sqrt{\rho^2 + (z - z')^2}} dz dz' ,$$

where $\varphi_{e1}(z)$ is the electron envelope function at the lowest conduction subband $e1$. The Fourier transform of $U(\rho)$ can be presented as

$$V_{\boldsymbol{q}} = \frac{2\pi e^2}{æ q} H(q) , \tag{5.78}$$

where the form-factor $H(q) = \int\int \exp(-q|z - z'|)\varphi^2_{e1}(z)\varphi^2_{e1}(z')dzdz'$ is smaller than unity. For $qa \ll 1$ (the large distance limit), one has $H(q) \cong 1$ and the interaction is exactly two-dimensional. In the opposite limiting case $qa \gg 1$, the form-factor $H(q)$ is inversely proportional to q and, therefore, $V_{\boldsymbol{q}} \propto q^{-2}$ as in the case of 3D electron gas. The allowance for the form-factor reduces the electron-electron interaction $U(\rho)$ with increasing the QW thickness and spreading the electron wavefunctions along the growth direction which results in increasing the average distance between electrons. In the approximation of infinitely high barriers the $e1$ envelope function has a simple form $\varphi_{e1}(z) = \sqrt{2/a}\cos(\pi z/a)$ and the form-factor allows an analytic representation [5.34]

$$H(q) = \frac{-32\,\pi^4 + 32\,\pi^4 \mathrm{e}^{-qa} + 3\,(qa)^5 + 20\,(qa)^3\pi^2 + 32\,\pi^4 qa}{\left[(qa)^2 + 4\,\pi^2\right]^2 (qa)^2}\,. \tag{5.79}$$

Experimentally, the effect of electron-electron collisions on the spin dynamics has recently been demonstrated by Brand et al. [5.35]. In [5.33] only the case of a nondegenerate 2D electron gas has been treated quantitatively while the data [5.35] were obtained for a degenerate high-mobility gas. In [5.36, 5.37] the theory [5.33] was extended to arbitrary electron degeneracy and comparison was performed between the calculated temperature dependence of τ_s with the experiment [5.35].

A convenient form to represent the temperature dependence of the spin relaxation time is to write τ_s as

$$\tau_s^{-1} = \Omega_0^2 \tau^*, \tag{5.80}$$

where Ω_0 is the effective Larmor frequency at the Fermi energy at zero temperature and τ^* is a temperature-dependent parameter which can be compared with the momentum relaxation time τ_p obtained from measurement of the Hall mobility. The representation (5.80) is usefully applied in the scattering-dominated regime, where $\Omega_0 \ll \tau^{-1}$, realized at $T \sim 10$ K and higher. At the low temperature $T = 1.8$ K, the electron spin polarization evolves as heavily damped oscillations of frequency $\Omega_0 \approx 0.19$ ps^{-1} and τ^* is found from the exponential decay of these oscillations. Thus, instead of τ_s, the temperature dependence of the above defined time τ^* is presented in Fig. 5.7.

Values of τ^* extracted from the experiment are plotted in Fig. 5.7 by crosses together with the momentum relaxation time τ_p (full circles). The spin polarization was monitored by a time-resolved optical response of a sample in which the 2D gas was confined in a (001)-oriented 10-nm n-doped GaAs/AlGaAs QW well structure. Electron concentration was estimated to be $N_s = 1.86 \times 10^{11}$ cm^{-2}, and Hall measurements showed N_s to be approximately constant at T below 100 K. The transport relaxation time τ_p was extracted from the Hall mobility.

The inverse electron spin relaxation time for the D'yakonov-Perel' mechanism in the symmetric GaAs QW is given by

$$\frac{1}{\tau_{zz}^s} = \langle(\Omega_1^2 + \Omega_3^2)\tau_p\rangle\,, \tag{5.81}$$

where $\hbar\Omega_1 = 2\gamma_c k(\langle k_z^2\rangle - k^2/4)$, $\hbar\Omega_3 = \gamma_c k^3/2$, γ_c is the constant describing spin-orbit splitting of the conduction band in bulk GaAs, see (2.119), and $\langle k_z^2\rangle$ is the quantum mechanical average of the squared electron wave vector along the growth axis. In (5.81) electron-electron collisions are neglected. Note that as compared with (5.71) we take into account the cubic-$\boldsymbol{k}$ terms as well and ignore the SIA linear-$\boldsymbol{k}$ spin splitting. The dotted line in Fig. 5.7 presents

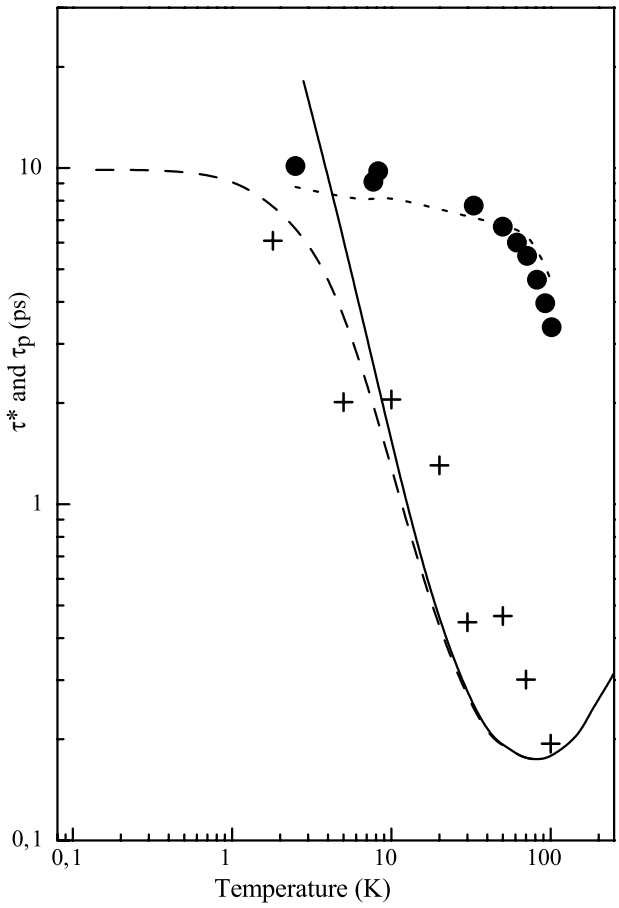

Fig. 5.7. Temperature dependencies of the scattering time τ^* controlling the D'yakonov-Perel' spin relaxation, see (5.80), and the transport scattering time τ_p which determines the mobility. Experimental data are represented by crosses (τ^*) and full circles (τ_p) [5.35]. Theoretical curves for τ^* are calculated neglecting either electron-electron scattering (*dotted*) or momentum scattering (*solid*) and taking into account both scattering mechanisms (*dashed*). From [5.37].

τ^* calculated from (5.81) with τ_p taken from the experiment (full circles). Definitely, this line does not fit experimental points (crosses) and, therefore, one can conclude that the account for momentum scattering processes only is not sufficient to explain the experimental results. The next step is to include electron-electron collisions into consideration and calculate the times τ_s and τ^* with allowance for both electron-electron and momentum scattering.

The quantum kinetic equation for the spin pseudovector taking into account both electron-electron collisions and elastic (or quasi-elastic) momen-

tum scattering changes its form from (5.73) to

$$\frac{\partial \boldsymbol{s}_{\boldsymbol{k}}}{\partial t} + \boldsymbol{s}_{\boldsymbol{k}} \times \boldsymbol{\Omega}_{\boldsymbol{k}} + \frac{\delta \boldsymbol{s}_k}{\tau_p} + \boldsymbol{Q}_{\boldsymbol{k}}\{\delta \boldsymbol{s}, f^0\} = 0\,, \tag{5.82}$$

where $\boldsymbol{Q}_{\boldsymbol{k}}\{\boldsymbol{s}, f^0\}$ is the electron-electron collision integral and τ_p is the momentum scattering time. For arbitrary degeneracy of the 2D electron gas but in the particular case of low spin polarization, the electron-electron scattering rate has the form [5.36]

$$\boldsymbol{Q}_{\boldsymbol{k}}\{\boldsymbol{s}, f\} = \frac{2\pi}{\hbar} \sum_{\boldsymbol{k}',\boldsymbol{p},\boldsymbol{p}'} \delta_{\boldsymbol{k}+\boldsymbol{k}',\boldsymbol{p}+\boldsymbol{p}'}\, \delta(E_k + E_{k'} - E_p - E_{p'}) \tag{5.83}$$

$$\times \left\{2V^2_{\boldsymbol{k}-\boldsymbol{p}} M(\boldsymbol{k}, \boldsymbol{k}', \boldsymbol{p}, \boldsymbol{p}') - V_{\boldsymbol{k}-\boldsymbol{p}} V_{\boldsymbol{k}-\boldsymbol{p}'} [M(\boldsymbol{k}, \boldsymbol{k}', \boldsymbol{p}, \boldsymbol{p}') + M(\boldsymbol{k}', \boldsymbol{k}, \boldsymbol{p}, \boldsymbol{p}')]\right\}.$$

Here

$$M(\boldsymbol{k}, \boldsymbol{k}', \boldsymbol{p}, \boldsymbol{p}') = \boldsymbol{s}_{\boldsymbol{k}} F(\boldsymbol{k}'; \boldsymbol{p}, \boldsymbol{p}') - \boldsymbol{s}_{\boldsymbol{p}} F(\boldsymbol{p}'; \boldsymbol{k}, \boldsymbol{k}'),$$

$F(\boldsymbol{k}_1; \boldsymbol{k}_2, \boldsymbol{k}_3) = f^0_{\boldsymbol{k}_1}(1 - f^0_{\boldsymbol{k}_2} - f^0_{\boldsymbol{k}_3}) + f^0_{\boldsymbol{k}_2} f^0_{\boldsymbol{k}_3}$ and $f^0_{\boldsymbol{k}}$ is the quasi-equilibrium Fermi-Dirac distribution function (5.65). For a nondegenerate electron gas, i.e., if $f^0_{\boldsymbol{k}} \ll 1$, equation (5.83) reduces to (5.76).

In [5.37] the spin-relaxation time governed by electron-electron collisions was calculated with allowance for the BIA linear-$\boldsymbol{k}$ term in $\boldsymbol{\Omega}_{\boldsymbol{k}}$ and fixed value of τ_p and using the statically screened 2D Coulomb potential for $V_{\boldsymbol{q}}$. The solid line in Fig. 5.7 shows temperature dependence of $\tau^* = \tau_s^{-1}\Omega_0^{-2}$ calculated taking into account electron-electron collisions only ($\tau_p = \infty$). A non-monotonous behavior of this time can be understood as follows. For a degenerate 2D electron gas, in the limit of low temperatures $\langle \Omega^2_{\boldsymbol{k}} \rangle$ tends to a constant value Ω_0^2, while the electron-electron scattering rate τ_{ee}^{-1} vanishes as $T^2 \ln T$. Therefore, if momentum scattering is neglected the scattering time $\tau^* \to \infty$. The allowance for electron momentum scattering stabilizes both τ_s^{-1} and τ^* at $T = 0$ (dashed curve). With rising the temperature the role of electron-electron collisions increases resulting in a decrease of τ^*. In the opposite limit of high temperatures the electron gas becomes nondegenerate in which case $\langle \Omega^2_{\boldsymbol{k}} \rangle \propto T$ and $\tau_{ee}, \tau^* \propto T$ so that the spin relaxation rate controlled by electron-electron collisions increases with temperature according to the T^2 law [5.33]. The dependence $\tau^*(T)$ exhibits a minimum near the transition from degenerate to nondegenerate statistics when the chemical potential of electron gas reaches the conduction band bottom. Figure 5.7 evidences, both experimentally and theoretically, that the D'yakonov-Perel' spin relaxation may be controlled by electron-electron collisions (which do not affect the mobility) in the same way as by any other carrier scattering process.

Now we briefly discuss other spin-relaxation mechanisms in semiconductor nanostructures. For bulk material the conduction-electron spin relaxation rate due to the *Elliott-Yafet mechanism* can be estimated as [5.25]

$$\frac{1}{\tau_s(E_e)} \sim \left(\frac{\Delta}{E_g+\Delta}\right)^2 \left(\frac{E_e}{E_g}\right)^2 \frac{1}{\tau_p(E_e)}\,,$$

where E_e is the electron kinetic energy, and the ratio E_e/E_g describes the extent of valence-band admixture in the conduction-band wavefunction. In QWs this rate transforms into [5.38, 5.39]

$$\frac{1}{\tau_s(E_e)} \sim \left(\frac{\Delta}{E_g+\Delta}\right)^2 \frac{E_{e1}E_e}{E_g^2} \frac{1}{\tau_p(E_e)} \tag{5.84}$$

and is proportional to the quantum-confinement energy E_{e1}. This is distinct from the D'yakonov-Perel' process related to the BIA linear-$\boldsymbol{k}$ terms which leads to the quadratic law $\tau_s^{-1} \propto E_{e1}^2$ because, for estimations, the average $\langle k_z^2\rangle$ can be approximated by $2m^*E_{e1}/\hbar^2$.

The spin-relaxation time of photoexcited electrons in p-doped QWs with the spin flip due to the electron-hole exchange interaction (Bir-Aronov-Pikus mechanism) is given by

$$\frac{1}{2\tau_s(\boldsymbol{k})} = \frac{2\pi}{\hbar} \sum_{\boldsymbol{p}\boldsymbol{p}'\boldsymbol{k}'} \sum_{jj'} f^h_{\boldsymbol{p}j} \left(1 - f^h_{\boldsymbol{p}'j'}\right)$$

$$\times \left|\langle \boldsymbol{k}', -1/2; \boldsymbol{p}', j' | V_{\rm exch} | \boldsymbol{k}, 1/2; \boldsymbol{p}, j\rangle\right|^2 \delta\left(E_{e1\boldsymbol{k}'} + E^h_{\boldsymbol{p}'j'} - E_{e1\boldsymbol{k}} - E^h_{\boldsymbol{p}j}\right)\,.$$

Here $V_{\rm exch}$ is the exchange interaction operator, $E^h_{\boldsymbol{p}j}$ is the hole energy in the state $(\boldsymbol{p}, j)$ and the factor $1 - f^h_{\boldsymbol{p}'j'}$ takes care for the hole not to be scattered into an occupied state. If only the $hh1$ subband is filled with holes forming a Fermi sea, the integration over the wave vectors leads to [5.40]

$$\frac{1}{\tau_s(k)} = \left(N_h a_{\rm B}^3 \omega_{\rm LT}\right)^2 (I_{hh} + I_{hl}) \frac{2m^*}{\hbar}\,, \tag{5.85}$$

where $a_{\rm B}$ and $\omega_{\rm LT}$ are the 3D-exciton Bohr radius and longitudinal-transverse splitting in bulk material related with the interband matrix element of the momentum operator according to (2.204), dimensionless k-dependent integrals I_{hh}, I_{hl} are contributed by hole scattering within the $hh1$ subband and to the $lh1$ subband, respectively. For small values of k, the electron-hole scattering keeps the holes within the heavy-hole subband and $I_{hl} = 0$. Moreover, the exclusion principle reduces the phase space available for the degenerate holes to be scattered by slow electrons. As a result, $\tau_s(k)$ exhibits a strong increase with decreasing the electron kinetic energy E_{e1k} [5.40]. For E_{e1k} exceeding the splitting between the $hh1$ and $lh1$ subbands, the integrals I_{hh} and I_{hl} become comparable.

The effective spin-relaxation mechanisms in bulk materials and QW structures are strongly suppressed for localized carriers. As a result the electron spin relaxation via interaction with nuclei becomes the dominant mechanism in semiconductor QDs at low temperatures [5.41–5.46]. The process is facilitated by the disparity of the characteristic time scales of the three processes

that determine the relaxation, namely, the period of the electron procession in the hyperfine field of the frozen fluctuation of the hyperfine field of the nuclei, the period of the nuclear spin precession in the hyperfine field of the electron, and the nuclear spin relaxation time in the dipole-dipole field of its nuclear neighbors. For GaAs QDs containing 10^5 nuclei, they are estimated to be ~ 1 ns, $\sim 1\,\mu$s and $\sim 100\,\mu$s, respectively. The last of these times is so long that many other electron spin relaxation mechanisms are more important on this time scale, and the effect of the nuclear dipole-dipole interactions on the electron spin relaxation can be neglected. In an ensemble of identical QDs the nuclear hyperfine fields are randomly oriented. Therefore, even though each electron spin processes in a coherent fashion in the frozen hyperfine field of its own dot, the ensemble average spin will decrease.

In bulk material the free heavy- and light-hole states in the degenerate band Γ_8 are characterized by a strong coupling between the wave vector and the angular momentum component (Chap. 2). As a result, ordinary scattering of a hole caused by spin-independent perturbations leads to a remarkable loss of the hole spin memory. The quantum confinement splits the heavy- and light-hole states, and quenches the spin relaxation for holes when the hole's in-plane kinetic energy is small compared with the $hh1$-$lh1$ separation distance. Nevertheless, the dominant mechanism of *hole spin relaxation* in p-doped QWs is the hole spin-flip scattering due to the spin mixing of heavy- and light-hole states [5.38,5.47,5.48]. It can be considered a modified Elliott-Yafet mechanism where the role of $\boldsymbol{k}$-dependent *interband* spin mixing is played by the *intersubband* mixing.

5.3.3 Effect of Quantum Confinement on the Electron g Factor

The Electron-Spin Resonance (ESR) frequency is determined by the electron effective Landé factor or the g factor (or gyromagnetic ratio). This important band parameter describes the Zeeman splitting of electron-spin sublevels in a magnetic field, and shows up not only in ESR experiments but also in various magneto-optical phenomena, especially in photoluminescence and light scattering.

In general, for a pair of Kramers-conjugate states, the Zeeman contribution to the electron effective Hamiltonian is written as

$$\mathcal{H}_{\boldsymbol{B}} = \frac{1}{2}\,\mu_B \sum_{\alpha\beta} \sigma_\alpha g_{\alpha\beta} B_\beta\,, \tag{5.86}$$

where σ_α ($\alpha = x, y, z$) are the Pauli matrices, $\boldsymbol{B}$ is the magnetic field, μ_B is the Bohr magneton and, for a low-symmetry system, the real tensor $g_{\alpha\beta}$ is characterized by nine linearly independent components. The ESR frequency is found from $\hbar\omega = \Delta_{\boldsymbol{B}}$, where the Zeeman splitting of the spin sublevels equals to

$$\Delta_{\boldsymbol{B}} = \mu_B \sqrt{\sum_{\alpha} \left(\sum_{\beta} g_{\alpha\beta} B_{\beta} \right)^2} \,. \tag{5.87}$$

If the system possesses a uniaxial symmetry, then the tensor $g_{\alpha\beta}$ has only two linearly independent components which are traditionally denoted by

$$g_{\parallel} \equiv g_{zz} \,,\; g_{\perp} \equiv g_{xx} = g_{yy}$$

with z being the principal axis. In this case (5.87) reduces to

$$\Delta_{\boldsymbol{B}} = \mu_B B \sqrt{g_{\parallel}^2 \cos^2\theta + g_{\perp}^2 \sin^2\theta} \,, \tag{5.88}$$

where $B = |\boldsymbol{B}|$, and θ is the angle between $\boldsymbol{B}$ and z.

The effective g factor in a bulk semiconductor results from the second-order $\boldsymbol{k}\cdot\boldsymbol{p}$ perturbation theory [5.49]. We remind that within terms of second-order in the $\boldsymbol{k}\cdot\boldsymbol{p}$ interaction the electron effective Hamiltonian in an external magnetic field is expressed as

$$\mathcal{H}^{(c)}_{ss'}(\boldsymbol{K}) = \left(E_c^0 + \frac{\hbar^2 \boldsymbol{K}^2}{2m_0} \right) \delta_{ss'} + \sum_{n \neq c} \frac{\mathcal{H}_{sn} \mathcal{H}_{ns'}}{E_c^0 - E_n^0} + \frac{1}{2} g_0 \mu_B \boldsymbol{\sigma}_{ss'} \boldsymbol{B} \,, \tag{5.89}$$

where E_c^0 and E_n^0 are the electron energies at the bottom of the conduction band and in the lower or higher band $n \neq c$ at the Γ-point, $s, s' = \pm 1/2$, $g_0 \approx 2$ is the free-electron Landé factor,

$$\mathcal{H}_{sn}(\boldsymbol{K}) = \frac{\hbar}{m_0} \, \boldsymbol{K} \cdot \boldsymbol{p}_{cs,n} \,, \qquad \boldsymbol{K} = -\mathrm{i}\nabla - \frac{e}{c\hbar} \, \boldsymbol{A}(\boldsymbol{r}) \,, \tag{5.90}$$

$\boldsymbol{A}(\boldsymbol{r})$ is the vector-potential of the magnetic field, and $\boldsymbol{p}_{cs,n}$ is the momentum matrix element between the Γ-point electron states in the conduction band c and the band n. The commutator of the operators K_α and K_β is given by

$$K_\alpha K_\beta - K_\beta K_\alpha = \frac{\mathrm{i}e}{\hbar c} \sum_{\gamma} \delta_{\alpha\beta\gamma} B_\gamma \,,$$

where $\delta_{\alpha\beta\gamma}$ is the unit antisymmetric tensor of the third rank. This allows to write the Zeeman Hamiltonian for the conduction electrons as

$$\mathcal{H}_{\boldsymbol{B},ss'} = \frac{1}{2} \, \mu_B \sum_{\gamma} B_\gamma \left(g_0 \sigma_{\gamma,ss'} - \frac{2\mathrm{i}}{m_0} \sum_{n \neq c} \sum_{\alpha\beta} \delta_{\alpha\beta\gamma} \frac{p^{\alpha}_{cs,n} p^{\beta}_{n,cs'}}{E_c^0 - E_n^0} \right) . \tag{5.91}$$

For an electron in the lowest s-antibonding conduction band Γ_6 in a zinc-blende semiconductor with the T_d point symmetry, the g factor is isotropic, $g_{\alpha\beta} = g\delta_{\alpha\beta}$, with

$$g \equiv g_{zz} = g_0 + \frac{1}{m_0} \sum_{n \neq c} \frac{|p^+_{c,1/2;n}|^2 - |p^-_{c,1/2;n}|^2}{E^0_c - E^0_n}, \tag{5.92}$$

where $p^{\pm}_{c,s;n} = \langle c\Gamma_6, s|\hat{p}_x \pm \mathrm{i}\hat{p}_y|n\rangle$, the spin index $s = \pm 1/2$ and $\hat{\boldsymbol{p}}$ is the momentum operator. In typical zinc-blende semiconductors the main contribution to g comes from the upper valence bands Γ_8, Γ_7 and the electron g factor is written in the form

$$g = g_0 - \frac{4}{3}\frac{m_0 P^2}{\hbar^2}\frac{\Delta}{E_g(E_g+\Delta)} + \Delta g = g_0 - \frac{4}{3}\frac{|p_{cv}|^2}{m_0}\frac{\Delta}{E_g(E_g+\Delta)} + \Delta g, \tag{5.93}$$

where Δg is the contribution from remote bands considered as a small fitting parameter, other parameters have been introduced in Chap. 2, see (2.45, 2.48). Using for GaAs the values $2|p_{cv}|^2/m_0 = 28.9$ eV, $E_g = 1.52$ eV, $\Delta = 0.34$ eV, we obtain $g = -0.32$. Experiments yield $g_{\mathrm{exp}}(\mathrm{GaAs}) = -0.44$. The difference can be attributed to $\Delta g = -0.12$. We see that in bulk GaAs both g_0 and the contribution of the spin-orbit split valence bands Γ_8, Γ_7 cancel to a considerable extent. According to (5.93) the electron effective Landé factor depends strongly on the fundamental gap and the spin-orbit splitting of the topmost valence band. It varies in a wide range from a large negative value in narrow-gap semiconductors (e.g., about -50 in InSb) to -0.44 in GaAs to positive values $g \leq 2$ in wide-gap materials. In the solid solution $\mathrm{Al}_x\mathrm{Ga}_{1-x}\mathrm{As}$ the energy gap increases with increasing the content x. Consequently, the electron g factor vanishes for a certain composition $x_0 \approx 0.12$ and becomes positive for $x > x_0$. In particular, $g(\mathrm{Al}_{0.35}\mathrm{Ga}_{0.65}\mathrm{As}) \approx 0.5$ [5.50].

Obviously, an equation similar to (5.91, 5.92) can be used for heterostructures, particularly in QW structures and SLs [5.51]. In this case, however, the index n runs not only over the different bands but also over subbands or minibands formed as a result of the quantum confinement. On the other hand, low-dimensional structures allow efficient alternative approaches based on the spatial confinement of electron wave function [5.52, 5.53]. Before presenting results of calculation in the sophisticated Kane model we consider two simplified but physically transparent approaches.

In the first approximate method the electron g factor in a QW or SL consisting of the layers A and B, e.g., GaAs and AlGaAs, is obtained in an averaging procedure

$$g = g_{\mathrm{A}} w_{\mathrm{A}} + g_{\mathrm{B}} w_{\mathrm{B}}\,, \tag{5.94}$$

where $g_{\mathrm{A,B}}$ is the g factor in the corresponding bulk material and $w_{\mathrm{A,B}}$ is the probability to find an electron inside the layer A or B:

$$w_{\mathrm{A,B}} = \int \varphi^2_{e1}(z)\theta_{\mathrm{A,B}}(z)dz\,,$$

where $\theta_{\mathrm{A}} = 1$ inside the layers A and 0 in the layers B while $\theta_{\mathrm{B}} = 1 - \theta_{\mathrm{A}}$. With decreasing the QW width the value of $w_{\mathrm{A}} = 1 - w_{\mathrm{B}}$ varies from 1

to 0 and, therefore, the electron g factor varies from $g_{\rm A}$ to $g_{\rm B}$. Since in a GaAs/$Al_{0.35}Ga_{0.65}$As heterostructure the g factors $g_{\rm A}$ and $g_{\rm B}$ differ in sign, the electron g factor should change its sign at a certain well thickness. Moreover, $g_{\rm A}$ and $g_{\rm B}$ are close in absolute value and their contributions to the net g factor (5.94) remarkably cancel out within a wide range of the well thicknesses. In this case, the various corrections disregarded in (5.94) may play a noticeable role.

Another simplified method is based on the assumption of infinitely high barriers for both conduction and valence bands in which case the selection rules (2.152) allow nonzero matrix elements $\boldsymbol{p}_{cs\nu,vm\nu'}$ for the quantum-confined states with the same quantum number $\nu = \nu'$ only. Then the longitudinal and transverse g factors are given by

$$g_{\parallel,\perp} = g_0 - \frac{2}{3}\,\frac{|p_{cv}|^2}{m_0} R_{\parallel,\perp}\,, \tag{5.95}$$

where

$$R_\parallel = \frac{3}{E_g + E_{e1} + E_{hh1}} - \frac{1}{E_g + E_{e1} + E_{lh1}} - \frac{2}{E_g + \Delta + E_{e1} + E_{so1}}\,,$$

$$R_\perp = \frac{2}{E_g + E_{e1} + E_{lh1}} - \frac{2}{E_g + \Delta + E_{e1} + E_{so1}}\,,$$

E_{e1}, E_{n1} are the confinement energies in the lowest conduction ($e1$), heavy-hole ($hh1$), light-hole ($lh1$) and spin-orbit split ($so1$) subbands. The equations for $g_{\parallel,\perp}$ can be derived by using either the general equation (5.89) or equation (5.92) for $g_\parallel$ and the similar equation

$$g_\perp = g_0 - \frac{2}{m_0} \sum_{n \neq c} \frac{{\rm Re}\left\{p^+_{c,1/2;n} p^z_{n;c,-1/2}\right\}}{E^0_c - E^0_n} \tag{5.96}$$

for $g_\perp$. It is clear that the contribution to $R_{\parallel,\perp}$ from the subband $n1$ is easily identified by the confinement energy E_{n1} in the corresponding denominator. In particular, the matrix elements $p^z_{n;c,\pm 1/2}$ vanish for the heavy-hole states and, therefore, the $hh1$ contribution to $R_\perp$ is absent. Neglecting the hole confinement energies we obtain an isotropic electron g factor renormalized as compared with (5.92) due to the replacement of E_g by $E_g + E_{e1}$. If we take into account the confinement energies E_{n1} in the corresponding denominators then we come to the following g-factor anisotropy

$$g_\perp - g_\parallel = \frac{2|p_{cv}|^2}{m_0} \left(\frac{1}{E_g + E_{e1} + E_{hh1}} - \frac{1}{E_g + E_{e1} + E_{lh1}} \right)\,. \tag{5.97}$$

According to (5.95, 5.97) the relative anisotropy of the g factor is given by

$$\frac{g_\perp - g_\parallel}{g_\perp} \approx \frac{3}{2}\,\frac{E_{lh1} - E_{hh1}}{\Delta}\,\frac{E_g + \Delta}{\eta E_g}\,, \tag{5.98}$$

where

$$\eta = 1 - \frac{3}{2}\,\frac{E_g(E_g+\Delta)m_0}{\Delta|p_{cv}|^2}\,.$$

It follows then that in heterostructures the electron g factor should exhibit a remarkable anisotropy.

While deriving (5.95) we considered unstrained heterostructures with matched lattice constants. In structures with a noticeable lattice mismatch the strain-induced shifts, δE_c and δE_n, of the conduction and valence bands should be included into the calculation procedure. As a result in the simplified equations (5.95) the denominators $E_g + E_{e1} + E_{n1}$ are changed by $E_g + \delta E_c + E_{e1} + \delta E_n + E_{n1}$. Thus, the heavy- and light-hole states are split due to both confinement and stress caused by the lattice mismatch between the compositional materials. In the CdTe/CdMgTe heterosystem, these effects act in the same direction pushing the light-hole states towards higher energies and increasing the g-factor anisotropy [5.54].

Detailed measurements have been performed on the transverse electron g factor $g_\perp$ as a function of the well width a for GaAs/$Al_{0.3}Ga_{0.7}$As QW structures [5.55–5.57] and showed the sign change of $g_\perp$ at $a \approx 65$ Å. Moreover, a considerable difference between $g_\parallel$ and $g_\perp$ has been observed on A_3B_5 and A_2B_6 based heterostructures, namely in GaAs/AlGaAs, GaAs/AlAs, GaInAs/InP, and CdTe/CdMgTe, under optical orientation of free carriers in tilted magnetic fields [5.58–5.60], in Optically Detected Magnetic Resonance (ODMR) experiments [5.61, 5.62], by using quantum beat technique [5.63], and in resonant spin-flip Raman scattering [5.54, 5.64, 5.65].

In an explicit calculation, the Zeeman Hamiltonian is written as

$$\mathcal{H}_{\boldsymbol{B},ss'} = \frac{1}{2}\,g_0\,\mu_B\,\eta_{\alpha;ss'}B_\alpha + \langle e1,s|\delta H|e1,s'\rangle\,, \tag{5.99}$$

where $\eta_{\alpha;ss'} = \langle e1,s|\sigma_\alpha|e1,s'\rangle$ and the magnetic-field induced perturbation is given by

$$\delta H = -\frac{e}{c}\boldsymbol{A}\hat{\boldsymbol{v}}\,,$$

$\hat{\boldsymbol{v}}$ being the velocity operator. Note that, for a homogeneous magnetic field, the vector-potential is a linear function of the radius-vector $\boldsymbol{r}$. The difference between $\eta_{\alpha;ss'}$ and $\sigma_{\alpha,ss'}$ arises from an admixture in the state $|e1,s\rangle$ of the opposite spin $-s$, see (2.44, 2.47). Numerical estimates show that this difference is very small in all particular cases considered below and can be neglected.

In the Kane model, the velocity operator $\hat{\boldsymbol{v}} = \hbar^{-1}\partial H(\boldsymbol{k})/\partial\boldsymbol{k}$ is an 8×8 matrix with $\boldsymbol{k}$-independent components. Using the explicit form for this matrix we obtain the Zeeman Hamiltonian in the form

$$\langle e1,s|\frac{e}{c}\boldsymbol{A}\hat{\boldsymbol{v}}|e1,s'\rangle = \mathrm{i}\,\frac{e}{c\hbar}\int P\,\left[\,\left(\boldsymbol{A}\boldsymbol{v}_s^+\right)u_{s'} - u_s^+\left(\boldsymbol{A}\boldsymbol{v}_{s'}\right)\right]d\boldsymbol{r}\,. \tag{5.100}$$

This particular equation can be used while calculating the electron g factor in QWRs and QDs as well as the transverse g factor in QWs. Indeed, if the wave function is localized in the direction ζ the diagonal matrix element of the coordinate ζ is no more a functional and the matrix element of δH for $\boldsymbol{B} \perp \zeta$ can be calculated avoiding its transformation into the sum in (5.89). While calculating the longitudinal g factor in a QW one cannot find such a direction and needs other methods based on the application of (5.89), numerical calculation of the Landau levels and their spin splitting and so on [5.53].

It follows from the symmetry considerations that the electron g factor in a spherical QD or a cylindrical QWR is isotropic. Moreover, one can show that in these two particular cases (5.100) can be reduced to [5.53]

$$g = g_0 + [g_{\rm A}(E_{e1}) - g_0]\, w_{\rm A} + [g_{\rm B}(E_{e1}) - g_0]\, w_{\rm B} + [g_{\rm B}(E_{e1}) - g_{\rm A}(E_{e1})]\, V_{3-d}(R)\, f^2(R)\,, \tag{5.101}$$

where d is the dimensionality of a nanostructure, $d = 0$ for a QD and $d = 1$ for a QWR, V_n is a volume of the sphere in the n-dimensional space: $V_2 = \pi R^2$ and $V_3 = 4\pi R^3/3$, $g_{\rm A}(E)$ and $g_{\rm B}(E)$ are the values of $g(E)$ and $g(E - \Delta E_c)$ in the A and B materials, see (2.48), $w_{\rm A}$ and $w_{\rm B}$ are the integral $\int d\boldsymbol{r} f^2(r)$ for a QD or $\int d\boldsymbol{\rho} f^2(\rho)$ for a QWR taken respectively over the A and B volumes. Note that the sum $w_{\rm A} + w_{\rm B}$ slightly differs from unity because of an admixture of the valence band states in the conduction-band wave function. An important point is that equation (5.101) describes as well the transverse g factor in a QW of the width $a = 2R$. In this case the dimensionality $d = 2$, the volume $V_{3-d} = 2R$ and $f(R) \equiv f(a/2)$.

Figure 5.8 shows the dependence of the electron g factor on the radius R in QDs and QWRs calculated for the isomorphic nanostructure GaAs/AlGaAs and pseudomorphic structure $Ga_{0.47}In_{0.53}As$/InP. In addition, in the same graph, variation of the longitudinal and transverse g factors in a QW is presented. The parameters used in the calculation of the first heterosystem are as follows: $E_g = 1.52$ eV, $\Delta = 0.34$ eV, $2|p_{cv}|^2/m_0 = 28.9$ eV for bulk GaAs, and $E_g = 1.94$ eV, $\Delta = 0.32$ eV, $2|p_{cv}|^2/m_0 = 26.7$ eV for bulk GaAs/$Al_{0.35}Ga_{0.65}As$, the band offset ratio V_h:V_c = 2:3. The contribution of remote bands is taken into account by adding the constant $\Delta g = -0.12$ to the Kane-model values of g. For the second heterosystem the following parameters were used: $E_g = 0.813$ eV, $\Delta = 0.356$ eV, $2|p_{cv}|^2/m_0 = 25.5$ eV for bulk $Ga_{0.47}In_{0.53}As$, and $E_g = 1.423$ eV, $\Delta = 0.108$ eV, $2|p_{cv}|^2/m_0 = 20.4$ eV for InP, the valence band offset $V_h = 0.356$ eV, the contribution from remote bands $\Delta g = -0.13$. With increasing R the curves approach the bottom value of g in the bulk material A, in agreement with (5.101) where, for $R \to \infty$, $w_{\rm A}$ saturates to unity and values of $w_{\rm B}, E_{e1}$ and $V_{3-d}(R)f^2(R)$ tend to zero. The asymptotic behavior of g at large R is described by $g(R) = g_{\rm A}(0) + \Delta g + (R_d/R)^2$ with the hierarchy $R_0 > R_1 > R_2^{\perp} > R_2^{\parallel}$, where $R_2^{\perp,\parallel}$ characterize the convergence of $g_{\perp}$ and $g_{\parallel}$ in QWs. In the opposite limit, $R \to 0$, the

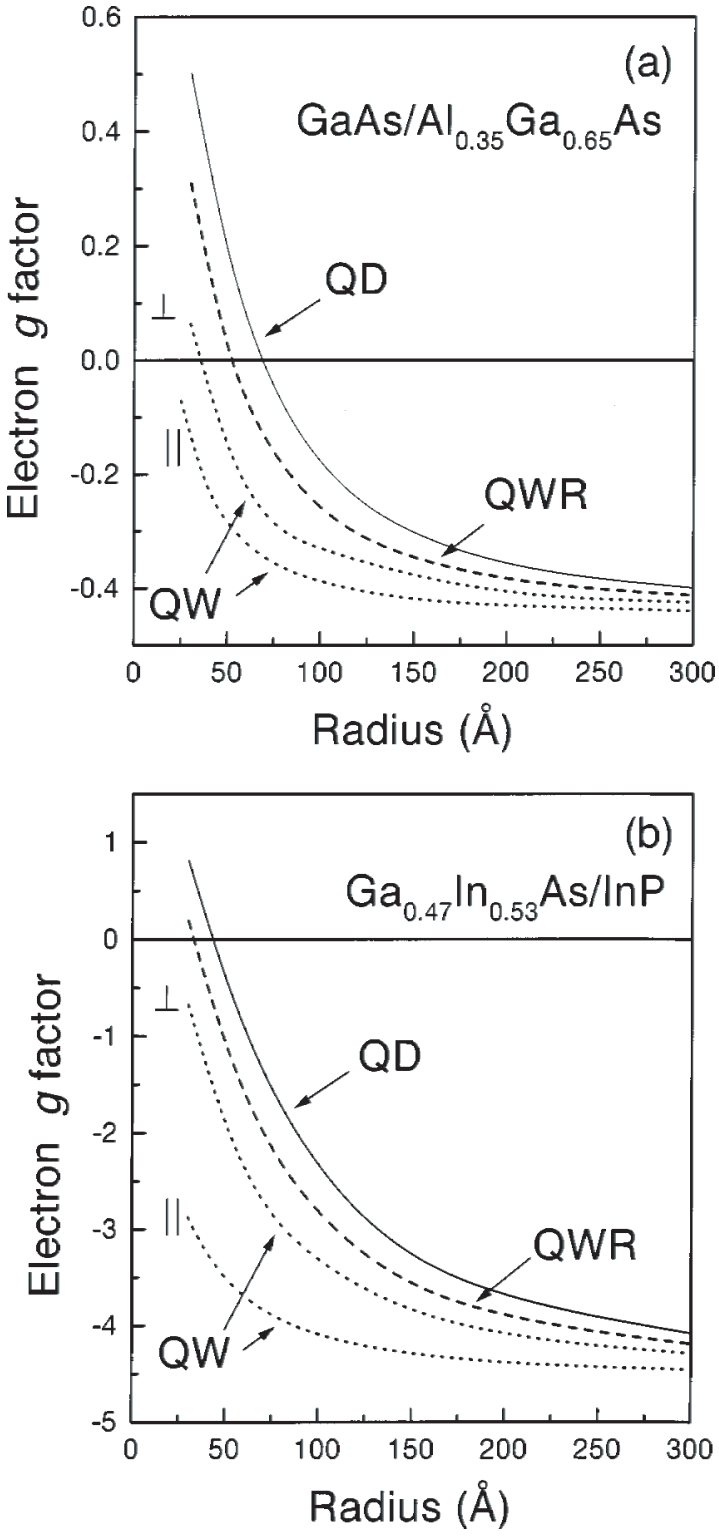

Fig. 5.8. The electron g factor calculated as a function of the radius R in spherical quantum dots (*solid*), cylindrical quantum wires (*dashed*) and quantum wells (*dotted*, $R = a/2$) for the heteropairs GaAs/$Al_{0.35}Ga_{0.65}As$ (**a**) and $Ga_{0.47}In_{0.53}As$/InP (**b**). [5.53]

curves $g(R)$ tend to the g factor value in the bulk barrier semiconductor, $g_{\rm B}(0) + \Delta g = 0.57$ in $Al_{0.35}Ga_{0.65}As$ and 1.2 in InP. The relation $g^{\rm QD} > g^{rmQWR} > g^{\rm QW}$ can be understood taking into account that the reduction in dimensionality enhances the role of the electron spatial confinement. The estimation shows that the contribution of the term proportional to $f^2(R)$ in (5.101) is not relatively small. In general, an approximate description of the dependence $g(R)$ is not applicable in the simple form $g_{\rm A}(E)w_{\rm A} + g_{\rm B}(E)w_{\rm B} + \Delta g$. Thus, Fig. 5.8 demonstrates main features of the effect of dimensionality on the electron g factor.

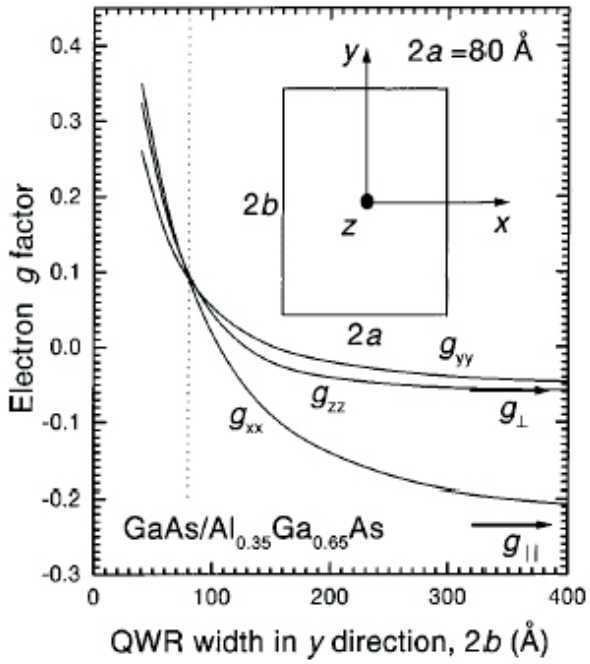

Fig. 5.9. The electron g factor components $g_{\alpha\alpha}$ ($\alpha = x, y, z$) in a GaAs/AlGaAs rectangular QWR vs. the length, $2b$, of one side. The other side, $2a$, is kept constant. The insert depicts the orientation of the coordinate system. The arrows indicate values of the transverse and longitudinal g factors in the 80 Å-thick QW. [5.53]

In rectangular QWRs, the tensor $g_{\alpha\beta}$ is characterized by the three different diagonal components, g_{xx}, g_{yy} and g_{zz}. The corresponding Kane-model electron wave functions were discussed in Chap. 2, see Fig. 2.3. Figure 5.9 shows the dependence of $g_{\alpha\alpha}$ ($\alpha = x, y, z$) in $GaAs/Al_{0.35}Ga_{0.65}As$ QWRs on one of the rectangular sizes while another size is kept constant and equal to $2a = 80$ Å. With increasing b the components g_{yy} and g_{zz} converge on the

electron transverse g factor in a QW of the thickness 80 Å and the component g_{xx} approaches the QW value of $g_{\parallel}$. In a square-shaped QWR, $b = a$, the two components g_{xx} and g_{yy} coincide as the symmetry predicts. Moreover, one can see from Fig. 5.9 that at the point $b = a$ the anisotropy $|g_{zz} - g_{xx}|$ is in fact quite small because, as it follows from (2.66), the function $h_z(x, y)$ in (2.65) vanishes at the four lines $x = 0, y = 0, y = x, y = -x$ and its values are too suppressed to produce a significant contribution to g.

A theory of the Zeeman splitting of electron spin states in biased QW structures was developed in [5.52]. The electric-field induced in-plane anisotropy of the g factor, due to the nonzero off-diagonal components g_{xy}, g_{yx}, was predicted by Kalevich and Korenev [5.66] and observed by Hallstein et al. [5.67].

In heterostructures, the heavy-hole effective g factor exhibits a strong anisotropy. Moreover, in the approximation of axial symmetry the in-plane $hh1$-hole g factor is zero at all. Kiselev and Moiseev developed a theory of the Zeeman spin splitting of size-quantized heavy holes in QWs and SLs in the multi-band envelope-function approximation, with a satisfactory agreement with experiment (see [5.68] and references therein). As far as in-plane magnetic fields are concerned, the transverse effective g factor $g_{h\perp}$ in the subband $hh1$ is nonzero due to the anisotropic parameter q in (2.31) and can be written as

$$g_{h\perp} = -3(q_{\mathrm{A}} w_{\mathrm{A}} + q_{\mathrm{B}} w_{\mathrm{B}}) \,, \tag{5.102}$$

where as before the indices A and B refer to the well and barrier compositional materials, and $w_{\mathrm{A,B}}$ is the probability to find a heavy hole in the quantum well or barrier. From comparison between theory and experiment on hole spin quantum beats in n-modulation-doped GaAs/AlGaAs QW structures a value of $|g_{h\perp}|$ was found to be 0.04 ± 0.01 [5.69] which is smaller than the longitudinal g factor, $g_{h\parallel}$, almost by two orders of magnitude.

5.3.4 Spin Quantum Beats in Photoluminescence

In order to elucidate the main idea of transient quantum beats let us first consider a general two-level quantum system with the initial state which is a linear superposition

$$\psi(t = 0) = C_1|1\rangle + C_2|2\rangle$$

of the two eigenstates $|1\rangle$ and $|2\rangle$ with the eigenenergies E_1, E_2. The wave function of the unperturbed system varies in time as

$$\psi(t) = \mathrm{e}^{-\mathrm{i}E_1 t/\hbar} C_1|1\rangle + \mathrm{e}^{-\mathrm{i}E_2 t/\hbar} C_2|2\rangle \,.$$

The detector is assumed to react to the particular state $|D\rangle = \bar{C}_1|1\rangle + \bar{C}_2|2\rangle$. Since the scalar product of $|D\rangle$ and $|t\rangle \equiv \psi(t)$ equals to

$$\langle D|t\rangle = \exp\left(-\mathrm{i}E_1 t/\hbar\right)\{\bar{C}_1^* C_1 + \bar{C}_2^* C_2 \exp\left[\mathrm{i}(E_1 - E_2)t/\hbar\right]\} \,,$$

one has for the signal registered by the detector

$$|\langle D|t\rangle|^2 = |\bar{C}_1 C_1|^2 + |\bar{C}_2 C_2|^2 + 2\,\mathrm{Re}\left\{\bar{C}_1 C_1^* \bar{C}_2^* C_2 \exp\left[\mathrm{i}(E_1 - E_2)t/\hbar\right]\right\} .$$

Thus, if $\psi(t=0)$ and $|D\rangle$ are not the pure states $|1\rangle$, $|2\rangle$ then the signal has an oscillating component with the oscillation period $T = 2\pi\hbar/|E_1 - E_2|$.

As an example we take

$$C_1 = C_2 = \frac{1}{\sqrt{2}} \quad \text{and} \quad \bar{C}_1 = \pm\bar{C}_2 = \frac{1}{\sqrt{2}} . \tag{5.103}$$

Then the squared scalar product $|\langle D|t\rangle|^2$ describing the measured signal is equal to $0.5\{1 \pm \cos\left[(E_2 - E_1)t/\hbar\right]\}$.

Now we will illustrate the idea of quantum beats by the example of the *transient Hanle effect*. We assume that the pulsed photoexcitation generates at $t = 0$ spin-polarized photoelectrons in the conduction band. We use the notations $n^0 \equiv n(t=0)$ and $\boldsymbol{s}^0 = (0, 0, s_z^0)$ for the initial electron density and spin density, where $s_z^0 = æ P_c^0 n_0/2$ and P_c^0, æ are introduced in (5.53). The time dependence of n and $\boldsymbol{s}$ in an external magnetic field $\boldsymbol{B} \perp z$ can be derived by solving equation (5.55) where the derivatives dn/dt and $d\boldsymbol{s}/dt$ are added in the left-hand sides and the steady-state generation rates g, $\dot{\boldsymbol{s}}$ are set to zero. For $\boldsymbol{B} \parallel x$, the solutions $n(t)$, $s_x(t)$ are easily written: $n(t) = n^0 \exp(-t/\tau_0)$, $s_x = 0$. As for two other components of $\boldsymbol{s}$, it is convenient to transform a pair of two equations for the real components s_y, s_z into one equation for the complex combination $s_+ = s_z + i s_y$

$$\frac{ds_+}{dt} + \left(\frac{1}{T} + \mathrm{i}\Omega_L\right) s_+ = 0 . \tag{5.104}$$

For the initial condition $s_+(t=0) = s_z^0$, its solution is

$$s_+(t) = s_z^0 \exp\left[-t\left(\frac{1}{T} + \mathrm{i}\Omega_L\right)\right] .$$

From this it follows that

$$s_z(t) = s_z^0 \mathrm{e}^{-t/T} \cos\Omega_L t\,,\ s_y(t) = -s_z^0 \mathrm{e}^{-t/T} \sin\Omega_L t\,.$$

The intensities of the PL circularly-polarized components are related to the total intensity I and the Stokes parameter P_c by $I_\pm = I(1 \pm P_c)/2$. Taking into account that, according to (5.53), $P_c = æ p = 2æ s_z/n$, we obtain for the transient Hanle effect

$$I_\pm \propto \mathrm{e}^{-t/\tau_0} \pm æ^2 P_c^0 \mathrm{e}^{-t/T} \cos\Omega_L t\,. \tag{5.105}$$

In order to analyze (5.105) in terms of the quantum beats we rewrite the spinor wave function $\psi(t)$ of a photoelectron as a linear combination of the spin eigenstates $|1\rangle, |2\rangle$ in the magnetic field $\boldsymbol{B} \parallel x$ which, in fact, are eigenstates of the Pauli matrix σ_x, namely

$$|1\rangle = \frac{1}{\sqrt{2}} \begin{bmatrix} 1 \\ 1 \end{bmatrix}, |2\rangle = \frac{1}{\sqrt{2}} \begin{bmatrix} 1 \\ -1 \end{bmatrix} .$$

We assume the initial electron spin to be polarized along z and neglect, for simplicity, the spin relaxation and decay due to the electron recombination. Then, the electron state is described by the time-dependent wave function

$$\psi(t) = \frac{1}{\sqrt{2}} \left(e^{-\mathrm{i}\Omega_L t/2}|1\rangle + e^{\mathrm{i}\Omega_L t/2}|2\rangle \right) . \tag{5.106}$$

For interband optical transitions $hh1 \rightarrow e1$ in a QW structure the factor æ in (5.105) equals -1. If the analyzer detects the circularly polarized photons, either σ_+ or σ_-, its action is equivalent to projecting $\psi(t)$ upon the state $|D\rangle = (|1\rangle \mp |2\rangle)/\sqrt{2}$, respectively. Therefore, in this particular case the coefficients C_1, C_2 and $\bar{C}_1, \bar{C}_2$ are indeed determined by (5.103). As a result we obtain $\langle D|t\rangle = \mathrm{e}^{-\mathrm{i}\Omega_L t/2}(1 \mp \mathrm{e}^{\mathrm{i}\Omega_L t})/2$ or $I_\pm \propto |\langle D|t\rangle|^2 = (1 \mp \cos \Omega_L t)/2$ with the quantum-beat period $2\pi/\Omega_L$. Allowance for the finite lifetime and spin relaxation leads to a multiplication of unity by e^{-t/τ_0} and $\cos \Omega_L t$ by $\mathrm{e}^{-t/T}$ in agreement with (5.105).

Note that, in a tilted magnetic field with $B_z \neq 0, B_x \neq 0$, equation (5.105) is expanded to

$$I_\pm \propto \mathrm{e}^{-t/\tau_0} \pm æ^2 P_c^0 \mathrm{e}^{-t/T} \left[1 - \left(\frac{\Omega_\perp}{\Omega_L} \right)^2 (1 - \cos \Omega_L t) \right] ,$$

where $\Omega_L = \sqrt{\Omega_\parallel^2 + \Omega_\perp^2}$, $\hbar\Omega_\parallel = g_\parallel \mu_B B_z$, $\hbar\Omega_\perp = g_\perp \mu_B B_x$ and the uniaxial anisotropy of the g factor is taken into account. Quantum beats in the exciton PL are mentioned in Sect. 5.5.

5.4 Hot Photoluminescence in Quantum-Well Structures

By the term *hot photoluminescence* of free carriers we mean the emission arising due to the radiative recombination of photoelectrons with their kinetic energies exceeding the average energy of the thermalized electrons. The emission occurs during the photoelectron energy relaxation to the conduction-band bottom and is usually related to band-to-acceptor transitions [5.70–5.73]. The hot-electron energy distribution is non-Maxwellian and, at low temperatures and low doping level, has a discrete character because of the consecutive emission of longitudinal optical phonons by the hot electrons.

The hot PL spectroscopy can be used to measure the valence subband dispersion in QW structures and SLs [5.73]. To simplify the picture let us ignore the in-plane anisotropy, or warping, of the QW subbands. Then to obtain the subband dispersion information, monochromatic photons are absorbed in a QW to generate hot electrons of energy E_e and hot holes of energy E_h. Most

of the hot electrons relax by phonon emission. However, a few of them immediately recombine radiatively at a neutral acceptor intentionally introduced as a dopant into the well and emit photons of the energy E_{PL}. By measuring the hot PL energy for a given initial photon energy $\hbar\omega$, values of E_e and E_h may be directly derived from the energy and wave-vector conservation laws

$$E_e(k) = E_{PL} - E_g + E_a \,, \qquad (5.107)$$
$$E_h(k) = \hbar\omega - E_{PL} - E_a \,.$$

Here $k = |\boldsymbol{k}|$, $\boldsymbol{k}$ is the electron wave vector, E_g is the QW band gap and E_a is the binding energy of a hole at the acceptor. The conduction-subband dispersion, $E_e(k)$, is relatively simple and can be readily derived by using independent information. Therefore, the wave vector k is obtained from the first equation (5.107). According to (5.107), a value of $E_h(k)$ equals to $\hbar\omega - E_g - E_e(k)$. By measuring the hot PL as a function of laser photon energy, the dispersion of the valence subbands can be mapped out.

The spin optical orientation for thermalized and hot electrons mostly differs quantitatively and, with some modifications, the principles formulated in Sect. 5.3.1 are valid for circular polarization of hot PL as well. A quite new phenomenon is the linear polarization of hot PL. It appears under optical excitation by linearly-polarized light and depends on the direction of the light-polarization unit vector $\boldsymbol{e}$. It is due to the *alignment* of photoelectron momenta which, in turn, is related to the form of the valence-band wave functions in semiconductors with a degenerate valence band. First we explain this phenomenon for a bulk semiconductor with a zinc-blende lattice. For transitions from the heavy- and light-hole subbands, hh and lh, to the conduction band c, the transition rate $W_{c,j}$ ($j = hh, lh$) is a function of the angle θ between the electron wave vector $\boldsymbol{k}$ and the polarization unit vector $\boldsymbol{e}$. Neglecting the warping of the valence band, one obtains, see, e.g., [5.74]

$$W_{c,j}(\boldsymbol{k}) \propto 1 + \alpha_j \mathrm{P}_2(\cos\theta) \,, \qquad (5.108)$$

where $\mathrm{P}_2(t) = (1/2)(3t^2 - 1)$ is the second Legendre polynomial and $\alpha_{hh} = -1, \alpha_{lh} = 1$. Note that for $\alpha = -1$ the transition rate is just proportional to $\sin^2\theta$. Thus, the momenta $\hbar\boldsymbol{k}$ of electrons excited from the heavy-hole subband are mostly normal to $\boldsymbol{e}$ and the initial distribution of electrons photoexcited from the light-hole subband is stretched along $\boldsymbol{e}$. Recombination of the hot photoelectrons with the anisotropic distribution in the $\boldsymbol{k}$-space leads to a linear polarization of the hot PL. In accordance with (5.108) the distribution function of the relaxing hot electrons is given by

$$f_{\boldsymbol{k}} = \bar{f}(E_e)[1 + \alpha(E_e)\mathrm{P}_2(\cos\theta)] \,, \qquad (5.109)$$

where $\bar{f}$ is the isotropic part of the distribution function and α is the parameter of anisotropy dependent on the electron kinetic energy E_e. The hot-PL intensity is determined by the integral

$$I(\omega') \propto \int [1 + \alpha_r \mathrm{P}_2(\cos\theta')] f_{\boldsymbol{k}} d\Omega \,, \tag{5.110}$$

where $d\Omega$ is an element of the solid angle, ω' is the selected PL frequency, ω' and k are related by $E_e(k) + E_g - E_a = \hbar\omega'$, and θ' is the angle between $\boldsymbol{k}$ and the polarization unit vector, $\boldsymbol{e}'$, of the secondary radiation. The band-to-acceptor optical matrix element is proportional to the Fourier component, $\Psi_a(\boldsymbol{k})$, of the spinor wave function of the bound-to-acceptor hole. At large k, the function $\Psi_a(\boldsymbol{k})$ is formed by heavy-hole states and the anisotropy parameter α_r is close to $\alpha_{hh} = -1$. Substituting $f_{\boldsymbol{k}}$ from (5.109) into (5.110) and integrating over the solid angle one obtains

$$I(\omega') \propto 1 + \frac{\alpha(E_e)\alpha_r}{5} \, \mathrm{P}_2(\cos\chi) \,, \tag{5.111}$$

where χ is the angle between $\boldsymbol{e}$ and $\boldsymbol{e}'$. In the back-scattering geometry, the degree of linear polarization of the hot PL is given by

$$P = \frac{I_\parallel - I_\perp}{I_\parallel + I_\perp} = \frac{3\alpha(E_e)\alpha_r}{20 + \alpha(E_e)\alpha_r} \,,$$

where $I_\parallel, I_\perp$ are the intensities of the radiation polarized parallel and perpendicular to the initial polarization $\boldsymbol{e}$. For $\alpha_r = -1$ and $\alpha_j = \mp 1$ we obtain $P = 1/7$ and $P = -3/9$, respectively. Thus, the sign of polarization for the radiation of electrons excited from the heavy-hole subband coincides with that of the exciting light, and for the electrons excited from the light-hole subband, the PL polarization has the opposite sign.

In bulk semiconductors the linear polarization P weakly depends on the initial photoelectron kinetic energy. The main feature of the hot-electron PL in QWs, as compared with bulk crystal, is its strong dependence on the kinetic energy E_e. Values of P in the 2D structures vary from $P = 0$ at $E_e = 0$ up to $P = 0.5$ at kinetic energies exceeding the confinement energy. This result can be understood taking into account that the valence-subband wave functions at $k_x = k_y = 0$ are pure states of heavy and light holes. Therefore, under optical excitation at the band edge $E_{g,hh}^{rmQW} = E_g + E_{e1} + E_{hh1}$ or $E_{g,lh}^{\mathrm{QW}} = E_g + E_{e1} + E_{lh1}$, the optical transition rate is independent of the angle φ between $\boldsymbol{e}$ and the 2D wave vector $\boldsymbol{k}_\parallel$, the anisotropic alignment in the $\boldsymbol{k}_\parallel$-space is absent and $P = 0$. However, at $k_\parallel \neq 0$ each subband state is a hybrid of heavy- and light-hole states and the alignment becomes possible. Similarly to (5.108), the angular dependence of the 2D-photoelectron distribution function can be presented as

$$W_{c,hh}^{\mathrm{QW}}(\boldsymbol{k}_\parallel) \propto 1 + \alpha^{2D}(k_\parallel) \cos 2\varphi \,. \tag{5.112}$$

In order to estimate the anisotropy parameter α^{2D} for transitions $hh1 \to e1$, we remind that, in a bulk semiconductor, the transition rate $W_{c,hh}(\boldsymbol{k})$ is proportional to $\sin^2\theta$ and, for $\boldsymbol{e} \parallel x$, the latter can be rewritten as the ratio

$$\frac{k_y^2 + k_z^2}{k_x^2 + k_y^2 + k_z^2} \,. \tag{5.113}$$

Replacing k_z^2 by the mean value $\langle k_z^2 \rangle \sim (\pi/a)^2$, where a is the QW width, and k_x^2, k_y^2 by

$$\frac{1}{2}\, k_\parallel^2 (1 \pm \cos 2\varphi)$$

we obtain

$$\alpha^{2D} = -\frac{k_\parallel^2}{k_\parallel^2 + \langle k_z^2 \rangle} \,.$$

A rigorous theoretical study [5.75], taking into account the $\boldsymbol{k}_\parallel$-governed heavy-light mixing, slightly modifies the dependence of the linear polarization P on the electron energy E_e as compared with the above simple consideration.

The width of the zero-LO-phonon hot-PL peak in bulk and QW samples is caused by the warping of the hole subbands as well as by inhomogeneous broadening of the acceptor levels. The low- and high-energy edges of the peak correspond to electrons excited with the lateral wave vector $\boldsymbol{k}_\parallel \parallel \{100\}$ and $\boldsymbol{k}_\parallel \parallel \{110\}$, respectively. If excitation of hot PL is performed in the configuration $\boldsymbol{e} \parallel [110]$ the electrons with $\boldsymbol{k}_\parallel \parallel \{100\}$ are not aligned and the low frequency edge should be unpolarized. Conversely, electrons with $\boldsymbol{k}_\parallel \parallel \{110\}$ contribute to the high energy edge of the zero-phonon peak and their recombination should be polarized. Therefore, the polarization is expected to grow from the low to high frequency edge, in agreement with experimental observations on MQWs and SLs [5.73, 5.76].

5.5 Polarized Photoluminescence of Excitons

5.5.1 Fine Structure of Exciton Levels in Nanostructures

If allowance is made for free-carrier spin, then the ground state $n = 1$ of an exciton is degenerate, even in the case of simple bands. For direct-gap Γ-point excitons, the ground-state degeneracy is equal to the product of the conduction- and valence-band degeneracies at $\boldsymbol{k} = 0$. The wave functions of the ground state transform according to the representation $D_{\rm exc} = \Gamma_e \times \Gamma_h$, where the representations Γ_e and Γ_h characterize the symmetry of electron and hole states at the extremum point. The representation $D_{\rm exc}$ is reducible and may be decomposed into irreducible representations of the point group of the semiconductor system, bulk material or nanostructure. The electron-hole exchange interaction partially removes the degeneracy and splits the $1s$-exciton level into states transforming according to the irreducible representations. In the present subsection we touch the main aspects of the electron-hole interaction in semiconductors and briefly recall the fine structure of excitonic levels in QWs, QWRs and QDs.

A consistent theory of electron-hole exchange interaction in semiconductors has been developed by Pikus and Bir [5.77] and Denisov and Makarov [5.78]. In the effective-mass approximation, the Coulomb-interaction operator between an electron and a hole in a semiconductor crystal includes three contributions, describing, respectively, the direct, or intraband, Coulomb interaction (U_C) and the long-range ($U_{\text{exch}}^{\text{long}}$) and short-range ($U_{\text{exch}}^{\text{short}}$) exchange interaction. We introduce the two-particle excited states of the crystal $|m, \boldsymbol{k}_e; n, \boldsymbol{k}_h\rangle$, where $\boldsymbol{k}_{e,h}$ is the wave vector of the electron or hole, indices m and n number the degenerate states of the electron in the conduction band and the hole in the valence band at $\boldsymbol{k}_{e,h} = 0$ (for definiteness, a direct-gap semiconductor with cubic symmetry and an extremum at the Γ point is considered). Then the matrix elements of the U_C and $U_{\text{exch}}^{\text{long}}$ operators between these states can be written as

$$\langle m', \boldsymbol{k}'_e; n', \boldsymbol{k}'_h | U_C | m, \boldsymbol{k}_e; n, \boldsymbol{k}_h \rangle = -\frac{1}{V} \frac{4\pi e^2}{æ_0 |\boldsymbol{k}_e - \boldsymbol{k}'_e|^2} \, \delta_{m'm} \delta_{n'n} \, \delta_{\boldsymbol{k}_e + \boldsymbol{k}_h, \boldsymbol{k}'_e + \boldsymbol{k}'_h} \,, \tag{5.114}$$

$$\langle m', \boldsymbol{k}'_e; n', \boldsymbol{k}'_h | U_{\text{exch}}^{(\text{long})} | m, \boldsymbol{k}_e; n, \boldsymbol{k}_h \rangle = \frac{1}{V} \frac{4\pi e^2 \hbar^2}{æ_b m_0^2 E_g^2} \frac{(\boldsymbol{K} p_{m'\bar{n}'})(\boldsymbol{K} p_{m\bar{n}})^*}{K^2} \, \delta_{\boldsymbol{k}_e + \boldsymbol{k}_h, \boldsymbol{k}'_e + \boldsymbol{k}'_h} \,. \tag{5.115}$$

Here $\boldsymbol{K}$ is the total wave vector $\boldsymbol{k}_e + \boldsymbol{k}_h = \boldsymbol{k}'_e + \boldsymbol{k}'_h$; E_g is the band gap; $\boldsymbol{p}_{m\bar{n}}$ is the matrix element of the momentum operator, calculated between the electronic Bloch functions $|m, \boldsymbol{k} = 0\rangle$ and $|\bar{n}, \boldsymbol{k} = 0\rangle$ (the hole state $n, \boldsymbol{k}$ and the electron state $\bar{n}, -\boldsymbol{k}$ are coupled to each other by the time-inversion operator); $æ_0$ and $æ_b$ are the dielectric constants, low-frequency and high-frequency (at the electron-hole-pair excitation frequency), and V is the volume of the crystal. The interaction represented by (5.115) can be interpreted as a result of the virtual recombination and generation of an electron-hole pair. This equation can be derived as well by one more method taking into account the macroscopic electric field generated by the electron-hole pair and the self-consistent effect of this field on the energy of the pair. It is worth to note that in (5.115) the retarding electron-photon interaction is neglected. The generalized form of this equation taking into account the successive emission and absorption of a transverse photon by an electron-hole pair can be found in [5.79].

The Fourier components of the Coulomb potential with the wave vectors $\boldsymbol{b} + \boldsymbol{k}'_e - \boldsymbol{k}_e$, where $\boldsymbol{b}$ represents a nonzero reciprocal-lattice vector, contribute to the short-range interaction. When k_e and k_h are small enough to satisfy the criterion of the applicability of the effective-mass method, operator $U_{\text{exch}}^{\text{short}}$ has the character of a contact interaction and can be represented in the form

$$\langle m', \boldsymbol{k}'_e; n', \boldsymbol{k}'_h | U_{\text{exch}}^{(\text{short})} | m, \boldsymbol{k}_e; n, \boldsymbol{k}_h \rangle = \Delta_{m'n',mn} a_0^3 \delta(\boldsymbol{r}_e - \boldsymbol{r}_h) \,, \tag{5.116}$$

where a_0 is the lattice constant and the factor a_0^3 is separated out in order to have the dimension of energy for the coefficients $\Delta_{m'n',mn}$. The dependence of these coefficients on the band indices is found from symmetry considerations, while their absolute magnitudes are determined by comparing theory with experiment on studies of the fine structure of exciton levels. The number of linearly independent coefficients coincides with the number of irreducible representations contained in the direct product $\Gamma_e \times \Gamma_h$. For illustration, let us consider the pair of bands Γ_6 and Γ_7 in GaAs-type semiconductors: $\Gamma_6 \times \Gamma_7 = \Gamma_2 + \Gamma_{15}$. It is convenient to go to a basis of electron-hole excitations in which the three states $|\nu, \boldsymbol{k}_e, \boldsymbol{k}_h\rangle$ ($\nu = x, y, z$) are optically active in the polarization $\boldsymbol{e} \parallel \nu$, while the optical transition to the fourth state $|\Gamma_2, \boldsymbol{k}_e, \boldsymbol{k}_h\rangle$ is forbidden. The long-range exchange interaction given by (5.114) involves only the states $|\nu, \boldsymbol{k}_e, \boldsymbol{k}_h\rangle$ and has in the new basis the form

$$\langle \nu', \boldsymbol{k}'_e, \boldsymbol{k}'_h | U_{\text{exch}}^{(long)} | \nu, \boldsymbol{k}_e, \boldsymbol{k}_h \rangle = \frac{4\pi}{æ_b V} \left(\frac{e\hbar p_0}{m_0 E_g} \right)^2 \frac{K_{\nu'} K_\nu}{K^2} \, \delta_{\boldsymbol{K}',\boldsymbol{K}} \,, \qquad (5.117)$$

where p_0 is the interband matrix element of the momentum operator for the optical transition to the state $|\nu\rangle$, see also (2.204).

The short-range interaction splits the exciton quartet $\Gamma_6 \times \Gamma_7(1s)$ into a dipole-allowed triplet Γ_{15} and an optically-inactive singlet Γ_2. The long-range exchange interaction splits the $1s$ exciton into states longitudinal and transverse with respect to the exciton wave vector $\boldsymbol{K}$. The longitudinal-transverse splitting is expressed via the microscopic parameter p_0 as

$$\hbar\omega_{\text{LT}} = \frac{4}{æ_b a_{\text{B}}^3} \left(\frac{e\hbar p_0}{m_0 E_g} \right)^2 \,, \qquad (5.118)$$

where a_{B} is the 3D-exciton Bohr radius.

The ground state $e1$-$hh1(1s)$ of a heavy-hole exciton in zinc-blende-based QWs is also fourfold degenerate but, in contrast to the previous case of the $\Gamma_6 \times \Gamma_7(1s)$ exciton, the exciton sublevels are characterized by the angular momentum component $M = s + j = \pm 1, \pm 2$, where $s = \pm 1/2$ and $j = \pm 3/2$ are the electron and hole spin components. In accordance with the multiplication law $\Gamma_6 \times \Gamma_6 = \Gamma_1 + \Gamma_2 + \Gamma_5$ for a QW structure of the D_{2d} symmetry, the short-range exchange interaction splits the state $e1$-$hh1(1s)$ into a radiative doublet Γ_5 which is dipole-active in the $\boldsymbol{e} \perp z$ polarization and corresponds to $M = \pm 1$ and two close-lying dipole-forbidden singlet levels Γ_1 and Γ_2 which are the symmetrized and antisymmetrized linear combinations of the exciton states with $M = \pm 2$. The long-range exchange interaction splits the longitudinal and transverse exciton states lifting the energy of the longitudinal exciton by

$$E_{\text{LT}}^{\text{QW}} = \frac{2\pi}{æ_b} \left(\frac{e\hbar p_0}{m_0 E_g} \right)^2 f^2(0) P(K) \, K \equiv \mathcal{C}(K) \, K \,, \qquad (5.119)$$

where $K = |\boldsymbol{K}|$, $\boldsymbol{K}$ is the in-plane wave vector of the 2D exciton, $f(\boldsymbol{\rho})$ is the envelope function describing the relative electron-hole motion,

$$P\,(K) = \int dz' \int dz\; \varphi_{e1}(z')\varphi_{hh1}(z')\; \varphi_{e1}(z)\varphi_{hh1}(z)\; \mathrm{e}^{-K|z-z'|}$$

and $\varphi_{e1}(z), \varphi_{hh1}(z)$ are the single-particle size-quantized functions. For small values of K satisfying the condition $Ka \ll 1$, the function $P(K)$ or the coefficient $\mathcal{C}$ is constant. Hence the long-range exchange interaction in a QW vanishes linearly when $\boldsymbol{K}$ goes to zero. This also means that no longitudinal-transverse splitting is expected for the exciton excitation with light propagating along the growth axis of the well. For $Ka \ll 1$, the longitudinal-transverse splitting and the coefficient $\mathcal{C}$ can be expressed in terms of the exciton radiative damping Γ_0 defined by (3.18) as

$$E_{\mathrm{LT}}^{\mathrm{QW}} = \hbar\Gamma_0\,\frac{K}{k}\;,\; \mathcal{C} = \frac{\hbar\Gamma_0}{k}\;. \tag{5.120}$$

where $k = n_b(\omega_0/c)$.

In the following we will use the two pairs of basis states for the $e1$-$hh1(1s)$ exciton quartet. The first set $|M, \boldsymbol{K}\rangle$ is characterized by a certain exciton angular momentum component $M = \pm 1, \pm 2$. The matrix element of the optical transition into the state $|M, \boldsymbol{K}\rangle$ is given by

$$\mathcal{M}_{\pm 1} = \mathcal{M}_0(e_x \mp ie_y)\;,\; \mathcal{M}_{\pm 2} = 0\;, \tag{5.121}$$

where $\mathcal{M}_0$ is independent of the light polarization $\boldsymbol{e}$. In the second basis the optically-active states are replaced by the excitonic states Γ_5 polarized along the fixed axes $\alpha = x, y$. It is worth to mention that in the basis $|\alpha\boldsymbol{K}\rangle$ the effective Hamiltonian for the states Γ_5 can be written as a 2×2 matrix

$$\mathcal{H}_{\mathrm{exc}} = E_{\mathrm{exc}}^0 + \frac{\hbar^2 K^2}{2M} + \frac{\mathcal{C}(K)}{K}\begin{bmatrix} K_x^2 & K_xK_y \\ K_xK_y & K_y^2 \end{bmatrix}\;. \tag{5.122}$$

The spin-dependent part of this matrix can be conveniently presented in the form

$$\frac{1}{2}\,\mathcal{C}(K)\,K\begin{bmatrix} \cos 2\Phi & \sin 2\Phi \\ \sin 2\Phi & -\cos 2\Phi \end{bmatrix}\;,$$

where Φ is the angle between $\boldsymbol{K}$ and x.

Now we consider the fine structure of 0D excitons and focus on the anisotropic splitting of the radiative doublet in semiconductor nanostructures, namely, heavy-hole excitons that are localized at a particular well-width fluctuations in type-I QWs, localized at a particular interface in type-II heterostructures, or confined by asymmetrical QDs. Despite the obvious differences between these three kinds of excitonic states their exchange splitting can be described by a common exchange-interaction matrix which in the basis $|M\rangle$ taken in the order $|1\rangle, |-1\rangle, |2\rangle, |-2\rangle$ may be written as follows

$$\hat{\mathcal{H}}_{\rm exch} = \frac{1}{2}\begin{bmatrix} \delta_0 & {\rm e}^{-{\rm i}\Phi_2}\delta_2 & 0 & 0 \\ {\rm e}^{{\rm i}\Phi_2}\delta_2 & \delta_0 & 0 & 0 \\ 0 & 0 & -\delta_0 & {\rm e}^{-{\rm i}\Phi_1}\delta_1 \\ 0 & 0 & {\rm e}^{{\rm i}\Phi_1}\delta_1 & -\delta_0 \end{bmatrix} . \tag{5.123}$$

Here the constants $\delta_0, \delta_1, \delta_2$ refer, respectively, to the quartet splitting into the doublets $|\pm 1\rangle$ and $|\pm 2\rangle$, nonradiative-doublet splitting into the states $(|2\rangle \pm {\rm e}^{{\rm i}\Phi_1}|-2\rangle)/\sqrt{2}$, and radiative-doublet splitting into the states $(|1\rangle \pm {\rm e}^{{\rm i}\Phi_2}|-1\rangle)/\sqrt{2}$ which are dipole-active along the rectangular axes rotated around the structure principal axis z by the angle $\Phi_2/2$ with respect to the fixed axes x and y. Note that the splitting δ_0 retains even in the uniaxial-symmetry approximation, a nonzero value of δ_1 appears taking into account the tetragonal symmetry D_{2d} of an ideal QW, and the δ_2-governed splitting is completely related to the low symmetry of an exciton-localizing potential. We will also use the frequencies Ω_j $(j = 0, 1, 2)$ defined by $\hbar\Omega_0 = \delta_0$, $\hbar\Omega_1 = \delta_2 \cos\Phi_2$, $\hbar\Omega_2 = \delta_2 \sin\Phi_2$. Then the matrix (5.123) for the two states $|\pm 1\rangle$ is rewritten as

$$\hat{\mathcal{H}}_{\rm exch} = \frac{\hbar}{2}\begin{bmatrix} \Omega_0 & \Omega_1 - {\rm i}\Omega_2 \\ \Omega_1 + {\rm i}\Omega_2 & \Omega_0 \end{bmatrix} . \tag{5.124}$$

We first discuss the energy and exchange splitting of an exciton localized at a fluctuation in the width of a type-I QW. Beyond the limits of the considered localization island, the QW is assumed to contain N monomolecular layers (in GaAs, the width of a monolayer is $a_0/2 = 2.8$ Å). One of the interfaces is flat while the other is shifted in the region of the island by a monolayer increasing the QW width here to $(N+1)a_0/2$. If the linear dimensions of the island exceed the exciton 2D Bohr radius, the envelope of the exciton wave function can be approximated by (2.188). If the shape of the island is anisotropic, the function $F(X, Y)$ in (2.188) is as well anisotropic which results in a nonzero value of δ_2 in (5.123). Introducing the 2D Fourier transform

$$F(K_x, K_y) = \int dX dY \, {\rm e}^{-{\rm i}\boldsymbol{K}\boldsymbol{R}_\parallel} \, F(X, Y)$$

we can present this splitting in the form [5.79]

$$\delta_2 = \frac{\hbar\Gamma_0}{S} \sum_{K>k} \frac{K_x^2 - K_y^2}{k\sqrt{K^2 - k^2}} \, F^2(\boldsymbol{K}) \, , \tag{5.125}$$

where the retardation is taken into account, as a consequence K is replaced by $\sqrt{K^2 - k^2}$ and the summation is performed over $K > k$.

Goupalov et al. [5.79] calculated the splitting δ_2 for a rectangular island of the dimensions L_x, L_y, see the inset in Fig. 5.10. The function $F(X, Y)$ was found as a solution of the 2D Schrödinger equation

$$\mathcal{H}_{\rm loc} F(X, Y) = -\varepsilon \, F(X, Y), \tag{5.126}$$

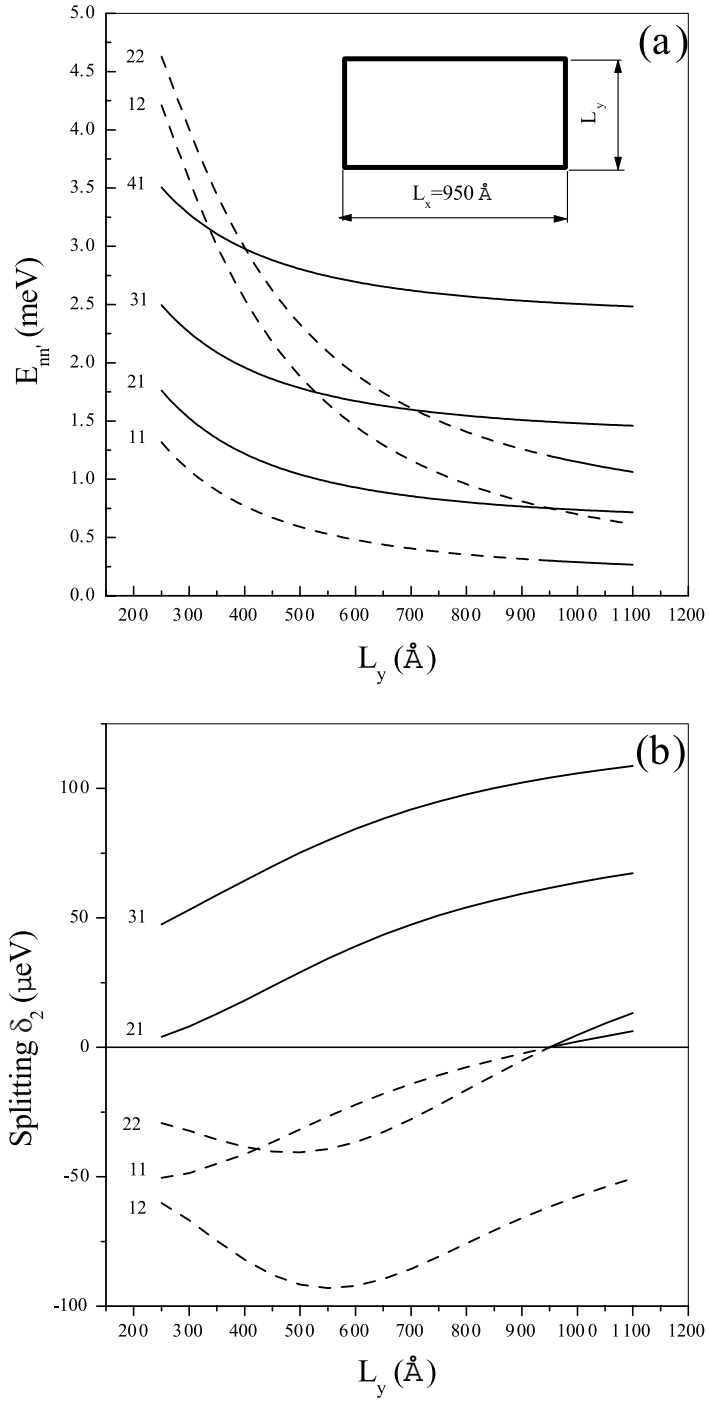

Fig. 5.10. (**a**)Energy levels $E_{nn'}$ of the localized exciton. (b) The splitting between localized states $|n, n', x\rangle$ and $|n, n', y\rangle$ as a function of L_y for a fixed value of L_x = 950 Å in a GaAs/$Al_{0.3}Ga_{0.7}$As QW of the width 28 Å (10 monomolecular layers). The parts of curves corresponding to negative and positive values of δ_2 are shown by dashed and solid lines, respectively. [5.79]

$$\mathcal{H}_{\rm loc} = -\frac{\hbar^2}{2M}\left(\frac{\partial^2}{\partial X^2}+\frac{\partial^2}{\partial Y^2}\right) - V\theta\left(\frac{L_x}{2}-|X|\right)\theta\left(\frac{L_y}{2}-|Y|\right)\,,$$

where V is the energy difference between the $1s$-exciton levels in the two perfect QWs differing in the width by one monomolecular layer, ε is the localization energy referred to the free-exciton energy in the thinner QW. While calculating δ_2 the approximation of the factorized envelope function was used and $F(X,Y)$ was taken in the form of a product $F_x(X)F_y(Y)$, where $F_x(X)$, $F_y(Y)$ are found self-consistently from (5.126). The localized states $|nn'\rangle$ are labelled by a pair of integer quantum numbers nn', e.g., 11, 21, 22 etc., describing the exciton in-plane confinement in the x and y directions.

Figure 5.10 illustrates the dependence of the energy and splitting of the ground and excited states on the island dimension. Note that $E_{nn'} = V - \varepsilon_{nn'}$ is the localized-exciton energy referred to the free exciton energy in the wider QW. Due to the long-range exchange interaction the level $E_{nn'}$ is split into two sublevels $E_{nn',x}, E_{nn',y}$ polarized along the x and y directions, respectively. According to (5.125), the sign of the splitting $\delta_2 \equiv E_{nn',x} - E_{nn',y}$ is mainly determined by the sign of the difference of the mean squares $\langle K_x^2\rangle$ and $\langle K_y^2\rangle$. When $n = n'$, the splitting of the $E_{nn'}$ level is evidently negative if $L_y < L_x$ and positive if $L_y > L_x$, and this agrees with curves 11 and 22 in Fig. 5.10. As the quantum number n (or n') increases, the dispersion $\langle K_x^2\rangle$ (or $\langle K_y^2\rangle$) increases. Therefore, for close-lying L_x and L_y, the signs of the differences $E_{nn',x} - E_{nn',y}$ and $n - n'$ coincide. If the sides of a rectangular island are rotated with respect to the fixed axes x, y by the angle Φ then, in the spin Hamiltonian (5.123), the angle Φ_2 is nonzero and equal to 2Φ.

Gammon et al. [5.10, 5.11] studied the PL of GaAs/AlGaAs QWs in the optical near-field regime and measured the PL spectrum of a single QD formed by a large monolayer high island. They report a fine structure splitting of 20-50 μeV and linear polarization of the split sublevels for both the ground and excited states of the localized exciton. The sequence of signs of this difference observed for the ground and four excited states of the localized exciton [5.11] is reproduced in Fig. 5.10 for values L_y lying between 420 Å and 480 Å.

In type-II GaAs/AlAs(001) SLs, the radiative level of localized heavy-hole excitons $e1$-$hh1(1s)$ was found to be split into the sublevels polarized along the [110] and [1$\bar{1}$0] directions in the interface plane [5.80–5.85]. Moreover, it was established that in the same sample there exist simultaneously two classes of excitons with equal absolute values but opposite signs of the energy difference between the dipole-active sublevels $E_{[110]}$ and $E_{[1\bar{1}0]}$ polarized along $x \parallel [1\bar{1}0]$ and $y \parallel [110]$, i.e., δ_2 is nonzero and $\Phi_2 = 0$ or π if the reference axes are x and y. This anisotropic exchange splitting of excitonic levels cannot be explained in terms of the long-range exchange interaction in excitons localized by laterally-anisotropic islands because the exciton oscillator strength in the type-II heterostructures is too small. The exchange-interaction anisotropy was related in [5.86–5.88] to the heavy-light hole mixing under normal hole

incidence on the (001) interface. Then the pair of wave functions at the bottom of the lowest heavy-hole subband $hh1$ can be written as

$$\psi^{(hh1)}_{\pm 3/2} = F(z)\,|\Gamma_8, \pm 3/2\rangle \pm \mathrm{i}G(z)\,|\Gamma_8, \mp 1/2\rangle + \mathrm{i}G_{so}(z)\,|\Gamma_7, \mp 1/2\rangle\,. \quad (5.127)$$

As compared with (3.116) an admixture of the spin-orbit-split valence band Γ_7 is included into $\psi^{(hh1)}$. The real envelope functions $F(z)$ and $G(z)$, $G_{so}(z)$ are even and odd with respect to the reflection $z \to -z$ for the origin $z = 0$ taken in the center of a GaAs well. The functions $G(z)$, $G_{so}(z)$ are proportional to the heavy-light hole mixing constant $t_{l\text{-}h}$ in the boundary conditions for the hole envelope function, see (3.115). Excitons contributing to the low-temperature PL of undoped type-II SLs are bound two-particle excitations localized by the structure imperfections in the plane of interfaces with an X-electron and a Γ-hole confined inside two neighboring AlAs and GaAs layers. This presupposes the existence of localized excitons with a left- and right-hand-side electron labelled in the following as the XL and XR states. Let the localization length exceeds the exciton Bohr radius $\tilde{a}$, describing the in-plane relative motion of the electron-hole pair. Then the anisotropic exchange splitting of the XL and XR levels is given by [5.88]

$$\begin{aligned}\delta_2 &= \left(E_{[110]} - E_{[1\bar{1}0]}\right)_{L,R} \quad (5.128)\\ &= \frac{16a_0^3}{\sqrt{3}\pi a_{\mathrm{B}}^2}\varepsilon_0 \int F(z)[G(z) + \sqrt{2}G_{so}(z)]\,[u^2_{L,R}(z) + v^2_{L,R}(z)]\,dz\,,\end{aligned}$$

where $u_{L,R}(z)$ and $v_{L,R}(z)$ are the X_1 and X_3 envelopes of an X-electron confined, respectively, in the left- and right-hand AlAs layer. ε_0 determines the bulk electron-hole short-range exchange interaction taken in the form

$$V_{\mathrm{exch}} = -\varepsilon_0 a_0^3\,\delta(\boldsymbol{r}_e - \boldsymbol{r}_h)\,\boldsymbol{\sigma}_e \cdot \boldsymbol{\sigma}_h\,, \quad (5.129)$$

where $\sigma_{e\alpha}, \sigma_{h\alpha}$ are the electron and hole spin Pauli matrices. Taking into account that $u^2_L(z) = u^2_R(-z)$, $v^2_L(z) = v^2_R(-z)$, $F(z)$ is even and $G(z), G_{so}(z)$ are odd, one immediately obtains opposite signs of the splitting for XL and XR states. This explains the two classes of excitons observed experimentally. Figure 5.11 shows the calculated dependence of the anisotropic exchange splitting of the radiative doublet in GaAs/AlAs SLs as a function the SL period d for a fixed ratio of the GaAs layer thickness, a, and the AlAs layer thickness, b. Experimental values of δ_2 measured by optically detected magnetic resonance and quantum beats technique are presented as well.

The Molecular-Beam-Epitaxy (MBE) grown InGaAs/GaAs-like QDs have a shape of pyramids with the height parallel to the growth direction $z \parallel [001]$ and the base oriented along the $\langle 100\rangle$ directions [5.89]. In case of the square base, QDs are characterized by the C_{2v} point symmetry for which $\hbar\Omega_1 = \delta_2 \cos\Phi_2 = 0$, $\hbar\Omega_2 = \delta_2 \sin\Phi_2 \neq 0$. In the general case of a rectangular base the symmetry is reduced to C_2 and both Ω_1 and Ω_2 are nonzero.

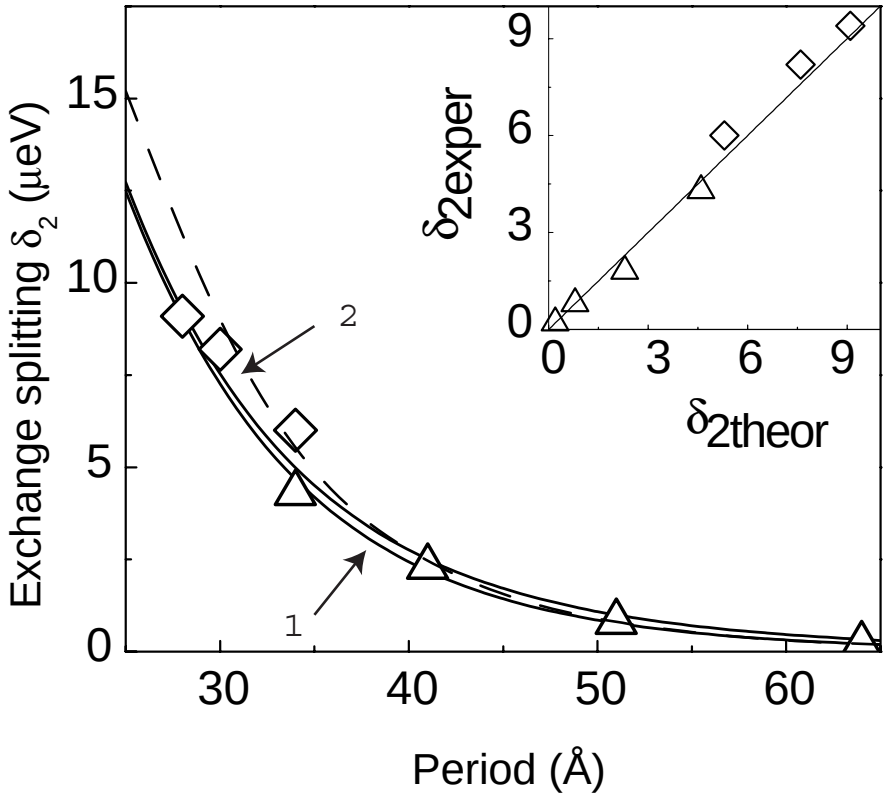

Fig. 5.11. Anisotropic exchange splitting of the radiative doublet as a function of the period of type-II GaAs/AlAs SL. Triangles [5.80] and rhombes [5.83] show experimental results, solid and dashed curves are calculated by using slightly different models. According to [5.87].

For free heavy-hole excitons in ideal QWs of the symmetry D_{2d} the spin Hamiltonian contains the term in (5.122) proportional to δ_0 and representing the long-range exchange interaction as well as the terms in (5.123) proportional to δ_0, δ_1 and representing the short-range exchange interaction.

In an external magnetic field the exciton spin-Hamiltonian includes, in addition to (5.123), the Zeeman contribution

$$\mathcal{H}_B = \mu_B \left[\left(g_{e\parallel} s_z + \mathcal{K} g_0 J_z \right) B_z + g_{e\perp} \, \boldsymbol{s}_\perp \cdot \boldsymbol{B}_\perp \right] \ , \qquad (5.130)$$

where $s_z = (1/2)\boldsymbol{\sigma}$ and J_z are the z-components of the electron spin $s = 1/2$ and hole angular momentum $J = 3/2$. We neglect the Zeeman splitting of heavy-hole states in an in-plane magnetic field. In the Faraday configuration, $\boldsymbol{B} \parallel z$, the split quartet levels are given by

$$E_{1,2} = \frac{\delta_0}{2} \pm \frac{1}{2}\sqrt{\delta_2^2 + (g_{h\parallel} - g_{e\parallel})^2 \mu_B^2 B_z^2}\,,$$
$$E_{3,4} = -\frac{\delta_0}{2} \pm \frac{1}{2}\sqrt{\delta_1^2 + (g_{h\parallel} + g_{e\parallel})^2 \mu_B^2 B_z^2}\,, \tag{5.131}$$

where we define the hole longitudinal g factor as

$$g_{h\parallel} = 3g_0\mathcal{K}\,. \tag{5.132}$$

With increasing the field, the level 2 goes downward, the level 3 goes upward and, at a particular value of B_z, they cross each other. Near the crossing point the states 2, 3 can be strongly mixed even by a weak symmetry-breaking potential that couples radiative and nonradiative states. Owing to the larger population of the nonradiative state the intensity of emitted light increases. This effect known as the level-anticrossing can lead to a remarkable nonthermal exciton spin polarization or alignment of exciton oscillating dipole moment under unpolarized excitation resulting in an appearance of circular or linear PL polarization near the crossing point. Depending on the exciton effective g factors the level 3 can also cross the level 1 at a higher value of the magnetic field where the field-induced PL polarization is opposite to that related with the 2-3 anticrossing [5.90, 5.91].

If the anisotropic-exchange constants δ_1, δ_2 are zero then at zero magnetic field the radiative and nonradiative levels are doubly degenerate. The transverse magnetic field (*Voigt* configuration) mixes the excitonic state $m = \pm 1$ with the state $m = \pm 2$ resulting in the shift of the levels

$$\frac{1}{2}\left[\delta_0 \pm \sqrt{\delta_0^2 + (g_{e\perp}\mu_B B)^2}\right] \tag{5.133}$$

and retaining the double degeneracy. The degeneracy is removed in some extent only if δ_1 or/and δ_2 are nonzero.

We turn now to the fine structure of the ground-state exciton level in cubic and hexagonal NanoCrystals (NCs) of the spherical form. Due to the confinement of electrons and holes in all three directions, the exchange splitting of excitonic levels increases as R^{-3} with decreasing the dot radius R and is strongly enhanced as compared with that in bulk semiconductors. Large exchange splittings were observed in CdSe NCs embedded in glassy materials and polymer films [5.92–5.94].

In order to make transparent the comparison between the short- and long-range exchange contributions to the splitting of excitonic levels we first consider optical transitions between the simple conduction band Γ_6 and the simple valence band Γ_7 in semiconductors of the crystal class T_d. In this case the 1s-exciton level is four-fold degenerate taking into account the electron and hole spin degeneracy. As well as in the case of bulk semiconductor, the direct product $\Gamma_6 \times \Gamma_7$ is decomposed into the Γ_{15} and Γ_2 irreducible representations. It is also convenient to use the spin basis $|\Gamma_{15}, \nu\rangle$ ($\nu = x, y, z$) and

$|\Gamma_2\rangle$ rather than $|m,n\rangle$ $(m,n=\pm 1/2)$. The state $|\Gamma_{15},\nu\rangle$ is optically active for the light polarized along the α direction while the state $|\Gamma_2\rangle$ is inactive. In the chosen basis non-zero components of the short- and long-range terms can be expressed as

$$\mathcal{H}^{(\mathrm{short})}_{\nu'\nu}\left(\boldsymbol{k}'_e,\boldsymbol{k}'_h,\boldsymbol{k}_e,\boldsymbol{k}_h\right)=\Delta^{\mathrm{bulk}}_{ST}\pi a_{\mathrm{B}}^3\,\delta_{\nu\nu'}\,\delta_{\boldsymbol{K}K'},\tag{5.134}$$
$$\mathcal{H}^{(\mathrm{long})}_{\nu'\nu}\left(\boldsymbol{k}'_e,\boldsymbol{k}'_h,\boldsymbol{k}_e,\boldsymbol{k}_h\right)=\hbar\omega_{\mathrm{LT}}\pi a_{\mathrm{B}}^3\frac{K_\nu K_{\nu'}}{K^2}\,\delta_{\boldsymbol{K}K'}$$

in terms of the bulk exciton Bohr radius a_{B}, the singlet-triplet splitting $\Delta^{\mathrm{bulk}}_{\mathrm{ST}}$ and the longitudinal-transverse splitting $\hbar\omega_{\mathrm{LT}}$ of the bulk exciton level. According to (5.134) for an exciton confined within a spherical QD of the radius $R\ll a_{\mathrm{B}}$, the singlet-triplet splitting is given by [5.95]

$$\Delta^{\mathrm{QD}}_{\mathrm{ST}}(R)=\pi\,C\left(\Delta^{\mathrm{bulk}}_{\mathrm{ST}}+\frac{1}{3}\,\hbar\omega_{\mathrm{LT}}\right)\left(\frac{a_{\mathrm{B}}}{R}\right)^3\,,\tag{5.135}$$

where

$$C=\int\limits_0^\pi\frac{\sin^4 x}{x^2}\,dx\approx 0.67.$$

While deriving (5.135), equation (2.89) for the single-particle envelope function quantum-confined in a spherical QD is used assuming the barrier to be infinitely high. Taking for reasonable estimations $\Delta^{\mathrm{bulk}}_{ST}\sim 0.1$ meV, $\hbar\omega_{\mathrm{LT}}\sim 1$ meV we obtain that, among the two terms in (5.135), the long-range contribution to the splitting $\Delta^{\mathrm{QD}}_{\mathrm{ST}}$ prevails. It should be mentioned that the long-range contribution

$$\hbar\delta\omega_0^{(\mathrm{long})}=\frac{\pi}{3}C\left(\frac{a_{\mathrm{B}}}{R}\right)^3\hbar\omega_{\mathrm{LT}}$$

to $\Delta^{\mathrm{QD}}_{\mathrm{ST}}$ can also be derived from equation (3.134) for the renormalized resonance frequency of the exciton assuming $qR\to 0$ and replacing $\Phi(\boldsymbol{r})$ by

$$(2\pi Rr^2)^{-1}\sin^2(\pi r/R)\,.$$

At finite values of qR one has to use a more general equation (3.134). Moreover, in this case the damping Γ_{SQD} defined by (3.135) becomes nonzero, it determines the radiative decay of the 0D exciton and is connected by $\Gamma_{SQD}=(2\tau_0)^{-1}$ with the exciton radiative lifetime τ_0. A large long-range contribution to the electron-hole exchange interaction in semiconductor QDs has been also considered by using a many-body approach based on atomistic pseudopotential wave functions [5.96].

Note that in case of different high-frequency dielectric constants $æ_b^{(1)}$ and $æ_b^{(2)}$, respectively inside and outside the dot, the second term in (5.135) should be multiplied by the factor [5.95, 5.97]

$$1 + \frac{3}{2\pi C}\,\frac{æ_b^{(2)} - æ_b^{(1)}}{æ_b^{(1)} + 2æ_b^{(2)}}\,. \tag{5.136}$$

For $\Gamma_6 \times \Gamma_8$ excitons the valence band Γ_8 is described by the 4×4 Luttinger Hamiltonian containing the three band parameters γ_1, γ_2 and γ_3. The ground state of a hole confined in a spherical QD has the symmetry Γ_8 and is characterized by the angular momentum component $n = \pm 3/2, \pm 1/2$. In the spherical approximation, $\gamma_2 = \gamma_3$, the four ground-state wave functions can be written as

$$\sum_{n'} \Psi_{n'}^{(n)}(\boldsymbol{r})\,|n'\rangle,$$

where $|n'\rangle$ ($n' = \pm 3/2, \pm 1/2$) are the Bloch functions,

$$\Psi_{n'}^{(n)}(\boldsymbol{r}) = C_{n'n}(\boldsymbol{r}),$$

$$\hat{C}(\boldsymbol{r}) = \frac{1}{\sqrt{4\pi}}\left\{R_0(r) - R_2(r)\,\left[\left(\boldsymbol{J}\cdot\frac{\boldsymbol{r}}{r}\right)^2 - \frac{5}{4}\right]\right\},$$

J_α ($\alpha = x, y, z$) are the angular momentum matrices in the Γ_8 basis, $R_0(r)$ and $R_2(r)$ are the radial functions introduced in [5.92] and reflecting the fact that the envelopes $\Psi_{n'}^{(n)}(\boldsymbol{r})$ are formed by coupled S ($L = 0$) and D ($L = 2$) states.

The short-range exchange interaction has the form [5.92]

$$\mathcal{H}_{\text{short}}\,(\boldsymbol{k}_e', \boldsymbol{k}_h', \boldsymbol{k}_e, \boldsymbol{k}_h) = -\frac{2}{3}\,\varepsilon_0\,a_0^3\,(\boldsymbol{\sigma}\cdot\boldsymbol{J})\,\delta_{\boldsymbol{K}\boldsymbol{K}'}, \tag{5.137}$$

where ε_0 is a constant. For the long-range exchange we obtain [5.97]

$$\begin{aligned}
&\mathcal{H}_{\text{long}}\,(\boldsymbol{k}_e', \boldsymbol{k}_h', \boldsymbol{k}_e, \boldsymbol{k}_h) \qquad (5.138)\\
&= \frac{4\pi}{æ_b}\left(\frac{\hbar e|p_{cv}|}{m_0 E_g}\right)^2 \delta_{\boldsymbol{K}\boldsymbol{K}'}\,\frac{1}{K^2}\,\left\{\frac{3}{8}K^2 - \frac{1}{6}(\boldsymbol{J}\cdot\boldsymbol{K})^2 - \frac{1}{9}K^2(\boldsymbol{\sigma}\cdot\boldsymbol{J})\right.\\
&+ \frac{1}{6}\left[(\boldsymbol{\sigma}\cdot\boldsymbol{J})\left((\boldsymbol{K}\cdot\boldsymbol{J})^2 - \frac{5}{4}K^2\right) + \left((\boldsymbol{K}\cdot\boldsymbol{J})^2 - \frac{5}{4}K^2\right)(\boldsymbol{\sigma}\cdot\boldsymbol{J})\right]\\
&\left.- \frac{1}{3}\left[(\boldsymbol{\sigma}\cdot\boldsymbol{K})(\boldsymbol{J}\cdot\boldsymbol{K}) - \frac{1}{3}K^2(\boldsymbol{\sigma}\cdot\boldsymbol{J})\right]\right\},
\end{aligned}$$

where $p_{cv} = \langle S|\hat{p}_x|X\rangle$ is the interband matrix element of the momentum operator.

In hexagonal crystals one has to add the crystal splitting term

$$\hat{\mathcal{H}}_{\text{cr}} = -\frac{\Delta_{\text{cr}}}{2}\left(J_z^2 - \frac{5}{4}\right)$$

to the Luttinger Hamiltonian. If a value of the crystal splitting Δ_{cr} is small as compared with the characteristic confinement energy the combined electron-hole exchange interaction in QDs of the radius $R \ll a_{\text{B}}$ is described by the Hamiltonian [5.97]

$$\hat{H}_{\rm exch} = -\bar{\eta}\,(\boldsymbol{\sigma}\cdot\boldsymbol{J})\,. \tag{5.139}$$

Here

$$\bar{\eta} = \left(\frac{a_{\rm B}}{R}\right)^3 \left[\chi(\beta)\,\hbar\omega_{\rm TF} + \frac{\pi}{9}\,\zeta(\beta)\,\hbar\omega_{\rm LT}\right]\,,$$

$$\hbar\omega_{\rm TF} = \frac{2}{\pi}\,\left(\frac{a_0}{a_{\rm B}}\right)^3\,\varepsilon_0\,,$$

$\hbar\omega_{\rm LT}$ is given by (2.204), $\chi(\beta)$ and $\zeta(\beta)$ are coefficients dependent on the ratio $\beta = m_{lh}/m_{hh}$ between the light- and heavy-hole effective masses. For $\beta = 0.3$ one has $\chi(\beta) \approx 0.77$ and $\zeta(\beta) \approx 0.62$. Note that $\hbar\omega_{\rm TF}$ is the short-range exchange induced splitting between the bulk exciton states with $n = \pm 1$ and $n = \pm 2$, and $\hbar\omega_{\rm LT}$ is the longitudinal-transverse splitting for a free exciton propagating perpendicular to the hexagonal axis of the bulk wurtzite-lattice crystal. Inset in Fig. 5.12a presents exciton level diagrams described by the Hamiltonian

$$-\frac{\Delta}{2}\left(J_z^2 - \frac{5}{4}\right) - \bar{\eta}\,(\boldsymbol{\sigma}\boldsymbol{J})\,,$$

where $\Delta = \Delta_{cr}\,v(\beta)$ with $v(\beta) \approx 0.94$ for $\beta = 0.3$. The excitonic sublevels are labelled in accordance with the value of total angular-momentum component on the C_6 axis. The splitting, $\Delta_{\rm TF}^{\rm QD}(\bar{\eta})$, between the $M = \pm 2$ and lower $M = \pm 1$ states of a 0D exciton is given by

$$\Delta_{\rm TF}^{\rm QD}(\bar{\eta}) = 2\bar{\eta} + \frac{\Delta}{2} - \sqrt{4\bar{\eta}^2 + \frac{\Delta^2}{4} - \bar{\eta}\Delta}\,. \tag{5.140}$$

If the long-range exchange contribution is neglected the parameter $\bar{\eta}$ in (5.140) is replaced by

$$\eta = \left(\frac{a_{\rm B}}{R}\right)^3 \chi(\beta)\,\hbar\omega_{\rm TF}\,,$$

which is smaller than $\bar{\eta}$ by ~ 4. Note that this result has alternatively been derived in [5.100] from consideration of resonant Rayleigh scattering of light by a QD following the procedure described in Sect. 3.2.1. Figures 5.12a and 5.12b present the measured and calculated dependence of the splittings $\Delta_{\rm TF}^{\rm QD}$ and Δ_1, Δ_2 on the nanocrystal radius.

In [5.101] the electron-hole exchange interaction is analyzed in the framework of the empirical tight-binding method. It is demonstrated that *inter-atomic* and *intra-atomic* (or intrasite) contributions to the long-range interaction enter in an inequivalent way. In particular case of the $\Gamma_6 \times \Gamma_7$ exciton in a spherical dot, the long-range singlet-triplet splitting is given by

$$\Delta_{ST,\,\rm long}^{\rm QD} = \frac{\pi}{3}\,C\,\hbar\left(\omega_{\rm LT} - \omega_{\rm LT}^{\rm (intra)}\right)\,\left(\frac{a_{\rm B}}{R}\right)^3\,, \tag{5.141}$$

where $\omega_{\rm LT}$ is the longitudinal-transverse splitting for the bulk exciton and $\omega_{\rm LT}^{\rm (intra)}$ is the contribution to $\omega_{\rm LT}$ caused by the intra-atomic transitions.

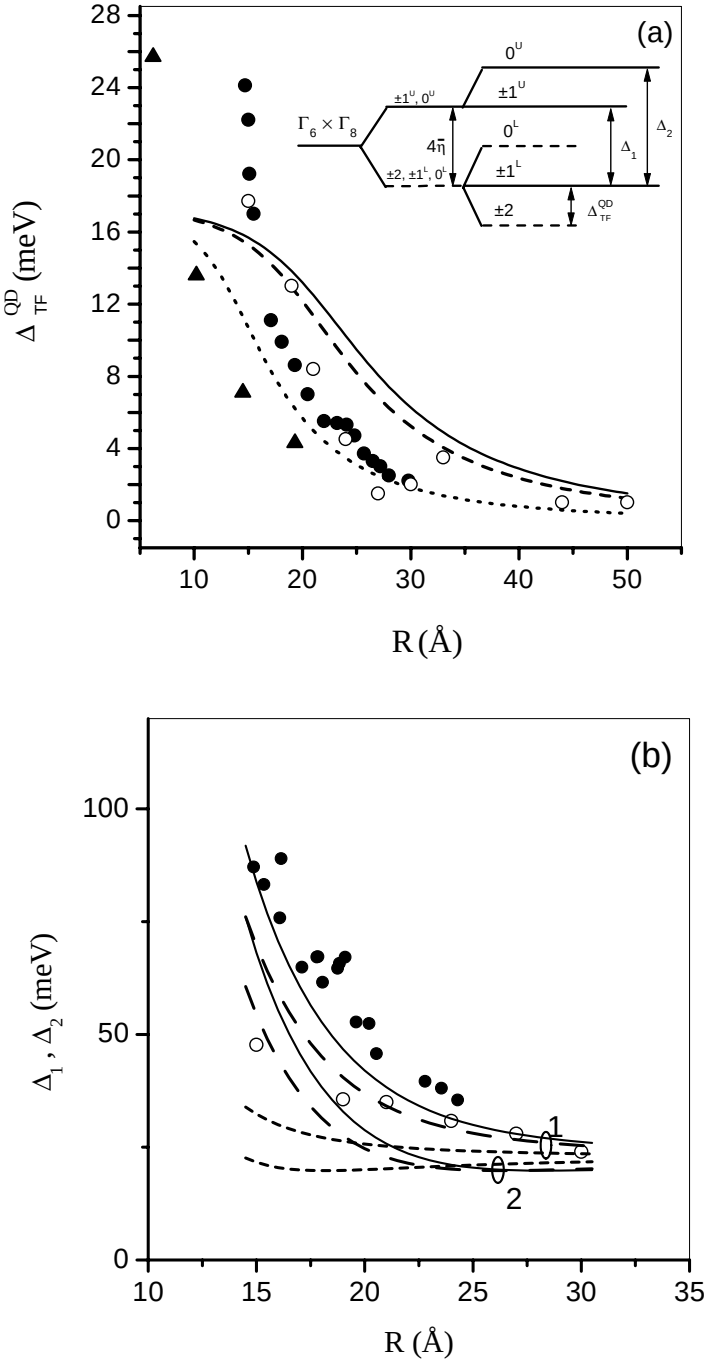

Fig. 5.12. Dependence of the splitting $\Delta_{\mathrm{TF}}^{\mathrm{QD}}$ (**a**) and Δ_1, Δ_2 (**b**) on crystal radius for $æ_1 = 8.4$ and $æ_2 = 2.25$ (*solid*) and $æ_1 = æ_2 = 8.4$ (*dashed*), taking into account both the short-range and long-range exchange contributions. The inset shows diagram of exciton level splitting into five sublevels for a hexagonal nanocrystal. For conveniency, the fine structure obtained neglecting crystal-field splitting is also shown. The dotted lines present the calculation performed neglecting long-range exchange interaction. In figure (**a**), the filled [5.93] and open [5.98] circles refer to the experimental values of the splitting, and the triangles are the splitting $\Delta_{\mathrm{TF}}^{\mathrm{QD}}$ calculated using the pseudopotential method [5.96]. In figure (**b**), the experimental values of the splitting are shown by the filled [5.99] and open [5.98] circles. According to [5.97].

Thus as compared to the envelope function approach valid for $\omega_{\rm LT}^{\rm (intra)} = 0$, the splitting (5.141) differs by a factor

$$\frac{\omega_{\rm LT} - \omega_{\rm LT}^{\rm (intra)}}{\omega_{\rm LT}} = 1 - \left(\frac{M_{cv}^{\rm (intra)}}{M_{cv}^{\rm (inter)} + M_{cv}^{\rm (intra)}} \right)^2 ,$$

where $M_{cv}^{\rm (inter)}, M_{cv}^{\rm (intra)}$ are the contributions to the interband optical matrix element due to the inter- and intra-atomic transitions in the tight-binding approach. For Frenkel excitons where $M_{cv}^{\rm (inter)}$ can be ignored, $\Delta_{\rm ST,\,long}^{\rm QD} = 0$.

5.5.2 Optical Orientation and Alignment of Free Excitons in Quantum Wells

Similarly to free carriers, exciton spins (or angular momenta) can be optically oriented. In the absence of an external magnetic field spin-polarized excitons are generated under optical pumping with circularly polarized photons: due to spin-orbit coupling of electronic states the selection rules for optical interband transitions provide a conversion of photon polarization into exciton spin orientation. This immediately follows from (5.121) for the matrix elements,

$$M_m = \sum_{\alpha=x,y} M_{m,\alpha} e_\alpha \, ,$$

of exciton optical excitation. Indeed, under normal incidence of the σ_+-polarized light one has $e_x = 1/\sqrt{2}, e_y = {\rm i}/\sqrt{2}$ and

$$M_1 \propto e_- \neq 0 \, , \; M_{-1} \propto e_+ = 0 \, ,$$

whereas, for the σ_- photons, $M_1 = 0$, $M_{-1} \neq 0$, in agreement with the angular momentum conservation law $m_{\rm exc} = m_{\rm phot}$, where $m_{\rm exc}$ and $m_{\rm phot}$ are the z components of exciton and photon angular momenta. In accordance with the same selection rule, $m_{\rm phot} = m_{\rm exc}$, the radiative recombination of spin-polarized excitons results in the PL circular polarization thus making possible optical detection of the spin polarization. The optical orientation of excitonic spins is a particular case of the more general phenomenon, namely, the *selective optical excitation* of excitonic sublevels. Another example of the selective excitation is the so-called *optical alignment* of excitons by linearly polarized radiation: in contrast to the optical orientation which means just the photoinduced difference in the populations of the exciton states $|m\rangle$ with the spin $m = \pm 1$, the linearly-polarized light can excite preferentially the exciton state $(|1\rangle + {\rm e}^{{\rm i}\Phi}|-1\rangle)/\sqrt{2}$ with a definite direction of oscillating electric-dipole moment (a value of the phase Φ is determined by the direction of the light polarization plane).

Optical orientation and alignment of excitons can be described by using the exciton spin-density matrix. The method is especially applicable to bound

and localized excitons. It can be easily used for free 2D excitons in QWs if the $\boldsymbol{K}$- and spin-dependent density matrix can be presented as a product of a matrix ρ depending only on the electron- and hole-spin indices and a distribution function $f(\boldsymbol{K})$ depending only on the exciton wave vector. This kind of factorization is possible if the momentum relaxation time τ_p is much shorter than the exciton lifetime τ_0 and the spin relaxation time τ_s.

If the exciton state is represented by a wave function $\Psi = \sum_m c_m \Psi_m$, where Ψ_m is one of the basis functions, then the spin-density matrix will be $\rho_{mm'} = c_m c^*_{m'}$. For a mixed state, the product $c_m c^*_{m'}$ is averaged over the statistical ensemble. The diagonal components ρ_{mm} determine the probability to find an exciton in the state m, and the off-diagonal components, $\rho_{mm'}$ with $m \neq m'$, the correlation between the m and m' states. For a pure state $|\rho_{mm'}|^2 = \rho_{mm}\rho_{m'm'}$. The PL polarization density matrix (3.227) and the exciton spin-density matrix are related by

$$d_{\alpha\beta} \propto \sum_{mm'} M^*_{m,\alpha} M_{m',\alpha'} \rho_{mm'} \,. \tag{5.142}$$

For heavy-hole quartet excitons in QWs the optical matrix elements are given by (5.121).

Similarly to the kinetic equation (5.56) for spin-polarized photoelectrons, in the steady-state regime of photoexcitation the exciton spin-density matrix satisfies the equation

$$\left(\frac{\partial \rho}{\partial t}\right)_{rec} + \left(\frac{\partial \rho}{\partial t}\right)_{s.r.} + \frac{\mathrm{i}}{\hbar}\left[\rho, \mathcal{H}_{\mathrm{exch}} + \mathcal{H}_{\boldsymbol{B}}\right] + \hat{G} = 0 \,. \tag{5.143}$$

The terms on the left-hand side take account of the exciton recombination, spin relaxation, exchange and Zeeman interaction in the presence of magnetic field $\boldsymbol{B}$, $\hat{G}$ is the generation matrix. Let $|m\rangle$ be the basis states $|s_z, J_z\rangle$ of the $e1$-$hh1(1s)$ exciton with the angular momentum component $m = s_z + J_z = 2, 1, -1, -2$.

Generally, there are two recombination channels, a radiative and a non-radiative (including dissociation), characterized for the state m by the times $\tau_0^{(m)}$ and $\tau_i^{(m)}$, respectively. This allows to write the recombination term in (5.143) in the form

$$\left(\frac{\partial \rho}{\partial t}\right)_{rec} = -\frac{\rho_{mm'}}{\tau_{mm'}} \,, \tag{5.144}$$

where

$$\frac{1}{\tau_{mm'}} = \frac{1}{2}\left(\frac{1}{\tau_m} + \frac{1}{\tau_{m'}}\right) \,, \quad \frac{1}{\tau_m} = \frac{1}{\tau_0^{(m)}} + \frac{1}{\tau_i^{(m)}} \,.$$

The generation matrix G depends on the conditions of exciton formation. In the case of resonance excitation, it is defined by

$$G_{mm'} \propto \sum_{mm'} M_{m,\alpha} M^*_{m',\beta} d^0_{\alpha\beta} \,, \tag{5.145}$$

where $d^0_{\alpha\beta}$ is the polarization density matrix of the initial radiation. As in Chap. 3, see (3.228), the light polarization is characterized by the circular polarization degree, P_c, and the degrees of linear polarization, P_l and $P_{l'}$, referred to the two pairs of rectangular axes labelled here as x, y and x', y'.

In order to make transparent the description of polarized PL we give here a simplified description of the optical orientation and alignment of excitons. For resonant excitation conditions and in the absence of exciton spin relaxation between the pairs $m = \pm 1$ and $m = \pm 2$, the optically-inactive sublevels remain unpopulated, the only nonzero components of the density matrix $\rho_{mm'}$ are those with $m, m' = \pm 1$ and the $e1$-$hh1(1s)$ exciton acts as a two-level system. Recall that any two levels can be considered as two states of an effective 3D *pseudospin* with $S = 1/2$. The 2×2 spin density matrix $\rho_{mm'}(m, m' = \pm 1)$ is expressed in terms of the average pseudospin $\boldsymbol{S}$ as

$$\hat{\rho} = N\left(\frac{1}{2} + \boldsymbol{S}\cdot\tilde{\boldsymbol{\sigma}}\right), \tag{5.146}$$

where $\tilde{\sigma}_\alpha(\alpha = x, y, z)$ are the Pauli matrices and N is the steady-state exciton concentration. The pure exciton states $|1\rangle$ and $|-1\rangle$ are equivalent to the pseudospin polarized parallel or antiparallel to the z axis, respectively. The exciton states

$$|X\rangle = (|1\rangle + |-1\rangle)/\sqrt{2}\,,\ |Y\rangle = -\mathrm{i}\,(|1\rangle - |-1\rangle)/\sqrt{2}\,,$$

dipole-active along the x or y axis are described by a pseudospin with $S_x = 1/2$ or $S_x = -1/2$ respectively. Finally, the states $|X'\rangle = (|X\rangle + |Y\rangle)/\sqrt{2}$ or $|Y'\rangle = (|X\rangle - |Y\rangle)/\sqrt{2}$ polarized in the x' and y' directions correspond to a pseudospin with nonzero component $S_y = 1/2$ or $S_y = -1/2$. Thus, one can rewrite (5.142) as

$$P_l = 2S_x\,,\ P_{l'} = 2S_y\,,\ P_c = 2S_z\,. \tag{5.147}$$

The generation matrix $G_{mm'}$ for $m, m' = \pm 1$ can be expanded similarly to (5.146)

$$\hat{G} = G_0\left(\frac{1}{2} + \boldsymbol{S}^0\cdot\tilde{\boldsymbol{\sigma}}\right), \tag{5.148}$$

which allows to rewrite (5.145) in the form

$$S^0_x = \frac{1}{2}\,P^0_l\,,\ S^0_y = \frac{1}{2}\,P^0_{l'}\,,\ S^0_z = \frac{1}{2}\,P^0_c\,. \tag{5.149}$$

Here G_0 is the total generation rate of excitons, $P^0_l, P^0_{l'}$ and P^0_c characterize the initial light polarization, $\boldsymbol{S}^0$ is the exciton pseudospin at the moment of resonant excitation.

If the exciton is formed by binding of free electrons and holes into pairs, then $\hat{G}$ is proportional to the product $\hat{\rho}_e\hat{\rho}_h$ of single-particle spin-density

matrices at the moment of binding. In this case one may observe only exciton orientation.

In terms of the pseudospin Pauli matrices, the spin-dependent long-range exchange interaction is written as

$$\mathcal{H} = \frac{1}{2}\ (\tilde{\sigma}_x \Omega_x + \tilde{\sigma}_y \Omega_y)\ , \tag{5.150}$$

where

$$\hbar\Omega_x = \mathcal{C}K\cos 2\Phi\ ,\ \hbar\Omega_y = \mathcal{C}K\sin 2\Phi\ .$$

The longitudinal-transverse splitting of the exciton state produces a *motional narrowing* type of spin relaxation similar to the D'yakonov-Perel' mechanism considered in Sect. 5.3.2. Indeed, the off-diagonal terms of the Hamiltonian (5.150) represent an effective magnetic field in the (x, y) plane. If such a field is fixed then, in the absence of a real external magnetic field, the pseudospin will process about this field which results in a spin decoherence in the exciton ensemble. In the multi-scattering regime, the exciton wave vector $\boldsymbol{K}$ is changed by each scattering event, the effective field is randomly oscillating and the exciton spin decoherence is slowed down. If $\boldsymbol{K}$ changes faster than the pseudospin procession, i.e. if $\mathcal{C}K\tau_p^{(2)} \ll 1$, then one has for the exciton spin relaxation times [5.102]

$$\frac{1}{\tau_{zz}^s} = \frac{2}{\tau_{xx}^s} = \frac{2}{\tau_{yy}^s} = \langle \Omega_K^2 \tau_p^{(2)} \rangle\ , \tag{5.151}$$

where $\Omega_K = \sqrt{\Omega_x^2 + \Omega_y^2} = \mathcal{C}K$ and $\tau_p^{(2)}$ is the momentum scattering time for the angular harmonics $\cos 2\Phi,\ \sin 2\Phi$ of the free-exciton distribution function. It should be noted that the times $T_{s1} \equiv \tau_{zz}^s$ and $T_{s2} \equiv \tau_{xx}^s = \tau_{yy}^s$ describe the relaxation of exciton optical orientation and alignment, respectively. The factor of 2 is easily understood by using the fact that the in-plane pseudospin, say S_x, is only affected by the y component of the depolarizing field, whereas the longitudinal polarization S_z is relaxed by both x and y components. Therefore, the theory predicts that the PL experiments with linearly polarized light should exhibit a longer spin-relaxation rate driven by exchange than those performed with circularly polarized light.

In terms of the pseudospin (5.143) reduces to

$$\frac{\boldsymbol{S}}{\tau} - \left(\frac{\partial \boldsymbol{S}}{\partial t}\right)_{s.r.} + \boldsymbol{S} \times \boldsymbol{\Omega}_{\parallel} = \frac{\boldsymbol{S}^0}{\tau}\ , \tag{5.152}$$

where τ is the exciton lifetime in the state $m = \pm 1$, the spin-relaxation term $-(\partial \boldsymbol{S}/\partial t)_{s.r.}$ has the components

$$\left(\frac{S_x}{T_{s2}}\ ,\ \frac{S_y}{T_{s2}}\ ,\ \frac{S_z}{T_{s1}}\right)\ ,$$

T_{si} $(i = 1, 2)$ are the longitudinal and transverse pseudospin relaxation times including those described by (5.151). In addition, the pseudospin precession in an external longitudinal magnetic field $\boldsymbol{B} \parallel z$ is taken into consideration with the exciton Larmor frequency $\boldsymbol{\Omega}_\parallel$ given by $(0, 0, g_\parallel \mu_B B_z/\hbar)$ and the effective exciton g factor given by $g_\parallel = g_{h\parallel} - g_{e\parallel}$. Note that in weak magnetic fields satisfying the condition $\Omega_\parallel \tau_p \ll 1$ one can neglect the field effect on the pseudospin relaxation times T_{si} [5.102].

At zero magnetic field, the polarizations of the secondary and primary radiations are related by

$$P_l = \frac{T_2}{\tau_0}\, P_l^0\ ,\ P_{l'} = \frac{T_2}{\tau_0}\, P_{l'}^0\ ,\ P_c = \frac{T_1}{\tau}\, P_c^0\ , \tag{5.153}$$

where

$$\frac{1}{T_i} = \frac{1}{\tau} + \frac{1}{T_{si}}\ .$$

In a longitudinal magnetic field $\boldsymbol{B} \parallel z$, the PL circular polarization remains unaffected while $P_l, P_{l'}$ change to

$$P_l(B_z) = \frac{P_l(0) - \Omega_\parallel T_2 P_{l'}(0)}{1 + \left(\Omega_\parallel T_2\right)^2}\ ,\ P_{l'}(B_z) = \frac{\Omega_\parallel T_2 P_l(0) + P_{l'}(0)}{1 + \left(\Omega_\parallel T_2\right)^2}\ , \tag{5.154}$$

where $P_l(0), P_{l'}(0)$ are zero-field polarizations given by (5.153). One can see that, under linearly-polarized excitation in a longitudinal magnetic filed, the plane of polarization of the exciton radiation is rotated around z by the angle $\theta = (1/2) \arctan \Omega_\parallel T_2$, while the degree of linear polarization, $P_{\rm lin} = \sqrt{P_l^2 + P_{l'}^2}$, decreases by the factor $[1 + (\Omega_\parallel T_2)^2]^{1/2}$.

Physically, equation (5.154) can be derived by using the following intuitive approach. Optical pumping in the polarization $\boldsymbol{e}_0 \parallel x$ excites the electric-dipole moment $\boldsymbol{d}_0$ of the exciton oscillator directed along the x axis. In a longitudinal magnetic field this dipole will rotate around z axis with angular frequency $\Omega_\parallel/2$. Hence, for the exciton created at $t = 0$ the components of the vector $\boldsymbol{d}$ exhibit the quantum beats

$$d_x(t) = d_0 \cos \frac{\Omega_\parallel t}{2}\ ,\ d_y(t) = d_0 \sin \frac{\Omega_\parallel t}{2}\ ,$$

$$d_{x'}(t) = d_0 \cos\left(\frac{\Omega_\parallel t}{2} - \frac{\pi}{4}\right)\ ,\ d_{y'}(t) = d_0 \sin\left(\frac{\Omega_\parallel t}{2} - \frac{\pi}{4}\right).$$

Taking into account the finite exciton lifetime and spin-relaxation time the PL intensity $I_\alpha(t)$ in the polarization α shows damped oscillations

$$I_\alpha(t) \propto \mathrm{e}^{-t/T_2} d_\alpha^2(t)\ .$$

On the other hand, the steady-state intensity I_α is related with the time-integrated quantum beats $I_\alpha(t)$ by

$$I_\alpha = \tau \int I_\alpha(t)\, dt \propto \int \mathrm{e}^{-t/T_2} d_\alpha^2(t)\, dt\,.$$

Substituting $d_{x,y}^2 = (d_0^2/2)(1 \pm \cos\Omega_\parallel t)$, $d_{x',y'}^2 = (d_0^2/2)(1 \pm \sin\Omega_\parallel t)$ and integrating over t we obtain the Stokes parameters (5.154) for $P_l(0) = 1$, $P_{l'}(0) = 0$.

In the absence of an anisotropic exchange interaction ($\delta_{1,2} = 0$) and spin relaxation ($T_{si} \to \infty$), the transverse magnetic field $\boldsymbol{B} \perp z$ does not affect the PL polarization but can change the PL intensity [5.103]. The latter effect occurs because the effective lifetime of resonantly-excited excitons increases with increasing the field in the presence of both radiative and nonradiative recombination channels.

In this subsection we concentrated on the polarized PL of free heavy-hole excitons. The secondary radiation of light-hole excitons can be considered in the same way with allowance for nonzero optical matrix elements in both polarizations $\boldsymbol{e} \parallel z$ and $\boldsymbol{e} \perp z$.

5.5.3 Optical Orientation and Alignment of Zero-Dimensional Excitons

Neglecting, for simplicity, the exciton spin relaxation one can obtain for the PL circular polarization under resonant circularly-polarized excitation in the longitudinal magnetic field [5.82]

$$P_c(B_z) = P_c^0 \frac{1 + \Omega_\parallel^2 \tau^2}{1 + \left(\Omega_\parallel^2 + \Omega_1^2 + \Omega_2^2\right)\tau^2}\ , \tag{5.155}$$

where the exchange-related frequencies $\Omega_{1,2}$ are introduced in (5.124) and τ is the 0D-exciton lifetime in the radiative states $m = \pm 1$. If the exciton lifetime τ is long enough so that $\max(\Omega_{1,2}\tau) \gg 1$ then, because of the exchange, the exciton optical orientation is quenched. With increasing the magnetic field the PL circular polarization is restored and reaches a value of P_c^0 as B_z tends to ∞. Thus, the magnetic field suppresses the depolarizing effect of anisotropic exchange interaction and permits to observe the optical orientation of excitons even if $\max(\Omega_{1,2}\tau) \gg 1$.

As in the previous subsection, the behavior of exciton optical orientation and alignment is very convenient to interpret physically in terms of the exciton pseudospin. In a longitudinal magnetic field, the pseudospin Hamiltonian is a sum of the exchange term (5.124) and the $\tilde{\sigma}_z$-dependent Zeeman term

$$\mathcal{H} = \frac{\hbar}{2}\left(\tilde{\sigma}_x\Omega_x + \tilde{\sigma}_y\Omega_y + \tilde{\sigma}_z\Omega_\parallel\right)\ . \tag{5.156}$$

The pseudospin $\boldsymbol{S}$ rotates around the vector $\boldsymbol{\Omega} = (\Omega_1, \Omega_2, \Omega_\parallel)$ with the effective Larmor frequency $\Omega = \sqrt{\Omega_1^2 + \Omega_2^2 + \Omega_\parallel^2}$. In the realistic case

$$\sqrt{\Omega_1^2 + \Omega_2^2} \gg \frac{1}{\tau} \tag{5.157}$$

the pseudospin precession around $\boldsymbol{\Omega}$ leads to a depolarization of the initial spin component perpendicular to $\boldsymbol{\Omega}$ while the component parallel to $\boldsymbol{\Omega}$ remains unchanged. This means that the steady-state value of $\boldsymbol{S}$ is obtained by projecting $\boldsymbol{S}^0$ onto the $\boldsymbol{\Omega}$ direction, i.e., $\boldsymbol{S} = \boldsymbol{\Omega}(\boldsymbol{\Omega} \cdot \boldsymbol{S}^0)/|\boldsymbol{\Omega}|^2$. Therefore, the relation between the secondary and primary polarizations can be presented in the following form

$$P_i = \Lambda_{ij} P_j^0 \ \ (i, j = l, l', c) \,, \tag{5.158}$$

with the matrix $\hat{\Lambda}$ given by

$$||\Lambda_{ij}|| = \frac{1}{\Omega_1^2 + \Omega_2^2 + \Omega_\parallel^2} \begin{bmatrix} \Omega_1^2 & \Omega_1\Omega_2 & \Omega_1\Omega_\parallel \\ \Omega_1\Omega_2 & \Omega_2^2 & \Omega_2\Omega_\parallel \\ \Omega_1\Omega_\parallel & \Omega_2\Omega_\parallel & \Omega_\parallel^2 \end{bmatrix} . \tag{5.159}$$

One can see that, for nonzero anisotropic exchange splitting δ_2, the longitudinal magnetic field restores the PL circular polarization and induces the linear polarization under circularly polarized excitation. It also follows that, under linearly polarized excitation, the magnetic field gives rise to two additional effects: suppression of the alignment and polarization conversion with an appearance of circular polarization in the PL.

In [5.85], instead of measuring the PL polarization degrees P_l, $P_{l'}$ and P_c under a fixed position of the polarizer, the modulation technique is applied where the analyzer is in a fixed position and the sample is pumped by the incident light changing its polarization from circular or linear to orthogonal at a certain frequency. The measured values are then the effective polarization degrees

$$\rho_\alpha^l = \frac{I_\alpha^{110} - I_\alpha^{1\bar{1}0}}{I_\alpha^{110} + I_\alpha^{1\bar{1}0}} \,,\ \rho_\alpha^{l'} = \frac{I_\alpha^{100} - I_\alpha^{010}}{I_\alpha^{100} + I_\alpha^{010}} \,,\ \rho_\alpha^c = \frac{I_\alpha^{\sigma+} - I_\alpha^{\sigma-}}{I_\alpha^{\sigma+} + I_\alpha^{\sigma-}} \,, \tag{5.160}$$

where I_β^α designates the PL intensity in the configuration (α, β) of the polarizer and analyzer, and α, β are linear polarizations along the axes [100], [010], [110], [1$\bar{1}$0] or circular polarizations σ_+, σ_-. The theory shows that, under resonant excitation conditions and neglecting the level anticrossing effects, the set (5.160) is equivalent to the values of P_l^α, $P_{l'}^\alpha$ and P_c^α, where α indicates the polarizer position.

Figure 5.13 displays the dependencies $\rho_\alpha^c(B_z)$ and $\rho_\alpha^l(B_z)$ measured on one of the type-II GaAs/AlAs SL samples at the PL spectral maximum ($\lambda =$ 6684 Å). It is seen from Fig. 5.13a that $\rho_{\sigma_+}^c(B_z)$ rapidly increases and saturates from 2.5% to 5% in weak magnetic fields $B_\parallel \approx 20$ G and then gradually increases up to the level of 20% at $B_z = 2.5$ kG. Figure 5.13b clearly demonstrates the field-induced orientation-to-alignment conversion: $\rho_{110}^c(B_z)$

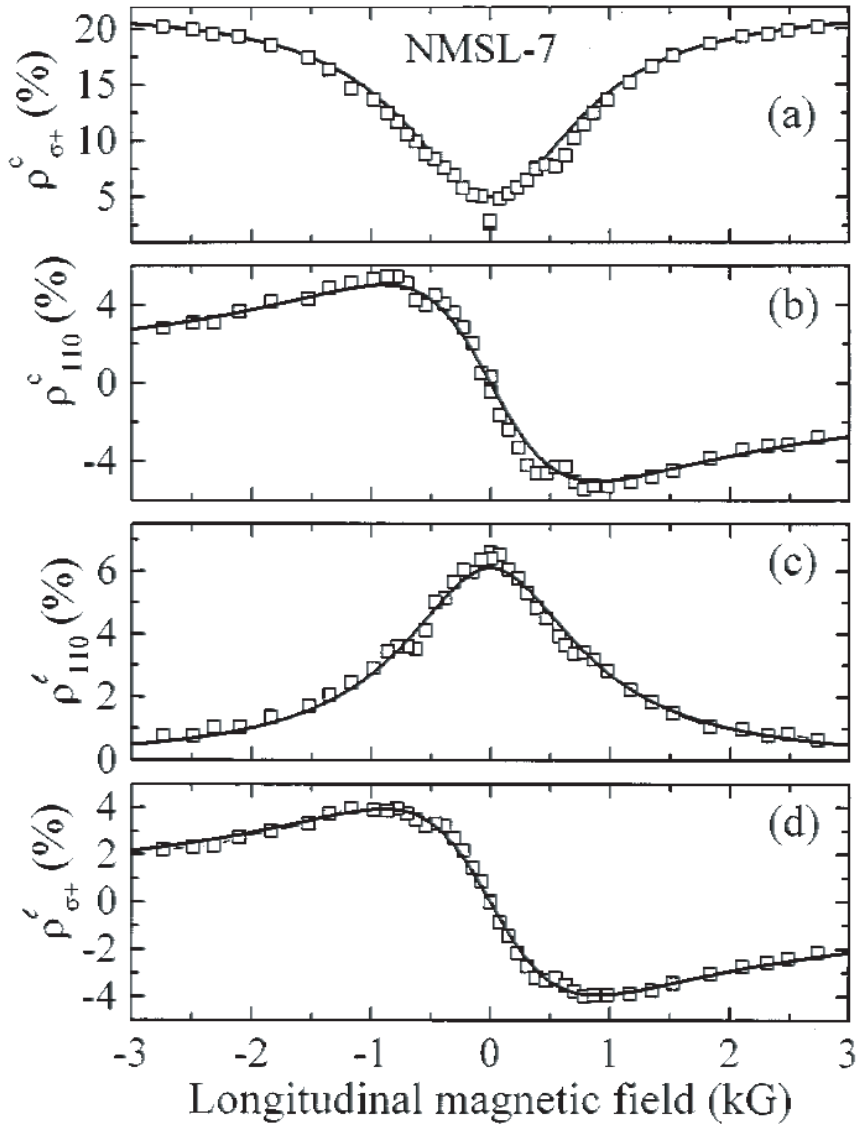

Fig. 5.13. Effect of the longitudinal magnetic field on optical orientation and alignment of localized excitons in a type-II GaAs/AlAs SL: (**a**)$\rho^c_{\sigma_+}$, (**b**) ρ^c_{110} , (c) ρ^l_{110} , (d) $\rho^l_{\sigma_+}$. Experimental data (T = 4.2 K) are shown as points. Solid curves are theoretical fits. From [5.85].

reaches a maximum value of 5% at $B_z \approx 0.7$ kG and reverses its sign under the field inversion. Moreover, $\rho^c_{110}(B_z)$ differs in sign from the measured dependence $\rho^c_{1\bar{1}0}(B_z)$. The effect of longitudinal magnetic field upon the optical alignment is illustrated in Fig. 5.13c. Note that the main variation of ρ^l_{110} takes place at the same magnetic fields $B_z \approx 0.7$ kG as for the function $\rho^c_{\sigma_+}(B_z)$ in Fig. 5.13a. Figure 5.13d shows that the orientation-to-alignment conversion effect is reversible: the experimental dependencies $\rho^c_{110}(B_z)$ and $\rho^l_{\sigma_+}(B_z)$ are close to each other.

The solid curves in Fig. 5.13 are theoretical fits by using the theory taking into account the exchange splitting with $\Omega_1 \neq 0, \Omega_2 = 0$ in accordance with the mechanism of anisotropic exchange interaction in GaAs/AlAs short-period type-II SLs discussed in Sect. 5.5.1. The fast low-field increase of $\rho^c_{\sigma_+}$ in Fig. 5.13a is attributed to a spatially separated electron-hole pairs characterized by small values of exchange splitting. In the analysis this contribution is taken into account by adding a constant value of 5% to the theoretical curve $\rho^c_{\sigma_+}(B_z)$. Except for this narrow region the experimental data can be described taking additionally into consideration the exciton spin relaxation between the radiative and nonradiative states and possible losses in the orientation and alignment during the quasi-resonant photoexcitation process [5.85]. Since in type-II GaAs/AlAs SLs there are two kinds of localized excitons with Ω_1 differing in sign, the calculated circular-to-linear and linear-to-circular conversion terms have to be multiplied by the imbalance factor

$$f = \frac{N^{(+)} - N^{(-)}}{N^{(+)} + N^{(-)}} ,$$

where $N^{(\pm)}$ denotes the concentration of excitons localized at the AlAs-on-GaAs and GaAs-on-AlAs interfaces, respectively. Thus, the magnetic-field-induced conversion between the circular and linear polarizations suggests an effective method to measure an important structural parameter, namely, the imbalance factor f. The curves in Fig. 5.13 are calculated for $\delta_2 = 1.8$ μeV and $f = 0.9$. Since in type-II GaAs/AlAs SLs the frequency Ω_2 is zero and $\Omega_1\tau \gg 1$, the theory in full agreement with experiment predicts no optical alignment in the cw excitation regime for the incident light polarized along the [100] or [010] axis, $\Lambda_{l'l'} = 0$, and no l'-c or c-l' polarization conversion, $\Lambda_{cl'} = \Lambda_{l'c} = 0$.

5.5.4 Photoluminescence of Neutral and Charged Quantum Dots

Figure 5.14 displays the effective polarization degrees of photoluminescence ρ^l_α, $\rho^{l'}_\alpha$, ρ^c_α measured as a function of the longitudinal magnetic field (the Faraday geometry) on InAlAs QDs in an AlGaAs matrix [5.104]. The PL was recorded at the wavelength 6890 Å under quasiresonant excitation with $\lambda = 6764$ Å. The main experimental findings are observations of (a) the optical alignment of excitons for any in-plane direction of linear polarization

of the exciting light, and (b) magnetic-field-induced conversion of the $\langle 110 \rangle$ alignment to orientation but no similar conversion of the $\langle 100 \rangle$ alignment. The MBE-grown InGaAs/GaAs-like QDs have a shape of pyramids with the height parallel to the growth direction $z \parallel [001]$ and the base oriented along the $\langle 100 \rangle$ directions [5.89]. In case of the square base, QDs are characterized by the C_{2v} point symmetry for which $\hbar\Omega_1 = \delta_2 \cos\Phi_2 \neq 0$ and $\hbar\Omega_2 = \delta_2 \sin\Phi_2 = 0$. In the general case of a rectangular base the symmetry is reduced to C_2 and Ω_1, Ω_2 are both nonzero. The experimental results on InAlAs QDs can be explained by assuming that the positive and negative values of Ω_2 are equally probable, the average value of Ω_1 is nonzero, and the mean-square values of Ω_1^2 and Ω_2^2 are comparable. It follows then that the components Λ_{ij} odd in Ω_2 vanish after averaging over the ensemble of QDs. As a result the secondary and primary polarizations are related by the matrix $\langle \Lambda_{ij}^{(+)} \rangle$ where

$$\langle \hat{\Lambda}^{(+)} \rangle = \frac{1}{\Omega_1^2 + \Omega_2^2 + \Omega_\parallel^2} \begin{bmatrix} \Omega_1^2 & 0 & \Omega_1\Omega_\parallel \\ 0 & \Omega_2^2 & 0 \\ \Omega_1\Omega_\parallel & 0 & \Omega_\parallel^2 \end{bmatrix}$$

and the angle brackets mean averaging over the distribution of Ω_1 and Ω_2. While calculating the theoretical curves in Fig. 5.14 the Gaussian distribution

$$P(\Omega_1, \Omega_2) = \frac{1}{2\pi\tilde{\Omega}_1\tilde{\Omega}_2} \exp\left[-\frac{(\Omega_1 - \langle\Omega_1\rangle)^2}{\tilde{\Omega}_1^2}\right] \exp\left(-\frac{\Omega_2^2}{\tilde{\Omega}_2^2}\right),$$

was assumed, allowance for nonzero average value of Ω_1 was made and the dispersion parameters $\tilde{\Omega}_1, \tilde{\Omega}_2$ were found from the fitting procedure.

The studies of spin dynamics in self-organized InAs/GaAs QDs under pulsed photoexcitation supplement the continuous wave QD spectroscopy experiments. The best fit of the experimental data on time-resolved optical orientation, optical alignment and linear-to-circular polarization conversion leads to the anisotropic exchange splitting $\delta_2 = 135$ eV in InAs/GaAs QDs obtained after a nominal deposition of 2.2 InAs monolayers [5.105]. These experiments also evidence a spin relaxation quenching in semiconductor QDs at low temperature compared to bulk or 2D structures and bring experimental support to proposals using electron spins in QDs for quantum information encoding and processing in a solid-state system.

Cortez et al. [5.106] have demonstrated a possibility to manipulate the spin of the resident electron in an n-doped QD using nonresonant optical excitation. The time dependence of the luminescence and circular polarization of the ground state emission under excitation in the wetting layer is shown in Fig. 5.15. To interpret the set of obtained experimental results the following scenario can be proposed providing a simplified description of the three-particle complex (or QD *trion*) dynamics. Let us consider that the dots contain ideally a single resident electron and that at most a single electron-

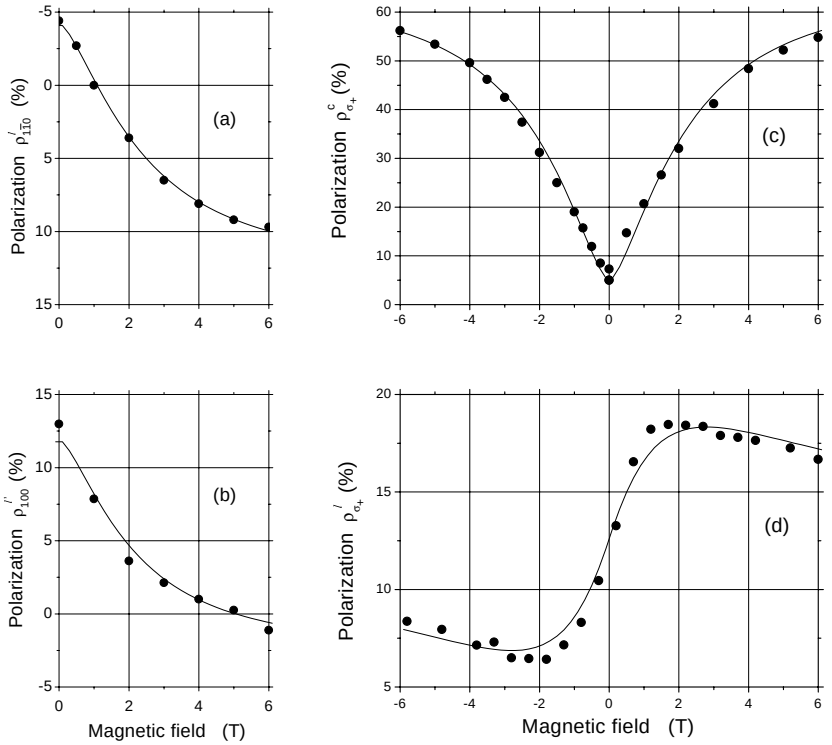

Fig. 5.14. Effect of the longitudinal magnetic field on optical orientation and alignment of excitons confined in $In_{0.45}Al_{0.55}As/Al_{0.3}Ga_{0.7}As$ QDs: (**a**) $\rho^{l}_{1\bar{1}0}(B_z)$, (**b**) $\rho^{l'}_{100}(B_z)$, (**c**) $\rho^{c}_{\sigma_+}(B_z)$, (**d**) $\rho^{l}_{\sigma_+}(B_z)$. Solid curves are theoretical fits taking into account the anisotropy of generation and recombination in the axes $[1\bar{1}0]$ and [110]. From [5.104].

hole pair is optically injected in a dot. Moreover, the heavy holes photogenerated in the wetting layer or barrier are assumed to lose completely their spin polarization.

When a photocreated pair is captured by a QD, the injected electron (say with spin $\downarrow$ for σ_+ excitation) relaxes in a few ps down the first excited electron state $p_c^{\downarrow}$ while the heavy hole relaxes down to its ground state. If the resident and photoinjected electrons have antiparallel spins the latter thermalize very rapidly to the ground state s_c, the electrons form the ground state singlet S_0 and the corresponding radiative recombination yields unpolarized luminescence. When both electrons have parallel spins (say $\downarrow\downarrow$) they form a triplet state T_{-1} and cannot relax to the ground state S_0 without spin reversal. Depending on the hole spin, the trion formed with T_{-1} electrons is either bright (the hole in the state $s_h^{\uparrow}$) or dark ($s_h^{\downarrow}$). The bright trion can recombine radiatively with σ_+ polarization and leaves a $p_c^{\downarrow}$ electron which

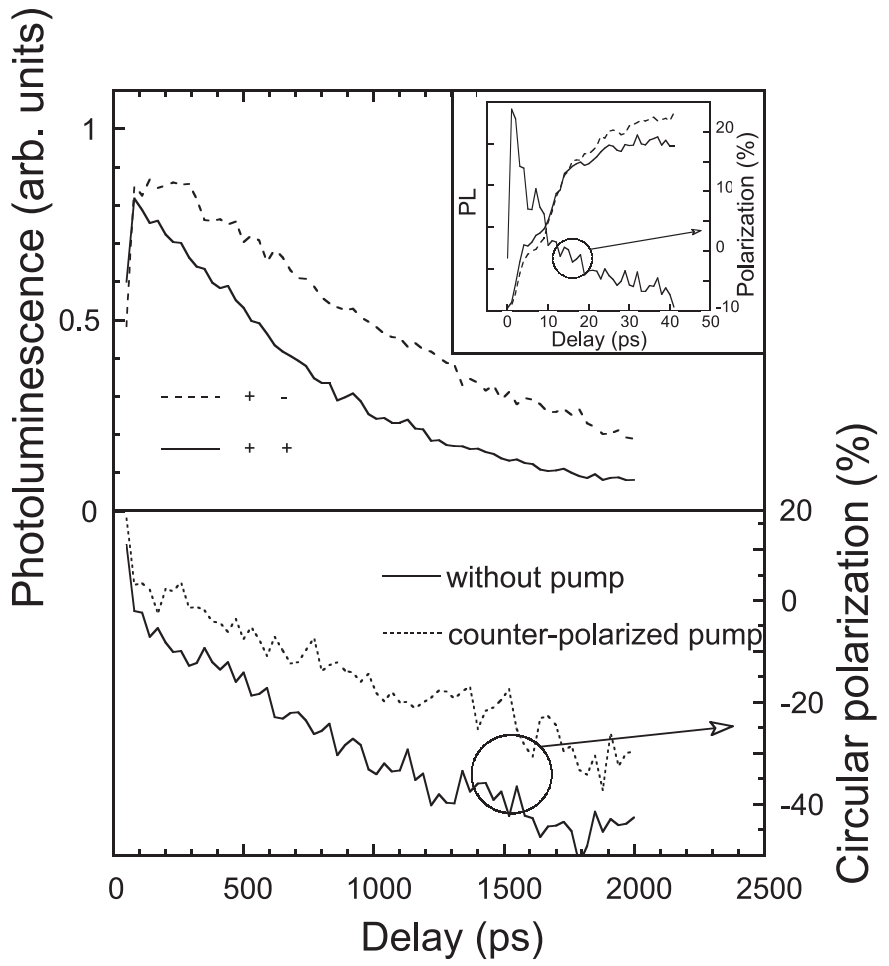

Fig. 5.15. Top: time-resolved photoluminescence detected at 1.15 eV under circularly polarized excitation at 1.44 eV of the *n*-doped QD sample. The inset shows a blowup of the fast dynamics at short times. Bottom: the corresponding circular polarization is shown (*dark* line), as well as the polarization in the presence of a counterpolarized pump pulse 10 ns earlier (*grey* line). From [5.106].

will further thermalize to the ground state $s_c^{\downarrow}$. This explains the observation of copolarized PL at the very beginning of the recombination process (see inset in Fig. 5.15). The anisotropic electron-hole exchange interaction causes a simultaneous spin reversal of the hole and one electron. This flip-flop is followed by an irreversible relaxation of the electron subsystem to the S_0 singlet state. The radiative recombination of the resulting frozen trion produces then counterpolarized light, due to the hole spin state. This path is much faster than the direct recombination. It is this mechanism that is assigned to

the reversal of PL polarization after a few tens of picoseconds in Fig. 5.15. In the case of the dark trion T_{-1} with the hole $s_h^{\downarrow}$ the most likely process is the single particle spin flip of an electron, maybe due to the effect of spin-orbit interaction and dot shape anisotropy. This electron spin-flip relaxation is due to the slow increase of counter polarization during the recombination lifetime. Finally one can conclude that the spin of the electron remaining in the dot after recombination of the photoinjected electron-hole pair is polarized, with an increase of the spin $\downarrow$ population (for σ_+ excitation). This allows to write and read the spin state of the resident electron in n-doped QDs.

5.6 Interface-Induced Linear Polarization of Photoluminescence

In Sect. 3.3.3 we considered the in-plane anisotropy of type-I heterostructures where both electrons and holes are confined within the same layers. Now we will concentrate on type-II heterostructures with no-common atoms, like InAs/AlSb [5.107, 5.108], ZnSe/BeTe [5.109, 5.110], CdS/ZnSe [5.111], where electrons and holes are confined in adjacent layers and the interband optical transitions are indirect in the real space. The PL measurements in type-II structures are preferential because, for the indirect transitions, the oscillator strength is very small and the transmission experiments are much less sensitive to the possible anisotropy.

Figure 5.16 demonstrates a giant in-plane optical anisotropy of BeTe/ZnSe heterostructures. In order to detect the anisotropy signal induced by a single interface the PL from high-quality ZnSe/BeTe double barrier structure was studied. The layer sequence is shown in Fig. 5.16c together with current-voltage characteristics. The samples are as symmetrical as possible and comprise lattice matched BeZnSe contact layers, undoped ZnSe spacer layers. They act as electron emitters under applied bias voltage and BeTe/$Zn_{1-x}Mn_xSe$/BeTe double-barrier structure with $x = 0$ or $x = 0.1$. All the normal and inverted interfaces are grown under Zn and Te termination and contain the Zn-Te and Te-Zn chemical bonds. PL is excited by an Ar-ion laser. The heterostructures demonstrate pronounced resonant-tunneling features which become less pronounced under illumination. Figures 5.16a and 5.16b present the PL spectra measured for two studied samples and detected in the linear polarization, P_l, along the $[1\bar{1}0]$ and [110] axes. The emission lines EL and ER originate from the spatially indirect transitions involving electrons from the ZnSe emitters and photoholes from the BeTe layers. The lines WL, WR observed only in the second sample are due to the quantum-well electrons. Splitting between the EL and ER lines can be attributed to small charge-asymmetry of the emitters.

One can see that the lines EL and ER are strongly polarized and, moreover, polarized orthogonally. The interpretation of these lines is confirmed by their behavior in an electric field under applied voltage. Positive electric

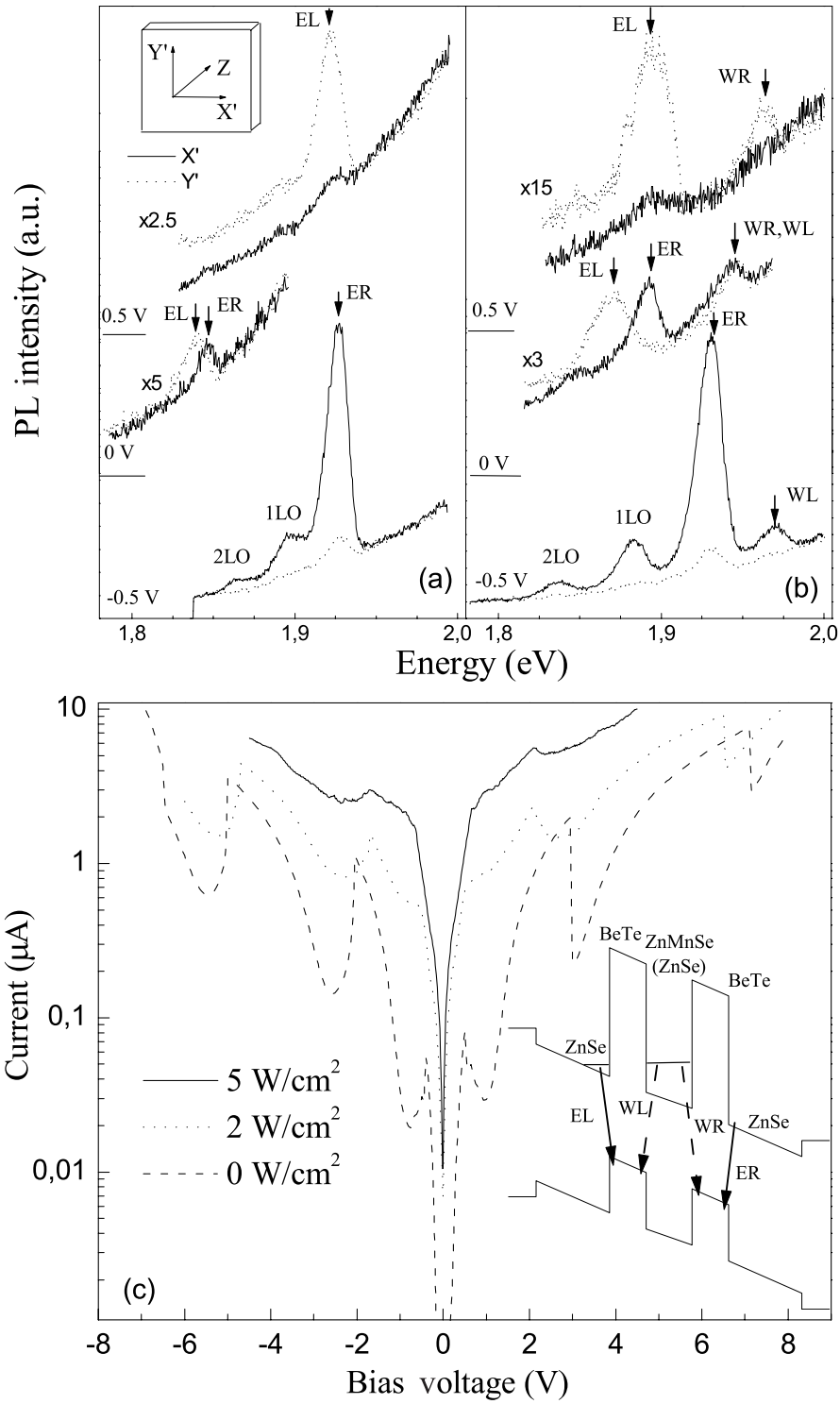

Fig. 5.16. The polarized PL spectra at different bias voltages (**a**, **b**) and I-V characteristics (**c**) measured at T = 1.6 K in the double-barrier resonant-tunneling structure BeTe/$Zn_{1-x}Mn_xSe$/BeTe shown in the inset. Solid and dotted spectra are taken for the analyzer orientation along the x' and y' axes of the (001)-grown samples. The spectra in (**a**) and the curves in (**c**) are obtained in the 40 Å/50 Å/40 Å structure with the Mn content $x = 0.1$; the spectra in (**b**) are obtained in the sample with pure ZnSe middle layer. [5.109]

fields push off electrons from the rightmost interface and form a triangular potential near the leftmost interface pressing electrons towards this interface. As a result the relative intensity of the EL line increases and that for the ER line vanishes. A field reversal leads to an exchange of the role played by the interfaces, in this case it is the line ER that survives at negative biases. The surviving line is as strongly polarized as it was at zero bias. Thus one concludes that the radiation contributed by indirect optical transitions at a particular interface between BeTe and ZnSe has very high linear polarization and this polarization is almost insensitive to the electric field. The fact of nonzero lateral polarization is a natural consequence of the C_{2v} point symmetry of a single interface in a (001)-grown heterostructure. However, giant values of this polarization need a theoretical explanation.

The temperature- and incident-power dependencies of the PL polarization in ZnSe/BeTe MQWs was studied in [5.110]. Complete sets of data on time-resolved and time-integrated spectra of the PL intensity and linear polarization P_l were obtained. The aim was to clarify whether the observed polarization is induced by localization of carriers at anisotropic defects and interface imperfections or it is an intrinsic property of the heterostructure. The crucial point is the stability of polarization against changes in various external and internal conditions, namely, against an increase in the excitation power by more than 7 orders of magnitude, against the temperature increase from 1.7 K to 300 K, and, in addition, there are no remarkable changes in the linear polarization with applying an external magnetic field up to 7 T. Under such conditions the PL spectrum exhibits tremendous modifications, its intensity changes by many orders of magnitude, the spectral maximum moves upwards or downwards by 200÷400 meV and the PL band halfwidth varies within broad limits as well. In contrast, the PL linear polarization degree remains stable varying between the limits of 50% and 75% and is almost constant within the halfwidth of the spectral band. All this means that any theoretical interpretation of the available experimental results should be based on intrinsic microproperties of a single (001) heterojunction between two semiconductors with a zinc-blende-like lattice.

In type-II ZnSe/BeTe systems the conduction- and valence-band offsets are very large. The penetration depth for an electron into the BeTe layer and for a hole into the ZnSe layer has the order of the lattice constant. Therefore in such a system the wave functions of an electron and a hole participating in the spatially indirect radiative recombination overlap remarkably only over few atomic planes. For calculations of optical matrix elements in this case the conventional envelope-function approximation is invalid. One must instead use microscopic pseudopotential or tight-binding models.

In the following we outline a tight-binding theory suitable for the calculation of interband optical transitions on a type-II heterojunction [5.112]. Let us consider a periodic CA/C′A′ heterostructure grown along the axis [001] and consisting of alternating layers of binary compounds CA and C′A′ with

different cations and anions. The electron wave function in the tight-binding method is written in the form

$$\psi(\boldsymbol{r}) = \sum_{n,\alpha} C_n^{\alpha b} \phi_{n\alpha}(\boldsymbol{r}) \,. \tag{5.161}$$

Here $\phi_{n\alpha}(\boldsymbol{r})$ are the planar orbitals, n is the number of the atomic plane, and α is the orbital state index. For clarity, the coefficients in expansion (5.161) are supplied with an additional superscript $b = a$ for the anion ($n = 2l$, where l is an integer) and $b = c$ for the cation ($n = 2l + 1$). For the states with a zero lateral wave vector, i.e. for the states with $k_x = k_y = 0$, the planar orbitals are related to the atomic orbitals Φ_α^b by

$$\phi_{n\alpha} = \sum_{n_1,n_2} \Phi_\alpha^b(\boldsymbol{r} - \boldsymbol{a}_n - n_1\boldsymbol{o}_1 - n_2\boldsymbol{o}_2) \,,$$

where n_1, n_2 are arbitrary integers, $\boldsymbol{o}_1 = (a_0/2)(1,1,0)$, $\boldsymbol{o}_2 = (a_0/2)(1,-1,0)$, a_0 is the lattice constant of the face-centered cubic lattice, $\boldsymbol{a}_n$ is the position of any atom on the n-th atomic plane. We remind that the distance between neighboring cation and anion planes equals $a_0/4$.

In the tight-binding method the wave equation for an electron with the energy E transforms into the system of linear equations for the coefficients $C_n^{\alpha b}$

$$\left(E_n^{\alpha b} - E\right) C_n^{\alpha b} + \frac{1}{2} \sum_{n' \neq n, \alpha'} V_{n,n'}^{\alpha b, \alpha' b'} C_{n'}^{\alpha' b'} = 0 \,. \tag{5.162}$$

Here $E_n^{\alpha b}$ are the diagonal atomic energies, and $V_{n,n'}^{\alpha b, \alpha' b'} = V_{n',n}^{\alpha' b', \alpha b}$ are the off-diagonal tight-binding parameters for the pair n, n'.

In the sp^3 tight-binding model, the atomic s- and p-orbitals are taken into account only. Hence, the pair of superscripts α, b runs through eight values $sa, sc, p_{x'}a, p_{y'}a, p_{x'}c, p_{y'}c, p_z a$ and $p_z c$. Taking into account the symmetry considerations, the orbitals

$$p_{x'} = \frac{p_x - p_y}{\sqrt{2}} \,,\; p_{y'} = \frac{p_x + p_y}{\sqrt{2}}$$

oriented along $[1\bar{1}0]$ and $[110]$ are used instead of the orbitals $p_x \parallel [100]$, $p_y \parallel [010]$. Neglecting the spin-orbit interaction, the tight-binding Hamiltonian in a homogeneous semiconductor crystal is described by nine parameters $E_{sa}, E_{ca}, E_{sp}, E_{pa}, V_{ss}, V_{xx}, V_{xy}, V_{sa,pc} = V_{pc,sa}$ and $V_{sc,pa} = V_{pa,sc}$.

For the electron states with zero lateral wave vector, eight coupled linear equations for the coefficients $C_n^{\alpha b}$ are decoupled into three independent sets of equations: four for s and p_z orbitals, two for $p_{x'}$ orbitals and two for $p_{y'}$ orbitals.

In calculating the matrix elements for optical transitions we apply the relation between the velocity and coordinate operators

$$\hat{\boldsymbol{v}} = \frac{\mathrm{i}}{\hbar}(\mathcal{H}\boldsymbol{r} - \boldsymbol{r}\mathcal{H})\,, \tag{5.163}$$

where $\mathcal{H}$ is the Hamiltonian. Taking the latter in the form $H^{b'b}_{\alpha'\alpha}(\boldsymbol{R}', \boldsymbol{R})$ and introducing the matrix elements of the coordinate $\boldsymbol{r}_{\alpha\alpha'}(\boldsymbol{R}, \boldsymbol{R}')$ we can find the tight-binding matrix elements of the velocity $\boldsymbol{v}^{b'b}_{\alpha'\alpha}(\boldsymbol{R}', \boldsymbol{R})$. Here $\boldsymbol{R} = \boldsymbol{a} + \boldsymbol{\tau}_b$ is the position of the atom specified by the location of an elementary cell, $\boldsymbol{a}$, and the location $\boldsymbol{\tau}_b$ of the atom of sort b within the cell. Usually only intrasite matrix elements

$$\boldsymbol{r}_{\alpha'\alpha}(\boldsymbol{R}', \boldsymbol{R}) \equiv \langle \boldsymbol{R}', \alpha' | \boldsymbol{r} | \boldsymbol{R}, \alpha \rangle = (\boldsymbol{R}\,\delta_{\alpha'\alpha} + \boldsymbol{r}_{\alpha'\alpha})\,\delta_{\boldsymbol{R}',\boldsymbol{R}} \tag{5.164}$$

are taken into account with $\boldsymbol{r}_{\alpha'\alpha}$ describing the inter-orbital transitions within a single atomic site. In the tight-binding model of Lew Zan Voon and Ram-Mohan [5.113] the inter-orbital matrix elements $\boldsymbol{r}_{\alpha'\alpha}$ are ignored. Then the velocity matrix elements contain only *inter-atomic* contributions and can be unambiguously expressed in terms of the tight-binding parameters as

$$\boldsymbol{v}^{b'b}_{\alpha'\alpha}(\boldsymbol{R}', \boldsymbol{R}) = \frac{\mathrm{i}}{\hbar}\,(\boldsymbol{R} - \boldsymbol{R}')H^{b'b}_{\alpha'\alpha}(\boldsymbol{R}', \boldsymbol{R})\,. \tag{5.165}$$

It is seen that according to this theory the intra-atomic terms with $\boldsymbol{R} = \boldsymbol{R}'$ are indeed equal to zero, and the inter-atomic terms are directed along the vector $\boldsymbol{R} - \boldsymbol{R}'$, i.e., along the chemical bond between the atoms $\boldsymbol{R}$ and $\boldsymbol{R}'$. In this case, the inter-atomic transitions between the planes $2l, 2l-1$ and $2l, 2l+1$ cause the emission of photons polarized in the direction of the axes $x' \parallel [1\bar{1}0]$ and $y' \parallel [110]$, respectively.

The optical matrix elements corresponding to the emitted photons polarized along the axes x' and y' are written as

$$M_j = \mathrm{i}\frac{a_0}{4\hbar}\sum_l V_l^j\,, \tag{5.166}$$

$$V_l^{x'} = V_{sa,pc}C_{2l}^{sa*}C_{2l-1}^{p_{x'}c} + V_{pa,sc}C_{2l-1}^{sc*}C_{2l}^{p_{x'}a} - V_{xy}\left(C_{2l}^{p_z a*}C_{2l-1}^{p_{x'}c} - C_{2l-1}^{p_z c*}C_{2l}^{p_{x'}a}\right),$$
$$V_l^{y'} = V_{sa,pc}C_{2l}^{sa*}C_{2l+1}^{p_{y'}c} + V_{pa,sc}C_{2l+1}^{sc*}C_{2l}^{p_{y'}a} + V_{xy}\left(C_{2l}^{p_z a*}C_{2l+1}^{p_{y'}c} - C_{2l+1}^{p_z c*}C_{2l}^{p_{y'}a}\right).$$

Here, M_j is the interband matrix element of the velocity operator, $V_l^{x'}$ is the contribution to $M_{x'}$ from the inter-atomic transitions between the anion plane $2l$ and the cation plane $2l-1$, $V_l^{y'}$ is the similar contribution to $M_{y'}$ from transitions between the planes $2l$ and $2l+1$, $C_n^{sb}, C_n^{p_z b}$ are the coefficients of the s- and p_z-orbitals in expansion (5.161) for the electron states in the lowest conduction band Γ_1, $C_n^{p_j b}$ is the p_j-orbital coefficient for the p_j hole states in the valence band.

It is important to stress the principal difference between calculations of optical matrix elements in type-I and type-II structures. The interband optical matrix element is proportional to the overlap integrals between the

electron and hole wave functions. In type-I structures, the overlap integral is contributed by the whole QW layer, one needs to know the coefficients of admixture of heavy- and light-hole states in the hole wave function at the lowest hole subband $hh1$. In this case the detailed information about behavior of the wave function near interfaces is not needed and the coefficients of admixture can be found from the effective boundary conditions imposed on the hole envelope functions, as it was realized in Sect. 3.3.3. In type-II structures, the behavior of the hole wave function inside the layer, where a hole is confined, can be calculated as well by imposing the boundary conditions on the envelopes. However, in this case the calculation of interband matrix elements requires the knowledge of microscopic behavior of the wave functions at the interfaces and the transition oscillator strength is strongly affected by an anisotropic orientation of interface chemical bonds. Thus one has to go forward beyond the generalized envelope function approaches.

The results of calculation of the $e1$-$hh1$ PL linear polarization

$$P_{\text{lin}} = \frac{I_{1\bar{1}0} - I_{110}}{I_{1\bar{1}0} + I_{110}}$$

are presented in Fig. 5.17. The tight-binding parameters for the ZnSe and BeTe layers can be chosen from the data on band structures of the corresponding bulk semiconductors. Note that the constants of lattices ZnSe and BeTe are close to each other, i.e., ZnSe/BeTe constitute a heteropair with matched lattice constants. However, they are different from those of the volume semiconductor ZnTe or BeSe. For this reason, the tight-binding coefficients for interface atoms can be considered as independent parameters of the theory. The three upper curves have been calculated for the ZnTe-like interface, while the three lower curves correspond to the BeSe-like interface. Each curve corresponds to a particular value of diagonal energy assumed for the p-like atomic orbital at the interface Zn atoms either at the interface Be atoms. From this figure we conclude that the theory allows high degrees of the PL linear polarization in type-II heterostructures. Moreover, as a rule the polarization follows the orientation of interface chemical bonds. Allowance for intra-atomic transitions modifies the PL polarization but leaves unchanged a possibility for the polarization to be very high.

The above-discussed lateral anisotropy is related to the tetrahedral orientation of the chemical bonds along the $\langle 111 \rangle$ directions and can be described by the reduced point-group symmetry C_{2v}. An ideal QW structure with two equivalent interfaces has the higher symmetry D_{2d}. It is uniaxially isotropic, because the chemical bonds at the opposite interfaces lie in mutually orthogonal planes, $(1\bar{1}0)$ and (110), and their contributions to the anisotropy cancel. Thus, in ideal QW structures the in-plane anisotropy of single interfaces is *hidden*. However, under special conditions it can reveal itself through a linear polarization of vertically emitted radiation. Such is the case in the presence of an electric field applied normal to the plane of the well (Fig. 5.16) or in asymmetric QWs with different profiles of nonabrupt normal and inverted

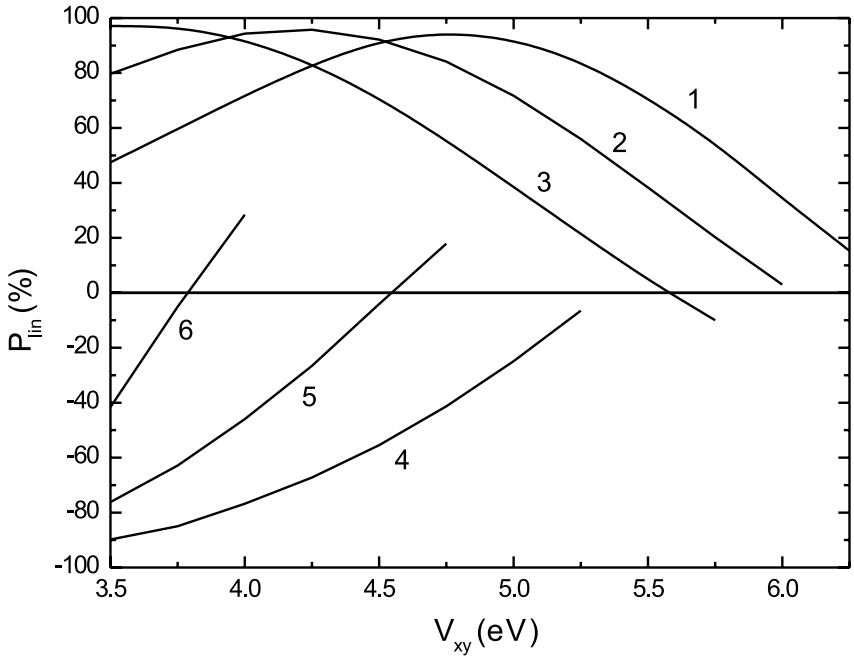

Fig. 5.17. Linear polarization of the photoluminescence in the ZnSe/BeTe heterostructure as a function of the tight-binding parameter V_{xy} at the Zn-Te interface (*curves* 1, 2 and 3) or Be-Se interface (*curves* 4, 5 and 6). Curves 1, 2 and 3 are calculated, respectively, for the diagonal energy $E_{pc} = 5, 6, 7$ eV for the interface Zn atom and curves 4, 5 and 6 for $E_{pc} = 3, 4, 5$ for the interface Be atom. For the other interface parameters, mean values, for example, $E_{sa}(\mathrm{ZnTe}) = [E_{sa}(\mathrm{ZnSe}) + E_{sa}(\mathrm{BeTe})]/2$, etc, were used. [5.112]

interfaces, and/or for heteropairs with no common atoms and with different kinds of chemical bonds at the abrupt interfaces (Sect. 3.3.3).

In [5.114,5.115] a method was proposed to uncover the hidden anisotropy of ideal QWs without breaking their invariance to the mirror-rotation operation S_4 and reducing the uniaxial symmetry. The method is based on the analysis of the magnetic-field induced elliptical polarization of the photoexcited system consisting of optically anisotropic subsystems. Indeed, the indirect radiative recombination at a type-II (001) interface between two zinc-blende-lattice semiconductors, like BeTe and ZnSe, can be modelled by light-emitting 2D dipole oscillators. It suffices to assume that each oscillator can equally oscillate along the planar axes x' and y' and the coupling of x' dipoles with the x'-polarized light differs from the y'-y' coupling by a factor of Λ. The circular oscillations $x' \pm \mathrm{i}y'$ effectively describe the electron-hole states $|-1/2, 3/2\rangle$ and $|1/2, -3/2\rangle$ and are characterized by the optical matrix elements for emission

$$M_{-1/2,3/2} = M_0(e^*_{x'} + \mathrm{i}\Lambda e^*_{y'}) \,,\; M_{1/2,-3/2} = M_0(e^*_{x'} - \mathrm{i}\Lambda e^*_{y'}) \,, \tag{5.167}$$

where M_0 is a constant and $\boldsymbol{e}$ is the polarization unit vector of an emitted photon. In fact, the model uses only one (real) parameter Λ which is the ratio, $p_{cv,y'}/p_{cv,x'}$, of the interband matrix elements of the momentum operator. According to (5.167), a photon emitted by the oscillation $x' + \mathrm{i}y'$ or $x' - \mathrm{i}y'$ is elliptically polarized with the principal axes of the ellipse parallel to x', y' and the degrees of linear and circular polarization are given by

$$\begin{aligned} P_l^0 &= \frac{|M(\mathbf{e} \parallel x')|^2 - |M(\mathbf{e} \parallel y')|^2}{|M(\mathbf{e} \parallel x')|^2 + |M(\mathbf{e} \parallel y')|^2} = \frac{1-\Lambda^2}{1+\Lambda^2} \,, \\ P_c^0 &= \frac{|M(\sigma^+)|^2 - |M(\sigma^-)|^2}{|M(\sigma^+)|^2 + |M(\sigma^-)|^2} = \pm\frac{2\Lambda}{1+\Lambda^2} \,. \end{aligned} \tag{5.168}$$

Here the sign $\pm$ coincides with the circularity of the oscillation. For each oscillation the emitted photon is *completely elliptically polarized* and the total degree of polarization P satisfies the condition

$$P^2 = (P_l^0)^2 + (P_c^0)^2 = 1 \,. \tag{5.169}$$

At zero magnetic field, the states $|-1/2, 3/2\rangle$ and $|1/2, -3/2\rangle$ are equally populated. Due to that the emission is linearly polarized with $P_l = P_l^0$ but lacks circular polarization, $P_c = 0$. In the presence of a longitudinal magnetic field the electron and hole spin states are split and, therefore, thermally populated. At high magnetic fields the carriers are completely polarized. It follows from (5.169) that the circular polarization under saturation differs from $\pm 100\%$ and amounts to

$$P_c^{sat} = \pm\sqrt{1 - (P_l^0)^2} \equiv P_c^0. \tag{5.170}$$

If, due to the structure asymmetry, the contributions, $J_i(\hbar\omega)$ and $J_n(\hbar\omega)$, to the spectral intensity from the normal (n) and inverted (i) interfaces are different then the linear polarization is given by

$$P_l = \frac{P_{l,n} + \eta(\hbar\omega)\, P_{l,i}}{1 + \eta(\hbar\omega)} = \frac{1 - \eta(\hbar\omega)}{1 + \eta(\hbar\omega)}\; P_l^0, \tag{5.171}$$

where $\eta(E) = J_i(E)/J_n(E)$. The degree of circular polarization at saturating magnetic fields is determined by

$$P_c^{sat} = \pm\frac{\sqrt{1 - P_{l,n}^2} + \eta(E)\sqrt{1 - P_{l,i}^2}}{1 + \eta(E)} = \pm\sqrt{1 - (P_l^0)^2} \tag{5.172}$$

which is identical with (5.170). Due to the function $\eta(\hbar\omega)$ the linear polarization P_l has a spectral dependence. In contrast, P_c^{sat} is spectrally independent and determined by only one parameter, P_l^0, of an individual interface in agreement with the experiment results presented in Fig. 5.18.

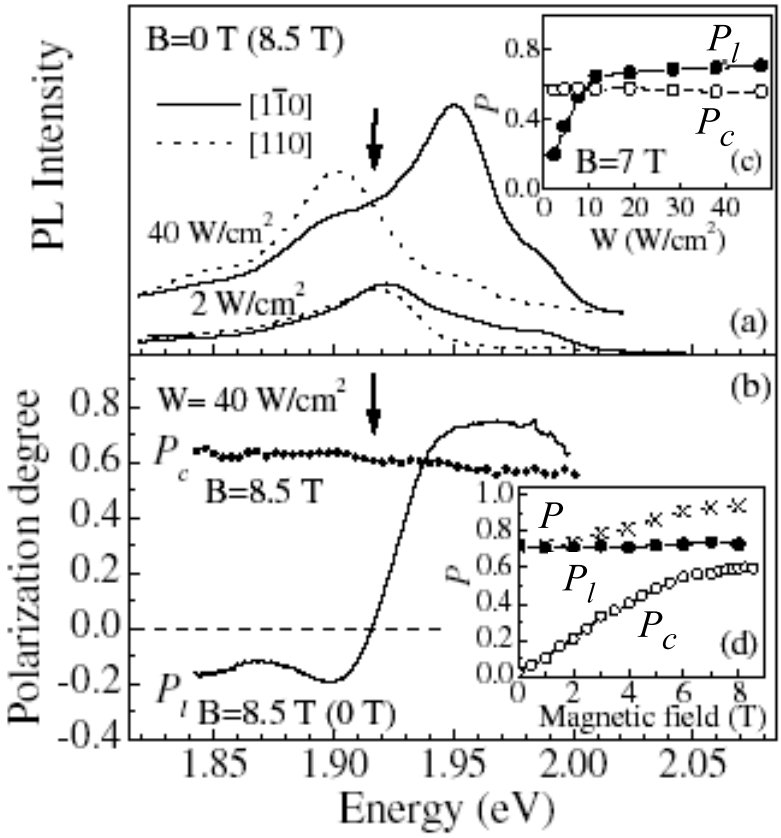

Fig. 5.18. (**a**) Linearly polarized PL spectra of 100 Å/50 Å ZnSe/BeTe MQWs. $B = 0$ (magnetic field of 8.5 T does not modify the spectra). (**b**) Spectral variation of the PL linear and circular polarizations measured at $B = 8.5$ T. $P_l(E)$ is identical at $B = 0$ and 8.5 T. Insets: Polarization of the indirect PL detected at 1.95 eV vs. excitation density (**c**) and magnetic field at $W = 40$ W/cm^2 (**d**). Lines are the guide to the eye. T = 1.6 K. From [5.115].

6 Light Scattering

He loads the clouds with moisture;
he scatters his lightning through them.

Job **37***: 11*

Under scattering of light one understands the appearance, in the medium illuminated by an external source, of new electromagnetic waves with frequencies and/or propagation directions different from those of the initial wave. Note that neither specular reflection nor refraction on a smooth macroscopical boundary between two media are attributed to scattering processes.

In bulk semiconductors the light can be scattered (i) by *free carriers*, namely, by *charge-density fluctuations* (single-particle excitations and plasmons) and *spin-density fluctuations* (spin-flip transitions), (ii) by phonons, optical (Raman scattering) or acoustic (Brillouin or Mandelshtam-Brillouin scattering), and (iii) by static imperfections and inhomogeneities inside the medium (Rayleigh scattering), see Sect. 6.2. In QW and QWR structures, contributions to the scattering (i) can come not only from intrasubband transitions but also from *intersubband transitions*, i.e. from intersubband charge- and spin-density excitations (Sect. 6.3). The Raman effect is enriched with scattering by *folded* acoustic phonons (Sect. 6.4) as well as by *confined* and *interface* optical phonons (Sect. 6.5). The spin-flip and double-resonance Raman spectroscopy is considered in Sects. 6.6 and 6.7, respectively.

6.1 The Physics of Light Scattering

In order to elucidate elastic and inelastic scattering of light by using the simplest possible model we consider a localized electric dipole with the moment P satisfying the equation of motion for a classical oscillator

$$\left(\frac{d^2}{dt^2} + \omega_0^2\right) P(t) = qE_0 \cos \omega t \,, \tag{6.1}$$

where ω_0 is the dipole eigenfrequency, ω and E_0 are the frequency and electric-field amplitude of the incident monochromatic light wave, the coefficient q characterizes the interaction between the dipole and the electric field. Let us assume that, for any reason, this coefficient varies periodically in time and it can be presented as a sum of constant and alternating contributions

$$q = q_0 + q_1 \cos \Omega t \,, \tag{6.2}$$

where q_0, q_1 are constant coefficients and Ω is the modulation frequency, in the following we are interested in the limiting case $\Omega \ll \omega_0$. The solution of (6.1) with q chosen in the form (6.2) consists of three harmonics

$$P(t) = \sum_{0,\pm 1} P_n \cos{(\omega + n\Omega)t} \tag{6.3}$$

with the amplitudes

$$P_0 = \frac{q_0}{\omega_0^2 - \omega^2} E_0 \ , \ P_{\pm 1} = \frac{q_1}{\omega_0^2 - (\omega \pm \Omega)^2} E_0 \ .$$

Thus, time variation of the dipole moment is a triple-harmonic oscillation at the initial frequency ω and two other, combinational, frequencies $\omega \pm \Omega$. The forced oscillations of the dipole moment give birth to secondary light waves at the same frequency ω (Rayleigh scattering) and two new frequencies $\omega + \Omega$ and $\omega - \Omega$ (Raman scattering). In a real system, the modulation frequency Ω can be any phonon frequency or the energy spacing between two eigenstates of the system related to $\hbar$.

It is instructive to consider a little more complicated model containing two dipoles with the moments $P(t), P'(t)$ that satisfy the set of two equations

$$\begin{aligned} \frac{d^2 P(t)}{dt^2} + \omega_0^2 P(t) &= q_0 E_0 \cos \omega t \ , \\ \frac{d^2 P'(t)}{dt^2} + {\omega'_0}^2 P'(t) &= q'(t) P(t) \ . \end{aligned} \tag{6.4}$$

In the case under consideration the incident light directly interacts only with the first dipole characterized by the resonance frequency ω_0 and the fixed coefficient $q = q_0$. Oscillation of the second dipole appears because of the linear coupling between the dipoles with the coupling coefficient being time modulated, namely $q'(t) = q'_0 + q'_1 \cos \Omega t$. Under stationary excitation the first dipole oscillates with the frequency ω of the primary light wave whereas the oscillation of the second dipole is a superposition of three harmonics

$$P'(t) = \sum_{0,\pm 1} P'_n \cos{(\omega + n\Omega)t} \ , \tag{6.5}$$

$$P'_0 = \frac{q_0 q'_0}{(\omega_0^2 - \omega^2)({\omega'_0}^2 - \omega^2)} E_0 \ , \ P'_{\pm 1} = \frac{q_0 q'_1}{(\omega_0^2 - \omega^2)[{\omega'}_0^2 - (\omega \pm \Omega)^2]} E_0 \ .$$

It follows then that the oscillation amplitudes P'_{+1}, P'_{-1} and, hence, amplitudes of the scattered wave at the corresponding frequencies $\omega \pm \Omega$ should increase enormously as the condition of the double optical resonance $\omega = \omega_0$ and $\omega + \Omega = \omega'_0$ (or $\omega - \Omega = \omega'_0$) is being approached. A real example of the double optical resonance is presented in Sect. 6.7.

In what follows we will use the notations ω_1, $\boldsymbol{q}_1$, $\boldsymbol{e}_1$ and ω_2, $\boldsymbol{q}_2$, $\boldsymbol{e}_2$ for the frequency, wave vector and polarization unit vector of the initial (primary) and scattered (secondary) electromagnetic waves, respectively. If a particle, or quasiparticle, involved in the act of scattering collides with a photon and changes its energy and wave vector from $E_1, \boldsymbol{k}_1$ to $E_2, \boldsymbol{k}_2$, the conservation laws read

$$\hbar\omega_1 + E_1 = \hbar\omega_2 + E_2 \ , \ \boldsymbol{q}_1 + \boldsymbol{k}_1 = \boldsymbol{q}_2 + \boldsymbol{k}_2 \ . \tag{6.6}$$

If the scattering of a photon is accompanied by emission or absorption of an excitation characterized by the frequency Ω and wave vector $\boldsymbol{Q}$ the conservation laws take the form

$$\omega_1 = \omega_2 + \Omega \ , \ \boldsymbol{q}_1 = \boldsymbol{q}_2 + \boldsymbol{Q} \ , \tag{6.7a}$$

$$\omega_1 + \Omega = \omega_2 \ , \ \boldsymbol{q}_1 + \boldsymbol{Q} = \boldsymbol{q}_2 \ . \tag{6.7b}$$

In the process a (or b) the photon frequency decreases (increases), it is the so-called scattering in the *Stokes* (or *anti-Stokes*) spectral region. One can also introduce the transferred wave vector and frequency

$$\boldsymbol{q} = \boldsymbol{q}_1 - \boldsymbol{q}_2 \ , \ \omega = \omega_1 - \omega_2 \ . \tag{6.8}$$

In the presence of absorption in the medium at the frequency ω_1 or ω_2 the expression for $\boldsymbol{q}$ will contain the real parts of the wave vectors. For the collision (6.6), one has $\boldsymbol{q} = \boldsymbol{k}_2 - \boldsymbol{k}_1$, $\omega = (E_2 - E_1)/\hbar$, and, for the scattering described by (6.7a) or (6.7b), $\boldsymbol{q} = \pm\boldsymbol{Q}$, $\omega = \pm\Omega$.

In terms of the Damen, Porto and Tell notation [6.1], scattering configurations are usually described by four symbols, two inside a parenthesis and two outside, for example, $x(yz)y$, $z(xx)\bar{z}$ or $z(\sigma^+, \sigma^-)\bar{z}$. The symbols inside are, left to right, the polarization of the incident and of the scattered light, while ones to the left and right of the parenthesis are the propagation directions of the incident and scattered light, respectively. Thus, the configuration $x(yz)y$ means that $\boldsymbol{q}_1 \parallel x$, $\boldsymbol{e}_1 \parallel y$, $\boldsymbol{q}_2 \parallel y$, $\boldsymbol{e}_2 \parallel z$, i.e., it corresponds to incoming light along the x direction with linear polarization y and the scattered light collected on the y direction with linear polarization z. The symbol $\bar{z}$ means the axis reversed with respect to z so that the configuration $z(\sigma^+, \sigma^-)\bar{z}$ corresponds to the σ^+ circularly-polarized incident light with the wave vector $\boldsymbol{q}_1 \parallel z$ backscattered and detected in the σ^- polarization.

QW structures lack the translational symmetry along the growth axis z. Therefore, the requirement of conservation of the wave-vector z-components should be excluded from (6.6, 6.7). Similarly, the restrictions imposed on the wave vectors by these equations are lifted in two cross-sectional directions in the case of a quantum wire and removed at all in a QD structure.

Phenomenologically, the light scattering can be described by adding to the material relation between the dielectric polarization and electric field, $P_\alpha = \chi^0_{\alpha\beta} E_\beta$, a contribution

$$\delta\chi_{\alpha\beta}(\boldsymbol{r}, t)\, E_\beta$$

caused by fluctuations of the dielectric susceptibility. If $\delta\chi \propto \exp(\mp \mathrm{i}\Omega t \pm \mathrm{i}\boldsymbol{Q}\boldsymbol{r})$, then the wave equation for the total electric field $\boldsymbol{E}$ contains an inhomogeneous term proportional to

$$\exp(-\mathrm{i}\omega_1 t \mp \mathrm{i}\Omega t)\ \exp(\mathrm{i}\boldsymbol{q}_1\boldsymbol{r} \pm \mathrm{i}\boldsymbol{Q}r)\,,$$

which serves as a source for secondary light waves. In the phenomenological description the spectral intensity of the scattered light is proportional to the squared fluctuation of the susceptibility,

$$I(\omega_2, \boldsymbol{q}_2) \propto \langle|\delta\chi(\boldsymbol{q}_1 - \boldsymbol{q}_2, \omega_1 - \omega_2)|^2\rangle\ E_0^2(\omega_1, \boldsymbol{q}_1)\,, \tag{6.9}$$

where E_0 is the amplitude of the initial wave, $\delta\chi(\boldsymbol{q}, \omega)$ is the space and time Fourier-component of the fluctuation $\delta\chi(\boldsymbol{r}, t)$, and the angular brackets denote the averaging over the energy and wave-vector distribution of quasiparticles involved in the scattering.

We start the microscopical description from the simplest resonant light scattering which is the resonant fluorescence of two-level quantum systems (atoms, impurity centers in the crystalline matrix, localized excitons, QDs etc.). The spectral intensity of the scattered light is given by

$$I(\boldsymbol{e}_2, \omega_2|\boldsymbol{e}_1, \omega_1) \propto |M|^2\delta(\omega_2 - \omega_1) \tag{6.10}$$

with the scattering matrix element being

$$M \propto \frac{(\boldsymbol{e}_2^* \cdot \boldsymbol{d}_{if})(\boldsymbol{e}_1 \cdot \boldsymbol{d}_{fi})}{\omega_0 - \omega_1 - \mathrm{i}\Gamma} E_0\,.$$

Here E_0 is the amplitude of the initial wave, $\hbar\omega_0$ is the energy spacing between the ground, $|i\rangle$, and excited, $|f\rangle$, states; $\boldsymbol{d}_{fi}$ is the dipole-moment matrix element for the optical transition $|i\rangle + \hbar\omega_1 \to |f\rangle$, the damping rate Γ is equal to $(2\tau_f)^{-1}$ with τ_f being the lifetime of the excited state $|f\rangle$ (the ground state lifetime is assumed to be infinite). Note that for the process under consideration the frequencies ω_2 and ω_1 coincide.

The expression for I can be rewritten in the equivalent form

$$I(\boldsymbol{e}_2, \omega_2|\boldsymbol{e}_1, \omega_1) \propto w_{if}^{(\mathrm{em})}\ \tau_f\ w_{fi}^{(\mathrm{abs})}\,, \tag{6.11}$$

$$w_{fi}^{(\mathrm{abs})} \propto |\boldsymbol{e}_1 \cdot \boldsymbol{d}_{fi}|^2\ E_0^2\ \frac{1}{\pi}\frac{\Gamma}{(\omega_0 - \omega_1)^2 + \Gamma^2}\,,$$

$$w_{if}^{(\mathrm{em})} \propto |\boldsymbol{e}_2^* \cdot \boldsymbol{d}_{if}|^2\ \delta(\omega_2 - \omega_1)\,.$$

Such a secondary-emission process can be considered as *light scattering* because the spectrum of the secondary radiation is tied to the initial light frequency ω_1 and shifts with shifting this frequency. On the other hand, the same process has features of the *photoluminescence* because it can be described in terms of a two-step process with a real intermediate state. Thus, the optical

phenomenon under consideration may be interpreted as both Rayleigh resonant scattering and resonant photoluminescence. Bearing this in mind they use sometimes the general term 'resonant secondary emission'. Note that, under optical excitation by a non-monochromatic light with $E_0(\omega_1)$ being a smooth function of ω_1 in the vicinity of ω_0, we obtain for the radiation spectrum

$$I(\omega_2) \propto \frac{1}{\pi} \frac{\Gamma}{(\omega_0 - \omega_2)^2 + \Gamma^2} E_0^2(\omega_0). \tag{6.12}$$

In most cases, however, the difference between the two phenomena can be justified. Indeed, in light scattering defined in the traditional way the excited states of a system are virtual, whereas in conventional photoluminescence the emission of the secondary photon is usually preceded by multiple transitions of the system between different real excited states.

In 1982, Hegarty et al. [6.2] reported for the first time a resonant enhancement of the Rayleigh scattering at the heavy-hole exciton transitions of GaAs/AlGaAs MQW structures. A systematic study of resonant Rayleigh scattering in semiconductor single QWs is presented in [6.3]. It is shown that, although the participation of propagating exciton states cannot be completely excluded, the main contribution to the resonant Rayleigh scattering comes from excitonic states localized (or confined) by 2D growth islands formed at the well interfaces during the growth process. A theory of steady-state scattering of light via 2D-excitons from a QW with rough interfaces has been developed in [6.4].

6.2 Light Scattering in Bulk Semiconductors

6.2.1 Scattering by Free Carriers

We define the differential light-scattering cross-section as

$$\frac{d^2\sigma}{d\omega d\Omega} = \frac{\hbar\omega_2}{J_1 V} \frac{\Delta W}{\Delta\omega_2 \Delta\Omega_2}\,, \tag{6.13}$$

where V is the emitting volume, the energy-flux density, J_1, of the primary radiation is related with the mean number of photons $\bar{N}_{\boldsymbol{q}_1}$ through

$$J_1 = \frac{c\hbar\omega_1}{V\sqrt{æ(\omega_1)}} \bar{N}_{\boldsymbol{q}_1}\,. \tag{6.14}$$

ΔW is the scattering rate in the frequency region $\Delta\omega_2$ and within a solid angle $\Delta\Omega_2$ inside the medium of the dielectric constant $æ_b$. Note that the quantity $d^2\sigma/d\omega d\Omega$ is defined in (6.13) as the scattering cross-section per unit volume and has the dimension $\mathrm{cm}^{-1}\mathrm{s}$ rather than $\mathrm{cm}^2\mathrm{s}$. The spectral intensity, $I(\omega_2)$, of the secondary radiation propagating in vacuum in a unit

solid angle is connected with the intensity J_1^0 incident on a semi-infinite crystal by the relation

$$I(\omega_2) = \frac{(1-R)^2}{æ(\omega_2)} \int\limits_0^\infty J_1^0 \mathrm{e}^{-(K_1+K_2)z} \frac{d^2\sigma}{d\omega d\Omega}\, dz \qquad (6.15)$$
$$= \frac{(1-R)^2 J_1^0}{æ(\omega_2)(K_1+K_2)} \frac{d^2\sigma}{d\omega d\Omega}\,.$$

Here, K_i is the absorption coefficient for the light of frequency ω_i $(i=1,2)$, R is the reflection coefficient, and the difference between $R(\omega_1)$ and $R(\omega_2)$ is neglected. For the sake of simplicity, we consider the geometry of backscattering under normal incidence of the primary wave. While writing (6.15), we have taken into account that for radiation backscattered perpendicular to the surface the ratio of the solid angles $d\Omega_2^0/d\Omega_2$ in vacuum and in the crystal is equal to the squared refractive index $æ(\omega_2)$.

In the limiting case of a rarefied plasma where the Coulomb interaction between electrons may be disregarded, one has

$$\Delta W = \frac{V q_2^2 \Delta q_2 \Delta\Omega_2}{(2\pi)^3} \frac{2\pi}{\hbar} \frac{2\pi\hbar c^2}{V æ(\omega_1)\omega_1} \bar{N}_{\boldsymbol{q}_1} \frac{2\pi\hbar c^2}{V æ(\omega_2)\omega_2} r_0^2 \left(\frac{m_0}{m^*}\right)^2$$
$$\times |\boldsymbol{e}_1 \cdot \boldsymbol{e}_2^*|^2 \sum_{\boldsymbol{k}s} f_{\boldsymbol{k}s}(1 - f_{\boldsymbol{k}+\boldsymbol{q},s})\, \delta(E_{\boldsymbol{k}+\boldsymbol{q}} - E_{\boldsymbol{k}} - \hbar\omega)\,, \qquad (6.16)$$

where s is the electron spin index, $r_0 = e^2/(m_0c^2)$ is the classical electron radius, m^* is the effective mass, $E_{\boldsymbol{k}} = \hbar^2k^2/(2m^*)$ and $f_{\boldsymbol{k}}$ is the equilibrium electron distribution function. The electron-photon interaction operator used in deriving (6.16) and written in the second-quantization representation has the following form

$$\mathcal{H}_{\text{el-phot}} = \frac{e^2}{m^*c^2} c_{\boldsymbol{q}_1} c_{\boldsymbol{q}_2}^\dagger (\boldsymbol{A}_1 \cdot \boldsymbol{A}_2^*) \sum_{\boldsymbol{k}s} a_{\boldsymbol{k}+\boldsymbol{q},s}^\dagger a_{\boldsymbol{k}s}\,, \qquad (6.17)$$

where

$$\boldsymbol{A}_i = \left(\frac{2\pi\hbar c^2}{V æ(\omega_i)\omega_i}\right)^{1/2} \boldsymbol{e}_i \qquad (i=1,2)\,,$$

$c_{\boldsymbol{q}}^\dagger, c_{\boldsymbol{q}}$ are the creation and annihilation operators for the photons and $a_{\boldsymbol{k}s}^\dagger, a_{\boldsymbol{k}s}$ are those for the electrons.

Substituting (6.14, 6.16) into (6.13) and neglecting the frequency dependence of æ, we come to

$$\frac{d^2\sigma}{d\omega d\Omega} = r_0^2 \left(\frac{m_0}{m^*}\right)^2 \left(\frac{\omega_2}{\omega_1}\right)^2 |\boldsymbol{e}_1 \cdot \boldsymbol{e}_2^*|^2\, \hbar \frac{2}{V}$$
$$\times \sum_{\boldsymbol{k}} f_{\boldsymbol{k}}(1 - f_{\boldsymbol{k}+\boldsymbol{q}}) \delta(E_{\boldsymbol{k}+\boldsymbol{q}} - E_{\boldsymbol{k}} - \hbar\omega)\,, \qquad (6.18)$$

with the factor 2 accounting for spin degeneracy.

The scattering cross-section (6.18) can be expressed in terms of the electronic susceptibility

$$\chi_{\rm el}(\omega,\boldsymbol{q}) = \frac{e^2}{q^2}\frac{2}{V}\sum_{\boldsymbol{k}}\frac{f_{\boldsymbol{k}}-f_{\boldsymbol{k}+\boldsymbol{q}}}{E_{\boldsymbol{k}+\boldsymbol{q}}-E_{\boldsymbol{k}}-\hbar(\omega+{\rm i}\Gamma)}\ . \tag{6.19}$$

Indeed, using the relation

$$f_{\boldsymbol{k}}-f_{\boldsymbol{k}+\boldsymbol{q}} = f_{\boldsymbol{k}}(1-f_{\boldsymbol{k}+\boldsymbol{q}})\left(1-{\rm e}^{-\hbar\omega/k_BT}\right)$$

valid for the equilibrium distribution and the identity

$${\rm Im}\left\{\frac{1}{\varepsilon-{\rm i}\hbar\Gamma}\right\} = \pi\delta(\varepsilon)$$

we can rewrite (6.18) as

$$\frac{d^2\sigma}{d\omega d\Omega} = r_0^2\left(\frac{m_0}{m^*}\right)^2\left(\frac{\omega_2}{\omega_1}\right)^2|\boldsymbol{e}_1\cdot\boldsymbol{e}_2^*|^2\frac{\hbar q^2}{\pi e^2}\,(1+N_\omega)\,{\rm Im}\left\{\chi_{\rm el}(\omega,\boldsymbol{q})\right\}\ , \tag{6.20}$$

where

$$N_\omega = \left[\exp\left(\hbar\omega/k_BT\right)-1\right]^{-1}\ .$$

It follows from (6.19) that, in equilibrium and for the isotropic electron spectrum, the susceptibility $\chi_{\rm el}(\omega,\boldsymbol{q})$ is independent of the direction of the wave vector $\boldsymbol{q}$. Note also that

$${\rm Im}\left\{\chi_{\rm el}(-\omega,\boldsymbol{q})\right\} = -{\rm Im}\left\{\chi_{\rm el}(\omega,\boldsymbol{q})\right\}\ .$$

In Stokes scattering the transferred frequency ω is positive and $N_\omega > 0$, whereas, in the anti-Stokes process, $\omega < 0$, $N_\omega < 0$ and $1+N_\omega = -N_{|\omega|}$. Therefore, the relation

$$\frac{(1+N_{-\omega}){\rm Im}\left\{\chi_{\rm el}(-\omega,\boldsymbol{q})\right\}}{(1+N_\omega){\rm Im}\left\{\chi_{\rm el}(\omega,\boldsymbol{q})\right\}}$$

defining the intensity ratio of the anti-Stokes and Stokes scattering lines is equal to $\exp\left(-\hbar\omega/k_BT\right)$.

Since the operator (6.17) is proportional to the Fourier component of the electron-density operator

$$\rho_{\boldsymbol{q}} = \frac{1}{V}\sum_{\boldsymbol{k}s}a^\dagger_{\boldsymbol{k}+\boldsymbol{q},s}a_{\boldsymbol{k}s}\ , \tag{6.21}$$

(6.20) gives the cross-section of light scattering by charge-density fluctuations in a rarefied plasma. With allowance made for Coulomb correlations, the

differential cross-section of scattering by charge-density fluctuations takes on the form

$$\frac{d^2\sigma}{d\omega d\Omega} = r_0^2 \left(\frac{m_0}{m^*}\right)^2 \left(\frac{\omega_2}{\omega_1}\right)^2 |\boldsymbol{e}_1 \cdot \boldsymbol{e}_2^*|^2 \frac{\hbar q^2}{4\pi\pi e^2} \times (1+N_\omega)\, æ_\infty^2 \mathrm{Im}\left\{-\frac{1}{\chi(\omega,\boldsymbol{q})}\right\}, \tag{6.22}$$

with the dielectric function

$$æ(\omega,\boldsymbol{q}) = æ_\infty + æ_{\mathrm{el}}(\omega,\boldsymbol{q})\,,\ æ_{\mathrm{el}}(\omega,\boldsymbol{q}) = 4\pi\chi_{\mathrm{el}}(\omega,\boldsymbol{q})\,. \tag{6.23}$$

For simplicity, the contribution of optical phonons is here neglected and will be discussed in the next subsection. The expressions (6.18) and (6.22) differ in the factor $æ_\infty^2/|æ(\omega,\boldsymbol{q})|^2$ accounting for the screening of the charge fluctuations appearing in the system. For a low-density plasma, $|æ_{\mathrm{el}}| \ll æ_\infty$ and this factor is close to unity. Equation (6.22) describes the scattering both from single-particle excitations with the transferred frequency $\omega = (E_{\boldsymbol{k}+\boldsymbol{q}} - E_{\boldsymbol{k}})/\hbar$ and collective plasma oscillations, or *plasmons*, whose frequency satisfies the equation

$$æ(\omega,\boldsymbol{q}) = 0\,. \tag{6.24}$$

Expression (6.17) for the operator $\mathcal{H}_{\text{el-phot}}$ describing light scattering by free electrons is valid provided the photon energy $\hbar\omega_i$ is small compared to the energy separation $E_c^0 - E_l^0$ from the other bands $l \neq c$. If this condition is not met, one has to start from a more general expression

$$\mathcal{H}_{\text{el-phot}} = r_0 c_{\boldsymbol{q}_1} c^\dagger_{\boldsymbol{q}_2} A_1 A_2 \sum_{\boldsymbol{k}ss'} \gamma_{s's} a^\dagger_{\boldsymbol{k}+\boldsymbol{q},s} a_{\boldsymbol{k}s}\,, \tag{6.25}$$

where $A_i = |\boldsymbol{A}_i|$,

$$\gamma_{s's} = (\boldsymbol{e}_1 \cdot \boldsymbol{e}_2^*)\,\delta_{s's} + \frac{1}{m_0}{\sum_l}' \left[\frac{(\boldsymbol{e}_1 \cdot \boldsymbol{p}_{cs',l})(\boldsymbol{e}_2^* \cdot \boldsymbol{p}_{l,cs})}{E_c^0 - E_l^0 - \hbar\omega_1} + \frac{(\boldsymbol{e}_2^* \cdot \boldsymbol{p}_{cs',l})(\boldsymbol{e}_1 \cdot \boldsymbol{p}_{l,cs})}{E_c^0 - E_l^0 + \hbar\omega_2}\right]. \tag{6.26}$$

In accordance with the expression of the reciprocal effective-mass tensor $m^{-1}_{\alpha\beta}$ in terms of the $\boldsymbol{k}\cdot\boldsymbol{p}$ theory, for $\hbar\omega_i \ll |E_c^0 - E_l^0|$ we obtain

$$\gamma_{s's} = \delta_{s's} \sum_{\alpha\beta} \frac{m_0}{m_{\alpha\beta}}\, e_{1\alpha} e_{2\beta}\,.$$

In crystals of cubic symmetry,

$$m_{\alpha\beta} = m^*\delta_{\alpha\beta}\,,\ \gamma_{s's} = \frac{m_0}{m^*}(\boldsymbol{e}_1 \cdot \boldsymbol{e}_2^*)\delta_{s's}$$

and (6.25) reduces to (6.17).

The matrix $\boldsymbol{\gamma}$ can be conveniently represented as a linear combination of four 2×2 matrices $\hat{I}$, σ_x, σ_y and σ_z. For zinc-blende-lattice crystals, this decomposition has the form

$$\boldsymbol{\gamma} = A(\boldsymbol{e}_1 \cdot \boldsymbol{e}_2^*)\,\hat{I} - \mathrm{i}B(\boldsymbol{e}_1 \times \boldsymbol{e}_2^*) \cdot \boldsymbol{\sigma}\,, \tag{6.27}$$

where

$$A = 1 + \frac{2|p_{cv}|^2}{3m_0}\left(\frac{2E_g}{E_g^2 - (\hbar\omega_1)^2} + \frac{E_g + \Delta}{(E_g + \Delta)^2 - (\hbar\omega_1)^2}\right)\,,$$

$$B = \frac{2|p_{cv}|^2}{3m_0}\,\hbar\omega_1\left(\frac{1}{E_g^2 - (\hbar\omega_1)^2} - \frac{1}{(E_g + \Delta)^2 - (\hbar\omega_1)^2}\right)\,.$$

While deriving these equations we neglected the difference between the frequencies ω_1 and ω_2 and included into the sum over l in (6.26) only the contributions of the upper valence bands Γ_8 and Γ_7. It was also assumed that the energies $|E_g - \hbar\omega_1|$, $|E_g + \Delta - \hbar\omega_1|$ exceed the mean electron kinetic energy, the thermal energy k_BT for the nondegenerate plasma and the Fermi energy E_F for the degenerate electron gas. Substituting (6.27) into (6.25), we obtain

$$\mathcal{H}_{\text{el-phot}} = r_0 c_{\boldsymbol{q}_1} c^\dagger_{\boldsymbol{q}_2} A_1 A_2 [A(\boldsymbol{e}_1 \cdot \boldsymbol{e}_2^*)\rho_{\boldsymbol{q}} - 2\mathrm{i}B(\boldsymbol{e}_1 \times \boldsymbol{e}_2^*) \cdot \boldsymbol{s}_{\boldsymbol{q}}]\,, \tag{6.28}$$

where the charge-density operator ρ is defined according to (6.21) and $\boldsymbol{s}_{\boldsymbol{q}}$ is the Fourier component of the electron-spin density operator

$$\boldsymbol{s}_{\boldsymbol{q}} = \frac{1}{2V}\sum_{\boldsymbol{k}s's} \boldsymbol{\sigma}_{s's} a^\dagger_{\boldsymbol{k}+\boldsymbol{q},s'} a_{\boldsymbol{k}s}\,.$$

As follows from (6.25), the light can be scattered not only by fluctuations of the electron density, but also by those of the spin density as well. The first contribution to the cross-section is described by (6.22) where the ratio m_0/m^* has to be replaced by the coefficient A. For the cross-section of spin-dependent scattering, we obtain

$$\begin{aligned}\frac{d^2\sigma}{d\omega d\Omega} &= r_0^2 B^2 \left(\frac{\omega_2}{\omega_1}\right)^2 |\boldsymbol{e}_1 \times \boldsymbol{e}_2^*|^2 \hbar \frac{2}{V}\sum_{\boldsymbol{k}} f_{\boldsymbol{k}}(1 - f_{\boldsymbol{k}+\boldsymbol{q}})\delta(E_{\boldsymbol{k}+\boldsymbol{q}} - E_{\boldsymbol{k}} - \hbar\omega) \\ &= r_0^2 B^2 \left(\frac{\omega_2}{\omega_1}\right)^2 |\boldsymbol{e}_1 \times \boldsymbol{e}_2^*|^2 \frac{\hbar q^2}{\pi e^2}\,(1 + N_\omega)\,\mathrm{Im}\{\chi_{\text{el}}(\omega, \boldsymbol{q})\}\,. \end{aligned} \tag{6.29}$$

Since the spin-density fluctuations are not accompanied by violation of neutrality, they are not screened and, therefore, the differential cross-section (6.29) does not contain the factor $\text{æ}_\infty^2/|\text{æ}(\omega, \boldsymbol{q})|^2$. It should be mentioned that (6.29) includes both the contribution due to spin-flip scattering $\boldsymbol{k}, 1/2 \to \boldsymbol{k}+\boldsymbol{q}, -1/2$ or $\boldsymbol{k}, -1/2 \to \boldsymbol{k}+\boldsymbol{q}, 1/2$ which is proportional to $|(\boldsymbol{e}_1 \times \boldsymbol{e}_2^*)_+|^2$ and $|(\boldsymbol{e}_1 \times \boldsymbol{e}_2^*)_-|^2$, respectively, and that due to spin-dependent spin-conserving

scattering $\boldsymbol{k}, s \to \boldsymbol{k}+\boldsymbol{q}, s$ ($s = \pm 1/2$) which is proportional to $|(\boldsymbol{e}_1 \times \boldsymbol{e}_2^*)_z|^2$, where z is the spin quantization axis and

$$(\boldsymbol{e}_1 \times \boldsymbol{e}_2^*)_\pm = (\boldsymbol{e}_1 \times \boldsymbol{e}_2^*)_x \pm \mathrm{i}(\boldsymbol{e}_1 \times \boldsymbol{e}_2^*)_y \,.$$

In a classical magnetic field $\boldsymbol{B} \parallel z$, the electron spin states are split and the transferred frequency in spin-flip scattering $s \to -s$ is given by

$$\hbar\omega = E_{\boldsymbol{k}+\boldsymbol{q}} - E_{\boldsymbol{k}} - 2sg\mu_B B_z \,, \tag{6.30}$$

where g is the electron g factor. In a quantizing magnetic field, contributions to light scattering arise not only from the spin-flip processes, but also from carrier transitions between the Landau levels.

Besides the above two light-scattering mechanisms related to charge- and spin-density fluctuations, there exist others, in particular, scattering by energy fluctuations taking into account the nonparabolicity of the free-carrier spectrum, by mass fluctuations in a many-valley semiconductor with anisotropic effective masses, by collective electron-hole plasma oscillations, and scattering involving carrier transitions between different subbands, e.g., between the heavy and light-hole subbands.

6.2.2 Scattering by Phonons

The main contribution to the phonon-assisted light scattering comes from the indirect interaction of photons with the lattice through the electron subsystem rather than from the direct photon-phonon interaction. Lattice vibrations produce in the medium a transient optical SL, and it is from the latter that the scattering occurs. Therefore, the efficiency of scattering by acoustic or optical phonons is inherently connected with the intensity of the corresponding fluctuations, $\delta\chi_{\alpha\beta}(\boldsymbol{r}, t)$, of the medium susceptibility, see (6.9). As a result, the differential scattering cross-section can be represented in the form

$$\frac{d^2\sigma}{d\omega d\Omega} = \left(\frac{\omega_2}{c}\right)^4 V^2 \int \frac{dt}{2\pi} \mathrm{e}^{\mathrm{i}\omega t} \langle \delta\chi^\dagger(\boldsymbol{q}, t)\delta\chi(\boldsymbol{q}, 0)\rangle \,, \tag{6.31}$$

where

$$\delta\chi(\boldsymbol{q}, t) = \frac{1}{V} e_{2\alpha}^* e_{1\beta} \int \delta\chi_{\alpha\beta}(\boldsymbol{r}, t)\mathrm{e}^{\mathrm{i}\boldsymbol{q}r} d\boldsymbol{r} \,. \tag{6.32}$$

In such a semiphenomenological description, the fluctuation $\delta\chi_{\alpha\beta}$ can be expanded in the normal coordinates of lattice vibrations written in the second-quantization representation. Consequently, $\delta\chi_{\alpha\beta}$ is an operator acting on the wave function of the phonon subsystem, the angular brackets in (6.31) denoting the thermodynamic average of the operator product.

The operator $\delta\chi_{\alpha\beta}$ involved in the calculation of the cross-section of scattering by *acoustic phonons* is a linear combination of the deformation tensor components u_{lm}, namely,

$$\delta\chi_{\alpha\beta}(\boldsymbol{r},t)=\frac{\partial\chi_{\alpha\beta}}{\partial u_{lm}}u_{lm}(\boldsymbol{r},t)\,, \tag{6.33}$$

where $\partial\chi_{\alpha\beta}/\partial u_{lm}$ is the tensor of elasto-optical coefficients,

$$u_{lm}=\frac{1}{2}\left(\frac{\partial u_l}{\partial x_m}+\frac{\partial u_m}{\partial x_l}\right)\,,$$

the displacement vector

$$\begin{aligned}&\boldsymbol{u}(\boldsymbol{r},t) \\ &=\sum_{\boldsymbol{Q}\nu}\left(\frac{\hbar}{2\rho\Omega_{\boldsymbol{Q}\nu}V}\right)^{1/2}\left(\mathrm{e}^{-\mathrm{i}\Omega_\nu t+\mathrm{i}\boldsymbol{Q}\boldsymbol{r}}\boldsymbol{e}_{\boldsymbol{Q}\nu}b_{\boldsymbol{Q}\nu}+\mathrm{e}^{\mathrm{i}\Omega_\nu t-\mathrm{i}\boldsymbol{Q}\boldsymbol{r}}\boldsymbol{e}^*_{\boldsymbol{Q}\nu}b^\dagger_{\boldsymbol{Q}\nu}\right)\,,\end{aligned} \tag{6.34}$$

ρ is the density of material, $\Omega_\nu\equiv\Omega_{\boldsymbol{Q}\nu}$ and $\boldsymbol{e}_{\boldsymbol{Q}\nu}$ are the frequency and polarization unit vector of the phonon of the ν-th branch with the wave vector $\boldsymbol{Q}$, and $b^\dagger_{\boldsymbol{Q}\nu}$ and $b_{\boldsymbol{Q}\nu}$ are the phonon creation and annihilation operators. In a piezoelectric, $\delta\chi_{\alpha\beta}$ includes, in addition to the deformation contribution, also an electro-optical term

$$\left(\partial\chi_{\alpha\beta}/\partial\mathcal{E}_n\right)_{u_{lm}=0}\mathcal{E}_n(\boldsymbol{r},t)\,,$$

where $\partial\chi_{\alpha\beta}/\partial\mathcal{E}_n$ is the electro-optical tensor and $\mathcal{E}_n$ are the components of the electric field $\boldsymbol{E}$ induced by acoustic oscillations ($n=x,y,z$). Substituting the expression for $\delta\chi_{\alpha\beta}$ into (6.31) and averaging over the equilibrium phonon distribution, we obtain for the Brillouin scattering

$$\begin{aligned}\frac{d^2\sigma}{d\omega d\Omega}=&\left(\frac{\omega_2}{c}\right)^4\frac{\hbar q^2}{2\rho\Omega_{\boldsymbol{q}\nu}}\left|\frac{\partial\tilde{\chi}_{\alpha\beta}}{\partial u_{lm}}e^*_{2\alpha}e_{1\beta}e_{\boldsymbol{q}\nu,l}\frac{q_m}{q}\right|^2 \\ &\times\left[(N_{\boldsymbol{q}\nu}+1)\delta(\omega-\omega_{\boldsymbol{q}\nu})+N_{\boldsymbol{q}\nu}\delta(\omega+\omega_{\boldsymbol{q}\nu})\right]\,.\end{aligned} \tag{6.35}$$

Here, $N_{\boldsymbol{q}\nu}$ are the phonon occupation numbers, the vector $\boldsymbol{e}_{\boldsymbol{q}\nu}$ is for simplicity considered real, and $\partial\tilde{\chi}_{\alpha\beta}/\partial u_{lm}$ includes both the deformation and electro-optical contributions

$$\frac{\partial\tilde{\chi}_{\alpha\beta}}{\partial u_{lm}}=\left(\frac{\partial\chi_{\alpha\beta}}{\partial u_{lm}}\right)_{\boldsymbol{E}=0}+\left(\frac{\partial\chi_{\alpha\beta}}{\partial\mathcal{E}_n}\right)_{u_{lm}=0}\frac{\partial\mathcal{E}_n(\boldsymbol{q})}{\partial u_{lm}(\boldsymbol{q})}\,.$$

Under ordinary conditions, $\hbar\Omega_{\boldsymbol{q}\nu}\ll k_BT$ and $N_{\boldsymbol{q}\nu},(N_{\boldsymbol{q}\nu}+1)\approx k_BT/\hbar\Omega_{\boldsymbol{q}\nu}$. Note that in (6.35) we replaced $\boldsymbol{Q}$ by $\boldsymbol{q}$ because, due to the wave-vector conservation law (6.7), $|\boldsymbol{Q}|=|\boldsymbol{q}|$.

Now we turn to light scattering by *longitudinal optical phonons* in undoped GaAs-like binary semiconductor crystals. In this case one uses the expansion

$$\delta\chi_{\alpha\beta}(\boldsymbol{r},t)=\frac{\partial\chi_{\alpha\beta}}{\partial u_l}u_l(\boldsymbol{r},t)+\frac{\partial\chi_{\alpha\beta}}{\partial\mathcal{E}_l}\mathcal{E}_l(\boldsymbol{r},t)\,, \tag{6.36}$$

where $u_l, \mathcal{E}_l$ are the components of the displacement vector $\boldsymbol{u}$ and the electric field $\boldsymbol{E}$ induced by this displacement. Usually, the vector $\boldsymbol{u}$ is defined as the relative shift of the cation and anion sublattices multiplied by $\sqrt{\bar{\rho}}$, where $\bar{\rho}$ is the reduced-mass density

$$\bar{\rho} = \rho \frac{M_a M_c}{(M_a + M_c)^2} = \frac{1}{\Omega_0} \left(\frac{1}{M_a} + \frac{1}{M_c} \right)^{-1} ,$$

$\rho = (M_a + M_b)/\Omega_0$ is the density, M_a and M_c are the anion and cation masses, and Ω_0 is the volume of the crystal primitive cell. In the second-quantization representation, the operators $\boldsymbol{u}$ and $\boldsymbol{E}$ can be written as

$$\boldsymbol{u} = \frac{\beta}{\Omega_{TO}^2 - \omega^2} \boldsymbol{E} \, , \; \beta = \Omega_{TO} \sqrt{\frac{æ_0 - æ_\infty}{4\pi}} \, , \; \boldsymbol{E} = -\nabla\varphi \, , \tag{6.37}$$

$$\varphi(\boldsymbol{r}, t) = \mathrm{i} \left(\frac{2\pi\hbar\Omega_{LO}}{V æ^*} \right)^{1/2} \sum_{\boldsymbol{Q}} \frac{1}{Q} \left(\mathrm{e}^{-\mathrm{i}\Omega t + \mathrm{i}\boldsymbol{Q}r} b_{\boldsymbol{Q}} - \mathrm{e}^{\mathrm{i}\Omega t - \mathrm{i}\boldsymbol{Q}r} b_{\boldsymbol{Q}}^\dagger \right) , \tag{6.38}$$

where $\Omega \equiv \Omega_{LO}$, $æ^* = æ_0 æ_\infty/(æ_0 - æ_\infty)$, $b_{\boldsymbol{Q}}^\dagger, b_{\boldsymbol{Q}}$ are the creation and annihilation operators for the longitudinal optical phonons. By using (6.31, 6.32, 6.36, 6.38) we come to

$$\begin{aligned} \frac{d^2\sigma}{d\omega d\Omega} = {} & \frac{2\pi\hbar\Omega_{LO}}{æ^*} \left(\frac{\omega_2}{c} \right)^4 \left| \chi'_E - \frac{S}{\Omega_{TO}} \chi'_u \right|^2 \\ & \times \left[(N_\omega + 1)\delta(\omega - \Omega_{LO}) + N_{|\omega|} \delta(\omega + \Omega_{LO}) \right] , \end{aligned} \tag{6.39}$$

where

$$S = \frac{æ_\infty}{\sqrt{4\pi(æ_0 - æ_\infty)}}$$

and

$$\chi'_E = \frac{\partial\chi_{\alpha\beta}}{\partial\mathcal{E}_l} e^*_{2\alpha} e_{1\beta} \frac{q_l}{q} \, , \; \chi'_u = \frac{\partial\chi_{\alpha\beta}}{\partial u_l} e^*_{2\alpha} e_{1\beta} \frac{q_l}{q} \, .$$

In the T_d-class crystals one has

$$\frac{\partial\chi_{\alpha\beta}}{\partial\mathcal{E}_l} = \frac{\partial\chi_{xy}}{\partial\mathcal{E}_z} |\delta_{\alpha\beta l}| \, , \; \frac{\partial\chi_{\alpha\beta}}{\partial u_l} = \frac{\partial\chi_{xy}}{\partial u_z} |\delta_{\alpha\beta l}| \, ,$$

where $\delta_{\alpha\beta l}$ is the unit antisymmetrical tensor of the third rank and x, y, z are the principal axes [100], [010], [001]. If the phonon damping Γ is taken into account, the function $\delta(\omega - \Omega_{LO})$ in (6.39) should be replaced by

$$-\frac{2}{\pi} \frac{æ^*}{\Omega_{LO}} \operatorname{Im} \left\{ \frac{1}{æ(\omega)} \right\} ,$$

where $æ(\omega)$ is the dielectric function

$$æ(\omega) = æ_\infty + æ_{\rm phon}\ ,\ æ_{\rm phon} = \frac{(æ_0 - æ_\infty)\Omega_{TO}^2}{\Omega_{TO}^2 - \omega^2 - 2i\Gamma\omega}\ . \tag{6.40}$$

In a doped semiconductor with polar optical vibrations, the dielectric function includes both the phonon and electron contributions

$$æ(\omega, \boldsymbol{q}) = æ_\infty + æ_{\rm el} + æ_{\rm phon}\ . \tag{6.41}$$

In the region of the variables q and ω satisfying the inequality $qv \ll \omega$, where v is the root-mean-square electron velocity, the electron contribution can be written in the form

$$æ_{\rm el} = -æ_\infty \frac{\omega_{\rm pl}^2}{\omega(\omega + {\rm i}\gamma)}\ , \tag{6.42}$$

where the 3D plasmon frequency is

$$\omega_{\rm pl} = \left(\frac{4\pi e^2 N}{æ_\infty m^*}\right)^{1/2}\ . \tag{6.43}$$

The equation for longitudinal waves, $æ(\omega) = 0$, has two solutions, ω_+ and ω_-, that determine the frequencies of the mixed plasmon-phonon modes. The cross-section of light scattering by each of these collective oscillations consists of an electronic contribution determined by the interaction (6.17, 6.28) and a phonon contribution associated with the deformation and electro-optical mechanisms of modulation of the dielectric susceptibility (6.36). These contributions are proportional to the polarization-dependent factors

$$T_1 = |\boldsymbol{e}_2^* \cdot \boldsymbol{e}_1|^2 \quad \text{and} \quad T_2 = \left|\,|\delta_{\alpha\beta l}|e_{2\alpha}^* e_{1\beta}\frac{q_l}{q}\right|^2\ ,$$

respectively.

For the sake of completeness, we present here also an expression for the cross-section of scattering by *transverse optical phonons* in zinc-blende-lattice crystals

$$\frac{d^2\sigma}{d\omega d\Omega} = \left(\frac{\omega_2}{c}\right)^4 \frac{\hbar}{2\Omega_{TO}} \left|\frac{\partial \chi_{xy}}{\partial u_z}\right|^2 \sum_{\nu=1,2} ||\delta_{\alpha\beta l}|e_{2\alpha}^* e_{1\beta} e_{\boldsymbol{q}\nu,l}|^2 \times [(N_\omega + 1)\delta(\omega - \Omega_{TO}) + N_{|\omega|}\delta(\omega + \Omega_{TO})]\ , \tag{6.44}$$

where the index ν enumerates two states of a transverse phonon with the polarization unit vectors $\boldsymbol{e}_{\boldsymbol{q}\nu} \perp \boldsymbol{q}$. The above equation is valid in the limiting case $q \gg \omega\sqrt{æ_\infty}/c$ realized in usual experiments on light scattering by phonons (with the exception for small-angle scattering with $q \ll q_{1,2}$). In this case the excitation of a transverse optical phonon is not accompanied by an appearance of a substantial transverse electric field due to the polariton effect, so that the electro-optical contribution in (6.36) can be disregarded.

6.3 Scattering by Intersubband and Intrasubband Excitations

We turn now to inelastic light scattering by intersubband electron excitations $e\nu \to e\nu'$ in an n-doped QW structure with the completely occupied valence-band states and partially occupied conduction-band states. As well as for the two-level quantum systems discussed in Sect. 6.1, the light scattering

$$e\nu + \hbar\omega_1 \to e\nu' + \hbar\omega_2$$

is a second-order process. It includes absorption of a primary photon accompanied by transition of an electron from the valence subband $v\nu''$ into the conduction subband $e\nu'$ followed by emission of a secondary photon and transition of an equilibrium conduction electron $e\nu$ into the empty state in the subband $v\nu''$. We assume the photon energy $\hbar\omega_1$ to lie close to the QW band gap and, therefore, take into account only resonant contribution to the second-order matrix element. Then, similarly to (6.10), we can write for the spectral intensity of scattered light

$$I(\boldsymbol{e}_2, \omega_2 | \boldsymbol{e}_1, \omega_1) \propto \sum_{i'i} |M_{i'i}|^2 f_i \, (1 - f_{i'}) \, \delta(E_{i'} + \hbar\omega_2 - E_i - \hbar\omega_1) \,, \quad (6.45)$$

$$M_{i'i} \propto E_0 \sum_{i''} \frac{\langle i'|\boldsymbol{e}_1 \cdot \hat{\boldsymbol{p}}|i''\rangle\langle i''|\boldsymbol{e}_2^* \cdot \hat{\boldsymbol{p}}|i\rangle}{E_{i'} - E_{i''} - \hbar\omega_1} \,.$$

Here $|i\rangle, |i'\rangle, |i''\rangle$ are the electron states in the subbands $e\nu$, $e\nu'$ and $v\nu''$, respectively, E_i is the electron energy in the state $|i\rangle$, $\langle i'|\hat{\boldsymbol{p}}|i''\rangle$ is the interband matrix element of the momentum operator. Taking into account (6.45) and neglecting the Coulomb interaction between the carriers and the valence-subband mixing, the differential cross-section of Raman scattering by intersubband excitations in a single QW can be presented as

$$\begin{aligned} \frac{d^2\sigma}{d\omega d\Omega} &= \frac{\hbar\omega_2}{J_1 S} \frac{\Delta W}{\Delta\omega_2 \Delta\Omega_2} \\ &= \frac{\hbar}{c^4} \left(\frac{\omega_2}{\omega_1}\right)^2 \frac{1}{S} \sum_{\nu'\nu\boldsymbol{k}} \sum_{s's} |e_{2\alpha}^* e_{1\beta} R_{\alpha\beta}(\nu' s', \nu s)|^2 \\ &\quad \times f_{\nu\boldsymbol{k}} \, (1 - f_{\nu'\boldsymbol{k}}) \, \delta(E_{e\nu'\boldsymbol{k}} + \hbar\omega_2 - E_{e\nu\boldsymbol{k}} - \hbar\omega_1) \end{aligned} \quad (6.46)$$

with S being the QW area and $\boldsymbol{R}$ being the light-scattering tensor

$$R_{\alpha\beta}(\nu' s', \nu s) = \frac{e^2}{m_0^2} \sum_{v\nu''} \frac{i_{e\nu', v\nu''} i_{e\nu, v\nu''}}{E_{e\nu'\boldsymbol{k}} - E_{v\nu''\boldsymbol{k}} - \hbar\omega_1} \sum_m p^{\beta}_{cs', vm} p^{\alpha}_{vm, cs} \,. \quad (6.47)$$

Here the index v indicates the series of valence subbands, heavy-hole, light-hole and spin-orbit-split, m is the hole spin index, $p^{\alpha}_{cs,vm}$ is the interband

matrix element of the operator $\hat{p}_\alpha$ calculated between the bulk Bloch functions, and $i_{e\nu',v\nu''}$ are the overlap integrals. We consider the backscattering geometry when the incident and scattered waves propagate in opposite directions, perpendicularly to the interface plane. Because of the wave-vector conservation, see (6.6), in this case the 2D wave vector $\boldsymbol{k}$ of an electron involved in the scattering process is conserved.

For the pair of conduction band Γ_6 and valence band Γ_7 in a semiconductor of T_d symmetry, the components

$$V_{s's}(v) = \sum_m (\boldsymbol{e}_1 \cdot \boldsymbol{p}_{cs',vm})(\boldsymbol{e}_2^* \cdot \boldsymbol{p}_{vm,cs})$$

can be presented in the following matrix form

$$\hat{V}(\text{s-o}) = \frac{1}{3}|p_{cv}|^2[\boldsymbol{e}_2^* \cdot \boldsymbol{e}_1 - \mathrm{i}\boldsymbol{\sigma} \cdot (\boldsymbol{e}_2^* \times \boldsymbol{e}_1)] \,. \tag{6.48}$$

The matrices $\hat{V}$ for transitions from the heavy- and light-hole states may be written in the simple form similar to (6.48) if the heavy-light hole mixing is ignored. In this case, one has

$$\hat{V}(\text{hh}) = \frac{1}{2}|p_{cv}|^2[\boldsymbol{e}_2^* \cdot \boldsymbol{e}_1 - e_{2z}^* e_{1z} + \mathrm{i}\sigma_z(\boldsymbol{e}_2^* \times \boldsymbol{e}_1)_z] \,,$$

$$\hat{V}(\text{lh}) = \frac{1}{6}|p_{cv}|^2[\boldsymbol{e}_2^* \cdot \boldsymbol{e}_1 + 3e_{2z}^* e_{1z} + 2\mathrm{i}\boldsymbol{\sigma} \cdot (\boldsymbol{e}_2^* \times \boldsymbol{e}_1) - 3\mathrm{i}\sigma_z(\boldsymbol{e}_2^* \times \boldsymbol{e}_1)_z] \,.$$

The diagonal and off-diagonal components of the matrix $\hat{V}$ describe the scattering from spin-conserving and spin-flip intersubband excitations, respectively.

In symmetrical QWs, the parity of electron envelope functions is conserved. Therefore it is conserved as well for scattering by intersubband excitations, e.g., the scattering is allowed for the transitions $e1 \to e3$ and forbidden for $e1 \to e2$. In real conditions, a deviation from the selection rules in parity may be due to additional scattering of the light-excited electron-hole pairs by static defects, and hybridization of the heavy and light hole states with $\boldsymbol{k} \neq 0$. Indeed, if hybridization is included, the combination $e_{2\alpha}^* e_{1\beta} R_{\alpha\beta}(\nu' s', \nu s)$ contains contributions of the type

$$e_{2z}^*(\boldsymbol{k} \cdot \boldsymbol{e}_1) \,,\; e_{2z}^*(\boldsymbol{k} \times \boldsymbol{e}_1)_z \sigma_z \,,\; (\boldsymbol{e}_2^* \times \boldsymbol{e}_1)_z(\boldsymbol{k} \cdot \boldsymbol{\sigma}) \quad \text{etc.} \,,$$

transforming according to the representation B (or Γ_2) of the D_{2d} group, see (4.17). In asymmetrical QWs, particularly in one-side δ-doped QWs, the main reason for scattering from $e2$-$e1$ intersubband transitions is asymmetrical shape of the electron envelopes $\varphi_{e\nu}(z), \varphi_{v\nu}(z)$ which allows $i_{e\nu',v\nu''}$ and $i_{e\nu,v\nu''}$ to be simultaneously nonzero.

Equation (6.46) was derived in the single-particle approximation. In this case, the transferred photon energy $\hbar\omega$ coincides with the difference between

the single-particle energies $E_{i'i} = E_{i'} - E_i$. The inclusion of Coulomb interaction between electrons results in renormalization of the intersubband excitation energy. For the $e1 \to e2$ transitions in a single QW, the renormalized energies, E_{CD} and E_{SD}, of the charge- and spin-density intersubband excitations can be written as

$$E_{CD}^2 = E_{21}^2(1 + \alpha_{21} - \beta_{21})\,, \tag{6.49}$$

$$E_{SD}^2 = E_{21}^2(1 - \beta_{21})\,. \tag{6.50}$$

The parameters α_{21}, β_{21} describe the depolarization and exchange-correlation (exciton) effects, they have been introduced in Chap. 4, see (4.12). Note that the length L_{21} in (4.13) can be also presented in the form

$$L_{21} = \int\limits_{-\infty}^{\infty} dz \left[\int\limits_{-\infty}^{z} dz' \varphi_2(z')\varphi_1(z') \right]^2 .$$

Note that as soon as the dispersion of the dielectric constant æ is taken into account the constant $æ_b$ in (4.13) should be replaced by the function $æ(\omega) = æ_\infty + æ_{\rm phon}$. As a result we obtain a mixed excitation of the intersubband plasmon and LO phonon satisfying the dispersion equation

$$\frac{\omega_{21,\rm pl}^2}{\omega_{21}^2 - \omega^2} + \frac{\Omega_{LO}^2 - \omega^2}{\Omega_{TO}^2 - \omega^2} = 0\,, \tag{6.51}$$

where $\omega_{21,\rm pl}^2$ is defined by (4.14) with $æ_b$ replaced by $æ_\infty$ and, for simplicity, the exchange-correlation correction is neglected. Equation (6.51) has two solutions

$$\omega_\pm^2 = \frac{1}{2}\left\{\omega_{21}^2 + \omega_{21,\rm pl}^2 + \Omega_{LO}^2 \right. \tag{6.52}$$

$$\left. \pm \left[\left(\omega_{21}^2 + \omega_{21,pl}^2 + \Omega_{LO}^2\right)^2 - 4\left(\omega_{21}^2\Omega_{LO}^2 + \omega_{21,\rm pl}^2\Omega_{TO}^2\right) \right]^{1/2} \right\} .$$

Figure 6.1 presents spectra of light scattering by intersubband charge- and spin-density excitations measured on a GaAs/AlGaAs SQW structure in parallel and crossed polarizations. The excitation-energy difference, $E_{CD} - E_{SD}$, is seen to exceed 2 meV. In addition, the spectra of Fig. 6.1 show single-particle intersubband excitations. In the normal-incidence backscattering geometry, the energy of these excitations coincides with the bare single-particle spacing E_{21}. In the oblique-incidence backscattering geometry, the scattered wave vector equals to $q = 2\sin\theta(\omega_1/c)$ (θ is the incidence angle) and the energies of single-particle intersubband excitations cover a continuum bounded by $E_{21} \pm \hbar q v_F$, where v_F is the Fermi velocity.

Raman scattering by collective and single-particle intersubband excitation has been observed not only in QW structures [6.5–6.13] but also in quantum

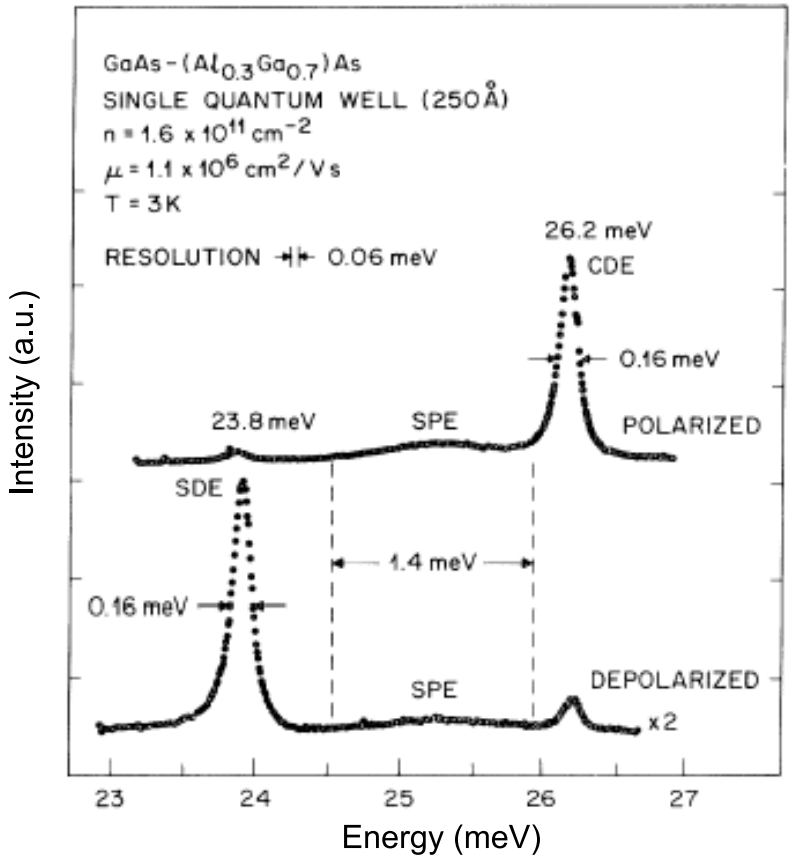

Fig. 6.1. Inelastic-light-scattering spectra of intersubband excitations of the high-mobility 2D electron gas in a GaAs/AlGaAs QW. The peaks of spin-density excitations (SDE), charge-density excitations (CDE), and single-particle excitations (SPE) are shown. From [6.5].

wires [6.14–6.16]. Decca et al. [6.17] have studied inelastic light scattering in GaAs/AlGaAs double QWs and observed excitations associated with transitions between two lowest $e1$ subbands, symmetric and antisymmetric. They have uncovered a new aspect of electron-electron interactions in the 2D electron gas in the studied structure when both subbands are densely populated, i.e. when the ratio $\eta = \Delta_{SAS}/E_F$ reaches some critical value. Here E_F is the Fermi energy and Δ_{SAS} is the symmetric-antisymmetric splitting which can be easily varied by changing the thickness and Al content of the barrier. The excitation spectra in 0D systems can be revealed in light-scattering as well.

For example, Lockwood et al. [6.17] have probed, by inelastic light scattering, shell structure and electronic excitations of many-electron QDs.

Not only inter- but also *intrasubband excitations* contribute to the light scattering from electrons in 2D and 1D nanostructures. For 2D electrons, the dispersion of plasma oscillations exhibits a square-root behavior

$$\omega_{\rm pl}^{2D}(q) = \left(\frac{2\pi e^2 N_s q}{æ_\infty m^*}\right)^{1/2} , \tag{6.53}$$

where $\boldsymbol{q}$ is the 2D plasmon wave vector. In a periodic MQW structure, the plasmon frequency depends on the 3D wave vector $\boldsymbol{Q}$ and differs from (6.53) in a structural factor [6.18]

$$\omega_{\rm pl}^{\rm MQW}(\boldsymbol{Q}) = \omega_{\rm pl}^{2D}(Q_\parallel) S^{1/2}(\boldsymbol{Q}) ,$$

$$S(\boldsymbol{Q}) = \frac{\sinh Q_\parallel d}{\cosh Q_\parallel d - \cos Q_z d} , \tag{6.54}$$

where $Q_\parallel = \sqrt{Q_x^2 + Q_y^2}$ and d is the structure period. In the weak coupling limit $Q_\parallel d \gg 1$ realized in thick-barrier MQWs or for plasmons with short wavelengths, the interaction between plasmons in different wells may be neglected, $S(\boldsymbol{Q}) \to 1$ and $\omega_{\rm pl}^{\rm MQW}(\boldsymbol{Q}) \to \omega_{\rm pl}^{2D}(Q_\parallel)$. In the strong coupling limit $Q_\parallel d \ll 1$, the plasmons are characterized by a linear dispersion law (*acoustical plasmons*)

$$\omega_{\rm pl}^{\rm MQW}(\boldsymbol{Q}) = v(Q_z) Q_\parallel$$

with the velocity

$$v(Q_z) = \left(\frac{2\pi e^2 N_s}{æ_\infty m^*} \frac{1}{1 - \cos Q_z d}\right)^{1/2} .$$

Of interest is also the particular case $(Q_z d)^2 \ll (Q_\parallel d)^2 \ll 1$, where $S(\boldsymbol{Q}) \approx 2/(Q_\parallel d)$,

$$\omega_{\rm pl}^{\rm MQW}(\boldsymbol{Q}) \approx \left(\frac{4\pi e^2 N_s}{æ_\infty m^* d}\right)^{1/2} ,$$

and the plasma oscillations regain the 3D character. Interaction of plasmons with polar optical phonons is included in (6.53,6.54) by replacing $æ_\infty$ with $æ_\infty + æ_{\rm phon}$.

The intrasubband plasmons in a QWR which correspond to oscillations of the charge density in the direction of the wire exhibits an almost linear dispersion [6.19–6.21]. For a cylindrical wire of the radius R, the dispersion of the 1D plasmon frequency in the long-wavelength limit $|q|R \ll 1$ can be presented analytically

$$\Omega_{\rm pl}^{1D}(q) = \left[\frac{2N_{1D}e^2}{æ_b m^*} \ln\left(\frac{2}{|q|R}\right)\right]^{1/2} |q| ,$$

where N_{1D} is the 1D electron density, æ$_b$ is the background dielectric constant and q is the plasmon wave vector.

6.4 Scattering by Folded Acoustic Phonons

The investigation of acoustic phonons in bulk semiconductors by light scattering spectroscopy is usually limited to the sub-meV range since the wave vector conservation only allows the observation of phonons which are very close to the Brillouin zone center, the Γ-point. In contrast to a bulk crystal, semiconductor SLs exhibit zone-folding of the bulk acoustic dispersion into minibands or minibranches, as shown in Chap. 2. Because of the artificial periodicity along the growth direction, each acoustic branch folds within the new Brillouin zone, $|Q_z| \leq \pi/d$, into a series of minibranches with forbidden minibands at the folding points $Q_z = 0, \pm\pi/d$. As a result, acoustic modes with energies of several meV appear at the superstructure Brillouin-zone center and can be easily detected in light scattering experiments.

To describe light scattering from folded acoustic phonons in terms of photoelastic mechanism, we expand, similarly to (6.32), the dielectric susceptibility fluctuation at frequency ω_1 in components of the deformation tensor

$$\delta\chi_{\alpha\beta}(\boldsymbol{r},t) = P_{\alpha\beta\lambda\mu}(z)\, u_{\lambda\mu}(\boldsymbol{r},t)\,. \tag{6.55}$$

In contrast to (6.32) written for a homogeneous semiconductor, here the elasto-optical, or photoelastic, coefficients $P_{\alpha\beta\lambda\mu} = \partial\chi_{\alpha\beta}/\partial u_{\lambda\mu}$ depend on z changing stepwise at the SL interfaces and retaining their values within each layer [6.22]. One can conveniently expand the tensor $\boldsymbol{P}$ in a Fourier series

$$\boldsymbol{P}(z) = \sum_m \boldsymbol{P}^{(m)}\, \mathrm{e}^{\mathrm{i}G_m z} \tag{6.56}$$

and the lattice displacement $\boldsymbol{u}$ in the eigenstates of folded acoustic phonons

$$\boldsymbol{u}^{(l)}_{\boldsymbol{Q}}(\boldsymbol{r}) = \mathrm{e}^{i\boldsymbol{Q}r} \sum_m \boldsymbol{u}^{(l)}_{\boldsymbol{Q}m}\, \mathrm{e}^{\mathrm{i}G_m z}\,, \tag{6.57}$$

where $G_m = 2\pi m/d$ ($m = 0, \pm 1...$), and $l = 0, \pm 1, \pm 2...$ is the folded-phonon branch index. Using (6.56, 6.57), we obtain

$$\begin{aligned}\delta\chi_{\alpha\beta}(\boldsymbol{q}) &\equiv \frac{1}{V}\int \delta\chi_{\alpha\beta}(\boldsymbol{q})\, \mathrm{e}^{\mathrm{i}\boldsymbol{q}r} d\boldsymbol{r} \\ &= \sum_m P^{(-m)}_{\alpha\beta\lambda\mu} u_{\boldsymbol{q}m,\lambda} \mathrm{i}(q_\mu + G_m\delta_{\mu z})\,.\end{aligned} \tag{6.58}$$

where $\boldsymbol{q}$ is the transferred wave vector. Bearing in mind to consider the light backscattering by longitudinal acoustic (LA) phonons in the parallel configuration $z(xx)\bar{z}$ or $z(yy)\bar{z}$, we focus on the coefficient $P_{xxzz} \equiv P_{12}$ that

relates $\delta\chi_{xx}, \delta\chi_{yy}$ with u_{zz}. Its values in the layers A and B are labelled as $P_{\rm A}$ and $P_{\rm B}$. Then the expansion (6.56) reduces to

$$P_{12}(z) = \sum_{m=-\infty}^{m=\infty} P^{(m)}\, {\rm e}^{{\rm i}G_m z}\,, \tag{6.59}$$

where

$$P^{(0)} = \frac{1}{d}\,(aP_{\rm A} + bP_{\rm B})\,,$$

$$P^{(m)} = (P_{\rm A} - P_{\rm B})\frac{1}{\pi m}\sin\frac{\pi m a}{d} \quad (m \neq 0)\,.$$

For GaAs/AlGaAs-type SLs, the modulation of photo-elastic coefficients plays a more essential role than the mixing in (6.57) of the various space harmonics. This allows to start the description of light scattering from the approximation of straight-line dispersion valid for $\varepsilon = 0$, see (2.137). In this approximation, the correlation function for fluctuations $\delta\chi_{\alpha\beta}$ in (6.31) can be evaluated by setting

$$u_z(z) = \left(\frac{\hbar}{2\rho\Omega_K V}\right)^{1/2}\left(b_K {\rm e}^{{\rm i}Kz} + b_K^\dagger {\rm e}^{-{\rm i}Kz}\right)\,. \tag{6.60}$$

Here

$$K = Q \quad \text{for } \; l = 0\,,\; K = \pm\left(\frac{2\pi|l|}{d} + |Q|\,\frac{l}{|l|}\right) \quad (l \neq 0)\,, \tag{6.61}$$

$\Omega_K = \bar{s}|K|$, b_K and $b_K^\dagger$ are the annihilation and creation operators for a phonon with the 3D wave vector $(0, 0, K)$. Notice that here K is the phonon wave vector in the extended-zone scheme and Q is that in the reduced-zone scheme. The second-order quantization allows to average correctly the square $|\delta\chi|^2$. We remind that

$$\left\langle b_K b_K^\dagger \right\rangle = 1 + N_{\Omega_K}\,,\; \left\langle b_K^\dagger b_K \right\rangle = N_{\Omega_K}\,,$$

where N_{Ω_K} is the phonon occupation number. Substituting the expansion (6.59) for P_{12} and equation (6.60) for $u_z(z)$ into (6.55) and taking into account that $u_{zz} = \partial u_z/\partial z$ we obtain

$$\delta\chi_{xx}(z) = \delta\chi_{yy}(z) = {\rm i}K\left(\frac{\hbar}{2\rho\Omega_K V}\right)^{1/2} \times \tag{6.62}$$
$$\times\,\left(b_K {\rm e}^{{\rm i}Kz} - b_K^\dagger {\rm e}^{-{\rm i}Kz}\right)\sum_m P^{(m)} {\rm e}^{{\rm i}G_m z}\,.$$

It follows then that the intensity of the light scattered from the l-th mode into the Stokes region of the spectrum can be written as

$$I(\boldsymbol{e}_2,\omega_2|\boldsymbol{e}_1,\omega_1) \propto |\boldsymbol{e}_2^*\cdot\boldsymbol{e}_1|^2\left(\frac{2\pi|l|}{d}+|Q|\,\mathrm{sign}\{l\}\right)P^{(l)2} \times (N_{\Omega_K}+1)\delta(\omega_1-\omega_2-\Omega_K)\delta_{q_1,q_2+Q}\,. \tag{6.63}$$

Thus, in the scattering spectrum, one should observe doublets $\pm|l|$ with an $|l|$-independent splitting

$$\Delta\Omega = \Omega_{|l|}-\Omega_{-|l|} = 2\bar{s}q \approx 2\frac{\bar{s}}{c}\omega_1\sqrt{æ(\omega_1)}\,, \tag{6.64}$$

where Ω_l is Ω_K for K related with l by (6.61).

The exact Stokes shift is obtained by changing Ω_K in the δ-function by the exact dispersion Ω_{lQ} of folded acoustic phonons, see (2.135). For small $|Q| \ll 2\pi/d$, the deviation from the straight-line dispersion is described by

$$\Omega_{lQ} = \frac{\bar{s}}{d}\left\{2\pi|l|+\frac{l}{|l|}\left[\varepsilon^2\sin^2\left(\frac{\Omega_l^0}{s_\mathrm{A}}a\right)+(Qd)^2\right]^{1/2}\right\}\,, \tag{6.65}$$

where $\Omega_l^0 = 2\pi|l|\bar{s}/d$ and ε is introduced in (2.136).

In (001)-grown SLs of the point symmetry D_{2d}, the folded acoustic-phonon vibrations $\pm|l|$ at $Q=0$ correspond to the irreducible representations A_1 and B_2 [6.23, 6.24]. For the above photoelastic mechanism, the mode A_1 is scattering-active whereas the mode B_2 is forbidden. Therefore, in the limit of small transferred wave vector q realized in forward Raman scattering, only one mode of the split doublet can be excited. At typical backscattering q-values the A_1 and B_2 components are mixed enough, the zone-center selection rules are relaxed, both branches $\pm|l|$ have nonzero scattering intensity well described by (6.63) and appear as doublets in the scattering spectrum. TA modes in this geometry are forbidden. Note that the doublet center-of-mass is independent of the excitation frequency ω_1 or the scattering angle, in contrast to the Brillouin scattering from the lowest branch $l=0$. Hence, the scattering by folded acoustic phonons with $l=\pm1,\pm2...$ is not called Brillouin, but Raman scattering.

The first unambiguous Raman observation of phonon folding in an artificial semiconductor SL was reported by Colvard et al. [6.25]. Figure 6.2 presents Raman scattering spectra in a GaAs/$Al_{0.3}Ga_{0.7}$As SL (a = 42 Å, b = 8 Å). In the parallel polarizations, $\boldsymbol{e}_2 \parallel \boldsymbol{e}_1$, one can see three doublets with $|l| = 1, 2, 3$. In accordance with the selection rules, there is no scattering from folded LA phonons in the crossed geometry $\boldsymbol{e}_2 \perp \boldsymbol{e}_1$. The peak at 160 cm^{-1} is attributed to 2TA scattering. Figure 6.3 shows Raman spectra in the acoustic frequency range measured in the $z(yy)\bar{z}$ configuration on hexagonal (wurtzite-lattice) GaN/$Al_{0.28}Ga_{0.72}$N SLs with three different periods [6.26]. Only the first folded doublet is observed for each sample. Here z is directed along the hexagonal c-axis. In agreement with theory, the doublet splitting is almost the same in all three cases while the shift of the doublet center-of-mass increases with decreasing the SL period. Forward and backward Raman scattering spectra are compared in [6.27]. Folded acoustic phonons in

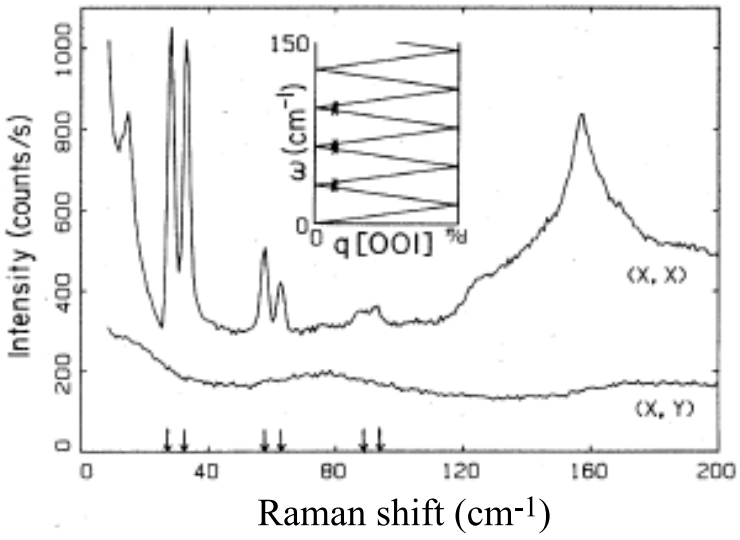

Fig. 6.2. Spectrum of light scattering by folded acoustic phonons in $GaAs/Al_{0.3}Ga_{0.65}As$ SL with $a = 42$ Å, $b = 8$ Å. Pump wavelength $\lambda_1 = 5145$ Å, T = 300 K. The inset sketches phonon dispersion by Rytov's model. The arrows specify the peak positions derived from X-ray diffraction data. From [6.25].

GaAs/AlAs SLs grown on non-(001)-oriented substrates have been studied by means of Raman scattering by Spitzer et al. [6.28]. A strong magnetic-field enhancement of Raman scattering on folded LA phonons in a SL has been reported by Mirlin et al. [6.29]. Raman spectroscopy on folded acoustic phonons in BeTe/ZnSe SLs has been applied for determination of sound velocity in BeTe [6.30]. Localized folded acoustic phonon modes in SLs with structural defect layers have been analyzed in [6.31].

Raman-scattering spectroscopy of nanocrystals or QDs [6.32, 6.33] allows to reveal the vibrational characteristics of nanoparticles that are intermediate between the bulk and molecular states. A theory of Raman scattering by acoustic vibrations in spherical nanocrystals embedded in a dielectric matrix was developed by Goupalov and Merkulov [6.34]. Since the sound velocities and the densities of the studied semiconductor nanocrystals and silicate-glass matrix differ insignificantly, the acoustic phonon modes in a nanocrystal are not completely confined, and they can transfer into continuum phonons of the matrix. This gives rise to a substantial broadening of the corresponding Raman lines. For the spheroidal fully-symmetric phonons being purely longitudinal, the line shape is given by

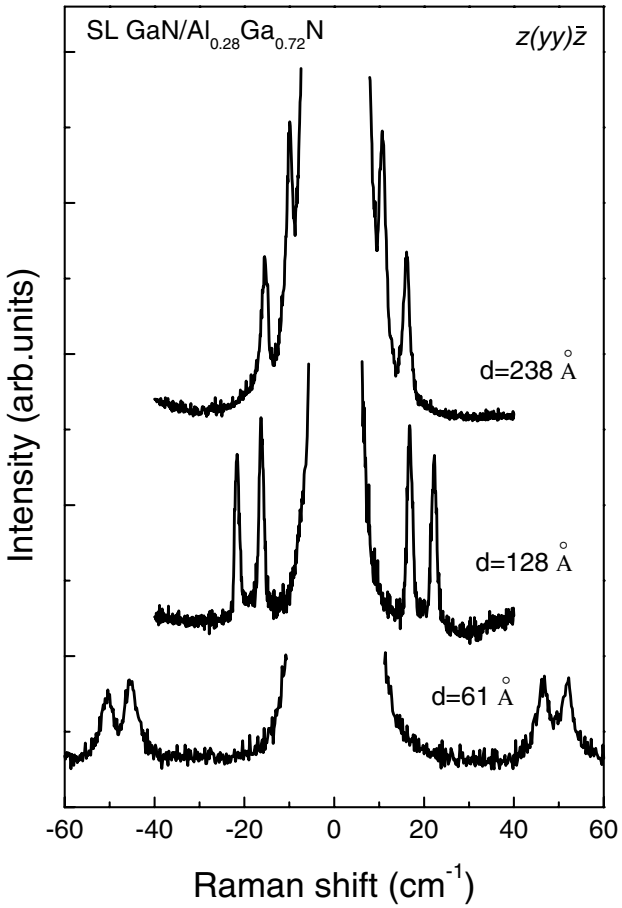

Fig. 6.3. Raman spectra of $GaN/Al_{0.28}Ga_{0.72}N$ SLs with different periods $d = 61$, 128 and 238 Å. $\lambda_1 = 488$ nm, T = 300 K. From [6.26].

$$I(\omega, R) \propto \frac{1}{R^3} I_1\left(q_{\text{in}} R\right) I_2\left(q_{\text{in}} R\right) \left(N_{|\omega|} + \frac{1 \pm 1}{2} \right) ,$$

where ω is the transferred frequency, R is the nanocrystal radius, $q_{\text{in}} = |\omega| / c_{LA}^{(\text{in})}$, $c_{LA}^{(\text{in})}$ is the longitudinal sound velocity in the nanocrystal, the sign $\pm$ corresponds to the Stokes and anti-Stokes components, and the functions $I_1(x), I_2(x)$ have been presented in [6.34]. The function $I_1\left(q_{\text{in}} R\right)$ has a broad peak at $q_{\text{in}} R \sim \pi$ with the half maximum of the same order and reflects the fact that, in the simple model of interaction of quantum-confined carriers with bulk phonons, the interaction is optimal for phonon wave vectors q of the order of π / R. The function $I_2(q_{\text{in}} R)$ has a series of narrow peaks contributed by different confined-phonon modes, the peak width being determined by the

conversion of a confined phonon into a bulk acoustic phonon propagating in the matrix.

6.5 Scattering by Confined and Interface Optical Phonons

In optical spectroscopy, in addition to the propagating folded acoustical phonons, the confined optical phonons and interface phonon modes in semiconductor QWs and SLs have received considerable attention and are reasonably well understood.

In order to provide insight into the optical phonon structure of QWs or SLs, let us consider an isolated slab of the thickness a. Optical vibrations are confined within the slab and are equivalent to those in the infinite crystal whose wave vectors are given by $\pm m\pi/a$, m being an integer. In a multilayered structure, optical phonon modes are confined within individual layers, provided that the optical branches of the constituent materials do not overlap. Particularly, this is the case of GaAs/AlAs or GaSb/AlSb SLs. The series of phonons labelled by m are termed *confined phonons*.

In the normal-incidence backscattering from (001)-grown heterostructures, only LO phonons with zero in-plane wave vector are involved. Then, in the dielectric-continuum approximation, the displacement vector $\boldsymbol{u}$ and the induced electric field $\boldsymbol{E} = -\nabla\Phi$ are parallel to the growth direction z and depend only on z. Three different models are usually employed for an analytical description of the confined optical modes [6.35]. In the *slab model* the electric field potential $\Phi(z)$ has nodes at the interfaces so that, for the A-like mode m confined in the layer A, $\Phi_m(z)$ and the LO displacement $u_m(z) \propto \mathcal{E}_z(z)$, see (6.37), take the form

$$\Phi_m(z) \propto \begin{cases} \cos\frac{m\pi z}{a}\,, & m = 1,3,5... \\ \sin\frac{m\pi z}{a}\,, & m = 2,4,6... \end{cases}\,,$$

$$u_m(z) \propto \begin{cases} \sin\frac{m\pi z}{a}\,, & m = 1,3,5... \\ -\cos\frac{m\pi z}{a}\,, & m = 2,4,6... \end{cases}\,. \tag{6.66}$$

However, with such a choice of $\Phi(z)$, the field $\mathcal{E}_z$ is discontinuous at the boundary between the layers A and B and the displacement $u_z(z)$ becomes discontinuous as well. In the *guided phonon model* [6.36], the ionic displacements vanish at the interfaces. Therefore, the electric potential and vibrational amplitudes of the confined, or "guided", modes are given by

$$\Phi_m(z) \propto \begin{cases} \sin\frac{m\pi z}{a}\,, & m = 1,3,5... \\ \cos\frac{m\pi z}{a}\,, & m = 2,4,6... \end{cases}, \qquad (6.67)$$

$$u_m(z) \propto \begin{cases} -\cos\frac{m\pi z}{a}\,, & m = 1,3,5... \\ \sin\frac{m\pi z}{a}\,, & m = 2,4,6... \end{cases}.$$

Huang and Zhu [6.37] proposed a relatively simple model (*Huang-Zhu model*) for which both electric potential and displacement have nodes at the interfaces. In this model which is now generally accepted, the scalar electric potential is given by

$$\Phi_m(z) \propto \begin{cases} \sin\frac{\pi\mu_m z}{a} + C_m\frac{z}{a}\,, & m = 3,5... \\ \cos\frac{m\pi z}{a} - (-1)^{m/2}\,, & m = 2,4,6... \end{cases}, \qquad (6.68)$$

where μ_m and C_m are constants determined by the condition that $\Phi_m(z)$ and its derivative both vanish at the interfaces $z = \pm a/2$. These conditions can be presented in the form [6.37]

$$\tan\frac{\pi\mu_m}{2} = \frac{\pi\mu_m}{2}\,,\; C_m = -2\sin\frac{\pi\mu_m}{2}\,.$$

An important point to stress is that $m = 1$ mode is excluded in (6.68) because this mode is associated with the interface mode considered in Chap. 2. For B-like confined optical modes, the thickness a is replaced by b and the point $z = 0$ is taken at the mid-point of the corresponding layer B.

The confined phonon frequency can be estimated from $\Omega_m = \Omega_{LO}(q_m)$, where $\Omega(q)$ is the bulk LO dispersion and $q_m = m\pi/a$ is the phonon quantized wave vector. For small values of q, $\Omega(q)$ can be approximated by a parabolic function

$$\Omega(q) \approx \Omega(0) - \frac{\hbar q^2}{2\bar{M}}\,,$$

where $\bar{M}$ is the parameter (the phonon effective mass) describing the dispersion of longitudinal modes.

In the D_{2d} point group, the confined LO phonons have the A_1 or B_2 symmetry. In the following we analyze the scattering selection rules for the phonon modes written in the form (6.67) or (6.68), which is equivalent. Accordingly, for the phonon modes with even m, the scalar electric potential $\Phi_m(z)$ has the A_1 symmetry and the displacement envelope function $u_m(z)$ transforms according to the representation B_2, whereas, for phonons with odd m, Φ_m and $u_m(z)$ correspond to the B_2 and A_1 representations.

Microscopically, light scattering by phonons in an undoped sample is described as a third-order process with the compound matrix element

$$\sum_{nn'} \frac{M_{0n'}\, V_{n'n}\, M_{n0}}{(E_{n'} - \hbar\omega_1 \pm \hbar\Omega - \mathrm{i}\hbar\Gamma_{n'})(E_n - \hbar\omega_1 - \mathrm{i}\hbar\Gamma_n)}\,, \tag{6.69}$$

where M_{n0} is the matrix element of the one-photon transition from the ground state of the structure, $|0\rangle$, to the excited state $|n\rangle$ which is an unbound electron-hole pair or exciton characterized by the excitation energy E_n and the damping rate Γ_n, $V_{n'n}$ is the matrix element of electron-phonon interaction including the interaction between a phonon with a hole, Ω is the phonon frequency. Note that in (6.69) only resonant contribution is taken into account. Before scattering occurs, the electronic subsystem is in the ground state $|0\rangle$, there are $N(\omega_1)$ incident photons, no photons with the frequency ω_2 and N phonons with the frequency Ω and wave vector $\boldsymbol{q}$. After scattering occurs, the electronic subsystem again finds itself in the ground state, the number of incident photons decreases by one, a photon ω_2 is created and the number of phonons is increased by one in the Stokes Raman scattering or decreased by one in the anti-Stokes process. According to (6.69), in the first step of the three-step scattering process, the incident photon excites the electronic subsystem to the intermediate state $|n\rangle$. Then a phonon induces scattering from $|n\rangle$ to another intermediate state $|n'\rangle$. Finally, the electronic subsystem returns to the ground state with emission of the scattered photon.

Since $M_{n0} \propto \boldsymbol{e}_1 \cdot \boldsymbol{j}_{n0}$ and $M_{0n'} \propto \boldsymbol{e}_2^* \cdot \boldsymbol{j}_{0n'}$ where $\boldsymbol{j}_{n0}$ is the matrix element of the current-density operator, the scattered intensity is proportional to

$$I(\boldsymbol{e}_2, \omega_2 | \boldsymbol{e}_1, \omega_1) \propto |e_{2\alpha}^* R_{\alpha\beta} e_{1\beta}|^2 [(N_\Omega + 1)\delta(\omega - \Omega) + N_\Omega \delta(\omega + \Omega)]\,, \tag{6.70}$$

where N_Ω is the phonon occupation number and we introduced the *scattering tensor*, or *Raman tensor*, defined as

$$R_{\alpha\beta} = \sum_{nn'} \frac{j_{0n'}^{\alpha}\, V_{n'n}\, j_{n0}^{\beta}}{(E_{n'} - \hbar\omega_1 \pm \hbar\Omega - \mathrm{i}\hbar\Gamma_{n'})(E_n - \hbar\omega_1 - \mathrm{i}\hbar\Gamma_n)}\,. \tag{6.71}$$

In polar semiconductors the electron-phonon interaction $\hat{V}$ can be separated into long- and short-range parts. The long-range part, $\hat{V}_F$, is the Fröhlich interaction induced by the macroscopic electric fields. On the other hand, the short-range part, $\hat{V}_{DP}$, is the deformation-potential interaction, also found in nonpolar materials.

Linearly independent components of the Raman tensor $R_{\alpha\beta}$ can be found by the method of invariants. The principal rule here reads as follows. Let $\hat{V} = \sum_i \hat{V}_i$ be the perturbation due to optical phonon modes enumerated by the index i and the operators $\hat{V}_i$ transform according to the irreducible representation D_μ of the system point group. Then, in light scattering induced by the perturbations $\hat{V}_i$, the quantities $R(D_\mu, i) = e_{2\alpha}^* R_{\alpha\beta} e_{1\beta}$ should transform under point-symmetry operations according to the representation D_μ. In particular, for perturbations of the symmetry A_1, B_2 and E in a (001)-grown QW or SL we have

$$
\begin{aligned}
R(A_1) &= R_{1,\parallel}\,|e^*_{2x}e_{1x} + e^*_{2y}e_{1y}|^2 + R_{1,zz}e^*_{2z}e_{1z}\,, \\
R(B_2) &= R_2(e^*_{2x}e_{1y} + e^*_{2y}e_{1x})\,, \\
R(E,1) &= R_3e^*_{2z}e_{1y} + R_4e^*_{2y}e_{1z}\,,\ R(E,2) = R_3e^*_{2z}e_{1x} + R_4e^*_{2x}e_{1z}\,,
\end{aligned}
\tag{6.72}
$$

where R's are scalar coefficients. To derive (6.72), we have to recall that as basis functions of the above three irreducible representations one may choose the functions x^2+y^2 or z^2 (representation A_1), xy (B_2), yz and xz (E), where $x \parallel [100]$, $y \parallel [010]$. According to (6.72), the Raman tensors $R_{\alpha\beta}(D_\mu, i)$ can be represented in the following matrix form

$$
\begin{aligned}
\boldsymbol{R}(A_1) &= \begin{bmatrix} R_{1,\parallel} & 0 & 0 \\ 0 & R_{1,\parallel} & 0 \\ 0 & 0 & R_{1,zz} \end{bmatrix},\ \boldsymbol{R}(B_2) = \begin{bmatrix} 0 & R_2 & 0 \\ R_2 & 0 & 0 \\ 0 & 0 & 0 \end{bmatrix}, \\
\boldsymbol{R}(E,1) &= \begin{bmatrix} 0 & 0 & 0 \\ 0 & 0 & R_4 \\ 0 & R_3 & 0 \end{bmatrix},\ \boldsymbol{R}(E,2) = \begin{bmatrix} 0 & 0 & R_4 \\ 0 & 0 & 0 \\ R_3 & 0 & 0 \end{bmatrix}.
\end{aligned}
\tag{6.73}
$$

For long-wavelength optical vibrations in bulk GaAs, the displacements have the F_2 symmetry. Following the symmetry reduction $T_d \to D_{2d}$, this representation of the group T_d transforms to the representations $B_2 + E$ of the group D_{2d}, compare Tables A.2 and A.5. Therefore, for the deformation-potential mechanism of electron-phonon interaction, the Raman tensors for phonons of the polarization $\boldsymbol{u} \parallel x, y, z$ in GaAs coincide with the tensors $\boldsymbol{R}(E,1)$, $\boldsymbol{R}(E,2)$ and $\boldsymbol{R}(B_2)$, where one has to set $R_2 = R_3 = R_4$. Taking into account the symmetry of confined LO modes, we conclude that the deformation-potential-induced scattering is allowed for the modes with odd m, i.e. with the even envelope $u_m(z)$.

In bulk GaAs the Fröhlich-interaction-induced scattering is "dipole-forbidden" with the matrix element $V_{n'n}$ being proportional to the phonon wave vector q. In QWs and SLs, q is replaced by the much larger confinement wave vector $q_m = m\pi/a$. This enhancement of the Fröhlich contribution allows to observe the Raman scattering by confined modes with even m, where the function $\Phi_m(z)$ is even and the function $u_m(z)$ is odd. Under optical excitation far away from all interband resonances the deformation-potential term dominates (m odd), but under resonance photoexcitation the Fröhlich term becomes stronger (m even).

Figure 6.4 shows Raman spectra for scattering by confined LO phonons measured on GaAs/AlAs SLs made up of 400 double layers with the layer thicknesses $a = 20$ Å, $b = 60$ Å. When excited under nonresonant conditions, the cross-sections of scattering by the phonons LO_{2l+1} and LO_{2l} observed in the $z(xy)\bar{z}$ and $z(xx)\bar{z}$ polarizations, respectively, are comparable in order of magnitude. In accordance with theoretical predictions, under resonant excitation, $\hbar\omega_{1,2} \approx E^0_{e1,hh1}$, one observes scattering by LO_{2l} phonons. The presence of the same LO_{2l} lines (though of a considerably lower intensity) in the crossed geometry $z(xy)\bar{z}$ can be attributed to the influence of static

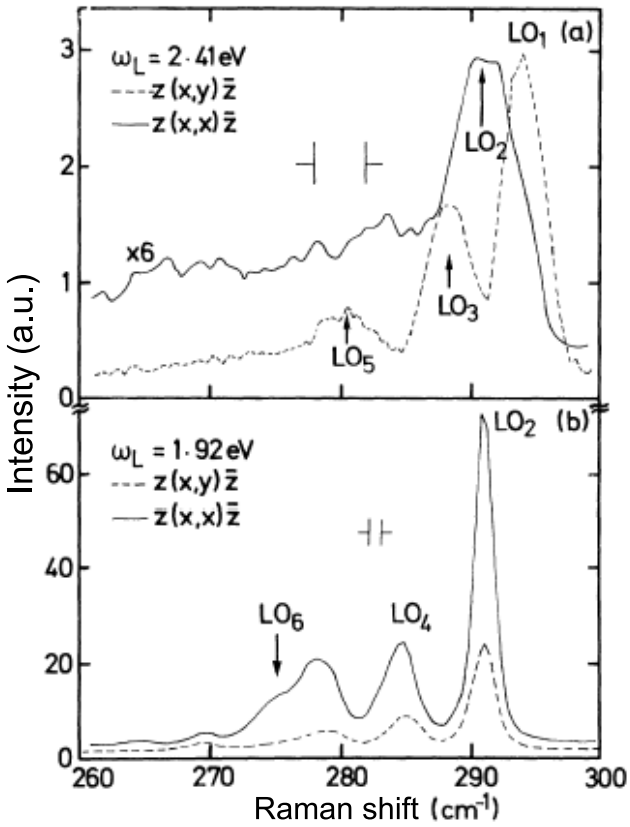

Fig. 6.4. Nonresonant (**a**) and resonant (**b**) Raman scattering spectra for GaAs/AlAs SL with $a = 20$ Å, $b = 60$ Å. The peak to the right of LO_6 phonon frequency is due to the interface mode. From [6.38].

defects on the Fröhlich interaction of carriers with optical phonons. Raman scattering from SLs and QWs has become an attractive alternative to inelastic neutron scattering for determining the bulk-phonon dispersion [6.39–6.42].

As compared to the confined optical phonons, observation of the interface modes was more difficult [6.43]. Nakayama et al. [6.44] have performed the first Raman study of the interface mode dispersion by changing the angle of incident light. A detailed investigation of interface modes was undertaken using micro-Raman backscattering from (010) and $(1\bar{1}0)$ surfaces of (001)-grown SLs [6.45]. Then it was realized that, when finite phonon dispersion is taken into account, the interface modes are partially mixed with nearby confined phonon modes [6.37, 6.46].

Most experiments on Raman scattering by confined and interface optical phonons were performed on heterostructures grown on (001)-oriented sub-

strates. However, there are many scattering studies carried out on SLs grown on differently oriented substrates, see, e.g., [6.47].

6.6 Spin-Flip Raman Spectroscopy

In electron spin-flip Raman scattering, the spin of an electron involved in the scattering process reverses and, in the presence of an external magnetic field $\boldsymbol{B}$, the incident photon energy $\hbar\omega_1$ changes to $\hbar\omega_1 - |g|\mu_B B$ and $\hbar\omega_1 + |g|\mu_B B$ for the Stokes and anti-Stokes shifted waves, respectively, where g is the electron effective g factor. Hence, spin-flip Raman scattering spectroscopy can be used for a direct measurement of g factors of electrons as well as holes or excitons in semiconductors and semiconductor nanostructures [6.33, 6.48–6.51].

According to (6.27), in cubic-symmetry semiconductors the spin-flip scattering cross-section is proportional to

$$\frac{d^2\sigma_{sf}}{d\omega d\Omega} \propto \left|(\boldsymbol{e}_1 \times \boldsymbol{e}_2^*) \times \frac{\boldsymbol{B}}{B}\right|^2 . \tag{6.74}$$

In the backscattering geometry, this selection rule allows the scattering only if the magnetic field has a nonzero component perpendicular to the light propagation direction. The same rule holds for light normally incident and backscattered from a QW structure or SL. This rule can be understood by taking into account that, in the Faraday geometry with $\boldsymbol{B} \parallel \boldsymbol{q}_1 \parallel z$, the angular momentum component projected onto the z axis should be conserved

$$s_{1z} + M_1 = s_{2z} + M_2 , \tag{6.75}$$

where s_{1z}, s_{2z} is the electron spin component $\pm 1/2$ in the initial and final states and $M_{1,2}$ is the circular-photon angular momentum component ± 1. In the spin-flip transition the electron changes the z component of its spin by $\Delta s_z = \pm 1$ whereas, in the backscattering process, the photon angular-momentum component either remains unchanged, $M_1 = M_2$, or changes by $\Delta M = \pm 2$. In both cases (6.75) is not satisfied and the scattering becomes allowed only at tilted magnetic fields when the spin quantization direction differs from that of light incidence. The spin-flip Raman scattering described by (6.74) is observed in crossed linear polarizations $z(xy)\bar{z}$, $z(yx)\bar{z}$ or parallel circular polarizations $z(\sigma^+, \sigma^+)\bar{z}$, $z(\sigma^-, \sigma^-)\bar{z}$. Note that in the notation $z(\sigma^\eta, \sigma^\lambda)\bar{z}$ the sign η or λ is determined by the sign of the angular momentum component of the incident or scattered photon on the same axis, in the following the axis z. Using this nomenclature, the conventional specular reflection of σ^η-circularly polarized light from an isotropic medium occurs in the configuration $z(\sigma^\eta, \sigma^\eta)\bar{z}$.

To illustrate the specific features of this kind of inelastic light scattering in heterostructures, we focus, in what follows, on resonant Raman scattering due to spin reversal transitions, or spin flips, of acceptor-bound holes in

QWs [6.48, 6.52, 6.53]. Sapega et al. [6.48] reported strong spin-flip-related Raman scattering in p-type GaAs/$Al_xGa_{1-x}As$ (001)-oriented MQWs in an external magnetic field. The experiment was performed in the backscattering Faraday configuration $z(\sigma^{\eta}, \sigma^{\lambda})\bar{z}$. This scattering is shown to be related to transitions within the magnetic-field-split ground state of the neutral acceptor into the $\pm 3/2$ sublevels and involves the angular-momentum reversal transitions $+3/2 \rightarrow -3/2$ or $-3/2 \rightarrow +3/2$ of a hole bound to an acceptor (peaks labelled H in Fig. 6.5). The effect exhibits resonance behavior and the scattering efficiency is significant only within a narrow frequency region between the low-energy edge of the photoluminescence spectrum and the fundamental-absorption edge of the heterostructure. The polarization of the Stokes and anti-Stokes components is found to depend on the excitation energy.

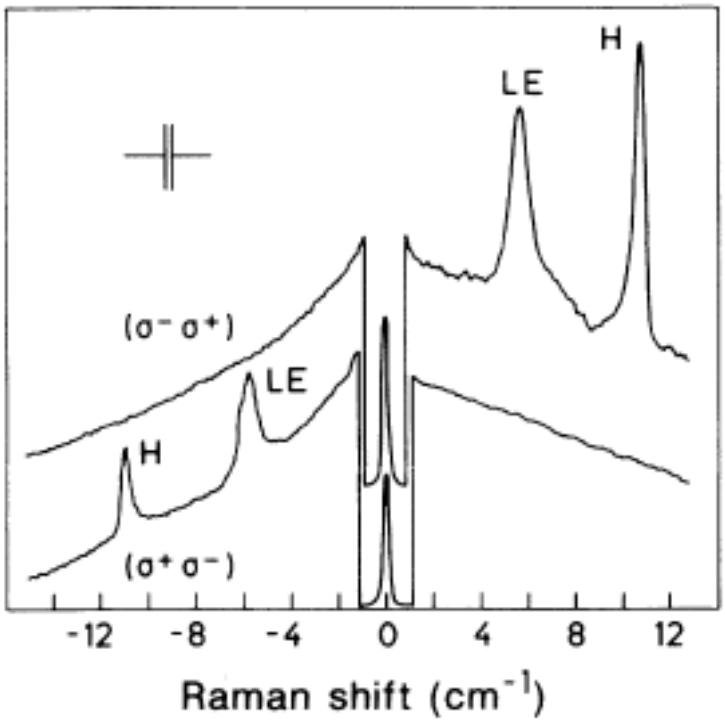

Fig. 6.5. Raman spectra of a Be-doped 46Å/110Å GaAs/$Al_xGa_{1-x}As$ MQWs measured in (σ^-, σ^+) (*upper* spectrum) and (σ^+, σ^-) (*lower*) configurations in a magnetic field $B = 10$ T and for excitation energy $\hbar\omega = 1.628$ eV. H labels the hole spin-flip Raman peak, LE the localized-exciton angular-momentum-flip peak. [6.48]

Two pure limiting cases observed at the edges of the scattering resonance profile can be discriminated in experiment. When excited with circularly polarized light at the *long-wavelength edge* of the resonance profile, the backscattering line, which is also completely polarized, is observed in the $z(\sigma^+,\sigma^-)\bar{z}$ or $z(\sigma^-,\sigma^+)\bar{z}$ configurations (Fig. 6.5) and is not seen in $z(\sigma^+,\sigma^+)\bar{z}$ or $z(\sigma^-,\sigma^-)\bar{z}$. Each of the (σ^+,σ^-), (σ^-,σ^+) spectra contains either the Stokes or anti-Stokes component in such a way that, if the $z(\sigma^-,\sigma^+)\bar{z}$ reveals a Stokes shift, then in the opposite geometry only the anti-Stokes component is present. Under circularly-polarized photoexcitation at the *short-wavelength edge*, one observes both the Stokes and anti-Stokes scattering lines simultaneously. These lines are circularly polarized with the polarization as high as 80%. The sign of the backscattered-light polarization coincides with that of specularly reflected light, thus implying that the scattering occurs predominantly in the $z(\sigma^+,\sigma^+)\bar{z}$ and $z(\sigma^-,\sigma^-)\bar{z}$ configurations. The intensity ratio of the Stokes and anti-Stokes components can be approximated with good precision by $\exp(|\hbar\omega|/k_BT)$, where ω is the transferred photon frequency, $\omega_1-\omega_2$, proportional to the magnetic field B_z. This scattering is observed only in p-type samples which confirms its interpretation as a process accompanied by a $\pm 3/2 \to \mp 3/2$ spin flip of the hole bound to an acceptor resulting from its exchange interaction with the hole in a photo-excited exciton. Thus, at least two different mechanisms are identified to contribute to the bound-hole-related spin-flip Raman scattering denoted as processes A and B and contributing, respectively, to the long- and short-wavelength edges of the resonance profile. The process B involves three-particle complexes, A^0LE, which can be considered as a localized exciton neighboring a neutral acceptor and weakly perturbed by it. The process A is associated with excitons bound to neutral acceptors, denoted A^0X, acting as intermediate states and occurs due to acoustic-phonon-assisted spin-flip of an electron in such a complex.

We remind that the neutral-acceptor ground state of Γ_8 symmetry is four-fold degenerate in a bulk GaAs crystal. Because of the confinement effect of the barriers, this state splits into two close-lying levels E_h and E_l with the hole spin components $\pm 3/2$ and $\pm 1/2$. Under a magnetic field $\boldsymbol{B}$ parallel to z each of them splits into

$$E_{h,\pm 3/2} = \pm\frac{3}{2}\, g_h \mu_B B_z\ ,\ E_{l,\pm 1/2} = \Delta_C \pm \frac{1}{2}\, g_l \mu_B B_z\ , \tag{6.76}$$

where the hole energy is referred to the zero-field position of the h level and Δ_C is the zero-field h-l splitting. In the first approximation, the values of g factors, g_h and g_l, coincide. In addition to the strongest $\pm 3/2 \to \mp 3/2$ Raman lines, two other acceptor-related lines are observed. Their polarization properties and magnetic-field behavior (Fig. 6.6) indicate that they originate from the $\pm 3/2 \to \mp 1/2$ interlevel transitions.

Now we describe in greater detail the scattering process B that occurs under resonant excitation of A^0LE complexes. In this case a $\sigma^\pm$ photon excites an A^0LE complex $|s,j,m\rangle$ with $s+j=\pm 1$, where $m=\pm 3/2$ is the

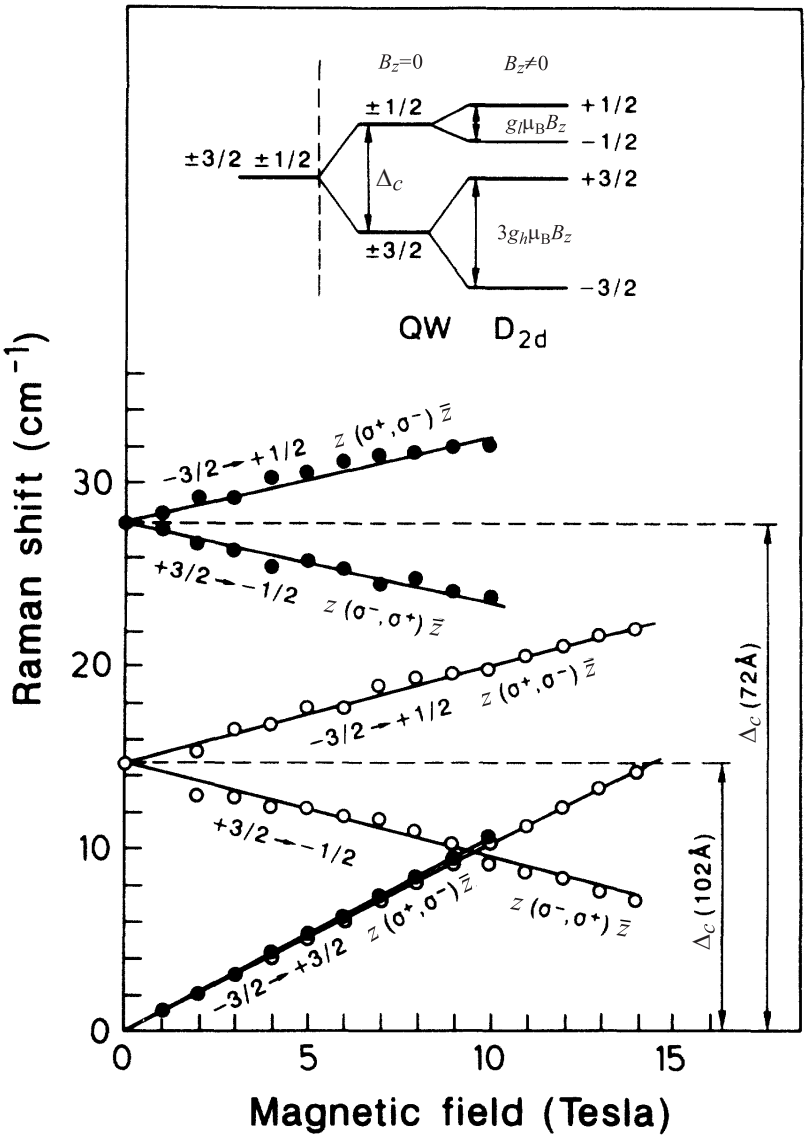

Fig. 6.6. Magnetic-field dependence of the Raman shifts of $-3/2 \rightarrow +3/2$, $+3/2 \rightarrow -1/2$, and $-3/2 \rightarrow +1/2$ lines for the 102Å/110Å (*open* circles) and 72Å/110Å (*full* circles) GaAs/Al_xGa_{1-x}As MQW structures. Δ_C denotes the "crystal-field" splitting of the acceptor ground state into two Kramers doublets at zero magnetic field. The inset shows the scheme of neutral acceptor energy levels at zero and nonzero z component of the magnetic field. [6.53]

initial spin of an acceptor-bound hole and $s = \pm 1/2$, $j = \pm 3/2$ are the spin indices of an electron and a hole in the photoexcited localized exciton. At the next stage the hole j in the exciton induces a flip $m \to -m$ of the bound hole as a result of a flip-stop-like exchange interaction described as [6.54]

$$\hat{V}_{\text{exch}} = (\Delta_{hh}\sigma_+^A + \Delta_{hh}^*\sigma_-^A)\,\sigma_z^{LE}\,, \tag{6.77}$$

where Δ_{hh} is a complex coefficient and $\sigma_\pm = (\sigma_x \pm \mathrm{i}\sigma_y)/2$. Here we use the Pauli matrices $\sigma_\alpha^{LE}, \sigma_\alpha^A$ operating on the exciton or acceptor bound-hole states $\pm 3/2$ in the basis $-\uparrow (X + \mathrm{i}Y)/\sqrt{2}, \downarrow (X - \mathrm{i}Y)/\sqrt{2}$. At the final stage the localized exciton (s, j) in the complex $|s, j, -m\rangle$ annihilates, emitting a photon of the same circular polarization, but the neighboring bound hole has now the reversed spin $-m$ and the secondary photon energy $\hbar\omega_2$ differs from the initial energy $\hbar\omega_1$ by $\pm|\Delta_A|$, where $\Delta_A = 3g_h\mu_B B_z$ with the minus and plus signs corresponding to Stokes and anti-Stokes scattering. Note that the interaction (6.77) flips the acceptor spin while leaving s and j invariant. Such an interaction becomes possible because the two holes in the complex A^0LE have different centers of in-plane localization, $\boldsymbol{\rho}_A$ and $\boldsymbol{\rho}_{LE}$. An existence of the in-plane direction $\boldsymbol{\rho}_A - \boldsymbol{\rho}_{LE}$ reduces the symmetry of the complex and allows nonzero values of Δ_{hh}. It is this reduction of symmetry that lifts the restrictions imposed by the conservation of the angular-momentum component $m + M$ in the backscattering process B. Indeed, in this process values $m_1 + M_1$ and $m_2 + M_2$ differ by ± 3 because the acceptor-bound hole changes its angular momentum by $\Delta m = \pm 3$ and the photon angular momentum is unchanged, $\Delta M = 0$.

As mentioned above, the A^0X-mediated scattering process A can be considered as a double spin flip because it includes an acoustic-phonon-induced spin flip of an electron in the photoexcited complex A^0X. The acoustic-phonon energy equals $|g_{e\|}\,\mu_B B_z|$ and, therefore, the Raman-shift energy is given by $(3g_h - g_{e\|})\mu_B B_z$, i.e. it also depends on the electron g factor. The interpretation of the process A is confirmed by measurements of Raman spectra under tilted magnetic fields [6.53] in which case the selection rules allow the A^0X-mediated backscattering without the assistance of an acoustic phonon and the Raman shift is given by $\Delta_A = 3g_h\mu_B B_z$.

Coming back to Fig. 6.5, we note that, besides the line H related to the spin flips of acceptor-bound holes, one can see a line with a smaller Raman shift, denoted as LE. It is assigned to Raman scattering by flipping the angular momentum, $s + j$, of a photoexcited localized exciton through interaction with acoustic phonons. This line is observed both in doped and undoped QWs.

The Raman shift of the interlevel scattering $\pm 3/2 \to \mp 1/2$ displays a strong dependence on the well width: $\Delta_C = 7.3$, 3.5 and 2 meV for the MQWs with the same barrier thickness $b = 110$ Å and the QW thickness $a = 46$, 72 and 102 Å, respectively. A value of Δ_C measured on one structure increases monotonically with increasing $\hbar\omega_1$. This can be understood

taking into consideration that the lower-energy excitation probes neutral acceptors with higher binding energy. Their states are less affected by barrier confinement and, hence, the splitting Δ_C is smaller.

Using Raman scattering in the absence of any applied magnetic field, Jusserand et al. [6.55–6.57] demonstrated spin splitting of the electron subbands in QW structures due to the inversion asymmetry (Chap. 2). They observed a double peak in the crossed-polarization scattering spectra of intrasubband excitations in an n-type modulation doped GaAs/$Al_xGa_{1-x}As$ SQW. Changing the angle of the sample surface normal with respect to the incident and scattered wave vectors allows one to study the scattering efficiency as a function of the transferred wave-vector in-plane component

$$\boldsymbol{q}_{\parallel} = \boldsymbol{q}_{1\parallel} - \boldsymbol{q}_{2\parallel} \, .$$

At small temperatures and $q_{\parallel} \ll k_F$, k_F being the Fermi wave vector, all involved electron states lie very close to the Fermi surface and the transferred photon frequency is given by

$$\hbar\omega = \frac{\hbar^2}{m^*} q_{\parallel} k_F \cos\left(\phi_k - \phi_q\right) \pm \Delta E(k, \phi_k) \, ,$$

where ϕ_k, ϕ_q are the azimuth angles of $\boldsymbol{k}$ and $\boldsymbol{q}_{\parallel}$, $\Delta E(k, \phi_k)$ is the spin splitting and the sign + (−) refers to the spin-down—spin-up (spin-up—spin-down) transitions. From an analysis of the Raman-scattering signal, Jusserand et al. obtained an overall understanding of the in-plane anisotropy of the electron spin splitting and showed that, in the studied samples, the Rashba contribution to the splitting induced by the asymmetric potential is of comparable magnitude to the bulk-inversion-asymmetry term.

6.7 Double Resonance in Raman Scattering

In optical spectroscopy the double resonance is defined as enhancement in the intensity of secondary emission under conditions where (i) the energies, $\hbar\omega_1$ and $\hbar\omega_2$, of the incident and secondary photons coincide with those of two interband excitations and (ii) the difference $\hbar(\omega_1 - \omega_2)$ equals to the energy of one or few optical phonons. This effect which can be described in terms of both resonant Raman scattering and resonant photoluminescence has been observed in bulk materials as well as in QW structures. The role of the interband excitations is typically played by excitons. The enhancement in the Raman scattering efficiency follows from (6.5) or (6.71) if differences $\omega_0 - \omega$, $\omega_0' - (\omega \pm \Omega)$ in (6.5) or $E_n - \hbar\omega_1$, $E_{n'} - \hbar\omega_1 \pm \hbar\Omega \equiv E_{n'} - \hbar\omega_2$ in (6.71) vanish simultaneously.

In bulk GaAs, the double Raman resonance was first realized by means of uniaxial stress, which splits the Γ_8 valence band into the heavy-hole

$(\Gamma_8, \pm 3/2)$ and light-hole $(\Gamma_8, \pm 1/2)$ subbands [6.58]. In this case the resonant intermediate states n, n' in (6.71) are the excitons formed by an electron and a heavy or light hole, respectively. In resonant magneto-Raman scattering, a double resonance occurs if the separation of the valence Landau levels in nonmagnetic semiconductors or Zeeman splitting between the states $|\Gamma_8, 3/2\rangle$, $|\Gamma_8, -3/2\rangle$ in semimagnetic semiconductors equals the energy of an optical phonon [6.59, 6.60].

Semiconductor nanostructures open new possibilities for realization of the double resonance conditions because resonant states for incoming and outgoing beams can be excitons attached to different size-quantized subbands in QWs or QWRs and quantum-confined levels in QDs. For example, Kleinman et al. [6.61, 6.62] observed the doubly resonant LO-phonon Raman scattering in GaAs/Al_xGa_{1-x}As QWs due to the following process

$$\hbar\omega_1 \rightarrow X_{e1\text{-}hh3} \rightarrow X_{e1\text{-}hh1} + \mathrm{LO} \rightarrow \hbar\omega_2 + \mathrm{LO}\,,$$

where $X_{e\nu'\text{-}hh\nu}$ denotes the exciton involving an $e\nu'$ electron and $hh\nu$ hole. In the sample containing QWs of the thickness $a = 140$ Å separated by 193-Å $x = 0.33$ alloy barriers, the excitation-energy interval between the $X_{e1\text{-}hh3}$ and $X_{e1\text{-}hh1}$ excitons is close to $\hbar\Omega_{LO}$. As the incident and scattered photons go into resonance with these excitons, a very strong single-LO peak is seen in emission, its intensity being comparable in amplitude to the main photoluminescence broad peak. The scattering peak intensity as a function of the excitation photon energy $\hbar\omega_1$ shows a sharp maximum with a width of ≈ 4.2 meV, in agreement with FWHM $= (4 \pm 1)$ meV seen for the $X_{e1\text{-}hh1}$ exciton in the photoluminescence excitation spectrum.

The double-resonance conditions can be adjusted by external fields. Calle et al. [6.63, 6.64] observed the effect setting the outgoing and incoming channels on the light-hole excitons $X_{e1\text{-}lh3}$, $X_{e1\text{-}lh1}$ and varying the strength of the applied magnetic field. Agulló-Rueda et al. [6.65] could induce a double resonance by applying a variable electric field to a GaAs/$Al_{0.35}Ga_{0.65}$As SL with $a = 30$ Å and $b = 35$ Å and forming the Stark ladder (Sect. 3.3.2). The incoming resonance was set on the intrawell interband transition $lh1, n_0 \rightarrow e1, n_0$ and outgoing resonance was tuned to the transition $lh1, n_0 \rightarrow e1, n_0 - 1$, where n_0 is the index of the Wannier-Stark localized state. According to (3.206) the corresponding value of the electric field is determined by $|e|Fd = \hbar\Omega_{LO}$ which gives $F \approx 56$ kV/cm in very good agrement with the value $F \approx 60$ kV/cm at which a maximum of the Raman intensity is observed.

In the cited studies resonant states for incoming and outgoing photons were 1s-excitons attached to different size-quantized subbands or to different Landau levels. Here we discuss one more double optical resonance. It is observed on the states $e1$-$hh1(2s)$ and $e1$-$hh1(1s)$ belonging to the same excitonic series and related to the lowest electron and hole subbands $e1$ and $hh1$ [6.66]. GaAs-based heteropairs does not suit for an observation of the $2s$-$1s$ resonance, because in the corresponding heterostructures the exciton binding energy and, hence, the $2s$-$1s$ energy separation, $\hbar\omega_{21}$, is several

times smaller than the LO phonon energy ≈ 37 meV. A suitable object is a CdTe-based QW structure because (i) in CdTe, the LO-phonon energy is relatively low, $\hbar\Omega_{LO} = 21$ meV , (ii) in QWs CdTe/$Cd_{1-x}Mn_xTe$ (or CdTe/$Cd_{1-x}Mg_xTe$) the energy spacing $\hbar\omega_{21}$ remarkably increases as a result of the quantum confinement effect and differs from $\hbar\Omega_{LO}$ just by a few meV, (iii) in the magnetic field oriented along the growth axis z, the $2s$-exciton level undergoes a strong diamagnetic blue shift and the condition $\omega_{21} = \Omega_{LO}$ is fulfilled in a moderate field $B < 10\,T$. The double $2s$-$1s$ resonance was observed in the backscattering Faraday geometry for circularly polarized analyzer and polarizer. In both photoluminescence and photoluminescence excitation spectra the intensity of the sharp 1LO-replica was found to increase rapidly with tuning to the double resonance conditions (Fig. 6.7). An important fact is that a strong 1LO-line has been observed not only in parallel circular polarizations but also in the crossed $z(\sigma^+,\sigma^-)\bar{z}$ or $z(\sigma^-,\sigma^+)\bar{z}$ configuration.

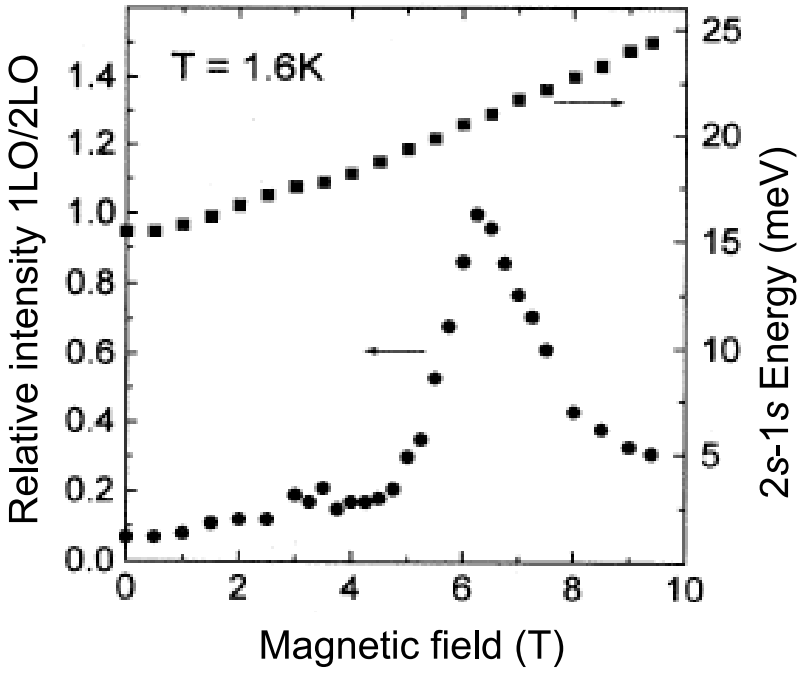

Fig. 6.7. The magnetic field dependence (*circles*) of the ratio between intensities of the 1LO- and 2LO- lines under double $2s$-$1s$ resonance observed in the CdTe/$Cd_{0.86}Mn_{0.14}Te$ 85 Å/95 Å MQW structure. *Squares* show the $2s$-$1s$ energy spacing as a function of the magnetic field. [6.66]

Let us consider two possible mechanisms of the doubly-resonant $2s$-$1s$ secondary emission. For the direct doubly-resonant one-phonon Raman scattering,

$$\hbar\omega_1 \to X_{e1\text{-}hh1}(2s, \boldsymbol{K}=0) \to X_{e1\text{-}hh1}(1s, \boldsymbol{K}=0) + \mathrm{LO} \to \hbar\omega_2 + \mathrm{LO}\,,$$

optical excitation of the $2s$ exciton is followed by the LO-phonon-assisted transition to the bottom of the $1s$-exciton subband and then by emission of a photon from the $1s$ state. However, the analysis shows that the vertical transition $2s \to 1s + \mathrm{LO}$ is ineffective. Really, in a bulk semiconductor, such a transition is forbidden in the dipole approximation, i.e. the corresponding matrix element $V^{\mathrm{LO}}_{1s,2s} \propto q_z$, where q_z is the scattered wave vector (the difference between wave vectors of the incident and secondary photons). Remind that by similar reason in resonant spectra of secondary emission of perfect crystals the 1LO-line is much weaker than the 2LO line. On the other hand, in the 2D approximation the exciton envelope function Ψ_{ns} is factorized so that

$$\Psi_{ns} = f_{ns}(\rho)\varphi_{e1}(z_e)\varphi_{h1}(z_h) \tag{6.78}$$

with the same single electron and hole envelopes $\varphi_{e1}, \varphi_{h1}$ for $1s$ and $2s$ states. Here $f_{ns}(\rho)$ is the envelope function describing the relative electron-hole motion in the (x, y) plane and $\rho = [(x_e - x_h)^2 + (y_e - y_h)^2]^{1/2}$. The condition of orthogonality between $f_{1s}(\rho)$ and $f_{2s}(\rho)$ immediately makes zero the matrix element $V^{\mathrm{LO}}_{1s,2s}$ since, for backscattering of normally-incident light, the exciton-phonon interaction operator is ρ-independent. Thus, the value of $V^{\mathrm{LO}}_{1s,2s}$ can be nonvanishing only due to the Coulomb-potential effect upon the electron or hole confinement along the z direction. Furthermore, for the direct process the exciton polarization cannot undergo a remarkable change which contradicts to the presence of the strong 1LO-line in the spectra observed in the crossed circular polarizations.

The more realistic mechanism

$$\hbar\omega_1 \to X_{e1\text{-}hh1}(2s, \boldsymbol{K}=0) \to X_{e1\text{-}hh1}(1s, \boldsymbol{K}\neq 0)$$
$$\to X_{e1\text{-}hh1}(1s, \boldsymbol{K}=0) + \mathrm{LO} \to \hbar\omega_2 + \mathrm{LO}$$

can be described as follows: the $2s$-exciton is first scattered from the bottom of the $2s$ branch to the "hot" $1s$ states characterized by large in-plane center-of-mass wave vectors, $\boldsymbol{K}$, then it is multi-scattered by elastic random potential of the heterostructure and only afterwards emits a LO-phonon. Obviously the second mechanism has more grounds to be interpreted as a luminescence rather than Raman scattering. It should be mentioned that similar static scattering processes with a large momentum transfer were suggested by Kleinman et al. [6.62] and Gubarev et al. [6.60] in order to interpret their results on doubly resonant LO-phonon-assisted secondary emission respectively in GaAs/$\mathrm{Al}_x\mathrm{Ga}_{1-x}$As QWs and bulk semimagnetic semiconductor $\mathrm{Cd}_{0.95}\mathrm{Mn}_{0.05}\mathrm{Te}$.

The concept of double resonance in Raman scattering is very productive. The double-resonance spectroscopy has been used to study the light confinement in semiconductor planar microcavities with MQWs as an active layer [6.67]. Kipp et al. [6.68] have reported on Raman scattering by electron charge- and spin-density excitations of a modulation-doped QW embedded inside a microcavity. Under conditions of optical double resonance, when both the exciting laser and the scattered light are in resonance with the cavity modes which is achieved by a variation of incidence and scattering angles, electronic excitations can be selectively enhanced. The enhancement factor between the single-resonant case, when only the incoming light is in resonance with the cavity, and the double-resonant case, when the outgoing light also is in resonance with the cavity, amounts up to three orders of magnitude. Linear and nonlinear optical properties of quantum microcavities is considered in the next chapter.

7 Nonlinear Optics

Two are better than one,
because they have a good return for
their work;
If one falls down,
his friend can help him up...
Though one may be overpowered,
two can defend themselves.

Ecclesiastes **4***: 9-12*

Many nonlinear effects can be phenomenologically described by expanding the electric polarization $\boldsymbol{P}$ in powers of the light-wave electric field

$$\begin{aligned} P_\alpha(\boldsymbol{r},t) \; &= \chi^{(1)}_{\alpha\beta}(\omega)E_\beta(\omega,\boldsymbol{k})\exp\left(\mathrm{i}\boldsymbol{k}\cdot\boldsymbol{r}-\mathrm{i}\omega t\right) \\ &+ \chi^{(2)}_{\alpha\beta\gamma}(\omega_1,\omega_2)E_\beta(\omega_1,\boldsymbol{k}_1)E_\gamma(\omega_2,\boldsymbol{k}_2)\exp\left[\mathrm{i}(\boldsymbol{k}_1+\boldsymbol{k}_2)\cdot\boldsymbol{r}-\mathrm{i}(\omega_1+\omega_2)t\right] \\ &+ \chi^{(3)}_{\alpha\beta\gamma\delta}(\omega_1,\omega_2,\omega_3)E_\beta(\omega_1,\boldsymbol{k}_1)E_\gamma(\omega_2,\boldsymbol{k}_2)E_\delta(\omega_3,\boldsymbol{k}_3) \\ &\quad\times\exp\left[\mathrm{i}(\boldsymbol{k}_1+\boldsymbol{k}_2+\boldsymbol{k}_3)\cdot\boldsymbol{r}-\mathrm{i}(\omega_1+\omega_2+\omega_3)t\right]+\;... \end{aligned} \tag{7.1}$$

Here ω_j is the frequency, $\boldsymbol{k}_j$ the wave vector, $\boldsymbol{E}(\omega_j,\boldsymbol{k}_j)$ the amplitude of the j-th constituent of the electromagnetic field. For single crystals or short-period SLs, $\boldsymbol{r}$ is the 3D radius-vector while, in QW structures, $\boldsymbol{r}$ is a vector with the components x, y, z_l, where z_l is the position of the l-th well, for instance, the coordinate of its center (the choice of point z_l within a well is arbitrary if its width a is small compared with the light wavelength). Similarly, in a QWR directed along z, the coordinates of $\boldsymbol{r}$ in (7.1) are (x_l, y_l, z), where x_l, y_l give the position of the wire in the (x, y) plane. The frequencies in (7.1) may assume both positive and negative values, the corresponding amplitudes being related through

$$\boldsymbol{E}^*(\omega,\boldsymbol{k}) = \boldsymbol{E}(-\omega,-\boldsymbol{k})\,.$$

For the sake of simplicity, we neglect in (7.1) the spatial dispersion of the susceptibility, i.e., the dependence of $\chi^{(n)}$ on $\boldsymbol{k}, \boldsymbol{k}_1, \boldsymbol{k}_2$...

The first-order susceptibility $\chi^{(1)}$ describes the conventional linear response. The second-order susceptibility $\chi^{(2)}$ describes the generation of optical harmonics at the sum or difference frequency (three-wave mixing), in particular, at $\omega_1 = \omega_2$, second-harmonic generation. The special case $\omega_1 = -\omega_2$ is considered in the next chapter devoted to photogalvanic effects. The third-order susceptibility $\chi^{(3)}$ describes a variety of phenomena, namely, third-harmonic generation (at $\omega_1 = \omega_2 = \omega_3$), two-photon absorption of a monochromatic light wave (two of the three values of ω_j coincide, the third one differing from them in sign, e.g., $\omega_2 = \omega_3 = -\omega_1$) or two monochromatic

waves (two of the three frequencies differ in sign and do not coincide with the third, e.g., $\omega_1 = -\omega_2 \neq \pm\omega_3$), a photoinduced change in the absorption or reflection of a probe beam linear in pump-beam intensity (photoabsorption or photoreflection), photoinduced gyrotropy or birefringence, four-wave mixing of three light waves $\omega_j, \boldsymbol{k}_j$ $(j = 1, 2, 3)$ accompanied by generation of a new harmonic at the frequency $\omega_1 + \omega_2 - \omega_3$ and the wave vector $\boldsymbol{k}_1 + \boldsymbol{k}_2 - \boldsymbol{k}_3$. Degenerate four-wave mixing is a particular case of the latter where two beams with the coinciding frequencies and different propagation directions, $\boldsymbol{k}_1 \neq \boldsymbol{k}_2$, interact and induce a new spatial harmonic $2\boldsymbol{k}_1 - \boldsymbol{k}_2$ or $2\boldsymbol{k}_2 - \boldsymbol{k}_1$.

In this chapter we discuss, one after another, the two-photon absorption (Sect. 7.1), biexciton optical spectroscopy (Sect. 7.2), resonant four-wave mixing (Sect. 7.3) and second-harmonic generation (Sect. 7.4) in nanostructures. Linear and nonlinear optical properties of quantum microcavities are considered in Sect. 7.5.

7.1 Two-Photon Absorption

Two-photon absorption is an elementary excitation process in which two photons simultaneously give their energies to the medium. The two quanta are chosen such that the system under study cannot absorb either quantum separately. Conservation of energy then demands that the sum of the energies of the two photons be the energy of the electronic transition.

Two-photon spectroscopy has properties that distinguish it from one-photon spectroscopy, and therefore it represents an alternative spectroscopic technique that provides valuable complementary information on the band structure of solids. Indeed, because the selection rules for two-photon transitions are different from those ruling linear absorption, the excited states which are not accessible in conventional linear optics can be observed. Also, the added opportunity in varying the relative polarization and the frequencies of the absorbed photons increases the flexibility of the two-photon technique.

For a monochromatic light wave $\boldsymbol{A} = \mathrm{e}^{-\mathrm{i}\omega t} A\boldsymbol{e} + \text{c.c.}$ propagating in a bulk intrinsic semiconductor, the second-order perturbation theory yields the two-photon transition rate in the form

$$W^{(2)}(\boldsymbol{e}, \omega) = \frac{2\pi}{\hbar} \left(\frac{eA}{cm_0} \right)^4 \sum_{\boldsymbol{k}} \sum_{cv} \left| M_{cv}^{(2)}(\boldsymbol{e}, \omega; \boldsymbol{k}) \right|^2 \delta(E_{c\boldsymbol{k}} - E_{v\boldsymbol{k}} - 2\hbar\omega) \,. \quad (7.2)$$

Here, $A, \boldsymbol{e}, \omega$ are the scalar vector-potential amplitude, polarization unit vector and frequency of the light wave, respectively, c and v are the conduction and valence band indices for which the argument of the δ-function can vanish. The second-order (composite) matrix element of the two-photon transition is defined as

$$M_{cv}^{(2)}(\boldsymbol{e}, \omega; \boldsymbol{k}) = \sum_r \frac{(\boldsymbol{e} \cdot \boldsymbol{p}_{c\boldsymbol{k}, r\boldsymbol{k}})(\boldsymbol{e} \cdot \boldsymbol{p}_{r\boldsymbol{k}, v\boldsymbol{k}})}{E_{r\boldsymbol{k}} - E_{v\boldsymbol{k}} - \hbar\omega} \,, \quad (7.3)$$

$\boldsymbol{p}_{r\boldsymbol{k},v\boldsymbol{k}}$ is the matrix element of the momentum operator taken between the Bloch states $(r,\boldsymbol{k})$ and $(v,\boldsymbol{k})$, and the index r stands for all possible intermediate states, both filled and unoccupied. Note that we take into consideration only dipole-allowed transitions and assume the photon wave vector to be zero.

In the two-quantum process described by (7.2, 7.3), the first photon is absorbed creating a virtual electron-hole pair. The absorption of the second photon then leads to the virtual state being taken into the final pair state. Here, for simplicity, we ignore the Coulomb interaction modifying the free-pair excited states into the discrete and continuum excitonic states.

The two-photon absorption coefficient $K^{(2)}$ is related to $W^{(2)}$ through

$$K^{(2)} = \hbar\omega \frac{dW^{(2)}}{dI} = 2\hbar\omega \frac{W^{(2)}}{I} \tag{7.4}$$

and with the nonlinear susceptibility, through the expression

$$K^{(2)} \propto \mathrm{Im}\left\{\chi^{(3)}_{\alpha\beta\gamma\delta}(-\omega,\omega,\omega) e^*_\alpha e^*_\beta e_\gamma e_\delta\right\} I\,.$$

Dual-beam two-photon spectroscopy employs two light sources of high and low power densities [7.1]. Usually, the pump beam is fixed and the other, the probe, is allowed to vary its frequency. The frequencies ω_1, ω_2 of the pump and probe beams are chosen to satisfy the conditions

$$\hbar\omega_1 < E_g/2\,,\ \hbar\omega_2 < E_g < \hbar\omega_1 + \hbar\omega_2\,.$$

The first condition prevents the absorption of two photons from the intense beam, i.e., $W^{(2)}(\boldsymbol{e}_1,\omega_1) = 0$. Due to low intensity of the second beam, its two-photon absorption can be ignored and, therefore, the main contribution to the interband optical transitions comes from simultaneous absorption of two photons from different beams. For the biharmonic vector potential

$$\boldsymbol{A} = \mathrm{e}^{-\mathrm{i}\omega_1 t} A_1 \boldsymbol{e}_1 + \mathrm{e}^{-\mathrm{i}\omega_2 t} A_2 \boldsymbol{e}_2 + \text{c.c.}\,,$$

the two-photon probability rate is given by

$$W^{(2)}(\boldsymbol{e}_1,\omega_1;\boldsymbol{e}_2,\omega_2) = \frac{2\pi}{\hbar}\left(\frac{e}{cm_0}\right)^4 A_1^2 A_2^2 \tag{7.5}$$
$$\times \sum_{\boldsymbol{k}} \sum_{cv} \left| M^{(2)}_{cv}(\boldsymbol{e}_1,\omega_1;\boldsymbol{e}_2,\omega_2;\boldsymbol{k}) \right|^2 \delta(E_{c\boldsymbol{k}} - E_{v\boldsymbol{k}} - \hbar\omega_1 - \hbar\omega_2)\,,$$

$$M^{(2)}_{cv}(\boldsymbol{e}_1,\omega_1;\boldsymbol{e}_2,\omega_2;\boldsymbol{k}) \tag{7.6}$$
$$= \sum_r \frac{(\boldsymbol{e}_2\cdot\boldsymbol{p}_{c\boldsymbol{k},r\boldsymbol{k}})(\boldsymbol{e}_1\cdot\boldsymbol{p}_{r\boldsymbol{k},v\boldsymbol{k}})}{E_{r\boldsymbol{k}} - E_{v\boldsymbol{k}} - \hbar\omega_1} + \frac{(\boldsymbol{e}_1\cdot\boldsymbol{p}_{c\boldsymbol{k},r\boldsymbol{k}})(\boldsymbol{e}_2\cdot\boldsymbol{p}_{r\boldsymbol{k},v\boldsymbol{k}})}{E_{r\boldsymbol{k}} - E_{v\boldsymbol{k}} - \hbar\omega_2}\,.$$

It is worth to mention that, if the light wave is quasimonochromatic, the probability rate (7.2) derived for a single laser source should be multiplied by

the correlation factor $g_2 = \langle I^2 \rangle / I^2$, where the angular brackets denote averaging over the intensity distribution (with $\langle I \rangle \equiv I$). For multimode radiation with a random phase distribution, $g_2 = 2$, and for a biharmonic wave with close frequencies, $\omega_1 \approx \omega_2$, one has

$$g_2 = 1 + 2I_1 I_2 / I^2 \,,$$

where I_1 and I_2 are intensities of the biharmonic components, the total intensity being $I = I_1 + I_2$.

Several methods are used to study two-photon absorption including measurements of the light transmission through the sample, the two-photon-absorption-induced photoluminescence and the change in the conductivity under two-photon excitation.

Transitions $v \to c$ which occur in real semiconductors can reach the final state by using any path through every intermediate state r which is available. In typical direct-gap semiconductors with electric-dipole-allowed interband optical transitions at the extremum point Γ, the two-photon absorption in the frequency region near the fundamental edge is mainly contributed by the intermediate states r in the initial and final bands, v and c, respectively. Therefore, in (7.3), both interband and intraband matrix elements of the momentum operator appear. At small values of the electron wave vector $\boldsymbol{k}$, the former matrix elements are constant whereas the latter are proportional to k. In other words, for allowed one-photon interband transitions, the two-photon transitions are "allowed-forbidden". For interband transitions near the fundamental edge E_g, the frequency dependence of the one- and two-photon transitions rates (or absorption coefficients $K^{(1)}, K^{(2)}$) is given by

$$W^{(1)}(\omega) \propto (\hbar\omega - E_g)^{1/2} \,,\; W^{(2)}(\omega) \propto (\hbar\omega_1 + \hbar\omega_2 - E_g)^{3/2} \,. \tag{7.7}$$

It is worth to mention that, in noncentrosymmetric crystals, the allowance for linear-$\boldsymbol{k}$ spin-dependent terms in the intraband electron Hamiltonians as well as the intermediate states r in the third bands different from v and c leads to an "allowed-allowed" contribution to $M_{cv}^{(2)}$. However, this contribution practically plays no essential role and can be neglected. Now, if the Coulomb interaction is taken into account and the final excited state is an exciton, then s-excitons are observed in one-photon spectra while the two-photon spectra reveal p-exciton states not accessible in linear optics.

Equations (7.2, 7.3) or (7.5, 7.6) can be used to describe two-photon absorption in nanostructures as well, while bearing in mind that the indices c, r and v should include the numbering of minibands in SLs, subbands in QWs [7.2–7.5] or QWRs [7.6, 7.7] and discrete levels in QDs [7.8, 7.9]. A unified theory for two-photon absorption spectra of Wannier–Mott excitons in a low-dimensional semiconductor of an arbitrary dimension $d = 0, 1, 2, 3$ is presented in [7.10].

In the case of a single QW, the summation in (7.2) is performed over the 2D electron wave vector $\boldsymbol{k}_\parallel$. Note that the two-photon absorption rate,

$W^{(2)}_{SQW}$, in a QW is the number of 2D electrons created per unit area per unit time. In MQWs, similarly to (4.6), the two-photon absorption coefficient is connected with $W^{(2)}_{SQW}$ by

$$K^{(2)}(\omega) = 2\hbar\omega \frac{W^{(2)}_{SQW}(\omega)}{I(a+b)} \,.$$

If the quantum-confinement energy is small compared to the band gap E_g, then the calculation of the composite matrix element $M^{(2)}_{e\nu' s,v\nu j}(\boldsymbol{k}_\parallel)$ for a QW does not require a special summation over virtual states. For instance, for two-photon transitions between simple bands v, Γ_7 and c, Γ_6 in a GaAs-based QW, one has

$$M^{(2)}_{e\nu' s,v\nu j}(\boldsymbol{k}_\parallel) = \int \varphi_{e\nu'}(z) M^{(2)}_{cs,vj}(\boldsymbol{k}_\parallel, \hat{k}_z) \varphi_{h\nu'}(z)\, dz \,, \tag{7.8}$$

where $\hat{k}_z = -\mathrm{i}\partial/\partial z$ and $M^{(2)}_{cs,vj}(\boldsymbol{k}_\parallel, k_z) \equiv M^{(2)}_{cs,vj}(\boldsymbol{k})$ is the matrix element entering (7.2). Optical transitions between the valence and conduction subbands with coinciding index ν belong to allowed-forbidden type and, at small $k_\parallel$, $M^{(2)}_{e\nu s,v\nu j}(\boldsymbol{k}_\parallel) \propto k_\parallel$. The optical transitions with $\Delta\nu \equiv \nu' - \nu = \pm 1$ are forbidden for one-photon absorption and allowed-allowed for two-photon absorption. Bearing this in mind, we come to conclusion that, in a 2D nanostructure, the exponents 1/2 and 3/2 in the frequency dependence of the transition rates (7.7) are changed, namely

$$W^{(1)}_{2D}(\mathrm{a}, \omega) \propto (\hbar\omega - E_g)^0 = \mathrm{const} \,,\; W^{(2)}_{2D}(\text{a-f}, \omega) \propto \hbar\omega_1 + \hbar\omega_2 - E_g \tag{7.9}$$

for band-to-band optical transitions with $\Delta\nu = 0$, and

$$W^{(1)}_{2D}(\mathrm{f}, \omega) \propto \hbar\omega - E_g \,,\; W^{(2)}_{2D}(\text{a-a}, \omega) \propto (\hbar\omega_1 + \hbar\omega_2 - E_g)^0 = \mathrm{const} \tag{7.10}$$

for transitions with $\Delta\nu = \pm 1$. Here the abbreviations "a", "f", "a-f" and "a-a" stand for "allowed", "forbidden", "allowed-forbidden" and "allowed-allowed", respectively.

Figure 7.1 presents one-beam two-photon excitation spectra of the photoluminescence due to recombination of the exciton $e1$-$hh1(1s)$ in GaAs/AlGaAs MQWs for two polarizations $\boldsymbol{e} \perp z$ (a), and $\boldsymbol{e} \parallel z$ (b). At the same time, one of the curves in Fig. 7.1a shows the frequency dependence of one-photon photocurrent with a clearly pronounced feature at the resonance frequency of the exciton $e1$-$hh1(1s)$, or $H1$-$C1(1s)$ in notation of [7.11]. In accordance with the selection rules for allowed-forbidden two-photon excitation of excitons, the strongly one-photon-allowed $1s$ state of the $e1$-$hh1$ exciton is absent in the two-photon spectrum. The onset of two-photon absorption occurs at the $2p$-exciton feature shown as the shaded area in Fig. 7.1a. The $2p$ assignment is confirmed by the weak $2s$-exciton feature seen in the linear spectrum.

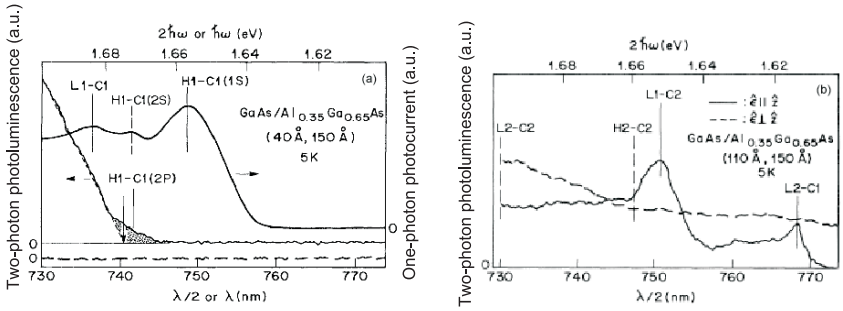

Fig. 7.1. (**a**) Single-photon (right scale) and two-photon (left scale) light absorption spectra in $GaAs/Al_{0.35}Ga_{0.65}As$ MQW structure. Single-photon spectrum was measured at normal incidence ($\boldsymbol{e} \perp z$). The dotted line below shows that for the sample with $a = 40$ Å there is no two-photon absorption in $\boldsymbol{e} \parallel z$ polarization within the wavelength range studied. Vertical lines indicate the predicted positions of exciton resonances. The vertical arrow indicates the threshold of $hh1 \rightarrow e1$ intersubband transitions. (**b**) Two-photon light absorption spectra for a similar structure but with wider QWs ($a = 110$ Å). The solid and dotted lines were measured in $\boldsymbol{e} \parallel z$ and $\boldsymbol{e} \perp z$ polarizations, respectively. The solid and dotted vertical lines indicate predicted positions of exciton resonances which are active, accordingly, in two-photon allowed-forbidden and one-photon allowed transitions. From [7.11].

The linear increase of two-photon absorption at higher energy as well as the plateau seen in linear absorption is in agreement with (7.9) for $d = 2$.

In the polarization $\boldsymbol{e} \parallel z$, other properties specific to the quantum confinement become apparent. In this case the two-photon transitions between subbands with the same index ν are not allowed, see (4.3). The $1s$-$hh2$ transition is also suppressed because of the selection rules for optical transitions from heavy-hole-subbands (Table 2.2). Therefore, for $\boldsymbol{e} \parallel z$, the onset of two-photon absorption occurs at the $e1$-$lh2$ transition. The next allowed transition is from $lh1$ to $e2$. The excitonic peaks $e1$-$lh2(1s)$ and $e2$-$lh1(1s)$ are followed by plateaus due to allowed-allowed two-photon transitions into the corresponding continuum states, in contrast to the linear frequency dependence for the $e1$-$hh1$ allowed-forbidden transitions.

The above selection rules are valid for symmetrical QWs. Shimizu [7.3] discussed what changes are expected in the two-photon spectra if one applies a static electric field F normal to the interface plane. In addition to the red shift due to the quantum-confined Stark effect (Sect. 3.4.1), selection rules for $\nu' - \nu$ are removed, since F causes parity mixing in subband envelope functions. An experimental study of electric-field-induced changes in the two-photon absorption spectra is performed by Fujii et al. [7.12]. Particularly, in agreement with theory, they observed growth and redshift of the exciton peak $1e$-$lh1(1s)$ which vanishes at zero bias.

Fröhlich et al. [7.13] performed two-photon magnetoabsorption measurements in GaAs/AlGaAs QW structures using as an intense radiation source a CO_2 laser with the photon energy $\hbar\omega_1 = 0.117$ eV that is much smaller than the band gap E_g. In these conditions, the transitions playing the dominant role in two-photon absorption are $v + \hbar\omega_2 \to c + \hbar\omega_1 \to c$ in which case the photon $\hbar\omega_2$ is absorbed at the first step, and $v + \hbar\omega_1 \to v + \hbar\omega_2 \to c$, where the interband transition is also induced by the photon $\hbar\omega_2$, and the intermediate states lie in the valence band. As a result, the principal contribution to the composite matrix element $M^{(2)}_{cs,vj}(\boldsymbol{k}_\parallel, \hat{k}_z)$ in (7.8) comes from the term proportional to $(\boldsymbol{e}_1 \cdot \boldsymbol{k}_\parallel)\boldsymbol{e}_2$. Therefore, one has the following selection rules for the transitions $hh1 \to e1$ for circularly polarized CO_2 radiation: $N_c - N_v = 1$ for σ_+ polarization, and $N_c - N_v = -1$ for σ_- polarization, where $N_{c,v}$ are the Landau-level indices in the conduction and valence subbands. The two-photon selection rules for inter-Landau-level transitions allowed Fröhlich et al. to determine the electron and hole cyclotron frequencies separately and, therefore, the effective masses m_e and m_{hh}.

Cingolani et al. [7.6] studied two-photon absorption in GaAs/AlGaAs quantum well wires of the 100Å×600Å cross-section along the x and y confined directions. In the studied sample, the wire width, L_y, along y is roughly 4 times longer than the 2D-exciton Bohr radius. Therefore, $1s$-excitons behave almost like 2D particles quantized as a whole along y while $2p$-excitons, having a larger extent of the relative motion, exhibit almost 1D character. The experiment [7.6] provides evidence for the strongly anisotropic selection rules in the in-plane polarizations $\boldsymbol{e} \parallel y$ and $\boldsymbol{e} \parallel z \perp y$. In particular, in the $\boldsymbol{e} \parallel z$ geometry the matrix elements of the two-photon process $(hh1, n_y) \to (e1, n'_y)$ do not vanish only for transitions with $n'_y = n_y$, where n_y is the index of lateral confinement, and are proportional to k_z (allowed-forbidden transition). Conversely, for $\boldsymbol{e} \parallel y$ only allowed-allowed transitions with $\Delta n_y \equiv n'_y - n_y \neq 0$ are possible. In terms of the $e1$-$hh1(1s)$ and $e1$-$hh1(2p)$ excitonic final states, this means that $1s$-excitons are excited in the $\boldsymbol{e} \parallel y$ geometry for $\Delta n_y \neq 0$ two-photon transitions whereas $2p$-excitons are accessible for $\Delta n_y = 0$ two-photon transitions in the polarization $\boldsymbol{e} \parallel z$.

For an array of spherical QDs randomly distributed in the 3D medium, one can introduce the effective absorption coefficient $K^{(2)}$ which is related to the two-photon transition rate, $W^{(2)}_{QD}$, in a single dot by

$$K^{(2)}(\omega) = 2\hbar\omega \frac{N}{I} \int dR f(R) W^{(2)}_{QD}(\omega) \,.$$

Here N is the concentration of QDs, R is the dot radius and $f(R)$ is the size distribution function. Analytical expressions for the absorpion coefficient $K^{(2)}(\omega)$ are derived by Fedorov et al. [7.9] for the strong confinement regime and the Lifshits-Slezov distribution

$$f(R) = \begin{cases} \frac{3^4}{2^{5/3}} \frac{\mathcal{R}^2}{R_0} \frac{\exp\left[1-(1-2\mathcal{R}/3)^{-1}\right]}{(\mathcal{R}+3)^{7/3}(3/2-\mathcal{R})^{11/3}} & \text{if} \quad \mathcal{R} < \frac{3}{2} \,, \\ 0 & \text{if} \quad \mathcal{R} > \frac{3}{2} \,, \end{cases}$$

where $\mathcal{R} = R/R_0$ and R_0 is the average QD radius.

7.2 Biexcitonic Nonlinearity

In nonlinear optics, there are two fundamentally different mechanisms of biexciton photogeneration. The first mechanism that dominates in studies of biexcitons in long-time scale measurements, e.g., photoluminescence measurements, is the binding of two incoherent excitons from a population of excitons. It is described by using the kinetic theory and calculating the exciton distribution function and the generation rate of biexcitons. It should be mentioned that generation of two spatially separated uncorrelated excitons and subsequent biexcitonic binding is possible only in systems with at least one direction of free motion, in bulk semiconductors and QW or QWR structures, but not in QDs. In the other mechanism, biexcitons are generated through a coherent two-photon excitation. Here we consider the latter mechanism on the basis of a three-level model including the ground state $|0\rangle$, the excitonic state $|X\rangle$ and the biexciton state $|XX\rangle$ [7.14, 7.15]. Taking into account the biexcitonic nonlinearity, the linear equation (3.44) for the exciton averaged polarization $P \equiv P_X$ in a QW is extended to

$$(\omega_0 - \omega - \mathrm{i}\Gamma)P_X = \xi\Gamma_0 E + \gamma_{\mathrm{bi}} B E^* \,, \tag{7.11}$$

where Γ, ξ, Γ_0 are the same parameters as in (3.44), B is the amplitude of the biexcitonic wave function, and γ_{bi} is proportional to the matrix element of the photon-induced exciton-biexciton transition. In addition to (7.11), an independent equation for B should be written. It has the form

$$[2(\omega_0 - \omega) - \delta_{\mathrm{bi}} - \mathrm{i}\Gamma_{\mathrm{bi}}]\, B = \gamma_{\mathrm{bi}} P_X E \,, \tag{7.12}$$

where $\hbar\delta_{\mathrm{bi}} \equiv \varepsilon_{\mathrm{bi}}, \Gamma_{\mathrm{bi}}$ are the biexciton binding energy and damping rate. Moreover, the relation (3.40) between E and P_X must be generalized to

$$E = E_0 + \frac{\mathrm{i}}{\xi}\,(P_X + P_{XX}) \,, \tag{7.13}$$

where $P_{XX} = (\gamma_{\mathrm{bi}}/\xi\Gamma_0) B P_X^*$ is the dielectric polarization due to the biexciton-exciton optical transition.

Assuming $\Gamma_0 \ll \Gamma$ we can consider E as an external electric field. Then, in the lowest nonvanishing approximation, the biexciton amplitude under single-beam optical excitation is given by

$$B \approx \frac{\xi\Gamma_0\gamma_{\mathrm{bi}}E^2}{(\omega_0 - \omega - \mathrm{i}\Gamma)\,[2(\omega_0 - \omega) - \delta_{\mathrm{bi}} - \mathrm{i}\Gamma_{\mathrm{bi}}]}$$

and, therefore,

$$|B|^2 = 2\pi\tau_{\rm bi}\left|\frac{\xi\Gamma_0\gamma_{\rm bi}E^2}{\omega_0-\omega-{\rm i}\Gamma}\right|^2 \Delta(2\omega_0-\delta_{\rm bi}-2\omega)\,.$$

Here we introduced the biexciton relaxation time $\tau_{\rm bi} = (2\Gamma_{\rm bi})^{-1}$ and the smoothed δ-function

$$\Delta(\Omega) = \frac{1}{\pi}\frac{\Gamma_{\rm bi}}{\Omega^2+\Gamma_{\rm bi}^2}\,.$$

The same result can be obtained by using the equation for the rate of two-photon excitation of biexcitons

$$W_{\rm bi}^{(2)}(\omega) \propto \left|\frac{\langle XX|\hat{V}|X\rangle\langle X|\hat{V}|0\rangle}{\omega_0-\omega}\right|^2 \delta(2\omega_0-\delta_{\rm bi}-2\omega)\,,$$

changing the real denominator $\omega_0-\omega$ into $\omega_0-\omega-{\rm i}\Gamma$ and smoothing the δ-function. Here $\hat{V}$ is the light-matter interaction operator, $\langle X|\hat{V}|0\rangle$ and $\langle XX|\hat{V}|X\rangle$ are the vacuum-exciton and exciton-biexciton optical matrix elements proportional to the electric field E.

Under normal incidence upon QWs of the D_{2d} symmetry, the polarization dependence of the two-photon probability rate is characterized by three coefficients

$$W_{\rm QW}^{(2)}(\boldsymbol{e},\omega) = I^2\left[a_1(\omega)+a_2(\omega)|\boldsymbol{e}\cdot\boldsymbol{e}|^2+a_3(\omega)(|e_x|^4+|e_y|^4)\right]\,. \qquad (7.14)$$

This expression is derived taking into account that $W^{(2)}$ should be an invariant of the D_{2d} point group and, for $\boldsymbol{e}\perp z$, linearly-independent invariant combinations of the products $e_\alpha^* e_\beta^* e_\gamma e_\delta$ are $|\boldsymbol{e}\cdot\boldsymbol{e}^*|^2 \equiv 1$, $|\boldsymbol{e}\cdot\boldsymbol{e}|^2$ and $|e_x|^4+|e_y|^4$. Note that any complex unit vector $\boldsymbol{A}$ satisfies the identity $|\boldsymbol{A}\cdot\boldsymbol{A}|^2+|\boldsymbol{A}\times\boldsymbol{A}^*|^2 = (\boldsymbol{A}\cdot\boldsymbol{A}^*)^2$. Therefore, $|\boldsymbol{e}\times\boldsymbol{e}^*|^2$ equals $1-|\boldsymbol{e}\cdot\boldsymbol{e}|^2$ and is expressed is terms of the chosen set of invariants. We remind that one-photon absorption for $\boldsymbol{e}\perp z$ is independent of the light polarization state. In the uniaxial approximation, the coefficient a_3 vanish and $W_{\rm QW}^{(2)}$ is insensitive to the in-plane polarization of the linearly polarized light. However, even in this case two-photon absorption is different for the linear and circular polarizations

$$W_{\rm QW}^{(2)}({\rm lin}) = (a_1+a_2)\,I^2\,,\; W_{\rm QW}^{(2)}({\rm circ}) = a_1 I^2\,. \qquad (7.15)$$

For allowed-forbidden two-photon transitions into the continuum electron-hole pair states, the ratio $\Lambda^{(2)} \equiv W_{\rm QW}^{(2)}({\rm lin})/W_{\rm QW}^{(2)}({\rm circ})$ characterizing the linear-circular dichroism differs from unity by few tens percent. The observed biexciton state is a singlet with the electron spins (as well as the hole angular momenta) being antiparallel. Hence, the two photons of the same circular polarization cannot excite biexcitons, the coefficient a_1 in (7.15) vanish and $\Lambda^{(2)}\to\infty$.

In 1970s, two-photon absorption measurements brought new experimental evidence for the existence of biexcitons, or excitonic molecules, in bulk semiconductors [7.16]. The two-photon PhotoLuminescence Excitation (PLE) spectrum reached a maximum at a frequency separation equal $\hbar(\omega_0 - \delta_{\rm bi}/2)$ in agreement with the energy conservation law $2\omega_0 - \delta_{\rm bi} = 2\omega$. The similar effect was observed on QW structures, ZnSe/ZnMnSe MQWs [7.17] and GaAs/AlGaAs SQWs [7.18, 7.19]. Using a micron-sized photoluminescence probe Brunner et al. [7.18] studied excitons and biexcitons bound to a single island-like defect, a 4 Å deep protrusion of the GaAs QW into the $Al_{0.35}Ga_{0.65}As$ barrier layer with the lateral size of about 400 Å. The PLE spectrum detected at the biexciton emission line $\omega_0 - \delta_{\rm bi}$ shows the resonant behavior at $\omega = \omega_0 - \delta_{\rm bi}/2$. In the studied structure, the excitation energy of the $e1$-$hh1$ ground-state exciton equals $\hbar\omega_0 = 1.6544$ eV and the biexciton binding energy $\hbar\delta_{\rm bi} = 4.2$ meV. The full width at half maximum of the two-photon resonance at $\hbar\omega = 1.6565$ eV is extremely narrow and even limited by the linewidth of the exciting laser beam, which is characteristic for the 0D excitations.

7.3 Degenerate Four-Wave Mixing

Time-resolved degenerate four-wave mixing has proven to be a powerful tool to provide much information on the exciton dynamics and loss of coherence as well as on nonlinear mechanisms of exciton-photon interaction in bulk semiconductors and QW structures. In a typical two-pulse self-diffraction setup (see inset in Fig. 7.2), a sequence of two coherent pulses 1 and 2 with the wave vectors $\boldsymbol{k}_1$, $\boldsymbol{k}_2$ are tuned to the exciton resonance, interfere and produce an excitonic grating. One of the two pulses, say, the pulse 2, is diffracted by this grating into the direction $\boldsymbol{k}_3 = 2\boldsymbol{k}_2 - \boldsymbol{k}_1$. The magnitude of the diffracted signal is then recorded as a function of the time delay $T = t_2 - t_1$ between the pulses.

Let us consider the four-wave mixing in a single QW sandwiched between semiinfinite barrier layers. We present the electric field of the incident two-pulse radiation in the form

$$\boldsymbol{E}(\boldsymbol{r}, t) = \mathrm{e}^{-\mathrm{i}\tilde{\omega}t}\left[\tilde{\boldsymbol{E}}_0^{(1)}(t)\mathrm{e}^{\mathrm{i}\boldsymbol{k}_1\cdot\boldsymbol{r}} + \tilde{\boldsymbol{E}}_0^{(2)}(t)\mathrm{e}^{\mathrm{i}\boldsymbol{k}_2\cdot\boldsymbol{r}}\right] + \text{ c.c.}\,, \tag{7.16}$$

where $\tilde{\omega}$ is the current frequency of the coherent light pulses and $\tilde{\boldsymbol{E}}_0^{(j)}(t)$ $(j = 1, 2)$ are the slowly varying amplitudes. For example, for Lorentzian pulses one can write the electric field inside the QW in the form

$$\boldsymbol{E}(x, t) = \mathrm{e}^{-\mathrm{i}\tilde{\omega}t}\left[\boldsymbol{E}_{0,1}\mathrm{e}^{-|t-t_1|/\tau_p}\mathrm{e}^{\mathrm{i}k_{1x}x} + \boldsymbol{E}_{0,2}\mathrm{e}^{-|t-t_2|/\tau_p}\mathrm{e}^{\mathrm{i}k_{2x}x}\right] + \text{ c.c.}\,,$$

where $\boldsymbol{E}_{0,j}$ are time-independent vectors. We assume (x, z) to be the plane of incidence in which case $\boldsymbol{k}_j = (k_{jx}, 0, k_{jz})$. Usually in four-wave mixing

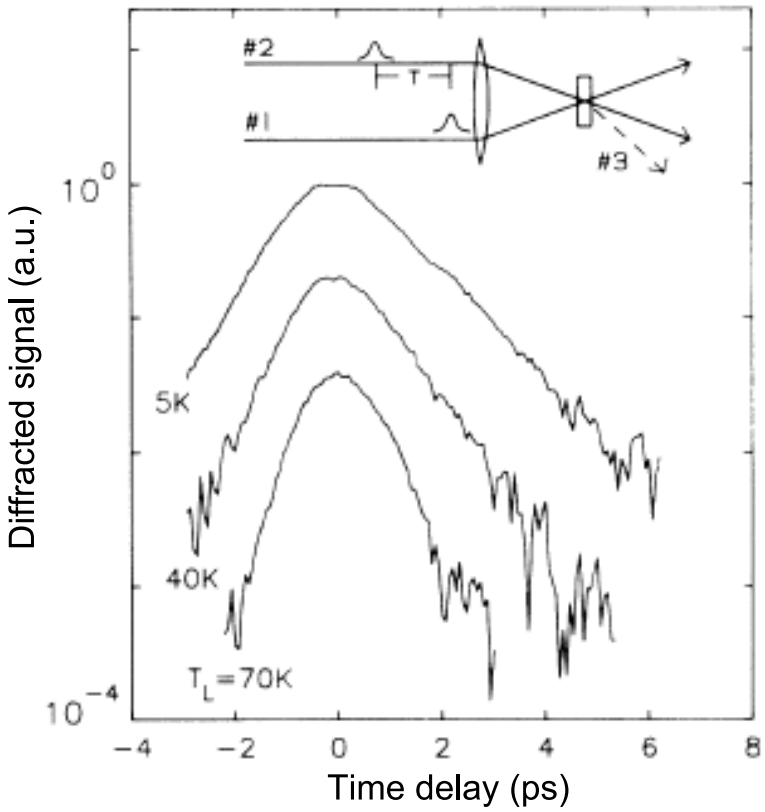

Fig. 7.2. Degenerate four-wave mixing signals in GaAs/AlGaAs MQWs vs. time delay for different temperatures and low excitation intensity. Inset: experimental configuration. From [7.20].

experiments the $\boldsymbol{k}_1$ and $\boldsymbol{k}_2$ vectors make small angles with the sample normal z. Thus, one may ignore an effect of the z component of the electric field and neglect angular dependence of the reflection and transmission. In the following we omit the exponential functions $\exp(\mathrm{i}k_{j,x}x)$ bearing in mind that $\tilde{\boldsymbol{E}}_0^{(1)}, \tilde{\boldsymbol{E}}_0^{(2)}$ and $\tilde{\boldsymbol{E}}_0^{(3)}$ describe amplitudes of the three waves $\boldsymbol{k}_1$, $\boldsymbol{k}_2$ and $\boldsymbol{k}_3 = 2\boldsymbol{k}_2 - \boldsymbol{k}_1$ independently detected.

For simplicity, we first assume the configuration of collinear polarized incident pulses, $\tilde{\boldsymbol{E}}_0^{(1)} \parallel \tilde{\boldsymbol{E}}_0^{(2)}$, which allows us to use the scalar amplitudes $\tilde{E}^{(j)}$ instead of the vectors $\tilde{\boldsymbol{E}}^{(j)}$. The basic equations describing the exciton dynamics in the QW are written as

$$\left[\frac{d}{dt} + \mathrm{i}(\omega_0 - \tilde{\omega}) + \Gamma + \Gamma_0\right] \tilde{P}(t) = \mathrm{i}\xi\Gamma_0\tilde{E}_0(t) + \mathrm{i}F_{NL}(t)\,, \tag{7.17}$$

$$\tilde{E}(t) = \tilde{E}_0(t) + \frac{\mathrm{i}}{\xi}\,\tilde{P}(t)\,. \tag{7.18}$$

They can be derived by extending equations (3.40) and (3.44) from mono- to quasimonochromatic waves, i.e., by changing

$$-\mathrm{i}\omega \quad \text{into} \quad \frac{d}{dt} - \mathrm{i}\tilde{\omega}\,,$$

and adding nonlinear term F_{NL} that gives rise to the third-order polarization. We consider the following two contributions to the nonlinearity

$$F_{NL}(t) = |\tilde{P}(t)|^2\left[\beta_1\tilde{P}(t) + \beta_2\tilde{E}(t)\right]\,, \tag{7.19}$$

the first of them (proportional to the coefficient β_1) describing an excitation-induced shift of the exciton resonant frequency and the second (proportional to β_2) being due to the optical-transition saturation. In the interpretation of [7.20], the corresponding contributions are called anharmonic-oscillator- and two-level-like nonlinear terms. According to (7.19) the polarization $\tilde{P}^{(3)}$ of the wave propagating in the direction $2\boldsymbol{k}_2 - \boldsymbol{k}_1$ is induced by

$$F_{NL}(t) = \tilde{P}^{(1)*}(t)\tilde{P}^{(2)}(t)\left[\beta_1\tilde{P}^{(2)}(t) + \beta_2\tilde{E}^{(2)}(t)\right]\,. \tag{7.20}$$

For the biexcitonic mechanism of nonlinearity, the term F_{NL} in (7.17) is given by $\gamma_{\mathrm{bi}}BE^*$ and the polarization $\tilde{P}_{XX} \propto B\tilde{P}_X^*$ should be added to the exciton polarization $\tilde{P} \equiv \tilde{P}_X$ in (7.18), see (7.11) and (7.13).

Equations (7.17)-(7.19) form a complete set allowing to calculate the four-wave mixing signal. The calculation procedure consists of solving (i) the linear equations (7.17, 7.18) for the polarization $\tilde{P}^{(1)}$ and the field $\tilde{E}^{(1)}$ induced by the initial pulse $E_0^{(1)}$, (ii) the same linear equations for the response $\tilde{P}^{(2)}, \tilde{E}^{(2)}$ to the pulse $E_0^{(2)}$, and (iii) the linear equation (7.17) for the polarization $\tilde{P}^{(3)}$ of the diffracted wave with the inhomogeneous term in the form of (7.20). Since $E_0^{(3)} \equiv 0$, the amplitude $\tilde{E}^{(3)}$ of the outgoing wave 3 is given by $(\mathrm{i}/\xi)\tilde{P}^{(3)}(t)$.

For short-pulse beams, we can approximate the time-dependence of $\tilde{E}_0^{(j)}$ by delta-functions

$$\mathcal{N}_j\,\delta(t - t_j)\,, \quad \text{where} \quad \mathcal{N}_j = \int\limits_{-\infty}^{\infty} dt\,\tilde{E}^{(j)}(t)\,.$$

Particularly, for a Lorentzian pulse, $\mathcal{N}_j = 2\tau_p E_{0,j}$. In this approximation the polarizations $\tilde{P}^{(1)}$ and $\tilde{P}^{(2)}$ are easily found

$$\tilde{P}^{(j)}(t) = \mathrm{i}\xi\Gamma_0\mathcal{N}_j\theta(t-t_j)\exp\left[\left(-\frac{1}{T_2}+\mathrm{i}\delta\right)(t-t_j)\right], \tag{7.21}$$

where $T_2 = (\Gamma+\Gamma_0)^{-1}$ is the polarization dephasing time and $\delta = \tilde{\omega}-\omega_0$ is the laser detuning. Substituting the solutions (7.21) into (7.20) we obtain

$$F_{NL}(t) = (\xi\Gamma_0)^2\mathcal{N}_1^*\mathcal{N}_2^2\theta(t-t_1)\theta(t-t_2)\mathrm{e}^{-\mathrm{i}\delta T}\mathrm{e}^{-(2t-t_1-t_2)/T_2}$$
$$\times\left[\mathrm{i}\beta_1'\xi\Gamma_0\mathrm{e}^{\mathrm{i}\delta(t-t_2)}\mathrm{e}^{-(t-t_2)/T_2}+\beta_2\delta(t-t_2)\right],$$

where $\beta_1' = \beta_1 + (\mathrm{i}/\xi)\beta_2$. We will not write the full solution for $\tilde{P}^{(3)}(t)$ but present only its dependence on the time delay T

$$\tilde{P}^{(3)}(t) = \mathcal{N}_1^*\mathcal{N}_2^2\begin{cases}\mathrm{e}^{-T/T_2}\mathrm{e}^{-\mathrm{i}\delta T}\theta(t-t_2)F_+(t-t_2) & \text{for}\quad T>0\,,\\ \mathrm{e}^{-2|T|/T_2}\mathrm{e}^{-2\mathrm{i}\delta T}\theta(t-t_1)F_-(t-t_1) & \text{for}\quad T<0\,,\end{cases} \tag{7.22}$$

where the functions $F_\pm$ are independent of T. It follows then that the time-integrated four-wave mixing signal

$$S^{(3)}(T) = \int_{-\infty}^{\infty} dt\,|\tilde{E}^{(j)}(t)|^2 \tag{7.23}$$

as a function of T is given by

$$S^{(3)}(T) = \begin{cases} S_+^{(3)}\mathrm{e}^{-2T/T_2} & \text{if}\quad T>0\,,\\ S_-^{(3)}\mathrm{e}^{-4|T|/T_2} & \text{if}\quad T<0\,,\end{cases} \tag{7.24}$$

where $S_\pm^{(3)}$ are coefficients proportional to $|\mathcal{N}_1|^2|\mathcal{N}_2|^4$. One can see that the slope of the function $\ln S^{(3)}(T)$ is independent of the detuning δ and, hence, the measured signal is controlled by the homogeneous dephasing time T_2 but not by the inhomogeneous broadening of the excitonic transition.

Figure 7.2 shows the time-integrated diffracted signals versus the time delay taken from a 170-Å GaAs/AlGaAs MQW structure. The signals are asymmetric in time delay and consist of exponentially rising ($T<0$) and decaying ($T>0$) wings. In accordance with (7.24) the rise time, τ_R, is about a factor of 2 smaller than the decay time, τ_D. Particularly, at low temperatures $\tau_R \approx 650$ fs and $\tau_R \approx 1150$ fs. With increasing lattice temperature, both the decay and rise times get shorter keeping the ratio ≈ 2.

According to (3.48, 3.49), in a QW structure with a top layer of finite thickness, the dephasing rate T_2^{-1} is modified to

$$\frac{1}{T_2} = \Gamma+\Gamma_0' \quad\text{with}\quad \Gamma_0' = \Gamma_0(1+r_{10}\cos 2\varphi_{0a})\,, \tag{7.25}$$

where the notations are the same as in (3.49).

In Chap. 3 we have shown that the dynamics of optical excitations in MQWs differs considerably from that in a nominally identical single QW and depends strongly on the number of QWs, N, and the interwell separation, d. A special situation arises in a resonant Bragg MQWs structure, where the period equals an integer multiple of half light wavelength at the exciton resonance frequency. In such a structure there exists a superradiant mode which is characterized by an N times enhanced radiative decay rate, see (3.92, 3.98). In Sect. 3.2.5 we discussed linear optical properties of the resonant Bragg structures. Hübner et al. [7.21] used femtosecond degenerate four-wave mixing to study light-induced collective effects in MQWs and clearly demonstrated efficient radiative coupling of excitons in high-quality Bragg MQW samples. The single QW displays an exponential signal yielding the decay time $\tau_D = 4.3$ ps. In agreement with the theoretical prediction, the MQWs exhibit an initial-stage decay which is remarkably faster as compared to the signal from the single QW. The experimentally observed two-stage decay of the Bragg structures indicates slight deviation of the periodicity from $\lambda(\omega_0)/2$. Note that the four-wave mixing in semiconductor microcavities is separately considered in Sect. 7.5.

Recently, Shackelette and Cundiff [7.22] have reexamined different nonlinear contributions to the optical Bloch equations in the density-matrix approach, including the saturation, local-field effect, excitation-induced shift of ω_0 and excitation-induced dephasing. They ignored the biexciton nonlinearity because, in the studied MQW structures containing 83-Å-thick $In_{0.14}Ga_{0.86}As$ wells and 80-Å-thick $GaAs_{0.71}P_{0.29}$ barriers, the same spectrally-resolved four-wave mixing signals were obtained for collinearly and cocircularly polarized pulses. However in many other heterostructures there exists strong biexcitonic contribution to four-wave mixing in the direction $2\boldsymbol{k}_2 - \boldsymbol{k}_1$ [7.23–7.26]. The first indication of this contribution in GaAs-based MQWs was discovered for negative delays by Feuerbacher et al. [7.23]. In their experiment the nonlinear interaction can be explained as a two-step process. In the first step, two photons of pulse 2 create a biexciton which then, in the second step, interacts coherently with pulse 1 and gives the measured four-wave mixing signal. Breunig et al. [7.26] have clearly demonstrated the coherent control of the biexcitonic polarization in measurements of the time-integrated spectrally-resolved four-wave mixing on a $ZnSe/ZnS_xSe_{1-x}$ single QW. The maximum energy of the laser pulses was set to the biexcitonic resonance and the narrow spectral width of the pulses allowed for exclusive excitation of the heavy-hole exciton-biexciton system. In the spectrally-resolved four-wave mixing signal, both the excitonic and biexcitonic resonances are observed for cross-linearly polarized pulses while the biexcitonic resonance is strongly suppressed in the case of cocircular excitation in agreement with spin selection rules for the formation of a bound biexcitonic state.

In addition to four-wave mixing, one can observe six-wave mixing in the direction $3\boldsymbol{k}_2 - 2\boldsymbol{k}_1$ or $3\boldsymbol{k}_1 - 2\boldsymbol{k}_2$ due to the second-order diffraction of the pulse pair [7.27, 7.28]. To describe this nonlinear signal one needs to start in the expansion (7.1) from the fifth-order susceptibility $\chi^{(5)}$ and consider participation of six waves in the buildup of a polarization in the corresponding direction. A microscopic theory based on the dynamics controlled truncation scheme, see for details [7.27], is able to reproduce the experimental results.

7.4 Second-Harmonic Generation

The second-harmonic generation is described in (7.1) by the third-rank tensor $\boldsymbol{\chi}^{(2)}(\omega_1, \omega_2)$ with $\omega_1 = \omega_2 \equiv \omega$. It is an elementary process of the annihilation of two light quanta $\hbar\omega$ and the creation of one new quantum with twice the energy. Obviously, the second-harmonic power is quadratic in the incident-pump power, as experimentally checked, e.g., by Seto et al. [7.29]. Neglecting the spatial dispersion of $\boldsymbol{\chi}^{(2)}(\omega, \omega)$ we conclude that the components $\chi^{(2)}_{\alpha\beta\gamma}$ are symmetrical with respect to interchange of the two last indices,

$$\chi^{(2)}_{\alpha\beta\gamma}(\omega, \omega) = \chi^{(2)}_{\alpha\gamma\beta}(\omega, \omega)\,. \tag{7.26}$$

Therefore, neglecting the spatial dispersion, the second-harmonic generation occurs only in piezoelectric crystals and nanostructures of the point symmetry belonging to the piezoelectric classes. For bulk crystals of the tetrahedral point group T_d, the symmetry reduces the number of linearly independent elements of $\boldsymbol{\chi}^{(2)}(\omega, \omega)$ to one and, in a frame of references with the axes x, y, z along the basic crystallographic directions [100], [010] and [001], one has

$$\chi^{(2)}_{\alpha\beta\gamma} = \begin{cases} \chi^{(2)}_{xyz} & \text{if} \quad \alpha \neq \beta \neq \gamma\,, \\ 0 & \text{otherwise}\,. \end{cases}$$

It is also useful to present the nonzero components of $\boldsymbol{\chi}^{(2)}(\omega, \omega)$ in the coordinate system $x' \parallel [1\bar{1}0], y' \parallel [110], z \parallel [001]$ rotated as compared to x, y, z around z by the angle -45°

$$\chi^{(2)}_{x'x'z} = \chi^{(2)}_{x'zx'} = \chi^{(2)}_{zx'x'} = -\chi^{(2)}_{y'y'z} = -\chi^{(2)}_{y'zy'} = -\chi^{(2)}_{zy'y'} = \frac{1}{2}\,\chi^{(2)}_{xyz}\,.$$

In a (001)-grown QW of the symmetry D_{2d}, there are two independent components

$$\chi^{(2)}_{x'x'z} = \chi^{(2)}_{x'zx'} = -\chi^{(2)}_{y'y'z} = -\chi^{(2)}_{y'zy'} \neq \chi^{(2)}_{zx'x'} = -\chi^{(2)}_{zy'y'}\,. \tag{7.27}$$

The point-group C_{2v} of an asymmetrical QW allows five linearly independent components $\chi^{(2)}_{x'x'z} = \chi^{(2)}_{x'zx'}$, $\chi^{(2)}_{y'y'z} = \chi^{(2)}_{y'zy'}$, $\chi^{(2)}_{zx'x'}$, $\chi^{(2)}_{zy'y'}$ and $\chi^{(2)}_{zzz}$. Except

$\chi^{(2)}_{zzz}$ that is zero in bulk and originates from the superstructure potential asymmetry, other components are nonzero also in a bulk semiconductor, they originate from both the bulk and structure inversion asymmetry. The symmetry increases from C_{2v} to C_{4v} when one uses the parabolic Hamiltonian for electrons in the conduction band, the Luttinger Hamiltonian for the valence band neglecting odd-$\boldsymbol{k}$ terms and the Bastard boundary conditions (2.34). In this case $\chi^{(2)}_{x'x'z}$ and $\chi^{(2)}_{y'y'z}$ or $\chi^{(2)}_{zx'x'}$ and $\chi^{(2)}_{zy'y'}$ equalize and the constitutive equations take the form [7.30]

$$P_{x'}(2\omega) = 2\chi^{(2)}_{x'x'z}E_{x'}(\omega)E_z(\omega)\ ,\ P_{y'}(2\omega) = 2\chi^{(2)}_{x'x'z}E_{y'}(\omega)E_z(\omega)\ , \qquad (7.28)$$

$$P_z(2\omega) = \chi^{(2)}_{zx'x'}\left[E^2_{x'}(\omega) + E^2_{y'}(\omega)\right] + \chi^{(2)}_{zzz}E^2_z(\omega)\ .$$

Within the independent-particle approximation the second-harmonic susceptibility can be expressed as (see, e.g., [7.31, 7.32])

$$\chi^{(2)}_{\alpha\beta\gamma}(\omega,\omega) \equiv \chi^{(2)}_{\alpha\beta\gamma}(\omega) \qquad (7.29)$$
$$\propto \frac{1}{V_d}\sum_{i_1,i_2,i_3}\frac{\langle i_1|p_\alpha|i_2\rangle\{\langle i_2|p_\beta|i_3\rangle\langle i_3|p_\gamma|i_1\rangle\}_s}{E_{i_2i_1}-2\hbar\omega}\left(\frac{f_{i_1i_3}}{E_{i_3i_1}-\hbar\omega}-\frac{f_{i_3i_2}}{E_{i_2i_3}-\hbar\omega}\right)\ .$$

Here V_d is the volume of the d-dimensional sample, i_1, i_2, i_3 denote quantum numbers labelling the electron states $|i\rangle$ and the eigen energies E_i, $E_{i_2i_1} = E_{i_2} - E_{i_1}$, $f_{i_1i_3} = f_{i_1} - f_{i_3}$, and f_i is the Fermi-Dirac distribution, the curly brackets $\{...\}_s$ mean a symmetrized form, e.g., $\{R_{\beta\gamma}\}_s = (R_{\beta\gamma}+R_{\gamma\beta})/2$. In general, the existing theoretical and experimental studies of the second-harmonic generation in nanostructures can be divided into two groups, depending on the light frequency ω: those dealing with energies $\hbar\omega$ in the region of valence-to-conduction *interband* transitions (see, e.g., [7.30, 7.33, 7.34] and references therein) and the second group using the photon energy in the region of *intraband intersubband* transitions [7.35–7.37]. In all cases, an enhancement of the nonlinear susceptibility as compared to the susceptibility of bulk materials was reported.

Atanasov et al. [7.30] addressed the problem of second-harmonic generation in asymmetrical QWs in the region of interband transitions including exciton effects. In the excitonic contribution to $\chi^{(2)}$, the energy differences $E_{i_2i_1}$, etc., in the denominators of (7.29) are replaced by the excitation energies of excitons attached to a pair of the corresponding subbands. As shown in [7.30], for step-like and double asymmetrical QWs, the inclusion of exciton states leads, particularly, to the sharp half-band-gap resonances at $\hbar\omega = E_{e\nu',h\nu;1s}/2$ for $\chi^{(2)}_{x'x'z}(\omega), \chi^{(2)}_{zzz}(\omega)$ and to the near-band-gap resonances at $\hbar\omega = E_{e\nu',h\nu;1s}$ for $\chi^{(2)}_{zx'x'}(\omega)$. Note that the resonant peaks of $|\chi^{(2)}_{zzz}(\omega)|$ are related with light-hole excitons only because the interband transitions from heavy-hole subbands are forbidden in the $\boldsymbol{e} \parallel z$ polarization. The theory predicts values of second-harmonic-generation susceptibility larger than in the

bulk. Jiang et al. [7.34] investigated second-order nonlinear optical properties of $Zn_{1-x}Cd_xSe/ZnSe$ asymmetric coupled QWs by using the reflective second-harmonic generation technique. The photon energy, $\hbar\omega = 1.17$ eV, of Nd:YAG (Yttrium Aluminum Garnet) laser was close to the half band gap of the studied structures and, therefore, conditions for the half-band-gap resonance were realized. Compared with the second-harmonic generation intensities in ZnSe bulk material, a significant enhancement of the signals (at least one order of magnitude) was observed due to the structure inversion asymmetry. Note also that the p-in/p-out intensity was two orders of magnitude larger than the s-in/s-out one.

The second-order susceptibility due to the intraband intersubband transitions can be greatly enhanced due to a possibility to realize the conditions of double resonance for three subbands 1, 2 and 3

$$E_2 - E_1 = E_3 - E_2 = \hbar\omega \,. \tag{7.30}$$

Replacing i_1, i_2, i_3 by 1, 3, 2, respectively, we obtain from (7.29) for the double-resonant contribution to the second-order susceptibility of a QW [7.36, 7.38, 7.39]

$$\chi^{(2)}_{\alpha\beta\gamma}(\omega) \propto \frac{1}{S}\sum_{\boldsymbol{k}} \frac{p^{\alpha}_{13}(\boldsymbol{k})\{p^{\beta}_{32}(\boldsymbol{k})p^{\gamma}_{21}(\boldsymbol{k})\}_s}{(E_{2\boldsymbol{k}} - E_{1\boldsymbol{k}} - \hbar\omega - \mathrm{i}\hbar\Gamma_{21})(E_{3\boldsymbol{k}} - E_{1\boldsymbol{k}} - 2\hbar\omega - \mathrm{i}\hbar\Gamma_{31})} \,, \tag{7.31}$$

where the dephasing constants $\Gamma_{i'i}$ are introduced into the energy denominators and, for simplicity, we omit the summation over the spin indices of the electron (or hole) states $|i\boldsymbol{k}\rangle$. The tuning to the double-resonance conditions can be achieved by varying parameters of an asymmetrically stepped QW or asymmetrical double QWs and/or applying an external electric field.

Enhancements as big as three orders of magnitude in $\chi^{(2)}$ were observed in doubly resonant experiments on n-doped QW structures with equal $e2$-$e1$ and $e3$-$e2$ transition energies [7.40, 7.41]. In these experiments, the only element of the susceptibility tensor that exhibits a strong double-resonant enhancement is $\chi^{(2)}_{zzz}$. Thus, the exciting and generated electric fields have to possess nonzero z-components which limits the usefulness of the element $\chi^{(2)}_{zzz}$ for device applications. In contrast to the conduction subbands, the hole energy dispersion is different for each valence subband, leading to a relatively low reduced density of states for intersubband transitions in p-doped QWs. Therefore, the double-resonance enhancements which can be obtained in the latter structures are expected to be lower. However, the presence of elements $\chi^{(2)}_{\alpha\beta\gamma}$ different from $\chi^{(2)}_{zzz}$ provides more functionality of the p-doped structures, since the incident and outgoing (second-harmonic) waves can have various polarizations. Bitz et al. [7.39] demonstrated second-harmonic generation in p-doped $GaAs/Al_xGa_{1-x}As$ asymmetrically stepped MQW structures using

the emission of a free-electron laser in the wavelength interval between 13 and 18 μm. In their samples the double-resonance conditions were realized for the transitions between the first heavy-hole, first light-hole and second heavy-hole subbands. The measured maximum enhancement by a factor of 16 in the second-harmonic susceptibility of the QWs with respect to that of bulk GaAs agrees with the theoretical expectations taking into account the quality of investigated samples.

For centrosymmetric materials, such as single Si or Ge crystals of the point group O_h, the second-harmonic generation is forbidden within the electric-dipole approximation. However, QW structures grown from these materials can lack such a center and allow the second-harmonic generation. Indeed, depending on the properties of an (001)-interface between the alloy $Si_{1-x}Ge_x$ and Si, its symmetry on average can be C_{2v} or C_{4v} [7.42]. The former point group describes the symmetry of an ideal heterointerface with the interfacial chemical bonds lying in the same plane. A nonideal interface containing monoatomic fluctuations has two kinds of flat areas with interfacial planes shifted with respect to each other by a quarter of the lattice constant a_0. The local symmetry of each area is C_{2v} as well. However if the both kinds are equally distributed, the interface overall symmetry increases up to C_{4v}. The both symmetries, C_{2v} and C_{4v}, allow the second-harmonic generation at a single interface. The symmetry of a $Si_{1-x}Ge_x$/Si QW structure containing two interfaces is described by one of five point groups: D_{2d} or D_{2h} in case of two ideal interfaces with odd or even number of monolayers between them; C_{2v} for a pair of ideal and rough interfaces; C_{4v} or D_{4h} for two non-ideal interfaces of the overall symmetry C_{4v} each. For QWs of the symmetry D_{2d}, C_{2v} and C_{4v} the contributions from the left- and right-hand-side interfaces to the second-harmonic generation do not compensate each other. Ghahramani et al. [7.32] performed a full-band-structure calculation of the components $\chi^{(2)}_{x'x'z}$ and $\chi^{(2)}_{zx'x'}$ for short-period Si_nGe_n SLs grown on the Si(001) substrates. They obtained that the bulk value of $\chi^{(2)}$ for SLs with odd $n = 1, 3, 5$ (point-group D_{2d}) is of the same order as that of bulk GaAs, one of the most commonly employed electro-optic semiconductor materials. Unfortunately, the presence of atomic height steps on the substrate and the incapability of precise control of layer thickness in SLs in the present molecular-beam epitaxy prevents up to now the realization of a macroscopic $\chi^{(2)}$ comparable to that of GaAs [7.43]. In addition, weak second-harmonic generation from GeSi nanostructures can arise from inhomogeneous strain, miscutting of the substrate, bulk quadruple mechanism. Zhang et al. [7.44] systematically analyzed contributions from different sources to the second-order susceptibility $\chi^{(2)}$ in two kinds of p-doped asymmetrical GeSi structures, namely, in $Si_{0.75}Ge_{0.25}/Si_{0.57}Ge_{0.43}$ step asymmetric QWs and electric-field biased Si_5Ge_5 SLs. The largest evaluated value of $\chi^{(2)}$ was found in the biased SL, under the electric field $F > 100$ kV/cm the main source of the nonlinear susceptibility arose due to the electric-field-induced asymmetry. In addition to

the second-harmonic generation, the linear and circular photogalvanic effects discussed in Chap. 8 can be used to question an existence of the inversion center in GeSe QW structures.

The further enhancement of $\chi^{(2)}$ has been demonstrated, both theoretically and experimentally, for intraband transitions in n- and p-doped QD structures [7.45,7.46]. In the study [7.46], the n-doped sample consisted of 30 layers of InAs/GaAs self-assembled QDs separated by 500-Å thick GaAs barriers and grown on the GaAs substrate. Second-harmonic power as a function of the pump photon energy shows a narrow peak at $\hbar\omega = 61$ meV superimposed on a background signal corresponding to the contribution of bulk GaAs. The peak is an enhancement due to the double resonance for the intersubband e_{100}-e_{000} (or p-s) and e_{110}-e_{100} (or d-p) transitions.

In [7.47], a quantum cascade laser is employed to demonstrate that intersubband optical transitions in stacked semiconductor QWs can function as a simultaneous source of fundamental pump and second-harmonic light.

7.5 Nonlinear Optical Phenomena in Quantum Microcavities

A natural way to enhance the light-matter interaction is to exploit band-edge resonances by tuning the incident-light frequency to the exciton-resonant spectral region. The quantum confinement of excitons in semiconductor nanostructures leads to the further increase in the resonant optical response. The photon confinement in quantum microcavities, i.e., in microcavities with embedded QW's shown schematically in Fig. 7.3, has opened a way for additional considerable enhancement of exciton-photon coupling [7.48]. Among reasons for the interest in these multi-layered structures, we mention the following three. First, the microcavities have potential applications in the development of low-threshold vertical-emitting lasers. Second, fundamental aspects of the interaction of confined photon modes (2D photons) with matter have opened a new field in quantum electrodynamics. And, finally, the quantum microcavities can be particularly interesting for nonlinear optics since a nonlinear response has a stronger dependence upon the coupling constant.

In the next subsection we introduce the two-oscillatory model of quantum microcavities and present the dispersion of 2D exciton-cavity polaritons. Other subsections are devoted to nonlinear optics of the microcavities.

7.5.1 Exciton Polaritons in a Quantum Microcavity

Semiconductor microcavity is a multilayer heterostructure consisting of an active layer B of the thickness L_b sandwiched between N_l pairs of the C_2/C_1 mirror, or Distributed Bragg Reflector (DBR), and N_r pairs of C_1/C_2 DBR grown on the substrate D. If one or few QWs (material A) are embedded

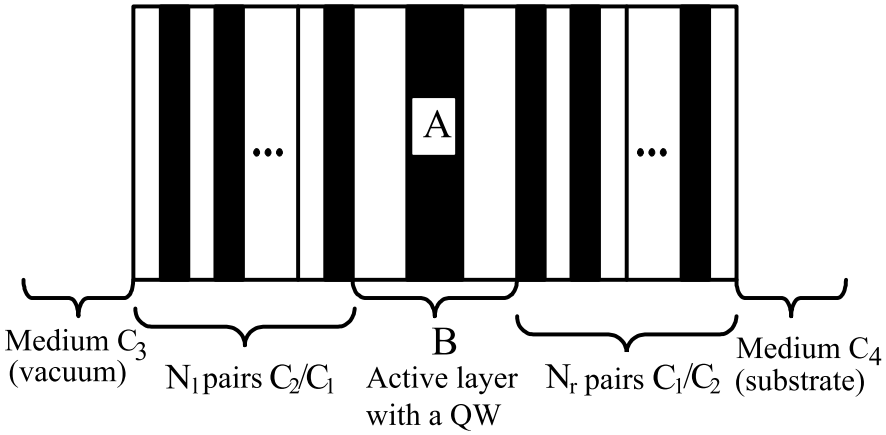

Fig. 7.3. Schematic representation of a quantum macrocavity.

inside the active layer the structure is called *Quantum Microcavity* (Fig. 7.3). As a rule we will consider the quantum microcavity with a single embedded QW.

The thickness L_b and the thicknesses a_1 and a_2 of the C_1 and C_2 layers in DBR's are assumed to satisfy the conditions

$$n_b \frac{\bar{\omega}}{c} L_b = N_b \pi \, , \; n_1 \frac{\bar{\omega}}{c} a_1 = n_2 \frac{\bar{\omega}}{c} a_2 = \frac{\pi}{2} \, , \tag{7.32}$$

where N_b is an integer that expresses the cavity length in half-wavelengths, n_i $(i = b, 1, 2)$ is the refractive index of the corresponding material, and $\bar{\omega}$ is an arbitrarily chosen frequency which turns out to be the resonance frequency of the microcavity, see below. In quantum microcavities, it is usually taken to lie close to the QW exciton resonance frequency ω_0.

Exciton-polariton modes in quantum microcavities can be modelled by a pair of two coupled classical oscillators, one of them representing an exciton in the QW and another representing the photon mode. Taking the averaged dielectric polarization $P(t)$ defined according to (3.41) and the electric field, $E(t)$, inside the QW as two variables for the two-oscillatory model we can write for them a standard set of equations

$$\begin{aligned} &\frac{d^2}{dt^2} P(t) + \omega_0^2 P(t) + 2\Gamma \frac{d}{dt} P(t) = q_1 E(t) \, , \\ &\frac{d^2}{dt^2} E(t) + \bar{\omega}^2 E(t) + 2\bar{\gamma} \frac{d}{dt} E(t) = q_2 P(t) \, . \end{aligned} \tag{7.33}$$

Here Γ, $\bar{\gamma}$ are the nonradiative damping rate of a bare 2D exciton and the damping rate of the bare-photon mode. The solution of (7.33) is sought in the exponential form $P(t) = P\mathrm{e}^{-\mathrm{i}\omega t}$, $E(t) = E\mathrm{e}^{-\mathrm{i}\omega t}$. If the damping constants

$\Gamma, \bar{\gamma}$ and the difference, $\omega_0 - \bar{\omega}$, of the bare resonance frequencies are small compared to these frequencies, (7.33) reduces to

$$(\omega_0 - \omega - \mathrm{i}\Gamma)P = \gamma_1 E \,, \tag{7.34a}$$

$$(\bar{\omega} - \omega - \mathrm{i}\bar{\gamma})E = \gamma_2 P \,, \tag{7.34b}$$

where, instead of q_1 and q_2, we introduced other parameters $\gamma_j = q_j/(2\bar{\omega})$. One of them is easily found from a comparison of (7.34a) with (3.44), namely,

$$\gamma_1 = \xi \Gamma_0 \,. \tag{7.35}$$

The expressions for $\bar{\gamma}$ and γ_2 are given below, see (7.51, 7.52, 7.55). From (7.34) we obtain the following complex eigenfrequencies of the mixed modes

$$\omega_\pm = \frac{1}{2}\left[\omega_0 + \bar{\omega} - \mathrm{i}(\Gamma + \bar{\gamma})\right] \pm \sqrt{\gamma_1\gamma_2 + \frac{1}{4}\left[\omega_0 - \bar{\omega} - \mathrm{i}(\Gamma - \bar{\gamma})\right]^2} \,. \tag{7.36}$$

Let us analyze the structure with $\bar{\omega}$ tuned exactly to ω_0. In the *weak-coupling regime* defined by the condition $(\Gamma - \bar{\gamma})^2 > 4\gamma_1\gamma_2$, one has for the eigenfrequencies

$$\omega_\pm = \bar{\omega} - \mathrm{i}\,\frac{\Gamma + \bar{\gamma}}{2} \pm \mathrm{i}\tilde{\gamma} \;,\; \tilde{\gamma} = \sqrt{\left(\frac{\Gamma - \bar{\gamma}}{2}\right)^2 - \gamma_1\gamma_2} \,,$$

i.e., their real parts coincide but the imaginary parts are different. In the *strong-coupling regime* where $(\Gamma - \bar{\gamma})^2 < 4\gamma_1\gamma_2$, the frequencies $\omega_\pm$ differ in the real part

$$\omega_\pm = \bar{\omega} \pm \tilde{\Omega} - \mathrm{i}\frac{\Gamma + \bar{\gamma}}{2} \;,\; \tilde{\Omega} = \sqrt{\gamma_1\gamma_2 - \left(\frac{\Gamma - \bar{\gamma}}{2}\right)^2} \,. \tag{7.37}$$

In the latter case the difference $\omega_+ - \omega_- = 2\tilde{\Omega}$ is called the *Rabi splitting*.

It is worth to mention that, as follows from Chap. 3, the conventional single-QW structures are open systems where the 2D electronic excitations (2D-excitons) interact with 3D photons, the renormalization of exciton resonance frequency, see (3.18), is small and the exciton-photon coupling leads mainly to the exciton radiative damping. In a quantum microcavity with thick DBR's of high quality, both excitonic and photonic states are size-quantized in the growth direction. As a result, the bare resonance frequencies $\omega_0, \bar{\omega}$ can be strongly renormalized. In real semiconductor microcavities the Rabi splitting amounts few meV and in some cases it can even exceed 10 meV. Now we turn to establishing the relation between $\gamma_2, \bar{\gamma}$ and parameters of the quantum microcavity.

The optical properties of the DBR's, or mirrors, are characterized by the amplitude reflection coefficients r_{mj}, r'_{mj} from the left, $j = l$, or right, $j = r$, mirror for the light incident, respectively, from the active layer and from the

external medium, vacuum or substrate, and the transmission coefficients t_{mj}, t'_{mj} through the mirror j defined in the similar way. In the following we ignore the difference between the refractive indices of the active layer and the QW. Then the amplitude reflection and transmission coefficients, $r_{\rm QW}$ and $t_{\rm QW}$, of a QW are given by (3.21).

Assuming the monochromatic light to be incident from the vacuum side under the angle θ_0, we can present the amplitude reflection and transmission coefficients for the whole quantum microcavity as

$$r_{QM} = r'_{ml} + \frac{t'_{ml}\tilde{r}t_{ml}\exp(\mathrm{i}\psi_b)}{1-\tilde{r}r_{ml}\exp(\mathrm{i}\psi_b)}\,, \qquad (7.38)$$
$$t_{QM} = \frac{t'_{ml}\tilde{t}\exp(\mathrm{i}\psi_b/2)}{1-\tilde{r}r_{ml}\exp(\mathrm{i}\psi_b)}\,,$$

where the transmission t_{QM} refers to the light field at the boundary between the second DBR and the substrate, the phase ψ_b is defined by

$$\psi_b = n_b\frac{\omega}{c}L_b\cos\theta_b\,, \qquad (7.39)$$

the value L_b includes the QW thickness, the angle θ_b and incidence angle in vacuum are connected by the Snellius relation $\sin\theta_0 = n_b\sin\theta_b$, and

$$\tilde{r} = r_{\rm QW} + \frac{t^2_{\rm QW}r_{mr}\exp(\mathrm{i}\psi_b)}{1-r_{\rm QW}r_{mr}\exp(\mathrm{i}\psi_b)}\,, \qquad (7.40)$$
$$\tilde{t} = \frac{t_{\rm QW}t_{mr}\exp(\mathrm{i}\psi_a/2)}{1-r_{\rm QW}r_{mr}\exp(\mathrm{i}\psi_a)}\,.$$

Substituting (7.40) into (7.38) we can present r_{QM}, t_{QM} as fractions with the denominator

$$D_{MC} = r_{ml}r_{mr}(t^2_{\rm QW}-r^2_{\rm QW})\exp(2\mathrm{i}\psi_b) + (r_{ml}+r_{mr})r\exp(\mathrm{i}\psi_b) - 1\,. \qquad (7.41)$$

The dispersion equation for the exciton polaritons in the structure of Fig. 7.3 is given by

$$D_{MC}(\omega, q_\parallel) = 0\,, \qquad (7.42)$$

where $q_\parallel$ is the exciton-polariton in-plane wave vector $(\omega/c)\sin\theta_0$. The dispersion equation for the photon mode in a semiconductor microcavity without embedded QWs (or empty cavity) is expressed by (7.41, 7.42) with $r_{\rm QW} = 0, t_{\rm QW} = 1$, i.e.,

$$r_{ml}r_{mr}\mathrm{e}^{2\mathrm{i}\psi_b} - 1 = 0\,. \qquad (7.43)$$

Let us denote by

$$r_m = \sqrt{R_m}\,\mathrm{e}^{\mathrm{i}\psi_m} \qquad (7.44)$$

the reflection coefficient under light incidence from the left upon the Bragg mirror

$$C_3(C_1/C_2)...(C_1/C_2)C_4$$

containing N pairs C_1/C_2 placed between the semi-infinite media C_3 and C_4 with the refractive indices n_3 and n_4. For a large number of pairs in the mirror, ω lying in the vicinity of $\bar{\omega}$ and $n_2 > n_1$ one can use the following approximate expressions [7.49–7.51, 7.53]

$$R_m \approx 1 - 4\frac{n_4}{n_3}\left(\frac{n_1}{n_2}\right)^{2N}, \tag{7.45}$$

$$\psi_m \approx \frac{\pi\alpha}{n_3}\frac{n_1 n_2}{n_2 - n_1}\frac{\omega - \beta\bar{\omega}}{\bar{\omega}},$$

where

$$\alpha = \frac{\cos^2\theta_1 \cos^2\theta_2}{\cos\theta_3},\ \beta = \frac{n_1\cos\theta_1 + n_2\cos\theta_2}{\cos\theta_1\cos\theta_2(n_1+n_2)} \tag{7.46}$$

and the angles θ_i are related to the photon in-plane vector by

$$q_\parallel = \frac{\omega}{c}\, n_i \sin\theta_i. \tag{7.47}$$

The further development is performed for zero $q_\parallel$ where ψ_b, ψ_m reduce to

$$\psi_b = \pi N_c\left(1 + \frac{\omega - \bar{\omega}}{\bar{\omega}}\right),\ \psi_m \approx \frac{\pi}{n_3}\frac{n_1 n_2}{n_2 - n_1}\frac{\omega - \bar{\omega}}{\bar{\omega}}, \tag{7.48}$$

but the final result for the polariton frequencies will then be rewritten in the general case of nonzero $q_\parallel$.

Taking into account that, for large numbers N_l and N_r, the reflectivity $R_{mj} = |r_{mj}|^2$ $(j = l, r)$ is close to unity we can approximate the square root $\sqrt{R_{mj}}$ by $1 - (1 - R_{mj})/2$ and obtain

$$r_{ml} r_{mr} \mathrm{e}^{2\mathrm{i}\psi_b} \approx 1 - \frac{1}{2}(1 - R_{ml}) - \frac{1}{2}(1 - R_{mr}) + 2\mathrm{i}\frac{\bar{L} + L_b}{c}(\omega - \bar{\omega}), \tag{7.49}$$

where $\bar{L}$ represents a mirror penetration length,

$$\bar{L} = \frac{\pi c}{\bar{\omega} n_b^2}\frac{n_1 n_2}{n_2 - n_1},$$

and R_{mj} is given by (7.45) with n_4 equal to 1 for $j = l$ and to the refractive index of the substrate for $j = r$. Substituting (7.49) into (7.43) we arrive at the equation for the photon eigenfrequency

$$\bar{\omega} - \omega - \mathrm{i}\bar{\gamma} = 0. \tag{7.50}$$

Here

$$\bar{\gamma} = \bar{\gamma}_l + \bar{\gamma}_r \tag{7.51}$$

and $\bar{\gamma}_{l,r}$ is the photon-mode damping due to the photon escape through the left or right mirror,

$$\bar{\gamma}_j = \frac{1}{8}\,(1 - R_{mj})\bar{\Gamma}\,,\ \bar{\Gamma} = \frac{2c}{n_b(\bar{L} + L_b)}\,. \tag{7.52}$$

As for the real part of the eigenfrequency, it indeed coincides with the frequency $\bar{\omega}$ introduced while choosing the layer thicknesses a_1, a_2 according to (7.32). Important parameters of a microcavity are the cavity *finesse* $F = \pi/(1 - R_m)$ and quality factor $Q = \bar{\omega}\bar{T}$, where $\bar{T}^{-1} = 2\bar{\gamma}$ is the rate at which the photon escape from the cavity.

When a QW is put in the cavity, optimal coupling of the electric field to the exciton is obtained when the electric field is maximum at the QW position. This is achieved at the cavity center in a λ-cavity with $N_b = 2$ in (7.32), and at the positions $L_b/3, 2L_b/3$ in the active layer for a $3\lambda/2$ cavity. The eigenfrequencies of exciton polaritons in a quantum microcavity can be found if we substitute (3.21, 7.45, 7.48) into (7.41, 7.42). For the particular case of a single QW placed in the center of the active layer and even N_b in order to have an antinode of the electric field in the center, the result reads

$$(\omega - \bar{\omega} + \mathrm{i}\bar{\gamma})(\omega - \omega_0 + \mathrm{i}\Gamma) = V^2\,, \tag{7.53}$$

where

$$V^2 = \frac{2c\Gamma_0}{n_b(\bar{L} + L_b)} = \bar{\Gamma}\Gamma_0\,. \tag{7.54}$$

Note that $2V$ determines the Rabi splitting in the strong-coupling regime. Equations (7.34) can be also presented in the similar form

$$(\omega - \bar{\omega} + \mathrm{i}\bar{\gamma})(\omega - \omega_0 + \mathrm{i}\Gamma) = \gamma_1\gamma_2\,.$$

Therefore, $\gamma_1\gamma_2 = V^2$ and, since $\gamma_1 = \xi\Gamma_0$, we have

$$\gamma_2 = \frac{V^2}{\gamma_1} = \frac{\bar{\Gamma}}{\xi}\,. \tag{7.55}$$

In terms of Γ_0, ξ and $\bar{\Gamma}$ equations (7.34) are written in the form

$$(\omega_0 - \omega - \mathrm{i}\Gamma)P = \xi\Gamma_0 E\,, \tag{7.56a}$$

$$(\bar{\omega} - \omega - \mathrm{i}\bar{\gamma})E = \bar{\Gamma}\left(\frac{1}{\xi}P - \mathrm{i}\frac{t'_{ml}}{2}E_0\right)\,. \tag{7.56b}$$

Here we included the field E_0 from the external light source placed in the left semi-space. The amplitudes, E_j, of the reflected and transmitted light waves can be calculated by solving (7.56) and using the following equations for the outgoing waves

$$E_j = \frac{t_{mj}}{2}E\,. \tag{7.57}$$

The eigenfrequencies of exciton polaritons with $q_\parallel \neq 0$ can be similarly derived taking into account that, at oblique incidence, the reflection and transmission coefficients $r_{\rm QW}, t_{\rm QW}$ are given by (3.51) and (3.53) for the s- and p-polarized light, respectively. On the other hand, the empty-cavity photon mode has the dispersion

$$\omega_{\rm phot}(q_\parallel) = \sqrt{\bar{\omega}^2 + (cq_\parallel/n_b)^2}\,,$$

which follows from the photon dispersion $\omega = (c/n_b)q = (c/n_b)\sqrt{q_z^2 + q_\parallel^2}$ in the active layer and the quantization of q_z in the microcavity. For small enough values of the in-plane wave vector, $q_\parallel \ll \bar{q} = (\bar{\omega}/c)n_b$, one has

$$\omega_{\rm phot}(q_\parallel) = \bar{\omega} + \frac{\hbar q_\parallel^2}{2\bar{m}} \tag{7.58}$$

with the 2D-photon effective mass being equal to

$$\bar{m} = \frac{n_b^2 \hbar \bar{\omega}}{c^2}\,. \tag{7.59}$$

In a quantum microcavity the exciton and photon modes are mixed to lead to the following dispersion of the upper and lower TE-polarized exciton-polariton branches

$$\omega_\pm(q_\parallel) = \frac{\omega_0 + \bar{\omega}}{2} + \frac{\hbar q_\parallel^2}{4\bar{m}} \pm \sqrt{V^2 + \left(\frac{\omega_0 - \bar{\omega}}{2} + \frac{\hbar q_\parallel^2}{4\bar{m}}\right)^2}\,, \tag{7.60}$$

where the exciton and photon-mode decay rates are ignored. Moreover, the exciton effective mass is set to infinity because the photon-mode mass $\bar{m}$ is extremely light and usually amounts 10^{-5}-$10^{-4}\ m_0$. For a quantum microcavity with ω_0 and $\omega_{\rm phot}$ coinciding at some particular value $\bar{k}_\parallel$, the dispersion (7.60) can be conveniently rewritten in the form

$$\omega_\pm(q_\parallel) = \omega_0 + \frac{\hbar(q_\parallel^2 - \bar{q}_\parallel^2)}{4\bar{m}} \pm \sqrt{V^2 + \left(\frac{\hbar(q_\parallel^2 - \bar{q}_\parallel^2)}{4\bar{m}}\right)^2}\,. \tag{7.61}$$

The dispersion of TM-polarized exciton polaritons in quantum microcavities was discussed in [7.53].

In the strong-coupling regime, the split frequencies $\omega_\pm$ reveal themselves as dips in the reflection spectra and peaks in the transmission or absorption spectra. For illustration of the strong-coupling regime, Fig. 7.4 shows the measured normal-incidence reflectivity of a λ cavity with quarter-wave pairs of AlAs ($n_1 = 2.95$) and GaAs ($n_2 = 3.61$) and with a single QW $In_{0.04}Ga_{0.96}As$ embedded in a GaAs active layer. The cavity-photon resonance was tuned to

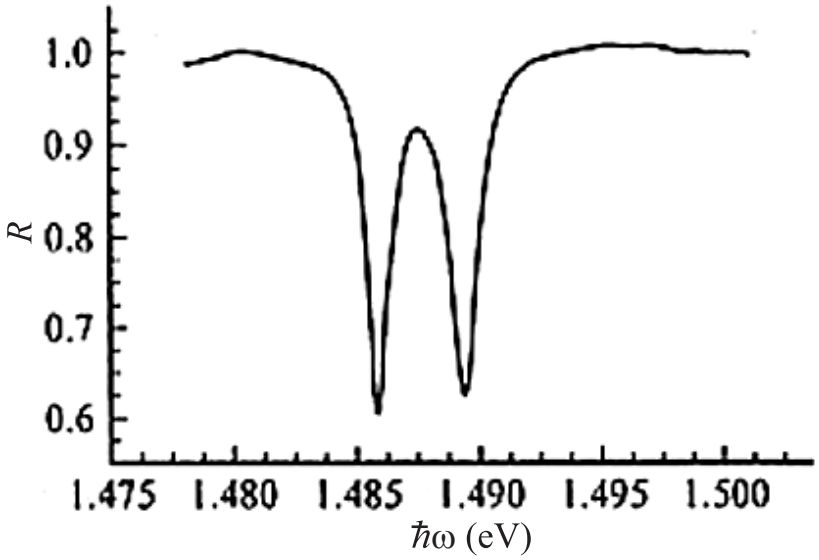

Fig. 7.4. Reflection spectrum from a quantum microcavity with a single QW embedded in the center of 1λ active layer. From [7.52].

the exciton resonance, $\bar{\omega} = \omega_0$. One can see two well-resolved reflectivity dips with a high splitting-to-linewidth ratio. The dip positions determine the energies, $\hbar\omega_{\pm}$, of the 2D-exciton–2D-photon coupled modes. The difference $\hbar(\omega_+ - \omega_-) \approx 3.5$ meV gives the Rabi splitting. The coherent interaction between the single-mode optical field and excitons in a QW leading to the Rabi splitting $\omega_+ - \omega_-$ can also be studied as quantum beats in the transient reflection or transmission spectra. It is worth to note that the Rabi splitting can be enhanced by inserting few QWs near the electric-field antinode of a λ-cavity or in different antinodes of a macrocavity with the thicker active layer [7.52, 7.53].

It is instructive to survey the existing variety of exciton-polariton quasiparticles focusing attention at the dimensionalities of bare exciton and photon states. In bulk semiconductors an exciton polariton is formed by a 3D exciton and a 3D photon. Heterostructures with QWs, quantum wires and quantum dots allow one to study coupling between 3D photons and 2D, 1D or 0D excitons, respectively. In a planar quantum microcavity, coupling of a 2D exciton in the embedded QW with a 2D photon confined in the cavity is realized. The 2D-1D and 2D-0D exciton-polariton states can be engineered in 2D microcavities with embedded quantum wires [7.54–7.57] and QDs or QD SLs [7.58, 7.59]. Gérard et al. [7.60] and Reithmaier et al. [7.61] have succeeded in further reducing the dimensionality of bare-photonic quantum states and fabricated laterally structured semiconductor microcavities

with three-dimensionally confined photons. In a cavity with the Bragg mirror stacks in the vertical direction and optical square-shaped lateral confinement, the optical mode spectrum splits into 0D levels given by

$$\omega_{\text{phot}} = \bar{\omega} + \frac{\hbar}{2\bar{m}} \left(\frac{\pi}{L}\right)^2 \left(\nu_x^2 + \nu_y^2\right) ,$$

where L is the lateral width and $\nu_{x,y} = 1, 2, ...$ are the lateral quantum numbers. Tridimensional light confinement was reported in an in-plane microcavity surrounded by a circular Bragg reflector [7.62]. The structure consists of deep concentric trenches etched in a $GaAs/Al_xGa_{1-x}As$ waveguiding heterostructure. In a wire-shaped microcavity with the lateral confinement along one direction, say along the x axis, the photon dispersion is described by a set of 1D modes

$$\omega_{\text{phot}}(q_y) = \bar{\omega} + \frac{\hbar}{2\bar{m}} \left[\left(\frac{\pi\nu_x}{L}\right)^2 + q_y^2\right] ,$$

where q_y is the photon wave vector along the optical-wire axis. Exciton-light coupling in cylindrical microcavities containing quantum wires was theoretically analyzed in [7.63].

Confined optical modes in semiconductor microcavities has opened a way for studies of mixing between 0D and 1D photons and ND excitons ($N = 2, 1, 0$) [7.64–7.69]. Recently Constantin et al. [7.70] have investigated in one study the coupling between 1D excitons and 3D, 2D, 1D and 0D photon states in high-finesse photon-well, photon-wire and photon-dot Bragg-air microcavites with embedded V-groove quantum wires. The interaction of electromagnetic waves and excitons is enhanced with decreasing the dimensionality of the states involved in the mixing.

7.5.2 Four-Wave Mixing in Microcavities

Turning to the nonlinear optical response of a QW microcavity in pump-probe experiments we first of all mention the exciton bleaching in the presence of free carriers generated under optical pumping, see, e.g., the review [7.52] and references therein. Physically, the pumping can lead to broadening of the exciton resonances, due to scattering of excitons by the photocarriers, and/or to a reduction in the exciton oscillator strength (described by the parameter Γ_0), due to the phase-filling and screening effects. If the former mechanism dominates then, with increased excitation, the transmission peaks at $\omega_\pm$ widen and reduce in height without a remarkable reduction in the splitting $\omega_+ - \omega_-$ [7.71]. Houdré et al. [7.72] studied a transition from the strong- to the weak-coupling regime due to the photoinduced loss of exciton oscillator strength. From carrier-density-dependent photoluminescence data, they conclude that the oscillator strength saturates as $(1 + N/N_{sat})^{-1/2}$ with $N_{sat} = 4.3 \times 10^{11}$ cm^{-2} at 100 K, where N is the density of electron-hole

pairs. Saba et al. [7.73] realized biexcitonic mechanism of the nonlinear optical response in a semiconductor microcavity. In pump-probe measurements they observed a crossover from exciton to biexciton polaritons: with increasing pump intensity the linear exciton-polariton doublet (7.61) evolves into a triplet polariton structure and finally into a shifted biexciton-polariton doublet.

The dynamics of exciton polaritons and the interplay between the coherent and incoherent processes in quantum microcavities has been revealed in a number of experiments on four-wave mixing carried out in cavities containing III-V or II-VI QWs [7.74–7.76]. Combining (7.17) with (7.56) we can switch the theoretical consideration of four-wave mixing from a single QW to a λ-cavity with a QW in its center and write the basic equations [7.77]

$$\left[\frac{d}{dt} + \mathrm{i}(\omega_0 - \tilde{\omega}) + \Gamma\right] \tilde{P}(t) = \mathrm{i}\xi\Gamma_0 \tilde{E}(t) + \mathrm{i}F_{NL}(t)\,, \tag{7.62a}$$

$$\left[\frac{d}{dt} + \mathrm{i}(\bar{\omega} - \tilde{\omega}) + \bar{\gamma}\right] \tilde{E}(t) = \bar{\Gamma}\left[\frac{\mathrm{i}}{\xi}\tilde{P}(t) + \frac{t'_{ml}}{2}\tilde{E}_0(t)\right] \tag{7.62b}$$

describing the nonlinear dynamics of exciton polaritons in the cavity.

We will analyze the degenerate four-wave mixing in a particular case where all three frequencies $\omega_0, \bar{\omega}$ and $\tilde{\omega}$ coincide and the incident pulses are short enough to overlap spectrally both resonance frequencies $\omega_\pm$ in (7.60). In this case the responses $\tilde{P}^{(n)}(t)$ and $\tilde{E}^{(n)}(t)$ to the pulses $n = 1, 2$ in the four-wave-mixing setup can be presented as

$$\tilde{P}_n(t) = \mathrm{i}t'_{ml}\xi\frac{\bar{\Gamma}\Gamma_0}{2\tilde{\Omega}}\mathcal{N}_n\theta(t - t_n)\exp\left[-\gamma(t - t_n)\right]\sin\left[\tilde{\Omega}(t - t_n)\right]\,, \tag{7.63}$$

$$\begin{aligned}\tilde{E}_n(t) = {} & \frac{t'_{ml}}{2}\bar{\Gamma}\mathcal{N}_n\theta(t - t_n)\exp\left[-\gamma(t - t_n)\right] \\ & \times\left\{\cos\left[\tilde{\Omega}(t - t_n)\right] - s\sin\left[\tilde{\Omega}(t - t_n)\right]\right\}\,,\end{aligned}$$

where $\gamma = (\Gamma + \bar{\gamma})/2$, $s = (\bar{\gamma} - \Gamma)/(2\tilde{\Omega})$ and $2\tilde{\Omega}$ is the Rabi splitting. For the two-level-like nonlinearity, the nonlinear source in (7.62a) can be transformed to

$$F_{NL}(t) = \mathrm{i}\theta(t)F_{NL}^{(0)}\mathrm{e}^{-\gamma T}\mathrm{e}^{-3\gamma t}\sin\left[\tilde{\Omega}(t + T)\right]\sin\tilde{\Omega}t(\cos\tilde{\Omega}t - s\sin\tilde{\Omega}t)\,, \tag{7.64}$$

$$F_{NL}^{(0)} = \frac{1}{8}\beta_2\left(t'_{ml}\bar{\Gamma}\right)^3\left(\xi\frac{\Gamma_0}{\tilde{\Omega}}\right)^2\mathcal{N}_1\mathcal{N}_2^2.$$

Here we assume pulse 1 to arrive before pulse 2, $t_2 > t_1$, and put $t_2 = 0$ in which case the interpulse time delay $T = -t_1 = |t_1|$. According to (7.64) the electric field of the self-diffracted wave $2\boldsymbol{k}_2 - \boldsymbol{k}_1$ can be presented as

$$\tilde{E}_3(t) = \mathrm{e}^{-\gamma T}[f_1(t)\cos\tilde{\Omega}T + f_2(t)\sin\tilde{\Omega}T]\,, \tag{7.65}$$

where the functions $f_1(t), f_2(t)$ are independent of T, and the time-integrated signal has the form [7.77]

$$S^{(3)}(T) = S\mathrm{e}^{-2\gamma T}[1 + a\sin(2\tilde{\Omega}T + \phi_0)]\,. \tag{7.66}$$

Thus, the signal $S^{(3)}(T)$ is a sum of monotonous and oscillating terms. The three parameters S, a, ϕ_0 entering (7.66) determine, respectively, the value of the monotonous term at zero delay, and the relative amplitude and initial phase of the oscillating term. A simple analytical form for these parameters follows if we assume γ to be small as compared with the Rabi splitting which implies the strong-coupling regime. Neglecting terms of the second and higher orders in $\gamma/\tilde{\Omega}$ we obtain for the parameters of the time-integrated signal

$$S = \frac{1}{12}\frac{1}{(8\gamma)^3}\left(\frac{\bar{\Gamma}|F_{NL}^{(0)}|}{\xi\tilde{\Omega}}\right)^2\,,\ a = \frac{\bar{\gamma}+5\Gamma}{\tilde{\Omega}}\,,\ \phi_0 = 0. \tag{7.67}$$

Figure 7.5 illustrates the calculated evolution of time-dependent self-diffracted signal, $|\tilde{E}^{(3)}(t)|^2$, with increasing the interpulse delay for the case $\tilde{\omega} = \omega_0 = \bar{\omega}$. The parameters used in the computation correspond to those of $Al_{0.2}Ga_{0.8}As$ λ-cavity with the distributed Bragg reflectors comprising 24 $Al_{0.4}Ga_{0.6}As$/AlAs stacks on the cavity front side (air interface) and 33 stacks on the substrate side. The refractive indices are as follows: $n_{ext,l} = 1$, $n_{ext,r} = 3.63$, $n_1 = 3.17$, $n_2 = 3.45$, $n_b = 3.54$. The calculated values of $\bar{\gamma}$ and $\bar{\Gamma}$ are 0.51 ps^{-1} and 117 ps^{-1}. A single QW was assumed to be embedded in the center of the active layer and values of $\Gamma = 1.0$ ps^{-1} and $\Gamma_0 = 0.05$ ps^{-1} were chosen for the exciton nonradiative and radiative damping rates. In this case the Rabi splitting $2\tilde{\Omega}$ equals to 4.8 ps^{-1}. The signal in Fig. 7.5 exhibits quantum beats between the exciton and cavity modes, and a significant beat-like modulation is exposed in the dependencies on both t and τ.

The analysis shows that, for the biexcitonic mechanism of nonlinearity with $\tilde{\Omega} \gg \delta_{\mathrm{bi}}$, the time-resolved four-wave-mixing signal exhibits $2\tilde{\Omega}$-oscillations modulated by the second period $T_{\mathrm{bi}} = 2\pi/\delta_{\mathrm{bi}}$ corresponding to the biexciton binding energy $\hbar\delta_{\mathrm{bi}}$. For comparable but incommensurable $\tilde{\Omega}$ and δ_{bi}, the nonlinear signal reveals damped irregular oscillatory behavior.

Kelkar et al. [7.76] spectrally resolved four-wave mixing signal as a function of time delay and observed well-defined temporal oscillations at both the cavitylike and heavy-hole-excitonlike resonances. The period of oscillations is measured to be 440 fs and matches well with the splitting of 9.5 meV between the two exciton-polariton modes.

7.5.3 Angle-Resonant Stimulated Polariton-Polariton Scattering

The further progress in the understanding of nonlinear optical properties of microcavities was stimulated by an observation of the previously overlooked scattering process shown in Fig. 7.6 [7.78–7.80]. In this process, two polaritons

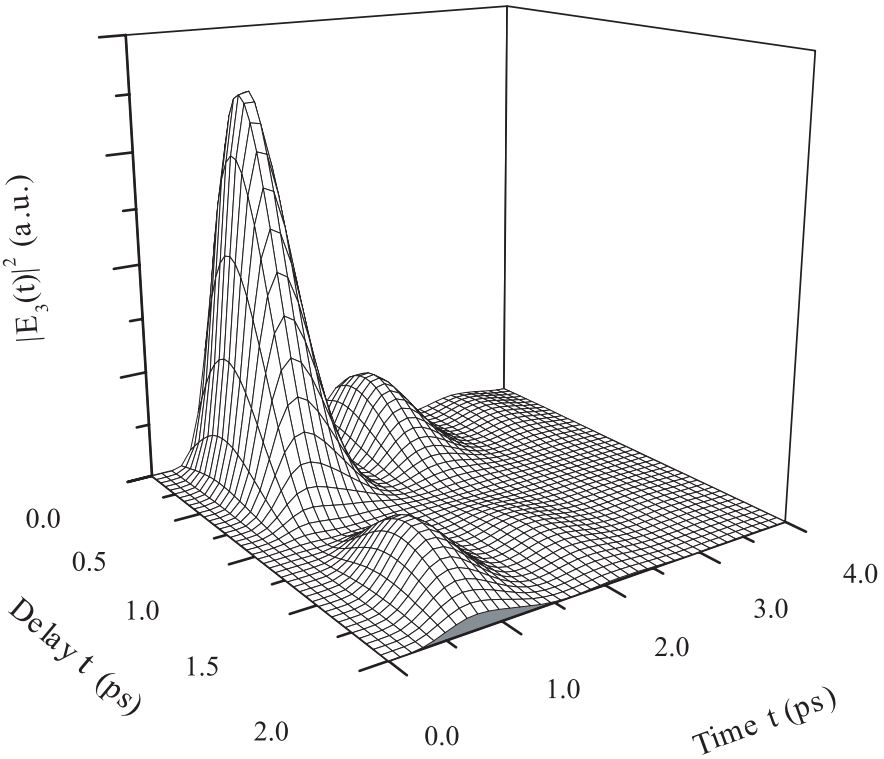

Fig. 7.5. The calculated time-resolved $2\boldsymbol{k}_2 - \boldsymbol{k}_1$ signal for different time delays between the light pulses. The real time t is referred to the peak of pulse 2. The pattern reveals the damped oscillatory behavior in both τ- and t-dependencies. From [7.77].

from the lower branch ω_- with the same in-plane wave vector $\boldsymbol{q}_p$ injected by the oblique-incidence pump are scattered within the branch ω_- into one "signal" polariton with $\boldsymbol{q}_\parallel = 0$ and one "idler" polariton with $\boldsymbol{q}_\parallel = 2\boldsymbol{q}_p$. Energy and momentum conservation restricts the range of $\boldsymbol{q}_p$ to those satisfying

$$2\omega_-(q_\parallel) = \omega_-(0) + \omega_-(2q_\parallel)\,. \tag{7.68}$$

For particles with a parabolic dispersion this scattering process is forbidden. As discussed in Sect. 7.5.1 the strong coupling between the excitons and photons in a micricavity produces two new dispersion branches of mixed quasiparticles. The lower branch $\omega_-(q_\parallel)$ has radically nonparabolic shape and allows extra scatterings to take part, in particular the process in Fig. 7.6. Substituting $\omega_-(q_\parallel)$ from (7.60) into (7.68) and considering a microcavity with the photon resonance $\bar{\omega}$ tuned to ω_0, we can come to the transcendental equation

$$\sqrt{1+4x^2} - \sqrt{4+x^2} + 1 - x = 0\,,$$

for the dimensionless variable $x = \hbar q_{\|}^2/(2\bar{m}V)$. This equation has two solutions, $x_1 = 0$ and $x_2 = 1$. Therefore, the above polariton-polariton scattering occurs for $q_p = \sqrt{2V\bar{m}/\hbar}$ and the critical, or "magic", angle of incidence is given by

$$\theta_p = \arcsin\left(cq_p/\omega_0\right) = \arcsin\left(n_b\sqrt{2\tilde{\Omega}/\omega_0}\right), \tag{7.69}$$

because, if the detuning $\bar{\omega} - \omega_0$ is zero and the damping rates are ignored, the Rabi splitting $2\tilde{\Omega}$ equals $2V$.

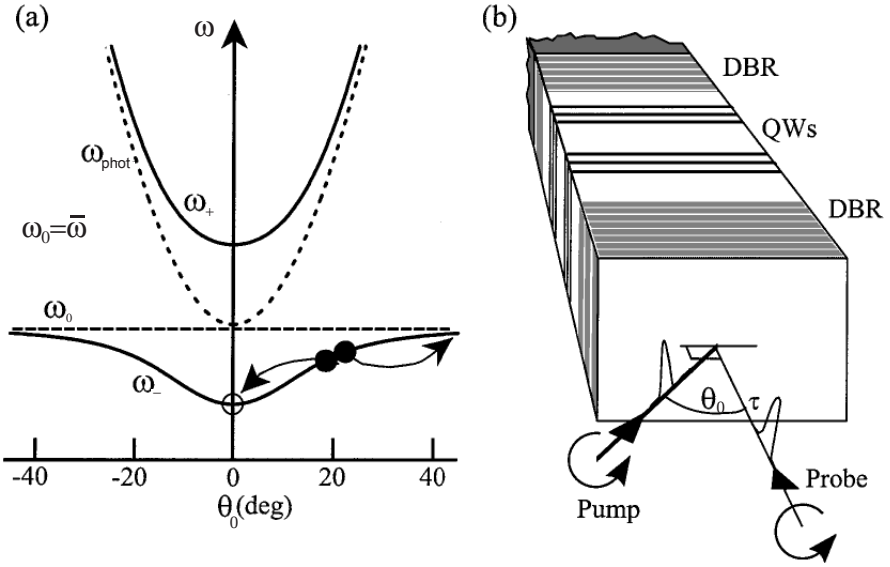

Fig. 7.6. (**a**) Polariton dispersion relation vs. incident angle θ_0 at zero detuning. Microcavity (exciton) frequencies $\omega_{\rm phot}$ (ω_0) shown dashed. Probe polariton (open circle) stimulates the scattering of pump polaritons (filled circles). (**b**) Sample structure and experimental geometry probed at normal incidence and time delay τ, while changing the pump angle θ_0. From [7.78].

The scattering under consideration was first observed by Savvidis et al. [7.78] in pump-probe experimental set-up shown in Fig. 7.6. The pump pulse excites resonantly the polaritons $\omega_-(q_p)$ at the magic angle θ_p. With a controlled delay a normally-incident probe pulse follows the pump one and the spectrally-resolved reflected signal is measured as a function of the pump intensity. The probe polaritons with $q_{\|} = 0$ stimulate the scattering of pump polaritons. Fig. 7.7 shows the reflected probe spectra when a broad-band 100 fs probe pulse (< 0.3 mW) is focused along the growth axis to a 50 μm spot on the sample. The no-pump spectrum has two dips revealing the exciton-polariton modes with the Rabi splitting $2\tilde{\Omega} \approx 7$ meV. This spec-

trum is radically modified when the pump pulse arrives, provoking narrow-band gains around the lower polariton of up to 70. These enormous gains for the injected pulses are observed when the pump is tuned to the vicinity of the lower-branch inflexion point and its incident angle is 16.5°. To confirm the gain is real, a narrow bandwidth probe centered at the lower polariton was used, producing the amplified spectrum shown in inset in Fig. 7.7. The observed angle-resolved stimulated amplification is a clear and impressive demonstration of the bosonic nature of cavity exciton polaritons.

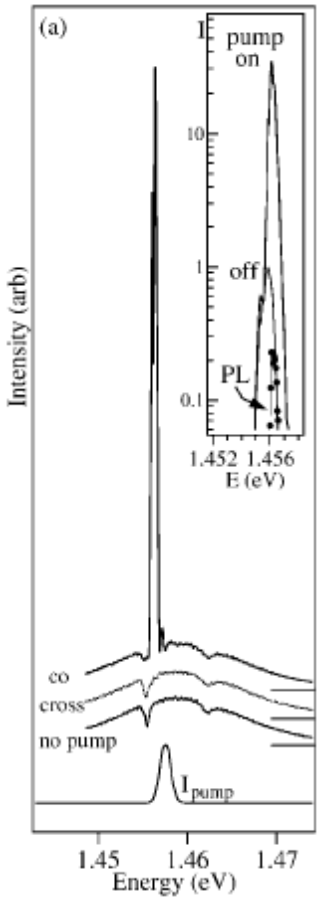

Fig. 7.7. Reflected probe spectra at $\tau = 0$ for pump off, co-, and cross-circularly polarized to the probe. Spectral oscillations are caused by interference between reflections from front and back of the sample. Pump spectrum on lower trace. Inset: Reflected narrow-band probe spectra at $\tau = 0$, with pump pulse on/off, together with pump PL without probe pulse (filled circles). From [7.78].

In the absence of the probe pulse, the pump luminescence collected in the same direction is over 2 orders of magnitude weaker. In [7.79, 7.80], the pump photoluminescence was studied in more detail under conditions of cw excitation of the similar QW microcavities. At low input powers I_p, the $\theta = 0°$ "signal" output is a linear function of I_p. The linear output-input regime is followed by a dramatic superlinear increase above the threshold pump density $I_p \sim 15$ W/cm^2. The bottom of the lower branch ω_- forms a "trap" for exciton polaritons. When driven by a cw laser at the magic angle, the polaritons are sucked into the trap, condensing into a macroscopic quantum state which efficiently emits light. Also clearly apparent in spectra is the "idler" mode (with the wave vector $2q_p$) observed at the angle $\varphi_0 = 35°$. It is more than an order of magnitude weaker than the signal.

A theory of the angle-resolved polariton amplifier has been proposed by Ciuti et al. [7.81]. They consider the excitation configuration of Fig. 7.6 with the probe and pump producing the polaritons with the wave vectors $q_\parallel = 0$ and $q_\parallel = \boldsymbol{q}_p$, respectively. Ciuti et al. present a close set of equations of motion for the polarizations $P_0 \equiv P(q_\parallel = 0)$, $P_1 \equiv P(\boldsymbol{q}_p)$ and $P_2 \equiv P(2\boldsymbol{q}_p)$ of the probe, pump and idler polaritons. For the steady-state regime with the probe electric field $E_{\text{probe}}(t) = \tilde{E}_{\text{probe}} \exp(-\mathrm{i}\omega t)$ and the pump electric field $E_{\text{pump}}(t) = \tilde{E}_{\text{pump}} \exp(-\mathrm{i}\omega_p t)$, one has

$$P_0 = \tilde{P}_0 \mathrm{e}^{-\mathrm{i}\omega t}\,,\; P_1 = \tilde{P}_1 \mathrm{e}^{-\mathrm{i}\omega_p t}\,,\; P_2 = \tilde{P}_2 \mathrm{e}^{-\mathrm{i}(2\omega_p - \omega)t}\,,$$

where $\omega_p = \omega_-(q_p)$, and the equations for the polarization amplitudes read

$$\{\mathrm{i}\,[\omega - \omega_-(0)] + \gamma\}\,\tilde{P}_0 = \Omega_{\text{int}} \tilde{P}_1^2 \tilde{P}_2^* + \mathcal{F}_{\text{probe}}\,, \tag{7.70a}$$

$$\gamma \tilde{P}_1 = \Omega_{\text{int}} \tilde{P}_0 \tilde{P}_1^* \tilde{P}_2 + \mathcal{F}_{\text{pump}}\,, \tag{7.70b}$$

$$\{\mathrm{i}[2\omega_-(q_p) - \omega - \omega_-(2q_p)] + \gamma\}\tilde{P}_2 = \Omega_{\text{int}} \tilde{P}_0^* \tilde{P}_1^2\,. \tag{7.70c}$$

Here $\mathcal{F}_{\text{probe}}, \mathcal{F}_{\text{pump}}$ are the probe and pump driving terms proportional to the amplitudes $\tilde{E}_{\text{probe}}$ and $\tilde{E}_{\text{pump}}$, $\hbar\Omega_{\text{int}}$ is the coupling energy of the polariton-polariton interaction and, for simplicity, the damping rate is taken the same for the three modes. Note that the frequencies ω_0, $\omega_-(q_p)$ and $\omega_-(2q_p)$ are slightly blueshifted with respect to the unperturbed lower polariton branch. The blueshift occurs due to the polariton-polariton interaction and is proportional to $|\tilde{P}_1|^2$.

Taking (7.70a) and complex conjugate of equation (7.70c) we have the linear inhomogeneous system that determines the quantities $\tilde{P}_0$ and $\tilde{P}_2^*$ as a function of $\tilde{P}_1$. With simple algebra, one finds that the probe polarization as function of ω has two complex poles

$$\tilde{P}_0 \propto \frac{\mathcal{F}_{\text{probe}}}{(\omega^{(+)} - \omega)(\omega^{(-)} - \omega)}\,,$$

$$\omega^{(\pm)} = \frac{1}{2}\left[\omega_-(0) + 2\omega_-(q_p) - \omega_-(2q_p) \pm \sqrt{\Theta}\right] + \mathrm{i}\gamma\,,$$

with

$$\Theta = [\omega_-(0) + \omega_-(2q_p) - 2\omega_-(q_p)]^2 - 4(\Omega_{\rm int}|\tilde{P}_1|^2)^2 \,.$$

The nonlinear response of the probe becomes singular when one of the poles is real. Such a condition is fulfilled when the energy conservation law (7.68) is satisfied and the threshold density given by $\Omega_{\rm int}|\tilde{P}_1|^2 = \gamma$ is reached. In this case $\omega^{(-)}$ becomes real and equal $\omega_-(0)$ while $\omega^{(+)} = \omega_-(0) + 2{\rm i}\gamma$. If the energy conservation is not satisfied, particularly if the pump incidence angle differs from the magic angle, the threshold density is higher and the amplification smaller. The singularity of the probe polarization at $\omega = \omega_-(0)$ is only formal and becomes finite if (7.70b) for the pump is consistently solved [7.81].

Similar angular-resolved probe-pump experiments have been performed as well in wire-shaped microcavities [7.82]. The experiments show that again, due to polariton-polariton scattering, a high optical gain is observed at $q = 0$ and at the idler state $2q_p$, but for photonic wires the polariton energies can be located on different subbranches from the pump.

7.5.4 Stimulated Spin Dynamics of Polaritons

According to Fig. 7.7, the scattering process introduced in [7.78] is highly polarization dependent. It is strong for co-circularly polarized pump and probe beams and completely suppressed for their opposite circular polarizations. It thus seemed possible to describe all the intermediate situations where both pump and probe are elliptically polarized by simply decomposing them into σ_+ and σ_- components and considering these components independently. However, this picture has been ruled out by the experiment of Lagoudakis et al. [7.83] who have reported unusual polarization properties of a microcavity excited resonantly at the magic angle. For example, in the case of a linearly-polarized pump pulse and circularly polarized probe pulse the observed signal was linearly polarized but in the polarization plane rotated by 45° with respect to the pump polarization. Figures 7.8a, b and c plot the intensity of polarization components of the emitted signal versus the helicity, $P_{{\rm pump},c}$, of the elliptically polarized pump. The main axis of the pump polarization ellipse is parallel to the incidence plane and the probe polarization is kept circular σ_+. The detected components are I_+, I_- (circular polarization), I_1, I_2 (linear polarization in the axes 1, 2 being parallel and perpendicular to the plane of pump incidence) and $I_{1'}, I_{2'}$ (linear polarization in the axes $1'$, $2'$), see (3.228). The polarization of the idler emission shows a similar behavior but differs in details from that of the signal. Kavokin et al. [7.84] have presented two models, phenomenological and pseudospin ones, in order to interpret the behavior of the polarized emission of resonantly excited microcavities. The intensities of the six polarization components calculated in the phenomenological model by using two fitting complex parameters are shown in Figs. 7.8d, e and f. The pseudospin model in [7.84] is based on representing the polariton polarized states in terms of the psedospin component

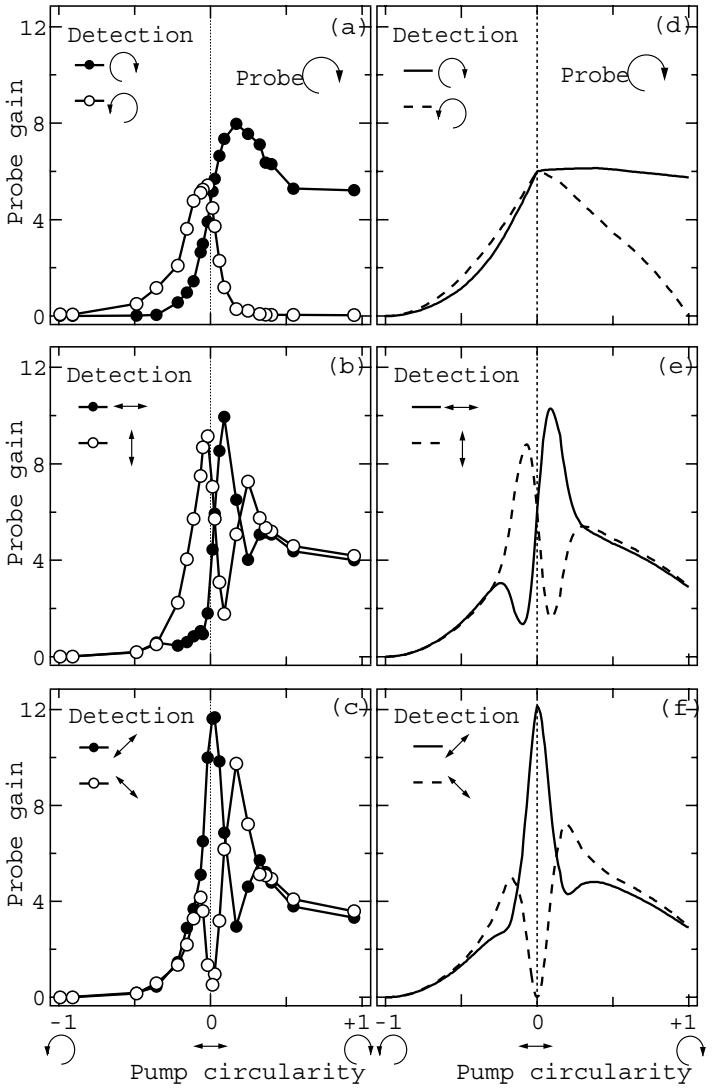

Fig. 7.8. Intensity of signal emission, decomposed into (**a**),(**d**) circular, (**b**),(**e**) linear, and (**c**),(**f**) linear diagonal polarizations, as a function of the pump circular polarization degree, where (**a**)-(**c**) show the experimental data and (**d**)-(**f**) show the theoretical predictions. The probe is σ_+ polarized. From [7.84].

S_z for circular polarization and S_x, S_y for linear polarization in the axes 1, 2 and $1'$, $2'$, in the same way as it is done in Sect. 5.5.2 for heavy-hole excitons. It is assumed that, due to exchange interaction, the pump pulse induces the splitting of the probe polaritons described by the Hamiltonian

$$\mathcal{H} = \frac{\hbar}{2} \left(\tilde{\sigma}_x \Omega_x + \tilde{\sigma}_z \Omega_z \right) . \tag{7.71}$$

similar to the Hamiltonian (5.150) or (5.156). Here $\tilde{\sigma}_x$, $\tilde{\sigma}_z$ are pseudo Pauli matrices, $\hbar\Omega_x$ is the pump-induced splitting proportional to the degree of pump linear polarization in the axes 1, 2 and $\hbar\Omega_z$ is proportional to $P_{\mathrm{pump},c}$. The probe psedospin rotates around the vector $(\Omega_x, 0, \Omega_z)$ with the angular velocity $\Omega = \sqrt{\Omega_x^2 + \Omega_z^2}$ which leads to the observed polarization phenomena. Concluding this chapter, we underline that spin dynamics of polaritons in photon-well, photon-wire and photon-dot microcavities can be an area rich on new effects and deserves the further study.

8 Photogalvanic Effects

And after the fire came a gentle whisper.

1 Kings **19***: 12*

Light propagating through a semiconductor and acting upon mobile carriers can generate a dc electric current, under short-circuit condition, or a voltage, in case of open-circuit samples. In this chapter we consider only the PhotoGalvanic Effects (PGE) which, by definition, appear *not* due to inhomogeneity of optical excitation of electron-hole pairs, as in the Dember and photoelectromagnetic effects, and *not* due to inhomogeneity of the sample, as in the conventional photovoltaic effect in *p*-*n* junctions. Phenomenologically, the PGE under consideration are described by the following equation

$$j_\lambda = I\left[\gamma_{\lambda\mu}\mathrm{i}(\boldsymbol{e}\times\boldsymbol{e}^*)_\mu + \chi_{\lambda\mu\nu}\frac{e_\mu e_\nu^* + e_\nu e_\mu^*}{2} + T_{\lambda\mu\nu\eta}q_\mu e_\nu e_\eta^*\right] \tag{8.1}$$

which relates the dc current density with the light intensity I, polarization $\boldsymbol{e}$ and wave vector $\boldsymbol{q}$. In a bulk semiconductor or superlattice the index λ runs over all three Cartesian coordinates x, y, z. In QW structures the free-carrier motion along the growth direction is quantized and the index λ enumerates two interface coordinates. In quantum wires and nanotubes the free movement is allowed only along one axis, the principal axis of the structure, and the coordinate λ is parallel to this axis. On the other hand, the light polarization unit vector $\boldsymbol{e}$ can be arbitrarily oriented in space and, therefore, $\mu, \nu = x, y, z$. Note that, for linearly polarized light, the complex conjugate vector $\boldsymbol{e}^*$ is parallel to $\boldsymbol{e}$ and the vector product $\boldsymbol{e}\times\boldsymbol{e}^*$ vanishes. However, for elliptically polarized electromagnetic wave, this product is nonzero, it is purely imaginary and proportional to the degree of circular polarization P_c. Note that, for a transverse wave, the vector $\mathrm{i}\,(\boldsymbol{e}\times\boldsymbol{e}^*)$ can be presented as a product $P_c\hat{\boldsymbol{o}}$, $\hat{\boldsymbol{o}}$ being a unit vector in the direction of light propagation.

The tensor $\boldsymbol{\gamma}$ in (8.1) relates components of the polar vector $\boldsymbol{j}$ and the axial vector $\boldsymbol{e}\times\boldsymbol{e}^*$, it is nonzero for point groups which allow optical activity or gyrotropy. The effect described by this tensor is called the *circular* PGE. It appears only under illumination with circularly polarized light and reverses direction when the sign of circular polarization is changed.

The effect described by the second term in (8.1) is called the *linear* PGE. The reason is that it is independent of the sign of circular polarization and usually measured under linearly polarized photoexcitation. The third-rank tensor $\boldsymbol{\chi}$ in (8.1) is invariant under interchange of indices μ and ν. There-

fore, the linear PGE can be observed in noncentrosymmetric media of the piezoelectric classes.

The third term on the right-hand side of (8.1) represents the photon drag effect. It is due to momentum transfer from photons to charge carriers and can be induced in both noncentrosymmetric and centrosymmetric systems.

We begin our study of the photocurrents from the circular PGE (Sect. 8.1). Then we consider its counterpart, the spin-galvanic effect (Sect. 8.2). In Sects. 8.3 and 8.4 we give an overview of the photon drag effect and the linear PGE. Next we discuss the saturation of the circular and linear PGE with increasing the light intensity (Sect. 8.5). The final section 8.6 is devoted to the circular PGE and other chirality effects in carbon nanotubes.

8.1 Circular Photogalvanic Effect in Quantum Well Structures

Physically, the circular PGE can be considered as a transformation of the photon angular momenta into a translational motion of free charge carriers. It is an electronic analog of mechanical systems which transmit rotatory motion to linear one like a screw thread or a plane with propeller. The effect was independently predicted by Ivchenko and Pikus [8.1], and Belinicher [8.2]. It was studied both theoretically and experimentally in bulk gyrotropic crystals (see the review article [8.3] and the book [8.4]), particularly in tellurium [8.5,8.6], and recently in zinc-blende- and diamond-based QW structures [8.7–8.10]. In this section we perform the symmetry analysis of the circular PGE in (001)- and (113)-grown QWs, present experimental data for demonstration and outline the microscopic theory of the effect under interband, intersubband and intrasubband optical transitions in QWs.

The three point groups D_{2d}, C_{2v} and C_s are particularly relevant in connection with the photogalvanic experiments on zinc-blende-based QW structures. Hereafter the Schönflies notation is used to label the point groups. In the international notation they are labelled as $\bar{4}2m, mm2$ and m, respectively. A (001)-grown QW with equivalent normal and inverted interfaces has the D_{2d} point-group symmetry. The point group reduces from D_{2d} to C_{2v} in symmetrical QWs with built-in electric fields or asymmetrical QWs, say compositionally stepped QWs, QWs with different profiles of the left and right interfaces, etc. If QWs are grown along the low-symmetry axis $[hhl] \neq [001]$, [111] and [110], the point group becomes C_s and contains only two elements, the identity and one mirror reflection plane $\sigma_{(1\bar{1}0)}$. In the cases $h = l = 1$ and $h = 1, l = 0$, the QW point symmetry increases up to C_{3v} and C_{2v}, respectively.

For the point group C_s, in the coordinate system $x \parallel [1\bar{1}0]$, $y \parallel [ll(\overline{2h})]$, $z \parallel [hhl]$ the y- and z-components of a polar vector and x-component of an axial vector are invariants (the representation A^+, see Table A.1), the x-component of a polar vector and y- and z-components of an axial vector

transform according to the representation A^-. As a result, the first term in (8.1) can be rewritten as

$$j_x = (\gamma_{xy} o_y + \gamma_{xz} o_z) I P_c \, , \; j_y = \gamma_{yx} o_x I P_c \, . \tag{8.2}$$

For the point group C_{2v}, in the coordinate system $x \parallel [1\bar{1}0]$, $y \parallel [110]$, $z \parallel [001]$ the component γ_{xz} is zero and (8.2) reduces to

$$j_x = \gamma_{xy} o_y I P_c \, , \; j_y = \gamma_{yx} o_x I P_c \, . \tag{8.3}$$

Finally, for the point group D_{2d}, in the above coordinate system the same equations are also valid but the higher symmetry imposes the condition $\gamma_{xy} = \gamma_{yx} \equiv \gamma$ on the $\boldsymbol{\gamma}$ tensor. One has

$$j_x = \gamma o_y I P_c \, , \; j_y = \gamma o_x I P_c \, . \tag{8.4}$$

It follows from (8.2)-(8.4) that, in QWs of the C_s symmetry, the circular PGE can be observed even under normal incidence of irradiation while, in QWs of the C_{2v} or D_{2d} symmetry, the circular photocurrent can be generated only under oblique incidence.

Figure 8.1 shows results of measurements carried out at room temperature on (113)-grown p-GaAs/AlGaAs MQWs under normal incidence (upper panel) and (001)-grown n-InAs/AlGaSb SQW structure under oblique incidence with an angle of incidence in vacuum $\theta_0 = -30°$ (lower panel). Optical excitation was performed by a high-power far-infrared pulsed NH_3 laser which yields strong linearly polarized emission at wavelengths λ between 35 and 280 μm corresponding to photon energies from 35 to 4.4 meV with power up to 100 kW. The linearly polarized light could be modified to an elliptically polarized radiation by applying a crystalline quartz $\lambda/4$ plate and changing the angle φ between the optical axis of the plate and the polarization plane of the laser radiation. Thus the helicity P_c of the incident light varies from -1 (left handed, σ_-) to $+1$ (right handed, σ_+) according to

$$P_c = \sin 2\varphi \, . \tag{8.5}$$

One can see from Fig. 8.1 that the photocurrent direction is reversed when the polarization switches from right-handed circular, $\varphi = 45°$, to left-handed, $\varphi = 135°$. Moreover, the experimental points are well fitted by the equation

$$j_\lambda(\varphi) = j_\lambda^0 \sin 2\varphi \tag{8.6}$$

with one scaling parameter.

In Fig. 8.2 closer look is taken at the dependence of the photocurrent on the angle of incidence θ_0 in configuration with the incidence plane normal to the axis x. According to (8.2) the photocurrent induced along x in (113)-oriented QWs is given by

$$j_x = (\gamma_{xy} \sin\theta + \gamma_{xz} \cos\theta) t_p t_s I_0 P_c \, , \tag{8.7}$$

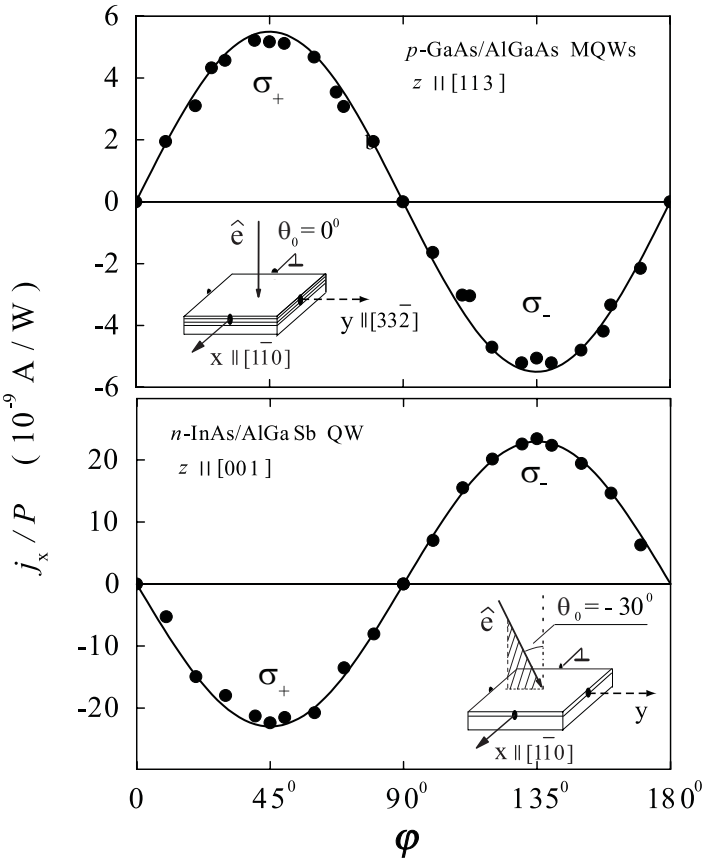

Fig. 8.1. Photocurrent in QWs normalized by the light power P as a function of the phase angle φ defining helicity. Measurements are presented for T = 300 K and $\lambda = 76$ μm. The insets show the geometry of the experiment. *Upper panel*: normal incidence of radiation on p-type (113)A-grown GaAs/AlGaAs QWs (symmetry class C_s). The current j_x flows along the $[1\bar{1}0]$ direction perpendicular to the mirror plane. *Lower panel*: oblique incidence of radiation with an angle of incidence $\theta_0 = -30°$ on n-type (001)-grown InAs/AlGaSb QWs (symmetry class D_{2d} or C_{2v}). Full lines are fitted using one parameter according to (8.6). [8.8]

where I_0 is the light intensity in vacuum, t_p and t_s are transmission coefficients after Fresnel's formula for linear p and s polarizations, θ is the refraction angle defined by $\sin\theta = \sin\theta_0/n$, and n is the index of refraction. In this case the circular PGE is observed at normal incidence. The fact that j_x is an even function of θ_0 means that in the sample under study the component γ_{xz} of the $\boldsymbol{\gamma}$ tensor is much larger as compared with γ_{xy}. In (001)-oriented samples where $\gamma_{xz} = 0$, a signal proportional to $\sin 2\varphi$ is observed only under

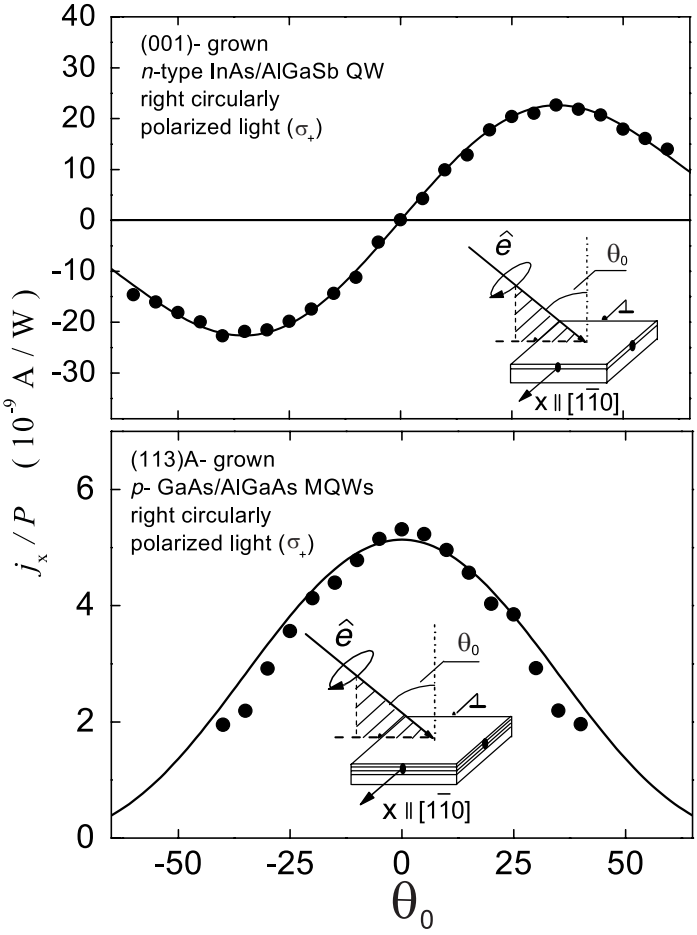

Fig. 8.2. Photocurrent in QWs normalized by the light power P as a function of the incidence angle θ_0 for right-circularly polarized radiation σ_+ measured perpendicularly to light propagation (T = 300 K, $\lambda = 76$ μm). *Upper panel*: n-type (001)-grown InAs/AlGaSb QWs. *Lower panel*: p-type (113)A-grown GaAs/AlGaAs QWs. Full lines are fitted using (8.7). From [8.8].

oblique incidence, and a variation of θ_0 in the plane of incidence changes the sign of the current j_x exactly at the point $\theta_0 = 0$.

Microscopically, a conversion of photon helicity into a current can be related to $\boldsymbol{k}$-linear terms in the effective Hamiltonian $\mathcal{H}^{(1)} = \beta_{lm}\sigma_l k_m$. The coefficients β_{lm} form a pseudotensor subjected to the same symmetry restriction as the pseudotensor $\boldsymbol{\gamma}$. The coupling between the spin Pauli matrices σ_l and the wave vector components k_m as well as spin-dependent selection rules

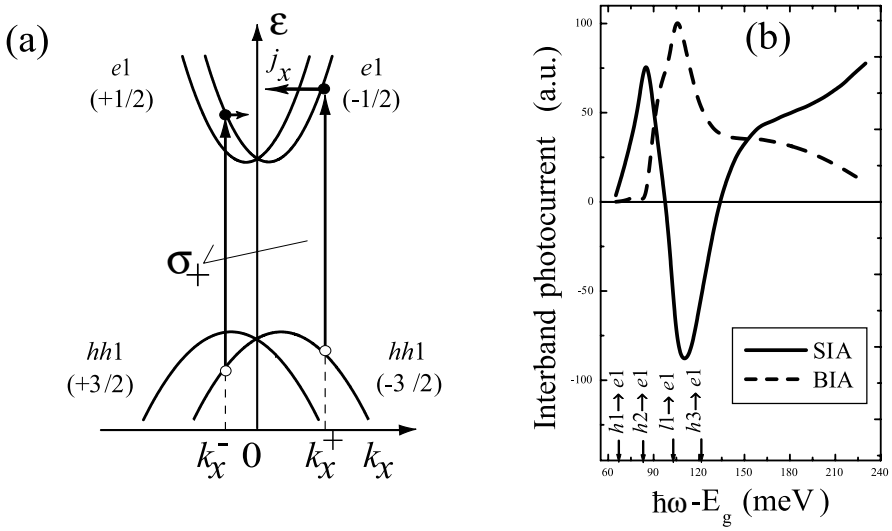

Fig. 8.3. (**a**) Microscopic picture describing the origin of spin polarized photocurrents. The essential ingredient is the spin splitting of the electron and/or hole states due to linear-$\boldsymbol{k}$ terms. (**b**) Calculated spectrum of the interband circular photocurrent due to SIA (*solid*) and BIA (*dashed*) electron spin splittings in a 100-Å wide QW. The arrows indicate the absorption edges for the four optical transitions. [8.11]

for electron optical transitions yield a net current sensitive to circularly polarized optical excitation. The circular PGE is most easily conceivable for direct optical transitions between the heavy-hole valence subband $hh1$ and conduction subband $e1$ in QWs of the C_s symmetry. For the sake of simplicity, we take the linear-$\boldsymbol{k}$ terms into account only in the conduction subband assuming the following parabolic dispersion in the $e1$ and $hh1$ subbands

$$E_{e1,\boldsymbol{k},\pm 1/2} = E_g^{QW} + \frac{\hbar^2 k^2}{2m_e} \pm \beta_e k_x \,,\; E^v_{hh1,\boldsymbol{k},\pm 3/2} = -\frac{\hbar^2 k^2}{2m_h} \,, \tag{8.8}$$

where E_g^{QW} is the bandgap renormalized because of the quantum confinement of electrons and holes. In Fig. 8.3a the allowed optical transitions are from $j = -3/2$ to $s = -1/2$ for the σ_+ polarization and from $j = 3/2$ to $s = 1/2$ for the σ_- polarization. Under circularly polarized radiation with a photon energy $\hbar\omega$ and for a fixed value of k_y the energy and momentum conservation allow transitions only from two values of k_x. For the σ_+ polarization these particular k_x values of photogenerated electrons are

$$k_x^{\pm} = \frac{\mu}{\hbar^2}\beta_e \pm \left[\frac{2\mu}{\hbar^2}(\hbar\omega - E_g^{QW}) - k_y^2 + \left(\frac{\mu}{\hbar^2}\beta_e\right)^2\right]^{1/2} \,, \tag{8.9}$$

where μ is the reduced electron-hole mass $m_e m_h/(m_e+m_h)$. The corresponding transitions are shown in Fig. 8.3a by the solid vertical arrows with their

"center-of-mass" shifted from the point $k_x = 0$ by $\beta_e \mu/\hbar^2$. Thus the average electron velocity in the excited state,

$$\bar{v}_{e,x} = \frac{\hbar(k_x^+ + k_x^-)}{2m_e} - \frac{\beta_e}{\hbar} = -\frac{\mu}{m_h}\frac{\beta_e}{\hbar}\,,$$

is nonzero and the contribution of $k_x^{\pm}$ photoelectrons to the current do not cancel as in the case $\beta_e = 0$. Consequently, a spin polarized net current in the x direction results. Changing the photon helicity from $+1$ to -1 inverts the current because the "center-of-mass" for this transitions is now shifted to $-\beta_e \mu/\hbar^2$. The asymmetric distribution of photoelectrons in the $\boldsymbol{k}$ space decays within the momentum relaxation time τ_p^e. However, under steady-state optical excitation new photocarriers are generated resulting in a dc photocurrent. The photohole contribution in considered in a similar way. Since the average hole velocity $\bar{v}_{h,x}$ coincides with $\bar{v}_{e,x}$, the final result for the interband circular photocurrent can be presented as

$$j_x = e\bar{v}_{e,x}(\tau_p^e - \tau_p^h)\frac{\eta_{cv} I}{\hbar\omega}P_c = -e(\tau_p^e - \tau_p^h)\frac{\beta_e}{\hbar}\frac{\mu}{m_h}\frac{\eta_{cv} I}{\hbar\omega}P_c\,,$$

where η_{cv} is the fraction of the energy flux absorbed in the QW due to the $hh1 \to e1$ transitions, different signs of the electron and hole contributions reflect opposite signs of the electron and hole charges. Note that the ratio $I/(\hbar\omega)$ is the flux of photons. If we add the term $\pm\beta_v k_x$ to the electron dispersion $E^v_{hh1,\boldsymbol{k},\pm 3/2}$ in the valence band we obtain

$$j_x = -e(\tau_p^e - \tau_p^h)\left(\frac{\beta_e}{m_h} + \frac{\beta_h}{m_e}\right)\frac{\mu}{\hbar}\frac{\eta_{cv} I}{\hbar\omega}P_c\,. \tag{8.10}$$

It should be mentioned that allowance for the energy dependence of the momentum relaxation times, $\tau_p^e(E_e)$ and $\tau_p^h(E_h)$, results in multiplication of the electron and hole contributions respectively by factors

$$1 + E_e\frac{d\ln\tau_p^e(E_e)}{dE_e}\,,\ 1 + E_e\frac{d\ln\tau_p^h(E_h)}{dE_h}\,, \tag{8.11}$$

where $E_{e,h}$ is the electron or hole energy. In the following these additional factors are as a rule disregarded.

Above we considered a particular mechanism of the circular PGE. Actually one can use the following general estimation for this effect

$$j_{\mathrm{CPGE}} = e\tau_p\frac{\beta}{\hbar}\frac{\eta I}{\hbar\omega}P_c\,, \tag{8.12}$$

where η is the relative absorbance for the considered optical transitions, β is a coefficient in the linear-$\boldsymbol{k}$ spin-dependent Hamiltonian and τ_p is a typical momentum relaxation time.

For more complicated band structures the previous simple consideration is invalid. Then one needs to use a sophisticated kinetic theory operating with the electron single-particle density matrix $\rho_{n'n}(\boldsymbol{k})$ and the following general equation of the electron current

$$\boldsymbol{j} = e \sum_{\boldsymbol{k}nn'} \boldsymbol{v}_{nn'}(\boldsymbol{k})\ \rho_{n'n}(\boldsymbol{k})\ . \tag{8.13}$$

Here, the indices n, n' enumerate the electronic states with a given value of $\boldsymbol{k}$ and $\boldsymbol{v}_{nn'}$ is the matrix element of the velocity operator. If the states $|\bar{n}, -\boldsymbol{k}\rangle$ and $|n, \boldsymbol{k}\rangle$ are related by the time inversion operation then one can write

$$\boldsymbol{v}_{\bar{n}\bar{n}'}(-\boldsymbol{k}) = -\boldsymbol{v}_{nn'}(\boldsymbol{k})\ .$$

This means that the current (8.13) is contributed only by the antisymmetrical component of the density matrix

$$\rho^{(-)}_{n'n}(\boldsymbol{k}) = \frac{1}{2}[\rho_{n'n}(\boldsymbol{k}) - \rho_{\bar{n}'\bar{n}}(-\boldsymbol{k})]\ . \tag{8.14}$$

For photoelectrons excited into the conduction subband $e1$ in a (001)-oriented QW and described by the effective 2×2 Hamiltonian

$$\mathcal{H} = E^0_{e1} + \frac{\hbar^2 k^2}{2m^*} + \beta_{xy}\sigma_x k_y + \beta_{yx}\sigma_y k_x\ , \tag{8.15}$$

(8.13) reduces to

$$\boldsymbol{j} = e \sum_{\boldsymbol{k}} \mathrm{Tr}\left\{\hat{\boldsymbol{v}}(\boldsymbol{k})\rho^{(e)}(\boldsymbol{k})\right\}\ , \tag{8.16}$$

and similar equation can be written for the photohole contribution. Here $\rho^{(e)}(\boldsymbol{k})$ is the spin-density matrix and the velocity operator $\hat{\boldsymbol{v}}(\boldsymbol{k}) = \hbar^{-1}\partial\mathcal{H}/\partial\boldsymbol{k}$ has the components

$$\hat{v}_x(\boldsymbol{k}) = \frac{\hbar k_x}{m^*} + \frac{\beta_{yx}}{\hbar}\sigma_y\ ,\ \hat{v}_y(\boldsymbol{k}) = \frac{\hbar k_y}{m^*} + \frac{\beta_{xy}}{\hbar}\sigma_x\ . \tag{8.17}$$

In the momentum-relaxation time approximation, one has

$$\boldsymbol{j} = e \sum_{\boldsymbol{k}} \tau_p^e \mathrm{Tr}\left\{\hat{\boldsymbol{v}}(\boldsymbol{k})\dot{\rho}^{(e)}(\boldsymbol{k})\right\}\ , \tag{8.18}$$

where components of the spin-density generation matrix $\dot{\rho}^{(e)}$ are given by

$$\begin{aligned}\dot{\rho}^{(e)}_{s's}(\boldsymbol{k}) = \frac{\pi}{\hbar}\sum_{v,j} M_{e1,s';v,j}(\boldsymbol{k})M^*_{e1,s;v,j}(\boldsymbol{k}) \\ \times\left[\delta\left(E_{e1,\boldsymbol{k},s'} - E^e_{v\boldsymbol{k}j} - \hbar\omega\right) + \delta\left(E_{e1,\boldsymbol{k},s} - E^e_{v\boldsymbol{k}j} - \hbar\omega\right)\right]\ ,\end{aligned} \tag{8.19}$$

$M_{e1,s;v,j}(\boldsymbol{k})$ is the matrix element of the interband optical transition $(v\boldsymbol{k}j) \to (e1, \boldsymbol{k}, s)$. As soon as linear-$\boldsymbol{k}$ spin-dependent terms are taken into account

in the electron Hamiltonian and the light is circularly polarized, the antisymmetrical component of the generation matrix $\dot{\rho}^{(e)}_{s's}(\boldsymbol{k})$ is nonzero. The photohole contribution to the photocurrent is considered in a similar way.

The spectral behavior of the interband circular PGE calculated for (001)-grown QWs is presented in Fig. 8.3b. The four band edges $j\nu \rightarrow e1$ are indicated by arrows. As the photon energy approaches the bandgap $e1$-$hh1$ the photocurrent tends to zero. This can be understood taking into account that, for QWs of the C_{2v} or D_{2d} symmetry, the circular photocurrent appears only under oblique incidence, the optical transitions have to be allowed both in the in-plane and normal-to-plane polarizations, but for purely heavy hole states the interband transitions in the polarization $\boldsymbol{e} \parallel z$ are forbidden. The circular photocurrent due to the $hh1 \rightarrow e1$ becomes nonzero because of an admixture of light-hole states in the heavy-hole subband $hh1$ at $\boldsymbol{k} \neq 0$. At small values of $\hbar\omega - E_g^{QW}$ the photocurrent is proportional to $(\hbar\omega - E_g^{QW})^2$ for the BIA linear-$\boldsymbol{k}$ term (2.113) in the electron Hamiltonian ($\beta_{xy} = \beta_{yx}$) and to the first order of $\hbar\omega - E_g^{QW}$ for the SIA linear-$\boldsymbol{k}$ term ($\beta_{xy} = -\beta_{yx}$) [8.11]. One can see from Fig. 8.3b that the spectral variations of the BIA and SIA contributions to the photocurrent differ dramatically in the whole frequency region studied.

Since the characteristic spin splitting is usually small as compared with the inhomogeneous broadening and kinetic energy of free carriers the photocurrents generated under interband, intersubband or intrasubband optical excitation are mainly contributed by terms linear in the coefficients β. In this case one can write the following general relation between the photogalvanic tensor $\boldsymbol{\gamma}$ and tensor $\boldsymbol{\beta}^{(\nu)}$ describing the linear-$\boldsymbol{k}$ terms in the ν-th conduction or valence subband ν

$$\gamma_{\lambda\mu} \propto \beta^{(\nu)}_{\mu\lambda} \,. \tag{8.20}$$

In particular, the BIA and SIA terms give rise to independent contributions to the circular PGE and one has

$$j_x \propto IP_c(\beta^{(\nu)}_{BIA} - \beta^{(\nu)}_{SIA})o_y \,,\; j_y \propto IP_c(\beta^{(\nu)}_{BIA} + \beta^{(\nu)}_{SIA})o_x \,, \tag{8.21}$$

where

$$\beta^{(\nu)}_{BIA} = (\beta^{(\nu)}_{xy} + \beta^{(\nu)}_{yx})/2 \,,\; \beta^{(\nu)}_{SIA} = (\beta^{(\nu)}_{xy} - \beta^{(\nu)}_{yx})/2 \,.$$

Note that in Chap. 2 the coefficients β_{BIA} and β_{SIA} are introduced as $-\beta_1$ and β_2, see (2.113) and (2.114). It is instructive to rewrite equations (8.21) in terms of the current components in the principal axes $x_1 \parallel [100]$, $x_2 \parallel [010]$ and obtain

$$j_1 \propto IP_c(\beta^{(\nu)}_{BIA}o_1 - \beta^{(\nu)}_{SIA}o_2) \,,\; j_2 \propto IP_c(-\beta^{(\nu)}_{BIA}o_2 + \beta^{(\nu)}_{SIA}o_1) \tag{8.22}$$

where o_1, o_2 are the components of the unit vector $\hat{\boldsymbol{o}}$ along x_1 and x_2. It is worth to mention that the BIA and SIA linear-$\boldsymbol{k}$ terms give rise to many spin-dependent phenomena in QWs such as an existence of beats in the Shubnikov-de Haas oscillations, spin relaxation, splitting in polarized Raman scattering

spectra, and positive anomalous magnetoresistence. However, in (001)-grown QWs, the BIA and SIA spin-orbit splittings cannot be distinguished in these experiments, particularly if one of the splitting mechanisms is dominating and the electron energy dispersion is uniaxially invariant. On the other hand, the circular PGE suggests a clear and effective way to identify the spin-splitting mechanism in (001)-oriented QWs: under oblique optical excitation by the circularly polarized light with the plane of incidence containing the principal axis 1 or 2, the BIA- and SIA-related circular photocurrents are respectively parallel and perpendicular to the incidence plane.

Next we turn to a more detailed discussion of the circular PGE for the $e1 \to e2$ intersubband transitions. The circular photocurrent is a sum of two contributions

$$\boldsymbol{j} = \boldsymbol{j}^{(e2)} + \boldsymbol{j}^{(e1)} \tag{8.23}$$

$$= e \sum_{\boldsymbol{k}} \left[\tau_p^{(2)} \mathrm{Tr} \left\{ \hat{\boldsymbol{v}}^{(e2)}(\boldsymbol{k}) \dot{\rho}^{(e2)}(\boldsymbol{k}) \right\} + \tau_p^{(1)} \mathrm{Tr} \left\{ \hat{\boldsymbol{v}}^{(e1)}(\boldsymbol{k}) \dot{\rho}^{(e1)}(\boldsymbol{k}) \right\} \right] ,$$

respectively, due to the asymmetry of distribution in $\boldsymbol{k}$-space of electrons excited to the subband $e2$ and electrons that stay in the subband $e1$. Here $\tau_p^{(\nu)}$ is the electron momentum relaxation time in the subband ν. The generation matrix $\dot{\rho}^{(e2)}(\boldsymbol{k})$ for incoming electrons is similar to (8.19). Therefore, it will suffice to present here the expression for the generation matrix in the $e1$ subband

$$\dot{\rho}^{(e1)}_{s's}(\boldsymbol{k}) = -\frac{\pi}{\hbar} \sum_j M_{e2,j;e1,s}(\boldsymbol{k}) M^*_{e2,j;e1,s'}(\boldsymbol{k}) \tag{8.24}$$

$$\times \left[f^0(E_{e1,\boldsymbol{k}s}) \delta \left(E_{e2,\boldsymbol{k}j} - E_{e1,\boldsymbol{k}s} - \hbar\omega \right) + f^0(E_{e1,\boldsymbol{k}s'}) \delta \left(E_{e2,\boldsymbol{k}j} - E_{e1,\boldsymbol{k}s'} - \hbar\omega \right) \right]$$

where the indices j, s, s' enumerate the spin-split eigenstates and the factor -1 means that the electrons are outgoing from the $e1$ subband. Note that the order of indices s, s' in the product $M_{e2,j;e1,s}(\boldsymbol{k}) M^*_{e2,j;e1,s'}(\boldsymbol{k})$ differs from that for incoming electrons, see (8.19).

In order to make the physics more transparent we will first consider the intersubband circular photocurrent generated under normal incidence in QWs of the C_s symmetry, say in (113)-grown QWs, and use the appropriate coordinate system x, y, z with $z \parallel [113]$. The electron energy spectrum is given by

$$E_{e\nu,\boldsymbol{k},s} = E^0_\nu + \frac{\hbar^2 k^2}{2m^*} \pm \beta_\nu k_x \, , \tag{8.25}$$

where $\beta_\nu = \beta^{(\nu)}_{zx}$ and, for the sake of simplicity, we neglect nonparabolicity effects assuming the effective mass m^* to be the same in both subbands. For the direct $e2$-$e1$ transitions, the energy and momentum conservation laws read

$$E_{21} + 2(s'\beta_2 - s\beta_1)k = \hbar\omega \, .$$

where E_{21} is the Γ-point gap $E^0_2 - E^0_1$ and $s', s = \pm 1/2$. In Chap. 4 we showed that, in the polarization $\boldsymbol{e} \perp z$, the direct intersubband absorption is

weakly allowed only for the spin-flip transitions, $(e1,-1/2) \to (e2,1/2)$ for σ_+ photons and $(e1,1/2) \to (e2,-1/2)$ for σ_- photons. Particularly, under the σ_+ photoexcitation the electrons involved in the transitions have the fixed x-component of the wave vector

$$k_{21} = \frac{\hbar\omega - E_{21}}{\beta_2 + \beta_1} \tag{8.26}$$

and velocity

$$v_x^{(e\nu)} = \frac{\hbar k_{21}}{m^*} + \frac{\beta_\nu}{\hbar}\,. \tag{8.27}$$

It follows then that the circular photocurrent can be written as

$$j_x^{(e1)} = e\left(v_x^{(e2)}\tau_p^{(2)} - v_x^{(e1)}\tau_p^{(1)}\right)\frac{\eta_{21} I}{\hbar\omega} P_c\,, \tag{8.28}$$

where η_{21} is the absorbance or the fraction of the energy flux absorbed in the QW due to the transitions in consideration, $v_x^{(e\nu)}$ is given by (8.27) and minus in the right-hand side means that the $e1$-electrons are removed in the optical transitions.

As indicated in Sect. 4.1.1, in available QW structures the inhomogeneous broadening Δ_{21} of the gap E_{21} exceeds the width δ_{21} of absorption spectrum in an ideal QW. The inhomogeneous broadening is taken into consideration by multiplying the photocurrent $\boldsymbol{j}$ as a function of E_{21} by the distribution function $F(E_{21})$ of the gaps E_{21} and integrating over E_{21}. Since $\delta_{21} \ll \Delta_{21}$ the function F can be expanded in powers of $E_{21} - \hbar\omega$ and it is enough to keep the first two terms

$$F(E_{21}) \approx F(\hbar\omega) + \frac{dF(\hbar\omega)}{d\,\hbar\omega}(E_{21} - \hbar\omega)\,. \tag{8.29}$$

The convolution of the current (8.28) with the inhomogeneous distribution function (8.29) leads to

$$j_x = \frac{e}{\hbar}(\beta_2 + \beta_1)\left[\tau_2\,\eta_{21}(\hbar\omega) + (\tau_1 - \tau_2)\,\bar{E}\,\frac{d\,\eta_{21}(\hbar\omega)}{d\,\hbar\omega}\right]\frac{IP_c}{\hbar\omega}\,, \tag{8.30}$$

where $\eta_{21} \propto F(\hbar\omega)$ is the absorbance calculated, neglecting the linear-$\boldsymbol{k}$ terms but taking into account the inhomogeneous broadening. $\bar{E}$ is the mean value of the 2D electron energy, namely half of the Fermi energy E_F for a degenerate 2D electron gas and k_BT for a nondegenerate gas.

In case of the $e2$-$e1$ transitions in (001)-grown QWs one should start from the spin Hamiltonian

$$\mathcal{H}_\nu = E_{e\nu}^0 + \frac{\hbar^2 k^2}{2m^*} + \beta_{xy}^{(\nu)}\sigma_x k_y + \beta_{yx}^{(\nu)}\sigma_y k_x \tag{8.31}$$

and the intersubband matrix elements of the velocity operator (Chap. 4)

$$||\boldsymbol{e}\cdot\boldsymbol{v}_{s_z's_z}|| = \frac{\hbar}{m^*}k_z^{(2,1)}\begin{bmatrix} e_z & \Lambda(e_x-\mathrm{i}e_y) \\ -\Lambda(e_x+\mathrm{i}e_y) & e_z \end{bmatrix}, \tag{8.32}$$

$$\Lambda = \frac{E_{21}\Delta(2E_g+\Delta)}{2E_g(E_g+\Delta)(3E_g+2\Delta)},$$

written in the basis of spin states with $s_z = \pm 1/2$. In order to perform a calculation taking into account all powers of $\beta_{\lambda\mu}$ one needs to use (8.23) and (8.24) in a straightforward way. As soon as we are interested in contributions to photocurrents linear in β we can set all β's to zero except for one and proceed similarly to the C_s-symmetry case. For example, we retain the term $\beta_{yx}^{(\nu)}\sigma_y k_x$ in (8.31) and disregard the term proportional to $\beta_{xy}^{(\nu)}$. The corresponding current is induced in the x-direction perpendicularly to the plane (y,z) of oblique incidence:

$$j_x \propto \mathrm{i}(\boldsymbol{e}\times\boldsymbol{e}^*)_y = \mathrm{i}(e_z e_x^* - e_x e_z^*) = P_c\, o_y\,. \tag{8.33}$$

Then the eigenstates have a fixed spin component on the y axis and the spin split energies are determined by (8.25) where $\beta_\nu = \beta_{zx}^{(\nu)}$ is changed by $\beta_{yx}^{(\nu)}$ and $\pm$ means spin states with $s_y = \pm 1/2$. Since the component e_z is present in (8.33) and the spin under z-polarized transitions is conserved, see (8.32), only spin-conserving processes $(e1, s_y) \to (e2, s_y)$ contribute to the circular photocurrent j_x. From (8.32) one can find the corresponding matrix elements of the velocity operator

$$\langle e2, s_y|\boldsymbol{e}\cdot\hat{\boldsymbol{v}}_{s_z's_z}|e1, s_y\rangle = v_{21}(e_z + 2\mathrm{i}\Lambda s_y e_x)$$

and, hence,

$$|\langle e2, s_y|\boldsymbol{e}\cdot\hat{\boldsymbol{v}}_{s_z's_z}|e1, s_y\rangle|^2 = |v_{21}|^2(|e_z|^2 - 2\Lambda s_y P_c o_y)\,, \tag{8.34}$$

where the term quadratic in Λ is neglected. The second consequence of the spin conservation is that, instead of (8.26), the wave vector component k_x of electrons involved in the transitions is expressed not via the sum but via the difference of β coefficients

$$k_{21} = \frac{\hbar\omega - E_{21}}{\beta_{yx}^{(2)} - \beta_{yx}^{(1)}}\,.$$

The final result for the circular photocurrent reads

$$j_x = -\Lambda\frac{e}{\hbar}(\beta_{yx}^{(2)} - \beta_{yx}^{(1)})\left[\tau_2\,\eta_{21}(\hbar\omega) + (\tau_1-\tau_2)\,\bar{E}\,\frac{d\,\eta_{21}(\hbar\omega)}{d\,\hbar\omega}\right]\frac{IP_c}{\hbar\omega}\,o_y\,, \tag{8.35}$$

where η_{21} is the absorbance in the polarization $\boldsymbol{e} \parallel z$.

An important conclusion is that the photocurrents (8.30) and (8.35) change their signs within the resonance absorption spectrum. If the inhomogeneous broadening has a Gaussian character, i.e., if

$$F(E_{21}) = \frac{1}{\sqrt{\pi}\Delta_{21}} \exp\left[-\left(\frac{E_{21}-\bar{E}_{21}}{\Delta_{21}}\right)^2\right], \tag{8.36}$$

the inversion point lies at the photon energy

$$\hbar\omega_{inv} = \bar{E}_{21} + \frac{\tau_2}{\tau_1-\tau_2}\frac{\Delta_{21}^2}{2\bar{E}}\,. \tag{8.37}$$

Usually $\tau_1 > \tau_2$ and the inversion point should be blue-shift relative to the resonance energy $\bar{E}_{21}$ determined from light transmission spectral measurements. However, for $\tau_1 \gg \tau_2$ this blue shift is negligible. The sign inversion of the circular photocurrent in the resonant $e2$-$e1$ transition region has been recently observed in n-type GaAs/AlGaAs QW samples [8.12].

In contrast to electrons in the conduction band, the energy dispersion of holes in the valence band of QWs is essentially nonparabolic and intersubband absorption can involve simultaneously different pairs of subbands $hh\nu$ and $hh\nu'$. However, with some modifications of the theory and complications in calculations the intersubband circular CPE in p-doped samples can be considered in a way similar to that in n-QWs.

Now we turn to intrasubband optical transitions

$$(e1, \boldsymbol{k}, s) + \hbar\omega \to (e1, \boldsymbol{k}', s')$$

in the lowest electron subband $e1$. They are indirect in the $\boldsymbol{k}$ space, occur due to additional scattering by phonons or static imperfections and involve virtual intermediate states. This situation is realized in n-doped QWs for photon energies to be not high enough in order to excite direct intersubband transitions. The intrasubband photocurrent is given by the general equation (8.18) where the generation matrix is a sum of contributions due to the ingoing and outgoing electrons. The corresponding generation matrices have the form

$$\dot{\rho}^{(\mathrm{out})}_{s's}(\boldsymbol{k}) = -\frac{\pi}{\hbar}\sum_{\boldsymbol{k}'j} M^{\mathrm{ind}}_{\boldsymbol{k}'j,\boldsymbol{k}s} M^{\mathrm{ind}\,*}_{\boldsymbol{k}'j,\boldsymbol{k}s'} \tag{8.38}$$

$$\times\left[\left(f^0_{\boldsymbol{k}s'} - f^0_{\boldsymbol{k}'j}\right)\delta\left(E_{\boldsymbol{k}',j} - E_{\boldsymbol{k},s'} - \hbar\omega\right) + \left(f^0_{\boldsymbol{k}s} - f^0_{\boldsymbol{k}'j}\right)\delta\left(E_{\boldsymbol{k}',j} - E_{\boldsymbol{k},s} - \hbar\omega\right)\right],$$

$$\dot{\rho}^{(\mathrm{in})}_{j'j}(\boldsymbol{k}') = \frac{\pi}{\hbar}\sum_{\boldsymbol{k}s} M^{\mathrm{ind}}_{\boldsymbol{k}'j',\boldsymbol{k}s} M^{\mathrm{ind}\,*}_{\boldsymbol{k}'j,\boldsymbol{k}s} \tag{8.39}$$

$$\times\left[\left(f^0_{\boldsymbol{k}s} - f^0_{\boldsymbol{k}'j}\right)\delta\left(E_{\boldsymbol{k}',j} - E_{\boldsymbol{k},s} - \hbar\omega\right) + \left(f^0_{\boldsymbol{k}s} - f^0_{\boldsymbol{k}'j'}\right)\delta\left(E_{\boldsymbol{k}',j'} - E_{\boldsymbol{k},s} - \hbar\omega\right)\right].$$

Here $E_{\boldsymbol{k},s} \equiv E_{e1,\boldsymbol{k},s}$, $f^0_{\boldsymbol{k}s}$ is the electron distribution function in the $e1$ subband and $M^{\mathrm{ind}}_{\boldsymbol{k}j,\boldsymbol{k}s}$ is the matrix element of the indirect optical transition. In the second order of the perturbation theory it is given by

$$M^{\mathrm{ind}}_{\boldsymbol{k}'j,\boldsymbol{k}s} = \sum_n \left(\frac{V_{e1,\boldsymbol{k}',j;n\boldsymbol{k}} M_{n\boldsymbol{k};e1,\boldsymbol{k},s}}{E_{n\boldsymbol{k}} - E_{e1,\boldsymbol{k},s} - \hbar\omega} + \frac{M_{e1,\boldsymbol{k}',j;n\boldsymbol{k}'} V_{n\boldsymbol{k}';e1\boldsymbol{k}s}}{E_{n\boldsymbol{k}'} - E_{e1,\boldsymbol{k},s} \pm \hbar\Omega}\right), \tag{8.40}$$

where the index n enumerates the intermediate states, $M_{n'\boldsymbol{k};n\boldsymbol{k}}$ and $V_{n'\boldsymbol{k}';n\boldsymbol{k}}$ are the matrix elements of the electron-photon and electron-phonon or electron-defect interaction, Ω is the phonon frequency, the sign $\pm$ corresponds to emission and absorption of phonons. For the scattering by static defects Ω is set to zero. An important point is that indirect transitions via intermediate states in the same subband do not contribute to the circular PGE. The effect appears if virtual processes involve intermediate states in other bands or subbands, $n \neq e1$. The same takes place for intrasubband optical orientation of electronic spins in the conduction band. The latter is discussed in more detail in the next subsection in connection with the spin-galvanic effect.

8.2 Spin-Galvanic Effect

The mechanisms of the circular PGE discussed so far are linked with the asymmetry in the momentum distribution of carriers excited in optical transitions which are sensitive to the light's circular polarization due to selection rules. Now we discuss an additional possibility to generate a photocurrent sensitive to the photon helicity [8.13, 8.14]. In a system of free carriers with non-equilibrium spin-state occupation but equilibrium energy distribution within each spin branch, the spin relaxation or Larmor precession in an external magnetic field can be accompanied by generation of an electric current. Phenomenologically, this linkage between an electric current and the total electronic spin $\boldsymbol{s}$ is described by

$$j_\lambda = \sum_\mu Q_{\lambda\mu} s_\mu \,. \tag{8.41}$$

The symmetry of the second-order pseudotensor $\boldsymbol{Q}$ coincides with that of the tensor $\boldsymbol{\gamma}$ describing the circular PGE, see (8.1). Similarly, its non-vanishing components can exist in non-centrosymmetric systems belonging to one of the gyrotropic classes. In (001)-oriented QWs of the C_{2v} symmetry equation (8.41) reads

$$j_x = Q_{xy} s_y \,,\; j_y = Q_{yx} s_x \,. \tag{8.42}$$

If the non-equilibrium spin is produced by optical orientation and the spin s_μ is proportional to the degree of light circular polarization P_c the current generation can be reputed just as another mechanism of the circular PGE. However the non-equilibrium spin $\boldsymbol{s}$ can be achieved both by optical and non-optical methods, e.g., by electrical spin injection, and, in fact, (8.41) presents an independent effect called the *spin-galvanic effect*. Here we bear in mind spin-induced electric currents that appear under uniform distribution of the spin polarization in the 3D-, 2D- or 1D space, respectively, in a bulk semiconductor, a QW and a quantum wire. In this sense the spin-galvanic effect differs from surface currents induced by inhomogeneous spin orientation [8.15] and other phenomena where the spin current is caused by gradients

of potentials, concentrations, etc., like spin-voltaic effect which occurs in inhomogeneous samples, e.g., the 'paramagnetic metal-ferromagnetic' junction or p-n junction.

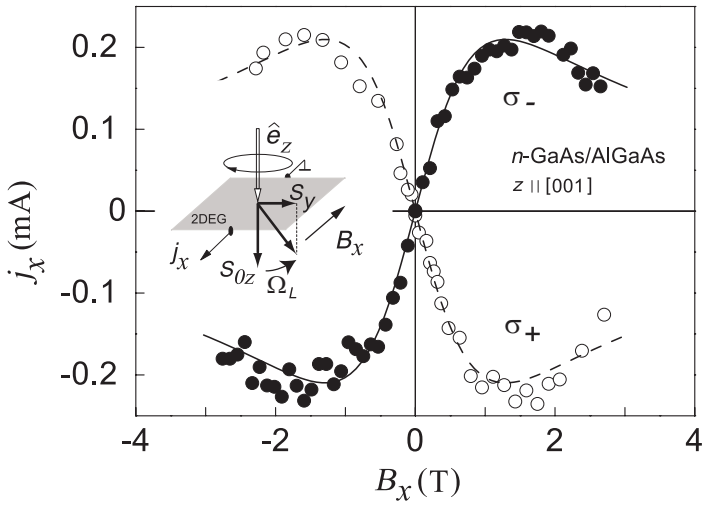

Fig. 8.4. Current j_x as a function of the magnetic field B for normally incident right-handed (*open* circles) and left-handed (*filled* circles) circularly polarized radiation at $\lambda = 148$ μm and radiation power 20 kW. Measurements are presented for an n-GaAs/AlGaAs single heterojunction at T = 4.2 K. Curves are fitted from (8.43) using the same value of the spin relaxation time τ_s and scaling of the j_x value for both the solid and dashed curves. From [8.14].

Usually the circular photogalvanic and spin-galvanic effects are observed simultaneously under illumination by circularly polarized light and do not allow experimental separation. However, they can be separated in time-resolved measurements. Indeed, after removal of light or under pulsed photoexcitation the circular photocurrent decays within the momentum relaxation time τ_p whereas the spin-galvanic current decays with the spin relaxation time. Next we consider a geometry of experiment under steady-state photoexcitation which allows to observe the spin-galvanic effect and exclude the circular PGE [8.14]. The geometry is depicted in inset in Fiq. 8.4. The circularly polarized light is incident normally to the interface plane (001) of a QW, the light absorption yields a steady-state spin orientation s_{0z} in the z direction proportional to the spin-generation rate $\dot{s}_z$. The symmetry of (001)-grown QWs forbids generation of a current proportional to the normal component of $\boldsymbol{s}$. To obtain an in-plane component of the spins, necessary for the spin-galvanic effect, a magnetic field $\boldsymbol{B} \parallel x$ is applied. Due to Larmor precession a non-equilibrium spin polarization s_y is induced,

$$s_y = -\frac{\Omega_L \tau_{s\perp}}{1+(\Omega_L \tau_s)^2}\, s_{0z}\,, \tag{8.43}$$

where $\tau_s = \sqrt{\tau_{s\parallel}\tau_{s\perp}}$, $\tau_{s\parallel}$, $\tau_{s\perp}$ are the longitudinal and transverse electron spin relaxation times, Ω_L is the Larmor frequency. The photocurrent measured in the x direction is depicted in Fig. 8.4 as a function of the magnetic field for two opposite circular polarizations of the light. In accordance with the phenomenological equations (8.42) and (8.43) the current j_x exhibits nonmonotonous variation with the magnetic field. Comparison with theory allows to find a product $g\tau_s$ and the spin relaxation time if the electron g-factor is known.

There are two different microscopical mechanisms of the spin-galvanic effect, namely, kinetic and relaxational [8.13]. The experimental data of Fig. 8.4 can be understood in terms of the kinetic mechanism. It is inherently connected with the spin dependency of matrix elements, $M_{\boldsymbol{k}'s',\boldsymbol{k}s}$, of electron scattering by impurities, other static defects and phonons. It is convenient to represent the 2×2 matrix $\hat{M}_{\boldsymbol{k}'\boldsymbol{k}}$ as a linear combination of the unit matrix $\hat{I}$ and Pauli matrices as follows

$$\hat{M}_{\boldsymbol{k}'\boldsymbol{k}} = A_{\boldsymbol{k}'\boldsymbol{k}}\hat{I} + \boldsymbol{\sigma}\cdot\boldsymbol{B}_{\boldsymbol{k}'\boldsymbol{k}}\,, \tag{8.44}$$

where $A^*_{\boldsymbol{k}'\boldsymbol{k}} = A_{\boldsymbol{k}\boldsymbol{k}'}$, $B^*_{\boldsymbol{k}'\boldsymbol{k}} = B_{\boldsymbol{k}\boldsymbol{k}'}$ due to hermiticity of the interaction and $A_{-\boldsymbol{k}',-\boldsymbol{k}} = A_{\boldsymbol{k}\boldsymbol{k}'}$, $B_{-\boldsymbol{k}',-\boldsymbol{k}} = -B_{\boldsymbol{k}\boldsymbol{k}'}$ due to the symmetry under time inversion. For the conduction subband $e1$ in a (001)-grown QW the electron-phonon deformation-potential Hamiltonian has the form

$$\mathcal{H}_{DP}(\boldsymbol{k}',\boldsymbol{k}) = \Xi_c \sum_{i=1,2,3} u_{ii} \tag{8.45}$$

$$+\Xi_{cv} L_{cv}\left\{u_{12}\left[\sigma_1(k'_2+k_2)-\sigma_2(k'_1+k_1)\right]+\sigma_3\left[u_{31}(k'_1+k_1)-u_{32}(k'_2+k_2)\right]\right\}.$$

Here $\boldsymbol{k}', \boldsymbol{k}$ are the electron final and initial wave vectors, u_{ij} are the strain tensor components induced by acoustic vibrations, Ξ_c and Ξ_{cv} are the conduction-band and interband deformation potential constants, the indices $1, 2, 3$ represent the principal axes [100], [010], [001],

$$L_{cv} = \frac{P\Delta}{3E_g(E_g+\Delta)}\,,\; P = -\mathrm{i}\frac{\hbar}{m_0}\langle S|\hat{p}_z|Z\rangle\,.$$

One can readily find the scalar $A_{\boldsymbol{k}'\boldsymbol{k}}$ and pseudovector $\boldsymbol{B}_{\boldsymbol{k}'\boldsymbol{k}}$ for this particular scattering mechanism. In the axes $x \parallel [1\bar{1}0]$, $y \parallel [110]$, $z \parallel [001]$ the first term in (8.45) remains invariant while the expression in braces in the second term of (8.45) becomes

$$\frac{1}{2}(u_{xx}-u_{yy})\left[\sigma_x(k'_y+k_y)-\sigma_y(k'_x+k_x)\right]+\sigma_z\left[u_{zx}(k'_y+k_y)+u_{zy}(k'_x+k_x)\right].$$

The spin-galvanic current observed in the geometry of Fig. 8.4 is caused by the asymmetric spin-flip scattering of spin-polarized electrons in the systems

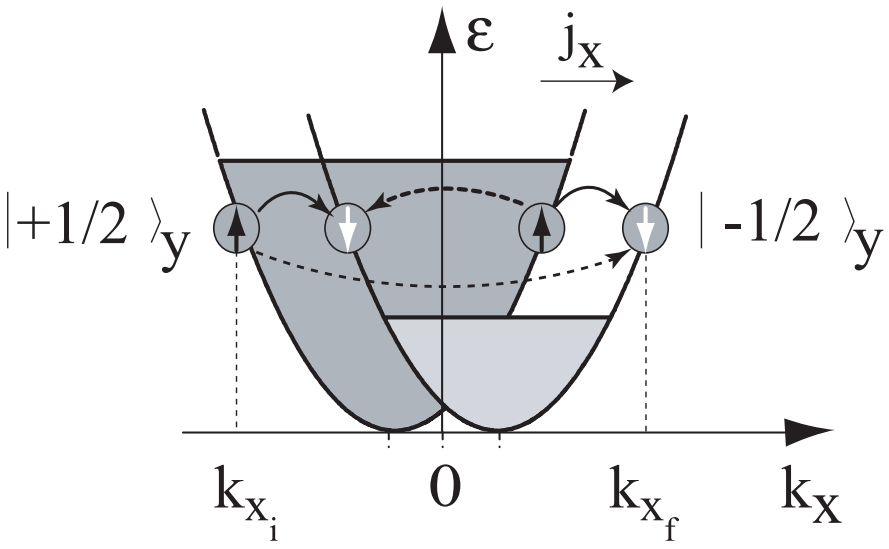

Fig. 8.5. Microscopic origin of the spin-galvanic current in the presence of $\boldsymbol{k}$-linear terms in the electron Hamiltonian. The $\sigma_y k_x$ term in the Hamiltonian splits the conduction band into two parabolas with the spin $\pm 1/2$ in the y direction. If one spin subband is preferentially occupied, asymmetric spin-flip scattering results in a current in the x direction. The rate of spin-flip scattering depends on the value of the initial and final $\boldsymbol{k}$-vectors. There are four distinct spin-flip scattering events possible, indicated by the arrows. The transitions sketched by dashed arrows yield an asymmetric occupation of both subbands and hence a current flow. If, instead of the spin-down subband, the spin-up subband is preferentially occupied the current direction is reversed.

with $\boldsymbol{k}$-linear contributions to the effective Hamiltonian. Figure 8.5 illustrates the electron energy spectrum with the $\beta_{yx}\sigma_y k_x$ term included. Spin orientation in the y direction causes an unbalanced population in the spin-down and spin-up branches. Spins oriented in the y direction are scattered along k_x from the higher filled branch, say the spin-up or $|1/2\rangle_y$ branch, to the less filled branch $|-1/2\rangle_y$. The matrix elements for these spin-flip processes are proportional to the components $B_{\boldsymbol{k}'\boldsymbol{k},x}$ and $B_{\boldsymbol{k}'\boldsymbol{k},z}$ of the vector $\boldsymbol{B}_{\boldsymbol{k}'\boldsymbol{k}}$ in (8.44).

Four different spin-flip scattering events are schematically sketched in Fig. 8.5 by arrows. Their probability rates depend on the values of the wave vectors of the initial and final states. Spin-flip transitions shown by solid arrows have the same rate. They preserve the symmetric distribution of carriers in the branches and, thus, do not yield a current. The two processes indicated by broken arrows are not equivalent and generate an asymmetric carrier dis-

tribution around the branch minima in each spin branch. This asymmetric distribution results in a current flow along the x direction.

In considering the relaxational mechanism of the spin-galvanic effect we can ignore spin-dependence of the scattering matrix elements but should retain quantum corrections of the order of $\mathcal{H}^{(1)}/\bar{E}$, where $\bar{E}$ is the average electron kinetic energy. We apply the spin density matrix formalism used in Chap. 5 while describing the electron spin relaxation and, in the same way, assume the following hierarchy of relaxation times to be fulfilled

$$\tau_p \ll \tau_\varepsilon \ll \tau_s, \tau_0 \,, \tag{8.46}$$

where $\tau_p, \tau_\varepsilon, \tau_s$ are, respectively, the electron momentum, energy and spin relaxation times, τ_0 is the electron lifetime in case of the interband optical photoexcitation.

The conditions (8.46) allow a straightforward solution of the kinetic equation for the electron spin density matrix

$$\frac{\partial \rho_{\boldsymbol{k}}}{\partial t} + \frac{\rho_{\boldsymbol{k}}}{\tau_0} + \left(\frac{\partial \rho_{\boldsymbol{k}}}{\partial t}\right)_{s.r.} + \frac{\mathrm{i}}{\hbar}\left[\mathcal{H}^{(1)}_{\boldsymbol{k}} + \mathcal{H}_{\boldsymbol{B}}, \rho_{\boldsymbol{k}}\right] + Q_{\boldsymbol{k}}\{\rho\} = G_{\boldsymbol{k}} \,, \tag{8.47}$$

where $G_{\boldsymbol{k}}$ is the generation matrix, $Q_{\boldsymbol{k}}\{\rho\}$ is the collision integral, $(\partial\rho_{\boldsymbol{k}}/\partial t)_{s.r.}$ is the spin relaxation term, $\mathcal{H}^{(1)}_{\boldsymbol{k}}$ and $\mathcal{H}_{\boldsymbol{B}}$ are the linear-$\boldsymbol{k}$ and Zeeman Hamiltonians. The current is given by the standard equation (8.16). In what follows we derive a contribution to the current linear in the coefficients $\beta_{\lambda\mu}$ governing $\mathcal{H}^{(1)}_{\boldsymbol{k}}$. It means that we retain only terms linear in $\mathcal{H}^{(1)}/\bar{E}$ and neglect quantum corrections of the order $\mathcal{H}_{\boldsymbol{B}}/\bar{E}$. In this approximation, in the state of thermal equilibrium the matrix $\rho_{\boldsymbol{k}}$ for electrons with non-equilibrium spin polarization $\boldsymbol{S}$ per particle can be written as

$$\rho^0_{\boldsymbol{k}} = \left\{f^0(\mathcal{H}'_{\boldsymbol{k}}), 1 + 2\boldsymbol{\sigma}\cdot\boldsymbol{S}\right\}_s \,, \tag{8.48}$$

where $f^0(E)$ is the Fermi-Dirac distribution function, $\{MN\}_s = (MN + NM)/2$, $\mathcal{H}'_{\boldsymbol{k}}$ is the electron effective Hamiltonian at zero magnetic field, i.e., the sum $E^0_{\boldsymbol{k}} + \mathcal{H}^{(1)}_{\boldsymbol{k}}$ with $E^0_{\boldsymbol{k}}$ being $\hbar^2k^2/(2m^*)$. Note that the total spin density $\boldsymbol{s}$ in (8.41) is a product of $\boldsymbol{S}$ and the electron density N_e. Practically, one should keep only zero- and first-order terms and replace (8.48) by

$$\rho^0_{\boldsymbol{k}} = f^0(1 + 2\boldsymbol{\sigma}\cdot\boldsymbol{S}) + \frac{\partial f^0}{\partial E}\mathcal{H}^{(1)}_{\boldsymbol{k}} + \frac{\partial f^0}{\partial E}\,\hbar\left(\boldsymbol{\Omega}^{(1)}_{\boldsymbol{k}}\cdot\boldsymbol{S}\right) \,, \tag{8.49}$$

where the angular frequency $\boldsymbol{\Omega}^{(1)}_{\boldsymbol{k}}$ is defined according to (2.116).

First of all we demonstrate that the distribution (8.49) leads to no electric current and the collision integral vanishes upon substitution of the matrix $\rho^0_{\boldsymbol{k}}$. In order to demonstrate the absence of current we notice that the sum

$$\boldsymbol{j} = e\sum_{\boldsymbol{k}} \mathrm{Tr}\left\{\hat{\boldsymbol{v}}(\boldsymbol{k})\rho^0_{\boldsymbol{k}}\right\}$$

after finding the trace reduces to three terms, namely

$$2e\sum_{\boldsymbol{k}}\frac{\hbar\boldsymbol{k}}{m^*}f^0\left(E^0_{\boldsymbol{k}}\right)\,,$$

$$2e\sum_{\boldsymbol{k}}f^0\left(E^0_{\boldsymbol{k}}\right)\nabla_{\boldsymbol{k}}\left(\boldsymbol{\Omega}^{(1)}_{\boldsymbol{k}}\cdot\boldsymbol{S}\right)\quad\text{and}\quad 2e\sum_{\boldsymbol{k}}\left(\boldsymbol{\Omega}^{(1)}_{\boldsymbol{k}}\cdot\boldsymbol{S}\right)\frac{\hbar\boldsymbol{k}}{m^*}\,\frac{df^0\left(E^0_{\boldsymbol{k}}\right)}{dE^0_{\boldsymbol{k}}}\,.$$

The first term vanishes because of the odd parity of $\boldsymbol{k}\,f^0\left(E^0_{\boldsymbol{k}}\right)$ while the second and third sums may be transferred into

$$\sum_{\boldsymbol{k}}\left[f^0\left(E^0_{\boldsymbol{k}}\right)\nabla_{\boldsymbol{k}}\left(\boldsymbol{\Omega}^{(1)}_{\boldsymbol{k}}\cdot\boldsymbol{S}\right)+\left(\boldsymbol{\Omega}^{(1)}_{\boldsymbol{k}}\cdot\boldsymbol{S}\right)\nabla_{\boldsymbol{k}}f^0\left(E^0_{\boldsymbol{k}}\right)\right]$$

$$=\sum_{\boldsymbol{k}}\nabla_{\boldsymbol{k}}\left[\left(\boldsymbol{\Omega}^{(1)}_{\boldsymbol{k}}\cdot\boldsymbol{S}\right)f^0\left(E^0_{\boldsymbol{k}}\right)\right]\,,$$

and also vanish. The second property, $Q_{\boldsymbol{k}}\{\rho^0\}\equiv 0$, can be checked if we write the collision integral for any particular mechanism of electron scattering. Say, for elastic scattering with spin-independent scattering matrix elements $V_{\boldsymbol{k}'\boldsymbol{k}}$ one has

$$Q_{\boldsymbol{k}}\{\rho\}=\frac{2\pi}{\hbar}\sum_{\boldsymbol{k}}N_i\left|V_{\boldsymbol{k}'\boldsymbol{k}}\right|^2 \times\left\{\delta\left(E^0_{\boldsymbol{k}}+\mathcal{H}^{(1)}_{\boldsymbol{k}}-E^0_{\boldsymbol{k}'}+\mathcal{H}^{(1)}_{\boldsymbol{k}'}\right),\rho_{\boldsymbol{k}}-\rho_{\boldsymbol{k}'}\right\}_s\,. \tag{8.50}$$

Here the curly brackets with the subscript s mean the antisymmetrization of matrices, N_i is the concentration of static defects and the δ-function is understood as

$$\delta\left(E^0_{\boldsymbol{k}}-E^0_{\boldsymbol{k}'}\right)+\left(\mathcal{H}^{(1)}_{\boldsymbol{k}}-\mathcal{H}^{(1)}_{\boldsymbol{k}'}\right)\frac{\partial}{\partial E^0_{\boldsymbol{k}}}\delta\left(E^0_{\boldsymbol{k}}-E^0_{\boldsymbol{k}'}\right)\,.$$

Substituting (8.49) into (8.50) and retaining zero- and first-order terms we obtain zero by using the identity

$$\left[F(E^0_{\boldsymbol{k}})-F(E^0_{\boldsymbol{k}'})\right]\frac{\partial}{\partial E^0_{\boldsymbol{k}}}\delta\left(E^0_{\boldsymbol{k}}-E^0_{\boldsymbol{k}'}\right)=-\delta\left(E^0_{\boldsymbol{k}}-E^0_{\boldsymbol{k}'}\right)\frac{\partial}{\partial E^0_{\boldsymbol{k}}}F(E^0_{\boldsymbol{k}})$$

for any analytical function $F(E)$.

We demonstrate the relaxational mechanism under conditions of interband optical orientation by circularly polarized light and then briefly discuss the intraband excitation. Since $\tau_\varepsilon\ll\tau_0$ it is not necessary to study the relaxation of the energy of hot photoelectrons to the bottom of the conduction band, and the generation matrix $G_{\boldsymbol{k}}$ in (8.47) can be written in the form

$$G_{\boldsymbol{k}}=(g/n)\left\{f^0\left(\mathcal{H}'_{\boldsymbol{k}}\right),1+2\boldsymbol{\sigma}\cdot\boldsymbol{S}_0\right\}_s\,, \tag{8.51}$$

where g is the rate of optical excitation of electrons in the conduction band, n is their density and $\boldsymbol{S}_0$ is the average spin of a photocreated electron relaxing to the conduction-band bottom. As in the case with ρ^0, one needs to expand (8.51) up to the first-order terms

$$G_{\boldsymbol{k}} = \frac{g}{n}\left[f^0(1+2\boldsymbol{\sigma}\cdot\boldsymbol{S}_0) + \frac{\partial f^0}{\partial E}\mathcal{H}^{(1)}_{\boldsymbol{k}} + \frac{\partial f^0}{\partial E}\,\hbar\left(\boldsymbol{\Omega}^{(1)}_{\boldsymbol{k}}\cdot\boldsymbol{S}_0\right)\right] .$$

We use the simple momentum-relaxation model and present the collision integral in the form

$$Q_{\boldsymbol{k}}\{\rho\} = \frac{\rho_{\boldsymbol{k}} - \rho^0_{\boldsymbol{k}}}{\tau_p} . \tag{8.52}$$

While solving the kinetic equation (8.47) we write the spin density matrix as

$$\rho_{\boldsymbol{k}} = \rho^0_{\boldsymbol{k}} + \delta\rho_{\boldsymbol{k}} \tag{8.53}$$

and assume $\delta\rho_{\boldsymbol{k}}$ to be a small correction. It is an odd function of $\boldsymbol{k}$.

Under steady-state photoexcitation $\rho_{\boldsymbol{k}}$ is time-independent, and the first term in the left-hand side of (8.47) vanishes. After averaging the terms of this equation over the vector $\boldsymbol{k}$ we obtain

$$\frac{g}{n} = \frac{1}{\tau_0}\,,\ \left(\frac{1}{\tau_0}+\frac{1}{\tau_s}\right)\boldsymbol{S} + \boldsymbol{S}\times\boldsymbol{\Omega}_L = \frac{1}{\tau_0}\boldsymbol{S}_0\,, \tag{8.54}$$

where $\boldsymbol{\Omega}_L$ is the Larmor vector frequency, and τ_s^{-1} is the spin relaxation rate including the contribution due to the Dyakonov-Perel' mechanism related to the term $(i/\hbar)[\mathcal{H}^{(1)}_{\boldsymbol{k}}, \rho_{\boldsymbol{k}}]$ in (8.47). These are the balance equations discussed in Chap. 5. Now we derive, from (8.47), an equation for $\delta f = \mathrm{Tr}\{\delta\rho/2\}$. It has the form

$$\frac{1}{\tau_0}\frac{\partial f^0}{\partial E}\,\hbar\left(\boldsymbol{\Omega}^{(1)}_{\boldsymbol{k}}\cdot\boldsymbol{S}\right) + \frac{\delta f_{\boldsymbol{k}}}{\tau_p} = \frac{1}{\tau_0}\frac{\partial f^0}{\partial E}\,\hbar\left(\boldsymbol{\Omega}^{(1)}_{\boldsymbol{k}}\cdot\boldsymbol{S}_0\right)$$

and, therefore, the correction $\delta f_{\boldsymbol{k}}$ is given by

$$\delta f_{\boldsymbol{k}} = \hbar\frac{\partial f^0}{\partial E}\frac{\tau_p}{\tau_0}\ \boldsymbol{\Omega}^{(1)}_{\boldsymbol{k}}\cdot(\boldsymbol{S}_0 - \boldsymbol{S})\,. \tag{8.55}$$

One can see that it is smaller than the last term in (8.49) by a factor of τ_p/τ_0. However, this is the correction contributing to the current and for a nondegenerate gas of photoelectrons one obtains

$$\boldsymbol{j} = 2e\sum_{\boldsymbol{k}}\frac{\hbar\boldsymbol{k}}{m^*}\,\delta f_{\boldsymbol{k}} = -eg\tau_p\nabla_{\boldsymbol{k}}\left(\boldsymbol{\Omega}^{(1)}_{\boldsymbol{k}}, \boldsymbol{S}_0 - \boldsymbol{S}\right) \tag{8.56}$$

or, according to (8.54),

$$\boldsymbol{j} = -eg\tau_0\tau_p\nabla_{\boldsymbol{k}}\left(\boldsymbol{\Omega}_{\boldsymbol{k}}^{(1)}, \frac{\boldsymbol{S}}{\tau_s} + \boldsymbol{S}\times\boldsymbol{\Omega}_L\right) . \tag{8.57}$$

If $\boldsymbol{S}$ is varying in time and the characteristic time of variation is long as compared to τ_p, τ_ε then (8.56) is generalized to

$$\boldsymbol{j} = -eg\tau_p\nabla_{\boldsymbol{k}}\left(\boldsymbol{\Omega}_{\boldsymbol{k}}^{(1)}, \boldsymbol{S}_0 - \boldsymbol{S} - \tau_0\frac{d\boldsymbol{S}}{dt}\right) , \tag{8.58}$$

which can be just as well converted into (8.57).

In order to consider the relaxational mechanism under intraband optical orientation of electronic spins in n-doped QWs the lifetime τ_0 in (8.47) should be set to infinity. The intraband generation matrix has the form

$$G_{\boldsymbol{k}} = 2\left\{f^0\left(\mathcal{H}'_{\boldsymbol{k}}\right), \boldsymbol{\sigma}\cdot\dot{\boldsymbol{S}}\right\}_s , \tag{8.59}$$

where $\dot{\boldsymbol{S}}$ is the spin generation rate per particle. Then we obtain for the correction $\delta f_{\boldsymbol{k}}$ contributing to the current

$$\delta f_{\boldsymbol{k}} = \hbar\frac{\partial f^0}{\partial E}\tau_p\,\boldsymbol{\Omega}_{\boldsymbol{k}}^{(1)}\cdot\dot{\boldsymbol{S}}$$

and for the current

$$\boldsymbol{j} = -eN_e\tau_p\nabla_{\boldsymbol{k}}\left(\boldsymbol{\Omega}_{\boldsymbol{k}}^{(1)}\cdot\dot{\boldsymbol{S}}\right) . \tag{8.60}$$

Under normal incidence of the light on a (001)-grown QW the vector $\dot{\boldsymbol{S}}$ is directed along z and the current is zero. Thus, the relaxational mechanism makes no contribution to the spin-galvanic current in the set-up of Fig. 8.4 and the latter is completely related to the kinetic mechanism.

The radiation of the CO_2 laser causes direct $e2$-$e1$ optical transitions in GaAs/AlGaAs MQWs. It can induce the resonant spin-galvanic current at normal incidence of radiation in the presence of an in-plane magnetic field, as this effect was observed under intrasubband transitions (Fig. 8.4). Since the spin generation rate $\dot{S}_z \propto K_\perp \propto K_z$, where $K_\perp, K_z$ are defined in (4.21) the spectral behavior of the spin-galvanic current must coincide with the absorption spectrum. One can see from Fig. 4.5 that the wavelength dependence of the spin-galvanic effect obtained between 9.2 μm and 10.6 μm, indeed, repeats the spectrum of the intersubband absorption.

8.3 Photon Drag Effect

In the calculation of the circular PGE, the photon momentum $\hbar\boldsymbol{q}$ was neglected. The photon drag effect described by the tensor $\boldsymbol{T}$ in (8.1) is entirely owing to the existence of a photon momentum. Classically, the momentum carried by electromagnetic waves can manifest itself through a radiation pressure on a surface as described already by Maxwell. Light pressure effects are

found in several fields of physics, namely, astrophysics, atomic and molecular physics, solid-state physics, including metals and semiconductors, bulk materials and nanostructures. If the absorption in a solid is caused by free-carrier optical transitions, intraband, interband, bound-to-continuum etc., these carriers acquire a directed motion due to momentum transfer from photons to the particles. In bulk crystals the photon drag current was first observed experimentally in the microwave region [8.16] and in quantum transitions between the valence subbands in Ge excited by a CO_2 laser [8.17, 8.18]. New features of the photon drag effect in a 2D electron gas were predicted by Vasko [8.19], Luryi [8.20], Grinberg and Luryi [8.21] and observed experimentally by Wieck et al. [8.22]

A reasonable estimation of the light-induced drift of quantum-confined carriers can be obtained on the basis of the following simple argument applied for example to a QW. If η is the relative absorbance and $q_\parallel$ is the photon in-plane wave vector component then the rate of momentum transfer per particle per unit area is given by

$$F = \hbar q_\parallel \frac{\eta I}{\hbar\omega N_e} \,.$$

This is nothing but the drag force acting upon each electron. It gives rise to a drift velocity $v_d = (\tau_p/m^*)F$ and a current density

$$j_{PD} = eN_e v_d = e\tau_p \frac{\hbar q_\parallel}{m^*} \frac{\eta I}{\hbar\omega} \,. \tag{8.61}$$

The same estimation follows from the momentum and energy conservation laws

$$E_{e2,\boldsymbol{k}+\boldsymbol{q}_\parallel} - E_{e1,\boldsymbol{k}} = \hbar\omega \tag{8.62}$$

for the direct interband optical transition $(e1, \boldsymbol{k}) \to (e2, \boldsymbol{k} + \boldsymbol{q}_\parallel)$. The kinetic energy $\hbar^2(\boldsymbol{k} + \boldsymbol{q})^2/(2m^*)$ has a linear-$\boldsymbol{k}$ term, $\hbar^2(\boldsymbol{k} \cdot \boldsymbol{q})/m^*$, which is reminiscent of the linear-$\boldsymbol{k}$ spin-dependent term in (8.8). One can see that the current (8.61) is obtained from the estimation (8.12) for the circular PGE as soon as the velocity, $\beta/\hbar$, related to the electron linear-$\boldsymbol{k}$ dispersion is substituted by the velocity, $\hbar q_\parallel/m^*$, of an electron with the momentum $\hbar q_\parallel$. Continuing this analogy we can use (8.10), change β_e by $\hbar^2 \boldsymbol{q}_\parallel/m_e$, set β_v to zero and P_c to -1, use the identity $m_e m_h/\mu = m_e + m_h \equiv M$ and finally come to the interband photon drag current induced under normal incidence

$$\boldsymbol{j} = e(\tau_p^e - \tau_p^h) \frac{\hbar \boldsymbol{q}_\parallel}{M} \frac{\eta_{cv} I}{\hbar\omega} \,. \tag{8.63}$$

The photon drag effect induced by the $e2$-$e1$ resonant transitions can be found from (8.30) by performing the replacement $\beta_2 + \beta_1 \to (\hbar^2 \boldsymbol{q}_\parallel/m^*)$, $P_c \to +1$, $\eta_{21}(\boldsymbol{e} \perp z) \to \eta_{21}(\boldsymbol{e} \parallel z)\,|e_z|^2$ which leads to

$$\boldsymbol{j} = e \frac{\hbar \boldsymbol{q}_\parallel}{m^*} |e_z|^2 \left[\tau_2\, \eta_{21}(\hbar\omega) + (\tau_1 - \tau_2)\, \bar{E}\, \frac{d\, \eta_{21}(\hbar\omega)}{d\, \hbar\omega} \right] \frac{I}{\hbar\omega} \,, \tag{8.64}$$

where for the sake of brevity η_{21} stands for $\eta_{21}(\boldsymbol{e} \parallel z)$. It is worth to note that $q_\parallel |e_z|^2 = q \sin^3\theta$. In Fig. 8.6 the spectral response of the photon drag effect in a modulation-doped GaAs/$Al_{0.35}Ga_{0.65}$As MQW structure is presented [8.23]. A Lorentzian absorption is taken for the fit using (8.64). The spectral line shape of the photon drag current yields a relaxation time ratio $\tau_1/\tau_2 = 1.6$.

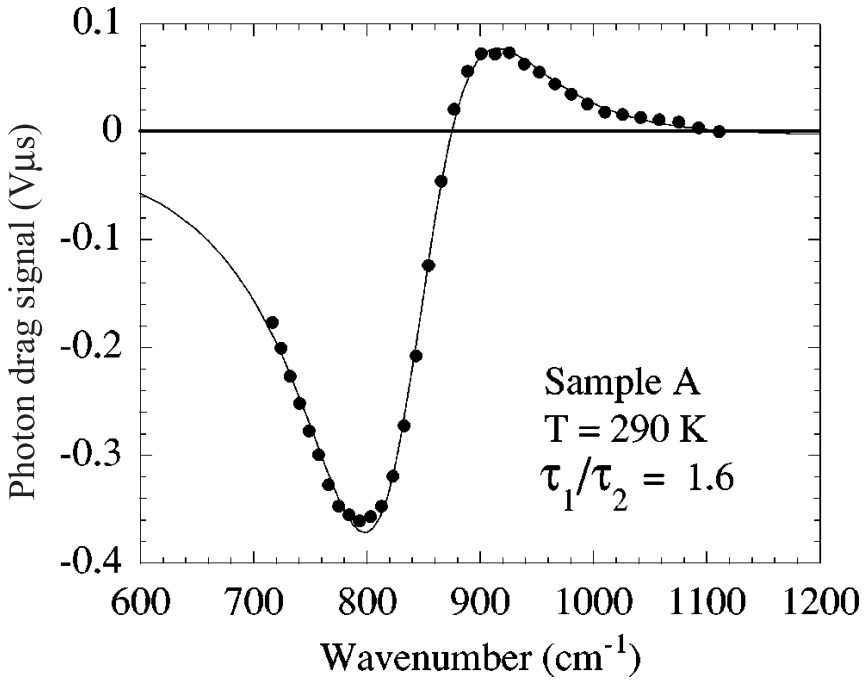

Fig. 8.6. Photon drag spectrum at room temperature of the modulation-doped GaAs/Al_xGa_{1-x}As MQW sample, measured at a micropulse intensity of 2.5 MW/cm^2. For a better signal to noise ratio, an integration is made over the entire macropulse of FELIX (5.6 μs). Solid line is the best fit according to (8.64). From [8.23].

It is instructive to compare equations (8.63, 8.64) derived for particular mechanisms with the general symmetry considerations. For QWs of the symmetry C_{2v}, the phenomenological description (8.1) gives for the photon drag effect

$$j_{PD,x} = q_x I \sum_{\mu=x,y,z} T_{xx\mu\mu} |e_\mu|^2 + q_y I T_{xyxy} \left(e_x e_y^* + e_y e_x^*\right) , \qquad (8.65)$$

$$j_{PD,y} = q_y I \sum_{\mu=x,y,z} T_{yy\mu\mu} |e_\mu|^2 + q_x I T_{yxyx} \left(e_x e_y^* + e_y e_x^*\right) .$$

In symmetrical QWs characterized by the symmetry D_{2d} some of the above coefficients $T_{\lambda\mu\nu\eta}$ are interrelated, namely

$$T_{xxzz} = T_{yyzz}\,,\; T_{xxxx} = T_{yyyy}\,,\; T_{xxyy} = T_{yyxx}\,,\; T_{xyxy} = T_{yxxy}\,. \qquad (8.66)$$

The photon drag current (8.63) corresponds to equal T_{xxxx} and T_{yyyy} while the photocurrent (8.64) is described by the coefficients $T_{xxzz} = T_{yyzz}$. For more complicated band structures these relations can be violated and, moreover, all other coefficients in (8.65) become nonzero.

8.4 Linear Photogalvanic Effect

For the linear PGE, the phenomenological equation (8.1) in QWs of the C_{2v} symmetry reduces to

$$j_{LPGE,x} = \chi_{xxz}\,(e_x e_z^* + e_z e_x^*)\,I\,,\; j_{LPGE,y} = \chi_{yyz}\left(e_y e_z^* + e_z e_y^*\right) I\,. \qquad (8.67)$$

In symmetrical QWs of the point-group D_{2d}, the pair of coefficients are linearly dependent, $\chi_{xxz} = -\chi_{yyz}$.

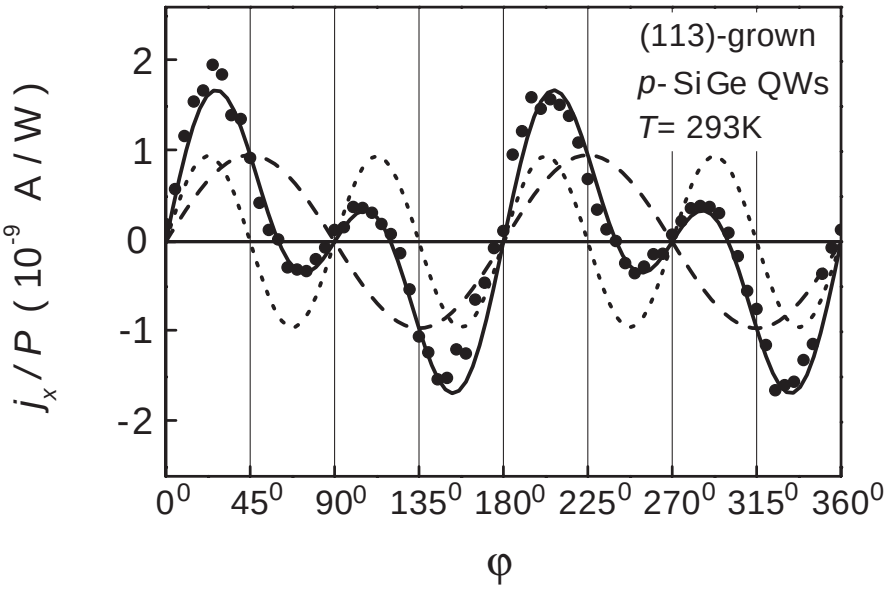

Fig. 8.7. Photogalvanic current in a (113)-grown $Si_{0.75}Ge_{0.25}$(5 nm)/Si single QW normalized by the light power P as a function of the phase angle φ. The results are obtained under normal-incidence irradiation at $\lambda = 280$ μm at room temperature. The full line is fitted according to (8.70). Broken and dotted lines show $j_x \propto \sin 2\varphi$ and $j_x \propto \sin 2\varphi \cos 2\varphi$, respectively. From [8.9].

The C_s symmetry allows both circular and linear PGEs for normal incidence because in this case the tensors $\boldsymbol{\gamma}$ and $\boldsymbol{\chi}$ have the additional nonzero components γ_{xz}, see (8.2), $\chi_{xxy} = \chi_{xyx}$, χ_{yxx} and χ_{yyy}. As a result, under normal incidence one has

$$j_x = \left[\gamma_{xz} P_c + \chi_{xxy}\left(e_x e_y^* + e_y e_x^*\right)\right] I\,,\; j_y = \left(\chi_{yxx}|e_x|^2 + \chi_{yyy}|e_y|^2\right) I\,. \quad (8.68)$$

In particular, for linearly polarized light

$$j_{LPGE,x} = I\chi_{xxy}\sin 2\alpha\,,\; j_{LPGE,y} = I\left(\chi_+ + \chi_-\cos 2\alpha\right)\,, \quad (8.69)$$

where $\chi_\pm = (\chi_{yxx} \pm \chi_{yyy})/2$ and α is the angle between the plane of polarization and x. Figure 8.7 presents the measured dependence of j_x and j_y as a function of the angle α and the fit to (8.69) for a p-type SiGe (113)-grown asymmetrical QW structure. In the experimental setup, where the laser light is linearly polarized along x and a $\lambda/4$ plate is placed between the laser and the sample, (8.68) takes the form

$$j_x = I\left(\gamma_{xz} + \chi_{xxy}\cos 2\varphi\right)\sin 2\varphi\,,\; j_y = I\left(\chi_+ + \chi_-\cos 2\varphi\right)\,, \quad (8.70)$$

where φ is the angle between the initial plane of linear polarization and the optical axis of the polarizer. The circular and linear polarizations of the incident light vary with φ in accordance to $P_c = \cos\varphi$, see (8.5), and $P_l = \sin\varphi$. In Fig. 8.7 experimental data and a fit to these functions are presented for the same p-type SiGe (113)-grown QW structure.

The linear PGE was observed in some insulators as early as the 1950s, and possibly even earlier, but was correctly identified as a novel phenomenon only in 1974-75 [8.24, 8.25]. In semiconductors, the linear PGE was first observed on tellurium [8.26, 8.27] and then studied in detail on p-GaAs [8.28].

Microscopically, a current of the linear PGE consists of the so-called ballistic and shift contributions [8.29–8.32]. The first of them is described by the conventional equation

$$\boldsymbol{j} = e\sum_{nn'} W_{n'n}(\boldsymbol{v}_{n'}\tau_p^{(n')} - \boldsymbol{v}_n\tau_p^{(n)})\,. \quad (8.71)$$

Here the index n describes all quantum numbers characterizing the electron eigenstates, namely the band and subband labels, spin sublevel and wave vector $\boldsymbol{k}$; the probability transition rate from the state n to n' is given by Fermi's golden rule

$$W_{n'n} = \frac{2\pi}{\hbar}\left|M_{n'n}\right|^2 (f_n - f_{n'})\delta(E_{n'} - E_n)\,, \quad (8.72)$$

$M_{n'n}$ is the transition matrix element, $\boldsymbol{v}_n$ and $\tau_p^{(n)}$ are the electron velocity and momentum relaxation time in the state n, f_n is the distribution function, or the occupation, of the state n. The energy E_n includes the photon or

phonon energy in the initial or final state. Equation (8.71) is a contribution to the general expression for the current (8.13) of diagonal components of the electron density matrix, $\rho_{nn} = f_n$, and of the velocity $\boldsymbol{v}_{nn} \equiv \boldsymbol{v}_n$. The ballistic current is nonzero only if one simultaneously includes in $M_{n'n}$ carrier interaction both with a photon and with another particle, a phonon, impurity or static defect, another electron or hole, including a geminate partner photocreated in the same photoabsorption process. In other words one needs to go beyond the Born approximation in calculating $M_{n'n}$.

The second contribution to the linear PGE current comes from inclusion in (8.13) of the nondiagonal components $\rho_{nn'}$ and $\boldsymbol{v}_{nn'}$ with $n' \neq n$. This current was shown [8.31] to originate from the shift of the wave packet's center-of-mass in quantum transitions and can be written as

$$\boldsymbol{j} = e \sum_{nn'} W_{n'n} \boldsymbol{R}_{n'n} \,. \tag{8.73}$$

For the shift in the real space we have

$$\boldsymbol{R}_{n'n} = -\left(\nabla_{\boldsymbol{k}} + \nabla_{\boldsymbol{k}'}\right) \Phi_{n'n} + \boldsymbol{\Omega}_{n'} - \boldsymbol{\Omega}_n \,, \tag{8.74}$$

where $\Phi_{n'n}$ is the phase of the transition matrix element, $\boldsymbol{k}$ and $\boldsymbol{k}'$ are the wave vectors in the states n and n', $\boldsymbol{\Omega}_n$ is the diagonal matrix element of the coordinate

$$\boldsymbol{\Omega}_n = \mathrm{i} \int u_n^* \nabla_{\boldsymbol{k}} u_n \, d\boldsymbol{r} \,,$$

and $u_n(\boldsymbol{r})$ is the Bloch periodical amplitude. In a steady-state regime, when the processes of generation, scattering and recombination are taken altogether into consideration, the contributions associated with $\boldsymbol{\Omega}_n$ vanish since they describe the static charge redistribution. The first term in the right-hand side of (8.74) can be rewritten as

$$\boldsymbol{R}_{n'n} = -\frac{\mathrm{Im}\left\{M_{n'n}^* \left(\nabla_{\boldsymbol{k}} + \nabla_{\boldsymbol{k}'}\right) M_{n'n}\right\}}{|M_{n'n}|^2} \,. \tag{8.75}$$

This form is useful for practical calculations. It is worthy of note that a shift of an electron under the quantum transition has a physical tie to the well-known Goos-Hänchen effect in classical optics [8.33]. In the latter, the totally reflected beam is spatially displaced with respect to a ray reflected by the geometrical interface between the two media. The physical connection becomes apparent when considering the totally reflected beam a superposition of plane waves and taking into account that the phase shift under reflection is a function of the angle of incidence [8.34, 8.35].

To illustrate, we estimate the linear PGE under the $hh1 \rightarrow e1$ interband transitions induced by linearly polarized light normally incident on a $[hhl]$-grown QW ($h \neq 0$). The shifts (8.75) become nonzero if both even and odd terms in $\boldsymbol{k}$ are included into the interband matrix elements. For transitions

from the heavy-hole subband the optical matrix elements can be presented by

$$M_{cv}(\boldsymbol{k}) \equiv M_{e1,\pm 1/2,;hh1,\pm 3/2}(\boldsymbol{k}) = \mp[\mathrm{i}M_0(e_x \pm \mathrm{i}e_y) + Q^{(\pm)}_{\lambda\mu} k_\lambda e_\mu] \,. \quad (8.76)$$

The first term on the right-hand side is the main contribution described by Table 2.2 while the complex coefficients $Q^{(\pm)}_{\lambda\mu}$ describe linear-$\boldsymbol{k}$ corrections. They satisfy the conditions

$$Q^{(-)}_{\lambda\mu} = Q^{(+)*}_{\lambda\mu} \,,\; Q^{(\pm)}_{\lambda\mu} = Q^{(\pm)}_{\mu\lambda} \,.$$

From (8.75) we obtain

$$R_{cv,\lambda}(\boldsymbol{k},\pm) = M_0^{-1} \left(e_x \mathrm{Re}\left\{Q^{(+)}\right\}_{\lambda\mu} + e_y \mathrm{Im}\left\{Q^{(+)}\right\}_{\lambda\mu} \right) e_\mu \,. \quad (8.77)$$

Now we can start from the interband matrix elements written in the principal axes x_0, y_0, z_0 and rewrite them in terms of x, y, z components. As a result, the ratios $Q^{(+)}_{\lambda\mu}/M_0$ can be presented as

$$\frac{Q_{xy}}{M_0} = \frac{Q_{yx}}{M_0} = \sin\theta \frac{P}{Q} \,,$$

$$\frac{Q_{xx}}{M_0} = \mathrm{i}\sin\theta \frac{P}{Q} \,,\; \frac{Q_{yy}}{M_0} = -3\mathrm{i}\sin\theta \frac{P}{Q} \,,$$

where the parameters P and Q are introduced in (3.210), and θ is the angle between the axes $[hhl]$ and $[001]$. Then from (8.73) and (8.77) we come to the shift contribution to the interband photocurrent

$$j_x = e\sin\theta \frac{\eta_{cv} I}{\hbar\omega} \frac{P}{Q} 2e_x e_y \,,\; j_y = e\sin\theta \frac{\eta_{cv} I}{\hbar\omega} \frac{P}{Q} \left(e_x^2 - 3\cos^2\theta e_y^2\right) \,. \quad (8.78)$$

Particularly, for QWs grown along [111] and characterized by the C_{3v} symmetry, we have $3\cos^2\theta = 1$ and obtain the polarization dependence $j_x \propto 2e_x e_y$, $j_y \propto e_x^2 - e_y^2$ which follows as well from the general symmetry considerations for the C_{3v} point group (Table A.4).

For the estimation of the ballistic photocurrent we should consider indirect interband transitions. Similarly to (8.40) the compound matrix element of the transition has the form

$$M^{\mathrm{ind}}_{e1,\pm 1/2;hh1,\pm 3/2}(\boldsymbol{k}',\boldsymbol{k}) \quad (8.79)$$
$$= \frac{V^c_{\boldsymbol{k}'\boldsymbol{k}} M_{cv}(\boldsymbol{k})}{E_{e1,\boldsymbol{k}} - E_{hh1,\boldsymbol{k}} - \hbar\omega - \mathrm{i}\gamma} + \frac{M_{cv}(\boldsymbol{k}') V^v_{\boldsymbol{k}'\boldsymbol{k}}}{E_{hh1,\boldsymbol{k}'} - E_{hh1,\boldsymbol{k}} \pm \hbar\Omega - \mathrm{i}\gamma} \,,$$

where $\gamma \to +0$ and $V^{c,v}_{\boldsymbol{k}'\boldsymbol{k}}$ are the scattering matrix elements in the conduction and valence bands. While calculating the square modulus of M^{ind}, the energy denominators are transformed using the identity

$$\frac{1}{E_i - E_j \pm \mathrm{i}\gamma}\bigg|_{\gamma\to+0} = \mathcal{P}\frac{1}{E_i - E_j} \mp \mathrm{i}\pi\delta(E_i - E_j)\,.$$

Only the terms containing the product of the real part for one of the denominators in (8.79) and the imaginary term for the other denominator contribute to the current. Therefore, the effect is due to the transitions where the energy conservation law holds not only between the initial and final states but also for one of the intermediate states as well. Formally it means that the following part

$$\pi\mathrm{Im}\left\{V^{c*}_{\boldsymbol{k}'\boldsymbol{k}}V^{v}_{\boldsymbol{k}'\boldsymbol{k}}M^{*}_{cv}(\boldsymbol{k})M_{cv}(\boldsymbol{k}')\right\}$$
$$\times\left(-\frac{\delta(E_{e1,\boldsymbol{k}} - E_{hh1,\boldsymbol{k}} - \hbar\omega)}{E_{hh1,\boldsymbol{k}'} - E_{hh1,\boldsymbol{k}}} + \frac{\delta(E_{hh1,\boldsymbol{k}'} - E_{hh1,\boldsymbol{k}})}{E_{e1,\boldsymbol{k}} - E_{hh1,\boldsymbol{k}} - \hbar\omega}\right)$$

of $|M^{\mathrm{ind}}|^2$ contains a contribution antisymmetrical in $\boldsymbol{k}$. Substituting this expression into (8.71) and taking into account the $\boldsymbol{k}$-dependent correction to $M_{cv}(\boldsymbol{k}')$ one can complete the calculation. The ballistic contribution to the photocurrent has the same order of magnitude as the shift contribution. Really, the antisymmetric part of $|M^{\mathrm{ind}}|^2$ is proportional to the product V^cV^v while the momentum relaxation times in (8.71) are proportional to $(V^c)^{-2}$ or $(V^v)^{-2}$ so that the dependence of the ballistic current on the absolute values of electron-photon or electron-defect coupling constants disappears.

The linear PGE can also be induced in noncentrosymmetric SLs, i.e., in a saw-tooth SL, and MQW structures, i.e., in MQWs with asymmetric double wells, under illumination with unpolarized light [8.36–8.39]. The photocurrent is generated along the growth direction z because of the lack of reflection symmetry $z \to -z$. Note that in MQWs the effect has a threshold at the edge of transitions between quantized and continuum states, the so-called bound-to-continuum or above-barrier transitions.

8.5 Saturation of Photocurrents at High Light Intensities

Here we discuss nonlinear behavior of the linear and circular PGEs, which will take place with increasing the light intensity due to saturation or bleaching of the absorption. Since the saturation effect was observed on p-doped QW structures [8.40] we consider direct intersubband optical transitions from the heavy-hole subband $hh1$ to higher subbands, say the $lh1$ subband.

Spin sensitive bleaching can be analyzed in terms of the following simple model taking into account both optical excitation and nonradiative relaxation processes. The probability rates for direct optical transitions from the $hh1$ states with $m = \pm 3/2$ to higher subbands are denoted as $W_\pm$. For linearly polarized light, W_+ and W_- are equal. For the circular polarization, right-handed, σ_+, or left-handed, σ_-, the rates $W_\pm$ are different but, due to time-inversion symmetry, satisfy the condition $W_+(\sigma_\pm) = W_-(\sigma_\mp)$. The

photoexcited holes are assumed to loose their spin orientation in the course of energy relaxation to the bottom of the $hh1$ subband, due to rapid spin relaxation in hot states. Thus, spin orientation occurs only in this subband. If p_+ and p_- are the 2D densities of heavy holes occupying the subbands $(hh1, +3/2)$ and $(hh1, -3/2)$, respectively, then the rate equations for $p_\pm$ can be written as

$$\frac{\partial p_+}{\partial t} + \frac{p_+ - p_-}{2\tau_s} = -W_+ + \frac{1}{2}(W_+ + W_-)\,, \tag{8.80}$$

$$\frac{\partial p_-}{\partial t} + \frac{p_- - p_+}{2\tau_s} = -W_- + \frac{1}{2}(W_+ + W_-)\,.$$

The second terms on the left-hand side describe the spin relaxation trying to equalize the population in the $(hh1, \pm 3/2)$ spin branches. The first terms on the right-hand side describe the removal of holes from the $hh1$ subband due to photoexcitation while the second terms characterize the relaxation of holes which come down to the $(hh1, +3/2)$ and $(hh1, -3/2)$ states with equal rates. If the laser-pulse duration is longer than any relaxation time, the time derivatives in (8.80) can be omitted and, instead of this equation, we have

$$\frac{p_+ - p_-}{\tau_s} = -(W_+ - W_-)\,. \tag{8.81}$$

The hole-removal rates can be presented in the form

$$W_+ = \frac{1}{2}\frac{\eta I}{\hbar\omega}(1 - \rho_0 P_c)(1 + \rho)\,,\; W_- = \frac{1}{2}\frac{\eta I}{\hbar\omega}(1 + \rho_0 P_c)(1 - \rho)\,, \tag{8.82}$$

where ρ is the hole spin polarization degree $(p_+ - p_-)/(p_+ + p_-)$, η is a function of the light intensity I, the parameter ρ_0 is defined as the ratio $(W_- - W_+)/(W_- + W_+)$ for the σ_+-polarized radiation of low enough intensity where η is constant and $W_\pm$ is proportional to I. The factors $1 \pm \rho_0 P_c$ take into account the sensitivity of optical transitions to the circular polarization of light and spin of involved particle. The factors $1 \pm \rho$ take into account that the transition probability rate depends on the occupation number of the initial state and, hence, on the hole spin polarization. Substitution of (8.82) into (8.81) leads to the linear equation for ρ

$$\frac{p_s}{\tau_s}\,\rho = \frac{\eta I}{\hbar\omega}\,(\rho_0 P_c - \rho)\,, \tag{8.83}$$

where p_s is the hole density and we rewrote $p_+ - p_-$ as $p_s\rho$. The solution reads

$$\rho = \rho_0 P_c \frac{\tau_s \eta I/(p_s \hbar\omega)}{1 + [\tau_s \eta I/(p_s \hbar\omega)]}\,. \tag{8.84}$$

Bleaching of absorption with increasing the intensity of linearly-polarized light is described phenomenologically by the function

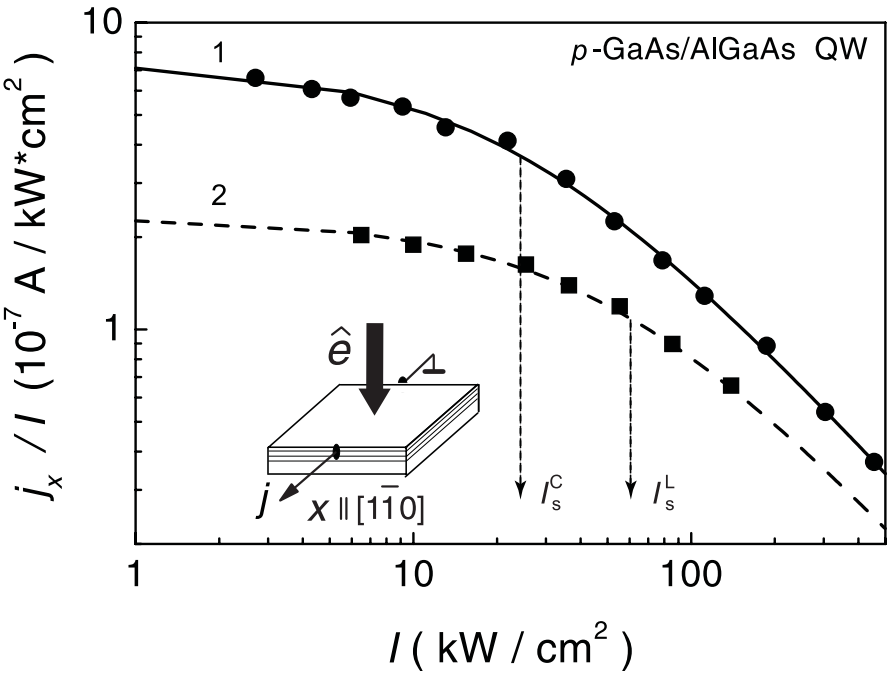

Fig. 8.8. Photogalvanic current j_x normalized by the intensity I as a function of I for circularly (*curve* 1) and linearly (*curve* 2) polarized radiation at T = 20 K. The inset shows the geometry of the experiment; $\hat{\boldsymbol{e}}$ indicates the direction of the incoming light. The current j_x flows along $[1\bar{1}0]$ direction at normal incidence of radiation on p-type (113)A-grown GaAs/AlGaAs QWs. In order to obtain the circular PGE right or left circularly polarized light has been applied. To obtain the linear PGE linearly polarized radiation with the electric field vector $\boldsymbol{E}$ oriented at 45° to the x direction was used. The measurements are fitted to $j_x/I \propto 1/(I+I/I_s)$ with one parameter I_s for each state of polarization (*full line*: circular, *broken line*: linear). From [8.40].

$$\eta(I) = \frac{\eta_0}{1+\frac{I}{I_{se}}}\,, \tag{8.85}$$

where $\eta_0 = \eta(I \to 0)$ and I_{se} is the characteristic saturation intensity controlled by energy relaxation of the 2D hole gas. Since the photocurrent of linear PGE, j_{LPGE}, induced by the linearly polarized light is proportional to ηI, one has

$$\frac{j_{\mathrm{LPGE}}}{I} \propto \frac{1}{1+\frac{I}{I_{se}}}\,. \tag{8.86}$$

The circular current j_{CPGE} induced by the circular polarized radiation is proportional to $W_+ - W_- \propto \rho$. Substituting $\eta(I)$ from (8.85) into (8.84) we find after some development

$$\frac{j_{\rm LPGE}}{I} \propto \frac{1}{1 + I\left(\frac{1}{I_{se}} + \frac{1}{I_{ss}}\right)}\,, \tag{8.87}$$

where $I_{ss} = p_s\hbar\omega/(\eta_0\tau_s)$.

The measurements illustrated in Fig. 8.8 indicate that the photocurrent j_x at a low power level depends linearly on the light intensity and gradually saturates with increasing intensity, $j_x \propto I/(1 + I/I_s^{\rm L,C})$, where $I_s^{\rm L,C}$ is the saturation parameter for linearly and circularly polarized radiation. This corresponds to a constant absorbance at low values of I and decreasing absorption with rising I. From (8.86, 8.87) we obtain

$$I_s^{\rm L} = I_{se}\,,\; I_s^{\rm C} = \frac{I_{se}I_{ss}}{I_{se} + I_{ss}}\,. \tag{8.88}$$

One can see from Fig. 8.8 that the measured saturation intensities $I_s^{\rm L,C}$ are different, namely $I_s^{\rm C} < I_s^{\rm L}$. This is in agreement with theory. The saturation of the absorption of linearly polarized radiation is governed by the energy relaxation time τ_ε whereas in case of the circular polarization it is governed by both τ_ε and τ_s. If τ_s is of the order of τ_ε or larger, the saturation becomes spin sensitive and the saturation intensity of circularly-polarized radiation drops below that for the linear polarization.

Taking into account that $I_{ss} = I_s^{\rm L}I_s^{\rm C}/(I_s^{\rm L} - I_s^{\rm C})$ and using the measured values of $I_s^{\rm L}$, $I_s^{\rm C}$ one can estimate the parameter $I_{ss} = p_s\hbar\omega/(\eta_0\tau_s)$ and even the time τ_s. The latter is possible if the absorbance η_0 is known from an independent experiment or theoretical calculation, see details in [8.40, 8.41].

8.6 Chirality Effects in Carbon Nanotubes

The point-group symmetry of a chiral medium makes no difference between polar and axial vectors. Thus, by definition, the chirality effects are those where a polar vector and an axial vector (or a pseudovector) are interconnected by a phenomenological equation. Here we consider chirality related effects in photogalvanic, electron-transport and optical properties of carbon nanotubes. For this purpose we apply the effective mass theory used previously in Chaps. 3, 4 for the analysis of absorption spectra of one-dimensional structures. It will be shown that the chiral properties are determined by terms in the electron effective Hamiltonian describing the coupling between the electron wave vector along the tube principal axis and the orbital momentum around the tube circumference (Chap. 2). We derive equations for the circular photocurrent and magneto-chiral dc electric currents, which are linear in the external magnetic field and quadratic in the bias voltage or amplitude of the electro-magnetic field. Moreover, we perform analytic estimations for the natural circular dichroism and magneto-spatial effect in the light absorption.

8.6.1 Circular Photocurrent in Nanotubes

In chiral nanotubes, the circular PGE is an electron analog of a screw thread or a plane with a propeller. In this case the tensor $\boldsymbol{\gamma}$ in the general phenomenological equation (8.1) has only one nonzero component γ_{zz} and the dc circular photocurrent is described by

$$j_{\mathrm{CPGE},z} = I\gamma\, \mathrm{i}(\boldsymbol{e}\times\boldsymbol{e}^*)_z\,, \tag{8.89}$$

where $\gamma \equiv \gamma_{zz}$ is a real coefficient. For a wave propagating along the nanotube principal axis z, one has instead of the above equation

$$j_{\mathrm{CPGE},z} = I\gamma P_c\,. \tag{8.90}$$

We remind that the circular photocurrent reverses its direction under inversion of the light circular polarization and vanishes for linearly-polarized excitation.

The consideration of the circular PGE and spin-galvanic effect in QWs in Sects. 8.1 and 8.2 is based on allowance of spin-dependent linear-in-$\boldsymbol{k}$ terms in the electron effective Hamiltonian. In carbon nanotubes the spin-orbit interaction is negligible and the similar role is played by the coupling between n and k_z described by (2.82). Here we take a chiral carbon nanotubes with $\nu = 1$, assume that the tube is n-doped and consider the direct intersubband optical transitions of electrons from the lowest to the first excited conduction subbands. Taking into account the conservation of the angular momentum z-component the allowed transitions are as follows: $(c, n = 0, k_z, K) \to (c, n = 1, k_z, K)$ under σ_+ excitation and $(c, 0, k_z, K) \to (c, -1, k_z, K)$ under σ_- excitation. In accordance with (8.90) they lead to circular photocurrents of opposite polarities.

In a 1D system with parabolic subbands, only two values of k_z satisfy the energy conservation law

$$E(c, 1, k_z^{\pm}, K) - E(c, 0, k_z^{\pm}, K) = \hbar\omega\,. \tag{8.91}$$

Their average value $\bar{k}_z = (k_z^+ + k_z^-)/2$ is nonzero because of the linear-k_z terms. The electron average velocities in the excited and initial subbands coincide and are equal to

$$\bar{v}_z = \frac{m_1\beta_1 - m_0\beta_0}{\hbar(m_1 - m_0)}\,.$$

It follows then that the photoexcited carriers contribute to an electric current before they loose their average velocity because of the momentum relaxation. Under the steady-state optical excitation this mechanism leads to the photocurrent

$$j_{\mathrm{CPGE},z} = eW_{10}\bar{v}_z(\tau_p^{(1)} - \tau_p^{(0)})P_c\,, \tag{8.92}$$

where W_{10} is the probability rate for the intersubband transitions and $\tau_p^{(n)}$ is the momentum scattering time in the n-th subband. We ignore in (8.91) the small frequency region where the terms linear-in-k_z exceed or are comparable with the terms quadratic in k_z. Then one can use the expression [8.42]

$$W_{1,0} = \frac{2\pi}{\hbar}\frac{2\pi e^2 I}{\omega^2 c n_\omega}\frac{1}{32}\left(\frac{\gamma}{\hbar}\frac{k_z}{k_{\perp,0}}\right)^2 f_c^0(E_0)\, g_{10}(\Delta_{10} - \hbar\omega) \tag{8.93}$$

derived for $\beta_n = 0$. Here I is the light intensity in units $energy \cdot length^{-1} \cdot time^{-1}$, $k_{\perp,0}$ is the size-quantized wave vector (2.78) at $n = 0$, the 1D reduced density of states equals to

$$g_{10}(E) = 2 \times \sum_{k_z} \delta(-\frac{\hbar^2 k_z^2}{2\mu_{10}} - E) = \frac{1}{\pi}\left(\frac{2\mu_{10}}{\hbar^2 E}\right)^{1/2} \theta(-E),$$

the factor of two makes allowance for the spin degeneracy, $\theta(x)$ is the step function, $-\mu_{10}^{-1}$ is the inverse reduced effective mass $m_1^{-1} - m_0^{-1}$ [since $m_1 > m_0$, a value of μ_{10} is positive and $g_{10}(E)$ is defined for negative values of E], and $f_c^0(E_0)$ is a value of the equilibrium distribution function at the energy $E_0 = (\hbar^2 k_z^2/2m_0) = (\mu_{10}/m_0)(\Delta_{10} - \hbar\omega) = 2(\Delta_{10} - \hbar\omega)$.

Equation (8.92) gives one of four possible contributions to the circular PGE. Three others are also related to the photoexcitation asymmetry in the k_z space. They arise due to the k_z dependence of the optical matrix element, momentum relaxation time and electron equilibrium distribution function. A sum of all four contributions is given by

$$j_{\mathrm{CPGE}} = eW_{1,0}(l_v + l_m + l_\tau + l_f)\,, \tag{8.94}$$

where the lengths l_v, l_m, l_τ, l_f are related to the photoexcitation asymmetry arising due to the k_z-dependence of the velocity and density of states (l_v), of the squared matrix element (l_m), of the momentum relaxation time (l_τ) and of the equilibrium distribution function (l_f). For the optical transitions under consideration the straightforward derivation results in [8.42]

$$l_v = \frac{3\beta_0}{\hbar}(\tau_p^{(1)} - \tau_p^{(0)})\,,\; l_m = \frac{2\beta_0}{\hbar}(\tau_p^{(1)} - 2\tau_p^{(0)})\,, \tag{8.95}$$

$$l_\tau = \frac{6\beta_0}{\hbar}\left(\tau_p^{(1)}\frac{d\ln\tau_p^{(1)}}{d\ln E_1} - \tau_p^{(0)}\frac{d\ln\tau_p^{(0)}}{d\ln E_0}\right)\,,$$

$$l_f = \frac{3\beta_0}{\hbar}(2\tau_p^{(0)} - \tau_p^{(1)})\frac{\Delta_{10} - \hbar\omega}{k_B T}[1 - f^0(E_0)]\,.$$

Here f^0 is the equilibrium distribution function, we assume that in equilibrium the upper subband $(c, 1, K)$ is unoccupied, and E_0 is the initial energy of an electron photoexcited from the subband $n = 0$. Obviously, the momentum relaxation time $\tau_p^{(1)}$ is shorter than $\tau_p^{(0)}$ because a photoelectron excited

to the subband $(c, n = 1)$ can be readily scattered to the subband $(c, n = 0)$. For crude estimations one can use the equation

$$j_{\mathrm{CPGE},z} = eW_{10}(\beta_0/\hbar)\tau_p P_c \tag{8.96}$$

which is just another form of the estimation (8.12). For the band parameters of carbon nanotubes, $L < 100$ Å and under the saturation of the optical transitions (high-intensity pulsed laser radiation), the photocurrent j_{CPGE} can amount a value of 10^{-9} A. It can be significantly enhanced in recently discovered carbon-nanotube crystals [8.43]. Note that in undoped nanotubes the circular PGE disappears because the contribution to the circular photocurrent due to interband optical transitions from (v, n, K) to $(c, n + 1, K)$ is completely compensated by that due to transitions from $(v, -n - 1, K')$ to $(c, -n, K')$ as a result of a particular charge conjugation symmetry of carbon nanotubes.

We conclude this subsection by comparing the circular photocurrent (8.96) with the photon drag current which is independent of the sign of the circular polarization. In accordance with (8.61) the photon drag effect is estimated as

$$j_{\mathrm{PD}} \sim eW_{1,0}\,\frac{\hbar q}{m_0}\tau_p\,, \tag{8.97}$$

where q is the photon wave vector (in vacuum $q = \omega/c$). Thus, for $\hbar\omega = 0.1$ eV we have $j_{\mathrm{CPGE}}/j_{\mathrm{PD}} \sim \beta_0 m_0/(\hbar^2 q) \approx 3$.

It is worth-while to remind that, in addition to the circular PGE, in noncentrosymmetric media a photocurrent of another kind can be induced by the electro-magnetic wave. It is the linear PGE described in (8.1) by a third-rank tensor $\chi_{\lambda\mu\nu}$ symmetrical with respect to interchange of the indices μ and ν. Ideal carbon nanotubes are unpolar with their principal axis, z, being two-sided which forbids nonzero components $\chi_{z\mu\nu}$. In $\mathrm{B}_x\mathrm{C}_y\mathrm{N}_z$ nanotubes the symmetry is reduced, the principal axis is polar and the linear PGE becomes allowed as predicted in [8.44]. In the next subsection we show that, in the presence of an external magnetic field $\boldsymbol{B} \parallel z$, the photocurrent can be induced by linearly-polarized or unpolarized photoexcitation even in an ideal carbon nanotube.

8.6.2 Magneto-Chiral Currents and Optical Absorption

Other chirality effects allowed in chiral nanotubes are as follows.

(a) *Magneto-chiral photogalvanic* effect described by

$$j_z = IB_z(\Lambda_{\parallel}|e_z|^2 + \Lambda_{\perp}|\boldsymbol{e}_{\perp}|^2)\,. \tag{8.98}$$

It was predicted in [8.1] for bulk gyrotropic crystals and observed first in QW structures [8.45,8.46] (e_z, $\boldsymbol{e}_{\perp}$ are the longitudinal and transverse components of the polarization unit vector $\boldsymbol{e}$, B_z is the external longitudinal magnetic

field). For the interband transitions $(v,0) \to (c,0)$ excited in an undoped carbon nanotube by the linearly polarized light $\boldsymbol{E} \parallel z$, one has the following estimation for the magneto-chiral photocurrent

$$j_z \sim eW_{00}^{cv}\tau_p\nu\frac{\beta}{\hbar}\frac{\Phi}{\Phi_0}\,,$$

where Φ is the magnetic flux, $B_zL^2/4$, passing through the cross section of a tube and Φ_0 is the magnetic flux quantum, ch/e. For $B_z = 10$ T and $L = 100$ Å, the ratio $\Phi/\Phi_0 \approx 2\cdot 10^{-2}$. While deriving the above equation we took into account that, in an external magnetic field, in the expression for the quantized value of k_n one should change n by $n + (\Phi/\Phi_0)$. Then, for $\nu \neq 0$, the band gaps $\Delta(K)$ and $\Delta(K')$ differ and the contributions from the K and K' valleys to the magneto-chiral photocurrent do not compensate each other.

(b) *Magneto-chiral conductivity* described by the second term in the current-field relation

$$j_z = \sigma F_z + \Lambda F_z^2 B_z \tag{8.99}$$

predicted for gyrotropic crystals [8.47] and simple spiral nanotubes [8.48] and observed recently by Rikken et al. in chiral carbon nanotubes [8.49] (F_z is the dc electric field, σ is the conventional conductivity). The magneto-chiral conductivity becomes nonzero if one takes into account that in the case of a chiral carbon nanotube the electron-phonon deformation potential has contributions both even and odd in k_z. For a doped nanotube with the Fermi energy E_F one can obtain [8.42]

$$\frac{\delta j_z}{j_z} = \frac{\Lambda F_z B_z}{\sigma} \sim \sin 3\theta \frac{eF_z\tau_p}{\hbar}\frac{\gamma}{\hbar}\frac{\Phi}{\Phi_0}\,,$$

where the parameter γ is the tight-binding parameter defined in (2.72). For $L = 70$ Å, $B_z = 10\,T$, $F_z\tau_p\gamma/\hbar = 0.01$ V and $E_F = 0.1$ eV we obtain $\delta j_z/j_z \sim 10^{-3}$.

(c) *Natural optical activity* and *circular dichroism*, the latter described by

$$W(\sigma_+) - W(\sigma_-) \propto q_z \tag{8.100}$$

with q_z being the z-component of the light wave vector and $W(\sigma_+), W(\sigma_-)$ being the absorption rates for the σ_+ and σ_- circularly-polarized radiation. For carbon nanotubes, the effects (c) were considered theoretically in the framework of the microscopic tight-binding model by Tasaki et al. [8.50]. Below we present an estimation for the natural dichroism derived for the interband optical transitions taking place in the vicinity of the gap, Δ_{10}^{cv}, between the $(v,1,K)$ valence and $(c,1,K)$ conduction bands

$$D \equiv \frac{W(\sigma_+) - W(\sigma_-)}{W(\sigma_+) + W(\sigma_-)} \sim \frac{\beta q_z}{\hbar\omega - \Delta_{10}^{cv}}\,.$$

The product βq_z can be estimated as 0.1 meV. It is instructive to present here as well an estimation for the magneto-induced dichroism

$$D \sim \frac{\Delta_{10}^{cv}}{\hbar\omega - \Delta_{10}^{cv}} \frac{\Phi}{\Phi_0} \,.$$

(d) *Magneto-chiral absorption* (or *emission*) described by the second term in the equation for the light absorption (emission) probability rate

$$W(B_z) = W^0 + \alpha B_z q_z \tag{8.101}$$

and observed in few chiral media, see [8.51,8.52] and references therein. Note that the first magneto-spatial dispersion effect was reported by Gross et al. [8.53]. The magneto-chiral correction is expected to be more remarkable for optical transitions in the vicinity of the gap Δ_{00}^{cv}. In this case it is given by

$$\frac{\delta W_{00}^{cv}}{W_{00}^{cv}} \equiv \frac{\alpha B_z q_z}{W^0} \sim \frac{\beta q_z \Delta_{00}^{cv}}{(\hbar\omega - \Delta_{00}^{cv})^2} \frac{\Phi}{\Phi_0} \,.$$

It is worth to mention effects which are inverse to the circular and magneto-chiral PGEs. In the absence of magnetic field the dc current in a carbon nanotube should induce the circular dichroism of the optical absorption or the circular polarization of the photoluminescence. Up to now the effect of the electric current on the optical activity has been observed only in bulk gyrotropic tellurium [8.54]. In the presence of an external magnetic field parallel to a nanotube the current j_z should induce a change in the photoluminescence intensity proportional to $j_z B_z$.

9 Conclusion

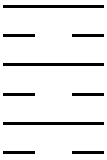

"It is not the end yet!"

Hexagram N 64 of Chinese "Book of Changes"

At the opening and concluding sessions of International Conferences on the Physics of Semiconductors (ICPS) the speakers are traditionally encouraged to describe in broad terms the state and future of semiconductor physics. In his introduction to the 6th ICPS (Exeter, 1962) Sir Nevill Mott predicted the death of semiconductor physics on about a ten year time scale. In the closing address at the 11th ICPS (Warsaw, 1972) J.J. Hopfield reminded those words of Mott. Nevertheless, he also expressed his own doubts in the future of semiconductor physics as a part of the fundamental physics and, among clear promises for continued science, mentioned "systems of lower dimensionality" and "opto-electronics". In fact, the expectations that in the seventies-eighties all fundamental problems would have been solved were rather strong. Surprisingly, the approaching crisis had been resolved in a positive way. It is true, nowadays the interest in investigation of bulk semiconductor crystals is limited. However, they represent only a small area of a big field occupied mainly by semiconductor nanostructures. L.J. Sham openly expressed his optimism in the program summary at the 17th ICPS (San Francisco, 1984) and predicted the continued flourishing of semiconductor physics. More recently, in his welcome address to participants of the 25th ICPS (Osaka, 2000), H. Yoshikawa emphasized that "semiconductor physics is one of the most important research areas of basic physics, and many important discoveries or the creation of new concepts in this area have greatly influenced the other research fields of basic science".

At present the optimism in liveliness of semiconductor physics is founded on the exciting progress in *nanotechnology*. The latter is aimed at the development and use of devices that have a size of only a few nanometers. The top-down and bottom-up approaches to produce nanostructures on a molecular level by a suitable sequence of chemical reactions or lithographic techniques may result in a close and efficient link between physics, chemistry and biology as it took place in physics and chemistry during 30 years after

appearance of the first semiconductor rectifiers and photocells at the end of 1920's.

Now it is widely accepted that basic studies are crucial to expose new ideas and opportunities to fabricate by design the three-dimensional complicated nanoobjects by using atoms, molecules, clusters, nanoparticles, superlattices, quantum wells, wires, dots, rings, nanotubes, nanomagnets etc. as building blocks. Optics can play an important role for the characterization and optimization of such objects provided it retains its freedom and status of fundamental science. For example, the extension of quantum electrodynamics to describe the interaction between N-dimensional ($N = 0, 1, 2, 3$) photons and N'-dimensional ($N' = 0, 1, 2, 3$) excitons has direct implication for the development of lasers based on quantum microcavities. The nanotechnology related to making artificial heterostructures of different dimensionalities needs the basic knowledge on interfaces and their properties. The interface physics seems to be growing out of its infancy. The better understanding in this area can be also achieved in the basic research of optical and transport interface-dependent phenomena, i.e., the phenomena dependent on the character and orientation of chemical bonds at the interface. And one more example: Semiconductor spintronics has reached a stage of understanding various mechanisms of spin injection, accumulation, detection and manipulation, both optical and nonoptical. But the common feeling is that novel conceptual ideas are needed to trigger the realization of effective spin devices.

Appendix. Character Tables of Point Groups

Below we present character tables of some point groups and examples of bases of irreducible representations.

Table A.1. Group C_s. The mirror plane σ_h is perpendicular to the axis x and contains the axes y, z. J_i are components of an axial vector.

	e	σ_h	
A^+	1	1	$y; z; yz; x^2; y^2; z^2; J_x$
A^-	1	-1	$x; xy; xz; J_y; J_z$

Table A.2. Group C_{2v}. The mirror planes σ_v, σ_v' are perpendicular to the axes x and y respectively, the two-fold rotation axis is parallel to z.

	e	C_2	σ_v	σ_v'	
A^+	1	1	1	1	$z; x^2; y^2; z^2$
A^-	1	1	-1	-1	$xy; J_z$
B^+	1	-1	1	-1	$y; yz; J_x$
B^-	1	-1	-1	1	$x; xz; J_y$

Table A.3. Group D_{2d}. The mirror-rotation axis S_4 is parallel to z, the mirror planes σ_d, σ_d' are perpendicular to the axes x and y respectively, the two-fold rotation axes u_2, u_2' are obtained from x, y by the rotation around z by 45°.

	e	C_2	2 S_4	2 u_2	2 σ_d	
A_1	1	1	1	1	1	$z^2; x^2 + y^2$
A_2	1	1	1	-1	-1	J_z
B_1	1	1	-1	1	-1	$x^2 - y^2$
B_2	1	1	-1	-1	1	$z; xy$
E	1	-2	0	0	0	$(x, y); (J_y, J_x); (xz, -yz)$

Table A.4. Group C_{3v}. The three-fold rotation axis is parallel to z, one of the mirror planes σ_v contains the axis x.

	e	$2C_3$	$3\sigma_v$	
A_1	1	1	1	$z; z^2; x^2+y^2$
A_2	1	1	-1	J_z
E	2	-1	0	$(x,y); (2xy, x^2-y^2); (xz,yz); (J_y, -J_x)$

Table A.5. Group T_d. The symmetry operation σ_d is mirror reflection with respect to one of these six planes: (110), (1$\bar{1}$0), (101), ($\bar{1}$01), (011), (01$\bar{1}$); x, y, z are the principal axes [100], [010] and [001], respectively.

	e	$8C_3$	$3C_2$	$6\sigma_d$	$6S_4$	
A_1	1	1	1	1	1	$x^2+y^2+z^2$
A_2	1	1	1	-1	-1	xyz; $\{J_xJ_yJ_z\}_s$
E	2	-1	2	0	0	$\sqrt{3}(x^2-y^2)$, $2z^2-x^2-y^2$
F_1	3	0	-1	-1	1	J_x, J_y, J_z
F_2	3	0	-1	1	-1	$(x,y,z); (yz, zx, xy)$

References

English translations of bibliographic data are given in square brackets.

References of Chapter 1

1.1 L.V. Keldysh: Fis. Tverd. Tela **4**, 2265 (1963).
1.2 L. Esaki, R. Tsu: IBM J. Res. Dev. **14**, 61 (1970).
1.3 R. Merlin, K. Bajema, R. Clarke, F.-Y. Juang, P.K. Bhattacharaya: Phys. Rev. Lett. **55**, 1768 (1985).
1.4 F. Laruelle, B. Etienne, Phys. Rev. **B 37**, 4816 (1988).
1.5 R.F. Kazarinov, R.A. Suris: Fiz. Tekh. Poluprovodn. **5**, 797 (1971) [Sov. Phys. Semicond. **5**, 707 (1971)].
1.6 J. Faist, F. Capasso, D.L. Sivco, C. Sirtori, A.L. Hutchinson, A.Y. Cho: Electron. Lett. **29**, 2230 (1993); Science **264**, 553 (1994).
1.7 R. Nötzel, N.N. Ledentsov, L. Däweritz, M. Hohenstein, K. Ploog: Phys. Rev. Lett. **67**, 3812 (1991).
1.8 E. Kapon, M.C. Tamargo, D.M. Hwang, Appl. Phys. Lett. **50**, 347 (1987).
1.9 X.-L. Wang, V. Valiotis, R. Grousson, M. Ogura: J. Cryst. Growth **213**, 19 (2000).
1.10 X.-L. Wang, M. Ogura, H. Matsuhata: J. Cryst. Growth **195**, 586 (1998).
1.11 Y.C. Chang, L.L. Chang, L. Esaki: Appl. Phys. Lett. **47**, 1324 (1985).
1.12 L. Pfeiffer, H.L. Störmer, K.W. Baldwin, K.W. West, A.R. Goñi, A. Pinczuk, R.C. Ashoori, M.M. Dignam, W. Wegscheider: J. Cryst. Growth **127**, 849 (1993).
1.13 W. Wegscheider, L.N. Pfeiffer, M.M. Dignam, A. Pinczuk, K.W. West, S.L. McCall, R. Hull: Phys. Rev. Lett. **71**, 4071 (1993).
1.14 S. Iijima: Nature (London) **354**, 56 (1991).
1.15 M.S. Dresselhaus, G. Dresselhaus, R. Saito: Phys. Rev. **B 45**, 6234 (1992).
1.16 A.N. Andriotis, M. Menon, D. Srivastava, L. Chernozatonskii: Phys. Rev. **B 65**, 165416 (2002).
1.17 M. Terrones, F. Banhart, N. Grobert, J.-C. Charlier, H. Terrones, P.M. Ajayan: Phys. Rev. Lett. **89**, 75505 (2002).
1.18 D. Bimberg, M. Grundmann, N.N. Ledentsov: *Quantum Dot Heterostructures* (John Wiley & Sons, Chichester 1999).
1.19 D. Leonard, M. Krishnamurthy, C.M. Reaves, S.P. DenBaars, P.M. Petroff: Appl. Phys. Lett. **63**, 3203 (1993).
1.20 N.N. Ledentsov, M. Grundmann, N. Kirstaedter, J. Christen, R. Heitz, J. Böhrer, F. Heinrichsdorff, D. Bimberg, S.S. Ruvimov, P. Werner, U. Richter, U. Gosele, J. Heydenreich, V.M. Ustinov, A.Yu. Egorov, A.E. Zhukov, P.S.

Kop'ev, Zh.I. Alferov: *Proc. 22nd Int'l Conf. Phys. Semicond.*, Vancouver, Canada, 1994, ed. by D.J. Lockwood (World Scientific, Singapore 1995) p. 1955.
1.21 M. Grundmann, J. Christen, N.N. Ledentsov, J. Böhrer, D. Bimberg, S.S. Ruvimov, P. Werner, U. Richter, U. Gösele, J. Heydenreich, V.M. Ustinov, A.Yu. Egorov, A.E. Zhukov, P.S. Kop'ev, Zh.I. Alferov: Phys. Rev. Lett. **74**, 4043 (1995).
1.22 V.A. Shchukin, N.N. Ledentsov, P.S. Kop'ev, D. Bimberg: Phys. Rev. Lett. **75**, 2968 (1995).
1.23 A.I. Ekimov, Al.L. Efros, A.A. Onushcenko: Solid State Commun. **56**, 921 (1985).
1.24 A.I. Ekimov: J. Lumin. **70**, 1 (1996).
1.25 W. Wegscheider, L.N. Pfeiffer, K.W. West: In *Festkörperprobleme/Advances in Solid State Physics*, ed. by R. Helbig (Vieweg, Wiesbaden, 1996) Vol. 35, p. 155.
1.26 M. Grundmann, D. Bimberg: Phys. Rev. **B 55**, 4054 (1997).
1.27 W. Wegscheider, G. Schedelbeck, G. Abstreiter, M. Rother, M. Bichler: Phys. Rev. Lett. **79**, 1917 (1997).

References of Chapter 2

2.1 D.J. BenDaniel, C.B. Duke: Phys. Rev. **152**, 683 (1966).
2.2 G. Bastard: Phys. Rev. **B 24**, 5693 (1981).
2.3 W.A. Harrison: Phys. Rev. **123**, 85 (1961).
2.4 R.A. Morrow, K.R. Brownstein: Phys. Rev. **B 30**, 678 (1984).
2.5 T. Ando, S. Wakahara, H. Akera: Phys. Rev. **B 40**, 11609 (1989).
2.6 N.F. Gashimzade, E.L. Ivchenko: Fiz. Tekhn. Poluprovodn. **25**, 323 (1991) [Sov. Phys. Semicond. **25**, 195 (1991)].
2.7 B.A. Foreman: Phys. Rev. **B 54**, 1909 (1996).
2.8 J.M. Luttinger, Phys. Rev. **102**, 1030 (1956).
2.9 S.S. Nedorezov: Fiz. Tverd. Tela **12**, 2269 (1970) [Sov. Phys. Solid State **12**, 1814 (1971)].
2.10 M. Altarelli, U. Ekenberg, A. Fasolino: Phys. Rev. **B 32**, 5138 (1985).
2.11 D.A. Broido, L.J. Sham: Phys. Rev. **B 31**, 888 (1985).
2.12 T. Uenoyama, L.J. Sham: Phys. Rev. **B 42**, 7114 (1990).
2.13 I.A. Merkulov, V.I. Perel, M.E. Portnoi: Zh. Eksp. Teor. Fiz. **99**, 1202 (1991) [Sov. Phys. JETP **72**, 669 (1991)].
2.14 R. Ferreira, G. Bastard: Phys. Rev. **B 43**, 9687 (1991).
2.15 L.E. Vorobjev, D.V. Donetskii, L.E. Golub: Pis'ma Zh. Eksp. Teor. Fiz. **63**, 928 (1996) [JETP Lett. **63**, 5138 (1996)].
2.16 I.L. Aleiner, E.L. Ivchenko: Pis'ma Zh. Eksp. Teor. Fiz. **55**, 662 (1992) [JETP Lett. **55**, 692 (1992)].
2.17 E.L. Ivchenko, A.Yu. Kaminski, I.L. Aleiner: Zh. Eksp. Teor. Fiz. **104**, 3401 (1993) [JETP **77**, 609 (1993).
2.18 E.L. Ivchenko, A.Yu. Kaminski, U. Rössler: Phys. Rev. **B 54**, 5852 (1996).
2.19 Y.-C. Chang, J. N. Schulman: Appl. Phys. Lett **43**, 536 (1983); Phys. Rev. **B 31**, 2069 (1985).
2.20 M.S. Kiledjian, J.N. Schulman, K.L. Wang, K.V. Rousseur: Surf. Sci. **267**, 405 (1992).

2.21 G. Edwards, J.C. Inkson: Solid State Commun. **89**, 595 (1994).
2.22 O. Krebs, P. Voisin: Phys. Rev. Lett. **77**, 1829 (1996).
2.23 V.A. Volkov, E.E. Takhtamirov: Uspekhi Fiz. Nauk **167**, 1123 (1997) [Physics-Uspekhi **40**, N 10 (1997)].
2.24 B.A. Foreman: Phys. Rev. Lett. **81**, 425 (1998).
2.25 G.F. Glinskii, K.O. Kravchenko: Fiz. Tverd. Tela **40**, 872 (1998) [Phys. Solid State **40**, 803 (1998)].
2.26 R. Magri, A. Zunger: Phys. Rev. **B 62**, 10364 (2000).
2.27 J.M. Luttinger, W. Kohn: Phys. Rev. **97**, 869 (1955).
2.28 G. Edwards, E.C. Valadares, F.W. Sheard: Phys. Rev. **B 50**, 8493 (1994).
2.29 E.O. Kane: J. Phys. Chem. Solids **1**, 249 (1957).
2.30 C.R. Pidgeon, R.N. Brown: Phys. Rev. **146**, 575 (1966).
2.31 H.-R. Trebin, U. Rössler, R. Ranvaud: Phys. Rev. **B 20**, 686 (1979).
2.32 R. Winkler, A.I. Nesvizhskii: Phys. Rev. **B 53**, 9984 (1996).
2.33 U. Rössler: Solid State Commun. **49**, 943 (1984).
2.34 M.E. Flatte, P.M. Young, L.-H. Peng, H. Ehrenreich: Phys. Rev. **B 53**, 1963 (1996).
2.35 A.E. Botha, M. R. Singh: Phys. Rev. **B 67**, 195334 (2003).
2.36 R.A. Suris: Fiz. Tekhn. Poluprovodn. **20**, 2008 (1986) [Sov. Phys. Semicond. **20**, 1258 (1986)].
2.37 M.V. Kisin, B.L. Gelmont, S. Luryi: Phys. Rev. **B 58**, 4605 (1998).
2.38 A.V. Rodina, A.Yu. Alekseev, Al.L. Efros, M. Rosen, B.K. Meyer: Phys. Rev. **B 65**, 125302 (2002).
2.39 A.A. Kiselev, E.L. Ivchenko, U. Rössler: Phys. Rev. **B 58**, 16353 (1998).
2.40 A.A. Kiselev, U. Rössler: Phys. Rev. **B 50**, 14283 (1994).
2.41 R. Rinaldi, R. Cingolani, M. Lepore, M. Ferrara, I.M. Catalano, F. Rossi, L. Rota, E. Molinari, P. Lugli, U. Marti, D. Martin, F. Morier-Gemoud, P. Ruterana, F.K. Reinhart: Phys. Rev. Lett. **73**, 2899 (1994).
2.42 A.A. Kiselev, U. Rössler: Semicond. Sci. Technol. **11**, 203 (1996).
2.43 W. Langbein, H. Gislason, J.M. Hvam: Phys. Rev. **B 54**, 14595 (1996).
2.44 E.L. Ivchenko, A.A. Kiselev: Pis'ma Zh. Eksp. Teor. Fiz. **58**, 31 (1993) [JETP Lett. **58**, 32 (1993)].
2.45 Ch. Gréus, L. Butov, F. Daiminger, A. Forchel, P.A. Knipp, T.L. Reinecke: Phys. Rev. **B 47**, 7626 (1993).
2.46 G. Bastard, J.Y. Marzin: Solid State Commun. **91**, 39 (1994).
2.47 Y.-K. Lin, Y.-N. Chen, D.-S. Chuu: Phys. Rev. **B 64**, 193316 (2001).
2.48 A. Jorio, R. Saito, C.M. Lieber, M. Hunter, T. McClure, G. Dresselhaus, M.S. Dresselhaus: Phys. Rev. Lett **86**, 1118 (2001).
2.49 P.R. Wallace: Phys. Rev. **71**, 622 (1947).
2.50 R. Saito, M. Fujita, G. Dresselhaus, M.S. Dresselhaus: Phys. Rev. **B 46**, 1804 (1992).
2.51 H. Ajiki, T. Ando: J. Phys. Soc. Jpn **62**, 1255 (1993); *ibid.* **62**, 2470 (1993); *ibid.* **64**, 4382 (1995).
2.52 H. Ajiki, T. Ando: Physica **B 201**, 349 (1994).
2.53 H. Ajiki, T. Ando: J. Phys. Soc. Jpn **65**, 505 (1996).
2.54 E.L. Ivchenko, B. Spivak: Phys. Rev. **B 66**, 155404 (2002); Physica **E 17**, 376 (2003).
2.55 C.L. Kane, E.J. Mele: Phys. Rev. Lett **78**, 1932 (1997).
2.56 S. Reich, J. Maultzsch, C. Thomsen, P. Ordejón: Phys. Rev. **B 66**, 35412 (2002).

2.57 S.B. Fagan, R.J. Baierle, R. Mota, A.J.R. da Silva, A. Fazzio: Phys. Rev. **B 61**, 9994 (2000).
2.58 D. Bimberg, M. Grundmann, N.N. Ledentsov: *Quantum Dot Heterostructures* (Wiley & Sons Ltd, Chichester, 1999).
2.59 P.C. Sercel, K.J. Vahala: Phys. Rev. **B 42**, 3690 (1990).
2.60 J.-Y. Marzin, G. Bastard: Solid State Commun. **92**, 437 (1994).
2.61 M. Grundmann, O. Stier, D. Bimberg: Phys. Rev. **B 52**, 11969 (1995).
2.62 O. Stier, M. Grundmann, D. Bimberg: Phys. Rev. **B 59**, 5688 (1999).
2.63 F.M. Peeters, V.A. Schweigert: Phys. Rev. **B 53**, 1468 (1996).
2.64 O. Voskoboynikov, C.P. Lee, O. Tretyak: Physica **E 10**, 107 (2001).
2.65 A. Wojs, P. Hawrylak, S. Fafard, L. Jacak: Phys. Rev. **B 54**, 5604 (1996).
2.66 F.B. Pederson, Y.-C. Chang: Phys. Rev. **B 53**, 1507 (1996).
2.67 Al.L. Efros, M. Rosen, M. Kuno, M. Nirmal, D.J. Norris, M.G. Bawendi: Phys. Rev. **B 54**, 4843 (1996).
2.68 S.V. Goupalov, E.L. Ivchenko: J. Crystal Growth **184/185**, 393 (1998).
2.69 S.V. Goupalov, E.L. Ivchenko: Fiz. Tverd. Tela **42**, 1976 (2000) [Phys. Sol. St. **42**, 2030 (2000)].
2.70 F.M. Peeters: Phys. Rev. **B 42**, 1486 (1990).
2.71 V. Fock: Z. Phys. **47**, 446 (1928).
2.72 C.G. Darwin: Proc. Cambridge Philos. Soc. **27**, 86 (1930).
2.73 P.W. Fry, I.E. Itskevich, D.J. Mowbray, M.S. Skolnick, J.J. Finley, J.A. Barker, E.P. O'Reilly, L.R. Wilson, I.A. Larkin, P.A. Maksym, M. Hopkinson, M. Al-Khafaji, J.P.R. David, A.G. Cullis, G. Hill, J.C. Clark: Phys. Rev. Lett. **84**, 733 (2000).
2.74 W. Sheng, J.-P. Leburton: Phys. Rev. **B 63**, 161301 (2001); Physica **E 17**, 50 (2003).
2.75 A.J. Williamson, L.W.Wang, A. Zunger: Phys. Rev. **B 62**, 12963 (2000).
2.76 J. Shumway, A.J. Williamson, A. Zunger, A. Passaseo, M. DeGiorgi, R. Cingolani, M. Catalano, P. Crozier: Phys. Rev. **B 64**, 125302 (2001).
2.77 A.D. Andreev, E.P. O'Reilly: Phys. Rev. **B 62**, 15851 (2000).
2.78 T. Saito, Y. Arakawa: Physica **E 15**, 169 (2002).
2.79 G. Dresselhaus: Phys. Rev. **100**, 580 (1955).
2.80 M.I. D'yakonov, V.Yu. Kachorovskii: Fiz. Tekhn. Poluprov. **20**, 178 (1986) [Sov. Phys. Semicond. **20**, 110 (1986)].
2.81 W. Knap, C. Skierbiszewski, A. Zduniak, E. Litwin-Staszewska, D. Bertho, F. Kobbi, J.L. Robert, G.E. Pikus, F.G. Pikus, S.V. Iordanskii, V. Mosser, K. Zekentes, Yu.B. Lyanda-Geller: Phys. Rev. **B 53**, 3912 (1996).
2.82 E.I. Rashba, V.I. Sheka: Fiz. Tverd. Tela, Collected Papers, Vol. 2, 162 (1959).
2.83 E.I. Rashba: Fiz. Tverd. Tela **2**, 1224 (1960) [Sov. Phys. Solid State **2**, 1109 (1960)].
2.84 F.G. Ohkawa, Y. Uemura: J. Phys. Soc. Jpn **37**, 1325 (1974).
2.85 F.T. Vas'ko: Pis'ma Zh. Eksp. Teor. Fiz. **30**, 574 (1979) [JETP Lett. **30**, 541 (1979)].
2.86 Yu.A. Bychkov, E.I. Rashba: Pis'ma Zh. Eksp. Teor. Fiz. **9**, 66 (1984) [JETP Lett. **39**, 78 (1984)].
2.87 B. Das, S. Datta, R. Reifenberger: Phys. Rev. **B 41** 8278 (1989).
2.88 E.A. de Andrada e Silva, G.C. Rocca, F. Bassani: Phys. Rev. **B 55**, 16293 (1997).
2.89 L. Wissinger, U. Rössler, R. Winkler, B. Jusserand, D. Richards: Phys. Rev. **B 58**, 15375 (1998).

2.90 P. Pfeffer, W. Zawadzki: Phys. Rev. **B 59**, 5312 (1999).
2.91 N.S. Averkiev, L.E. Golub, M. Willander: Fiz. Tekhn. Poluprov. **36**, 97 (2002) [Semiconducotrs **36**, 91 (2002)].
2.92 L. Vervoort, R. Ferreira, P. Voisin: Phys. Rev. **B 56**, 12744 (1997).
2.93 U. Rössler, J. Kainz: Solid State Commun. **121**, 313 (2002).
2.94 S.D. Ganichev, V.V. Bel'kov, L.E. Golub, E.L. Ivchenko, Petra Schneider, S. Giglberger, J. Eroms, J. DeBoeck, G. Borghs, W. Wegscheider, D. Weiss, W. Prettl: cond-mat/0306521.
2.95 R. Winkler: Phys. Rev. **B 62**, 4245 (2000).
2.96 M.V. Entin, L.I. Magarill: Phys. Rev. **B 64**, 85330 (2001).
2.97 E.A. de Andrada e Silva, G.C. La Rocca: Phys. Rev. **B 67**, 165318 (2003).
2.98 E.P. Pokatilov, S.I. Beril: phys. stat. sol. (b) **118**, 567 (1984).
2.99 B. Jusserand, M. Cardona: In *Light Scattering in Solids V*, ed. by M. Cardona, G. Güntherodt, Topics Appl. Phys., Vol. 66 (Springer, Berlin, Heidelberg, 1989) Chap.3.
2.100 R. Fuchs, K.L. Kliewer: Phys. Rev. **A 140**, 2076 (1965).
2.101 S.M. Rytov: Akust. Zh. **2**, 71 (1956) [Sov. Phys. - Acoust. **2**, 68 (1956)].
2.102 J.I. Frenkel: Phys. Rev. **37**, 17, 1276 (1931).
2.103 Excitons, eds. E.I. Rashba and M.D. Sturge (North-Holland, Amsterdam, 1982).
2.104 G.H. Wannier: Phys. Rev. **52**, 191 (1937).
2.105 N.F. Mott: Trans. Faraday Soc. **34**, 500 (1938).
2.106 R.L. Greene, K.K. Bajaj: Solid State Commun. **45**, 831 (1983).
2.107 B. Zhu, K. Huang: Phys. Rev. **B 36**, 8102 (1987).
2.108 B. Zhu: Phys. Rev. **B 37**, 4689 (1988).
2.109 E.L. Ivchenko, A.V. Kavokin, V.P. Kochereshko, G.R. Pozina, I.N. Uraltsev, D.R. Yakovlev, R.N. Bicknell-Tassius, A. Waag, G. Landwehr: Phys. Rev. **B 46**, 7713 (1992).
2.110 T. Fukuzawa, E.E. Mendez, J.M. Hong: Phys. Rev. Lett. **64**, 3066 (1990).
2.111 L.V. Butov, A.L. Ivanov, A. Imamoglu, P.B. Littlewood, A.A. Shashkin, V.T. Dolgopolov, K.L. Campman, A.C. Gossard: Phys. Rev. Lett. **86**, 5608 (2001).
2.112 A.V. Larionov, V.B. Timofeev, J.M. Hvam, K. Soerensen: Pis'ma Zh. Eksp. Teor. Fiz. ... (2002) [JETP Lett. **75**, 200 (2002)].
2.113 D. Scalbert, J. Cernogora, C. Benoit à la Guillaume, M. Maaref, F.F. Charfi, R. Planel: Solid State Commun. **70**, 945 (1989).
2.114 V. Voliotis, R. Grousson, P. Lavallard, E.L. Ivchenko, A.A. Kiselev, R. Planel: Phys. Rev. **B 49**, 2576 (1994).
2.115 T. Ando, H. Akera: Phys. Rev. **B 40**, 11619 (1989).
2.116 I.L. Aleiner, E.L. Ivchenko: Fiz. Tekh. Poluprovodn. **27**, 594 (1993) [Semiconductors **27**, 498 (1993)].
2.117 Y. Fu, M. Willander, E.L. Ivchenko, A.A. Kiselev: Phys. Rev. **B 47**, 13498 (1993).
2.118 C. Gourdon, D. Martins, P. Lavallard, E.L. Ivchenko, Yun-Lin Zheng, R. Planel: Phys. Rev. **B 62**, 16856 (2000).
2.119 J.W. Brown, H.N. Spector: Phys. Rev. **B 35**, 3009 (1987).
2.120 M.H. Degani, O. Hipólito: Phys. Rev. **B 35**, 93451 (1987).
2.121 R. Loudon: Am. J. Phys. **44**, 1064 (1976).
2.122 M.A. Lampert: Phys. Rev. Lett. **1**, 450 (1958).
2.123 D.A. Kleinman: Phys. Rev. **B 28**, 871 (1983).

2.124 R.C. Miller, D.A. Kleinman, A.C. Gossard, O. Munteanu: Phys. Rev. **B 25**, 6545 (1982).
2.125 L. Bányai, I. Galbraith, C. Ell, H. Haug: Phys. Rev. **B 36**, 6099 (1987).
2.126 T. Takagahara: Phys. Rev. B **39**, 10206 (1989).
2.127 M. Bayer, T. Gutbrod, A. Forchel, V.D. Kulakovskii, A. Gorbunov, M. Michel, R. Steffen, K.H. Wang: Phys. Rev. **B 56**, 2109 (1997).
2.128 T. Shimura, M. Matsuura: Phys. Rev. **B 58**, 4740 (1998).
2.129 K. Kheng, R.T. Cox, Y. Merle d'Aubigné, F. Bassani, K. Saminadayar, S. Tatarenko: Phys. Rev. Lett. **71**, 1752 (1993).
2.130 P. Kossacki: J. Phys.: Condens. Matter **15**, 471 (2003).
2.131 B. Stébé, A. Ainane: Superlatt. Microstruct. **5**, 545 (1989).
2.132 B. Stébé, G. Munschy, L. Stauffer, F. Dujardin, J. Murat: Phys. Rev. **B 56**, 12454 (1997).
2.133 R.A. Sergeev, R.A. Suris: Fiz. Tverd. Tela **43**, 714 (2001) [Phys. Solis State **43**, 476 (2001)].
2.134 A. Thilagam: Phys. Rev. **B 55**, 7804 (1996).
2.135 R.A. Sergeev, R.A. Suris: phys. stat. sol. (b) **227**, 387 (2001).
2.136 B. Szafran, B. Stébé, J. Adamowski, S. Bednarek: Phys. Rev. **B 66**, 165331 (2002).

References of Chapter 3

3.1 *Excitons*, eds.: E.I. Rashba, M.D. Sturge (North-Holland, Amsterdam, 1982).
3.2 E.L. Ivchenko, V.A. Kosobukin: Fiz. Tekhn. Poluprovodn. **22**, 24 (1988) [Sov. Phys. Semicond. **22**, 15 (1988)].
3.3 E.L. Ivchenko, V.P. Kochereshko, P.S. Kop'ev, V.A. Kosobukin, I.N. Uraltsev, D.R. Yakovlev: Solid State Commun. **70**, 529 (1989).
3.4 L.C. Andreani, F. Tassone, F. Bassani: Solid State Commun. **77**, 641 (1991).
3.5 E.L. Ivchenko: Fiz. Tverd. Tela **33**, 2388 (1991) [Sov. Phys. Solid State **33**, 1344 (1991)].
3.6 E.L. Ivchenko, A.V. Kavokin, V.P. Kochereshko, G.R. Pozina, I.N. Uraltsev, D.R. Yakovlev, R.N. Bicknell-Tassius, A. Waag, G. Landwehr: Phys. Rev. **B 46**, 7713 (1992).
3.7 V.A. Kosobukin: Fiz. Tverd. Tela **34**, 3107 (1992) [Sov. Phys. Solid State **34**, 1662 (1992)].
3.8 D.S. Citrin: Solid State Commun. **89**, 139 (1994).
3.9 L.C. Andreani: Phys. Lett. **A 192**, 99 (1994); Phys. Stat. Solidi (b) **188**, 29 (1995).
3.10 E.L. Ivchenko, A.I. Nesvizhskii, S. Jorda: Fiz. Tverd. Tela **36**, 2118 (1994) [Sov. Phys. Solid State **36**, 1156 (1994)].
3.11 V.P. Kochereshko, G.R. Pozina, E.L. Ivchenko, D.R. Yakovlev, A. Waag, W. Ossau, G. Landwehr, R. Hellmann, E.O. Göbel: *Proc. 22nd Int'l Conf. Phys. Semicond.*, Vancouver, Canada (1994), ed. by D.J. Lockwood (World Scientific, Singapore 1995) p. 1372; Superlatt. Microstruct. **15**, 471 (1994).
3.12 Y. Merle d'Aubigné, A. Wasiela, H. Mariette, T. Dietl: Phys. Rev. **B 54**, 14003 (1996).
3.13 V.A. Kosobukin, M.M. Moiseeva: Fiz. Tverd. Tela **37**, 3694 (1995) [Phys. Solid State **37**, 2036 (1995).

3.14 T. Stroucken, A. Knorr, P. Thomas, S.W. Koch: Phys. Rev. **B 53**, 2026 (1996).
3.15 Y. Boucher, Transfer matrix of a Dirac-like singularity of the dielectric permittivity, IEEE J. Quant. Electron. **33**, 265 (1997).
3.16 J.P. Prineas, C. Ell, E.S. Lee, G. Khitrova, H.M. Gibbs, S.W. Koch: Phys. Rev. **B 61**, 13863 (2000).
3.17 G.V. Astakhov, D.R. Yakovlev, V.P. Kochereshko, W. Ossau, J. Nürnberger, W. Fashinger, G. Landwehr: Phys. Rev. **B 60**, 8485 (1999).
3.18 G.V. Astakhov, V.P. Kochereshko, D.R. Yakovlev, W. Ossau, J. Nürnberger, W. Fashinger, G. Landwehr: Phys. Rev. **B 62**, 10345 (2000).
3.19 E.L. Ivchenko, P.S. Kop'ev, V.P. Kochereshko, I.N. Uraltsev, D.R. Yakovlev, S.V. Ivanov, B.Ya. Mel'tser, M.I. Kaliteevskii, Fiz. Tekhn. Poluprovodn. **22**, 784 (1988) [Sov. Phys. Semicond. **22**, 495 (1988)].
3.20 E.L. Ivchenko, V.P. Kochereshko, A.V. Platonov, D.R. Yakovlev, A. Waag, W. Ossau, G. Landwehr: Fiz. Tverd. Tela **39**, 2072 (1997) [Phys. Solid State **39**, 1852 (1997)].
3.21 E.L. Ivchenko, A.V. Kavokin: Fiz. Tekh. Poluprovodn. **25**, 1780 (1991) [Sov. Phys. - Semicond. **25**, 1070 (1991)].
3.22 E.L. Ivchenko, V.P. Kochereshko, I.N. Uraltsev: In *Semiconductors and Insulators: Optical and Spectroscopic Research*, ed. by Yu.I. Koptev, Ioffe Physicotechnical Institute Research Series, Vol. 12 (Nova Science, New York, 1992), p. 21.
3.23 E.L. Ivchenko, M. Willander: phys. status solidi (b) **215**, 199 (1999).
3.24 L.I. Deych, A.A. Lisyansky: Phys. Rev. **B 62**, 4242 (2000).
3.25 A. Kozhekin, G. Kurizki: Phys. Rev. Lett. **74**, 5020 (1995).
3.26 A. Kozhekin, G. Kurizki, B. Malomed: Phys. Rev. Lett. **81**, 3647 (1998).
3.27 I.H. Deutsch, R.J.C. Spreeuw, S.L. Rolston, W.D. Phillips: Phys. Rev. **A** 52, 1394 (1995).
3.28 M.R. Vladimirova, E.L. Ivchenko, A.V. Kavokin: Fiz. Tekh. Poluprovodn. **32**, 101 (1998) [Semiconductors **32**, 90 (1998)].
3.29 J. Sadowski, H. Mariette, A. Wasiela, R. André, Y. Merle d'Aubigné, T. Dietl: Phys. Rev. **B 56**, 1664 (1997).
3.30 J. Sadowski, H. Mariette, A. Wasiela, Y. Merle d'Aubigné, T. Dietl: J. Cryst. Growth **184/185**, 768 (1998).
3.31 S. Haas, T. Stroucken, M. Hübner, J. Kuhl, B. Grote, A. Knorr, F. Jahnke, S.W. Koch, R. Hey, K. Ploog: Phys. Rev. B **57**, 14860 (1998).
3.32 C. Ell, J. Prineas, T.R. Nelson, Jr., S. Park, H.M. Gibbs, G. Khitrova, S.W. Koch: Phys. Rev. Lett. **80**, 4795 (1998).
3.33 G.R. Hayes, J.L. Staehli, U. Oesterle, B. Deveaud, R.T. Phillips, C. Ciuti: Phys. Rev. Lett. **83**, 2837 (1999).
3.34 S. Nojima: Phys. Rev. **B 47**, 13535 (1993).
3.35 M.S. Belousov, V.L. Berkovits, A.O. Gusev, E.L. Ivchenko, P.S. Kop'ev, N.N. Ledentsov, A.I. Nesvizhskii: Fiz. Tverd. Tela **36**, 1098 (1994) [Sov.Phys. Solid State **36**, 596 (1994)].
3.36 G. Armelles, P. Castrillo, P.S. Dominguez, L. González, A. Ruíz, D.A. Contreras-Solorio, V.R.Velasco, F. Garsía-Moliner: Phys. Rev. **B 49**, 14020 (1994).
3.37 M.S. Belousov, E.L. Ivchenko, A.I. Nesvizhskii: Fiz. Tverd. Tela **37**, 1408 (1995) [Sov.Phys. Solid State **37**, 763 (1995)].
3.38 D. Gershoni, I. Brener, G.A. Baraff, S.N.G. Chu, L.N. Pfeiffer, K. West: Phys. Rev. **B 44**, 1930 (1991).

3.39 G. Armelles, P. Castrillo, J.A. Prieto, L. González, P.S. Dominguez, V.R.Velasco, D.A. Contreras-Solorio: *Proc. 22nd Int. Conf. Phys. Semicond.*, Vancouver, Canada, 1994, ed. by D.J. Lockwood (World Scientific, Singapore 1995), p. 1143.
3.40 R. Winkler, A.I. Nesvizhskii: Phys. Rev. **B 53**, 9984 (1996).
3.41 M. Nagelstrasser, H. Dröge, F. Fisher, T. Litz, A. Waag, G. Landwehr, H.-P. Steinrück: J. Appl. Phys. **83**, 4253 (1998).
3.42 O. Krebs, P. Voisin: Phys. Rev. Lett. **77**, 1829 (1996).
3.43 O. Krebs, W. Seidel, P. Voisin: Inst. Phys. Conf. Ser. No. 155: Chap. 12, *Proc. 23rd Int'l Symp. Compound Semiconductors* (St. Petersburg, Russia, 1996), ed. by M. S. Shur and R. A. Suris (1997), p. 859.
3.44 O. Krebs, W. Seidel, J. P. André, D. Bertho, C. Jouanin, P. Voisin: Semicond. Sci. Technol. **12**, 938 (1997).
3.45 E.L. Ivchenko, A.A. Toropov, P. Voisin: Fiz. Tverd. Tela **40**, 1925 (1998) [Phys. Solis State **40**, 1748 (1998)].
3.46 *Photonic Band Gaps and Localization*, ed. by C.M. Soukoulis, Proc. NATO, Adv. Sci. Inst. Series (Plenum, New York, 1993).
3.47 *Photonic Band Gaps Materials*, NATO Adv. Study Institute, Series E: Applied Sciences, ed. by C.M. Soukoulis, (Kluwer, Dordrecht, 1996), Vol. 315.
3.48 D.V. van Coevorden, R. Sprik, A. Tip, A. Lagendijk: Phys. Rev. Lett. **77**, 2412 (1996).
3.49 Yu.A. Vlasov, V.N, Astratov, O.Z. Karimov, A.A. Kaplyanskii, V.N. Bogomolov, A.V. Prokofiev: Phys. Rev. **B 55**, 13357 (1997).
3.50 Yu.A. Vlasov, Nan Yao, D.J. Norris: Adv. Mater. **11**, 165 (1999).
3.51 E.L. Ivchenko, A.V. Kavokin: Fiz. Tverd. tela **34**, 1815 (1992) [Sov.Phys. Solid State **34**, 968 (1992)].
3.52 F. Thiele, Ch. Fuchs, R. von Baltz: Phys. Rev. **B 64**, 205309 (2001).
3.53 E.L. Ivchenko, Y. Fu, M. Willander: Fiz. Tverd. Tela **42**, 1707 (2000) [Phys. Solid State **42**, 1756 (2000)].
3.54 G.Ya. Slepyan, S.A. Maksimenko, V.P. Kalosha, A. Hoffmann, D. Bimberg: Phys. Rev. **B 64**, 125326 (2001).
3.55 Yu. Kagan, A.M. Afanas'ev, I.P. Pertsev: Zh. Eksp. Teor. Fiz. **54**, 1530 (1968) [Sov. Phys. - JETP **27**, 819 (1969)].
3.56 A.I. Chumakov, G.V. Smirnov, A.Q.R. Baron, J. Arthur, D.E. Brown, S.L. Ruby, G.S. Brown, N.N. Salashchenko: Phys. Rev. Lett. **71**, 2489 (1993).
3.57 M.M. Sigalas, C.M. Soukoulis, C.T. Chan, K.M. Ho: Phys. Rev. **B 49**, 11080 (1994).
3.58 M.M. Voronov, E.L. Ivchenko: Fiz. Tverd. Tela **45**, 168 (2003) [Phys. Solid State **45**, 176 (2003)].
3.59 E.E. Mendez, F. Agullo-Rueda: J. Lumin. **44**, 223 (1989).
3.60 G.H. Wannier: Phys. Rev. **B 117**, 432 (1960).
3.61 J. Bleuse, G. Bastard, P. Voisin: Phys. Rev. Lett. **60**, 220 (1988).
3.62 E.E. Mendez, F. Agulló-Rueda, J.M. Hong: Phys. Rev. Lett. **60**, 2426 (1988).
3.63 V.G. Lyssenko, G. Valušis, F. Löser, T. Hasche, K. Leo, M.M. Dignam, K. Köhler: Phys. Rev. Lett. **79**, 301 (1997).
3.64 F. Agulló-Rueda, E.E. Mendez, H. Ohno, J.M. Hong: Phys. Rev. **B 42**, 1470 (1990).
3.65 S.V. Ivanov, P.S. Kop'ev, T.V. Shubina, A.A. Toropov,: Semicond. Sci. Technol. **8**, 357 (1993).

3.66 S.M. Cao, M. Willander, E.L. Ivchenko, A.I. Nesvizhskii, A.A. Toropov: Superlatt. Microstruct. **17**, 97 (1995).
3.67 S.M. Cao, M. Willander, A.A. Toropov, T.V. Shubina, B.Ya. Mel'tser, S.V. Shaposhnikov, P.S. Kop'ev, P.O. Holtz, J.P. Bergman, B. Monemar: Phys. Rev. **B 51**, 17267 (1995).
3.68 S.H. Kwok, H.T. Grahn, K. Ploog, R. Merlin: Phys. Rev. Lett. **69**, 973 (1992).
3.69 A.A. Toropov, E.L. Ivchenko, O. Krebs, S. Cortez, P. Voisin, J.L. Gentner: Phys. Rev. **B 63**, 35302 (2000). (1992).
3.70 R. Winkler: Phys. Rev. **B 51** 14395 (1995).
3.71 D.C. Reynolds, K.K. Bajaj, C. Leak, G. Peters, W. Theis, P.W. Yu, K. Alavi, C. Colvard, I. Shidlovsky: Phys. Rev. **B 37**, 3117 (1988); W.M. Theis, G. D. Sanders, C. E. Leak, D. C. Reynolds, Y.-C. Chang, K. Alavi, C. Colvard, I. Shidlovsky: Phys. Rev. **B 39**, 1442 (1989).
3.72 B. Zhu, K. Huang: Phys. Rev. B **36**, 8102 (1987); B. Zhu: Phys. Rev. **B 37** 4689 (1988).
3.73 H. Chu, Y.-C. Chang: Phys. Rev. **B 39**, 10861 (1989).
3.74 R.C. Miller, A.C. Gossard, G.D. Sanders, Y.-C. Chang, J. N. Schulman: Phys. Rev. **B 32**, 8452 (1985).
3.75 Y.-C. Chang, J. N. Schulman: Appl. Phys. Lett **43**, 536 (1983); Phys. Rev. **B 31**, 2069 (1985).
3.76 J. N. Schulman, Y.-C. Chang: Phys. Rev. **B 31**, 2056 (1985).
3.77 O. Krebs, D. Rondi, J.L. Gentner, L. Goldstein, P. Voisin: Phys. Rev. Lett **80**, 5770 (1998).
3.78 R.P. Seisyan, B.P. Zakharchenya: In *Landau Level Spectroscopy*, ed. by G. Landwehr and E.I. Rashba (North-Holland, Amsterdam, 1991) Vol. 1, p. 345.
3.79 S. Tarucha, H. Okamoto, Y. Twasa, N. Miura: Solid. State Commun. **52**, 815 (1984).
3.80 I.V. Lerner, Yu.E. Lozovik: Zh. Eksp. Teor. Fiz. **78**, 1167 (1980) [Sov. Phys. JETP **51**, 588 (1980)].
3.81 A.V. Kavokin, A.I. Nesvizhskii, R.P. Seisyan: Fiz. Tekh. Poluprovodn. **27**, 977 (1993) [Semiconductors **27**, 530 (1993)].
3.82 S.-R.E. Yang, L.J. Sham: Phys. Rev. Lett. **58**, 2598 (1987).
3.83 G.E.W. Bauer, T. Ando: Phys. Rev. **B 37**, 3130 (1988).
3.84 W. Edelstein, H.N. Spector, R. Marasa: Phys. Rev. **B 39**, 7697 (1989).
3.85 J. Puls, V.V. Rossin, F. Henneberger, R. Zimmermann: Phys. Rev. **B 54**, 4974 (1996).
3.86 H. Chu, Y.-C. Chang: Phys. Rev. **B 40**, 5497 (1989).
3.87 E.L. Ivchenko, A.V. Kavokin, V.P. Kochereshko, G.R. Pozina, I.N. Uraltsev, D.R. Yakovlev, R.N. Bicknell-Tassius, A. Waag, G. Landwehr: Phys. Rev. **B** 46, 7713 (1992).
3.88 C. Gourdon, G. Lazard, V. Jeudy, C. Testelin, E.L. Ivchenko, G. Karczewski: Solid State Commun. **123**, 299 (2002).
3.89 C. Gourdon, V. Jeudy, M. Menant, D. Rodichev, Le Anh Tu, E.L. Ivchenko, G. Karczewski: Appl. Phys. Lett. **82**, 230 (2003).

References of Chapter 4

4.1 T. Ando, A.B. Fowler, F. Stern: Electronic properties of two-dimensional systems. Rev. Mod. Phys. **54**, 437 (1982).

4.2 G. Beadie, W.S. Rabinovich, D.S. Katzer, M. Goldenberg: Phys. Rev. **B 55**, 9731 (1997).
4.3 F.T. Vasko, P. Aceituno, A. Hernández-Cabrera: Phys. Rev. **B 66**, 125303 (2002).
4.4 R.J. Warburton, C. Gauer, A. Wixforth, J.P. Kotthaus, B. Brar, H. Kroemer: Phys. Rev. **B 53**, 7903 (1996).
4.5 B.F. Levine, R.J. Malik, J. Walker, K.K. Choi, C.G. Bethea, D.A. Kleiman, J.M. Vandenberg: Appl. Phys. Lett. **50**, 273 (1987).
4.6 H.C. Liu, M. Buchanan, Z.R. Wasilewski: Appl. Phys. Lett. **72**, 1682 (1998).
4.7 S.A. Tarasenko, E.L. Ivchenko, V.V. Bel'kov, S.D. Ganichev, D. Schowalter, P. Schneider, M. Sollinger, W. Prettl, V.M. Ustinov, A.E. Zhukov, L. E. Vorobjev: J. Superconductivity: Incorporating Novel Magnetism **16**, 419 (2003).
4.8 M. Helm: Semicond. Sci. Technol. **19**, 557 (1995).
4.9 H.H. Chen, Y.-H. Wang: IEEE J. Quant. Electron. **32**, 471 (1996).
4.10 L.E. Vorobjev, D.V. Donetskii, L.E. Golub: Pis'ma Zh. Eksp. Teor. Fiz. **63**, 928 (1996) [JETP Lett. **63**, 5138 (1996)].
4.11 E. Towe, L.E. Vorobjev, S.N. Danilov, Yu.V. Kochegarov, D.A. Firsov, D.V. Donetsky: Appl. Phys. Lett. **75**, 2930 (1999).
4.12 M. Agethe, E. Vass: Solid State Commun. **125**, 591 (2003).
4.13 B.C. Cavenett, E.J. Pakulis: Phys. Rev. **B 32**, 8449 (1985).
4.14 G. Belle, J.C. Maan, G. Wiegmann: Solid State Commun. **56**, 65 (1985).
4.15 T. Duffield, R. Bhat, M. Koza, F. DeRosa, D.M. Hwang, P. Grabbe, S.J. Allen, Jr.: Phys. Rev. Lett. **56**, 2724 (1986).
4.16 T. Duffield, R. Bhat, M. Koza, F. DeRosa, K.M. Rush, S.J. Allen, Jr.: Phys. Rev. Lett. **59**, 2693 (1987).
4.17 G. Brozak, E.A. de Andrada e Silva, L.J. Sham, F. DeRosa, P. Miceli, S.A. Schwarz, J.P. Harbison, L.T. Florez, S.J. Allen, Jr.: Phys. Rev. Lett. **64**, 471 (1990).
4.18 B. Lou, R. Sudharanan, S. Perkowitz: Phys. Rev. **B 38**, 2212 (1988).
4.19 O.K. Kim, W.G. Spitzer: J. Appl. Phys. **50**, 4362 (1979).
4.20 M. Göppert, M. Hetterich, A. Dinger, C. Klingshirn, K.P. O'Donnel: Phys. Rev. **B 57**, 13068 (1998).
4.21 M.F. MacMillan, R.P. Devaty, W.J. Choyke, M. Asif Khan, J. Kuznia: J. Appl. Phys. **80**, 2372 (1996).

References of Chapter 5

5.1 D. Gershoni, M. Katz, W. Wegscheider, L.N. Pfeiffer, R.A. Logan, K. Weat: Phys. Rev. **B 50**, 8930 (1994).
5.2 L.E. Golub, E.L. Ivchenko, A.A. Kiselev: J. Opt. Soc. Am. **B 13**, 1199 (1996).
5.3 L.E. Golub, S.V. Ivanov, E.L. Ivchenko, A.A. Kiselev, T.V. Shubina, A.A. Toropov, J.P. Bergman, G.R. Pozina, B. Monemar, M. Willander: phys. stat. sol. (b) **205**, 203 (1998).
5.4 S.D. Baranovskii, R. Eichmann, P. Thomas: Phys. Rev. **B 58**, 13081 (1998).
5.5 R. Zimmermann, E. Runge: phys. stat. sol. (a) **164**, 511 (1997).
5.6 S.A. Tarasenko, A.A. Kiselev, E.L. Ivchenko, A. Dinger, M. Baldauf, C. Klingshirn, H. Kalt, S.D. Baranovskii, R. Eichmann, P. Thomas: Semicond. Sci. Technol. **16**, 486 (2001).

5.7 J.-Y. Marzin, G. Bastard: Phys. Rev. Lett. **73**, 716 (1994).
5.8 K. Brunner, G. Abstreiter, G. Böhm, G. Tränkle, G. Weimann: Phys. Rev. Lett. **73**, 1138 (1994).
5.9 M. Grundmann, J. Christen, N.N. Ledentsov, J. Böhrer, D. Bimberg, S.S. Ruvimov, P. Werner, U. Richter, U. Gösele, J. Heydenreich, V.M. Ustinov, A.Yu. Egorov, A.E. Zhukov, P.S. Kop'ev, Zh.I. Alferov: Phys. Rev. Lett. **74**, 4043 (1995).
5.10 D. Gammon, S.W. Brown, T.A. Kennedy, E.S. Snow, B.V. Shanabrook, D.S. Katzer, D. Park: *Proc. 24th Int. Conf. Phys. Semicond.* (Jerusalem, Israel, 1998) (World Scientific, Singapore 1998) p. 164.
5.11 D. Gammon, E.S. Snow, B.V. Shanabrook, D.S. Katzer, D. Park: Phys. Rev. Lett. **76**, 3005 (1996).
5.12 Qiang Wu, R.D. Grober, D. Gammon, D.S. Katzer: Phys. Rev. Lett. **83**, 2652 (1999).
5.13 G. Finkelstein, H. Shtrinkman, I. Bar-Joseph: Phys. Rev. Lett. **74**, 976 (1995).
5.14 J.G. Tischler, A.S. Bracker, D. Gammon, D. Park: Phys. Rev. **B 66**, 81310 (2002).
5.15 B.M. Ashkinadze, E. Linder, E. Cohen, Arza Ron, L.N. Pfeiffer: Phys. Rev. **B 51**, 1938 (1995); B.M. Ashkinadze, E. Tsidilkovski, E. Linder, E. Cohen, Arza Ron, L.N. Pfeiffer: Phys. Rev. **B 54**, 8728 (1996).
5.16 L.E. Golub, E.L. Ivchenko, S.A. Tarasenko: Solid State Commun. **108**, 799 (1998).
5.17 C. Riva, F.M. Peeters, K. Vagra: Phys. Rev. **B 61**, 13873 (2000).
5.18 Y.-P. Feng, H.N. Spector: J. Phys. Chem. Solids **48**, 593 (1987); IEEE J. Quant. Electr. **24**, 1659 (1988).
5.19 T.S. Koh, Y.P. Feng, H.N. Spector: Solid State Commun. **104**, 407 (1997).
5.20 B.M. Ashkinadze, E. Cohen, Arza Ron, L.N. Pfeiffer: Phys. Rev. **B 47**, 10613 (1993).
5.21 L.E. Golub: Fiz. Tverd. Tela **39**, 1871 (1997) [Phys. Solid State **39**, 1673 (1997)].
5.22 G. Lampel: Phys. Rev. **20**, 491 (1968).
5.23 *Optical Orientation*, ed. F. Meier and B.P. Zacharchenya (Elsevier, Amsterdam, 1984).
5.24 G.E. Pikus, E.L. Ivchenko: In *Excitons* (North-Holland, Amsterdam, 1982) p. 205.
5.25 G.E. Pikus, A.N. Titkov: In *Optical Orientation*, ed. by F. Meier and B.P. Zakharchenya (North-Holland, Amsterdam, 1984) p. 73.
5.26 Pil Hun Song, K.W. Kim: Phys. Rev. **B 66**, 35207 (2002).
5.27 M.I. D'yakonov, V.I. Perel': Zh. Eksp. Teor. Fiz. **60**, 1954 (1971) [Sov. Phys. JETP **33**, 1053 (1971)]; Fiz. Tverd. Tela **13**, 3581 (1971) [Sov. Phys. Solid State, **13**, 3023 (1972)].
5.28 G.L. Bir, A.G. Aronov, G.E. Pikus: Zh. Eksp. Teor. Fiz. **69**, 1382 (1975) [Sov. Phys. Solid State **42**, 705 (1975)].
5.29 M.I. D'yakonov, V.Yu. Kachorovskii: Fiz. Tekhn. Poluprov. **20**, 178 (1986) [Sov. Phys. Semicond. **20**, 110 (1986)].
5.30 N.S. Averkiev, L.E. Golub: Phys. Rev. **B 60**, 15582 (1999).
5.31 E.L. Ivchenko: Fiz. Tverd. Tela **15**, 1566 (1973) [Sov. Phys. Solid State **15**, 1048 (1973)].

5.32 E.L. Ivchenko: P.S. Kop'ev, V.P. Kochereshko, I.N. Uraltsev, D.R. Yakovlev, Pis'ma Zh. Eksp. Teor. Fiz. **47**, 407 (1988) [JETP Lett. **47**, 486 (1988)].
5.33 M.M. Glazov, E.L. Ivchenko: Pis'ma Zh. Eksp. Teor. Fiz, **75**, 76 (2002) [JETP Lett. **75**, 403 (2002)]; J. Superconductivity: Incorporating Novel Magnetism **16**, 735 (2003).
5.34 M.M. Glazov, Fiz. Tverd. Tela **45**, 1108 (2003) [Phys. Solid State **45**, 1162 (2003)].
5.35 M.A. Brand, A. Malinowski, O.Z. Karimov, P.A. Mardsen, R.T. Harley, A.J. Shields, D. Sanvitto, D.A. Ritchie, M.Y. Simmons: Phys. Rev. Lett. **89**, 236601 (2002).
5.36 M.M. Glazov, E.L. Ivchenko: NATO Advanced Research Workshop St.-Petersburg, Russia, June 13-16, (2002); cond-mat/0301519.
5.37 M.M. Glazov, E.L. Ivchenko, M.A. Brand, O.Z. Karimov, R.T. Harley: Proc. 11th Internat. Symposium "Nanostructures: Physics and Technology", St.-Petersburg, Russia, Ioffe Institute, June 2003, p. 273.
5.38 N.S. Averkiev, L.E. Golub, M. Willander: J. Phys.: Condens. Matter **14**, 271 (2002).
5.39 A. Tackeuchi, T. Kuroda, S. Muto, Y. Nishikawa, O. Wada: Jpn. J. Appl. Phys. **38**, 4680 (1999).
5.40 M.Z. Maialle: Phys. Rev. **B 54**, 1967 (1996).
5.41 A.V. Khaetskii, Yu.V. Nazarov: Phys. Rev. **B 61**, 12639 (2000).
5.42 D. Gammon, Al.L. Efros, T.A. Kennedy, M. Rosen, D.S. Katzer, D. Park, S.W. Brown, V.L. Korenev, I.A. Merkulov: Phys. Rev. Lett. **86**, 5176 (2001).
5.43 A.V. Khaetskii, Yu.V. Nazarov: Phys. Rev. **B 64**, 125316 (2001).
5.44 I.A. Merkulov, Al.L. Efros, M. Rosen: Phys. Rev. **B 65**, 205309 (2002).
5.45 Y.B. Lyanda-Geller, I.L. Aleiner, B.L. Altshuler: Phys. Rev. Lett. **89**, 107602 (2002).
5.46 L.M. Wooda, T.L. Reinecker, Y.B. Lyanda-Geller: Phys. Rev. **B 66**, 161318 (2002).
5.47 T. Uenoyama, L.J. Sham: Phys. Rev. Lett. **64**, 3070 (1990).
5.48 R. Ferreira, G. Bastard: Phys. Rev. **B 43**, 9687 (1991).
5.49 L.M. Roth, B. Lax, S. Zwerdling: Phys. Rev. **114**, 90 (1959).
5.50 C. Hermann, C. Weisbush: In *Optical Orientation*, ed. by F. Meier and B.P. Zakharchenya (North-Holland, Amsterdam, 1984) p. 463.
5.51 E.L. Ivchenko, A.A. Kiselev: Fiz. Tehkn. Poluprovodn. **26**, 1471 (1992) [Sov. Phys. Semicond. **26**, 827 (1992)].
5.52 E.L. Ivchenko, A.A. Kiselev, M. Willander: Solid State Commun. **102**, 375 (1997).
5.53 A.A. Kiselev, E.L. Ivchenko, U. Rössler: Phys. Rev. **B 58**, 16353 (1998).
5.54 A.A. Kiselev, E.L. Ivchenko, A.A. Sirenko, T. Ruf, M. Cardona, D.R. Yakovlev, W. Ossau, A. Waag, G. Landwehr: J. Crystal Growth **184/185**, 831 (1998).
5.55 M.J. Snelling, G.P. Flinn, A.S. Plaut, R.T. Harley, A.C. Tropper, R. Eccleston, C.C. Phillips: Phys. Rev. **B 44**, 11345 (1991).
5.56 R.M. Hannak, M. Oestreich, A.P. Heberle W.W. Rühle, K. Köhler: Solid State Commun. **93**, 313 (1995).
5.57 L. Gravier, M. Potemski, M.D. Martin, E. Perez, L. Vina, K. Ploog, A. Fisher: *Proc. Int. Conf. Phys. Semicond.* (Berlin 1996), ed. by M. Scheffler and R. Zimmermann, (World Scientific, Singapore 1996) p. 2431.

5.58 E.L. Ivchenko, V.P. Kochereshko, I.N. Uraltsev, D.R. Yakovlev: In *High Magnetic Fields in Semiconductor Physics*, ed. by G. Landwehr, Springer Series in Solid-State Sci. (Springer, Berlin, Heidelberg 1992) Vol. 110, p. 533.
5.59 V.K. Kalevich, V.L. Korenev: Pis'ma Zh. Eksp. Teor. Fiz. **56**, 257 (1992) [JETP Lett. **56**, 257 (1992)].
5.60 V.K. Kalevich, B.P. Zakharchenya, O.M. Fedorova: Fiz. Tverd. Tela **37**, 287 (1995) [Phys. Solid State **37**, 154 (1995)].
5.61 P. Omling, B. Kowalski, B.K. Meyer, D.M. Hofmann, C. Wetzel, V. Härle, F. Scholz: Solid State Electron. **37**, 669 (1994).
5.62 B. Kowalski, P. Omling, B.K. Meyer, D.M. Hofmann, C. Wetzel, V. Härle, F. Scholz, P. Sobkowicz: Phys. Rev. **B 49**, 14786 (1994).
5.63 P. Le Jeune, D. Robart, X. Marie, T. Amand, M. Brousseau, J. Barrau, V. Kalevich, D. Rodichev: Semicond. Sci. Technol. **12**, 380 (1997).
5.64 A.A. Sirenko, T. Ruf, K. Eberl, M. Cardona, A.A. Kiselev, E.L. Ivchenko, K. Ploog: in: *High Magnetic Fields in Semiconductor Physics*, ed. by G. Landwehr and W. Ossau (World Scientific, Singapore 1996) p. 561.
5.65 A.A. Sirenko, T. Ruf, M. Cardona, D.R. Yakovlev, W. Ossau, A. Waag, G. Landwehr: Phys. Rev. **B 56**, 2114 (1997).
5.66 V.K. Kalevich, V.L. Korenev: Pis'ma Zh. Eksp. Teor. Fiz. **57**, 557 (1993) [JETP Lett. **57**, 571 (1993)].
5.67 S. Hallstein, M. Oestreich, W.W. Rühle, K. Köhler: *Proc. 12th Int. Conf. on High Magnetic Fields in the Physics of Semiconductors*, (Wuerzburg, 1996), ed. by G. Landwehr and W. Ossau (World Scientific, Singapore 1997) p. 593.
5.68 A.A. Kiselev, L.V. Moiseev: Fiz. Tverd. Tela **38**, 1574 (1996) [Phys. Solid State **38**, 866 (1996)].
5.69 X. Marie, T. Amand, P. Le Jeune, M. Paillard, P. Renucci, L.E. Golub, V.D. Dymnikov, E.L. Ivchenko: Phys. Rev. **B 60**, 5811 (1999).
5.70 B.P. Zakharchenya, P.S. Kop'ev, D.N. Mirlin, D.G. Polyakov, I.I. Reshina, V.F. Sapega, A.A. Sirenko: Solid State Commun. **69**, 203 (1989).
5.71 P.S. Kop'ev, D.N. Mirlin, D.G. Polyakov, I.I. Reshina, V.F. Sapega, A.A. Sirenko: Fiz. Tverd. Tela **24**, 1200 (1990) [Sov. Phys. - Semicond. **24**, 757 (1990).
5.72 D.N. Mirlin, V.I. Perel': Semicond. Sci. Technol. **7**, 1221 (1992).
5.73 J.A. Kash, M. Zachau, M.A. Tischler: Phys. Rev. Lett. **69**, 2260 (1992).
5.74 B.P. Zakharchenya, D.N. Mirlin, V.I. Perel', I.I. Reshina: Usp. Fiz. Nauk. **136**, 459 (1982) [Sov. Phys. Usp. **25**, 143 (1982)].
5.75 I.A. Merkulov, V.I. Perel, M.E. Portnoi: Zh. Eksp. Teor. Fiz. **99**, 1202 (1991) [Sov. Phys. JETP **72**, 669 (1991)].
5.76 V.F. Sapega, V.I. Perel', A.Yu. Dobin, D.N. Mirlin, I.A. Akimov: Phys. Rev. **B 56**, 6871 (1997).
5.77 G.L. Bir, G.E. Pikus: *Symmetry and strain-induced effects in semiconductors* (Nauka, Moscow, 1972; Wiley, New York, 1974).
5.78 M.M. Denisov, V.P. Makarov: phys. stat. sol. (b) **56**, 9 (1973).
5.79 S.V. Goupalov, E.L. Ivchenko, A.V. Kavokin: Zh. Eksp. Teor. Fiz. **113**, 703 (1998) [JETP **86**, 388 (1998)].
5.80 H. W. van Kesteren, E. C. Cosman, W. A. J. A. van der Poel, C. T. Foxon: Phys. Rev. **B 41**, 5283 (1990).
5.81 S. Permogorov, A. Naumov, C. Gourdon, P. Lavallard: Solid State Commun. **74**, 1057 (1990).

5.82 E.L. Ivchenko, V.P. Kochereshko, A.Yu. Naumov, I.N. Uraltsev, P. Lavallard: Superlatt. Microstruct. **10**, 497 (1991).
5.83 C. Gourdon, P. Lavallard: Phys. Rev. **B 46**, 4644 (1992).
5.84 P.G. Baranov, I.V. Mashkov, N.G. Romanov, P. Lavallard, R. Planel: Solid State Commun. **87**, 649 (1993).
5.85 R.I. Dzhioev, H.M. Gibbs, E.L. Ivchenko, G. Khitrova, V.L. Korenev, M.N. Tkachuk, B.P. Zakharchenya: Phys. Rev. **B 56**, 13405 (1997).
5.86 I.L. Aleiner, E.L. Ivchenko: Pis'ma Zh. Eksp. Teor. Fiz. **55**, 662 (1992) [JETP Lett. **55**, 692 (1992)].
5.87 E.L. Ivchenko, A.Yu. Kaminski, I.L. Aleiner: Zh. Eksp. Teor. Fiz. **104**, 3401 (1993) [JETP **77**, 609 (1993).
5.88 E.L. Ivchenko, A.Yu. Kaminski, U. Rössler: Phys. Rev. **B 54**, 5852 (1996).
5.89 M. Grundmann, O. Stier, D. Bimberg: Phys. Rev. **B 52**, 11969 (1995).
5.90 E.L. Ivchenko, A.Yu. Kaminskii: Fiz. Tverd. Tela **37**, 1418 (1995) [Sov. Phys. Solid State **37**, 768 (1995)].
5.91 C. Gourdon, I.V. Mashkov, P. Lavallard, R. Planel: Phys. Rev. **B 57**, 3955 (1998).
5.92 Al.L. Efros, M. Rosen, M. Kuno, M. Nirmal, D.J. Norris, M.G. Bawendi: Phys. Rev. **B 54** 4843 (1996).
5.93 M. Chamarro, C. Gourdon, P. Lavallard, O. Lublinskaya, A.I. Ekimov: Phys. Rev. **B 53** 1336 (1996).
5.94 U. Woggon, F. Gindele, O. Wind, C. Klingshirn: Phys. Rev. **B 54** 1506 (1996).
5.95 S.V. Goupalov, E.L. Ivchenko: J. Crystal Growth **184/185**, 393 (1998).
5.96 A. Franceschetti, L.W. Wang, H. Fu, A. Zunger: Phys. Rev. **B 58**, 13367 (1998).
5.97 S.V. Goupalov, E.L. Ivchenko: Fiz. Tverd. Tela **42**, 1976 (2000) [Phys. Solid State **42**, 2030 (2000)].
5.98 D.J. Norris, Al.L. Efros, M. Rosen, M.G. Bawendi, Phys. Rev. **B 53**, 16347 (1996).
5.99 M. Chamarro, M. Dib, C. Gourdon, P. Lavallard, O. Lublinskaya, A.I. Ekimov: Mater. Res. Soc. Symp. Proc. **454** 396 (1997).
5.100 S.V. Goupalov, P. Lavallard, G. Lamouche, D.S. Citrin: Fiz. Tverd. Tela **45**, 730 (2003) [Phys. Solid State **45**, 768 (2003)].
5.101 S.V. Goupalov, E.L. Ivchenko: Fiz. Tverd. Tela **43**, 1791 (2001) [Phys. Solid State **43**, 1867 (2001)].
5.102 M.Z. Maialle, E.A. de Andrada e Silva, L.J. Sham: Phys. Rev. **B 47**, 15776 (1993).
5.103 V.P. Kochereshko, E.L. Ivchenko, D.R. Yakovlev, F. Lavallard: Fiz. Tverd. Tela **40**, 2229 (1998) [Phys. Solid State **40**, 2024 (1998)].
5.104 R.I. Dzhioev, B.P. Zakharchenya, E.L. Ivchenko, V.L. Korenev, Yu.G. Kusrayev, N.N. Ledentsov, V.M. Ustinov, A.E. Zhukov, A.F. Tsatsul'nikov: Fiz. Tverd. Tela **40**, 858 (1998) [Phys. Solid State **40**, 790 (1998)].
5.105 M. Paillard, X. Marie, P. Renucci, T. Amand, A. Jbeli, J.M. Gérard: Phys. Rev. Lett. **86**, 1634 (2001).
5.106 S. Cortez, O. Krebs, S. Laurent, M. Senes, X. Marie, P. Voisin, R. Ferreira, G. Bastard, J.M. Gérard, T. Amand: Phys. Rev. Lett. **89**, 207401 (2002).
5.107 F. Fuchs, J. Schmitz, J.D. Ralston, P. Koidl, R. Heitz, A. Hoffmann: Superlatt. Microstruct. **16**, 35(1994).

5.108 F. Fuchs, J. Schmitz, N. Herres: *Proc. 23rd Int'l. Conf. Phys. Semicond.* (Berlin, 1996), ed. by M. Scheffler and R. Zimmermann (World Scientific, Singapore 1996) Vol. 3, p. 1803.
5.109 A.V. Platonov, V.P. Kochereshko, E.L. Ivchenko, G.V. Mikhailov, D.R. Yakovlev, M. Keim, W. Ossau, A. Waag, G. Landwehr: Phys. Rev. Lett. **83**, 3546 (1999).
5.110 D.R. Yakovlev, E.L. Ivchenko, V.P. Kochereshko, A.V. Platonov, S.V. Zaitsev, A.A. Maksimov, I.I. Tartakovskii, V.D. Kulakovskii, W. Ossau, M. Keim, A. Waag, G. Landwehr: Phys. Rev. **B 61**, 2421 (2000).
5.111 M. Schmidt, M. Grün, S. Petillon, E. Kurtz, C. Klingshirn: Appl. Phys. Lett. **77**, 85 (2000).
5.112 E.L. Ivchenko, M.O. Nestoklon: Zh. Eksp. Teor. Fiz. **121**, 747 (2002) [JETP **94**, 644 (2002)].
5.113 L.C. Lew Yan Voon, L.R. Ram-Mohan: Phys. Rev. **B 47**, 15500 (1993).
5.114 A.V. Platonov, D.R. Yakovlev, W. Ossau, V.P. Kochereshko, E.L. Ivchenko, L. Hansen, A. Waag, G. Landwehr, L.W. Molenkamp: phys. stat. sol (b) **229**, 689 (2002).
5.115 D.R. Yakovlev, A.V. Platonov, E.L. Ivchenko, V.P. Kochereshko, C. Sas, W. Ossau, L. Hansen, A. Waag, G. Landwehr, L.W. Molenkamp: Phys. Rev. Lett **88**, 257401 (2002).

References of Chapter 6

6.1 T.C. Damen, S.P.S. Porto, B. Tell: Phys. Rev. **142**, 570 (1966).
6.2 J. Hegarty, M.D. Sturge, C. Weisbuch, A.C. Gossard, W. Wiegmann: Phys. Rev. Lett. **49**, 930 (1982).
6.3 N. Garro, L. Pugh, R.T. Phillips, V. Drouot, M.Y. Simmons, B. Kardynal, D.A. Ritchie: Phys. Rev. **B 55**, 13752 (1997).
6.4 V.A. Kosobukin, A.V. Sel'kin: Physica **E 18**, 452 (2003).
6.5 A. Pinczuk, S. Schmitt-Rink, G. Danan, J.P. Vallarades, L.N. Pfeiffer, K.W. West: Phys. Rev. Lett. **63**, 1633 (1989).
6.6 G. Abstreiter, M. Cardona, A. Pinczuk: In *Light Scattering in Solids IV*, ed. by M. Cardona and M. Güntherodt, Topics Appl. Phys., Vol. 54 (Springer, Berlin, Heidelberg 1984) p. 5.
6.7 D. Gammon, B.V. Shanabrook, J.C. Ryan, D.S. Katzer: Phys. Rev. **B 41**, 12311 (1990).
6.8 J.C. Ryan: Phys. Rev. **B 43**, 12406 (1991).
6.9 S.L. Chuang, M.S.C. Luo, S. Schmitt-Rink, A. Pinczuk: Phys. Rev. **B 46**, 1897 (1992).
6.10 D. Gammon, B.V. Shanabrook, J.C. Ryan, D.S. Katzer, M.J. Yang: Phys. Rev. **B 68**, 1884 (1992).
6.11 M.S.C. Luo, S. L. Chuang, S. Schmitt-Rink, A. Pinczuk: Phys. Rev. **B 48**, 11086 (1993).
6.12 G. Brozak, B.V. Shanabrook, D. Gammon, D.S. Katzer,: Phys. Rev. **B 47**, 9981 (1993).
6.13 J. Wagner, J. Schmitz, F. Fuchs, J.D. Ralston, P. Koidl: Phys. Rev. **B 51**, 9786 (1995).
6.14 A.R. Goñi, A. Pinczuk, J.S. Weiner, J.M. Calleja, B.S. Dennis, L.N. Pfeiffer, K.W. West: Phys. Rev. Lett. **67**, 3298 (1991).

6.15 A.R. Goñi, A. Pinczuk, J.S. Weiner, B.S. Dennis, L.N. Pfeiffer, K.W. West: Phys. Rev. Lett. **70**, 1151 (1993).
6.16 A.Schmeller, A.R. Goñi, A. Pinczuk, J.S. Weiner, J.M. Calleja, B.S. Dennis, L.N. Pfeiffer, K.W. West: Phys. Rev. **B 49**, 14778 (1994).
6.17 D.J. Lockwood, P. Hawrylak, P.D. Wang, C.M. Sotomayor Torres, A. Pinczuk, B.S. Dennis: Phys. Rev. Lett. **77**, 354 (1996).
6.18 S. Das Sarma, J.J. Quinn: Phys. Rev. **B 25**, 7603 (1982).
6.19 S. Das Sarma, Q.P. Li: Phys. Rev. **B 32**, 1401 (1985).
6.20 A. Gold, A. Ghazali: Phys. Rev. **B 41**, 7626 (1990).
6.21 Q.P. Li, S. Das Sarma: Phys. Rev. **B 43**, 11768 (1991).
6.22 C. Colvard, T.A. Gant, M.V. Klein, R. Merlin, R. Fischer, H. Morkoc, A.C. Gossard: Phys. Rev. **B 31**, 2080 (1985).
6.23 J. Sapriel, J.C. Michel, J.C. Tolédano, R. Vacher, J. Kervarec, A. Regreny: Phys. Rev. **B 28**, 2007 (1983).
6.24 A. Bartels, T. Dekorsy, H. Kurz, K. Köhler: Physica **B 263-264**, 45 (1999).
6.25 C. Colvard, R. Merlin, M.V. Klein, A.C. Gossard, Phys. Rev. Lett. **45**, 298 (1980).
6.26 V.Yu. Davydov, A.A. Klochikhin, I.E. Kozin, V.V. Emtsev, I.N. Goncharuk, A.N. Smirnov, R.N. Kyutt, M.P. Scheglov, A.V. Sakharov, W.V. Lundin, E.E. Zavarin, A.S. Usikov: phys. stat. sol. (a) **188**, 863 (2001).
6.27 B. Jusserand, D. Paquet, F. Mollot, F. Alexandre, G. Le Roux: Phys. Rev. **B 35**, 2808 (1987).
6.28 J. Spitzer, Z.V. Popović, T. Ruf, M. Cardona, R. Nötzel, K. Ploog: Solid-State Electron. **37**, 753 (1994).
6.29 D.N. Mirlin, I.A. Merkulov, V.I. Perel', I.I. Reshina, A.A. Sirenko, R. Planel: Solid State Commun. **82**, 305 (1992).
6.30 V. Wagner, J. Geurtz, T. Gerhard, Th. Litz, H.-J. Lugauer, F. Fischer, A. Waag, G. Landwehr, Th. Walter, D. Gerthsen: Appl. Surface Sci. **123/124**, 580 (1998).
6.31 Ke-Qiu Chen, Xue-Hua Wang, Ben-Yuan Gu: Phys. Rev. **B 61**, 12075 (2000).
6.32 L. Saviot, B. Champagnon, E. Duval, A.I. Ekimov: J. Crystal Growth **184/185**, 370 (1998).
6.33 A.A. Sirenko, V.I. Belitsky, T. Ruf, M. Cardona, A.I. Ekimov, C. Trallero-Giner: Phys. Rev. **B 58**, 2077 (1998).
6.34 S.V. Goupalov, I.A. Merkulov: Fiz. Tverd. Tela **41**, 1473 (1999) [Phys. Solid State **41**, 1349 (1999)].
6.35 S. Rudin, T.L. Reinecke: Phys. Rev. **B 41**, 7713 (1990).
6.36 B.K. Ridley: Phys. Rev. **B 39**, 5282 (1989).
6.37 Kun Huang, B. Zhu: Phys. Rev. **B 38**, 13377 (1988).
6.38 A.K. Sood, J. Menéndez, M. Cardona, K. Ploog: Phys. Rev. Lett. **54**, 2111 (1985).
6.39 A.K. Arora, E.-K. Suh, A.K. Ramdas, F.A. Chambers, A.L. Moretti: Phys. Rev. **B 36**, 6142 (1987).
6.40 G. Fasol, M. Tanaka, H. Sakaki, Y. Horikoshi: Phys. Rev. **B 38**, 6056 (1988).
6.41 B. Jusserand, D. Paquet, F. Mollot: Phys. Rev. Lett. **63**, 2397 (1989).
6.42 D.J. Mowbray, M. Cardona, K. Ploog: Phys. Rev. **B 43**, 1598 (1991).
6.43 A.K. Sood, J. Menéndez, M. Cardona, K. Ploog: Phys. Rev. Lett. **54**, 2115 (1985).
6.44 M. Nakayama, M. Ishida, N. Sano: Phys. Rev. Lett. **38**, 6348 (1988).

6.45 R. Hessmer, A. Huber, T. Egeler, M. Haines, G. Tränkle, G. Weimann, G. Abstreiter: Phys. Rev. **B 46**, 4071 (1992).
6.46 G. Scamarcio, M. Haines, G. Abstreiter, E. Molinari, S. Baroni, A. Fischer, K. Ploog: Phys. Rev. **B 48**, 14356 (1993).
6.47 Z.V. Popović, M. Cardona, E. Richter, D. Strauch, L. Tapfer, K. Ploog: Phys. Rev. **B 40**, 1207, 3040 (1989); **41**, 5904 (1990).
6.48 V.F. Sapega, M. Cardona, K. Ploog, E.L. Ivchenko, D.N. Mirlin: Phys. Rev. **B 45**, 4320 (1992).
6.49 M.P. Halsall, S.V. Railson, D. Wolverson, J.J. Davies, B. Lunn, D.E. Ashenford: Phys. Rev. **B 50**, 11755 (1994).
6.50 A.A. Sirenko, T. Ruf, N.N. Ledentsov, A.Yu. Egorov, P.S. Kop'ev, V.M. Ustinov, A.E. Zhukov: Solid State Commun. **97**, 169 (1996).
6.51 A.A. Sirenko, T. Ruf, M. Cardona, D.R. Yakovlev, W. Ossau, A. Waag, G. Landwehr: Phys. Rev. **B 56**, 2114 (1997).
6.52 D.N. Mirlin, A.A. Sirenko: Fiz. Tverd. Tela **34**, 205 (1992) [Sov. Phys. Solid State **34**, 108 (1992)].
6.53 V.F. Sapega, T. Ruf, M. Cardona, K. Ploog, E.L. Ivchenko, D.N. Mirlin: Phys. Rev. **B 50**, 2510 (1994).
6.54 E.L. Ivchenko: Fiz. Tverd. Tela **34**, 476 (1992) [Sov. Phys. Solid State **34**, 254 (1992)].
6.55 B. Jusserand, D. Richards, H. Peirc, B. Etienne: Phys. Rev. Lett. **69**, 848 (1992).
6.56 D. Richards, B. Jusserand, G. Allan, C. Priester, B. Etienne: Solid-State Electron. **40**, 127 (1996).
6.57 L. Wissinger, U. Rössler, R. Winkler, B. Jusserand, D. Richards: Phys. Rev. **B 58**, 15375 (1998).
6.58 F. Cerdeira, E. Anastassakis, W. Kauschke, M. Cardona: Phys. Rev. Lett. **57**, 3209 (1986).
6.59 T. Ruf, R.T. Phillips, C. Trallero-Giner, M. Cardona: Phys. Rev. **B 41**, 3039 (1990).
6.60 S.I. Gubarev, T. Ruf, M. Cardona: Phys. Rev. **B 43**, 1551 (1991).
6.61 R.C. Miller, D.A. Kleinman, A.C. Gossard: Solid State Commun. **60**, 213 (1986).
6.62 D.A. Kleinman, R.C. Miller, A.C. Gossard: Phys. Rev. **B 35**, 664 (1987).
6.63 F. Calle, J.M. Calleja, F. Meseguer, C. Tejedor, C. López, K. Ploog: Phys. Rev. **B 44**, 1113 (1991).
6.64 L. Viña, J.M. Calleja, A. Cros, A. Canarero, T. Berendschot, J.A.A.J. Perenboom, K. Ploog: Phys. Rev. **B 53**, 3975 (1996).
6.65 F. Agulló-Rueda, E.E. Mendez, J.M. Hong: Phys. Rev. **B 38**, 12720 (1988).
6.66 D.R. Yakovlev, W. Ossau, A. Waag, G. Landwehr, E.L. Ivchenko: Phys. Rev. **B 52**, 5773 (1995).
6.67 A. Fainstein, B. Jusserand, Phys. Rev. **B 57**, 2402 (1998).
6.68 T. Kipp, L. Rolf, C. Schüller, D. Enler, Ch. Heyn, D. Heitmann: Phisica **E 13**, 408 (2002).

References of Chapter 7

7.1 J.J. Hopfield, J.M. Worlock, K. Park: Phys. Rev. Lett. **11**, 414 (1963).

7.2 H.N. Spector: Phys. Rev. **B 35**, 5876 (1987).
7.3 A. Shimizu: Phys. Rev. **B 40**, 1403 (1989).
7.4 A. Quattropani, A. Pasquarello: Phys. Rev. **B 42**, 9073 (1990).
7.5 A. Pasquarello, A. Quattropani: Phys. Rev. **B 41**, 12728 (1990).
7.6 R. Cingolani, M. Lepore, R. Tommasi, I.M. Catalano, H. Lage, D. Heitmann, K. Ploog, A. Shimizu, H. Sakaki, T. Ogawa: Phys. Rev. Lett. **69**, 1276 (1992).
7.7 F.L. Madarasz, F. Szmulowicz, F.K. Hopkins: Phys. Rev. **B 52**, 8964 (1995).
7.8 T. Takagahara: Phys. Rev. **B 39**, 10206 (1989).
7.9 A.V. Fedorov, A.V. Baranov, K. Inoue, Phys. Rev. **B 54**, 8627 (1996).
7.10 A. Shimizu, T. Ogawa, H. Sakaki: Phys. Rev. **B 45**, 11338 (1992).
7.11 K. Tai, A. Mysyrowicz, R.J. Fischer, R.E. Slusher, A.Y. Cho: Phys. Rev. Lett. **62**, 1784 (1989).
7.12 K. Fujii, A. Shimizu, J. Berquist, T. Sawada: Phys. Rev. Lett. **65**, 1808 (1990).
7.13 D. Fröhlich, R. Wille, W. Schlapp, G. Weimann: Phys. Rev. Lett. **61**, 1878 (1988).
7.14 L. Banyai, I. Galbraith, H. Haug, Phys. Rev. **B 38**, 3931 (1988).
7.15 T. Takagahara: Phys. Rev. **B 39**, 10206 (1989).
7.16 G.M. Gale, A. Mysyrowicz: Phys. Rev. Lett. **32**, 727 (1974).
7.17 Q. Fu, D. Lee, A. Myzyrovicz, A.V. Nurmikko, R.L. Gunshor, L.A. Kolodziejski: Phys. Rev. **B 37**, 8791 (1988).
7.18 K. Brunner, G. Abstreiter, G. Böhm, G. Tränkle, G. Weimann: Phys. Rev. Lett. **73**, 1138 (1994).
7.19 G. Chen, T.H. Stievater, E.T. Batteh, X. Li, D.G. Steel, D. Gammon, D.S. Katzer, D. Park, L.J. Sham: Phys. Rev. Lett. **88**, 117901 (2002).
7.20 K. Leo, M. Wegener, J. Shah, D.S. Chemla, E.O. Göbel, T.C. Damen, S. Schmitt-Rink, W. Schäfer: Phys. Rev. Lett. **65**, 1340 (1990).
7.21 M. Hübner, J. Kuhl, T. Stroucken, A. Knorr, S.W. Koch, R. Hey, K. Ploog: Phys. Rev. Lett. **76**, 4199 (1996).
7.22 J.M. Shackelette, S.T. Cundiff: Phys. Rev. **B 66**, 45309 (2002).
7.23 B.F. Feuerbacher, J. Kuhl, K. Ploog, Phys. Rev. **B 43**, 2439 (1991).
7.24 D.S. Kim, J. Shah, T.C. Damen, L.N. Pfeiffer, W. Schäfer: Phys. Rev. **B 50**, 5775 (1994).
7.25 H.P. Wagner, A. Schätz, W. Langbein, J.M. Hwam, A.L. Smirl: Phys. Rev. **B 60**, 4454 (1999).
7.26 H.G. Breunig, T. Voss, I. Rückmann, J. Gutovski: Phys. Rev. **B 66**, 193302 (2002).
7.27 V.M. Axt, S.R. Bolton, U. Neukirch, L.J. Sham, D.S. Chemla: Phys. Rev. **B 63**, 1559301 (2001).
7.28 T. Voss, H.G. Breunig, I. Rückman, J. Gutovski, V.M. Axt, T. Kuhn: Phys. Rev. **B 66**, 155301 (2002).
7.29 M. Seto, M. Helm, Z. Moussa, P. Boucaud, F.H. Julien, J.-M. Lourtioz, J.F. Nützel, G. Absreiter: Appl. Phys. Lett. **65**, 2969 (1994).
7.30 R. Atanasov, F. Bassani, V.M. Agranovich: Phys. Rev. **B 50**, 7809 (1994).
7.31 N. Bloembergen: *Nonlinear Optics*, (Benjamin, New York 1965).
7.32 E. Ghahramami, D.J. Moss, J.P. Sipe: Phys. Rev. **B 43**, 8990 (1991).
7.33 J. Khurgin: Phys. Rev. **B 38**, 4056 (1988).
7.34 Y. Jiang, J. Xu, W. Wang, X. Lu, X. Liu, G. Wang, F. Li: Phys. Rev. **B 63**, 125308 (2001).
7.35 M.M. Fejer, S.J.B. Yoo, R.L. Byer, A. Harwit, J.S. Harris, Jr.: Phys. Rev. Lett. **62**, 1041 (1989).

7.36 E. Rosencher, Ph. Bois: Phys. Rev. **B 44**, 11315 (1991).
7.37 M.J. Shaw, M. Jaros, Z. Xu, P.M. Fauchet, C.W. Rella, B.A. Richman, H.A. Schwettman, G.W. Wicks: Phys. Rev. **B 50**, 18395 (1994).
7.38 C. Lien, Y. Huang, T.-F. Lei: J. Appl. Phys. **75**, 2177 (1994).
7.39 A. Bitz, M. Marsi, E. Tuncel, S. Gürtler, J.L. Staehli, B.J. Vartanian, M.J. Shaw, A.F.G. van der Meer: Phys. Rev. **B 56**, 10428 (1997).
7.40 H.C. Chui, E.L. Martinet, G.L. Woods, M.M. Fejer, J.S. Harris, Jr., C.A. Rella, B.I. Richman, H.A. Schwettman: Appl. Phys. Lett. **64**, 3365 (1994).
7.41 E.L. Martinet, G.L. Woods, H.C. Chui, J.S. Harris, Jr., M.M. Fejer, C.A. Rella, B.I. Richman: Proc. SPIE **2139**, 331 (1994).
7.42 X. Xiao, C. Zhang, A.B. Fedorov, Z. Chen, M.M. Loy: J. Vac. Sci. Technol. B **15**, 1112 (1997).
7.43 D.J. Bottomley, J.-M. Baribeau, H.M. van Driel: Phys. Rev. **B 50**, 8564 (1994).
7.44 X. Zhang, Z. Chen, L. Xuan, S. Pan, G. Yang: Phys. Rev. **B 56**, 15842 (1997).
7.45 T. Brunhes, P. Boucaud, S. Sauvage, A. Lemaître, J.-M. Gérard, F. Glotin, R. Prazeres, J.-M. Ortega: Phys. Rev. **B 61**, 5562 (2000).
7.46 S. Sauvage, P. Boucaud, T. Brunhes, F. Glotin, R. Prazeres, J.-M. Ortega, J.-M. Gérard: Phys. Rev. **B 63**, 113312 (2001).
7.47 N. Owschimikow, C. Gmachl, A. Belyanin, V. Kocharovsky, D.L. Sivco, R. Colombelli, F. Capasso, A.Y. Cho: Phys. Rev. Lett. **90**, 43902 (2003).
7.48 C. Weisbuch, M. Nishioka, A. Ishikava, Y. Akarawa: Phys. Rev. Lett. **69**, 3314 (1992).
7.49 H.A. McLeod: *Thin-Film Optical Fibers*, 2nd edn. (Hilger, Bristol, UK, 1986).
7.50 L.C. Andreani, V. Savona, P. Schwendimann, A. Quattropani: Superlatt. Microstruct. **15**, 453 (1994).
7.51 V. Savona, L.C. Andreani, P. Schwendimann, A. Quattropani: Solid State Commun. **93**, 733 (1995).
7.52 G. Khitrova, H.M. Gibbs, F. Jahnke, M. Kira, S.W. Koch: Rev. Mod. Phys. **71**, 1591 (1999).
7.53 E.L. Ivchenko, M.I. Kaliteevskii, A.V. Kavokin, A.I. Nesvizhskii: J. Opt. Soc. Am. B **13**, 1061 (1996).
7.54 E.L. Ivchenko, A.V. Kavokin: Pis'ma Zh. Eksp. Teor. Fiz. **62**, 694 (1995) [JETP Lett. **62**, 710 (1995)].
7.55 A.V. Kavokin, E.L. Ivchenko, M.R. Vladimirova, M.I. Kaliteevskii, S.V. Goupalov: Superlatt. Microstruct. **23**, 389 (1998).
7.56 A.V. Kavokin, M.I. Kaliteevskii, M.R. Vladimirova: Phys. Rev. **B 54**, 1490 (1996).
7.57 C. Konstantin, E. Martinet, A. Rudra, E. Kapon: Phys. Rev. **B 59**, 7809 (1999).
7.58 M.V. Ustinov, A.E. Zhukov, N.A. Maleev, A.R. Kovsh, S.S. Mikhrin, B.V. Volovik, Yu.G. Musikhin, Yu.M. Shernyakov, M.V. Maximov, A.F. Tsatsul'nikov, N.N. Ledentsov, Zh.I. Alferov, J.A. Lott, D. Bimberg: J. Cryst. Growth **227/228**, 1155 (2001).
7.59 T. Schwarzl, W. Heiss, G. Springholz, H. Krenn, T. Fromherz, A. Raab, I. Vavra: Phys. Rev. **B 65**, 245321 (2002).
7.60 J.M. Gérard, D. Barrier, J.Y. Marzin, R. Kuszelewicz, L. Manin, E. Costard, V. Thierry-Mieg, T. Rivera: Appl. Phys. Lett. **69**, 449 (1996).
7.61 J.P. Reithmaier, M. Röhner, H. Zull, F. Schäfer, A. Forchel, P.A. Knipp, T.L. Reinecke: Phys. Rev. Lett. **78**, 378 (1997).

7.62 D. Ochoa, R. Houdré, M. Ilegems, H. Benisty, T.F. Krauss, C.J.M. Smith: Phys. Rev. **B 61**, 4806 (2000).
7.63 M.A. Kaliteevski, S. Brand, R.A. Abram, V.V. Nikolaev, M.V. Maximov, N.N. Ledentsov, C.M. Sotomayor Torres, A.V. Kavokin: Phys. Rev. **B 61**, 13791 (2000).
7.64 B. Ohnesorge, M. Bayer, A. Forchel, J.P. Reithmaier, N.A. Gippius, S.G. Tikhodeev: Phys. Rev. **B 56**, 4367 (1997).
7.65 J.M. Gérard, B. Sermage, B. Gayral, B. Legrand, E. Costard, V. Thierry-Mieg: Phys. Rev. Lett. **81**, 1110 (1998).
7.66 A.I. Tartakovskii, V.D. Kulakovskii, A. Forchel, J.P. Reithmaier: Phys. Rev. **B 57**, 6807 (1998).
7.67 M. Bayer, T.L. Reinecke, F. Weidner, A. Larionov, A. McDonald, A. Forchel: Phys. Rev. Lett. **86**, 3168 (2001).
7.68 G.S. Solomon, M. Pelton, Y. Yamomoto: Phys. Rev. Lett. **86**, 3903 (2001).
7.69 M.A. Kaliteevski, S. Brand, R.A. Abram, V.V. Nikolaev, M.V. Maximov, C.M. Sotomayor Torres, A.V. Kavokin: Phys. Rev. **B 64**, 115305 (2001).
7.70 C. Konstantin, E. Martinet, D.Y. Oberli, E. Kapon, B. Gayral, J.M. Gérard: Phys. Rev. **B 66**, 165306 (2002).
7.71 F. Jahnke, M. Kira, S.W. Koch, G. Khitrova, E.K. Lindmark, T.R. Nelson, Jr., D.V. Wick, J.D. Berger, O. Lyngnes, H.M. Gibbs, K. Tai: Phys. Rev. Lett. **77**, 5257 (1996).
7.72 R. Houdré, J.L. Gibernon, P. Pellandini, R.P. Stanley, U. Oesterle, C. Weisbuch, J. O'Gorman, B. Roycroft, M. Ilegems: Phys. Rev. **B 52**, 7810 (1995).
7.73 M. Saba, F. Quochi, C. Ciuti, U. Oesterle, J.L. Staehli, B. Deveaud, G. Bongiovanni, A. Mura: Phys. Rev. Lett. **85**, 385 (2000).
7.74 G. Bongiovanni, A. Mura, F. Quochi, S. Gürtler, J.L. Staehli, F. Tassone, R.P. Stanley, U. Oesterle, R. Houdré: Phys. Rev. **B 55**, 7084 (1997).
7.75 M. Shirane, C. Ramkumar, Yu.P. Svirko, H. Suzuura, S. Inouye, R. Shimano, T. Someya, H. Sakaki, M. Kuwata-Gonokami: Phys. Rev. **B 58**, 7978 (1998).
7.76 P.V. Kelkar, V.G. Kozlov, A.V. Nurmikko, C.-C. Chu, J. Han, R.L. Gunshor: Phys. Rev. **B 56**, 7564 (1997).
7.77 Y. Fu, M. Willander, E.L. Ivchenko, A.A. Kiselev: Pis'ma Zh. Eksp. Teor. Fiz. **64**, 749 (1996); Phys. Rev. **B 55**, 9872 (1997).
7.78 P.G. Savvidis, J.J. Baumberg, R.M. Stevenson, M.S. Skolnick, D.M. Whittaker, J.S. Roberts: Phys. Rev. Lett. **84**, 1547 (2000).
7.79 R.M. Stevenson, V.N. Astratov, M.S. Skolnick, D.M. Whittaker, M. Emam-Ismail, A.I. Tartakovskii, P.G. Savvidis, J.J. Baumberg, J.S. Roberts: Phys. Rev. Lett. **85**, 3680 (2000).
7.80 J.J. Baumberg, P.G. Savvidis, R.M. Stevenson, A.I. Tartakovskii, M.S. Skolnick, D.M. Whittaker, J.S. Roberts: Phys. Rev. **B 62**, 16247 (2000).
7.81 C. Ciuti, P. Schwendimann, B. Deveaud, A. Quattropani: Phys. Rev. **B 62**, 4825 (2000).
7.82 G. Dasbach, M. Schwab, M. Bayer, D.N. Krizhanovskii, A. Forchel: Phys. Rev. **B 66**, 201201 (2002).
7.83 P.G. Lagoudakis, P.G. Savvidis, J.J. Baumberg, D.M. Whittaker, P.R. Eastham, M.S. Skolnick, J.S. Roberts: Phys. Rev. **B 65**, 161310 (2002).
7.84 A. Kavokin, P.G. Lagoudakis, G. Malpuech, J.J. Baumberg: Phys. Rev. **B 67**, 195321 (2003).

References of Chapter 8

8.1 E.L. Ivchenko, G.E. Pikus: Pis'ma Zh. Eksp. Teor. Fiz. **27**, 640 (1978) [JETP Lett. **27**, 604 (1978)].
8.2 V.I. Belinicher: Phys. Lett. A **66**, 213 (1978).
8.3 V.I. Belinicher, B.I. Sturman: Usp. Fiz. Nauk **130**, 415 (1980) [Sov. Phys. Usp. **23**, 199 (1980)].
8.4 B.I. Sturman, V.M. Fridkin: *The Photovoltaic and Photorefractive Effects in Non-Centrosymmetric Materials* (Gordon and Breach, New York, 1992).
8.5 V.M. Asnin, A.A. Bakun, A.M. Danishevskii, E.L. Ivchenko, G.E. Pikus, A.A. Rogachev: Pis'ma Zh. Eksp. Teor. Fiz. **28**, 80 (1978); Solid State Commun. **30**, 565 (1979).
8.6 N.S. Averkiev, V.M. Asnin, A.A. Bakun, A.M. Danishevskii, E.L. Ivchenko, G.E. Pikus, A.A. Rogachev: Fiz. Tekh. Poluprovodn. **18**, 639 (1984); *ibid* **18**, 648 (1984).
8.7 S.D. Ganichev, H. Ketterl, W. Prettl, E.L. Ivchenko, L.E. Vorobjev: Appl. Phys. Lett. **77**, 3146 (2000).
8.8 S.D. Ganichev, E.L. Ivchenko, S.N. Danilov, J. Eroms, W. Wegscheider, D. Weiss, W. Prettl: Phys. Rev. Lett. **86**, 4358 (2001).
8.9 S.D. Ganichev, U. Rössler, W. Prettl, E.L. Ivchenko, V.V. Bel'kov, R. Neumann, K. Brunner, G. Abstreiter: Phys. Rev. **B 66**, 75328 (2002).
8.10 S.D. Ganichev, W. Prettl: J. Phys.: Condens. Matter **15**, 935 (2003).
8.11 L.E. Golub: Physica **E 17**, 342 (2003); Phys. Rev. **B 67**, 235320 (2003).
8.12 S.D. Ganichev, V.V. Bel'kov, Petra Schneider, E.L. Ivchenko, S.A. Tarasenko, W. Wegscheider, D. Weiss, D. Schuh, E.V. Beregulin, W. Prettl: Phys. Rev. **B 68**, 35319 (2003).
8.13 E. L. Ivchenko, Yu.B. Lyanda-Geller, G.E. Pikus: JETP Lett. **50**, 175 (1989); Zh. Eksp. Teor. Fiz. **98**, 989 (1990) [Sov. Phys. JETP **71**, 550 (1990)].
8.14 S.D. Ganichev, E.L. Ivchenko, V.V. Bel'kov, S.A. Tarasenko, M. Sollinger, D. Weiss, W. Wegscheider, W. Prettl: Nature **417**, 153 (2002).
8.15 N.S. Averkiev, M.I. D'yakonov: Sov. Phys. Semicond. **17**, 395 (1983).
8.16 H.E.M. Barlow: Proc. IRE **46**, 1411 (1958).
8.17 A.M. Danishevskii, A.A. Kastal'skii, S.M. Ryvkin, I.D. Yaroshetskii: Zh. Eksp. Teor. Fiz. **58**, 544 (1970) [Sov. Phys. JETP **31**, 292 (1970)].
8.18 A.F. Gibson, M.F. Kimmit, A.C. Walker: Appl. Phys. Lett. **17**, 75 (1970).
8.19 F.T. Vasko: Fiz. Tekh. Poluprovodn. **19**, 1319 (1985) [Sov. Phys. Semicond. **19**, 808 (1985)].
8.20 S. Luryi: Phys. Rev. Lett. **58**, 2263 (1987).
8.21 A.A. Grinberg, S. Luryi: Phys. Rev. **B 38**, 87 (1988).
8.22 A.D. Wieck, H. Sigg, K. Ploog: Phys. Rev. Lett. **64**, 463 (1990).
8.23 S. Graf, H. Sigg, K. Köhler, W. Bächtold: Phys. Rev. **B 62**, 10301 (2000).
8.24 A.M. Glass, D. von der Linde, T.J. Negran: Appl. Phys. Lett. **25**, 233 (1974).
8.25 A.M. Glass, D. von der Linde, D.H. Auston, T.J. Negran: J. Electr. Mater. **4**, 915 (1975).
8.26 K.H. Herrmann, R. Vogel: Proc. XI Int. Conf. Phys. Semicond, Warsaw, Poland, 1972 (Elsevier, Amsterdam, 1972) p. 870.
8.27 C.R. Hammond, J.R. Jenkins, C.R. Stanley: Optoelectronics **4**, 189 (1972).
8.28 A.V. Andrianov, E.L. Ivchenko, G.E. Pikus, R.Ya. Rasulov, I.D. Yaroshetskii: Zh. Eksp. Teor. Fiz. **81**, 2080 (1981) [Sov. Phys. JETP **54**, 1105 (1981)].

8.29 N. Kristoffel, A. Gulbis: Izv. A.N. Est. SSR **28**, 268 (1979).
8.30 R. von Baltz, W. Kraut: Phys. Lett. A **79**, 364 (1980).
8.31 V.I. Belinicher, E.L. Ivchenko, B.I. Sturman: Zh. Eksp. Teor. Fiz. **83**, 649 (1982) [Sov. Phys. JETP **56**, 359 (1982)].
8.32 E.L. Ivchenko, Yu.B. Lyanda-Geller, G.E. Pikus: Fiz. Tekh. Poluprovodn. **18**, 93 (1984) [Sov. Phys. Semicond. **18**, 55 (1984)].
8.33 F. Goos, H. Hänchen: Ann. Phys. Lpz. (6) **1**, 333 (1947); F. Goos, H. Lindberg-Hänchen: Ann. Phys. Lpz. (6) **5**, 251 (1949).
8.34 H.K.V. Lotsch: J. Opt. Soc. Am. **58**, 551 (1968).
8.35 H.K.V. Lotsch: Optik **32**, 116, 189, 299 and 553 (1970/71) .
8.36 F. Capasso, S. Luryi, W.T. Tzang, C.G. Bethea, B.F. Levine: Phys. Rev. Lett. **51**, 2318 (1983).
8.37 F.G. Pikus: Fiz. Tekh. Poluprovodn. **22**, 940 (1988) [Sov. Phys. Semicond. **22**, 594 (1988)].
8.38 C. Schönbein, H. Schneider, G. Bihlmann, K. Schwarz, P. Koidl: Appl. Phys. Lett. **68**, 973 (1995).
8.39 H. Schneider, S. Ehret, C. Schönbein, K. Schwarz, G. Bihlmann, J. Fleissner, G. Rränkle: Superlatt. Microstruct. **23**, 1289 (1998).
8.40 S.D. Ganichev, S.N. Danilov, V.V. Bel'kov, E.L. Ivchenko, M. Bichler, W. Wegscheider, D. Weiss, W. Prettl: Phys. Rev. Lett. **88**, 057401 (2002).
8.41 Petra Schneider, S.D. Ganichev, J. Kainz, U. Rössler, W. Wegscheider, D. Weiss, W. Prettl, V.V. Bel'kov, L.E. Golub, D. Schuh: phys. stat. sol. (b) **238**, 533 (2003).
8.42 E.L. Ivchenko, B. Spivak: Phys. Rev. **B 66**, 155404 (2002); Physica **E 17**, 376 (2003).
8.43 R.R. Schlitler, J.W. Seo, J.K. Gimzewski, C. Dunkan, M.S.M. Saifullmah, M.E. Welland: Science **292**, 1136 (2001).
8.44 P. Král, E.J. Mele, D. Tománek: Phys. Rev. Lett. **85**, 1512 (2000).
8.45 A.P. Dmitriev, S.A. Emel'yanov, S.V. Ivanov, P.S. Kop'ev, Ya.V. Terent'ev, I.D. Yaroshetskii: Pis'ma Zh. Eksp. Teor. Fiz. **54**, 279 (1991) [JETP Lett. **54**, (1991)].
8.46 Yu.A. Aleshchenko, I.D. Voronova, S.P. Grishechkina, V.V. Kapaev, Yu.V. Kopaev, I.V. Kucherenko, V.I. Kadushkin, S.I. Fomichev: Pis'ma Zh. Eksp. Teor. Fiz. **58**, 377 (1993) [JETP Lett. **58**, (1993)].
8.47 E.L. Ivchenko, G.E. Pikus: Izv. Akad. Nauk SSSR (ser. fizich.) **12**, 2369 (1983) [Bull. Acad. Sci. of the USSR, Phys. Ser., **47**, 81 (1983)].
8.48 O.V. Kibis: Phys. Solid State **43**, 2336 (2001).
8.49 G.L.J.A. Rikken, E. Raupach, V. Krstič, S. Roth: Mol. Phys. **100**, 1155 (2002).
8.50 S. Tasaki, K. Maekawa, T. Yamabe: Phys. Rev. **B 57**, 9301 (1998).
8.51 G.L.J.A. Rikken, E. Raupach: Nature **390**, 493 (1997).
8.52 G.L.J.A. Rikken, E. Raupach: Phys. Rev. **E 58**, 5081 (1998).
8.53 E.F. Gross, B.P. Zakharchenya, O.V. Konstantinov: Fiz. Tverd. Tela **3**, 305 (1961).
8.54 L.E. Vorobjev, E.L. Ivchenko, G.E. Pikus, I.I. Farbshtein, V.A. Shalygin, A.V. Shturbin: Pis'ma Zh. Eksp. Teor. Fiz. **29**, 485 (1979) [JETP Lett. **29**, 441 (1979)].

Index